Frank Czerwinski

Magnesium Injection Molding

Springer

Magnesium Injection Molding

Frank Czerwinski

Magnesium Injection Molding

Springer

Dr. Frank Czerwinski
Development Engineering
Husky Injection Molding Systems Ltd.
560 Queen St. S.
Bolton, Ontario
Canada L7E 5S5
FCzerwinski@husky.ca
FCzerwinski@sympatico.ca

ISBN-13: 978-0-387-72399-0 e-ISBN-13: 978-0-387-72528-4

Library of Congress Control Number: 2007928398

Printed on acid-free paper.

9 8 7 6 5 4 3 2 1

springer.com

To my Wife Celina and Son Marcin

Preface

The continuous quest for weight reduction, especially in ground and air transportation, has catalyzed the development of light metals and alloys. In this search, particular attention is being paid to magnesium, used at present in a diversity of applications, each one exploring a specific range of unique properties. As a result, the magnesium consumption by many important market sectors is growing at an impressive rate exceeding 10% per year.

In parallel with the alloy development the search continues for new techniques of converting magnesium into useful products in a safe and effective manner. Magnesium injection molding, commercialized in recent years, represents a modern technology that is clean and safe for workers as well as friendly for an environment. Extensive research, conducted at both the industrial and university levels, indicates that the technique exceeded its initial expectations. While combining key features of a number of processing techniques, magnesium injection molding is emerging as a universal technology, capable of implementing many conventional and novel processing routes. The routes are based on both the semisolid slurry and fully molten alloy with tightly controlled temperature. Despite well-advanced practice, the critical breakthrough is still hindered by slow progress in understanding key mechanisms, controlling the process at stages of slurry preparation and component forming.

The objective of this book, being the first one on magnesium injection molding, is to take the mystery out of this technique, to separate myths from facts and cover both the scientific background and the technological aspects as they are understood at present. For subjects where no literature data exist yet, the pioneering research was conducted to provide the scientifically credible explanations. The book contains fourteen chapters. Chaps. 1, 2 and 3 are dedicated to fundamentals of magnesium alloys, semisolid processing and injection molding machinery. Chap. 4 describes the corrosive and high temperature effects of magnesium on a variety of alloys. Chap. 5 provides the theory and practice of the injection molding process with broad comparison to plastic molding and metal die casting. Chaps. 6, 7 and 8 cover characteristics of the magnesium feedstock, its oxidation and melting behavior. The alloy transformations during molding, leading to generation of thixotropic slurries and unique microstructures after solidification, are presented in Chap. 9. Chap. 10 analyzes a correlation between the microstructure and properties of

molded alloys. The recently developed novel processing concepts: semisolid extrusion molding, near-liquidus molding, as well as the alloy and composite generation in a semisolid state, are described in chaps. 11, 12 and 13. Finally, Chap. 14 discusses the challenging aspects of processing the high temperature alloys of magnesium. A bibliography of related references will be found at the end of each chapter. The purpose is not only to give credit to original sources but also to provide a link to further information on details or controversies as well as to point out documents that are worthy of reading.

The book is intended for scientists and engineers from academia and industry who are involved in all fields of materials development, manufacturing and engineering. It will be of particular value for those involved in production, processing and application of magnesium, researching and practically implementing magnesium injection molding, die casting and other net-shape forming techniques. Moreover, the book will be valuable for those studying various aspects of semisolid processing of alloys and composites. Although some sections require advanced metallurgical knowledge, the fundamentals included will also allow beginners to understand the essence and gradually enter this fascinating interdisciplinary field.

Bolton, Ontario, 2007 Frank Czerwinski

Biography

Dr. Frank Czerwinski holds a Ph.D. degree in metallurgical engineering from McGill University, Montreal, Quebec, Canada and Ph.D. (Hons) and M.Sci. (Hons) degrees in materials science from the University of Mining and Metallurgy, Cracow, Poland. He has also completed post-doctoral studies at McMaster University, Hamilton, Ontario and at McGill University, Montreal, Quebec.

During his professional career, Dr. Czerwinski was a University Professor of materials and metallurgical engineering and the faculty member. He was also Manager and Principal Scientist of numerous research projects sponsored by universities, research institutions and industry. After years of university teaching and research he joined Husky Injection Molding Systems Ltd., Bolton, Ontario, Canada where he oversees the metallurgical aspects of development of injection molding machinery for plastics and metals.

Dr. Czerwinski is the author of a monograph in surface engineering as well as the author and co-author of several patents and over 140 research papers in peer-review scientific journals and conference proceedings. They cover areas of processing and heat treatment of steel, metallurgy of welding, electrodeposition, phase transformations in metals and alloys, high temperature corrosion, metallic and ceramic thin films and coatings, nanomaterials, grain boundary engineering, crystallographic texture, semisolid processing of alloys and analytical techniques of materials investigation.

Dr. Czerwinski is affiliated with Professional Engineers of Ontario, ASM International and The Minerals, Metals and Materials Society.

Contents

Preface . . . . . **vii**

1 Magnesium and Its Alloys **1**
1.1 Introduction 1
1.2 Market Development 1
1.2.1 Raw Metal Production 1
1.2.2 Raw Metal Consumption 4
1.3 Production Techniques of Pure Metal 9
1.3.1 Thermal Processes 10
1.3.2 Electrolytic Methods 10
1.3.3 Experimental Scale Processes 12
1.3.4 Recycling as a Source of the Secondary Metal 15
1.4 Fundamentals of Alloying 18
1.4.1 Role of Alloying Additions 18
1.4.2 Impurities 23
1.4.3 Strengthening Mechanisms 24
1.5 Alloys 29
1.5.1 Designations 29
1.5.2 Casting Alloys 29
1.5.3 Wrought Alloys 35
1.5.4 Alloys Manufactured by Non-Conventional Methods 38
1.6 Selected Properties of Alloys 40
1.6.1 Deformation Mechanisms 40
1.6.2 Superplastic Deformation 45
1.6.3 Mechanical Properties 46
1.6.4 Damping Capacity 49
1.6.5 EMI/RFI Shielding 49
1.6.6 Heat Dissipation 51
1.7 Processing Techniques 52
1.7.1 Casting 53
1.7.2 Forging 58
1.7.3 Rolling 59

1.7.4 Extrusion 60
1.8 Heat Treatment 61
1.8.1 Annealing. 62
1.8.2 Stress Relieving 62
1.8.3 Solution Treatment and Aging. 62
1.9 Surface Protection 65
1.9.1 Corrosion Nature 65
1.9.2 Metallurgical Factors Affecting Corrosion 67
1.9.3 Corrosion Prevention by Surface Treatments 68
1.10 Application Markets 73
1.10.1 Automotive 73
1.10.2 Aerospace 75
1.10.3 Consumer Electronics (3C) 75
1.10.4 General Purpose Market 76
1.11 Summary 76
References 76

2 Semisolid Processing — Origin of Magnesium Molding 81
2.1 Introduction 81
2.2 Origin of the Concept 81
2.2.1 Thixotropy 81
2.2.2 Semisolid Metal Processing. 82
2.3 Rheological Behavior of Semisolid Slurries 83
2.3.1 Newtonian and Non-Newtonian Fluids 83
2.3.2 Thixotropy and Pseudoplasticity 85
2.3.3 Experimental Relationships for Metallic Slurries 86
2.3.4 Models Describing Thixotropic Behavior 87
2.3.5 Flow Characteristics 91
2.4 Viscosity Measurements of Metallic Slurries 96
2.4.1 Rotational Instruments. 96
2.4.2 Compression Viscometer 99
2.4.3 Drop Forge Viscometer 99
2.4.4 Back Extrusion Viscometer 101
2.5 Rheological Measurements for Semisolid Magnesium Alloys 103
2.5.1 Isothermal Holding Measurements 103
2.5.2 Continuous Cooling Measurements. 104
2.5.3 Influence of Rest Time on Viscosity 106
2.6 Techniques of Generating Globular Structures 107
2.6.1 Melt Stirring/Agitation 107
2.6.2 Chemical Grain Refinement 110
2.6.3 Swirl Enthalpy Equilibration 110
2.6.4 Continuous Rheo-Conversion Process (CRP) 111
2.6.5 Liquidus/Sub-Liquidus Casting/Pouring 112
2.6.6 Rapid Slug Cooling 112

2.6.7 Controlled Slow Cooling . . . 113
2.6.8 Spray Forming . . . 113
2.6.9 Liquid Phase Sintering (LPS) . . . 115
2.6.10 Stress Induced Melt Activation (SIMA) . . . 115
2.7 Benefits of Semisolid Processing . . . 115
2.7.1 Structural Implications of Reduced Temperature . . . 116
2.7.2 Component's Integrity and Microstructure . . . 118
2.7.3 Present Limitations . . . 119
2.8 Suitability Criteria of Alloys for Semisolid Processing . . . 119
2.8.1 Solidification Range . . . 120
2.8.2 Temperature Sensitivity of Solid Fraction . . . 120
2.8.3 Thermodynamic Characteristics of Alloys for Semisolid Processing . . . 121
2.8.4 Morphological and Rheological Characteristics of the Slurry . . . 122
2.8.5 Applicability of Semisolid Processing for Magnesium Alloys . . . 122
2.9 Industrial Implementations of Major Semisolid Concepts . . . 124
2.9.1 Rheo- and Thixo- Processing Routes . . . 124
2.9.2 Thixocasting . . . 126
2.9.3 New Rheocasting (NRC) . . . 126
2.9.4 Semisolid Rheocasting (SSR) . . . 127
2.9.5 Sub-Liquidus Casting (SLC) . . . 128
2.9.6 Other Semisolid Techniques . . . 129
2.10 Origin and Progress of Magnesium Molding . . . 130
2.10.1 Technology Origin . . . 130
2.10.2 Commercialization Progress . . . 134
2.11 Present Applications and Future Opportunities for Magnesium Molding . . . 135
2.11.1 Consumer Electronics . . . 135
2.11.2 Automotive . . . 142
2.11.3 General Purpose Equipment . . . 144
2.12 Summary . . . 144
References . . . 145

3 Basic and Auxiliary Hardware . . . 149
3.1 Introduction . . . 149
3.2 Machine . . . 149
3.2.1 Clamp . . . 149
3.2.2 Injection Unit . . . 154
3.2.3 Machine Barrel Assembly . . . 155
3.2.4 Heating Systems for Barrel Assembly Components . . . 158
3.2.5 Injection Screw Assembly . . . 164
3.2.6 Feedstock Loading Devices . . . 166

3.2.7 Feedstock Drying and Preheating Devices 168
3.2.8 Protective Gas Supply to the Barrel 169
3.2.9 Mist Filtration Devices 169
3.2.10 Robots 169
3.2.11 Barrel and Screw Maintenance Stations 170
3.3 Slurry Distribution Systems 171
3.3.1 Cold Sprue 171
3.3.2 Hot Sprue 172
3.3.3 Hot Runner 172
3.4 Mold 174
3.4.1 General Features 174
3.4.2 Mold Heating–Cooling Systems 175
3.4.3 Mold Spray Equipment 177
3.4.4 Mold Vacuum Systems 178
3.5 Summary 180
References 180

4 Thermal and Corrosive Aspects of Processing Molten Magnesium 181
4.1 Introduction 181
4.2 High-Temperature Effect of Molten Magnesium Alloys on Other Materials 182
4.2.1 Property Degradation Due to Structural Changes 182
4.2.2 High Temperature Fatigue 188
4.2.3 Thermal Fatigue 192
4.2.4 Corrosion Fatigue 194
4.2.5 Creep and Stress Rupture 194
4.2.6 Oxidation 196
4.3 Corrosive Behavior of Molten Magnesium Alloys 199
4.3.1 Reactivity with Iron and Steel 199
4.3.2 Reactivity with Ni-Containing Alloys 202
4.3.3 Simultaneous Corrosion and Wear 210
4.4 Summary 212
References 214

5 Process Theory and Practice 215
5.1 Introduction 215
5.2 Key Processing Parameters 215
5.2.1 Injection Molding Sequence 215
5.2.2 Barrel Temperature Profile 218
5.2.3 Shot Size 220
5.2.4 Injection Profile 220
5.2.5 Recovery 223
5.3 Functions of the Injection Screw 223
5.3.1 Feedstock Conveying 223

5.3.2 Feedstock Melting . . . 225
5.3.3 Alloy Metering . . . 226
5.3.4 Output of Injection Screw . . . 227
5.3.5 Shear Function of an Injection Screw . . . 229
5.3.6 Alloy Mixing . . . 232
5.4 Function of the Non-Return Valve . . . 238
5.4.1 Role of Piston in Die Casting . . . 238
5.4.2 Role of the Non-Return Valve in Plastics Injection . . . 241
5.4.3 Role of the Non-Return Valve in Magnesium Molding . . . 241
5.5 Nozzle Plug—Principles of Thermal Gating . . . 242
5.5.1 Formation of the Nozzle Plug . . . 242
5.5.2 Mechanism of the Plug's Release and Disintegration . . . 245
5.5.3 Plug Nature During Induction Heating . . . 245
5.5.4 Slurry Transfer to the Mold Using Hot Sprue . . . 246
5.5.5 Slurry Distribution to the Mold Using Hot Runners . . . 249
5.6 Mold Processing . . . 251
5.6.1 Fluidity of Molten Metals . . . 252
5.6.2 Mold Filling Time . . . 256
5.6.3 Mold Temperature . . . 260
5.6.4 Mold Spraying Function . . . 261
5.6.5 Part Cooling After Ejection . . . 264
5.7 Common Defects . . . 264
5.7.1 Defect Classification and Characterization . . . 264
5.7.2 Identifying Defect Causes . . . 269
5.7.3 Defect Prediction by Flow Modeling . . . 277
5.8 Product Quality Control . . . 277
5.8.1 Dimensional Accuracy and Surface Quality . . . 277
5.8.2 Integrity of the Component . . . 277
5.8.3 Chemistry . . . 282
5.8.4 Metallography . . . 282
5.9 Summary . . . 282
References . . . 283

6 Feedstock Selection . . . 285
6.1 Introduction . . . 285
6.2 Techniques of Particulates Manufacturing . . . 285
6.2.1 Mechanical Comminution . . . 286
6.2.2 Techniques Based on Rapid Solidification . . . 288
6.3 Characterization of Particulates Manufactured by Mechanical Fragmentation . . . 290
6.3.1 Morphological Features . . . 290
6.3.2 Sieve Analysis . . . 292
6.3.3 Bulk Density . . . 295

6.3.4 External Defects 295
6.3.5 Phase Composition and Microstructure 296
6.4 Characterization of Rapidly Solidified Granules 297
6.4.1 Morphological Features 297
6.4.2 Dimensional Features 299
6.4.3 Bulk Density 301
6.4.4 External Defects 301
6.4.5 Stability of Chemical Composition. 303
6.4.6 Phase Composition 304
6.4.7 Internal Microstructure 305
6.4.8 Microstructure of Globules with External Defects 307
6.5 External Characteristics Affecting Injection Molding Applications 308
6.5.1 Mechanically Fragmented Chips 309
6.5.2 Rapidly Solidified Granules 309
6.6 Global Manufacturing Market of Magnesium Particulates. 310
6.7 Summary 312
References 312

7 Oxidation Behavior of the Feedstock 315
7.1 Introduction. 315
7.2 Oxidation Kinetics 315
7.2.1 Initial Stage Reaction 316
7.2.2 Transient and Steady Stage Reactions 318
7.3 Oxidation Surfaces 319
7.4 Oxide Growth Morphologies 320
7.4.1 Thin Films. 320
7.4.2 Nodular Features. 321
7.5 Internal Structure of Oxide Layers 324
7.6 Oxide Phase Composition. 326
7.7 Influence of Chemical Composition on Magnesium Oxidation 330
7.8 Evaporation Characteristics 332
7.9 Oxidation Mechanism. 334
7.9.1 Initial Oxidation—Thin Film Stage 334
7.9.2 Transient Stage—Oxide Ridges 334
7.9.3 Steady Stage Growth—Oxide Nodules 336
7.9.4 Role of Substrate Phases in Oxide Growth. 337
7.10 Ignition Behavior 338
7.11 Alloy Protection Against Oxidation and Ignition 339
7.11.1 Sulphur Hexafluoride SF_6 340
7.11.2 Sulphur Dioxide SO_2. 342
7.11.3 MagShield. 342
7.11.4 Other Methods 343
7.11.5 Protective Atmospheres for Heat Treatment. 345
7.11.6 Environmental Impact. 345

7.12 Implications for Injection Molding Practice 346
7.12.1 Advantages of Oxidation Kinetics and an Incubation Period 346
7.12.2 No Accumulation of Magnesium Vapour—Protection by an Inert Gas 347
7.12.3 Issues Caused by the Particulate Nature of the Feedstock 347
7.12.4 Advantage of Small Volume of Molten Alloy 347
7.13 Examples of Alloy Degradation from Injection Molding Practice 347
7.13.1 Magnesium Evaporation 348
7.13.2 Oxidation Within a Machine Nozzle During Stand-By Periods 349
7.13.3 Oxidation and Ignition During Equipment Maintenance 350
7.14 Summary 352
References 352

8 Melting Behavior of the Feedstock 355
8.1 Introduction 355
8.2 Factors Affecting Feedstock's Thermal Instability 355
8.2.1 Cold Deformation in Metals 355
8.2.2 Cold Deformation of Magnesium 356
8.2.3 Compression Deformation of As-Cast Ingot 357
8.2.4 Deformation in Mechanically Cut Chips 357
8.2.5 Deformation in Pellets Manufactured by Solid-State Extrusion 359
8.3 Solid-State Transformation During Heating 364
8.3.1 Phenomena During Annealing of Cold-Deformed Metal 365
8.3.2 Recrystallization Phenomena in Magnesium 366
8.3.3 Recrystallization of Cold-Deformed Ingot 367
8.3.4 Annealing Phenomena Within Mechanically Comminuted Chips 368
8.3.5 Annealing Phenomena in Extruded Pellets 370
8.4 Microstructure Evolution During Feedstock Melting 374
8.4.1 Nature of Non-Equilibrium Melting 375
8.4.2 Melting by Liquid Penetration Along Grain Boundaries 375
8.4.3 Assessment of The Solid to Liquid Ratio During Melting 376
8.4.4 Melting Mechanically Comminuted Chips 385
8.4.5 Melting of Extruded Pellets 387
8.5 Melting of As-Cast Ingot 392
8.6 Phenomena During Heating of Rapidly Solidified Granules 394

8.6.1 Features of As-Solidified Microstructure 395
8.6.2 Transformations During Heating in Solid State 396
8.6.3 Granule Melting 396
8.6.4 Common Melting Features of Particulate Feedstock 398
8.7 Microstructure Correlation Between the Solid and Semisolid State 399
8.7.1 Solid-State Grain Versus Semisolid-State Solid Globule 400
8.7.2 Size-Evolution of Solid Phase Within the Slurry 401
8.7.3 Internal Changes of the Globular Solid. 403
8.8 Summary 403
References 404

9 Alloy Transformations During Molding 407
9.1 Introduction 407
9.2 Factors Controlling Microstructure Evolution 407
9.2.1 Slurry Generation 408
9.2.2 Secondary Changes During Injection 409
9.2.3 Solidification Conditions 409
9.3 Solid-State Transformations During Initial Conveyance 409
9.4 Semisolid-State Transformations Within the Machine Barrel 412
9.4.1 Transformations Under a Regime of Partial Melting 414
9.4.2 Transformations Under a Regime of Complete Melting and Partial Re-Solidification 416
9.4.3 Effectiveness of Shear During Mold Filling 418
9.4.4 Transformations During Non-Conventional Processing 419
9.5 Transformations Associated with the Seal Plug 420
9.5.1 Role of Alloy Temperature in the Plug's Microstructure. 420
9.5.2 Changes During Reheating, Preceding the Plug's Release 420
9.5.3 Effect of Microstructure on Plug's Disintegration 421
9.5.4 Effect of Microstructure on Plug Flow Behavior Through the Mold Gate. 423
9.6 Theories of the Formation of Globular Structures During Melting and Solidification 425
9.6.1 Morphology of the Crystallization Front 425
9.6.2 Dendrite Description. 426
9.6.3 Segregation in Cast Structures 426
9.6.4 Globular Growth Due to Fragmentation of Dendrites 427
9.6.5 Development of Globular Forms During Melting. 428
9.6.6 Solidification of Remnant Liquid 429
9.7 Evolution of the Primary Solid Phase During Molding 429
9.7.1 Characteristics of the Primary Solid After Various Processing Routes 429

9.7.2 Particle Size Versus Solid Volume Fraction 430
9.7.3 Mechanisms Controlling the Solid Particle Evolution 431
9.8 Engineering Microstructure for Commercial Applications 436
9.8.1 Thick Wall Components 436
9.8.2 Thin Wall Components 437
9.9 Summary 439
References 439

10 Microstructure–Property Relationship for Molded Alloys 441
10.1 Introduction 441
10.2 Parameters Characterizing Thixotropic Structures After Solidification 441
10.2.1 Volume Fraction of the Primary Solid 442
10.2.2 Size of the Primary Solid Particles 443
10.2.3 Shape of the Primary Solid 443
10.2.4 Volume of Entrapped Liquid 446
10.2.5 Interfaces 446
10.3 General Constituents of Thixotropic Microstructures of Magnesium Alloys 447
10.3.1 Primary Solid 448
10.3.2 As-Solidified Liquid 448
10.3.3 Phase Composition 449
10.3.4 Structural Integrity 451
10.4 Internal Structure of the Primary Solid and Matrix 452
10.4.1 Entrapped Liquid in As-Cast State 452
10.4.2 Changes of Entrapped Liquid Due to Diffusion 452
10.4.3 Detailed Features of Molded Structures 454
10.5 Tensile Properties 456
10.6 Decohesion Characteristics 457
10.6.1 Failure Mode Under Cryogenic Conditions 459
10.7 Structure–Property Correlation 462
10.7.1 Role of Alloy Matrix 462
10.7.2 Role of Solid Particle Substructure 462
10.7.3 Role of Solid Particle Content 463
10.8 Attempts at a Quantitative Description of the Structure–Property Relationship 463
10.9 Structure–Property Correlation for Magnesium Alloys, Processed with Other Semisolid Techniques 465
10.10 Modification of Mechanical Properties by the Post-Molding Heat Treatment 466
10.11 Summary 466
References 467

11 Semisolid Extrusion Molding 469
11.1 Introduction 469
11.2 General Features of SSEM 469
11.2.1 Deformation Behavior of Slurries at Ultra High Solid Contents 470
11.2.2 Temperature Requirements for SSEM 471
11.3 Mold Filling Characteristics and Part Integrity 471
11.3.1 Flow Behavior of the High-Solid Slurries 471
11.3.2 Part Integrity 472
11.3.3 Mold Filling Time as the Critical Factor 474
11.3.4 Role of the Flow Mode 476
11.4 Structural Transformations During Molding and As-Solidified Structure 476
11.4.1 Structural Transformations During SSEM 476
11.4.2 General Microstructure After Solidification 477
11.4.3 Role of the Solidification Rate 478
11.4.4 Phase Composition 480
11.5 Characterization of Primary Solid 481
11.5.1 Factors Affecting Solid Distribution 481
11.5.2 The Size of Solid Particles and Its Change During Processing 482
11.6 Application Areas for SSEM 484
11.7 Summary 485
References 485

12 Near-Liquidus Molding 487
12.1 Introduction 487
12.2 Growth of Globular Structures by Nucleation 487
12.2.1 Mullins–Sekerka Stability Criterion of Globular Growth 488
12.2.2 Growth of Globular Forms During Non-Agitated Solidification 489
12.2.3 Growth of Globular Forms Under Forced Convection 491
12.3 The NLM Concept and Its Experimental Implementation 492
12.3.1 Technical Implications of the Preheating Range Required 493
12.3.2 Preheating Range for Mg–Al–Zn Alloys 493
12.4 Microstructure After NLM 494
12.4.1 Alloy's Structural Integrity 495
12.4.2 Matrix Morphology 497
12.4.3 Morphology of Solid Particles 498
12.4.4 Features of Die Cast Microstructure 499
12.4.5 Crystallographic Orientation 500

12.4.6 Phase Composition 500
12.4.7 Decohesion Characteristics 502
12.5 Tensile Properties 504
12.6 Structure-Property Correlation After NLM 505
12.6.1 Benefits of Reduced Temperatures During NLM 506
12.6.2 Melt Agitation During NLM 506
12.6.3 Separating the Microstructure and Internal Integrity 507
12.6.4 Influence Of Alloy's Chemistry 507
12.7 Application Areas of NLM 508
12.7.1 Thin-wall Molding 508
12.7.2 Matrix for Composites 508
12.8 Summary 510
References 510

13 Alloy and Composite Generation in a Semisolid State 513
13.1 Introduction 513
13.2 Concept of Semisolid-State Mixing 513
13.2.1 Methods of Practical Implementation 514
13.2.2 Phenomenology of Structural Transformations 514
13.3 Effect of Temperature on Semisolid-State Mixing 516
13.3.1 Chemistry and Phase Composition 517
13.3.2 Role of a Particulate Nature of the Feedstock During Mixing 520
13.3.3 Microstructure Evolution 521
13.3.4 Effect of Solid State Diffusion 523
13.4 Role of Other Parameters in Semisolid-State Mixing 523
13.4.1 Proportions of Mixed Ingredients 524
13.4.2 Differences in Melting Ranges 525
13.5 Tensile Properties of Alloys Created by Semisolid-State Mixing 526
13.5.1 Correlation of Strength and Elongation 526
13.5.2 Influence of Mixing Temperature on Properties 527
13.5.3 Applicability of the Rule of Mixtures 532
13.6 Generation of Magnesium Matrix Composites 532
13.6.1 Magnesium as a Composite's Matrix 533
13.6.2 Reinforcements Applicable for Magnesium 535
13.6.3 Challenges with Manufacture of the Magnesium Matrix Composites 536
13.6.4 Injection Molding as a Fabrication Method of Composites 536
13.7 Engineering Importance of Semisolid-State Mixing 540
13.7.1 Application to Conventional Alloys 540
13.7.2 Application to Immiscible Alloys 540
13.7.3 Application to Magnesium Matrix Composites 541
13.8 Summary 541
References 542

14 Molding Creep-Resistant Alloys 543
14.1 Introduction 543
14.2 Elements of Creep Deformation Theory 544
14.2.1 The Creep Deformation Curve 544
14.2.2 Creep Mechanisms 546
14.3 Creep in Magnesium and Its Alloys 547
14.3.1 Creep in Pure Magnesium 548
14.3.2 Factors Affecting Creep in Magnesium Alloys 548
14.4 Creep Control in Modern Commercial Alloys 550
14.4.1 Alloying Systems 551
14.4.2 Role of Alloy Processing in Creep Properties 553
14.5 Characteristics of Mg–5Al–2Sr Feedstock for Injection Molding 554
14.5.1 Alloy Chemistry and Melting Range 554
14.5.2 Effect of Sr on Phase Composition in As-Cast Ingot 555
14.5.3 General Microstructure 557
14.5.4 Ingot's Phases and Their Morphology 560
14.5.5 Changes During Manufacturing to Particulates 562
14.6 Effect of Semisolid Molding on Mg–5Al–2Sr Microstructure 563
14.6.1 Phase Composition 564
14.6.2 General Microstructure 565
14.6.3 Phase Morphology 569
14.7 Summary 570
References 573

Index 575

Erratum

The Publisher regrets that the presentation of figures 1.35, 2.11a, 2.31, 3.16b, 5.4, 5.24, and 5.29 in the book *Magnesium Injection Molding*, by Frank Czerwinski (ISBN 978-0-387-72399-0) was incorrect. The corrected figures are reprinted below.

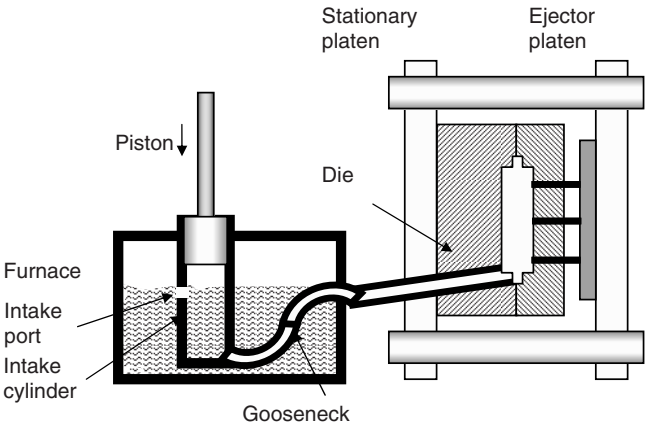

Fig. 1.35 The graphical illustration of a hot chamber die-casting machine

F. Czerwinski, *Magnesium Injection Molding*.

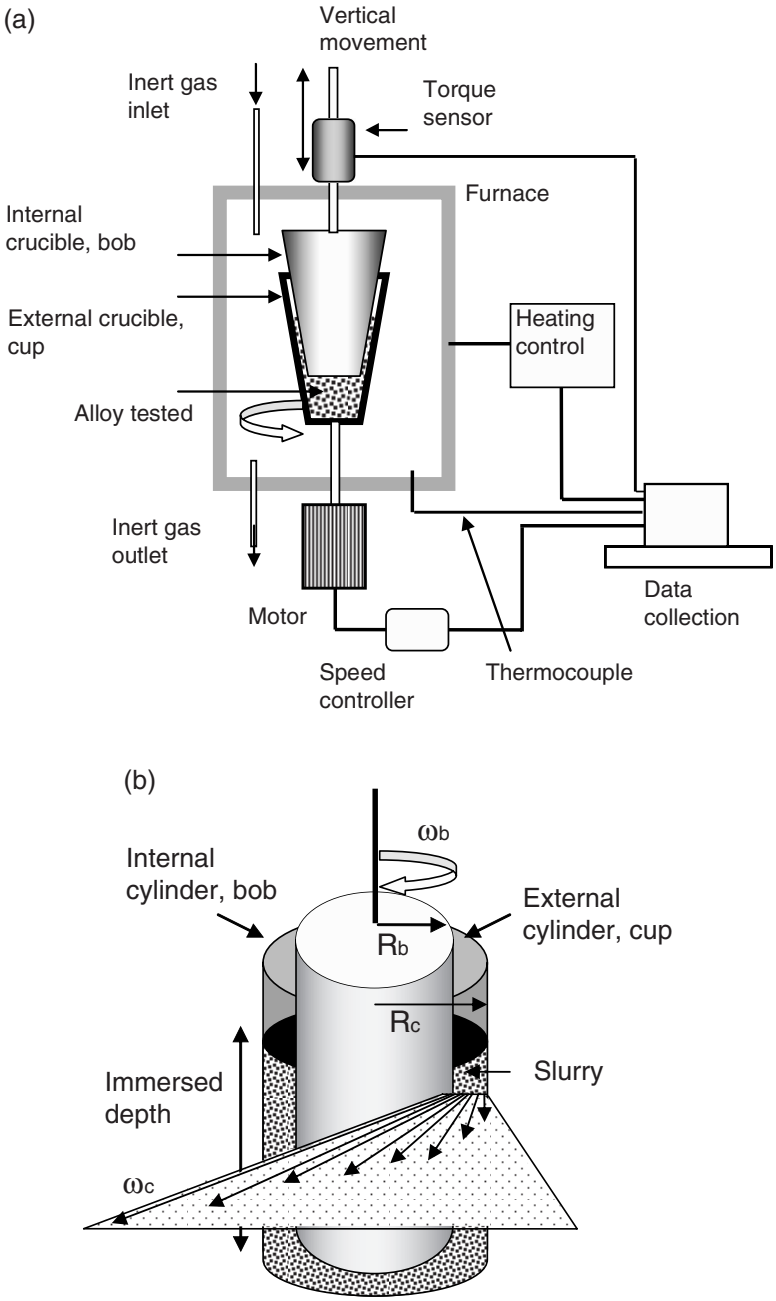

Fig. 2.11 A rotational viscometer based on Couette method **a** and a distribution of slurry's velocity between cup and bob within the Searle's instrument **b**

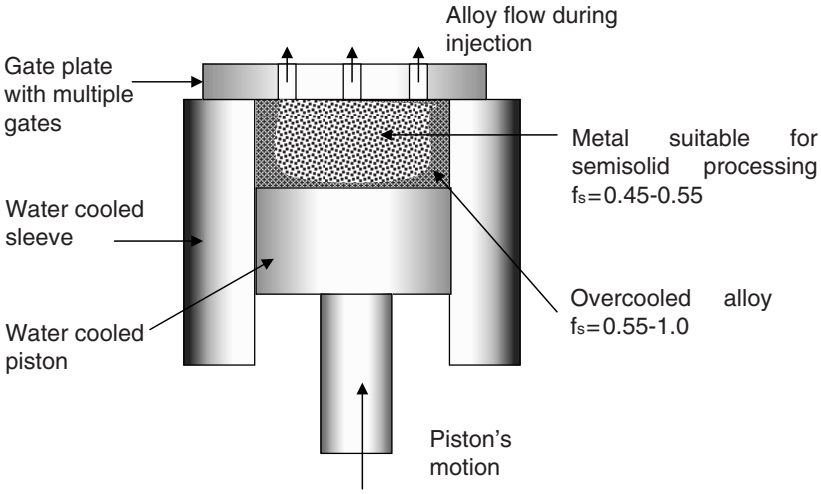

Fig. 2.31 The concept of sub-liquidus casting (SLC) developed by THT Presses Inc.

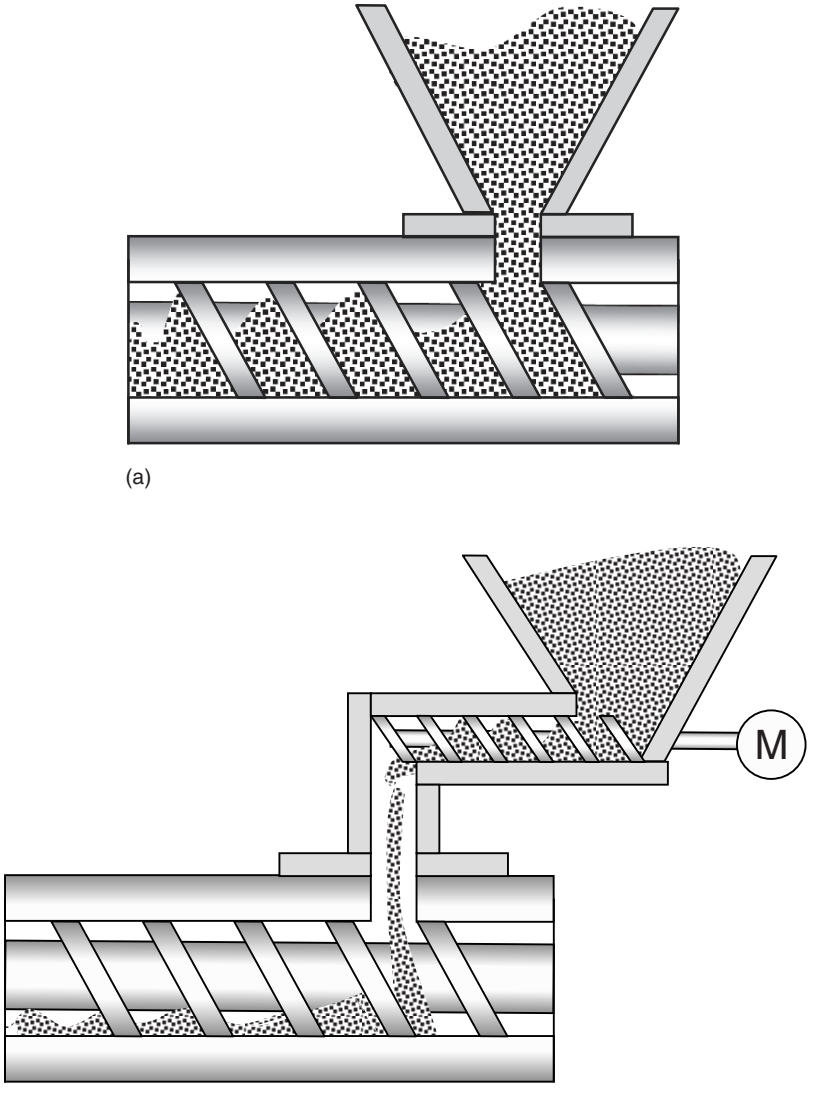

Fig. 3.16 The feeding techniques used in magnesium molding: **a** concept of uncontrolled dosing of the feedstock—flood feeding; **b** concept of controlled dosing of the feedstock—starve feeding

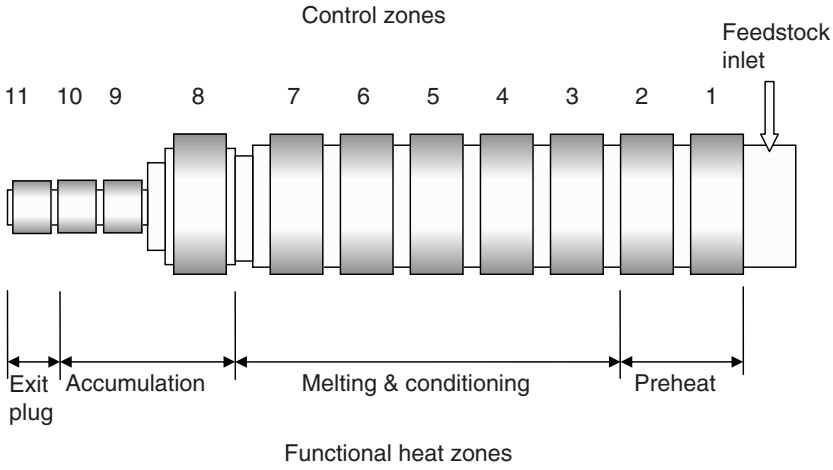

Fig. 5.4 The arrangement of control and functional heat zones along the magnesium flow path through the machine barrel and nozzle

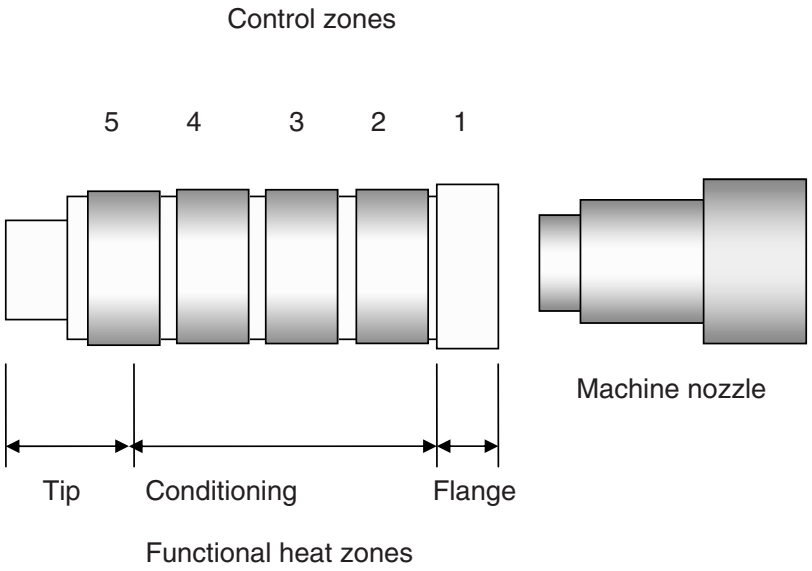

Fig. 5.24 The arrangement of control and functional heat zones along the magnesium flow path through the hot sprue

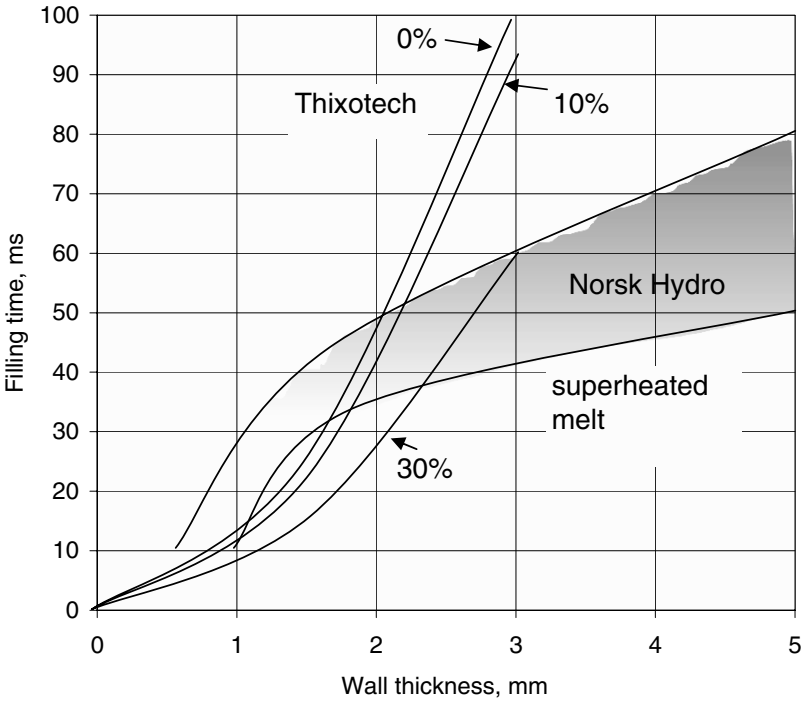

Fig. 5.29 Mold fill time during injection molding of magnesium alloys depending on wall thickness and initial solid content (Thixotech Inc. and Hydro Magnesium Inc.)

1
Magnesium and Its Alloys

1.1 Introduction

Magnesium belongs to alkaline earth metals, which occupy the second main group of the periodic table of elements. It was discovered in the eighteenth century and named after the ancient Greek district of Magnesia in Thessaly (Table 1.1). This silvery-white metal is the eighth most abundant element, comprising 2.7% of earth's crust. Due to high reactivity, magnesium is not found in elemental form in nature but only in chemical complexes, widely distributed in rock structures, seawater and lake brines.

The inherent advantages of magnesium include a unique blend of low density, high specific strength, stiffness, electrical conductivity, heat dissipation and absorption of vibration. When combined with easy machining, casting, forming and recycling, magnesium is seen as a very attractive material for a large volume of applications. In recent years the interest in magnesium has grown dramatically, which has spurred academic research and industrial trials to identify more efficient ways of manufacturing the primary metal, as well as a search for new alloys and extending areas of their application. This chapter contains the historical background, elements of physical metallurgy, a characterization of alloys and examples of application.

1.2 Market Development

The magnesium industry in its early stages was turbulent, driven by military applications and wars. A periodically volatile market was also recorded through later history but over the last quarter of the twentieth century a tremendous growth was achieved.

1.2.1 Raw Metal Production

Following a series of discoveries by western researchers, the magnesium market in the late nineteenth and early twentieth centuries was dominated by German industry. In

F. Czerwinski, *Magnesium Injection Molding*.

Table 1.1 The key milestones of magnesium discovery and early development

Year	Name	Country	Milestone
1754	Joseph Black	England	Discovery of magnesia during decomposition of calcium and magnesium carbonates
1808	Humphrey Davy	England	Establishing that magnesia represents the oxide of new metal magnesium
1828	Antoine-Alexander Bussy	France	Isolation of magnesium metal by fusion of anhydrous magnesium chloride with metallic potassium
1833	J. von Liebling & Michael Faraday	England	Production of magnesium metal by electrolytic reduction of the chloride
1852	Robert Bunsen	Germany	Production of magnesium metal from anhydrous magnesium chloride
1853	St. Claire Deville & Caron	France	Production of magnesium from anhydrous magnesium chloride by reduction with potassium in a heated closed container
1860	Johnson Matthey & Co	England	Commercial production based on Deville-Caron process
1886	IG Farbenidustry	Germany	Commercial production of magnesium by electrolysis of molten carnallite (Bunsen's cell)
1896	Chemische Fabrik Griesheim Elektron & Aluminium und Magnesium Fabrik	Germany	Full scale commercial production based on Bunsen's cell

1852, Robert Bunsen produced anhydrous magnesium employing ammonium chloride and improved electrolysis to permanently separate magnesium from chlorine (Table 1.1). In the late 1920's, K. Pistor and W. Moschel produced magnesium by a reduction of magnesium anhydrous chloride obtained by carbo-chlorination of magnesite:

$$MgO + C + Cl_2 = MgCl_2 + CO \tag{1.1}$$

$$2MgO + C + 2Cl_2 = 2MgCl_2 + CO_2 \tag{1.2}$$

The above technology, then owned by I.G. Farbenindustry, along with its subsequent modifications, affect the worldwide manufacturing of magnesium until today.

At the beginning of the twentieth century global production was around 10 tonnes per year (Fig. 1.1). Just before the World War I the production reached 350 tonnes, increasing further to over 3,000 tonnes in 1919. When during World War I the British blockade was imposed on Germany, being at that time the sole source of magnesium, seven plants were built in the US, the largest ones by Dow Chemicals and American Magnesium Company, later a subsidiary of Alcoa. The end of the war led to a decline in production to its pre-war level. As a result of the closure of magnesium plants, including American Magnesium Company in 1928, Dow Chemicals remained the only US producer until World War II.

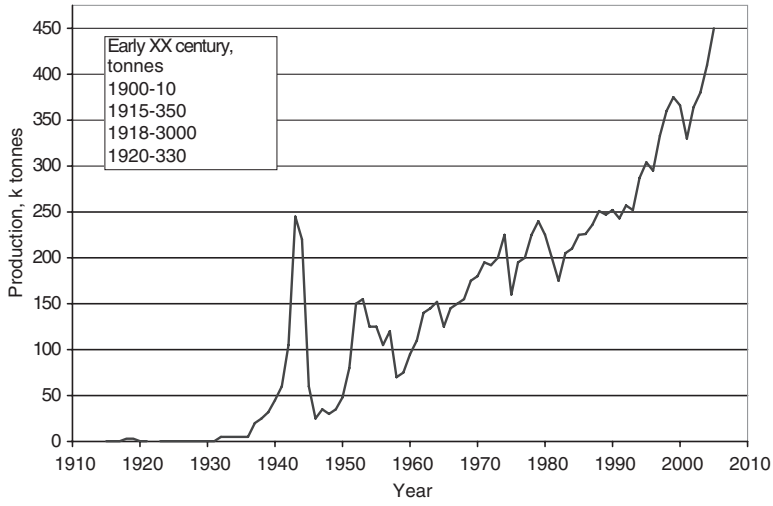

Fig. 1.1 The world production of primary magnesium metal (based on IMA and data combined from various sources)

During World War II magnesium production expanded enormously from 32,000 tonnes in 1939 to its peak of over 240,000 tonnes in 1944 with Germany, Great Britain, the USA and France as key players. Germany expanded existing facilities and built new plants in Austria and Norway, reaching an overall capacity of 34,000 tonnes. At the same time, the USA built fifteen new magnesium plants, expanding capacity by two orders of magnitude to 291,000 tonnes per year with a production of 184,000 tonnes in 1943.

After World War II, the global production contracted almost tenfold to near 20,000 tonnes in 1946. Germany was prohibited from the fabrication of magnesium, so facilities were disassembled and equipment moved to other countries. The post-war market was dominated for decades exclusively by Dow Chemicals. When the technology became more widespread, new players started production of raw metal. At this stage the access to cheap energy was the main factor. Norsk Hydro, after reconstruction of a German-built plant in Heroya, Norway, reached a capacity of 12,000 tonnes in 1950 and became the second largest supplier after Dow. Changing market and metal pricing, imports, and a natural catastrophe at its Freeport, Texas plant all contributed to Dow Chemical's exiting magnesium production in 1998, after over 80 years. As a result, Norsk Hydro, with plants in Norway and Canada, emerged as the largest supplier, covering about 25% of the world demand. For a short period, the Korean War led to reactivation of production to over 150,000 tonnes in 1953. As before, when the war ended the industry declined again and did not exceed the World War II level until the1980's.

The peace-driven growth, which started in the 1980's with several short-lasting slow-downs, led to the present level. According to International Magnesium Association (IMA) statistics, the total market climbed from 380,000 tonnes in 2003 to 410,000 tonnes in 2004, which translates to 8% growth. The IMA figures account for primary magnesium production and consequently do not consider

re-melting and recycling. According to Roskill Metals and Minerals reports, the secondary metal accounted for 230,000 tonnes in 2003. Moreover, the IMA statistics, continued in 2004 by Hydro Magnesium, exclude domestic demand in Russia and in China. After including all these components and China's domestic consumption of 50,000 tonnes, the world magnesium production in 2003 exceeded 660,000 tonnes.

The remarkable emergence of China as the world's largest source of magnesium continues to have a significant impact on the industry. The share of global supply from China grew from 5% in 1994 to over 65% in 2004 (Fig. 1.2). In 2005 the production grew by 8%, as compared to 2004, reaching 468,000 tonnes. While adding this potential to Western suppliers, along with the secondary metal production, the world's present capacity exceeds 900,000 tonnes, predicted as the consumption level by 2010. The major manufacturing centers of the primary metal in 2004 are listed in Table 1.2. As compared to the year 2000, a number of western companies abandoned the market, including North West Alloys, the USA (43,000 tonnes); Pechiney, France (18,000 tonnes); and Norsk Hydro, Norway (43,000 tonnes).

1.2.2 Raw Metal Consumption

Magnesium is used in a variety of applications including pyrotechnical, chemical, pharmaceutical and metallurgical. The primary focus of this volume is the metallurgical

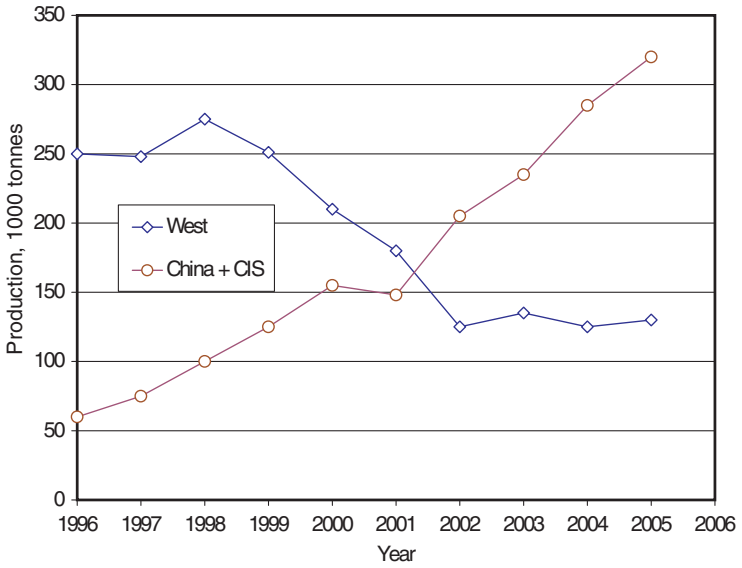

Fig. 1.2 The production of primary magnesium by Western countries and China (based on IMA data)

Table 1.2 The major manufacturers of primary magnesium in 2004

Country	Manufacturer	Capacity in tonnes per year as of 2004	Process type	Feed/Process features
Brazil	Rima	11,000	Thermal	Based on own reserves of dolomite which is reduced in a sillico-thermal processing under vacuum
Canada	Timminco Metals, Haley Station, Ontario	7,000	Thermal	Pidgeon process, calcined dolomite is reduced by ferrosilicon in a vacuum retort
Canada	Norsk Hydro, Becancour, Quebec	48,000	Electrolytic	Based on imported magnesite which is transformed to magnesium chloride then dehydrated and subjected to electrolysis
China	Shanxi Province, approx 70 plants Ningxia Province, approx 15 plants Henan Province, approx 50 plants	600,000+	Thermal	Pidgeon process with pilot-scale vertical retorts
Israel	Dead Sea Magnesium	33,000	Electrolytic	Electrolytic decomposition of carnallite hexahydrate
Kazakhstan	Ust-Kamenogorsk, Titanium Magnesium Works	14,000	Electrolytic	Process based on natural carnallite and magnesium chloride with top anode entry cell
Russia	Solikamsk Magnesium Works,	23,000	Electrolytic	Based on natural carnallite from Verhokamsk
Russia	Avisma, Berezniki Titanium Magnesium Works	30,000	Electrolytic	Bottom anode entry cell
USA	US Magnesium, Great Salt Lake, Utah	43,000	Electrolytic	Carbo chlorination and electrolytic decomposition in open or closed cells

segment, with major markets listed in Fig. 1.3. The key change over the decade from 1992 (Fig. 1.3.a) to 2002 (Fig. 1.3.b) is an almost threefold increase in die casting volume. As in previous years, the die casting segment was also the main growth area in 2004, increasing 13% compared to 2003 (Fig. 1.3.c). Aluminum remains the largest consumer of pure, non-recycled magnesium, and after 4% growth in 2004, has not yet been overtaken by die casting. In 2005 die casting grew at 8%, representing 34% of total demand. Looking forward, it is expected that die cast alloys will become the single largest segment. Moreover, the automotive demand for magnesium is anticipated to drive the growth. The present die casting portfolio is dominated by the automotive applications with structural components of vehicles taking almost one third of the entire market (Fig. 1.3d). Geographically, Europe is set to emerge as the largest region for magnesium consumption although demand in Asia is predicted to grow equally fast.

China's internal consumption in 2000 was only 25,500 tonnes with a structure shown in Fig. 1.4a. The consumption increased almost three fold up to 70,500 tonnes in 2004 [1]. China's consumption in 2005 grew again by 33%, reaching 105,500 tonnes. The structure of its 2005 market is shown in Fig. 1.4.b, where three segments represent 80% of total consumption: Al alloying–30,000 tonnes, steel desulfurization and iron inoculation–28,500 tonnes and die casting 25,900 tonnes. An increase in China's domestic consumption is accompanied by broadening of the application range.

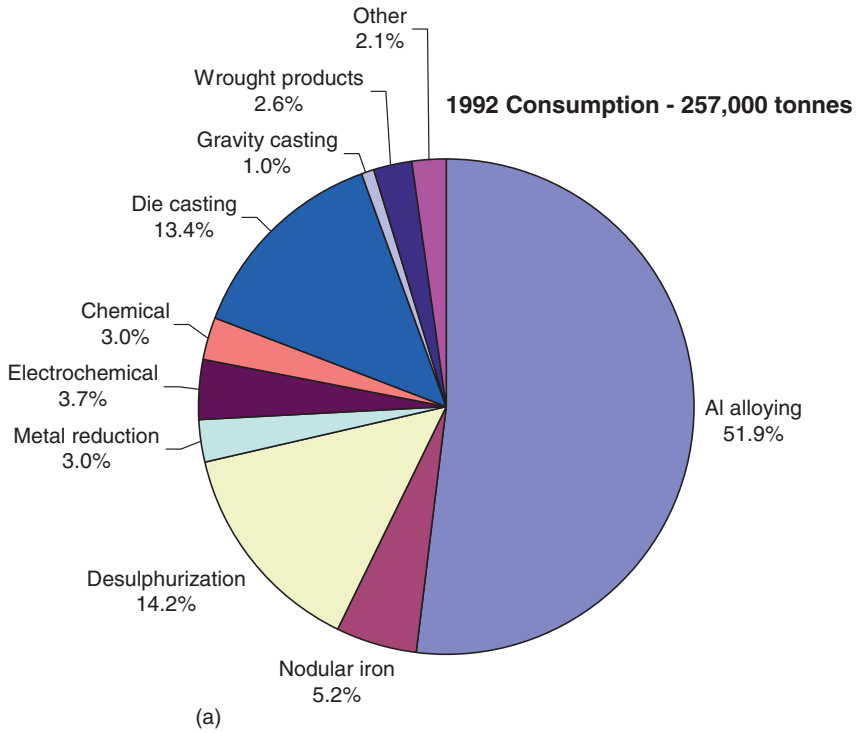

Fig. 1.3 (continued)

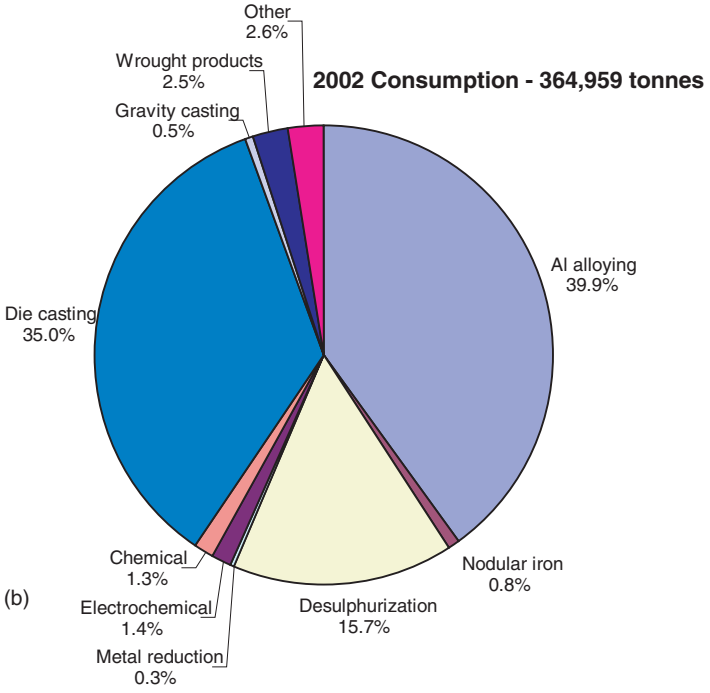

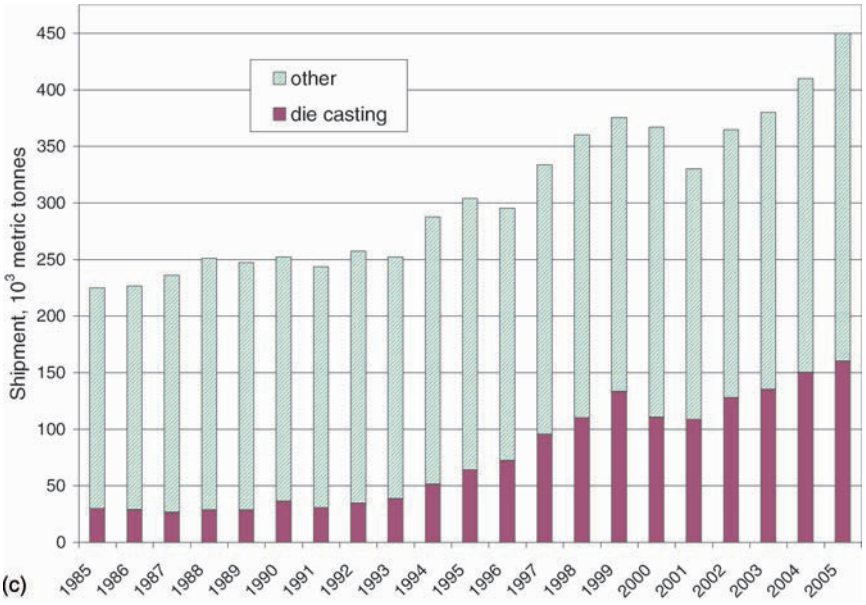

Fig. 1.3 (continued)

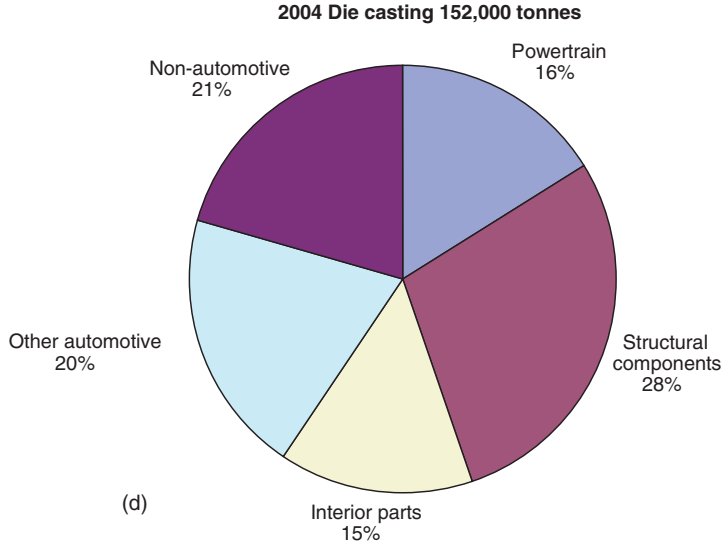

Fig. 1.3 The structure of world consumption of magnesium: **a** 1992; **b** 2002; **c** Growth of die casting segment over last two decades; **d** Structure of die casting segment in 2004 (based on IMA data)

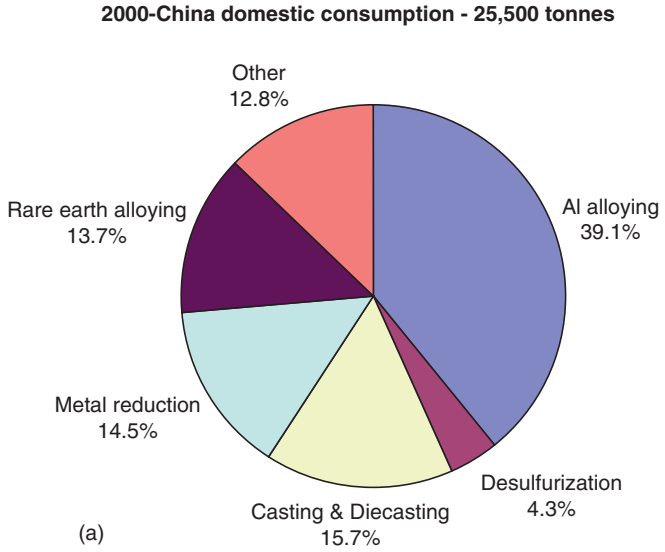

Fig. 1.4 (continued)

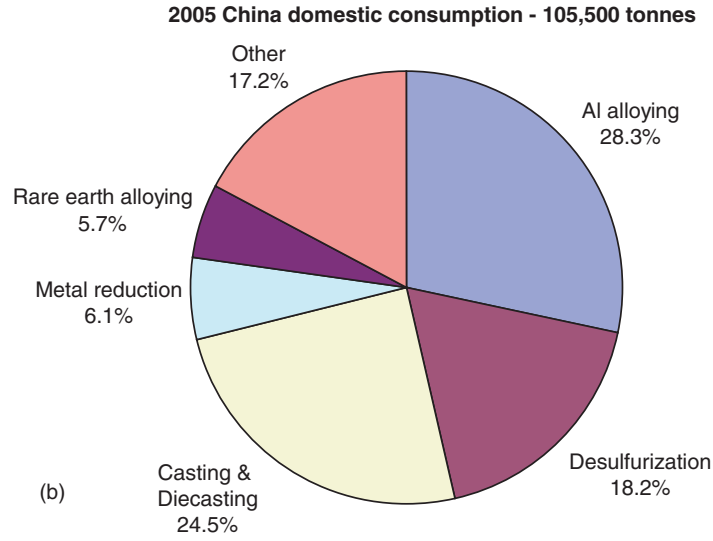

Fig. 1.4 The structure of domestic consumption of magnesium by China in **a** 2000 and **b** 2005; based on data from [81]

Table 1.3 The characteristics of minerals containing magnesium

Mineral's name	Chemical formula	Magnesium content, weight %
Brucite	$Mg(OH)_2$	41.7
Magnesite	$MgCO_3$	28.8
Serpentine	$3MgO \cdot 2SiO_2 \cdot 2H_2O$	26.3
Dolomite	$MgCO_3 \cdot CaCO_3$	13.2
Carnallite	$KCl \cdot MgCl_2 \cdot 6H_2O$	8.8
Lake brines	$MgCl_2$, $MgSO_4$	0.8
Seawater	$MgCl_2$, $MgSO_4$	0.14

1.3 Production Techniques of Pure Metal

Magnesium exists naturally within a number of minerals representing several chemical compounds. The major ones among them are listed in Table 1.3 in order of diminishing magnesium content. To extract metallic magnesium, two very different technologies are used commercially: thermal reduction of magnesium oxide in calcined dolomite and fused salt electrolysis of magnesium chloride. It was anticipated that the thermal process will gradually be replaced by electrolytic technology, covering in the early 1990s about three quarters of the world's capacity. However, the importance of the thermal route (mainly Pidgeon), well suited to developing economies such as that of China, increased to 46% in 2003 and to 87% in 2005. In addition to production of the primary metal from ores, the secondary metal is generated through recycling.

1.3.1 Thermal Processes

An advantage of the high temperature reduction is that dolomite requires just calcining to be used as a feedstock as compared to a complex purification needed to prepare the feedstock for the electrolytic route. Entry for this method is relatively easy, and it is also less capital intensive. Among many disadvantages, a batch type discontinuous production and high operating cost, in part due to the amount of heat consumed, are quoted. Energy consumption during the reduction step of the thermal route is between 17 and 20 kWh/kg as compared to 12-14 kWh/kg used during the electrolytic process. Thus to produce 1 kg of magnesium, up to 10-12 kg of coke is needed. There is also a negative environmental impact because about 40 kg CO_2 is released to the atmosphere during production of 1 kg of Mg. To prevent oxidation and combustion of exposed molten magnesium, sulphur hexafluoride, SF_6, is used. It is estimated that 95% of greenhouse gas emissions are due to SF_6 use. The remaining 5% is from calcinations of ores and fuel combustion.

The major thermal routes include the:

(i) Magnetherm process, developed by Pechiney in 1960, exploring electric resistance heating via an electrode at a temperature of 1550 °C in a vacuum of 0.05 atm;
(ii) Pidgeon process, which uses externally heated retort;
(iii) Brasmag process, where briquettes of ferrosilicon and dolime (calcined dolomite) particulates react within an internally-heated electric furnace.

The flow chart for the process developed by L.M. Pidgeon is shown in Fig. 1.5. Ferrosilicon is produced in an arc furnace, mixed with calcined dolomite and briquetted. Then the briquettes are heated in horizontal retorts. As a result of reduction following reaction (1.3) pure metal is isolated:

$$2MgO \cdot CaO + FeSi = Ca_2SiO_4 + 2Mg + Fe \quad (1.3)$$

After the Mg vapor condenses at the retort's cold end the metal is tapped to cast ingots.

1.3.2 Electrolytic Methods

There are a number of modifications of electrolytic isolation of magnesium from minerals. In general each of them contains two steps: hydrometallurgical preparation of the feedstock, followed by the electrolysis. The advanced process utilizing carnallite involves fluidized bed dryers, chlorinators, electrolysis cells and continuous magnesium refining furnaces. The electrolysis cells can be supplied by anhydrous carnallite melt, magnesium chloride and solid highly dehydrated carnallite. Electrolytic techniques are capable of attaining lower average total cost than thermal plants. Although this method is similar to the standard Hall process for Al, the knowledge level required for Mg is much higher.

During the electrolytic method of Magnola, Canada [2], the serpentine mine tailings are used as a raw material (Fig. 1.6). After crashing, drying and screening

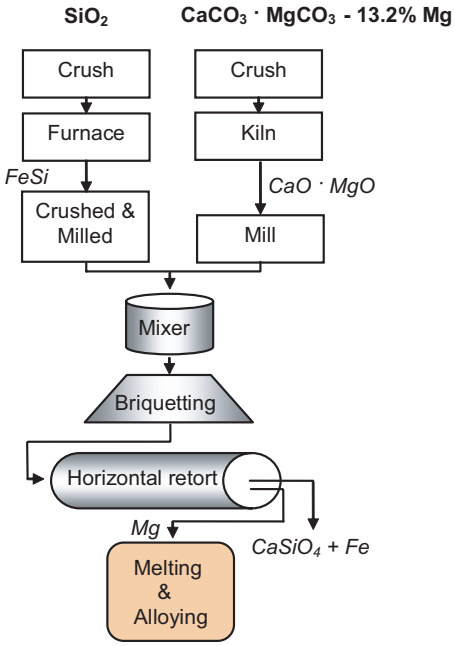

Fig. 1.5 The production flow chart of thermal process by L.M. Pidgeon

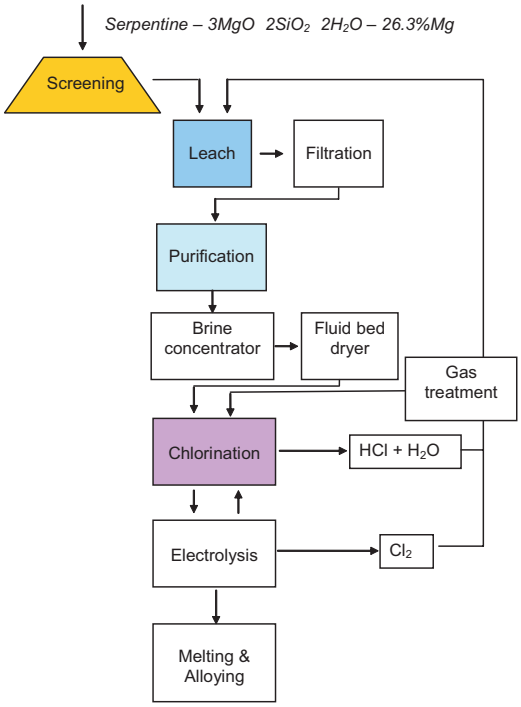

Fig. 1.6 The production flow chart of electrolytic process by Magnola

of serpentine ores ($3MgO \cdot 2SiO_2 \cdot 2H_2O$), magnesium is extracted through acid leach to form brine. The purified brine is subsequently dried to create granular magnesium chloride. Then the magnesium chloride granules are dissolved in an electrolyte and treated in a chlorination process. During the second stage, metallic magnesium is extracted by electrolysis. The Magnola electrolysis system is based on the Alcan Multi Polar Cell. The cell itself consists of an outer steel shell linked with a refractory brick layer resistant to corrosion by molten salt electrolyte, which is composed of $MgCl_2$, NaCl, $CaCl_2$ and MgF_2. The metallic magnesium is tapped and then cast into ingots.

1.3.3 Experimental Scale Processes

Continuous efforts are undertaken to increase effectiveness of both the thermal and electrolytic routes. At the same time, there are attempts to develop an original technology, more efficient than those presently existent.

1.3.3.1 Improved Thermal Process (Mintek)

An improvement of the thermal method, proposed by Mintek, South Africa, is summarized in Fig. 1.7. The Mintek Thermal Magnesium Process (MTMP) uses direct-current arc smelting technology to produce magnesium vapor from calcined dolomite at atmospheric pressure instead of under a vacuum, as is the case in the conventional thermal method. Subsequently, the vapor is condensed to liquid magnesium in a novel condenser [3]. The elimination of vacuum increases productivity by allowing the furnace and condenser to operate continuously without necessity to stop and break the vacuum to tap the magnesium from the condenser and slug from the furnace. It is claimed that the crude magnesium is of better quality than that produced by other thermal routes, particularly in regards to calcium.

1.3.3.2 Direct Extraction Using Solid Oxide Membrane (SOM)

The SOM is considered as an emerging generic technology for the extraction of metals from their oxide ores [4]. It is seen as an alternative for conventional processes used at present. The concept is shown in Fig. 1.8. When the applied electric potential between the anode and cathode exceeds the dissociation level of the oxide to be reduced, the desired metal cations are reduced at the cathode and oxygen anions migrate through the membrane and are oxidized at the anode. The electric potential applied between the electrodes can be increased as long as the potential across the melt-zirconia interface does not exceed the dissociation potential of the solid zirconia and undesired oxides are not reduced at the cathode.

The experimental electrolytic SOM cell operating at an anode current density of 1 A/cm^2 is shown in Fig. 1.9. The entire apparatus is contained and heated within the

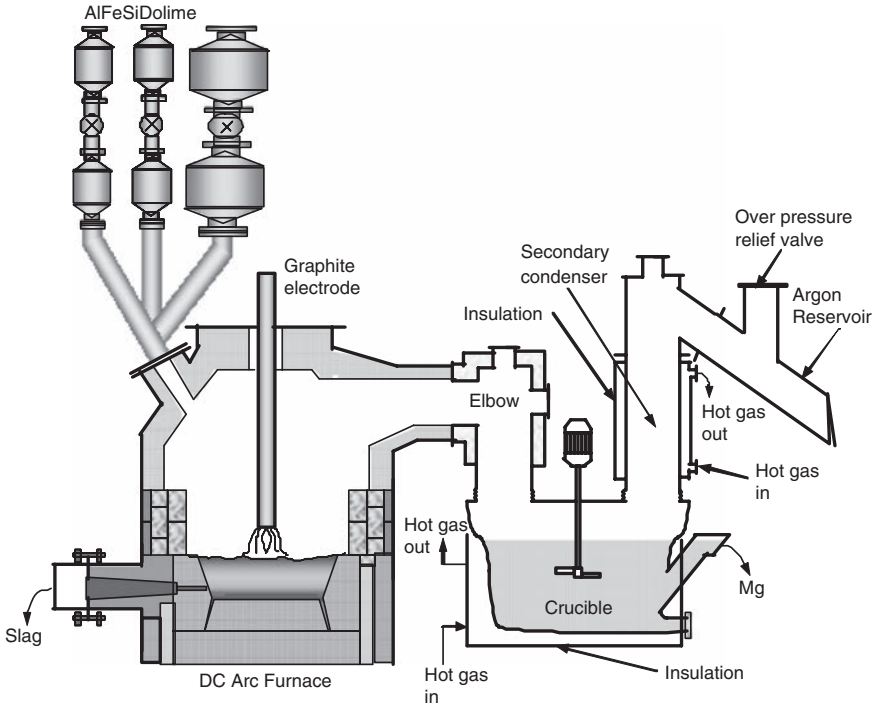

Fig. 1.7 The production flow sheet of experimental thermal process by MINTEK [3]

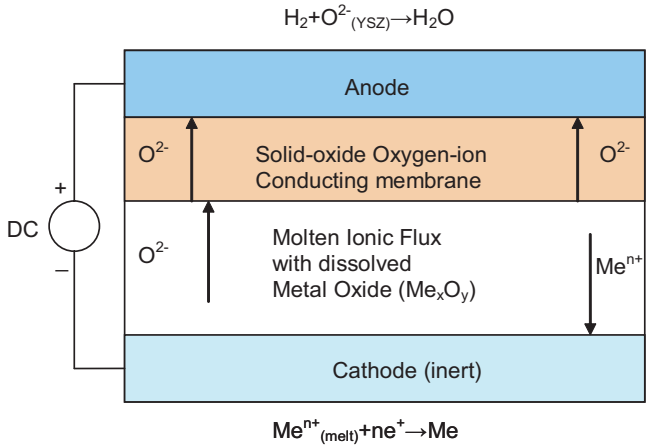

Fig. 1.8 The concept of direct magnesium production from magnesium oxide using Solid Oxide Membrane [4]

mullite reaction tube of a high temperature resistance furnace. The electrolysis chamber is maintained at 1150 °C while the condensation chamber is kept within range of 1100-1300 °C. Argon gas is introduced to protect the yttria-stabilized zirconia (YSZ) membrane from highly reducing the Mg vapor created. A tube connected to the

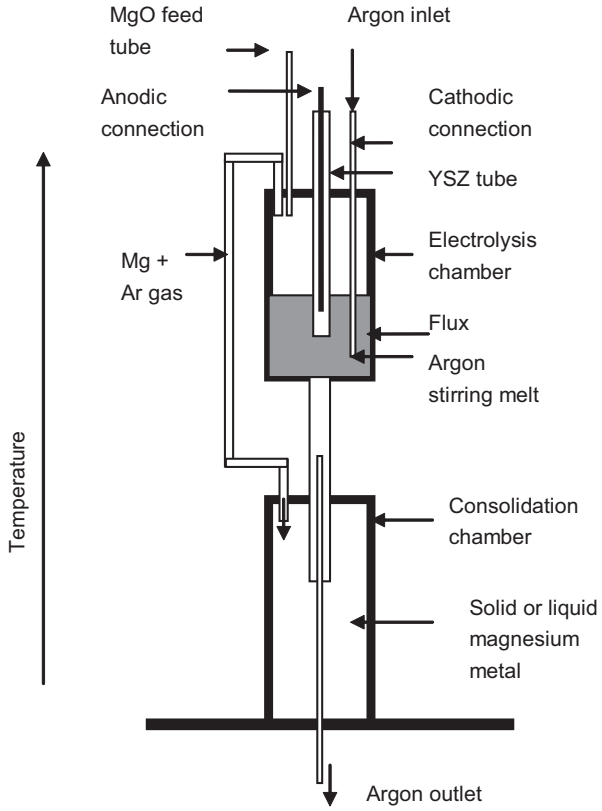

Fig. 1.9 The experimental setup for direct magnesium production from magnesium oxide using Solid Oxide Membrane [4]

instrument's top is used to supply MgO to the melt. The process is still in laboratory stage and the system can produce up to 1 kg of magnesium per day.

1.3.3.3 Carbothermic Reduction

The carbothermic reduction of magnesia has a potential of higher energy efficiency and higher productivity and is based on the reaction which produces a magnesium and carbon monoxide vapor:

$$MgO_{(s)} + C_{(s)} = Mg_{(g)} + CO_{(g)} \tag{1.4}$$

As can be deduced from the partial magnesium pressure associated with reaction (1.4), the reaction is favored at high temperatures, typically above 1700 °C (Fig. 1.10). While operating at lower temperatures the product gas should be diluted with an inert gas.

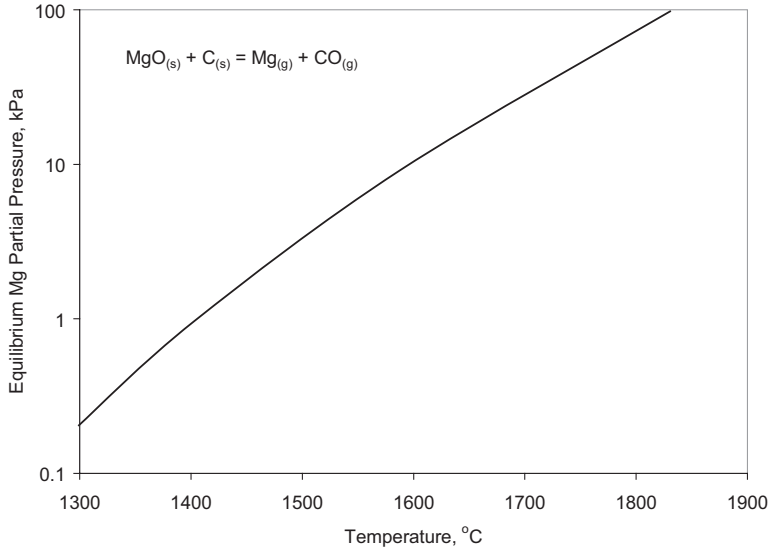

Fig. 1.10 The partial pressure of magnesium associated with the equilibrium of reaction (1.4) [5]

The major technical challenge is preventing the reverse reaction, achieved by rapid quenching of the vapor and dissolving magnesium in a metal solvent [5]. The rapid quenching explores the fact of passing hot gases at temperature between 1500 °C and 1800 °C through the expansion nozzle at supersonic velocity, achieving cooling rates over 10^6 °C per second. A schematic flow is shown in Fig. 1.11. The choice of carbon feed depends on the cost involved in removal of impurities and includes either metallurgical or petroleum coke, various coal chars, charcoal or graphite. The research is in progress to develop a high temperature solvent to quickly dissolve the reduced magnesium and bypass the classic reversion tendency.

1.3.4 Recycling as a Source of the Secondary Metal

Magnesium is a highly recyclable material, consuming only 5% of the energy required to produce the primary metal. The recycling capacities of Europe and the USA are listed in Table 1.4.

1.3.4.1 Scrap Classification

There is no common classification system for magnesium scrap. According to [6], new magnesium scrap is categorized into four classes. Type I represents the high-grade

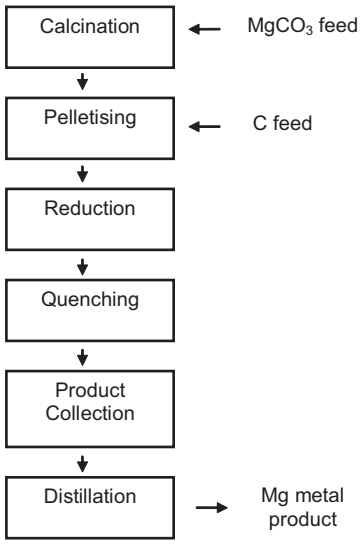

Fig. 1.11 A schematic flow chart of the carbothermic route of magnesium reduction [5]

Table 1.4 The magnesium recycling capacity of Europe [9] and US [6]

Company	Location	Capacity (tonnes per year)
Europe (2002)		
Hydro Magnesium	Porsgrunn, Norway	20,000
Magnesium Electron	Manchester, England	14,000
Magnesium Electron	Litvinov, Chech Rep.	10,000
REMAG	Delfzijl, Netherland	10,000
Hydro Magnesium	Bottrop, Norway	7,500
REMAG	Schalgotarjan, Hungary	5,000
Ecka Granules	St. Georgen, Austria	3,500
Others		5,000
Total		75,000
USA (1998)		
Alabama Cathodic Metals Inc.	Foley, AL	17,000
Garfield Alloys Inc.	Cleveland, OH	13,600
IMCO Recycling Inc.	Sapula, OK	15,000
Spectrulite Consortium Inc.	Madison, IL	15,000
Total		60,600

scrap, generated mainly by die casting, which includes clean rejected parts, melt spills, biscuits, runners, flashing, and overflows. Depending on the casting hardware, the amount of scrap generated in the foundry reaches typically 50% to 70%. Type II represents the oil-contaminated scrap and type III includes dross (oxide formed on the top surface of the melt) and sludge (contaminant particles accumulated at the bottom of a crucible or furnace). Type IV covers chips and fines. The broader classifications also exist, where scrap is divided into up to 9 classes. At present only the high quality scrap can easily be recycled into high purity alloys.

The old post-customer scrap requires more complex processing. It includes the rejected castings with coatings or contaminated with oil, parts with non-magnesium inserts, dross, sludge or oily machining chips. In addition, there are residues which cannot be recycled such as blastings or grindings, and they are disposed of after deactivation.

1.3.4.2 Recycling Technologies

Commercial recycling relies on two processes:

(i) flux-based, batch wise method where the refining flux, usually in the form of salts such as $MgCl_2$, KCl, $BaCl_2$ or CaF_2 is mixed with the melt to absorb any oxide particles. After reaction, dense conglomerates settle at the bottom of a crucible;
(ii) fluxless, continuous method where gas purging, melt filtration and conglomerate settling are explored.

Both techniques require chemistry correction, mainly removal of impurities such as Fe, Ni and Cu. The metallic contaminants are removed by pyrometallurgical refining after agents react with them, forming heavier conglomerates.

A separation of contaminants by a distillation, though feasible, is not widely exercised. In a distillation column, less volatile impurities are removed while the magnesium vapor condenses at the top of the column. A benefit of distillation is the possibility of Mg separation from all impurities. It may be carried out in a vacuum so the SF_6 protection is not required [7].

In the case of alloys containing reactive elements, these ingredients may react with conventional fluxes. To preserve the alloy chemistry either alkaline earth element fluxes or a special fluxless technology should be applied.

1.3.4.3 Techniques of Coating Removal

The specific issues during recycling of various housings are coatings that should be removed. A removal of coatings prior to recycling allows controlling and neutralizing the gaseous emissions and reduces the amount of moisture generated during melting. The following methods of coating removal are available:

(i) dry sand blasting, being dangerous due to the generation of dust and possible explosion;
(ii) wet blasting, when abrasives are mixed with water and injected at high speed;
(iii) chemical treatment, where the coated part is immersed in reactive solutions. To dissolve coating and at the same time not react with the magnesium base, solutions based on alkaline elements are effective [8];
(iv) thermal treatment, which is applicable to removal of organic coatings such as lacquer, paint or oil. The major techniques include: rotary kiln, belt decoater and fluidized bed decoater [9].

1.3.4.4 Recycling Circuit

The typical recycling flow chart is shown in Fig. 1.12. The first step is sorting the scrap into batches requiring the same recycling method. After shredding and thermal treatment to remove surface contaminants and coating, the scrap is subjected to briquetting. When the molten state is achieved, the purification process is conducted to remove all metallic and non-metallic inclusions.

1.4 Fundamentals of Alloying

Unalloyed magnesium, obtained from either the thermal or electrolytic route with different levels of purity, is not used for structural applications. For engineering applications, alloys are created that contain a number of different elements, including Al, Zn, Mn, Si, Zr, Ca, Ag, Li, Cu, alkaline or rare earth elements. The purpose of alloying additions is to improve strength and other properties of magnesium. Although alloying alters certain properties, the key features of magnesium-based alloys remain similar to those of pure magnesium. The major properties of pure magnesium are listed in Table 1.5.

1.4.1 Role of Alloying Additions

Aluminum: Solubility in magnesium reaches 12.7% at 437 °C and is reduced to 3% at 93 °C (Fig. 1.13). In the Mg-rich range, Al forms the $Mg_{17}Al_{12}$ phase,

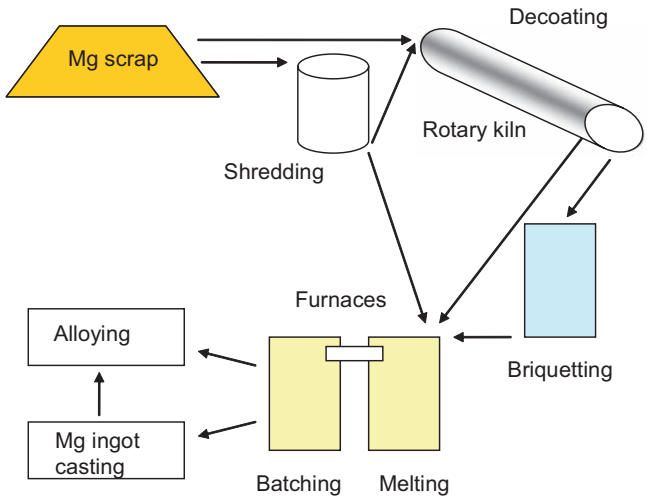

Fig. 1.12 The flow chart of magnesium recycling

Table 1.5 Properties of pure magnesium [91-95]

Property class	Specific property	Values	Unit	Remarks
Crystallography	Crystal structure	Hexagonal close-packed		20 °C
		a = 0.32092	nm	
		c = 0.52105	nm	
	Atomic volume	13.97	cm^3/mol	
	Burger's vector	0.321	nm	
Mass	Density-Solid phase	1.738	g/cm^3	20 °C
		1.650	g/cm^3	650 °C
	Volume change on solidification	4.2 volumetric, 1.5 linear	%	
	Volume change on cooling	5 volumetric, 1.7 linear	%	Cooling from 650 °C to 20 °C.
Mechanical	Young's modulus	45	GPa	
	Shear modulus	17.2	GPa	
	Ultimate tensile strength	80-180	MPa	
	Fracture elongation	1-12	%	
	Hardness	30-47	HB	
	Poisson's ratio	0.35		
	Viscosity	1.23	mPa s	650 °C
		1.13	mPa s	700 °C
	Surface tension	0.56	N/m	650 °C
	Solid-liquid interfacial free energy γ_{SL}	0.115	J/m^2	650 °C
Electrical	Resistivity	45.3	nΩ m	a axis
		37.8	nΩ m	c axis
Thermal	Melting point	650 ± 1	°C	
	Boiling point	1090	°C	
	Thermal expansion	26.1	µm°C	20-100 °C
		29.9		20-500 °C
	Thermal conductivity (solid phase)	156	W/m K	27 °C
		149		327 °C
		130		650 °C
	Thermal conductivity (liquid phase)	78	W/m K	650 °C
	Latent heat of fusion per mol	8.954	kJ/mol	
	Latent heat of fusion per unit volume	5.90	J/m^3	
	Heat of vaporization	127.4	kJ/mol	
	Specific heat capacity	1.025	kJ/kg K	20 °C
	Lattice diffusion $D_L = D_{oL}\exp\left(-\frac{Q_L}{RT}\right)$	$D_{oL}=1.0\times10^{-4}$ $Q_L=135$	m^2/s kJ/mol	

(continued)

Table 1.5 (continued)

Property class	Specific property	Values	Unit	Remarks
	Grain boundary diffusion $\delta D_b = \delta D_{ob} \exp\left(-\frac{Q_b}{RT}\right)$	$\delta D_{ob} = 5.0 \times 10^{-12}$ $Q_b = 92$	m^3/s kJ/mol	
	Core diffusion $a_c D_c = a_c D_{oc} \exp\left(-\frac{Q_c}{RT}\right)$	$a_c D_{oc} = 3.0 \times 10^{-23}$ $Q_c = 92$	m^4/s kJ/mol	
	Vapor pressure at 650 °C	360	Pa	

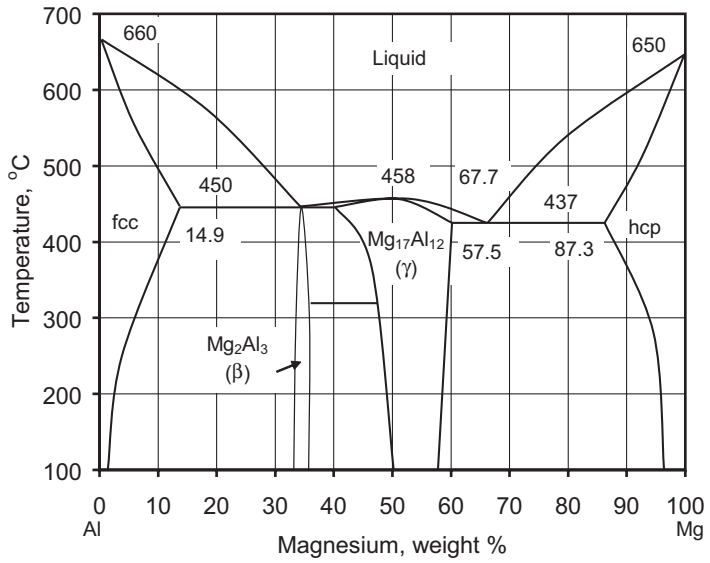

Fig. 1.13 The Mg–Al equilibrium phase diagram [82]

effective in preserving alloy properties to roughly 120 °C. Additions of Al improve room temperature strength, castability and corrosion resistance. Ductility and fracture toughness are gradually reduced with increasing Al content (Fig. 1.14).

Zinc: improves room temperature strength through solid solution effect. As shown in Fig. 1.15, the solubility of zinc is 6.2% at 341 °C and 2.8% at 204 °C. In addition zinc also improves fluidity of the melt, but contents above 2% decrease elongation at fracture—especially in the solution-treated condition—and can cause cracking. The ductility reduction is explained through preferential segregation of Zn to the $Mg_{17}Al_{12}$ phase, thus increasing its volume fraction.

Manganese: is added to control the iron content. The level of Mn additions depends on the mutual solubility of Fe and Mn in the presence of other alloying elements. Mn increases slightly the yield stress without marked influence on tensile strength.

Solubility of manganese is less than 1% at 482 °C. In alloys containing Al, Mn combines with Al forming MnAl, $MnAl_4$ and $MnAl_6$. All compounds may exist as single particles with the Al/Mn ratio decreasing to the particle center. After heat treatment the $MnAl_6$ phase predominates. The binary diagram Mg-Mn is shown in Fig. 1.16.

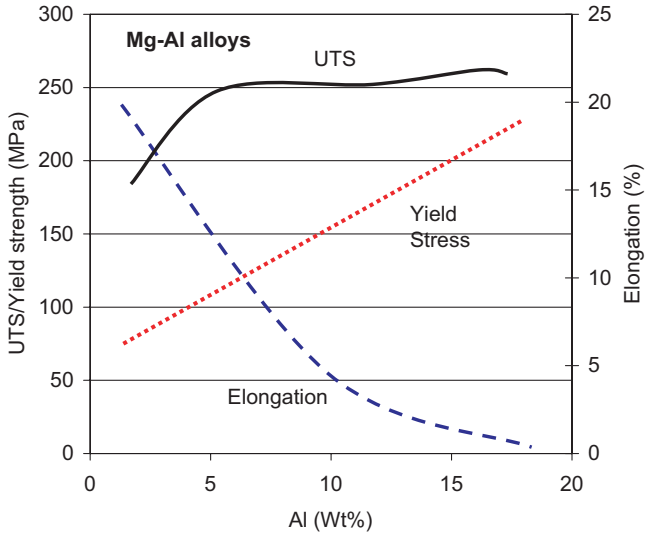

Fig. 1.14 The influence of Al content on mechanical properties of Mg–Al alloys [83]

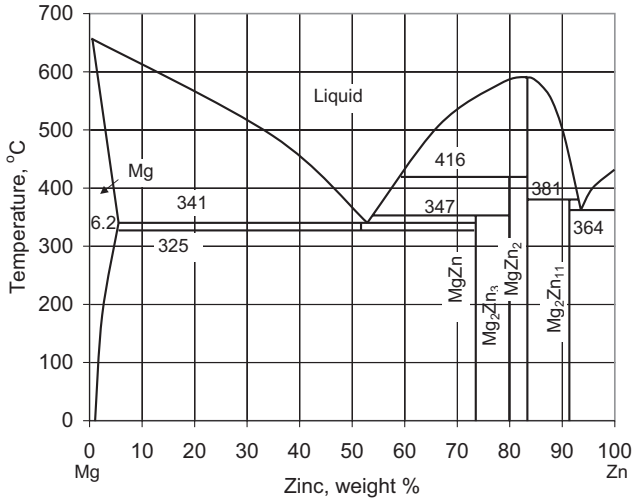

Fig. 1.15 The Mg–Zn equilibrium phase diagram [82]

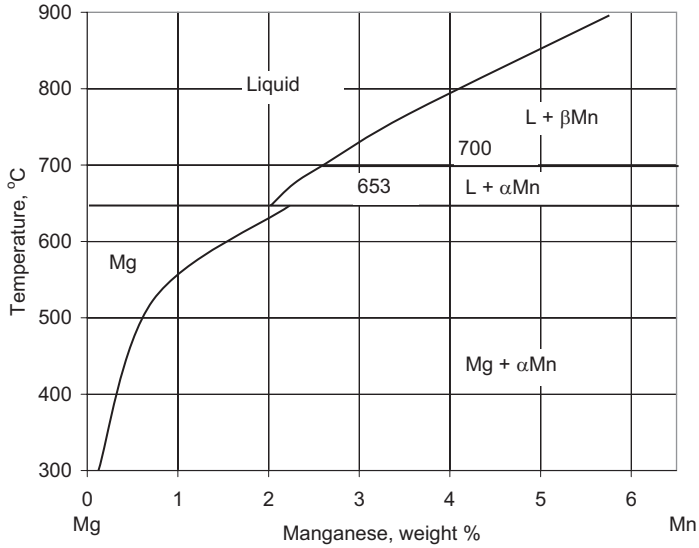

Fig. 1.16 The Mg–Mn equilibrium phase diagram [84]

Silicon: is added to increase the creep resistance by stable silazide precipitates. Addition of Si is limited by the liquid solubility to 1.7% at regular melt temperatures during casting (Fig. 1.17). Additions above 1.16%, which correspond to the Mg-Si eutectic point, cause the formation of coarse, blocky intermetallic particles that do not contribute to improvement in mechanical properties. At the same time Si additions reduce castability.

Calcium: is seen as an addition improving the creep resistance and grain size control. Its presence in an alloy reduces general processing behavior, e.g., causing sticking to the mold.

Zirconium: is a strong grain refiner and is added to pure Mg or alloys containing Zn, Ag, Y or Th. It has the same lattice type and nearly identical lattice constant as Mg. It also has a reasonable solubility limit in magnesium. As a result, Zr atoms play a strong role in growth restriction of Mg grains. Zr is capable of diminishing the grain coarsening effect of beryllium. For example, additions of 0.2% Zr to AZ92 contaminated with Be reduces grain size from 510 µm to 180 µm [10].

Beryllium: is added routinely in trace amounts in the order of 10-15 ppm to retard oxidation and ignition of molten alloy. It is also effective in removal of iron from magnesium melt: Additions as low as 0.2% allowed reduction of Fe in AZ63 alloy to 2 ppm [11]. Grain coarsening, however, restricts its use for anti-oxidation and anti-ignition purposes. Small Be additions increase the grain size in Mg-Al alloys up to one order of magnitude. It is suggested that Be might form carbides that are not effective as nucleation substrates for Mg and consume carbon, which could otherwise be used to form particles effective in grain refinement, e.g., Al_4C_3. According to recent findings, beryllium can

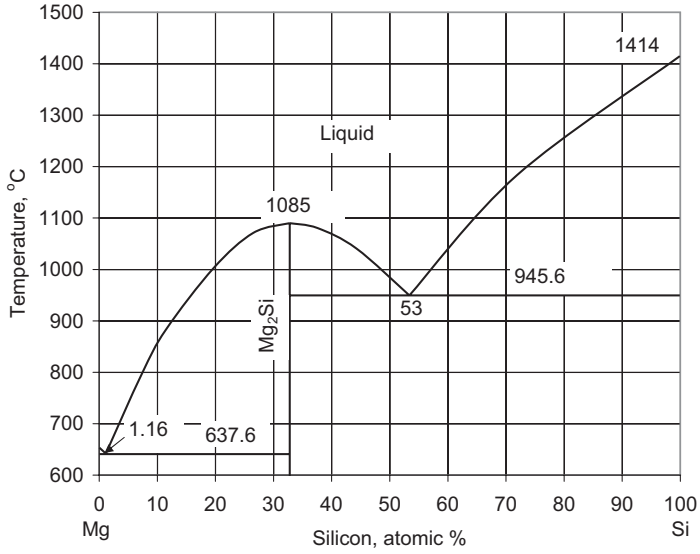

Fig. 1.17 The Mg–Si equilibrium phase diagram [84]

poison or considerably degrade any type of heterogeneous nucleus particles existing in melt by coating those particles with surface active surfactant [12].

1.4.2 Impurities

The quality of magnesium alloys depends on their purity. Of a number of elements, nickel and iron are the most detrimental. Some sources list copper as an impurity. Although copper, if present in contents over 0.05%, reduces corrosion resistance of Mg, it also improves the high temperature strength. Therefore, it is deliberately added as an alloying element, e.g., in Mg–Mn–Zn–Cu grades.

Nickel: is a harmful impurity, which strongly deteriorates the corrosion resistance. The allowed content in commercial alloys is 0.01–0.03wt%. To achieve high corrosion resistance the Ni content should be limited to 0.002wt% (ASTM B 94 standard).

Iron: strongly diminishes the corrosion resistance of magnesium alloys, similarly as nickel. Although the allowed content in commercial alloys is 0.01–0.03wt% for high corrosion resistance only 0.005wt% is allowed (ASTM B 94 standard).

During a process of creating magnesium alloys, Mn is added into the melt to reduce the content of Fe. The anhydrous $MnCl_2$ prill is introduced to molten metal at a temperature of over 700 °C. While mixed with the melt, Fe forms binary or ternary compounds with Mg, Al and Mn, which after temperature reduction to 640 °C settle at the bottom of the crucible as a sludge. There are concepts of removing iron

by treatment of molten magnesium with elemental Zr and Si. Also a boron-containing compound with a flux is proposed for this purpose [13].

1.4.3 Strengthening Mechanisms

The strengthening mechanisms of magnesium alloys include:

(i) grain boundary strengthening;
(ii) solid solution strengthening;
(iii) particle dispersion strengthening.

Of those mechanisms, the two first ones are the most effective. Particle dispersion strengthening is achieved after the separate heat treatment of alloys where solubility limits are exceeded.

1.4.3.1 Strengthening Due to Grain Size

Grain size is one of the most important characteristics determining alloy properties and mechanical strengthening, explored in engineering practice. The effect is caused by grain boundaries, inducing non-homogeneous deformation and introducing multiple slip. The grain-size dependence of the flow stress is expressed by the Hall–Petch equation [14]:

$$\sigma_o = \sigma_i + kd^{-1/2} \tag{1.5}$$

where:

σ_o is the yield stress;
σ_i–friction stress opposing motion of dislocations;
k–unpinning constant, measuring the extent to which dislocations are piled up at barriers;
d–grain diameter.

Experimental data indicate that for pure magnesium, the yield strength and tensile strength increase gradually with grain refinement and are accompanied by an increase of the elongation to failure (Fig. 1.18). For reduction in grain size of AZ91D alloy from 130 µm to 10 µm, assuming $k = 0.37$ MPa $m^{1/2}$, contribution from grain boundary strengthening was estimated for 84 MPa [15]. The fracture toughness, which is sensitive to yield strength, elongation to failure and strain hardening, was also improved by fine grain. The phenomenon is associated with an increase of the plastic zone size. The plain-strain fracture toughness K_{IC} was estimated by stretched zone analysis as 12.7–17.8 MPa $m^{1/2}$ [16].

Grain size control in magnesium alloys has a specific nature. Unlike aluminum, where reliable grain refiners are well established, a universal grain refinement system

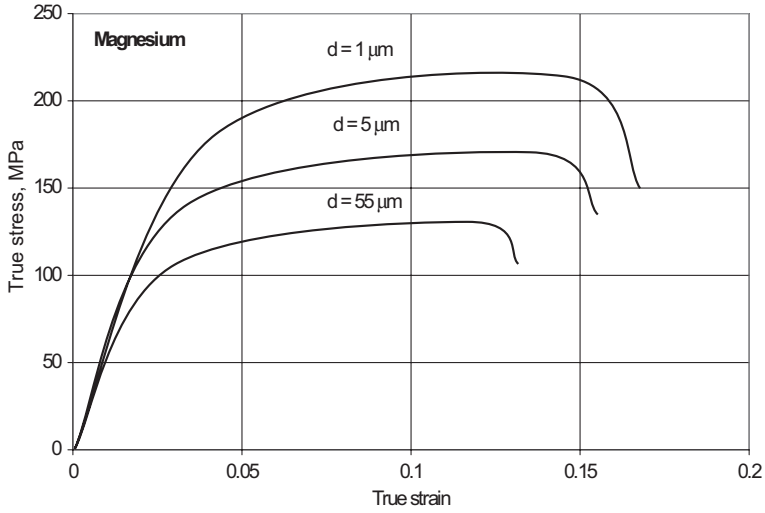

Fig. 1.18 The typical room temperature true stress versus true strain of pure Mg with different grain size. The grain size was modified by changing extrusion conditions [16]

does not exist for magnesium. The grain-size control is of particular importance for thick wall castings in which a fine grain structure cannot easily be obtained due to low cooling rates. Several grain-refining techniques have been developed to prevent formation of columnar structures and refinement of equiaxed grains:

(i) melt superheating;
(ii) carbon inoculation;
(iii) rapid cooling;
(iv) melt agitation;
(v) anhydrous ferritic chloride ($FeCl_3$) treatment;
(vi) alloying additions of Zr, Al or Zn.

The melt superheating method requires holding a melt at a temperature of 150-260 °C above the liquidus. As such, it consumes extra energy and leads to alloy deterioration due to oxidation and evaporation. Although the other method, called carbon inoculation, generates harmful gases, it offers some practical benefits. To achieve the grain refinement, the carbon-containing materials in gaseous or solid states, such as the organic carbons (C_2Cl_6), hexachlorobenzene is introduced into the melt. One of several interpretations of the mechanism involved, supported by a requirement of some Al within an alloy, assumes that carbon reacts with Al in the melt to form a large number of Al_4C_3 particles, acting as nucleation substrates for Mg crystals. There are elements such as Zr, Be and RE, which diminish the effect of carbon inoculation. The same Al_4C_3 particles are seen as suppressing grain growth following $FeCl_3$ additions to the molten alloy, a process especially effective in the presence of Mn and more than 3% of Al. It is suggested that C is liberated from the steel crucible after attack by HCl [17]. The most effective grain refiner is Zr, which appears to be a result of similarities

in crystal structures between Mg and Zr. However, Zr is not universally applied because the effect is poisoned by some alloying elements including Al. While Al and Zr are together they form stable Al–Zr intermetallics.

Recent experiments show that solute elements also restrict the grain growth. For example, Al in contents of 1%–5% causes significant grain refinement of magnesium and change from columnar to equiaxed grains. The growth restriction due to a solute diffusion in front of the moving solid/liquid interface is described by the growth restriction parameter (Q), quantifying the influence of solute on the solid growth rate. For a multi component system interaction between solutes is difficult to quantify. Thus estimation is conducted based on binary phase diagrams by summing the effect of each solute:

$$Q = \sum_{i=1}^{n} m_{L,i}(k_i - 1)C_{0,i} \tag{1.6}$$

where:

$m_{L,i}$ – liquidus slope for solute i;
k_i – partition coefficient of solute i;
$C_{0,i}$ – initial concentration of element i.

1.4.3.2 Strengthening Due to Solid Solution Effect

The factors, which control the tendency for the formation of substitutional solid solutions, are defined by Hume–Rothery [14]. If the sizes of two atoms, expressed by the lattice parameter, differ by less than 15%, it favors formation of solid solution. Also strong chemical affinity of two atoms is favorable. The relative valence is important and the solubility of a metal with the higher valence in a solvent of lower valence is more extensive. For a wide range of solubility a similarity in crystal structure is required.

The influence of several alloying elements on strengthening of Mg is given in Table 1.6 and Fig. 1.19. As seen, elements with large atom sizes generate potentially high strengthening. The practical effect is however diminished by relatively low solubility of these elements. A study of the contribution of combinations of Al, Zn, Si, Ce, Li and Ca to hardening of rapidly solidified Mg alloys revealed that for a Mg–Al–Zn system in which α–Mg solid solution is the major phase exhibiting hardening, the hardness (H) follows the relationship [18]:

$$H = H_o + K_1\left(X_{Zn} + \frac{1}{2}X_{Al}\right) \tag{1.7}$$

where:

H_o – constant, approximately of 50 kg/mm^2;
K_1 – constant with a value of 10 kg/mm^2;
X_{Zn}, X_{Al} – contents of Zn and Al in atomic %.

Table 1.6 Examples of Mg solid solution strengthening effect by several elements [85]

Element	Atom size difference, $\% \frac{DMg - DM}{DMg}$	Approximate solubility in Mg at 200 °C Wt%	Yield strength increase, % per wt % solute
Al	+10	3	25
Zn	+16	2	45
Ag	+9	5	23
Ce	−14	2	148
Ca	−24	1	110
Cu	+20	2	35
Th	−13	1	212

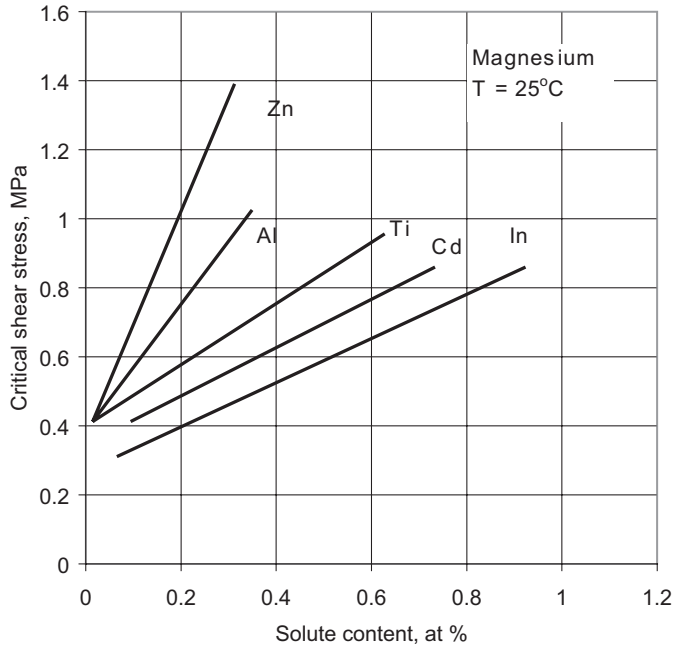

Fig. 1.19 The effect of solute content in Mg base solid solutions on the critical resolved shear stress for slip on the basal plane. Experiment was performed at room temperature [85]

Moreover, increments in hardening, resulting from further additions of Si, Ce or Li, are similar in magnitude as those found in the absence of Al or Zn.

A special role in solid solution strengthening of magnesium is ascribed to Zn. The maximum solid solution concentration of Zn in Mg is 2.4at% at 341 °C and 0.5at% at room temperature (earlier Fig. 1.15). The strain-hardening rate is low for dilute concentrations below 0.5at%, increasing monotonically above 1at%. An increase in the strain-hardening rate above 1at% Zn coincides with a decreasing of tensile elongation, which indicates that solid solution softening of secondary slip is gradually offset by the solid solution hardening at high solid concentrations [19]. It is argued that solute in solid solutions below 0.5at% Zn hardens the basal planes but softens the prismatic and possibly

pyramidal planes. Ductility of Mg-Zn alloys is largest at low and medium contents of Zn where the strain hardening is reduced. The effect is associated with increased activity of prismatic slip for lower strain and possibly pyramidal slip at larger strains above 10%.

The solution strengthening for AZ91D alloy (σ_{ss}), calculated as a difference between pure Mg with the same grain size equals [15]:

$$\sigma_{ss} \cong k_s c^{2/3} \tag{1.8}$$

where:

k_s–constant;
c–atom concentration.

According to formula (1.8), for high pressure die cast AZ91D with about 67% of Al atoms in solution and the rest in $Mg_{17}Al_{12}$ phase, the contribution of solid solution to the total strength was estimated as 60 MPa.

1.4.3.3 Particle Dispersion Strengthening

Magnesium alloys typically represent at least a two-phase structure where dispersed precipitates are surrounded by a matrix of Mg solid solution having single orientation. In such a case, the strengthening produced by the second phase particles is superimposed on effects from grain boundary and solid solution. The strengthening produced by finely dispersed particles within a matrix is called dispersion hardening. For identical volumes fractions and number of precipitates per unit volume, plate-shaped precipitates distributed on prismatic planes of magnesium matrix were most effective in dispersion strengthening [20].

The mean stress, σ_{disp}, due to the elastic $Mg_{17}Al_{12}$ particles within the Mg-Al matrix was described by the following equation [15] [21]:

$$\Delta\sigma_{disp} = 4\varphi\gamma\mu f\varepsilon^* \tag{1.9}$$

where:

γ is an accommodation factor, for disk-shaped particles within a matrix deforming by single slip equals to $\gamma = \frac{1}{2(1-\nu)}$ where ν is the Poisson's ratio,

φ is expressed by the relationship $\varphi = \frac{\mu^*}{(\mu^* - \Upsilon(\mu^* - \mu)}$

and μ is the shear modulus of matrix, estimated as 17.2 GPa, and μ^* is the shear modulus of dispersed particles, estimated as 24 GPa;
ε^* is the unrelaxed plastic strain;
f is a volume fraction of the dispersed phase.

Based on the formula (1.9), the particle dispersion strengthening within die cast AZ91D alloy is estimated for 5.4 MPa. This is less than 5% of total strengthening, estimated for grain boundaries and solid solution effects.

1.5 Alloys

The major distinction line separates magnesium alloys in terms of the method used for component manufacturing into cast and wrought. Both groups have subdivisions: where cast alloys are further divided into sand cast, permanent mold cast and die cast. Within the wrought group the rolled, extruded and forged alloys are distinguished. Finally, depending on the service conditions, alloys are classified as general purpose, high ductility and high temperature grades.

1.5.1 Designations

Of a number of designations used in various countries, the most frequently recognized internationally is that of the American Society for Testing and Materials (ASTM). The method is a four part letter-number system expressed as follows:

(i) the two first letters specify the principal alloying elements in order of reduced content, where: A–aluminum, B–bismuth, C–copper, D–cadmium, E–rare earth, F–iron, H–thorium, K–zirconium, L–lithium, M–manganese, N–nickel, P–lead, Q–silver, R–chromium, S–silicon, T–tin, W–yttrium, Y–antimony, Z–zinc;
(ii) the two next numbers specify the rounded-off percentages of the two principal alloying elements arranged in the same order as the first letters;
(iii) a letter that allows a distinction between alloys of the same base chemistry;
(iv) a letter followed by a number, which indicate the condition or temper where:
- F–as fabricated,
- O–annealed of wrought products,
- H–strain hardened (H1 plus one or more digits mean strain hardened only; H2 plus one or more digits mean strain hardened and then partially annealed; H3 plus one or more digits mean strain hardened and then stabilized);
- T–thermally treated other than F, O and H; it is followed by a number indicating the specific temper. Further details are provided in the section describing the heat treatment of alloys.

1.5.2 Casting Alloys

Magnesium cast alloys are divided into two groups: sand cast alloys with fine grain structure due to small additions of zirconium and die cast alloys with Al as the major alloying addition. The growing importance of thin-wall casting exerts pressure on alloys with high fluidity. Therefore, these alloys are presented here as a separate group along with the present trends in their development. The major alloy systems, and the nominal chemistries of individual grades along with their key features, are summarized in Table 1.7.

Table 1.7 Classification and nominal chemistries of cast magnesium alloys. All values in weight %. RE: rare earth mischmetal, which usually consists of Ce, La, Nd and Pr. Data from [24], [25], [96], Noranda, Hydro Magnesium, Magnesium Electron, Australian Magnesium Technology

Alloy group	Alloy grade	Al	Mn	Zr	Zn	Other	Solidus–Liquidus °C	Key characteristics
Sand and permanent mold casting								
Mg–Mn–Al	AM100A	10	0.1				463–595	Pressure tight, weldable
Mg–Mn–Al–Zn	AZ63A	6	0.15		3		455–610	Balanced strength and toughness at room temperature
	AZ81A	7.6	0.13		0.7		490–610	Good strength and excellent ductility
	AZ91C	8.7	0.13		0.7		470–595	General purpose alloy
	AZ92A	9	0.1		2		445–595	High strength, pressure tight
Mg–Mn–Zn–Cu	ZC63A		0.25		6	2.7Cu	465–635	Good castability, pressure tight, heat treatment required
Mg–Zr	K1A to F			0.7			650–650	High damping capacity, low thermal strength
Mg–Zn–Zr	ZK51A			0.7	4.6		560–640	Highest yield strength, possibility of casting complicated shapes
	ZK61A			0.7	6		530–635	Increased yield strength compared to ZK51
Mg–Zn–Zr–RE	ZE41A			0.7	4.2	1.2RE	525–645	Elevated temperature application, medium strength
	ZE63A			0.7	5.8	2.6RE	510–635	Thin wall castings
	EZ33A			0.6	2.7	3.3RE	545–645	Good strength and stability at elevated temperatures; rather difficult to cast
Mg–Au–Zr	EQ21A			0.7		1.5Ag	540–640	Creep resistance and yield strength up to 200 °C
	QE22A			0.7		2.5Ag	550–645	Good creep resistance up to 200 °C, high tensile strength

Mg–Zr–Y–RE	WE43A			0.7		4.0Y, 3.4RE	540–640	Good creep resistance up to 250 °C, good corrosion resistance
	WE54A			0.7		5.2Y, 3.0RE	545–640	High strength at elevated temperatures
Obsolete with thorium								
Mg–Au–Zr–Th	QH21A			0.7		2.5Ag, 1.0Th	535–640	Creep resistance up to 250 °C, good yield strength at high temperatures
Mg–Th–Zr	HK31A			0.7		3.3Th	590–650	Sand castings with high strength for use up to 350 °C
Mg–Th–Zr–Zn	HZ32A			0.7	2.1	3.3Th	550–650	Sand castings with moderate strength above 200 °C
	ZH62A			0.7	5.7	1.8	520–630	Very high yield strength, complex shape castings
Die casting								
Mg–Al–Zn–Mn	AZ91A, B, D, E	9	0.17		0.7		470–595	Excellent castability, good strength
Mg–Al–Mn	AM20	2.0	0.2				Liquidus 638	High ductility and impact strength
	AM50A	4.9	0.26				565–620	Excellent ductility and energy absorption
	AM60A, B	6.0	0.13				565–615	Good ductility-strength combination
Mg–Al–Si–Mn	AS21	2.2	0.2			1.0Si	Liquidus 632	Good creep resistance up to 150 °C
	AS41	4.2	0.3			1.0	595–617	Lower creep resistance than AS21 but higher strength at room temperature and better castability, automotive applications
Mg–Al–Mn–RE	AE42	4.0	0.1			2.5RE	594–625	Good strength and creep resistance up to 150 °C
	AE63	6.0				3.0RE		Better castability than AE42
Mg–Al–Sr	AJ52	5.2	0.5			2Sr	512–616	Good creep resistance up to 150-170 °C
	AJ62	6	0.5			2Sr	515–612	Better die castability than AJ52

(continued)

Table 1.7 (continued)

Alloy group	Alloy grade	Al	Mn	Zr	Zn	Other	Solidus–Liquidus °C	Key characteristics
Mg–RE	MEZ		0.3		0.35	2.5 RE	640–645	Good creep resistance up to 175 °C under load of 60 MPa; low ductility at room temperature
Thin-wall casting-High-fluidity								
Mg–Al–Zn	AZ10.1	10	0.2		1			High fluidity, moderate ductility
	AZ11.1	11	0.2		1			Excellent fluidity, lower ductility than AZ10.1
Mg–Al–Zn Sn	Mg12Al1Zn5Sn	12			1	5Sn	425–567	High fluidity, strength compared to AZ91
	Mg12Al3Zn5Sn	12			3	5Sn	411–556	High fluidity, room temperature strength of 300 MPa
Mg-Zn-Al	AM-lite	Chemistry not disclosed					330–585	Excellent fluidity, good electro-plating capabilities

1.5.2.1 Gravity Cast Alloys

The first group consists of eleven major systems with over twenty commercial chemistries. Three systems containing thorium are obsolete due to its hazardous radiation features. The major challenges include development of alloys well suited to the permanent mold process using a steel mold since even alloys designed for sand casting create problems. Moreover, non-reactive mold coatings are required to reduce a corrosive attack of molten magnesium alloy. According to recent experiments, low-pressure permanent mold casting can accelerate structural magnesium market growth since it allows casting magnesium components not feasible by other manufacturing techniques. While applying AM50 alloy to the front cradle of an automobile, high mechanical properties were achieved due to controlled solidification and tranquil mold fill [22]. The technique can incorporate internal cores allowing the casting of complex shapes. A gravity filling permanent mold casting exhibited an influence of the grain refinement on castability of alloys AZ91 and AM50. A trend was discovered that a reduction in grain size led to an increase in the level of internal porosity. Alloy AZ91, with grain refined by strontium, showed a higher level of porosity than AM50 with larger grains where strontium additions were not effective [23].

1.5.2.2 Die Cast Alloys

The commercial die casting alloys consist of five major systems with over fifteen individual chemistries. The three traditional systems of AZ, AM and AS were extended by AE and A–Sr groups. Two first systems of AZ and AM represent over 60% and 35% consumption, respectively, with the AS, AE and A–Sr together having around 5% of the market. The application of HK group (Mg–Th–Zn–Zr), with stable properties up to 350 °C, has to be stopped due to the radioactivity of Th.

1.5.2.3 Die Cast Alloys with High Fluidity

Thin wall applications, representing the majority of present injection molding, require alloys with high fluidity. The die casting alloy AZ91D is the present workhorse, representing the predominant volume of consumption by the thin-wall market. Since the alloy was designed a long time ago for general purposes, its application for thinner and lighter components, combined with a high quality surface finish, may not be optimal, causing surface defects and reducing the yield of production. There is a quest, therefore, for alloys that better suit this specific niche market. At present, the three major groups of alloys are promoted worldwide:

(i) Mg–Al–Zn alloys with increased content of Al;
(ii) Mg–Al–Zn–Sn alloys with increased contents of Al and Zn;
(iii) Mg–Zn–Al alloys with increased content of Zn.

The first group benefits from the fact that aluminum decreases solidus and liquidus temperatures and increases latent heat thus improving fluidity [24] (Fig. 1.20).

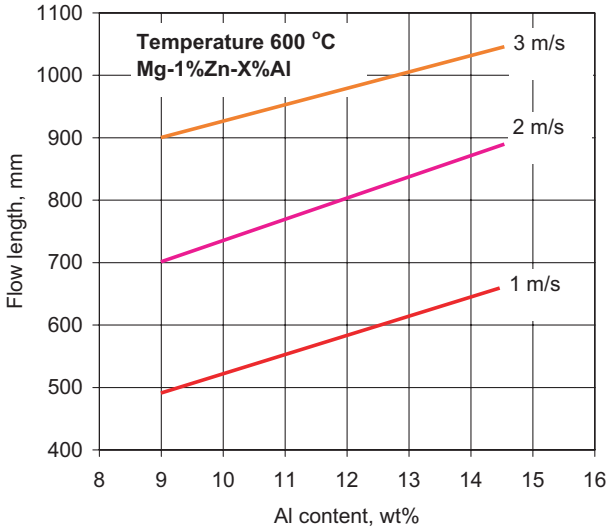

Fig. 1.20 The flow length of Mg–1%Zn–X%Al alloys with various contents of Al. A spiral mold with a flow path 2 mm thick and 15 mm wide [24]

At the same time it increases alloy strength at the expense of ductility. At aluminum contents exceeding roughly 13%, Mg–Al alloys become extremely brittle. In all alloys, the content of silicon is too low to have an impact on fluidity since to avoid deterioration in mechanical properties its content is kept below 1.4%. Although zinc also lowers the solidus-liquidus range, its content is kept below 0.8% to prevent casting cracks.

The major difference in Mg–Al–Zn–Sn alloys with increased contents of Al and Zn, as compared to the first group, is a substantially wider range for aluminum, zinc and a new addition of tin. The aluminum range suggested is from 12% to 20%, zinc content from 0.1% to 10% and tin from 0.1% to 15%. For commercial implementations, however, two alloys are proposed: Mg12Al1Zn5Sn and Mg12Al3Zn5Sn with aluminum content of 12% [25]. The Mg12Al1Zn5Sn alloy has a melting range of 425–567 °C, strength similar to AZ91D but elongation of only 1.5% which counts for 50% of the AZ91D level. An increased content of zinc to 3%, as it is in Mg12Al3Zn5Sn, reduces the melting range to 411 °C–556 °C and increases strength to 300 MPa. Elongation remains, however, at the very low level of 1.6%. The fluidity characteristics of both alloys, as compared to AZ91D, are shown in Fig. 1.21.

The third group of Mg–Al–Zn with increased Zn content, represented by the AM–lite, benefits from the influence of Zn. The AM–lite does not contain rare earth or other exotic elements [26]. Having a density of 2.02 g/cm^3, the alloy is half way between typical Mg based alloys and Al. The AM–lite has a better die castability than AZ91D and a much better surface finish. It is claimed that the alloy is particularly

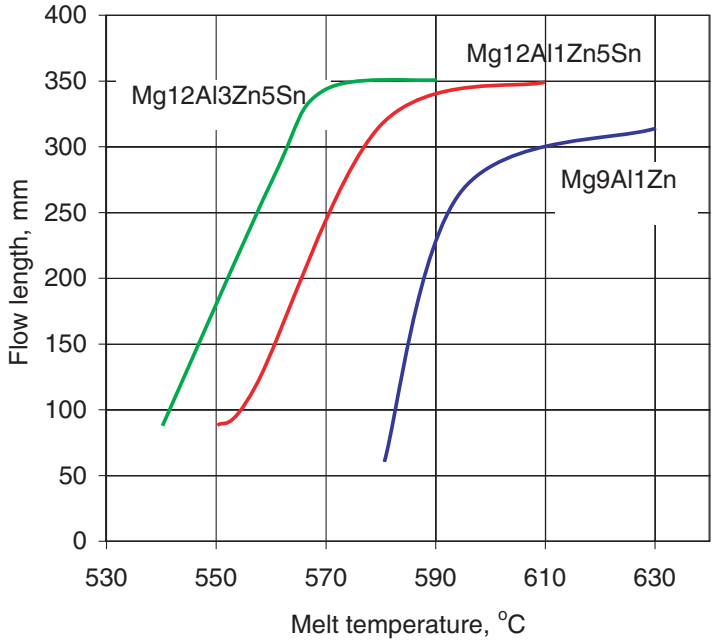

Fig. 1.21 The flow length of Mg12Al3Zn5Sn and Mg12Al1Zn5Sn alloys compared to Mg9Al1Zn. Injection molding, spiral mold with a flow channel of 10x1 mm [25]

well suited for decoratively finished products. The electroplating capabilities of the new alloy are better than AZ91 or Al and are rather similar to that of zinc.

1.5.3 Wrought Alloys

Wrought alloys account for 10-15% of all magnesium alloys due to their poor workability. The hot forming processes include rolling, extrusion and forging and are conducted at temperatures higher than 300 °C–350 °C but below 500 °C. The following cold work forming is limited to prevent cracking. There are seven commercial systems with approximately fifteen individual chemistries. Two systems containing thorium are obsolete. Typical extrusion grades include AZ80, ZK21, ZK60, ZC71, ZM21, ZM61 and AZ21X1. Grades such as AZ31, ZE10, M1A, ZM21, HM21, HK31 or ZK31 are used for rolling. For forging, AZ80, ZK60, AZ61 and HM21 are mainly used. Selected alloy systems, nominal chemistries of alloys along with their key features are summarized in Table 1.8. Due to higher cost of wrought alloys compared to die cast grades the use of the former is limited.

Table 1.8 Classification and nominal chemistries of wrought magnesium alloys. All values in weight %. Based on [96], [97], Magnesium Electron, Hydro Magnesium

Alloy group	Alloy grade	Al	Mn	Zr	Zn	Other	Solidus–liquidus, °C	Key characteristics
Mg–Mn	M1A		1.2				648–649	Wrought products with moderate mechanical properties, not heat treatable, mainly rolling
Mg–Mn–Zn	ZM21		1.0		2.0			Good forgability, medium strength, for rolling
Mg–Mn–Zn–Cu	ZC71		1.0		6.5	1.2Cu	465–600	Medium cost extrusion alloy with good mechanical properties and high elongation
Mg–Mn–Al–Zn	AZ10A	1.2	0.2		0.4		630–645	Low cost extrusion alloy with moderate strength and high elongation
	AZ21X1	2.0	0.15		1.2		Liquidus 645	Extrusions
	AZ31	3.0	0.3		1.0		605–630	General purpose alloy with moderate strength
	AZ61A	6.5	0.3		1.0		525–620	General purpose extrusions with good properties and moderate cost
	AZ80A	8.5	0.12		0.5		490–610	Extruded products and press forgings, heat treatable
Mg–Zn–Zr	ZK21A			0.45	2.3		626–642	Moderate strength extrusion alloy with good weldability
	ZK40A			0.45	4.0			High yield extrusion alloy, lower strength than ZK60
	ZK60A			0.45	5.5		520–635	Extruded products and press forgings with high strength and good ductility
Mg–Y–RE	WE43			0.7		4.0Y, 3.4RE	540–640	High temperature creep resistance up to 300 °C, long term exposure up to 200 °C

	WE54		0.7	5.2Y, 3.0RE	545–640	High strength, fully heat treatable, application to 300 °C, highly isotropic properties
Obsolete with Thorium						
Mg–Th–Zr	HK31A		0.6	3Th	590–650	Sheets and plates with excellent formability and high strength up to 315 °C
Mg–Th–Mn	HM21A	1.0		2Th	605–650	Sheets, plates, forgings applicable up to 340 °C
	HM31A	1.2		3Th	605–650	Extruded bars, rods, shapes for elevated temperature applications, moderate strength

1.5.4 Alloys Manufactured by Non-Conventional Methods

In addition to conventional metallurgy methods, magnesium alloys can be created by a number of other techniques including:

(i) vapor deposition;
(ii) electrodeposition;
(iii) mechanical milling;
(iv) severe plastic deformation (equal channel angular pressing–ECAP, equal channel angular extrusion– ECAE or torsion straining);
(v) rapid solidification (roller melt spinning, copper mold casting, thermal spray).

While some non-conventional alloys have unique chemistries, others are chemically the same as those manufactured by conventional metallurgy. Their properties are, however, unique due to microstructural features inherited during their generation.

1.5.4.1 Amorphous Alloys (Metallic Glasses)

In polycrystalline materials, the individual crystals, called grains, are separated by grain boundaries which are of an amorphous nature. Thus, the smaller the grain size the larger the fraction of grain boundaries, i.e., amorphous factor. The high contribution of amorphous state is, therefore, in nanocrystalline materials. Ultimately, when crystalline grains disappear completely, the amorphous factor represents 100% of the material volume. Due to the amorphous state, alloys exhibit very high strength, specific strength and elastic strain limit along with unusual combinations of other properties, e.g., simultaneously high strength and toughness. The latter is exactly opposite to the same relationship seen in a crystalline state.

The first amorphous metals were discovered in 1934 in Germany (Kramer, vapor deposition) and in 1957 in the United States [27]. The peak research interest was between 1975 and 1985, shifting later towards nanocrystalline structures. The first metallic glasses required an extremely high cooling rate of millions of degrees per second and as such had a form of thin ribbons, flakes or wires. Further developments, mainly by designing special compositions e.g., Pd–Cu–Si, Pd–Ni–P, Al–Y–Cu, Fe,Co,Ni, Zr–Ti–Cu–Ni–Be or Zr–Cu–Ni–Al systems, allowed a reduction in cooling rate, so bulk forms could be manufactured. Generally, the amorphous materials have complex stechiometry. During the most recent two decades a number of alloy families were developed which exhibit resistance to crystallization and readily form glass or vitrify to form bulk amorphous alloys or bulk metallic glasses. Those ones involving a Mg base are listed in Table 1.9.

The majority of research on magnesium based amorphous alloys was conducted for Mg-M–Ln system where M is the nickel or copper and Ln is a lanthanide element. In fact, the first Mg-based bulk metallic glasses were obtained for $Mg_{65}Cu_{25}Y_{10}$ chemistry [28, 29]. These alloys showed high compressive fracture strength up to 800 MPa. Moreover, the specific strength of 3×10^5 Nm/kg is twice that of crystalline Mg based alloys [30]. While tested in alkaline electrolytes, the $Mg_{65}Cu_{25}Y_{10}$

Table 1.9 The characteristics of magnesium based amorphous alloys

Composition	Form	Production method	Key properties	References
$Mg_{85}Zn_{12}Ce_3$	Ribbon	Rapid solidification	High tensile strength, significant plastic deformation	[29]
$Mg_{76.5}Ni_{23.5}$	Ribbon	Melt spinning	High strength, low ductility	[32]
$Mg_{65}Cu_{25}Y_{10}$	Bulk	Melt spinning	Compressive fracture strength of 800 MPa	[28]
$Mg_{87.5}Cu_5Y_{7.5}$				[88]
$Mg_{65}Cu_{20}Ag_5Y_{10}$	Bulk	Rapid solidification	Ag additions enhance glass forming abilities but reduces thermal stability of glass	[31]
$Mg_{65}Cu_{15}Ag_{10}Y_{10}$				
$Mg_{65}Cu_{10}Ag_{15}Y_{10}$				
$Mg_{65}Cu_{7.5}Ni_{7.5}Zn_5Ag_5Y_{10}$	4 mm thick strip	Copper mold casting		[33, 34]
$Mg_{70}Al_{20}Ca_{10}$	Bulk	Extrusion of atomized amorphous powders	Maximum strength of 600 MPa	[89]

alloy shows the lowest corrosion rate as compared to the crystalline state of the same chemistry and pure Mg. This is due to the highest tendency to form protective surface layers upon anodic polarization, caused by the effect of an alloying element and the structural homogeneity. It was revealed that partial substitution of Cu by Ag to form $Mg_{65}Cu_{20}Ag_5Y_{10}$, $Mg_{65}Cu_{15}Ag_{10}Y_{10}$ or $Mg_{65}Cu_{10}Ag_{15}Y_{10}$, improved the glass-forming ability of $Mg_{65}Cu_{25}Y_{10}$ alloys because of a significant reduction in crystal growth rate. At the same time the Ag additions reduced their thermal stability by allowing growth on quenched-on nuclei [31].

The amorphous ribbons were produced from the $Mg_{76.5}Ni_{23.5}$ binary compositions [32]. When tested at temperatures below 125 °C, alloys showed high strength and low ductility. Heating up to 150 °C caused crystallization of Mg and metastable $Mg_{5.5}Ni$ phase, which increases yield and causes embrittlement of the alloy. Above 150 °C, the alloy reaches maximum elongation of 35% at 200 °C due to the presence of an equilibrium between Mg and Mg_2Ni phases. The yield stress decreases with the test temperature. Another alloy is represented by $Mg_{85}Zn_{12}Ce_3$, obtained in a ribbon form after rapid solidification [29]. This alloy has a mixed structure of fine magnesium particles supersaturated with Zn and Ce in a crystalline state and an amorphous matrix. The high strength value in a quenched condition of 665 MPa is further increased to 930 MPa after short-term annealing at 110 °C. In another development, TiB_2 particles were used to reinforce the bulk metallic glasses $Mg_{65}Cu_{7.5}Ni_{7.5}Zn_5Ag_5Y_{10}$ [33]. In fact, the alloy matrix was produced earlier but always failed before yielding with irreproducible strength below 650 MPa [34]. The composite created by copper

mold casting maintained very high specific strength over 3.5×10^5 Nmkg^{-1}. The tensile strength was three times larger than for die cast AZ91C alloy.

It is clear that amorphous structure is thermally unstable and transforms to a crystalline state after heating. The amorphous magnesium alloys exhibit high thermal stability and the crystallization temperature may reach 0.64 of the melting temperature. Of several factors, a content of solute elements tends to increase the crystallization temperature.

1.6 Selected Properties of Alloys

Although the specific strength is emphasized as the key feature of magnesium alloys, there are also other properties that make them attractive for structural applications. The major properties are characterized below.

1.6.1 Deformation Mechanisms

Deformation of magnesium at low homologous temperatures occurs by crystallographic slip and twinning. Thus interaction between these two deformation mechanisms affects the resultant mechanical properties. Due to its hexagonal crystal structure and low tendency to twinning, magnesium and its alloys show a very limited forming ability at room temperature.

1.6.1.1 Slip

The common mechanism of plastic deformation is by the sliding of blocks of the crystal over one another. Sliding takes place on definite crystallographic planes and along specific directions, which together constitute the slip system. Generally the slip plane is characterized by the greatest atomic density while the slip direction is the closest-packed direction within this plane. For polycrystalline materials, cooperative displacements across grain boundary have to be matched so that the grains can deform in concert without cracking. To achieve this, five independent slip systems are required. For an independent slip system the slip displacement cannot be duplicated by a combination of displacements on other slip systems. Elements of crystallography, required to understand the description of crystal geometry, can be found in related handbooks [35].

The slip systems for hcp magnesium lattice are characterized in Table 1.10 and in Fig. 1.22a–c. Crystallographic slip in hcp single crystals is commonly observed on the basal $\{0001\}\langle 11\bar{2}0\rangle$ and prismatic $\{10\bar{1}0\}\ \langle 11\bar{2}0\rangle$ systems. The activation of a pyramidal slip system $\{10\bar{1}0\}\ \langle 11\bar{2}0\rangle$ in polycrystalline structures takes place due to large stresses generated within misoriented grain boundary regions. For magnesium

Table 1.10 Slip systems in hexagonal close packed structure of magnesium

Name of slip system	Slip plane	Slip direction	Number of non-parallel planes	Number of slip directions per plane	Number of geometrical slip systems	Number of independent slip systems
Basal	$\{0001\}$	$\langle 11\bar{2}0\rangle$	1	3	3	2
Prismatic	$\{10\bar{1}0\}$	$\langle 11\bar{2}0\rangle$	3	1	3	2
Pyramidal	$\{10\bar{1}1\}$	$\langle 11\bar{2}0\rangle$	6	1	6	4

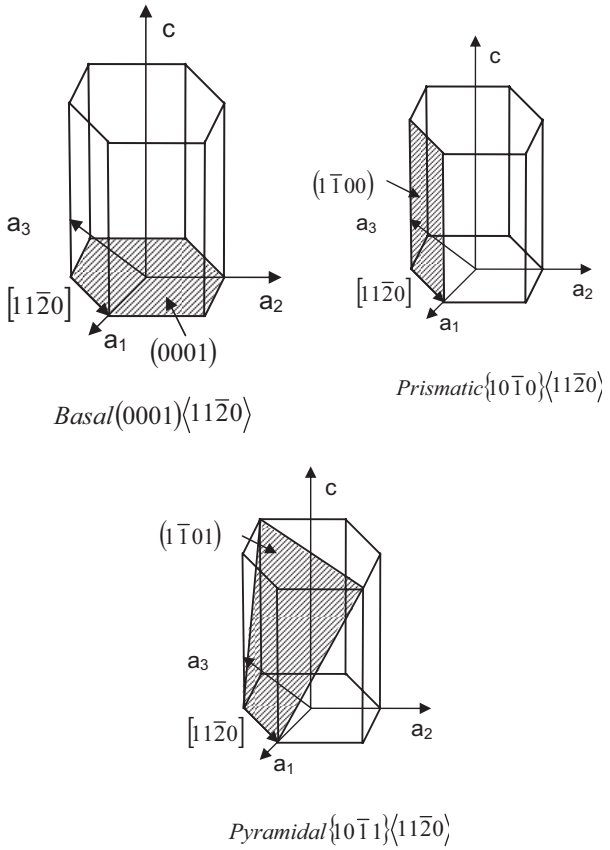

Fig. 1.22 The slip systems in hexagonal close packed system of magnesium: **a** basal system (0001) $\langle 11\bar{2}0\rangle$; **b** prismatic system $\{10\bar{1}0\}\langle 11\bar{2}0\rangle$ **c** pyramidal system $\{10\bar{1}1\}\langle 11\bar{2}0\rangle$ [37]

and its alloys the main deformation mode is through the basal slip. Although the prismatic and pyramidal slip is also observed, their critical resolved shear stress is about 100-fold greater than that of the basal slip [36].

Since basal slip provides only two independent slip systems, it adversely affects the conditions of simultaneous deformation of grains in a polycrystalline structure.

According to recent findings, crystallographic slip and twinning in Mg are insufficient to accommodate all possible imposed deformations on polycrystalline aggregates. It appears that phenomena associated with relative sliding and separation between neighboring grains become involved [37].

1.6.1.2 Twinning

Twinning represents the second mechanism by which a metal deforms. It is of importance for systems where deformation by slip is difficult. During mechanical twinning, there is no change in crystal structure but only a change in orientation of the crystal lattice. Deformation twinning relies on simple shear and is accompanied by the shape change. In contrast to slip, atoms move only a fraction of an interatomic distance relative to each other. When a single crystal is sheared by twinning, the sheared section preserves the structure and symmetry of the original crystal. The lattice of the twin is a mirror image of the parent lattice, and the plane of symmetry between the two portions is called the twinning plane.

Materials with closed-packed hexagonal lattices exhibit many types of twinning; however, for all hexagonal metals at low homologous temperatures, deformation twinning on $\{10\bar{1}2\}$ planes is the dominant mechanism, which allows for inelastic shape changes in the c-direction. For materials with $c/a < \sqrt{3}$, as is the case for magnesium with $c/a = 1.623$ (Table 1.5), the direction of shear is $[\bar{1}011]$ and the twinning occurs under tension parallel to the c-axis [37]. The schematic of twinning deformation is shown in Fig. 1.23. For magnesium the compressive stress applied parallel to the basal plane favors twinning whereas tensile stress with similar orientation does not produce this effect.

During a practical deformation, slip and twinning coexist and an example for Mg–Zn alloy is shown in Fig. 1.24. At low and intermediate stress-strain ranges, twinning accompanies first the basal then the basal and prismatic slips. At high stress-strain range, twinning is absent and deformation proceeds through basal, prismatic and pyramidal slips. The influence of temperature is shown in Fig. 1.25. While increasing

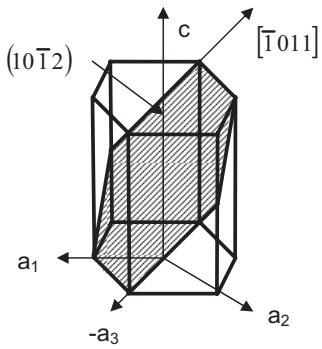

Fig. 1.23 The $\{10\bar{1}2\}\langle\bar{1}011\rangle$ tensile twinning system for magnesium [37]

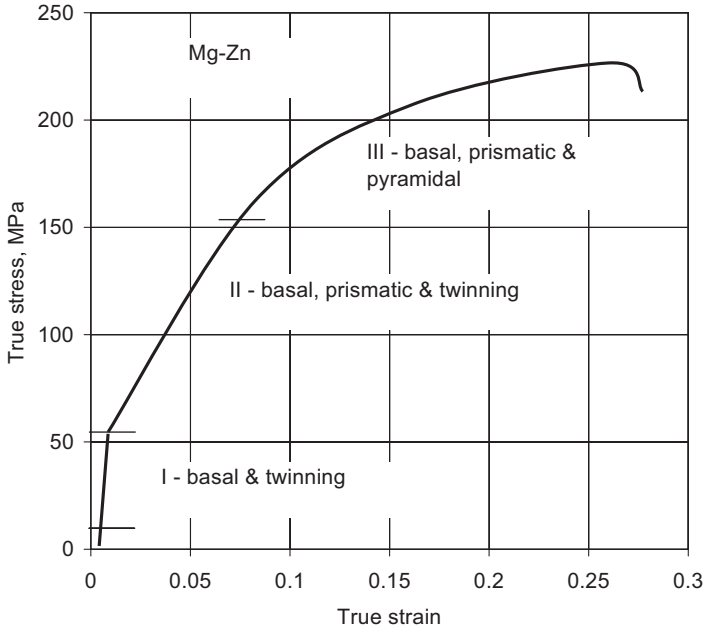

Fig. 1.24 Stages of tensile deformation modes in Mg–Zn alloys [19]

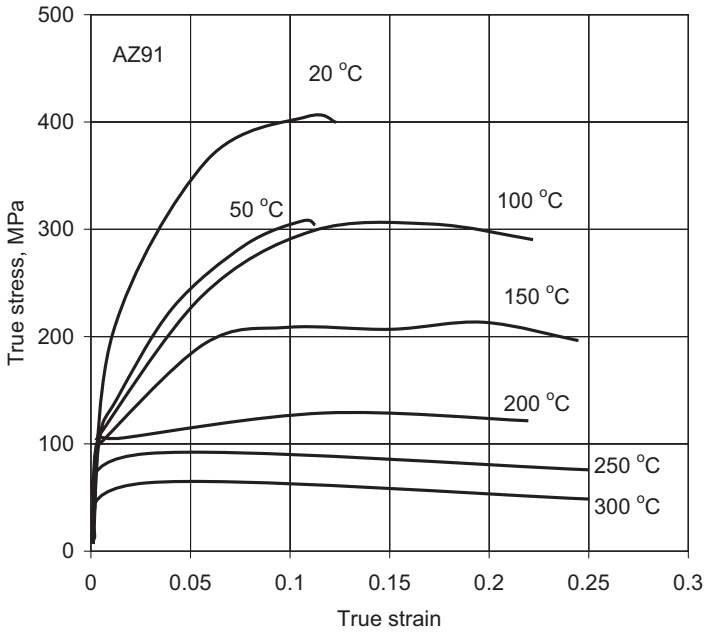

Fig. 1.25 The compression deformation curves of AZ91 alloy at various temperatures [86]

temperature, three deformation stages become less distinct, and above 150 °C they disappear completely. An example of Mg–9Al–1Zn microstructure with well-developed twins is shown in Fig. 1.26. The αMg grains, divided sometimes by sub-boundaries, are surrounded by blocky $Mg_{17}Al_{12}$ and eutectics of Mg–$Mg_{17}Al_{12}$. Twin colonies are more frequently present close to the eutectics than to the grain centers.

1.6.1.3 Texture Effect on Plastic Deformation

Plastic deformation of hexagonal metals such as magnesium is strongly influenced by the crystallographic texture. For pure Mg and AZ31 alloy a pronounced

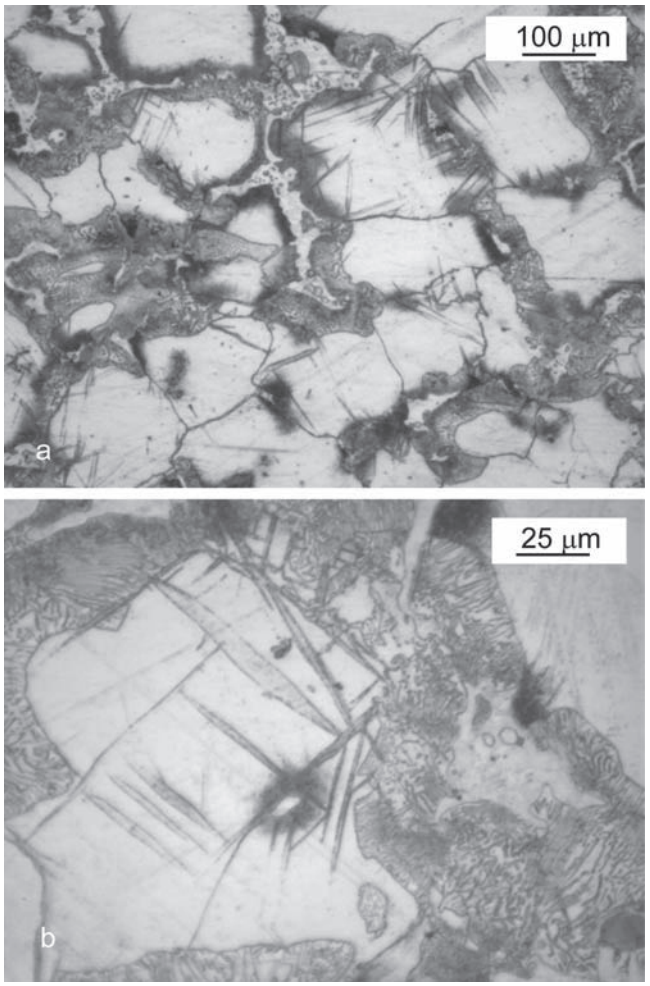

Fig. 1.26 The microstructure of Mg-9Al–1Zn alloy with deformation twins

basal texture reduces formability during plane-strain compression within a channel-die at 100 °C and 200 °C [38]. The deformation becomes inhomogeneous and is dominated by formation of shear bands. When the initial texture is selected so that basal planes are aligned parallel to the compression direction, non-basal (possibly prismatic) slip mechanisms are activated, leading to a more homogeneous deformation of large fracture strains and improved ductility at temperatures as low as 100 °C.

1.6.2 Superplastic Deformation

Superplasticity is defined as a state in which a solid crystalline material is deformed well beyond its typical breaking point, often exceeding 1000% during tension. Such a state is achieved in some fine-grained metals and ceramics at temperatures of typically half that of the absolute melting point. Thus requirements for a material to become superplastic include a fine grain size, typically below 10 μm, and a fine dispersion of thermally stable particles that act to pin the grain boundaries and maintain the fine grain structure at the high temperatures. The materials must also have a high strain rate sensitivity (>0.5) which prevents localized deformation at a reduced cross-section (necking). At the macroscopic scale, a superplastically deformed material experiences uniform deformation, rather than localized necking, preceeding fracture. Another cause of premature failure, namely a formation of internal cavities, is also inhibited.

Superplasticity has its origin in Russia where Bochvar and Sviderskaya, introduced in 1945 the term "sverhplastichnost" (ultrahigh plasticity) based on their studies of aluminum–zinc alloys [39]. They showed that a metallic material, when processed properly, could be stretched like molten glass at temperatures substantially lower than the melting level. Superplasticity in magnesium alloys was first reported for binary systems with Ni, Cu and Al. Also commercial alloys Mg–1.8Mn–0.25Ce and ZK60 with fine grain structure exhibit superplastic behaviour [40] [41]. A possibility of achieving low-temperature superplasticity in the AZ31 alloy was confirmed through processing using a combination of extrusion and equal channel angular pressing (ECAP) [42]. Equal channel angular extrusion (ECAE) is a process in which large shear strains can be imparted with no macroscopic shape change. According to [43], fine grained material AZ91 processed by ECAE exhibits superplastic behavior at temperatures 175 °C and 200 °C, which is close to 0.5 T_m of the melting point of pure magnesium. The effect is related to the small grain size.

Grain boundary sliding is the dominant deformation mechanism of the superplastic flow [44]. The stress concentrations during superplastic deformation are located at ledges along grain boundaries as well as at triple junctions and have to be accommodated. It is accepted that the grain boundary sliding is accommodated by slip, which involves sequential steps of glide and climb. Therefore the rate controlling

process is related to the dislocation movement which, in turn, is controlled by diffusion. At temperatures of 0.4÷0.6 T_m, diffusion is controlled by grain boundary transport and above 0.7T_m by lattice transport.

1.6.3 Mechanical Properties

Magnesium alloys exhibit attractive mechanical properties. Despite the low yield stress, the strength to weight ratio is superior to other commonly used materials (Fig. 1.27). The examples of room temperature mechanical properties for a selection of cast and wrought alloys are shown in Table 1.11. While analyzing properties of wrought alloys, it should be remembered that magnesium, as other metals with hexagonal crystal structure, shows a pronounced anisotropy of mechanical properties after deformation, attributed to the crystallographic texture that develops. The properties of cast alloys are based on casting of test bars under controlled laboratory conditions. Thus complications may eventually arise from an intricate shape of components.

1.6.3.1 Alloy Integrity Effect on Mechanical Properties

For complex parts, the properties are closely related to the quality of the casting and in particular to its internal integrity. The microstructure of a casting contains a

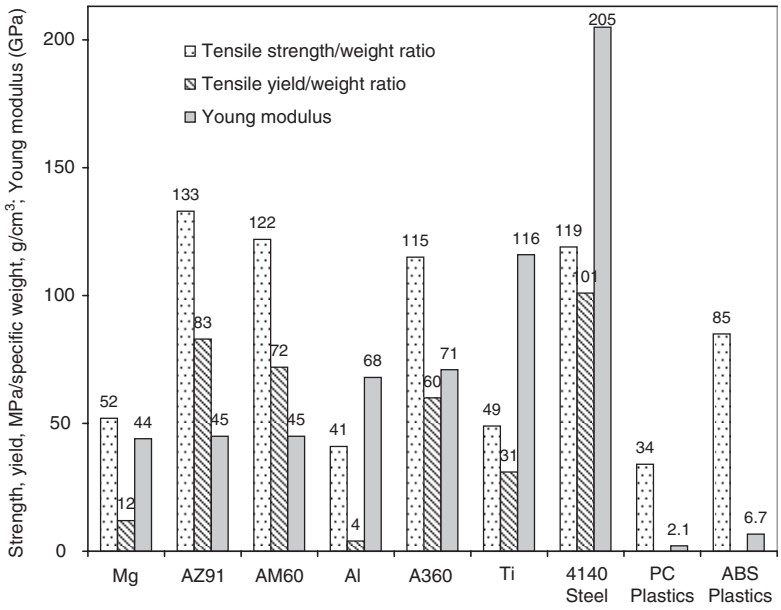

Fig. 1.27 A comparison of the strength to weight ratio and Young's modulus for two magnesium alloys and several other materials

Table 1.11 Room temperature properties of selected magnesium alloys. Data from: [96], [97], Noranda, Dead Sea Magnesium, Australian Magnesium Technology, Hydro Magnesium, Magnesium Elektron

		Specific density	UTS	Tensile YS	Compressive YS	Elongation	Hardness HB
Alloy grade	Temper	g/cm^3	MPa	MPa	MPa	%	
Sand and permanent mold							
AM100 A	F	1.83	150	83	83	2	53
AZ81A	T4	1.80	275	85	85	15	
AZ92A	F	1.83	170	100	100	3	
ZC63A	T6	1.87	210	125		4	
ZK61A	T6	1.83	310	195	195	10	70
ZE41	T5	1.82	208	140	140	3.5	62
ZE63A	T6	1.87	300	190	195	10	60–85
QE22A	T6	1.80	276	193	195	6	65–85
EZ33A	T5	1.80	160	110	110	3.5	50
Die cast							
AZ91	F	1.81	240	165	148	3	70
AM60	F	1.80	220	130		8	65
AM50	F	1.77	200	110	113	10	60
AM20	F	1.75	190	90	74	12	45
AS41	F	1.77	215	140	140	6	
AS21	F	1.76	175	110	106	9	55
AE42	F	1.79	230	145	103	10	60
AE44	F	1.82	245	142		10	62
AJ62	F	1.80	235	140		7	61
MRI 153M	F	1.82	250	170		6	72
MRI 230D	F	1.82	245	180		5	71
AM-lite	F	2.02	240	165	150	3.5	80 HB 90 HVN
Wrought							
M1A	rolled	1.77	240	180	76	7	48
ZM21	forged	1.80	200	124		9	
AZ21X1	extruded	1.77	240	130	130	9	
AZ31	extruded	1.77	250	180	97	15	49
AZ61	forged	1.80	300	220	125	12	55
AZ80	forged	1.80	330	230	170	12	
ZK21	rolled bar	1.80	260	195	135	4	
ZK40	extruded	1.83	275	250	140	4	
ZK60	extruded	1.83	340	260	230	11	80

certain amount of porosity resulting from shrinkage and gas evolution or entrapment during solidification. It was observed that shrinkage pores are topologically linked to gas pores. A number of studies have shown that there is a strong correlation between mechanical properties of cast magnesium alloys and their internal porosity. For ductile materials such as Mg alloys, the fracture strain and fracture stress dependence on an alloy's porosity can be predicted by the critical local strain model [45]. The model considers instability resulting from internal neck formation around an imperfection such as a pore [46].

The relationship between tensile ductility and porosity, measured by quantitative fractographic technique for AM50 alloy is shown in Fig. 1.28a [47]. A simple law power

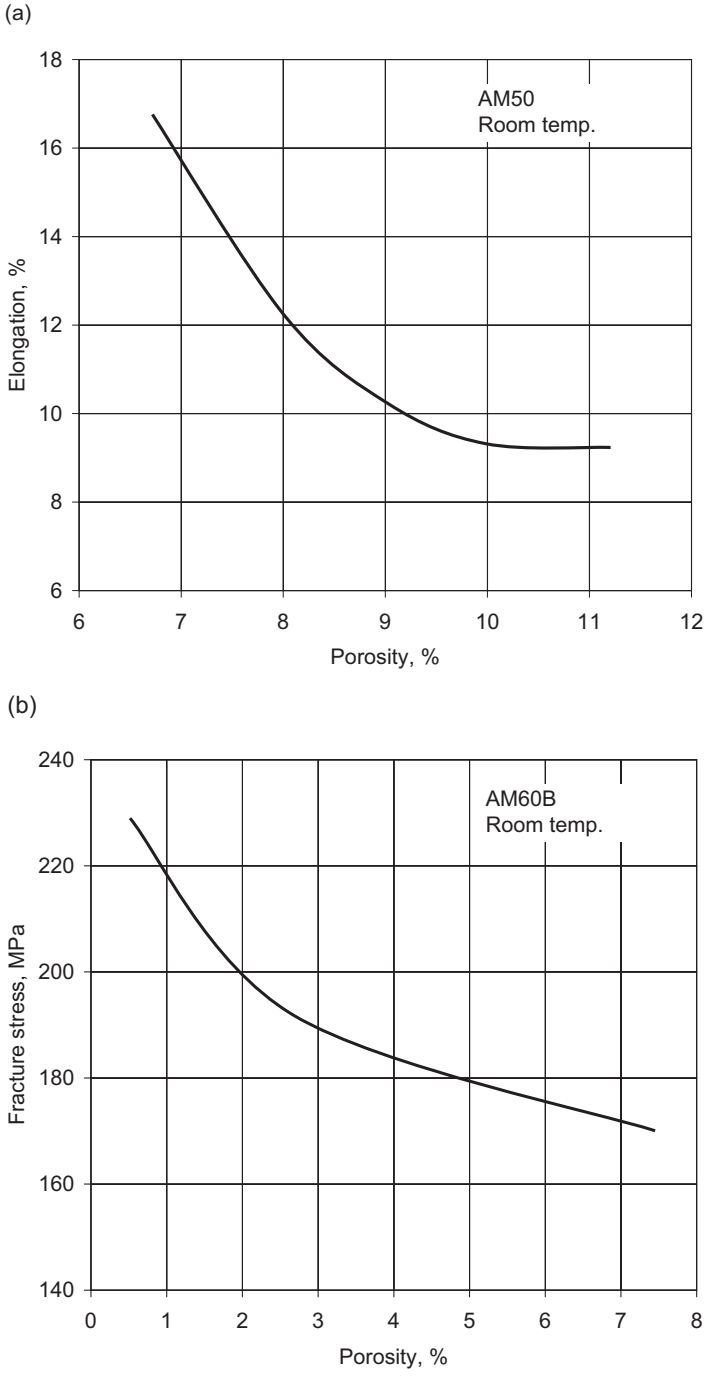

Fig. 1.28 The influence of porosity on mechanical properties for Mg–Al alloys: **a** tensile ductility of AM50 alloy tested at room temperature [47]; **b** the predicted and measured fracture stress as a function of the area fraction of porosity for AM60B [48]

equation correlates the tensile ductility and the area fraction of porosity detected on the fracture surface. Obviously, the fracture propagation path travels through individual and clustered pores. While considering the average volume fraction of porosity, no correlation with the tensile ductility was established. At higher temperatures the influence of porosity was diminished. Other data show that the tensile strength and ductility are mainly affected by the areal fraction of porosity and not the average volumetric porosity content measured by X-ray tomography (Fig. 1.28b) [48]. Thus, even a low fraction of porosity has a considerable effect on both the tensile fracture strain and stress.

1.6.4 Damping Capacity

A capacity for absorbing vibration energy and dissipating it in the form of heat is described as damping capacity. Damping is the term applied to any cause or effect that tends to reduce the amplitude of vibration whether it operates externally or is inherent in the vibrator itself. It has application for the attenuation of vibration and noise. Damping capacity of metals is usually measured from a vibration decay curve generated by the free vibration of a sample of the metal in a torsion pendulum. The damping capacity is generally independent of frequency but varies greatly with applied stress.

All metals and alloys exhibit some degree of damping capacity under the assumption that even at low stress no material is perfectly elastic. As a result, when the stress is applied repeatedly some energy is absorbed. For alloys there are several factors affecting damping:

(i) increasing alloying addition, particularly leading to generation of a second phase is detrimental;
(ii) wrought alloys have poorer damping capacity than castings;
(iii) a heat treatment increasing strength reduces damping.

Examples of damping capacity for several metals are shown in Fig. 1.29. Pure magnesium has substantially better damping capacity as compared to cast iron and aluminum. However, the damping capacity of very pure wrought magnesium is only half that measured for cast state (Fig. 1.30) [49]. For wrought magnesium, in turn, a sample orientation exerts significant effect. Accordingly, the damping for a single crystal of magnesium is highest when the basal plane of the crystal is inclined 45 degrees to the vibration direction [50].

1.6.5 EMI/RFI Shielding

The performance of any electronic device is affected by electromagnetic interference (EMI) and electrostatic discharge. A potential source of EMI is any circuit or device that carries an electrical current. EMI covers the frequency range from 1 Hz to 10^{22} Hz, which is generated by any circuit carrying electrical current. The radio

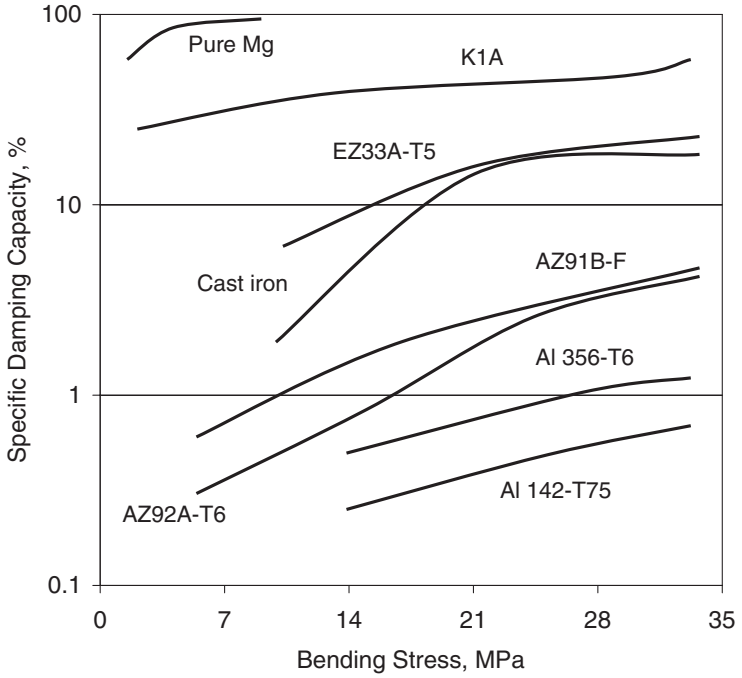

Fig. 1.29 The damping capacity of several sand cast alloys. Measurements were carried out by the cantilever beam method [49]

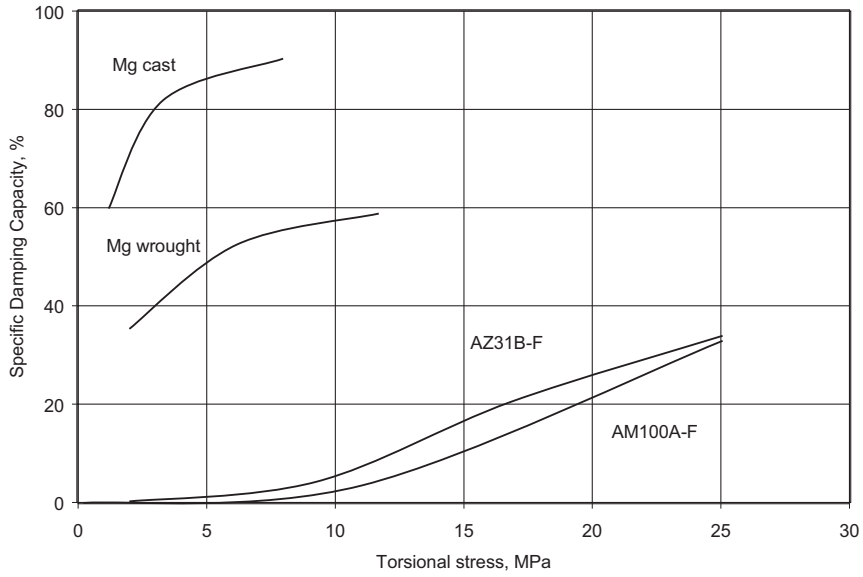

Fig. 1.30 The stress dependent damping capacity of Mg and Mg base alloys. Measurements were carried out by the torsion pendulum method. Extracted from [50]

interference frequency (RFI) is a type of EMI that covers a relatively small portion of the overall frequency from 10^3 Hz to 10^{10} Hz.

The amount of EMI shielding provided by a metal depends upon the nature and frequency of the radiation, the absorption and reflection components of the radiation, the conductivity and magnetic permeability of the metal and distance from the radiation source. While metals reflect and absorb EMI to a certain degree, plastics must rely on surface coating for reflection or incorporation of metal particles into interior enclosures to activate absorption. Magnesium provides advantages in EMI shielding over both plastics and alternative metals (Fig. 1.31). In the case of reflective shielding the weight-saving benefit of magnesium is valid for the entire frequency spectrum. For shielding by absorption, magnesium shows advantages at frequencies higher than 1MHz (Fig. 1.32). This is because as the frequency increases, the wall thickness required for a certain level of shielding effectiveness becomes smaller, reaching limitations in the metal fluidity and structural integrity of Al alloys, represented by A380 [51].

1.6.6 Heat Dissipation

A need for heat sinks is very common in electronic applications where aluminum is traditionally used. The ability of a material to dissipate heat under steady state

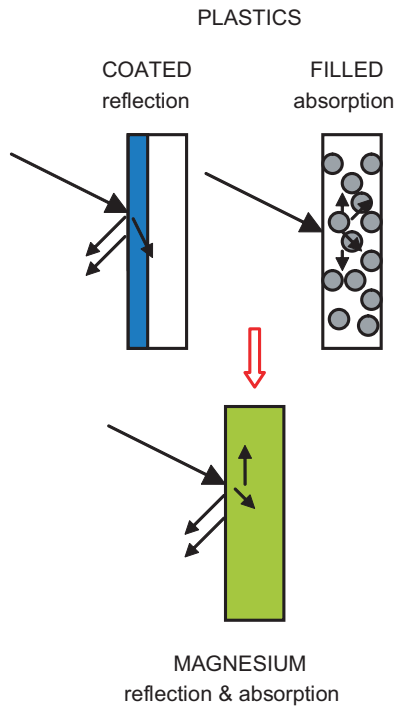

Fig. 1.31 The concept of EMI shielding in various materials: top left—plastics coated with metallic layer, protecting by reflection; top right—plastics filled with metallic particles—protecting by absorption; bottom: magnesium—protecting by reflection and absorption

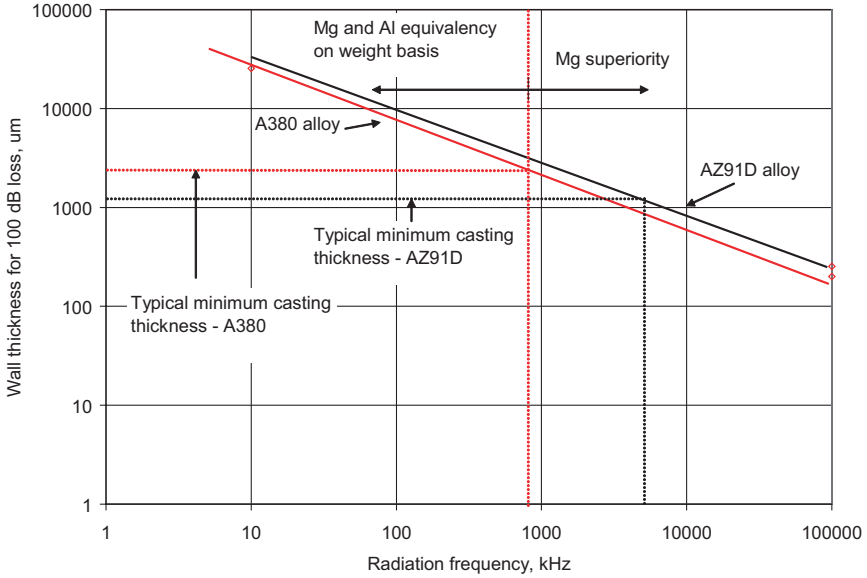

Fig. 1.32 The effect of frequency on the shielding thickness required to achieve 100 dB loss (Hydro Magnesium Technical Data)

conditions is determined by the lower thermal conductivity of Mg (see Table 1.5) than Al (210 W/m K for 6063 aged alloy). For transient conditions, thermal diffusivity, being similar for Mg and Al, is a controlling factor. For portable devices operating without fans under transient thermal conditions Mg dissipates heat at the same rate as Al. A lower specific density of Mg provides an advantage.

Both the thermal diffusivity and thermal conductivity depend on the content of alloying elements (Fig. 1.33). For a given chemistry, both parameters are affected by alloy microstructure, modified by the heat treatment. For a binary Mg-Al system, the solid solution of Al in Mg has lower conductivity than an alloy containing $Mg_{17}Al_{12}$ precipitates. Similar observations are reported for AM100 alloys after various thermal treatments [52].

1.7 Processing Techniques

Magnesium alloy components can be manufactured by all the conventional techniques including casting, forging, extruding and rolling. The choice of a method depends upon factors such as the configuration of the design, the application, the properties required, the total number of parts and the castability or formability of the alloy. In recent years, alternative techniques have been commercialized to improve the overall effectiveness of net shape forming. The most distinct technique of semisolid forming will be discussed in Chap. 2.

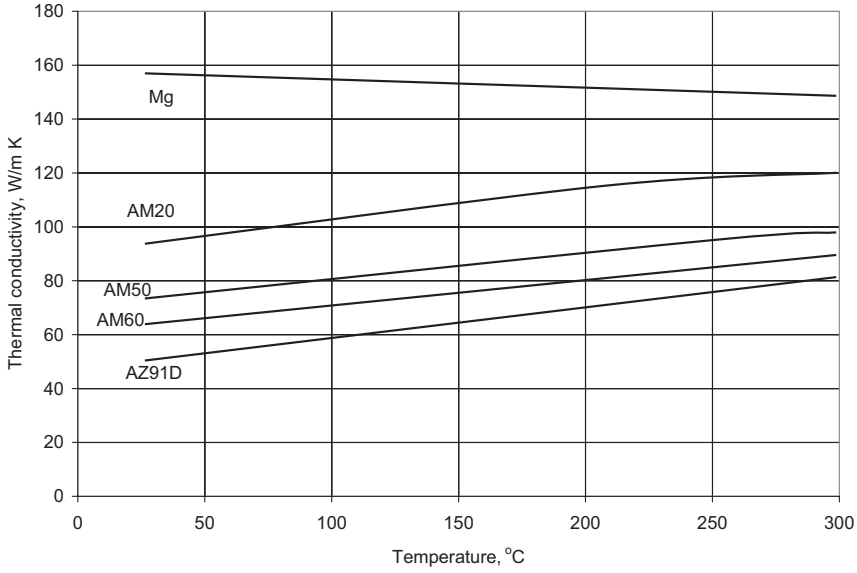

Fig. 1.33 The thermal conductivity for magnesium alloys as a function of temperature [52]

1.7.1 Casting

In practice, all casting processes can be adopted for magnesium alloys. Over the decades a number of solutions have emerged that utilize a variety of hardware. The major difference from a processing perspective is that metal is subjected to different pressures and gate velocities, as portrayed in Fig. 1.34.

1.7.1.1 Hot Chamber Die Casting

Die casting is the most popular technique to produce magnesium shape components. The process was invented by H.H. Doehler in 1910 for casting of zinc and extended several years later for aluminum [53]. The present solution is shown in Fig. 1.35. Hot chamber die casting means that the molten metal is transported directly into die via a heated channel called a "gooseneck," thus minimizing the heat loss. To achieve this, a significant portion of the metal injection system is immersed in the molten metal at all times. The benefit is that a molten metal needs to travel a short distance and the cycle time is reduced. At the same time the continuous contact with a molten alloy creates severe material problems. In addition to quick hardware deterioration, there are difficulties with sealing a plunger within the gooseneck. The static pressure of 20–30 MPa achieved is usually less than in the cold chamber process. The important feature of hot chamber is that after each injection cycle, molten metal is retracted back into the gooseneck.

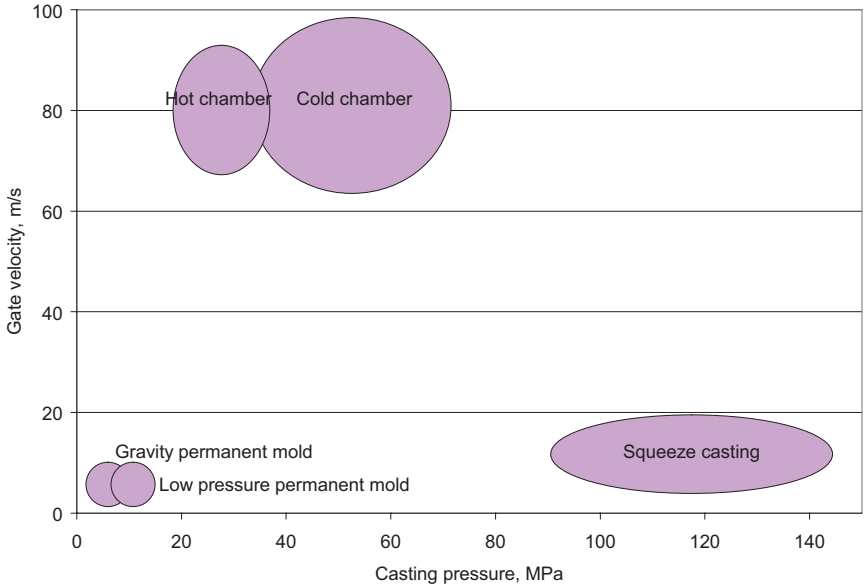

Fig. 1.34 The pressure versus gate velocity for common casting techniques

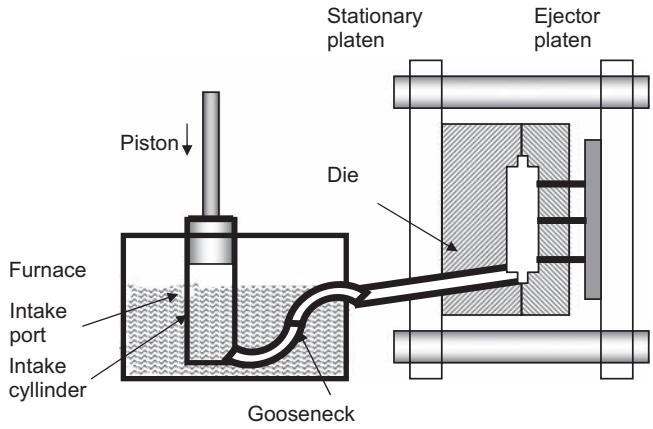

Fig. 1.35 The graphical illustration of a hot chamber die-casting machine

The hot chamber process is used for smaller parts up to 3 kg; there are, however, systems capable of casting parts up to 6 kg.

Traditional hot chamber die casting uses a two-part die, making it difficult to produce parts with complex geometries. To resolve this, multislide dies were introduced to use four perpendicular slides and the technique is called *multi-slide die casting*. In some cases, up to six slides may be added, at angles other than 90 deg.

The multislide die is made of a main die block, slide, crosshead and cover plate. Each die block has either a cavity and/or cores on its face that together form the complete cavity and runner system, allowing injection of liquid magnesium. The die blocks are mounted onto sliders, which fit into the crosshead, ensuring repeatable opening and closing. All the die components are held by a cover plate. At present, the technique is limited to small components with a projected area of 100 cm^2.

1.7.1.2 Cold Chamber Die Casting

The schematic diagram of the cold chamber is shown in Fig. 1.36. Cold chamber means that the molten metal passes through the cold shot sleeve while traveling from a furnace to the die cavity. Since the liquid metal is ladled (metered) into the shot sleeve during each injection cycle, an independent metering system is required. Unlike in a hot chamber, the shot sleeve is in contact with a molten metal for a small fraction of each injection cycle. The minimal exposure of shot sleeve to liquid metal, along with plunger lubrication, allows the generation of high pressure, typically of 30–70 MPa. The maximum size of casting is limited by the maximum locking force of the clamp, at present roughly 45,000 kN. This translates to the maximum projected area of 10,000 cm^2, being the size of a car door. The maximum weight of parts produced ranges up to 25 kg. When the same part can be cast by both techniques, the use of hot chamber is more economical. In addition to conventional die casting the high integrity high-vacuum die casting is often distinguished.

Conventional pressure die casting also shows limitations. Due to high injection rates, the volume of pores is significant, which excludes casting from subsequent heat treatment. Thin wall castings with long flow distances show variation in mechanical properties. In particular, the strength and elongation decrease with

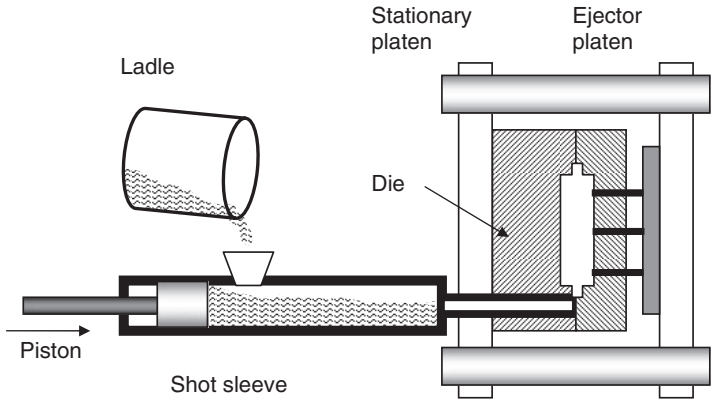

Fig. 1.36 The graphical illustration of a cold chamber die-casting machine

increasing distance from the gate. It means that the last filled area of the casting exhibits reduced mechanical properties.

1.7.1.3 Squeeze Casting

The essential feature of squeeze casting is that molten metal is introduced into a die with minimum turbulence and solidifies there under high pressure. The amount of pressure applied is significantly less than during forging but more than in die casting, reaching from 55 MPa to 300 MPa with most often an exploratory range of 80 MPa–110 MPa.

During direct squeeze casting, also called liquid metal forging, liquid metal is poured into the lower die segment (Fig. 1.37). When the alloy starts solidifying the upper half closes and the alloy solidifies completely under the high pressure that is applied. During indirect squeeze casting, which is similar to die casting, the molten metal is injected into the mold through a bigger gate as compared to die casting. This results in a gate velocity as low as 0.5 m/s.

The commercial squeeze casting machines are built as horizontal (HVSC horizontal clamping vertical injection) or vertical (VSC vertical clamping vertical injection) (Fig. 1.38). The key difference between a horizontal squeeze casting machine and the conventional die casting machine is that it includes a vertical shot sleeve and tilt-docking injection unit where, after die closure and pouring metal into the shot sleeve, the shot unit is tilted to an injection position, then docked while molten metal is injected into the mold cavity. The disadvantage of large gates is that trimming cannot be used to separate parts from runner systems and sawing is usually required. The cycle time for squeeze casting is longer than in die casting due to lower filling rates and longer solidification times.

The higher mechanical properties of squeeze cast magnesium alloys are caused by lower porosity and finer microstructure. The latter is attributed to the controlled

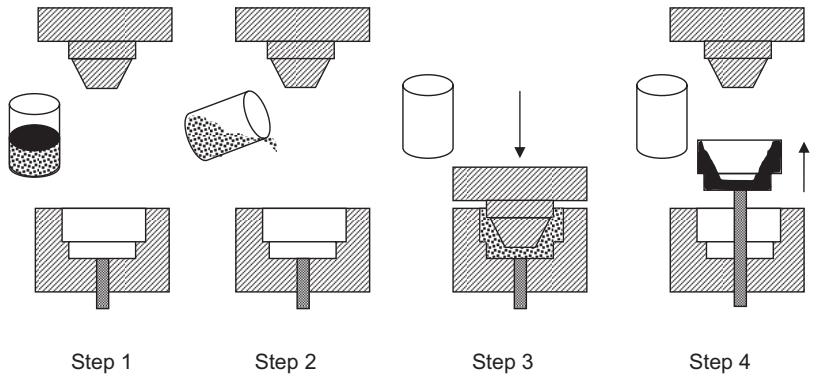

Fig. 1.37 The concept of direct squeeze casting: step 1—alloy melting; step 2—die filling; step 3—closing die and applying pressure; step 4—part ejection

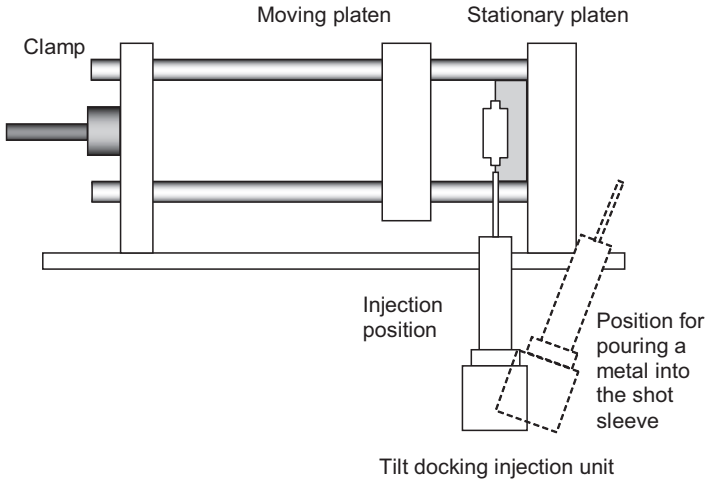

Fig. 1.38 The schematics of HVSC squeeze casting machine

solidification and applied high pressure. The high pressure can influence the solidification temperature since due to a shift in melting range the alloy is super-cooled.

1.7.1.4 Investment Casting

Investment casting is also known as the lost wax process. It is regarded as the precise manufacturing technique for components with complex shape, excellent surface finish and dimensional accuracy. The mold is made using wax or other materials, which are easy to melt away. Then the wax is multiply dipped in refractory slurry to form a skin after drying. After the wax is melted away in an oven, a mold is created that can be filled with a liquid metal. Pouring can be done using gravity, pressure or vacuum conditions. Due to the reactive nature of magnesium, special mold materials are required. The process was proven to be successful with cast magnesium alloys [54].

1.7.1.5 Permanent Mold and Sand Casting

Permanent mold casting utilizes a metal mold that resembles the component shape. It is less flexible than sand casting but allows the achievement of low production cost for larger part numbers. There are several variations of permanent mold casting. The simplest one is gravity casting where metal fills the mold under its own gravity. During low pressure permanent mold casting, up to 1 atm pressure is applied to the molten metal to allow complete filling and to compensate for any shrinkage during cooling. In another variation, called permanent mold vacuum casting, instead of external pressure a vacuum is applied to the permanent mold to improve filling, particularly of thin walled components.

1.7.1.6 Experimental Casting Techniques

In an attempt to minimize the disadvantages of conventional casting, several new techniques are at different stages of development. Their common purpose is to find a balance between cold chamber and hot chamber die castings. Some of them, which use the overheated melt, are described below.

In a technique developed by Sodick of Japan, a series of magnesium rods are fed into a heated cylinder with a temperature gradient ranging from well below solidus at the feeding point and above liquidus toward the exit [55]. The magnesium rod, being pushed forward, acts as a self-sealing plunger. After exceeding the melting range, the alloy is injected into the mold. An injection is executed through the transmission of pressure from a hydro-mechanical injection piston incorporating a screw mechanism and using a still-solid portion of the magnesium rod. After the shot is completed, the screw position is adjusted to compensate for the shorter feedstock length (Fig. 1.39).

Technology introduced by Takata of Japan starts from magnesium melting in a furnace. Then, the molten alloy is introduced to the first chamber, inclined to the base level. The second chamber, situated horizontally, plays the role of a shooting pot. It fills with molten alloy during the retracting motion of the piston. Thus the metal residing in both chambers is fully molten. During the first stage of injection, a portion of the alloy is moved back to the first chamber but the largest volume is transported to the mold [56].

Another process, based on fully molten alloy, was developed by Nissei Plastics Industrial, Japan [57]. First, the feedstock is preheated and transported by a screw into the melting section of the first barrel which is inclined to the machine base (Fig. 1.40). Such alignment allows the alloy to transport by gravity. An injection is executed by the hydraulically driven plunger.

1.7.2 Forging

The principle of forging is shaping a component by compressive forces (hammering or pressing) applied through various dies and tools. The common forging processes include open-die forging where the final product is the rough approximation

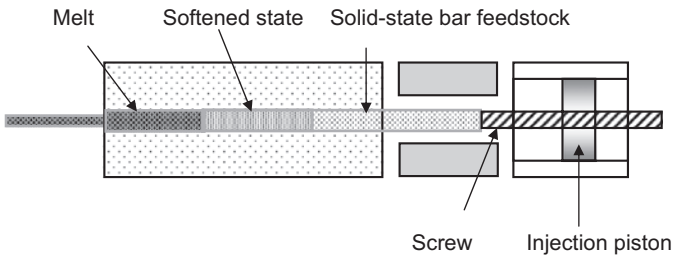

Fig. 1.39 The schematics of Sodick, Japan, solution for casting magnesium

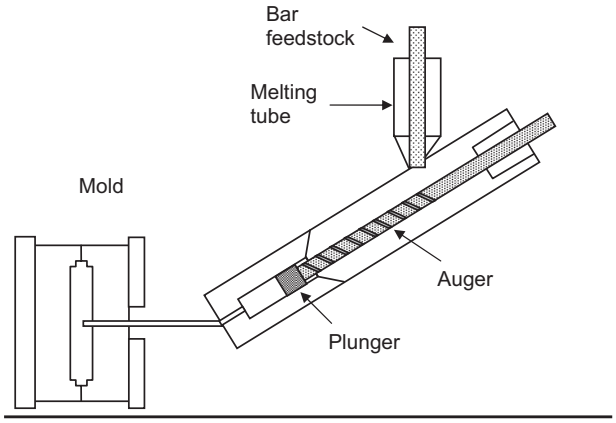

Fig. 1.40 The schematics of Nissei, Japan, solution for casting magnesium

of the die, frequently required during pre-forming. In close-die forging the alloy piece is deformed between two die halves to obtain the final shape of the part. Both methods are implemented using mechanical or hydraulic presses. A new method of near shape die forging is drop forging without flash, called precision forging.

Forging refines the grain structure. Only the forging process provides the advantage of grain orientation following the contour of the tool. Forging processes are particularly suitable for magnesium alloys. The plasticity of magnesium alloys increases at temperatures between 200 °C and 250 °C due to thermal activation of pyramid sliding planes in the hexagonal structure. Due to the sensitivity of magnesium alloys to temperature, the die control temperature is of importance.

During experimental forging of AZ31 alloy, squeeze casting was used to produce pre-forms [58]. Although use of squeeze casting is not attractive from a cost perspective it provides fine-grained structures and allows forging of complex shapes in one step. The macrostructure and microstructure are not significantly affected by forging speed used. For all forging speeds the microstructure depends upon location within the part with the most deformation, taking place within the mid section of the disc-shape component. Despite both processing steps, in the case of AZ31 alloy, internal defects in the form of small cracks and voids are still observed with no clear conclusion regarding their origin.

1.7.3 Rolling

Rolling is the process of plastic deformation of a metal by passing it between rolls. Historically, large volumes of magnesium sheets were manufactured during World War II, but the interest declined later. Depending on temperature, hot rolling and

cold rolling are distinguished with the former being easier and more popular but more expensive. Sheet production by hot rolling starts from slab with a typical cross section of 30 × 100 cm. Due to limited formability and low heat capacity, reheating has to be repeated several times to keep an alloy within the 250 °C–450 °C range and complete the process.

Although magnesium exhibits poor behavior during cold rolling, small additions of Ca, Th, Mn or RE, forming binary or ternary alloys, substantially improve cold rolling response. Early explanations attributed the improvement to the influence of alloying additions on the deformation structure and micro-texture [59]. It assumes that the deformation concentrates within bands inclined diagonally to the rolling plane, which are formed in regions subjected to $\{10\bar{1}1\}$ twinning followed by $\{10\bar{1}2\}$ secondary twinning. In these regions the easy glide basal planes are favorably aligned for the slip. The present experiments revealed that Mg–0.2Ce alloy is considerably easier to cold roll than pure Mg or AZ31 chemistry [60]. Although the precise reason is unclear, deformation texture and shear banding are suspected as controlling factors. In all cases the microstructure of cold rolled alloys exhibited shear bands, $\{10\bar{1}2\}$ twins and occasional $\{10\bar{1}1\}$-$\{10\bar{1}2\}$ double twins. The higher strain resulted in more frequent shear banding and less frequent $\{10\bar{1}2\}$ twinning. The deformation texture, expressed by the c-axis being parallel to normal direction, strengthened during strain increase, especially within the initial range up to 10%.

The production of magnesium alloy sheet at reasonable cost is likely by a combination of twin roll casting and hot rolling. The twin roll caster represents a special process capable of producing as-cast magnesium sheet with a thickness from 2.5 to 5 mm. The grain size is the crucial parameter for rolling and the coarse grain creates a high possibility of intercrystalline cracks. For AZ31 alloy the grain size after twin roll casting was 200 µm [61]. Further reduction in thickness down to 0.5 mm can be achieved using finish hot rolling equipment. A thickness reduction during each pass is from 10% to 40%.

1.7.4 Extrusion

Extrusion is a plastic deformation process in which a block of metal is forced to flow by compression through the die opening of a smaller cross section than the original billet. In practice, the cylindrical billet is placed in a closed container when a ram forces it to flow through a die orifice (Fig. 1.41). As a result the compressive or shear stresses are created enabling extensive deformation without tearing the material. The force required to cause extrusion depends on type of extrusion, temperature, extrusion ratio, speed and friction within the die. Two extrusion methods include direct extrusion and indirect extrusion. The benefit of extrusion is that excluding tail, no material is lost. Another type of extrusion is represented by hydrostatic extrusion where a hydrostatic medium is used to exert a pressure on the billet, forcing it to flow through the die. As a result, shear stresses are decreased

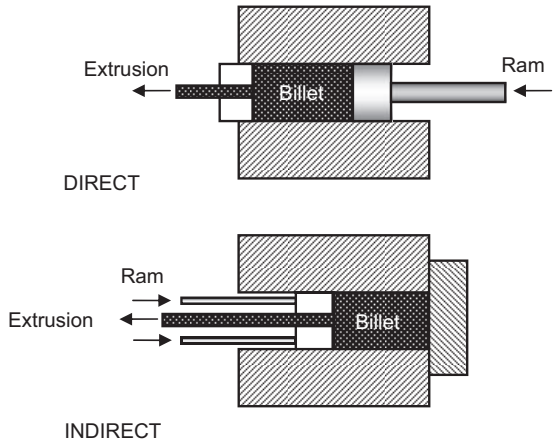

Fig. 1.41 The ideas of direct and indirect extrusion

within the die entrance, and formability is improved, which allow the reduction of preheating temperature.

Magnesium wrought alloys are practically extrudable. Experiments with hydrostatic extrusion of AZ31 alloy revealed that twinning plays a role before or during dynamic recrystallization, causing an increase in the $\langle 10.0 \rangle$ pole density of the fiber texture [62].

In magnesium the compressive stress applied parallel to the basal plane favors twinning, whereas tensile stress with similar orientation does not produce this effect. This leads to strong tension-compression asymmetry on extruded rods known to develop a texture where the basal planes $\{0001\}$ and the $\langle 10\bar{1}0 \rangle$ directions of the grains align mostly parallel to the rod's axis. Thus, in compression, yielding occurs at a stress level, which is almost half of this in tension. The asymmetry generated during deformation has an important effect on the design of the extruded structures. For example, in extruded magnesium beam the compressive side of the beam will deform much earlier than the tensile side does.

1.8 Heat Treatment

The purpose of heat treatment of magnesium alloys is to improve mechanical properties of a final product or modify properties required at a certain stage of processing. The major temper designations, used to specify the heat treatment state, are as follows:

T1-cooled and naturally aged; T2-annealed of cast products; T3-solution treated and cold worked; T4-solution heat treated; T5-cooled and artificially aged; T6-solution heat treated and artificially aged; T7-solution heat treated

and stabilized; T8- solution heat treated, cold worked and artificially aged; T9-solution heat treated, artificially aged and then cold worked; T10-cooled, artificially aged and cold worked. The most frequently implemented heat treatments are described below.

1.8.1 Annealing

Annealing is applied to restore the alloy's structure after cold deformation. Thus it is conducted on wrought alloys. The temperature required depends on the alloy grade and values may range from 290 °C to 450 °C. After holding at temperature for a period depending on the component size, slow cooling follows.

1.8.2 Stress Relieving

As opposed to annealing, which is used mainly with wrought alloys, stress relieving applies to both cast and wrought alloys. For wrought alloys the purpose is to remove stress generated during forming, straightening or welding. For castings, this heat treatment is performed to remove stress from casting to provide dimensional stability during machining or to avoid stress corrosion cracking during further service. The temperature–time parameters depend on the alloy chemistry and its state. The typical values are between 150 °C and 340 °C and a time period from several minutes to several hours.

1.8.3 Solution Treatment and Aging

This is a treatment which leads to precipitation hardening and consists of two stages:

(i) solution annealing, when alloy is heated to temperatures above the solvus line;
(ii) aging, when the solution annealed alloy is re-heated to cause precipitation of certain compounds.

The temperature-time parameters depend on the alloy chemistry and values for several typical alloys are listed in Table 1.12. The time and temperature are interdependent, and better effect is frequently achieved by lowering temperature and increasing time. The effect of strengthening due to precipitation hardening depends on the alloy chemistry. While for Mg–9Al alloy it is approximately 20%, for rare earth metals it is higher, and for Mg–5%Zn it is around 70%. The age hardening response of Mg–Al based alloys is, however, poor compared with age hardenable Al alloys. The shift of tensile curves after T4 and T6 heat treatments is shown in Fig. 1.42.

Table 1.12 The recommended parameters of solution treating and aging for magnesium castings and wrought products selected from [96]

		Solution treatment			Aging	
Alloy	Temper	Temp., °C	Time, h	Max temp. °C	Temp., °C	Time, h
AZ91	T4	413	16–24	418		
	T5				168	16
	T6	413	16–24	418	168	16
AZ63	T4	385	10–14	391		
	T5				260	4
	T6	385	10–14	391	218	5
AM100	T4	424	16–24	432		
	T5				232	5
	T6	424	16–24	432	232	5
WE43	T6	525	4–8	535	250	16
ZE63	T6	480	10–72	491	141	48
ZK61	T5				149	48
	T6	499	2	502	129	48
ZK60	T5				150	24
AZ80	T5				177	16–24

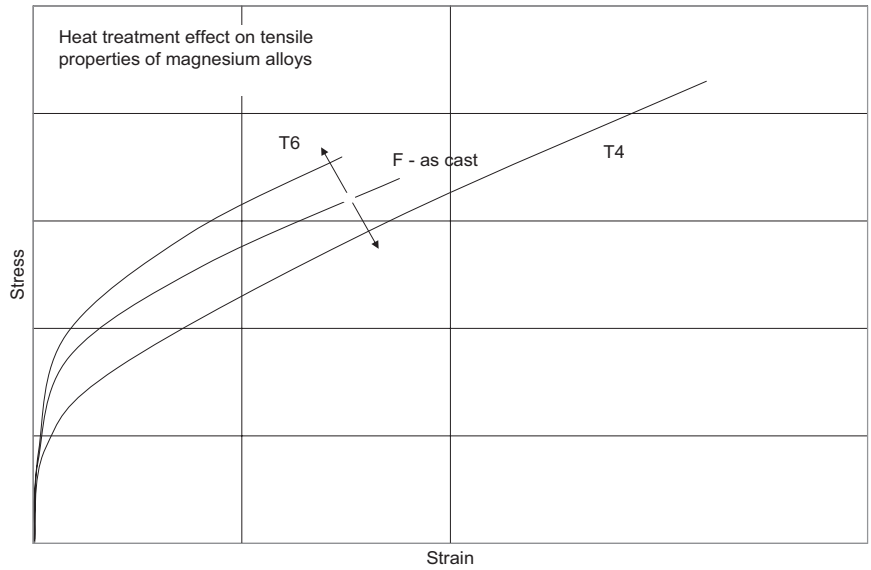

Fig. 1.42 The tendency of shift in tensile properties for Mg–Al–Zn alloys after T4 and T6 heat treatments

1.8.3.1 Precipitation Phenomena in Mg–Al–Zn Alloys

It is commonly accepted that $Mg_{17}Al_{12}$ phase with bcc structure is the only precipitate generated during aging following solution treatment in Mg–9Al–1Zn grade. The alloy strengthening is attributed to plate-like precipitate phases, formed

on prismatic or basal planes of Mg matrix. Two competitive precipitation mechanisms, acting simultaneously at aging temperatures, are identified:

(i) continuous precipitation which takes place via nucleation and growth of individual precipitates within the parent grains;
(ii) discontinuous precipitation, where nucleation and growth takes place on grain boundaries.

Despite high solubility of Al in Mg, reaching a maximum of 12.5%, the precipitation strengthening effect of roughly 20% is rather low. The reason is the large inter-precipitate spacing and unfavorable orientation of $Mg_{17}Al_{12}$ plate-like precipitates to block the basal slip.

An increase in Zn content in Mg–9%Al alloy to 2% increases the amount of precipitated phase by reducing the solid solubility of Al in Mg. The precipitate morphologies detected here are in general agreement with findings for aged AZ91D alloys where three morphologies of continuous precipitates were identified: plates with the primary habit plane parallel to the (0001) basal plane, laths with the primary growth direction perpendicular to the basal plane and laths lying at an angle to the basal plane. It was also reported that the number of continuous precipitates per unit volume in aged AZ91 decreases from $1 \times 10^{12}/mm^3$ at 70 °C to $1.5 \times 10^9/mm^3$ at 300 °C [63]. According to TEM observations, the most intensive precipitation is present for lower aging temperatures. However, their strengthening effect is limited since the continuous precipitates consist of coarsely dispersed plates lying parallel to the basal plane, and there are many opportunities for dislocations to glide between the precipitates.

1.8.3.2 Crystallography of Precipitates

Although various orientation relationships are quoted between the $Mg_{17}Al_{12}$ precipitates and Mg matrix, two are considered as dominant [64]:

i) the Burger orientation, where $(0001)_M$ represents the habit plane and precipitates are parallel to the basal plane of the Mg matrix:

$$(0001)_M \,//\, (011)_\gamma, \left[\bar{2}\bar{1}\bar{1}0\right]_M \,//\, \left[1\bar{1}1\right]_\gamma$$

ii) the Potter orientation

$$(0001)_M \text{ 2 deg from } (001)_\gamma, (01\bar{1}\bar{1})_M \,//(110)_\gamma, [2\bar{1}\bar{1}0]_M \,//[1\bar{1}\bar{1}]_\gamma$$

The above relationships are valid for both discontinuous and continuous type precipitates. The orientations of precipitates within a single matrix grain may be different where they may obey different variants of Burger or Potter orientations or both.

1.9 Surface Protection

Room temperature corrosion in various environments, including the atmospheric one, is a major disadvantage of magnesium, eliminating a number of its engineering applications. For some applications, the poor corrosion behavior can be compensated by surface treatments, coatings or combinations of both.

1.9.1 Corrosion Nature

The poor corrosion resistance of magnesium is associated with two issues:

(i) low protective behavior of the quasi-passive hydroxide film;
(ii) susceptibility to galvanic corrosion due to very low electronegative potential.

At room temperature, magnesium in air develops a gray oxide film on its surface. When combined with moisture, this film converts to magnesium hydroxide which is unstable in neutral or acidic ranges. As shown in Fig. 1.43, in neutral or low pH environments, magnesium dissolves as Mg^{+} and Mg^{2+} and the evolution of hydrogen accompanies this reaction. As a result the $Mg(OH)_2$ layer does not provide lasting protection. The protective properties are further diminished by certain ions, like: chloride, chlorate, bromide or sulfate, which break down the protective

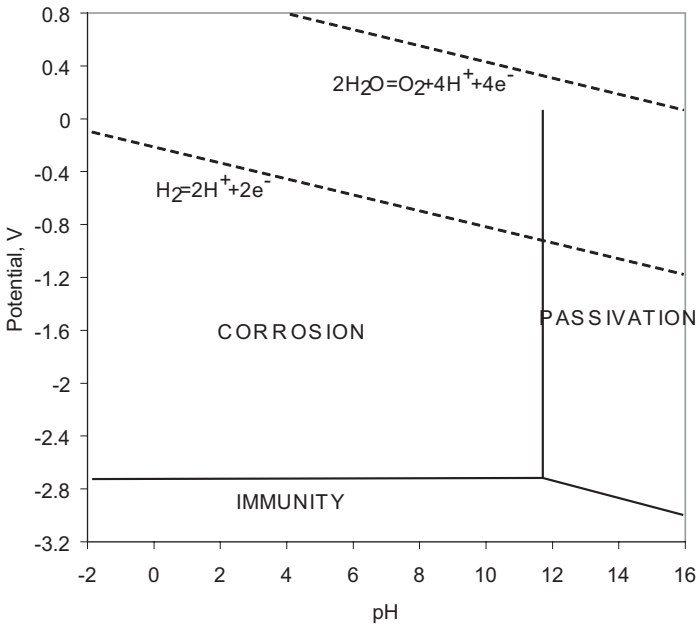

Fig. 1.43 Potential-pH diagram (Pourbaix) for magnesium–water system at 25 °C showing ranges of immunity, passivation and corrosion [87]

film. As compared to other metals, magnesium corrosion is below the level of aluminum alloys and significantly less than obtained under similar conditions on mild steel (Fig. 1.44).

The galvanic corrosion is caused by the very electronegative potential of Mg, being of -2.37 V ($Mg^{2+}+e^{-}\rightarrow Mg$). This is compared to the potential of – 0.44 V for ($Fe^{2+}+e^{-}\rightarrow Fe$) and -0.25 V for Ni ($Ni^{2+}+e^{-}\rightarrow Ni$). Examples of corrosion potentials are given in Table 1.13. The galvanic corrosion may take place internally due

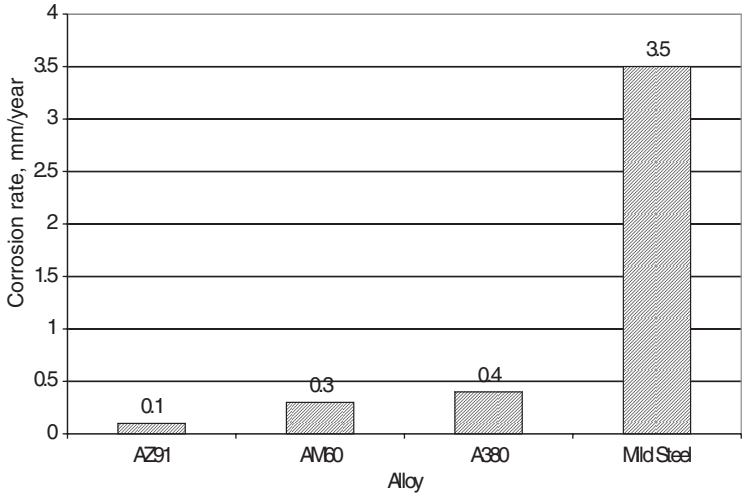

Fig. 1.44 The corrosion resistance of two magnesium alloys compared with aluminum alloy and a mild steel

Table 1.13 The standard electrode potentials versus normal hydrogen electrode at 25 °C

Electrode	Reaction	Potential, V	Remarks
Au, Au^{3+}	$Au^{3+} + e^{-} \rightarrow Au$	1.50	Noble–cathodic
Pt, Pt^{2+}	$Pt^{2+} + e^{-} \rightarrow Pt$	1.20	
Ag, Ag^{+}	$Ag^{+} + e^{-} \rightarrow Ag$	0.80	
Cu, Cu^{2+}	$Cu^{2+} + e^{-} \rightarrow Cu$	0.34	
H_2, H^{+}		0.00	Neutral
Sn, Sn^{2+}	$Sn^{2+} + e^{-} \rightarrow Sn$	−0.14	
Ni, Ni^{2+}	$Ni^{2+} + e^{-} \rightarrow Ni$	−0.25	
Co, Co^{2+}	$Co^{2+} + e^{-} \rightarrow Co$	−0.28	
Cd, Cd^{2+}	$Cd^{2+} + e^{-} \rightarrow Cd$	−0.40	
Fe, Fe^{2+}	$Fe^{2+} + e^{-} \rightarrow Fe$	−0.44	
Cr, Cr^{2+}	$Cr^{2+} + e^{-} \rightarrow Cr$	−0.74	
Zn, Zn^{2+}	$Zn^{2+} + e^{-} \rightarrow Zn$	−0.76	
Al, Al^{3+}	$Al^{3+} + e^{-} \rightarrow Al$	−0.17	
Mg, Mg^{2+}	$Mg^{2+} + e^{-} \rightarrow Mg$	−2.37	
Na, Na^{+}	$Na^{+} + e^{-} \rightarrow Na$	−2.71	
K, K^{+}	$K^{+} + e^{-} \rightarrow K$	−2.92	
Li, Li^{+}	$Li^{+} + e^{-} \rightarrow Li$	−3.02	Active–anodic

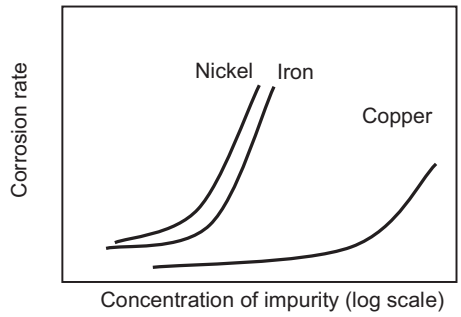

Fig. 1.45 The influence of Ni, Fe and Cu impurities on corrosion resistance of magnesium (schematics)

to other phases or impurities with more noble potential. This is why cathodic impurities of Fe, Ni or Cu are so harmful (Fig. 1.45).

When Mg is coupled with other metals, galvanic corrosion will occur externally. In this case, Mg will dissolve, playing a role as sacrificial electrode. The factors affecting external corrosion rate include the medium conductivity, the surface ratio of anode and cathode and the distance between them: High conductivity, larger surface ratio and smaller distance increase the corrosion rate. While considering alloys, their constituents should be taken into account. For example, pure Al is considered quite compatible. The Al alloys, containing metals with low hydrogen overvoltage such as Fe, Ni, Cu, 7000, 6000, 2000 series and cast alloy A380, cause galvanic corrosion.

1.9.2 Metallurgical Factors Affecting Corrosion

From an engineering perspective, the corrosion resistance of magnesium alloys is of primary concern rather that the behavior of pure magnesium. Therefore, factors that describe the alloy chemistry and microstructure are of importance: alloying elements, impurities, phase composition, grain size or crystallographic texture. A variety of factors affecting corrosion resistance are discussed in related publications [65].

1.9.2.1 Alloy Chemistry

Aluminum and manganese are among elements improving corrosion resistance. For cast Mg–Al alloys the Al effect depends on its content: While for contents higher than 8%, an increased Al causes improvements, for lower concentrations the opposite effect was recorded [66]. Zn is known to improve corrosion resistance. The positive influence of Mn is expressed by its tendency to combine with Fe thus reducing its detrimental effect. Zr improves the corrosion resistance: Alloys with 4% and 15% zirconium show the increased corrosion resistance of Mg–4Al [67]. However, increased Zr content to 32% and 50% reduces the corrosion resistance. In MEZ alloy, grain refining with Zr led also to an improvement in

corrosion resistance [68]. The corrosion was mostly confined within grains as compared to grain boundary attack, observed in the absence of Zr. It is suspected that in addition to removal of Fe, Zr stabilizes the Mg matrix, delaying the initiation of localized corrosion. Zr reduces the rate of anodic dissolution, passivates precipitated particles and provides more continuous coverage of grain boundaries by the corrosion resistant phase containing rare earths.

1.9.2.2 Alloy Microstructure

For a given chemistry, corrosion behavior is controlled by alloy microstructure, generated by the processing method. The rapid solidification, leading to fine and homogeneous microstructures, improves the corrosion resistance. The metastable or amorphous phases within the structure inhibit the corrosive attack. At the same time, there are data showing no improvement in corrosion resistance of AZ91D and AM60B after laser melting even though it generates metastable phases [69]. The higher solidification rates during die casting of AZ91D provided a benefit [70]. The effect was attributed to a higher content of $Mg_{17}Al_{12}$ phase in the surface layer of fine αMg with low porosity.

The AZ91D alloy after semisolid processing showed a corrosion rate 35% below the same alloy after die casting [71]. An improvement is explained by differences in composition of αMg. After semisolid casting the Al content in αMg was 3% as compared to 1.8% after die casting. The content of Zn in αMg after semisolid casting was also higher. The improvement is not associated with the $Mg_{17}Al_{12}$ phase, which after semisolid casting, is present as large discontinuous grains. Injection molding leads to improvement in corrosion resistance. This is because of phase distribution across the thickness of the molded part. While solid particles are located within the wall center, the solidified liquid, being richer in Al than in a fully molten state, is distributed close to the component surface.

1.9.3 Corrosion Prevention by Surface Treatments

A number of different surface protection techniques were developed and commercialized. The most frequently used are listed below. Although conventional treatments are based on anodizing, the laser surface alloying or thermal spraying is also used.

1.9.3.1 Electrolytic/Ion Plate Coating

Electrolytic coatings were found to be effective in improving the corrosion resistance of magnesium alloys. An example is the electroless nickel-phosphorus with a

thickness of approximately 10 µm, plated on the conversion treated surface [72]. The chemical conversion coating with a thickness of several microns is created by immersion for 1 h at 90 °C in a solution of NaOH, $Na_2SnO_3 \cdot 3H_2O$ and $NaCH_3COO \cdot 3H_2O$ with a weight ratio of 1:5:1, respectively. The presence of the conversion coating reduces the potential between Mg substrate and a Ni layer enhancing the corrosion resistance of the AZ91D alloy in 3.5% NaCl solution. Electroless nickel can also be applied onto a thin sublayer of copper or directly onto activated magnesium alloy. An example of Ni electroless coating, applied directly to AM60B alloy, is shown in Fig. 1.46.

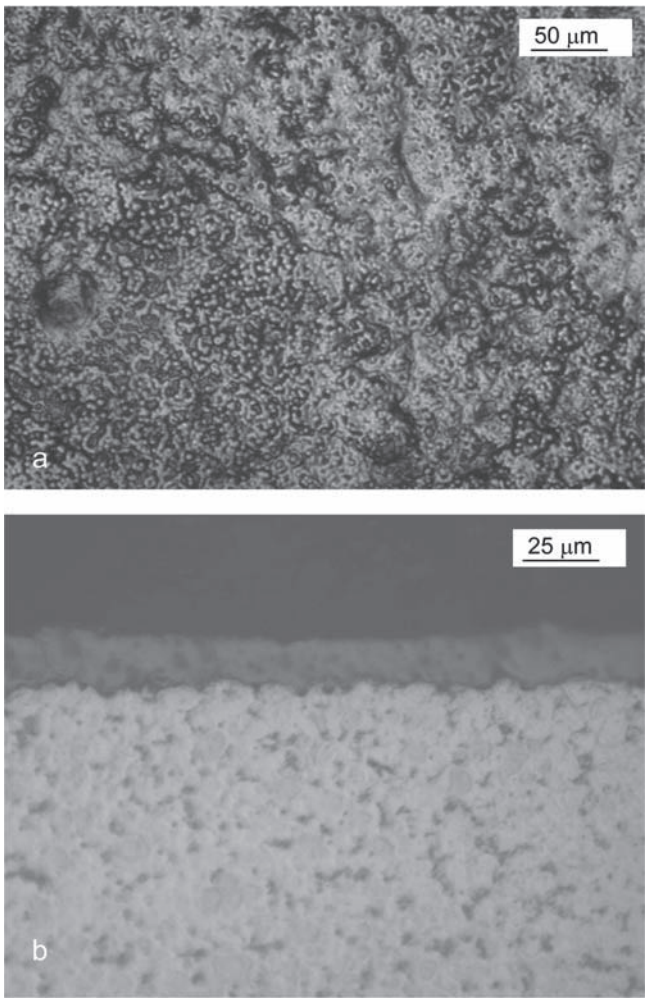

Fig. 1.46 The electroless Ni coating on AM60 alloy: **a** top view; **b** cross section

The dense Ti coatings with a thickness of 10 μm, deposited by ion plating, were also found to be effective. Electrochemical polarization indicates that the corrosion current density of Mg is reduced by one order of magnitude [73].

1.9.3.2 Electrolytic Microplasma Anodizing

Electrolytic microplasma anodizing represents a technology capable of forming hard and controlled porosity coatings on magnesium and its alloys. The technology is seen as intermediate between the conventional low voltage anodizing and the high energy plasma coatings, generated in a dry environment. Although the phenomenon of discharge in aqueous electrolyte was discovered in the nineteenth century, its application for coating generation was developed after the 1960s, mainly in Russia [74].

During the coating process, the electrochemical reactions which involve charge transfer at the electrode-electrolyte interface, are combined with the strong charge transfer effect across a wet plasma gas film between the electrode surface and the electrolyte [75]. The effects include local heating and plasma thermochemical reactions. The typical electrolytes, effective for Al alloys, include sodium aluminate, sodium hexametaphosphate, a mixture of sodium alkali, aluminate and hexametaphosphate. Other possibilities are colloidal solutions, e.g., based on liquid glass or solutions containing dispersed particles [76]. Due to a build up of internal stress during growth, thin coatings are subjected to cracking. The thin ceramic layer is easily penetrable by electric arc, so local melting takes place. After long-term exposure the coating is thick, and electric discharge to the substrate creates craters (Fig. 1.47). As the coating thickness increases further, its top surface becomes more uniform (Fig. 1.48).

The coating formed on AZ91D alloy by the commercialized process of electrolytic microplasma consists of a ceramic layer of magnesium aluminum oxide [77]. The external layer, typically 30–60 μm thick has a microhardness of 500–1000 HV and porosity over 15%. The bottom functional layer with a thickness up to 200 μm has microhardness of 900–2000 HV and reduced porosity in the range 2–15%. While the outer, porous layer provides an excellent adhesive base for subsequent painting, the presence of an inner, dense layer improves corrosion resistance.

1.9.3.3 Comprehensive Surface Treatments for Different Service Environments

The flow chart for the protection of a magnesium surface is shown in Fig. 1.49. For all treatments the basic stages include:

(i) cleaning;
(ii) passivation;
(iii) finish coat.

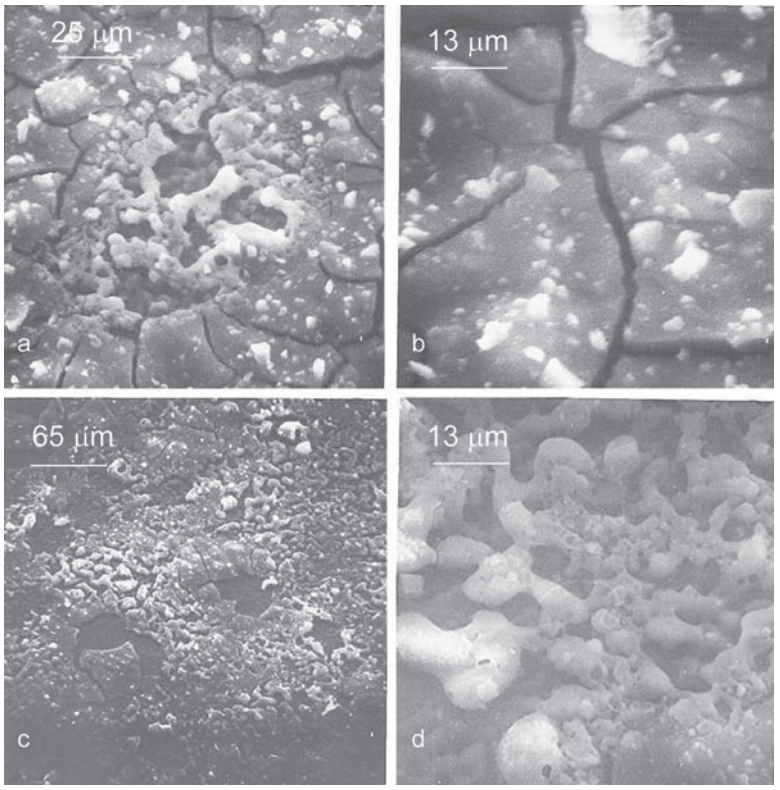

Fig. 1.47 Early stage of formation of ceramic coatings during electrolytic microplasma technology: **a,b** 10 s of deposition; **c,d** 30 s of deposition

Cleaning is conducted first by mechanical then by chemical processes aimed at removal of contaminants and activating the surface. Examples include grinding, shot pinning, water pressure, alkaline solvent and acid treatments.

Surface passivation is carried out by chemical conversion coatings or anodizing. The conversion coatings are based on chromate or phosphate routes. Fluoride anodizing is a cleaning treatment and is recommended prior to the first application of protective finishes. The treatment removes contamination with metallic debris from previous use. Chromate conversion coatings are applied prior to coatings with resins or paints. Hard anodizing results in the formation of a hard coating resistant to wear, but due to its porosity the coating is not resistant to corrosion. There are, however, anodized coatings that provide good corrosion protection. Surface sealing provides thin, flexible dense resin coatings on pretreated magnesium surfaces.

The painting of magnesium does not differ substantially from that of other metals. The protective painting of magnesium is performed on a chromate film,

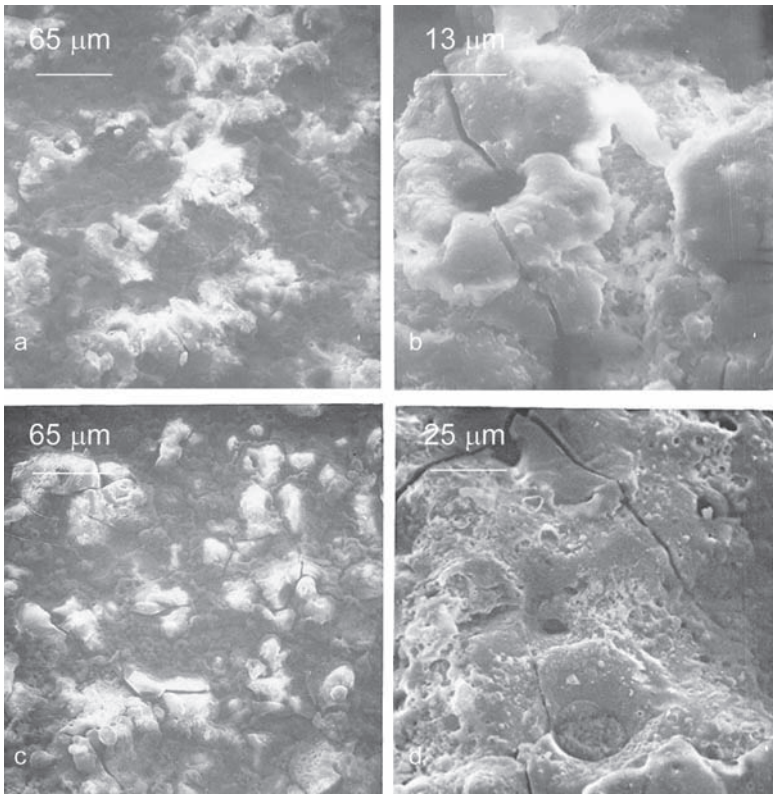

Fig. 1.48 Top view of typical coatings formed by electrolytic microplasma technology after long term deposition: **a,b** 1h; **c,d** 2h

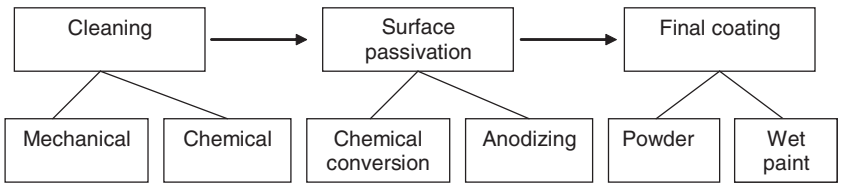

Fig. 1.49 Flow chart of surface treatments, available for magnesium alloys

surface sealed chromate conversion or hard anodic coating. Depending on application, paint may be a single layer or complex multilayer consisting of primer, filler, base and transparent surface coat. The paint should never be applied to bare magnesium.

Depending on particular application, a suitable surface protection should be given to the component surface. For aerospace and military applications, three ranges of service

environments are distinguished: (i) moderate; (ii) aggressive and (iii) very aggressive [78]. Accordingly, the number and kind of treatment stages differ substantially.

1.10 Application Markets

When assessing the market size and applications of today's magnesium industry an analogy is frequently used to aluminum industry of size 1.5 mln tonnes it was just after the World War II. Magnesium is used in a diverse range of markets and applications, each one exploring its unique properties. For decades, the automotive industry was seen as the greatest opportunities for structural magnesium. At the same time, magnesium alloy development has traditionally been driven by aerospace industry requirements. Application of magnesium for ground and air transportation vehicles reduces their total weight, reduces fuel consumption, toxic emissions and greenhouse gases, and increases recyclability, safety and handling. The potential reduction in fuel consumption, while converting from steel to aluminum or structural plastics and further to magnesium, reaches 50%–75%, 25%–35% and 20%–30%, respectively. Recent developments of electronics and telecommunications open new opportunities. It is clear that the magnesium industry must capitalize on an increasingly mobile, prosperous and environmentally aware society.

1.10.1 Automotive

Although an application of magnesium for pistons of internal combustion engines was developed in Germany in 1919–1920, the large-scale use of magnesium in the automotive industry originated at Volkswagen after World War II. Consumption by the Beetle car reached a peak in 1971 with an annual volume of 42,000 tonnes. Air-cooled engines and gearboxes were the main components with 20 kg of the vehicle weight. Later, however, magnesium was replaced by aluminum. Although there are applications of magnesium on high-visibility high volume vehicles, the general contribution to the total weight still remains low.

At present, the American auto industry uses about 70,000 tonnes per year of magnesium, which is equivalent to 3.5 kg per vehicle. There are, however, examples of higher volume with GM full size vans up to 26 kg, GM minivans up to 17 kg, Ford F-150 truck – 14 kg, Buick Park Avenue - 9.5 kg, Chrysler minivans - 6 kg (2001 data). For comparison, VW Passat, Audi A4 and A6 use roughly 14 kg, representing 1% of the vehicle weight, Mercedes SLK Roadster - 8 kg (2001 data). The assessment of present use and future opportunities is given in Table 1.14 with components potentially implantable in short to long time range. Magnesium is used for automotive components including seat frames, instrument panels, steering wheels, engine valve covers, intake manifolds and transmission housings. For example, of 62 mln steering wheels approximately 26 mln are made of magnesium. To improve a car's performance and driving

Table 1.14 The present and predicted uses of magnesium alloys in motor vehicles [90]

Component	Used on various VW/Audi vehicles kg	Possible in short term up to 5 years kg	Possible in medium term beyond 5 years kg	Possible in long term beyond 10 years kg
Drive train				
Manual/automatic gearbox housing	x	x		
Intake manifold	x			
Cylinder head cover	x			
Supports		x		
Oil sump, oil pump housing		x		
Crankcase			x	
Total	18	6–11	14–20	
Interior				
Steering wheel core	x			
Pedal brackets	x			
Steering column components	x			
Seat components, rear seat		x		
Other components	x	x	x	
Total	4	8–12	2–4	
Body				
Inner boot lid section	x			
Cast door, inner, 2 (4)		x		
Instrumental panel cross-car beam		x		
Mg-sheet application (interior/exterior)			x	x
Mg extrusion application			x	x
Total	3	20–34	8–12	15–20
Chassis				
Engine cradle/ sub-frame			x	
Wheels (5)				x
Suspension arms (front/rear)				x
Total	0	0	4–6	30–34
Grand total	25	34–57	28–42	45–54
Cumulative total		59–82	87–124	132–178

dynamics the center of gravity should be lowered and the weight distributed evenly. Therefore components reducing weight higher and in the front of the vehicle but also in the wheel/hub are especially attractive. An important achievement is seen in the new BMW six-cylinder engine, which has a hybrid magnesium aluminum block with

magnesium bedplate and cam cover. Another example is the Daimler Chrysler's new seven speed 7G-tronic gearbox with a magnesium casing.

As listed in Table 1.14, magnesium structures have potential to reduce vehicle mass by 100 kg. For 15-16 million automobiles built per year in North America, assuming additionally 25 to 125 kg of Mg translates to 375,000 tonnes to 2,000,000 tonnes of magnesium per year.

1.10.2 Aerospace

Magnesium fuel tanks, propellers and engine crankcases were applied in German aircraft in the early 1930's. The trend continued through the 1940's when the B-47 jet bomber had a total of 5,500 kg of magnesium sheet, extrusions and castings [79]. Magnesium was intensively used as a skin material on wing and tail, jet engine pods, cowling, gun enclosures and doors.

At present, commercial aircraft have very few magnesium parts. Helicopters contain some cast components, such as gearboxes, seats and pedals. Some cast and wrought magnesium parts are in satellites. The military industry uses much more magnesium, e.g., in wheels, radar antennas, radar bases, covers and missile elements.

1.10.3 Consumer Electronics (3C)

The thin-wall housing market of various appliances has historically been dominated by injection molded plastics. As compared to plastics, magnesium parts offer not only a metallic look and feel but also greater rigidity with no warpage or sink marks. Although magnesium has a higher specific gravity than plastics, its strength to weight ratio, impact resistance and rigidity are significantly higher, allowing the manufacture of components that are slimmer and lighter. In addition to thin wall and high strength, castings for the electronic industry require certain thermal and electrical properties. As shown earlier in this chapter, the properties required, including damping capacity, EMI/RFI shielding and heat dissipation, are inherent to magnesium.

Digitalization and the need for increased portability resulted in a rapid increase in application for information and communication technology (ICT) appliances for cameras, projectors, laptop computers, cell phones and television cabinets. Sony first used magnesium for its digital video camera, causing a reduction of noise and vibration, prevention of heat built-up inside the machine, electromagnetic shielding, and strength allowing smaller size. Today magnesium is used extensively by leading manufacturers such as Sony, Toshiba, Panasonic, Sharp, JVC, Hitachi, Minolta, and Nikon [80]. More details regarding this market segment are provided in Chap. 2.

1.10.4 General Purpose Market

This market represents sporting goods, household and office equipment. Particular applications include a number of sports and leisure uses as suspensions, frames and pedals of bicycles, archery equipment, camping equipment, tennis rackets and ski bindings, domestic and industrial hand tools. Recently magnesium use was extended to fashion accessories such as sunglasses and prescription frames.

1.11 Summary

Magnesium and its alloys have a unique position as engineering materials with low specific weight, vast resources and easy recyclability. As a result, magnesium faces a continuous growth in a variety of attractive applications. The alloys designed in the past do not always best suit modern techniques available for components manufacturing and new service environments. The knowledge of magnesium metallurgy is a key factor for designing alloys capable of fulfilling the demanding requirements of new markets in the 21st century.

References

1. Shukun M et al (2005) Uplift China's Pidgeon magnesium reduction processing level and develop recycling economy – China magnesium report. In: 62nd Annual World Magnesium Conference, Berlin, Germany, IMA, pp 13–25
2. Watson K et al (2000) The Magnola demonstration plant: A valuable investment in technology development and improvement. In HI Kaplan (ed) Magnesium Technology 2000, TMS, Nashville, TN, 27–30
3. Schoukens A, Curr T, and Abdellatif M (2007) Thermal production of magnesium. MINTEK, Pyrometallurgy Division, Randburg, South Africa, personal communication
4. Krishnan A, Lu X, and Pal UB (2005) Solid oxide membrane (SOM) for cost effective and environmentally sound production of magnesium directly from magnesium oxide. In NR Neelaleggham HI Kaplan, and BR Powell (eds) Magnesium Technology 2005, TMS, Warrendale, PA, pp 7–15
5. Brooks G et al (2006) The carbothermic route to magnesium. Journal of Metals 57(5):51
6. Kramer DA (1998) Magnesium recycling in the United States in 1998. In Flow studies for recycling metal commodities in the United States, US Geological Survey, Reston, VA, USA
7. Shang S et al (2001) Innovative vacuum distillation for magnesium recycling. In J Hryn (ed) Magnesium Technology 2001, TMS, Warrendale, PA, USA, pp 55–60
8. Kimura K, Nishii K, Kawarada M (2003) Recycling magnesium alloy housings for notebook computers. Fujitsu Scientific Technical Journal 38(1): 102–111
9. Hanko G, Macher G (2003) Technologies for efficient Mg-scrap recycling. In HI Kaplan (ed) Magnesium Technology 2003, TMS, Warrendale, PA, USA, pp 29–32
10. Busk RS, Phillips CW (1945) Transactions AIME 161:266
11. Holdeman GE (1942) US Patent 2,304,093, 8 Dec 1942
12. Cao P, Qian M, StJohn DH (2004) Grain coarsening of magnesium alloys by beryllium. Scripta Materialia 51:647–651
13. Green W et al (1993) Method for producing high purity magnesium alloys. US Patent 5,248,477, 28 Sept 28 1993

14. Dieter GE (1976) Mechanical Metallurgy. McGraw-Hill, New York
15. Caceres CH et al (2005) Section thickness, macrohardness and yield strength in high pressure die cast magnesium alloy AZ91. Materials Science and Engineering A 402:269–277
16. Somekawa H, Mukai T (2005) Effect of grain refinement on fracture toughness in extruded pure magnesium. Scripta Materialia 53:1059–1064
17. Emley EF (1966) Principles of magnesium technology. Pergamon Press, Oxford
18. Shaw C, Jones H (1997) The contribution of different alloying additions to hardening in rapidly solidified magnesium alloys. Materials Science and Engineering A 226–228:856–860
19. Blake AH, Caceres CH (2005) Solid solution effects on the tensile behaviour of concentrated Mg-Zn alloys. In NR Neelaleggham (ed) Magnesium Technology 2005, TMS, Warrendale, PA, pp 403–407
20. Nie JF (2003) Effects of precipitate shape and orientation on dispersion strengthening in magnesium alloys. Scripta Materialia 48:1009–1015
21. Caceres CH et al (2002) Effects of solidification and aging on the microstructure and mechanical properties of AZ91 alloy. Materials Science and Engineering A 325:344–355
22. Weiss D, Robison ST (2005) Magnesium driving to permanent mold. Modern Casting 95(9):26–29
23. Loughanne T et al (2005) The effect of grain refinement on the castability of magnesium permanent mould castings. In NR Neelaleggham (ed) Magnesium Technology 2005, TMS, Warrendale, PA, pp 309–314
24. Tukeda T et al (2003) Magnesium alloy excellent fluidity and materials thereof. US Patent 6,582,533 B2, 24 June 2003
25. Nakamura K et al (2004) High strength magnesium based alloy and Mg based casting alloy and article made of the alloy. US Patent 6,755,922 B2, 29 June 2004
26. Sweder TA et al (2006) AM-lite and AM-HP2 new magnesium alloys offer new opportunities. In SAE 2006 Congress, Detroit, USA, SAE, paper 06M–459
27. Klement W, Wilens R.H, Duwez P (1960) Nature 187:869
28. Inoue A (1995) Japan Institute of Materials (JIM) 36 (7):866–875
29. Kim G, Inoue A, Matsumoto T (1991) Increase of mechanical strength of Mg85Zn12Ce3 amorphous alloy by dispersion of ultrafine hcp particles. Materials Transactions JIM 32:875–878
30. Amiya K, Inoue A (2000) Materials Transactions JIM 41:1460
31. Magde SV, Greer AL (2004) Effect of Ag addition on the glass-forming ability and thermal stability of Mg-Cu-Y alloys. Materials Science and Engineering A 375–377:759–762
32. Perez P et al (2002) Mechanical behaviour of amorphous Mg-23.5Ni ribbons. In VIII Congreso National de Propiedades Mecanicas en Solidos, Gandia
33. Xu YK et al (2005) Mg-based bulk metallic glass composites with plasticity and gigapaskals strength. Acta Materialia 53:1857–1866
34. Inoue A et al (1991) Materials Transactions JIM 32:609
35. Cullity BD (1978) Elements of X-ray Diffraction. Addison-Wesley, New York
36. Kelly EW, Hosford WF (1968) Trans.AIME 242:5
37. Staroselsky A, Anand L (2003) A constitutive model for hcp materials deforming by slip and twinning: Application to magnesium alloy AZ31B. International Journal of Plasticity 19(10):1843–1864
38. Gehrmann R, Frommert MM, Gottstein G (2005) Texture effect on plastic deformation of magnesium. Materials Science and Engineering A 395:338–349
39. Kaibyshev OA (2005) Superplasticity: Microstructural Refining and Superplastic Roll Forming. In ISTC, Science and Technology Series, vol 3. Futureplast, Arlington, USA
40. Kaibyshev OA, Salikhov RR (1981) Effect of superplastic deformation on the structure and properties of alloy MA21. Metal Science and Heat Treatment 23(3):188–192
41. Watanabe H et al (2002) Low temperature superplasticity of a fine-grained ZK60 magnesium alloy processed by equal-channel-angular extrusion. Scripta Materialia 46:851–856
42. Somekawa H et al (2003) Low temperature diffusion bonding in a superplastic AZ31 magnesium alloy. Scripta Materialia 48:1249–1254

43. Mabuchi M et al (1997) Low temperature superplasticity in an AZ91 magnesium alloy processed by ECAE. Scripta Materialia 36:681–686
44. Watanabe H et al (1999) Effect of temperature and grain size on the dominant diffusion process for superplastic flow in AZ61 magnesium alloy. Acta Materialia 47(14): 3753–3758
45. Caceres CH et al (1999) The effect of Cu content on the level of microporosity in Al-Si-Cu-Mg casting alloys. Scripta Materialia 40(5):631–637
46. Ghosh AK (1977) Tensile instability and necking in materials with strain hardening and strain-rate hardening. Acta Metallurgica 25(12):1413–1424
47. Lee SG et al (2005) Variability in the tensile ductility of high pressure die cast AM50 Mg alloy. Scripta Materialia 53:851–856
48. Weiler JP et al (2005) Relationship between internal porosity and fracture strength of die cast magnesum alloy AM60B. Materials Science and Engineering A 395:315–322
49. Ericksen SC (1988) Magnesium's high damping capacity for automotive noise and vibration attenuation. In 45 World Magnesium Congress, Tokyo, 1998, IMA, pp 54–58
50. Jensen JW (1964) Magnesium damping capacity—causes and effects. In Magnesium Association Convention, 1964, pp 1–11
51. EMI shielding, Hydro Magnesium Brochure, 2005
52. Rudajevova A, Stanek M, Lukac P (2003) Determination of thermal diffusivity and thermal conductivity of Mg-Al alloys. Materials Science and Engineering A 341:152–157
53. Doehler HH (1951) Die castings. McGraw Hill, New York
54. Sin LS, Dube D (2004) Influence of process parameters on fluidity of investment cast AZ91D magnesium alloy. Materials Science and Engineering A 386:34–42
55. Moore S (2002) Magnesium Molding—technique expands options. Modern Plastics, July 2002:33
56. Kono K (1999) Method and apparatus for manufacturing metallic parts by fine die casting. US Patent 5,983,976, 16 Nov 1999
57. Moore S (2002) Thixotropic molding broadens processor capabilities. Modern Plastics March 2002:24–30
58. Tausing G, Ricketts NJ, Peck SR (2001) Forging of magnesium using squeeze cast preform. In J Hryn (ed) Magnesium Technology 2001, TMS, Warrendale, PA, pp 235–242
59. Couling SL, Pashak JF, Sturkey L (1959) Transactions ASM 51:94–107
60. Barnett MR, Bave MD, Bettles CJ (2004) Deformation microstructures and textures of some cold rolled Mg alloys. Materials Science and Engineering A 386:205–211
61. Lochte L, Westengen H, Rodseth J (2005) An efficient route to magnesium alloy sheet: Twin roll casting and rolling. In NR Neelaleggham (ed) Magnesium Technology 2005, TMS, Warrendale, PA, pp 247–252
62. Bohlen J et al (2005) Microstructure and texture development during hydrostatic extrusion of magnesium alloy AZ31. Scripta Materialia 53:259–264
63. Celotto S (2000) TEM study of continuous precipitation in Mg-9Al-1Zn alloy. Acta Materialia 48(8):1775–1787
64. Zhang MX, Kelly PM (2002) Crystallography of Mg17Al12 precipitates in AZ91D alloy. Scripta Materialia 48:647–652
65. Ghali E, Kainer KU (2004) General and localized corrosion of magnesium alloys: A critical review. Journal of Materials Engineering and Performance 13:7–23
66. Lunder O et al (1989) Corrosion Science 45:741
67. Juzeliunas E et al (2005) Structure and initial corrosion resistance of sputter deposited nanocrystalline Mg-Al-Zr alloys. Materials Science and Engineering A 395:411–416
68. Song G, StJohn D (2002) The effect of zirconium grain refinement on the corrosion behaviour of magnesium-rare earth alloy MEZ. Journal of Light Metals 2:1–16
69. Dube D et al (2001) Characterization and performance of laser melted AZ91D and AM60B. Material Science and Engineering A 299:38–45
70. Song G, Atrens A, Dargusch M (1999) Influence of microstructure on the corrosion of die cast AZ91D. Corrosion Science 41:249–273

71. Mathieu S et al (2002) Corrosion behaviour of high pressure die cast and semisolid cast AZ91D alloys. Corrosion Science 44:2737–2756
72. Wang F, Li Y, Huo H 2004) Corrosion of AZ91D magnesium alloy with a chemical conversion coating and electroless nickel layer. Corrosion Science 46:1467–1477
73. Yang K, Xu L, Zhang E (2005) Formation by ion plating of Ti-coating on pure Mg for biomedical applications. Scripta Materialia 53:523–527
74. Timoshenko AV, Magurova YV (1995) The effect of a cathodic component on AC microplasma oxidation of aluminum alloys. Protection of Metals 31(4):377–380
75. Stevens KT, John CG, Walsh FC (2003) Surface finishing of aluminum and magnesium alloys using plasma electrolytic oxidation. In HI Kaplan (ed) Magnesium Technology 2003, TMS, Warrendale, PA, p 89
76. Timoshenko AV et al (1994) The effect of silicates in sodium hydroxide solution on the structure of oxide coatings deposited on a D16T alloy by microarc oxidation. Protection of Metals 30(2):149–153
77. Shrestha S et al (2002) Improved corrosion performance of AZ91D magnesium alloy coated with the Keronite process. In HI Kaplan (ed) Magnesium Technology 2002, TMS, Warrendale, PA
78. MEL (2005) Surface treatments for magnesium alloys in aerospace and defence. Magnesium Elektron, Swinton, England
79. Brown RE (2002) Developments in magnesium wrought products rolling, forging and sheet casting. In 59th Annual World Magnesium Conference, Montreal, 2002, pp 25–32
80. Nakatsugawa I, Tsukeda T, Kitamura K (2002) Latest developments in magnesium use for thixomolding in Asia. In 59th Annual World Magnesium Conference, Montreal, 2002, 11–14
81. Shukun M et al (2006) China magnesium industry development report for 2005. In 63rd World Magnesium Conference, Beijing, IMA, pp 3–23
82. Metals Handbook (1973) 8th ed. vol. 8. American Society for Metals, Metals Park, Ohio
83. Westengen H, Bakke P, Albright, D (2005) Advances in Magnesium Alloy Development. Die Casting Engineer 49(6):26–32
84. Nayeb-Hashemi AA, Clark JB (1988) Phase diagrams of binary magnesium alloys. ASM International, Metals Park, Ohio
85. Brooks CR (1982) Heat treatment, structure and properties of non-ferrous alloys. ASM International, Metals Park, Ohio
86. Mathis K, Trojanova Z, Lukac P (2002) Hardening and softening in deformed magnesium alloys. Materials Science and Engineering A 324:141–144
87. Pourbaix M (1974) Atlas of Electrochemical Equilibria. In Aqueous Solutions, National Association of Corrosion Engineers
88. Kato A et al (1994) Consolidation and mechanical properties of atomized Mg-based amorphous powder. Materials Science and Engineering A 179–180:112–117
89. Kato A et al (1994) Microstructure and mechanical properties of bulk Mg70Ca10Al20 alloys produced by extrusion of atomized amorphous powders. Materials Science and Engineering A 179–180:707–711
90. Friedrich H, Schumann S (2002) Strategies for overcoming technological barriers to the increased use of magnesium in cars. In Transactions of Institute of Mining and Metallurgy (section c: mineral processing and extractive metallurgy), The Institute of Materials, Minerals and Mining, pp. C65–C71
91. CRC Handbook of Chemistry and Physics (1996) New York
92. Smithels Metals Reference Book, 8-th edition (2004) Elsevier
93. Shewmon P, Diffusion in Solids (1989) TMS Warrendale
94. Horst HJ and Asby MF (1982) Deformation Mechanism Map, Pergamon Press
95. Cannon JF (1974) J. Phys. Chem. Ref. Data Vol. 3, pp 781–824
96. Magnesium and Magnesium Alloys (1999) edited by M. Avedesian and H. Baker, ASM International, Materials Park, OH
97. Metals Handbook (1990) Vol 2. ASM International, Materials Park, OH

2
Semisolid Processing—Origin of Magnesium Molding

2.1 Introduction

The majority of techniques applicable for manufacturing net shape components from metals and their alloys, in principle, could be classified into two conventional routes restricted to either the solid or liquid state. The liquid state methods involve casting with a variety of modifications: gravity, high-pressure die casting, squeeze casting, etc. In contrast, the solid-state techniques require generally multi step operations following casting, such as homogenization of chemistry, hot working, cold working, forming, machining and eventually heat treatment. As a result, the properties of wrought components are predominantly superior to castings. The number of manufacturing steps and their complexity, however, contributes to a significantly higher cost of the final product. The economy factor represents the downside of many non-conventional manufacturing techniques, e.g., powder metallurgy. Thus, there is a continuous quest for a technology that would allow reducing cost and at the same time improving the properties.

The ultimate goal in this search is the single step manufacture of components with intricate shapes, sound structural integrity and properties comparable to the wrought state at a low cost similar to casting (Fig. 2.1). It is believed that the emerging technology of semisolid processing exhibits features that may satisfy these requirements. Although semisolid processing established itself already as a viable method of manufacturing, it is currently under intensive development, and a critical breakthrough is still expected. This chapter provides the basic characteristics of semisolid processing, including historical and technical backgrounds, major concepts and examples of their commercialization.

2.2 Origin of the Concept

2.2.1 Thixotropy

The phenomenon of thixotropy, which primarily referred to the reversible changes from a flowable fluid to a solid-like elastic gel, was discovered in 1923 by Schalek

F. Czerwinski, *Magnesium Injection Molding*.

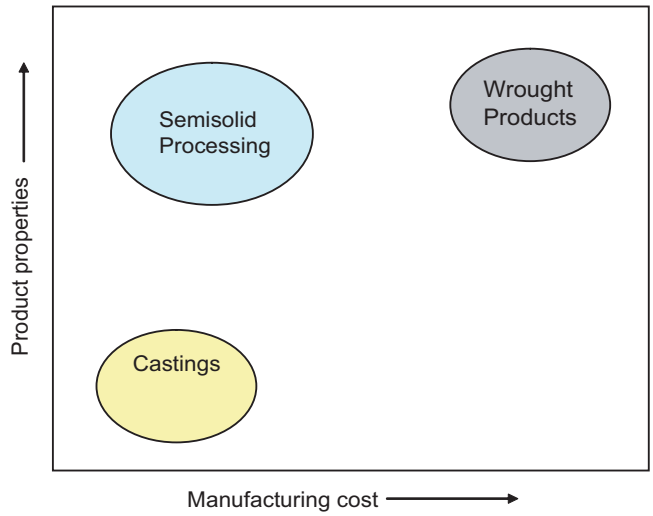

Fig. 2.1 The manufacturing cost versus properties relationship for cast and wrought components with the anticipated relationship for semisolid metal processing [60]

and Szegvari [1] within nonmetallic systems. The essence of their finding was the remarkable property of aqueous iron oxide gels, which were becoming completely liquid through gentle shaking alone to such an extent that the liquefied gel was hardly distinguishable from the original sol (Fig. 2.2). Previously, these kinds of physical changes had only been known to occur by modifying the temperature when gels would melt on heating and then re-solidify on cooling. The term *thixotropy* was introduced by Peterfi [2] in 1927 as a combination of two Greek words: *thixis*, meaning stirring or shaking and *trepo*, meaning turning or changing. During the following years, various systems were studied, including clays, oil suspensions, creams, drilling mud, flour doughs, flour suspensions, fiber greases, jellies, paints and starch pastes. Thixotropic behavior with the time response of the structure, that is itself changing with time, represents a great challenge for rheologists, and from this discovery until today it is differently understood by various parts of the scientific community [3].

2.2.2 Semisolid Metal Processing

Semisolid metal processing (SSP), sometimes referred to as semisolid metallurgy (SSM), was invented at Massachusetts Institute of Technology (MIT), USA, in 1971 by Flemings and co-workers [4, 5]. During experiments with Sn–15%Pb alloy they found that applying shear during solidification substantially reduced the stress measured. In fact, the stress at a given temperature below the liquidus was orders of magnitude less than when the alloy was cooled to that temperature

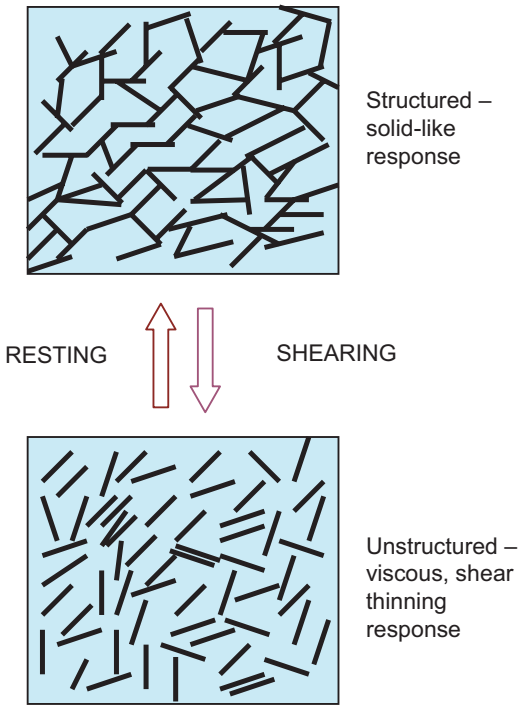

Fig. 2.2 The schematics of transient from the completely structured matter with solid-like response to completely unstructured matter with viscous, shear thinning response [60]

without shear. For a dendritic Sn–15%Pb composition with a solid fraction around 0.4, the maximum shear stress was 200 kPa. For the same solid fraction of the non-dendiric semisolid slurry the shear stress was only 0.2 kPa, i.e., three orders of magnitude less.

Semisolid metal processing represents one of the many engineering applications that utilize thixotropy. It should be pointed out that, although metallic alloys, sheared below their melting point, are described as thixotropic, in fact they exhibit mainly shear-thinning behavior.

2.3 Rheological Behavior of Semisolid Slurries

2.3.1 Newtonian and Non-Newtonian Fluids

An inherent feature of a fluid is that it cannot resist externally applied lateral force (shear), and under influence of this force it deforms continuously. In general, there is a relationship between shear stress and shear rate. For Newtonian fluids the shear

stress τ, defined as the force acting tangentially to a surface divided by the area of the surface, is proportional to the shear rate, $\dot{\gamma}$; where the constant of proportionality is called the viscosity, η:

$$\tau = \eta\dot{\gamma} \tag{2.1}$$

For non-Newtonian fluids the shear stress is not proportional to the shear rate. The viscosity is then termed the *apparent viscosity*, and it is dependent on the shear rate, pressure, temperature and time. The simplest empirical equation describing the viscosity η changes is based on power law model:

$$\eta = k\dot{\gamma}^{n-1} \tag{2.2}$$

where:

k – consistency index;
n – power-law exponent;
$\dot{\gamma}$ – shear rate.

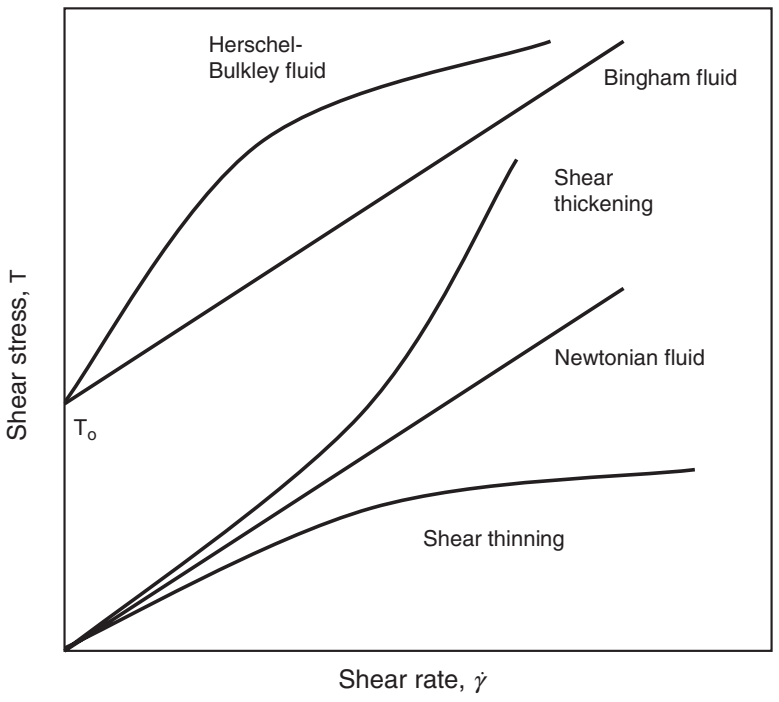

Fig. 2.3 Relationships between shear stress and shear rate for several rheological behaviors

A variety of behavior of different fluids is summarized in Fig. 2.3. When the power-low exponent $n < 1$, the viscosity of the fluid increases with the shear rate and the fluid exhibits shear thickening behavior. In the case, when $n > 1$, the viscosity decreases with the shear rate and the fluid exhibits shear thinning. There are also non-Newtonian fluids which require a certain shear stress to be deformed. When this stress is exceeded their flow is activated. The fluids, which after exceeding the threshold stress flow further as Newtonian, are called Bingham fluids. When further deformation follows a power low, the term Herschel-Bulkley fluids is valid.

2.3.2 Thixotropy and Pseudoplasticity

The system is described as thixotropic when a reduction in magnitude of its rheological properties, such as elastic modulus, yield stress and viscosity occurs reversibly and isothermally with a distinct time dependence on application of shear strain. The thixotropic material subjected to constant shear rate experiences a reduction in viscosity with time. After the material is allowed to rest for a period of time, the viscosity increases again (Fig. 2.4). The most frequent structural changes that produce thixotropy are those where the structure breaks down under high shear rate but recovers under low shear rate or when at rest. Therefore, thixotropy arises from changes in floc structural arrangement due to forces acting between suspended particles and breakdown due to the shear rate. For a limited number of materials the opposite changes are also possible when structure builds up under shear and disintegrates under rest, and this phenomenon is called *anti-thixotropy*. It was revealed in the 1930's that thixotropy was more pronounced in systems

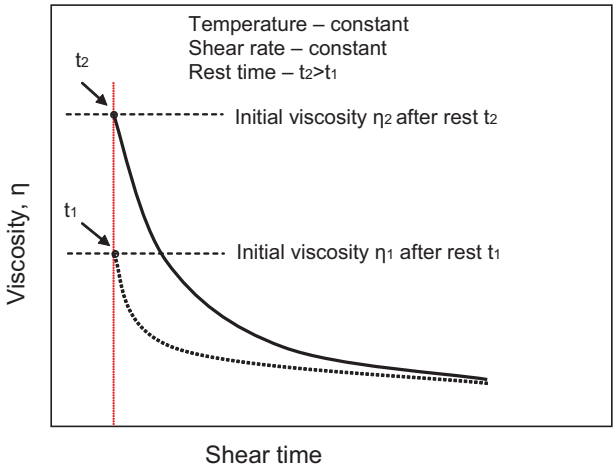

Fig. 2.4 The schematics of influence of the rest time on viscosity changes versus shear time

containing non-spherical particles because rotation and movement allowed for their alignment and dis-alignment in a three-dimensional structure [6].

Shear thinning, also referred to as pseudoplasticity, describes a decrease of viscosity with an increase in shear rate. Both terms are frequently confused since in real systems it is difficult to separate the time-dependent and time-independent behavior of the non-Newtonian fluid. An explanation of pseudoplastic behavior is the formation of agglomerates/clusters of favorably oriented solid particles at low shear rates, which increases viscosity. It is assumed that changes are reversible and high shear rates break down agglomerates, reducing viscosity. In general, all thixotropic materials exibit shear thinning but not all shear thinning fluids are thixotropic.

2.3.3 Experimental Relationships for Metallic Slurries

Rheological experiments with metallic slurries, using predominantly the Sn–Pb system, led to a number of findings [4, 7]. Measurements performed during continuous cooling describe viscosity changes at constant cooling rate or constant shear rate. It was found that the steady state apparent viscosity of non-Newtonian slurries depends on solid concentration the same way as it is observed for Newtonian slurries (Fig. 2.5). For constant solid fraction, a reduction in shear rate leads to an increase in viscosity. For measurements at constant shear rate, an increase in solid fraction leads to higher viscosity. The viscosity is highly sensitive to solid fraction for high solid fractions (typically above 0.6). For high liquid fractions small changes of viscosity are observed.

A measurement of shear-rate dependence of *steady-state viscosity* indicates the pseudoplastic i.e., shear thinning behavior (Fig. 2.6). For a slurry with a constant solid fraction, the steady state viscosity decreases with shear rate. At low shear rates

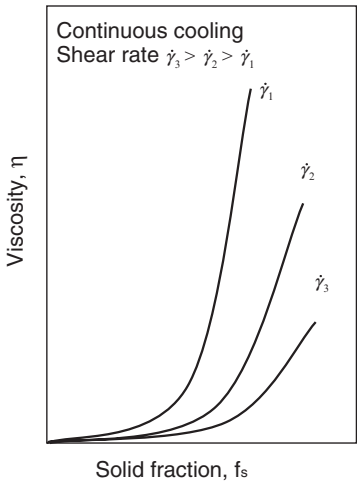

Fig. 2.5 The schematic graph characterizing changes of apparent viscosity versus solid fraction for different shear rates

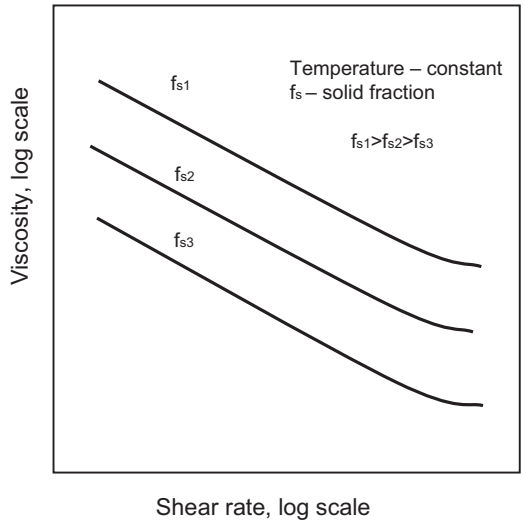

Fig. 2.6 The plot showing steady state apparent viscosity versus shear rate for various solid fractions

the bonds are formed between particles and viscosity is high. At high shear rates, structural connections between particles are broken, reducing resistance to flow. At steady state, there is equilibrium between formation and disappearance of connections between particles.

During semisolid processing the slurry is subjected to rapid change in shear rate, e.g., when thixocast billet is injected into die cavity. Such a rapid change in shear rate results in certain rheological response which depends on so-called transient behavior of the slurry [8]. The time dependence of *transient-state viscosity* means that at constant shear rate, viscosity slowly decreases with time. When the shear rate is rapidly reduced, a structure build up is experienced, and after a certain time, viscosity is settled at the new higher level as emphasized in schematics based on [8] and [9] in Fig. 2.7. By contrast, when the shear rate is rapidly increased, structure breakdown takes place and after a certain relaxation time, a new steady state condition is achieved with viscosity settled at the lower level.

2.3.4 Models Describing Thixotropic Behavior

In engineering practice, it is essential to know the effect of thixotropy on flow of a slurry during the filling of the mold. To achieve this, quantitative mathematical models of thixotropy are required. The issue is complex since thixotropy is within the subject of the thermodynamic theory of relaxation phenomena. The majority of the present theories can be divided into three groups [3]:

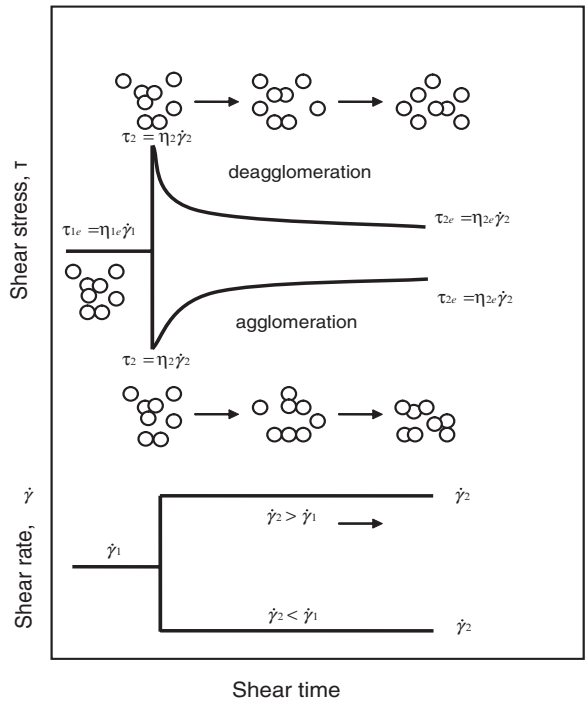

Fig. 2.7 Shear stress transient after changes in shear rates along with a schematic model of changes in semisolid material structure related to agglomeration and de-agglomeration

(i) indirect microstructural theories using general description microstructure with a scalar parameter;
(ii) theories using direct description of microstructure changes including number of bonds or description of the floc using fractal analysis;
(iii) theories using the viscosity data.

The purpose of a mathematic model is to express the complete thixotropic behavior in a consistent set of parameters and be able to fit the experimental data from the rheological tests. For metallic slurries, difficulties in modeling are caused in part by the fact that evolution of particle shape and size during shear is irreversible. This implies that viscosity depends not only on the shear but also on the slurry thermal history.

2.3.4.1 Microstructure as the Scalar Parameter: Indirect Theories

Theories based on structure models build equations derived from details of floc formation and break-up and the effect of the floc size on viscosity [9]. The viscosity η is derived using structural parameter λ that controls the floc size and shape:

$$\eta = \eta(\dot{\gamma}, \lambda) \tag{2.3}$$

where:

$\dot{\gamma}$ - shear rate.

The variation of the structural parameter with time $\frac{d\lambda}{dt}$ is expressed by:

$$\frac{d\lambda}{dt} = g(\dot{\gamma}, \lambda) \tag{2.4}$$

To describe the structure changes, it is proposed that the breakdown rate depends on shear rate and on the current structure [9]:

$$\frac{d\lambda}{dt} = a(1-\lambda) - b\lambda\dot{\gamma} \tag{2.5}$$

where:
a,b are kinetic data.
When $\dot{\gamma} = 0$, fluid is at rest, the viscosity is the zero-shear viscosity η_o and the structure is fully build up, then λ=1. As opposed to this, when shear rate is high, $\dot{\gamma} \to \infty$, the viscosity is η_∞ and the structure is fully broken down, λ=0.

The structural parameter λ is related to the stress τ or viscosity η by flow equations. According to reference [9], the relationship is as follows:

$$\eta = \frac{\tau_o}{\dot{\gamma}} + \frac{\tau_p}{\dot{\gamma}}\lambda + k\dot{\gamma}^{n-1} \tag{2.6}$$

where:

k, n, τ_p - constants;
τ_o - the yield stress.

2.3.4.2 Direct Structure Theories

The reaction kinetics was applied to thixotropy via a simple scheme that looked at the distribution of broken and unbroken bonds and the number of the broken bonds is linked to viscosity [10]. The rate of structure breakdown is expressed as:

$$-\frac{d(unbroken)}{dt} = k_1(unbroken)^n - k_2(broken)^m \tag{2.7}$$

where:
k_1 and k_2 are the rate constants for the breakdown and buildup, respectively.

In order to solve the above equation it is assumed that viscosity is linearly proportional to the amount of unbroken structure with a maximum value when completely structured - η_o and a minimum value when completely destructured - η_∞. The rate

constant k_2 is assumed to be independent of shear rate while the rate of breakdown constant k_1 is related to shear rate by a power-law expression.

Assuming that a structured liquid is made of flocs of randomly linked chains of particles, the rate equation is derived in the form [11]:

$$\frac{dN}{dt} = k_2 P - \left(k_o + k_1 \dot{\gamma}^m\right) N \tag{2.8}$$

where:

N – average number of links per chain;
k – rate constant describing Brownian collision;
k_o and k_1 – rate constants for the Brownian and shear contributions to breakdown;
P – the number of single particles per unit volume;
m – the constant less than unity.

Since at the equilibrium $\frac{dN}{dt}$ is zero

$$N_e = \frac{k_2 P}{k_o \left(1 + \frac{k_1}{k_o} \dot{\gamma}^m\right)} \tag{2.9}$$

Assuming subsequently that the viscosity is given by a constant η_∞ plus a viscous contribution proportional to the number of bonds N_e the following relationship is derived:

$$\frac{\eta_e - \eta_\infty}{\eta_o - \eta_\infty} = \frac{1}{1 + \frac{k_1}{k_o} \dot{\gamma}^m} \tag{2.10}$$

It is possible to use the non-equilibrium data to derive a thixotropic model as it was proved later by others.

2.3.4.3 Simple Viscosity Theories

In the simple viscosity theory the structural parameter λ is replaced by viscosity as a direct measure of structure [12]. According to this theory, the rate of change of viscosity $\frac{d\eta}{dt}$ rather than the change of structure is related to the viscosity difference between the steady state η_s and current values of viscosity η, not the structure difference, respectively:

$$\frac{d\eta}{dt} = K\left[\eta_s(\dot{\gamma}) - \eta\right]^n \tag{2.11}$$

where:

K, n – material constants.
According to another description, thixotropic breakdown is expressed as [13]:

$$\left(\eta_{\infty}-\eta\right)^{1-m}=\left[\left(m-1\right)kt+1\right]\left(\eta_{o}-\eta_{\infty}\right)^{1-m} \tag{2.12}$$

where:

η_o and η_∞ - the asymptotic values of viscosity η representing the fully structured and fully destructured states, respectively, measured at time t and any particular share rate;

k, m - material constants.

2.3.5 Flow Characteristics

Rheological models are very useful in predicting flow characteristics of liquids, e.g., during filling mold cavities. In semisolid processing the finite yield stress plays a critical role. Therefore, the process is controlled by relative contribution of gravity, viscous and plastic resistance. They affect the process differently in polymer processing with negligible inertia or metal processing with negligible inertia and gravity effects.

During a modeling that filled two-dimensional cavity by Bingham fluid at negligible gravity but different values of Reynolds (Re) and Bingham (Bi) numbers, five different flow patterns were identified: shell, mound, disc, bubble and transition [14, 15]. The morphology of these patterns exhibits a correlation with Reynolds and Bingham numbers. Shell type flow takes place at large Re but small Bi, mound flow at low Re and low Bi, bubble at larger Bi. Disc exists for conditions between shell and bubble. Patterns of shell, mound and disc do not exhibit significant un-yielded areas. As a result, filling is not substantially different than that expected for Newtonian fluids. When both inertia and plastic resistance are significant, the bubble flow takes place, which is characterized by increased spread of the filling slurry column near the entry. The patterns of transition and bubble are dominated by yielded and un-yielded surfaces. Flow associated with those patterns is different from Newtonian fluids and leads to flow instabilities and unpredictable die filling.

A number of computer codes were developed to correlate the viscosity of the alloy with flow behavior during filling the mold cavities. Earlier research using the finite element program ProCast 4.0 shows that during filling the simple shape cavity for low viscosities of 10^{-3} Pa s, typical for liquid metals, an irregular flow front suggesting turbulence is observed [16]. The flow advanced faster on both edges of the cavity. At high viscosities of 10^{1} Pa s, typical for metallic slurry, uniform filling with laminar flow was seen.

The flow modeling of semisolid slurry is often performed by incorporating special modules into commercial software for modeling the flow of molten alloy. A literature example describes simulations that fill a cavity with a cylindrical obstacle [17]. The model fitted the steady state flow curve for Sn–15%Pb to a Herschel–Bulkley model with a yield stress τ dependant on the solid fraction:

$$\tau = \tau_o\left(f_s\right) + \exp\left(Bf_s\right)k^*\kappa\dot{\gamma}^m \tag{2.13}$$

where:

B, k* coefficients;
κ – the structural parameter which describes the current state of agglomeration;
f_s – solid fraction;
τ_o – yield stress.

The model was incorporated into the computational fluid dynamics software. Then a high pressure die casting process was simulated with a semisolid alloy modeled as a Newtonian and as thixotropic fluid with f_s=0.5 and identical filling rates. The results demonstrate the different filling behavior of the thixotropic slurry, which flows more smoothly around the cylindrical obstacle.

The practical application of the FLOW-3D software (Flow Science Inc.) for evaluating filling patterns, based on specific process parameters and properties of Mg–9Al–1Zn magnesium alloy, is shown in Fig. 2.8 and 2.9. The cell phone housing with sections having a thickness of 0.4 mm is filled with alloy of different viscosities: 0.013 Pa s and 0.8 Pa s. The difference in viscosity was achieved by changes in temperature. In both cases the gate velocity and the fill time were the same. For alloy with a viscosity of 0.013 Pa s, the flow is turbulent with large air pockets left far behind the flow front (Fig. 2.8). For alloy with a viscosity of 0.8 Pa s, being higher by almost two orders of magnitude than the former one, the flow front is uniform. The sections filled at the end represent overflows, which are separated from the part and forwarded to recycling.

Another practical application of FLOW-3D software (Flow Science, Inc.) is depicted in Fig. 2.10. The part is the laptop case cover, gated from the center by a 20 mm diameter inlet. The average feeder thickness at a minimum inlet ring thickness is of 0.45 mm. The mold, made of AISI H13 steel, was preheated to 250 °C and assumed remaining constant. For the modeling of mold filling using fully molten Mg–9Al–1Zn alloy the melt temperature was assumed as 595 °C. For inlet velocity of 7.5 m/s, the fill time reached 20 ms with highly turbulent flow (Fig. 2.10a).

During flow modeling of the semisolid slurry at f_s = 0.2 at approximately 570 °C, the dynamic viscosity was temperature and strain dependant, and particular behaviors

Fig. 2.8 The FLOW-3D simulation of filling a cavity of cell phone housing with a weight of 5.3 g using magnesium alloy Mg-9Al-1Zn with a viscosity of 0.013 Pa s

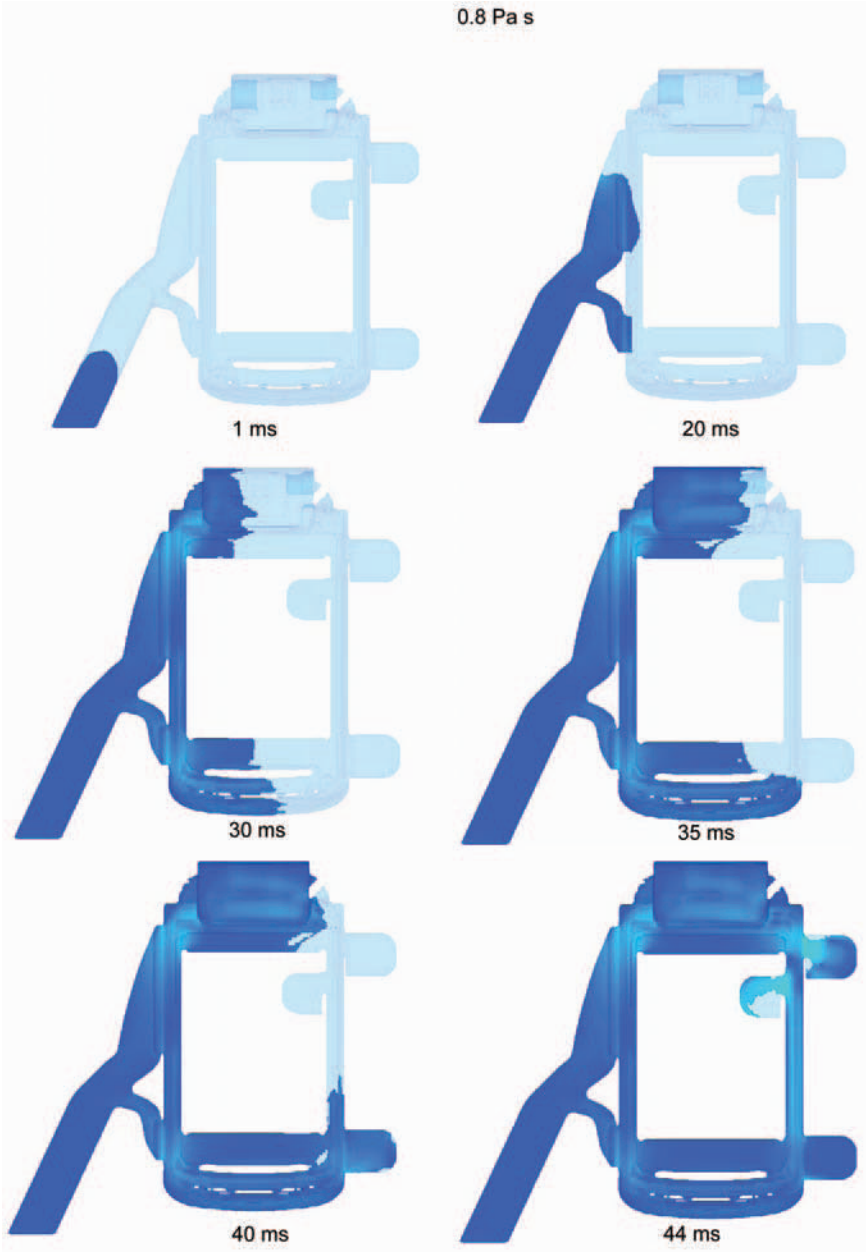

Fig. 2.9 The FLOW-3D simulation of filling a cavity of cell phone housing with a weight of 5.3 g using magnesium alloy AZ91D with a viscosity of 0.8 Pa s

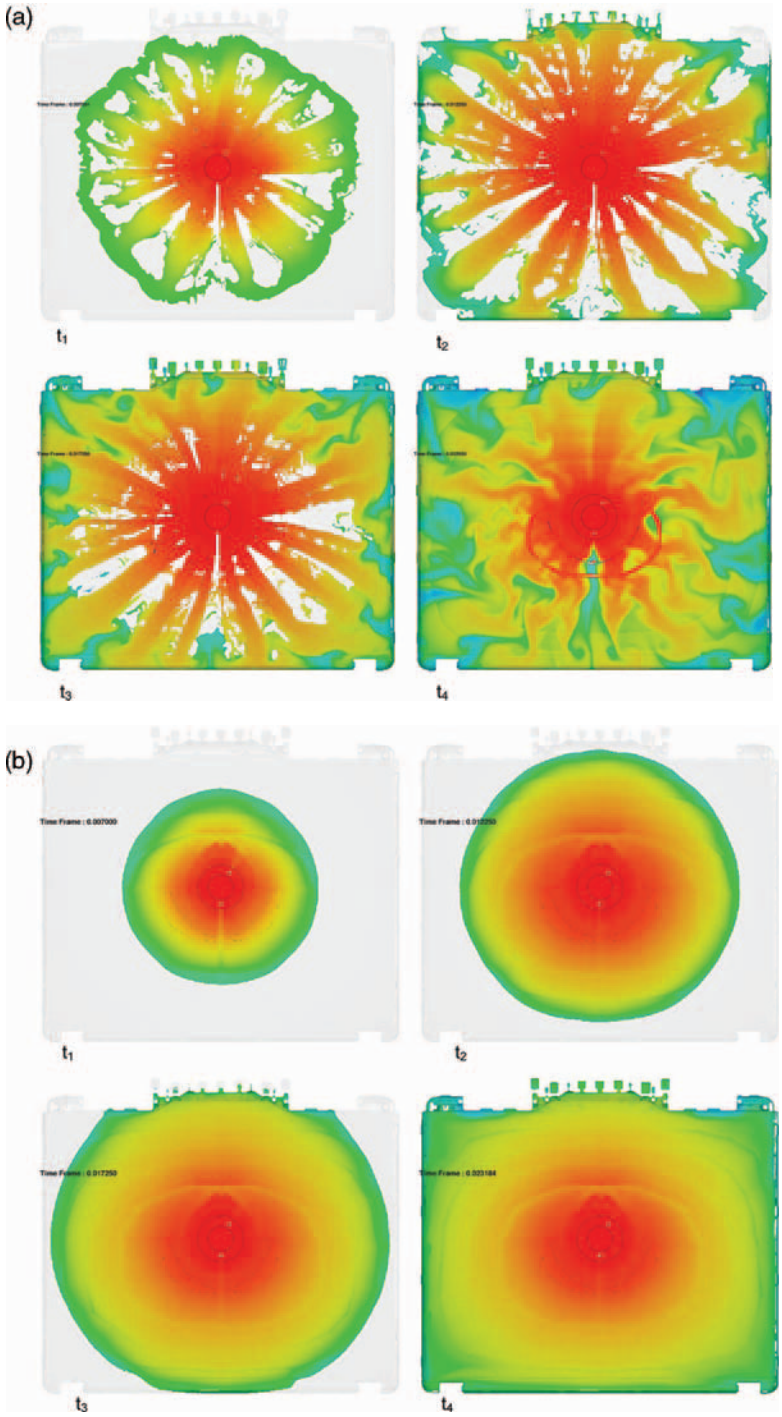

Fig. 2.10 The FLOW-3D simulation results showing differences in filling the thin wall housing (0.7 mm wall, 100 g weight) of a laptop with AZ91D alloy: **a** fully molten state at temperature of 595 °C; **b** semisolid state at f_s=0.2 and temperature of 570 °C

are presented later in this chapter. For the same fill time of 20 ms, a presence of solid essentially changed the mold filling behavior, creating highly laminar flow (Fig. 2.10b).

2.4 Viscosity Measurements of Metallic Slurries

Of a variety of techniques used for viscosity measurements of fluids, only a limited number is applicable to metallic slurries at high temperatures. Viscometers that can measure fluids with high viscosity are usually called rheometers. The rotational viscometers do not have sufficient torque to be applied for viscosity measurements of metallic slurries with high solid fractions. As a result other techniques should be used that introduce complexity and potentials for artifacts, e.g., related to nonuniform distribution of shear rate within the alloy volume. Those most frequently used are based on the material's compression, drop forge and back extrusion. Due to a number of factors affecting measurements the comparison of data generated by different techniques should be exercised with care. The comparison of viscosities of selected materials is listed in Table 2.1.

2.4.1 Rotational Instruments

In all the rotational methods the force required to rotate an object within the fluid indicates a viscosity. The techniques applicable to metals are based on a fluid flow through the gap between two coaxial cylinders, one or both rotating along their common axis. As opposed to other methods described below, rotational viscometers

Table 2.1 Typical viscosities of selected materials with a superimposed viscosity range, typical for metallic alloys in semisolid state

Viscosity, Pa s	10^{-5}	10^{-4}	10^{-3}	10^{-2}	10^{-1}	10^{0}	10^{1}	10^{2}	10^{3}	10^{4}	10^{6}	10^{8}	10^{12}
Non metallic materials		Acetone	Water	Olive oil	Yogurt	Glycerin	Honey, ketchup	Chocolate syrup	Molasses, bitumen				Molten glass
Metallic alloys			Liquid metals		Semisolid alloys at f_s=0.4								
					$\dot{\gamma} = 200s^{-1}$				$\dot{\gamma} = 0.001s^{-1}$				

use *in situ* prepared slurry. There are two classical geometries of instruments known as either Couette or Searle—distinguished by whether the external cylinder (cup) or internal cylinder (bob) rotates, respectively.

The Couette method is named in honor of its developer, Maurice Frederic Alfred Couette, professor of physics at the end of the 19th century at University of Angers, France. Viscosity measurements are conducted when the cup, rotating at a known velocity, creates a viscous drag to be exerted by the fluid residing in an annular space between both cylinders. This drag creates torsional forces in the bob, which are measured with a torque dynamometer. The range of shear rates may be changed by selecting rotor speed and using various cup-bob combinations. A design shown in Fig. 2.11a has cup and bob of conical shapes, allowing in situ adjustment of the space between them, i.e., the shear force. A classic Searle viscometer represents concentric cylinders where the inner cylinder (bob) is rotated by external weights. As with the Couette case, the space between cylinders is filled with a liquid alloy and subjected to torsional forces created this time by the bob. Both instruments are equipped with systems for heating and accurate control of temperature.

The shear rate $\dot{\gamma}$, generated by a cylindrical viscometer (Fig. 2.11b), is described by the relationship [18]:

$$\dot{\gamma} = \frac{2\omega R_c R_b}{R_c^{\,2} - R_b^{\,2}} \tag{2.14}$$

where:

ω – angular speed of the motor;
R_c – inner radius of the outer cylinder (cup);
R_b – radius of the inner cylinder (bob).
The torque signal recorded is then used to determine the viscosity η:

$$\eta = \frac{M\left(R_c^{\,2} - R_b^{\,2}\right)}{4\pi h \omega R_c^{\,2} R_b^{\,2}} \tag{2.15}$$

where ;

M – torque of the inner cylinder;
h – immersed depth of the inner cylinder;
R_c, R_b, ω defined in (2.14).

The typical measurements with rotational viscometers include:

(i) shearing and continuous cooling of overheated melt;
(ii) transient and steady state measurements for constant solid fraction and constant shear rate where initial conditions are specifically defined;
(iii) shearing following partial solidification or re-melting.

Advantages of rotational methods include flexibility in experiment design and well specified flow parameters.

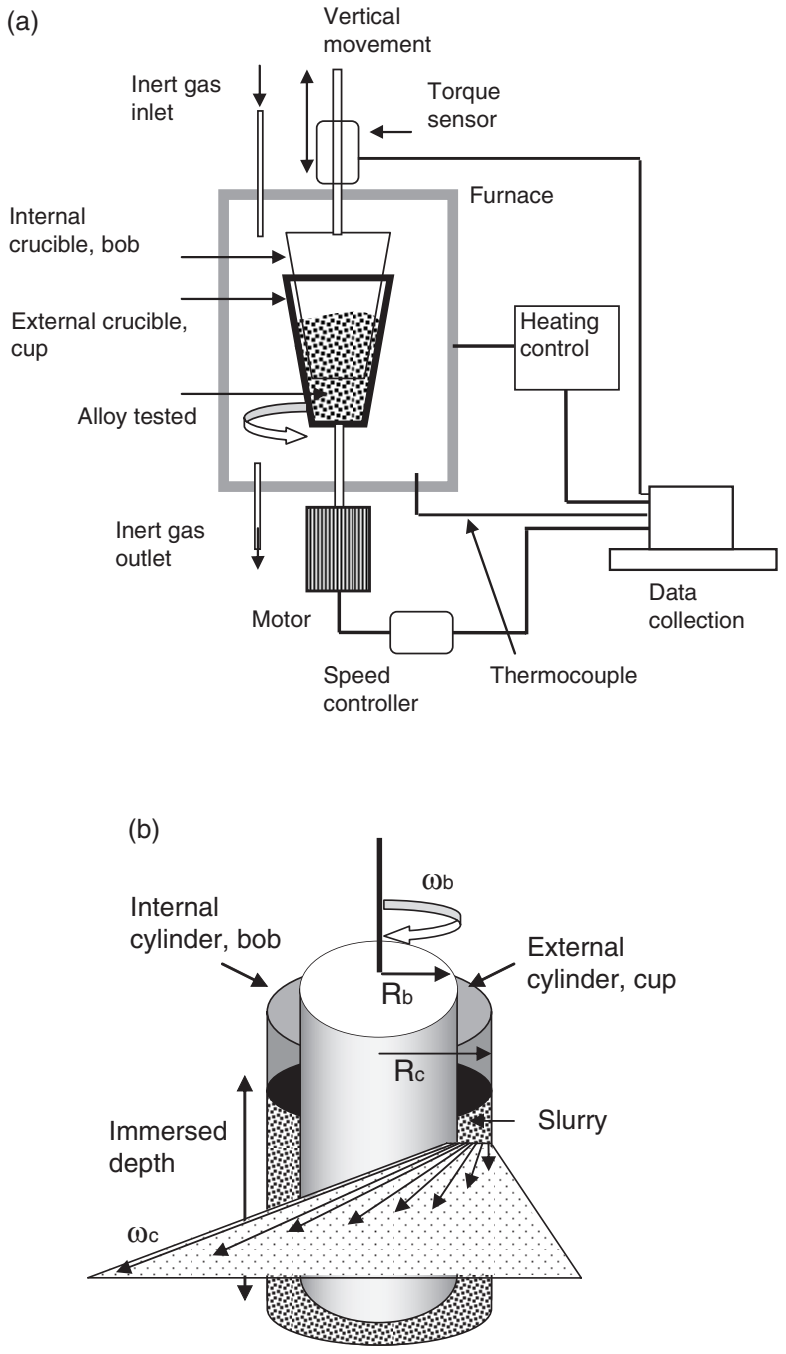

Fig. 2.11 A rotational viscometer based on Couette method **a** and a distribution of slurry's velocity between cup and bob within the Searle's instrument **b**

2.4.2 Compression Viscometer

During rheological measurements with a compression test the material is placed between two parallel plates, surrounded by the furnace walls and attached to the crossheads of a tensile machine. After the required temperature is reached, the compression is performed under either constant deformation or constant load at various crosshead speeds. The typical compression curve for low solid fractions exhibits a maximum followed by stress reduction apparently caused by the sample cracking. At high solid fraction the stress remains practically constant, as the sample flows homogeneously.

During the compression tests, the average value of the shear rate, $\dot{\gamma}$ is expressed [19]:

$$\dot{\gamma} = \frac{1}{2}\sqrt{\frac{V}{\pi h_c^{\,3}}}\dot{\varepsilon} \tag{2.16}$$

where:

V – sample volume;
h_c – sample height after test;
$\dot{\varepsilon}$ – compression rate.

The apparent viscosity η is calculated from the compression test using the following formula [19]:

$$\eta = \frac{2\pi h_c^{\,4}}{3V^2\dot{\varepsilon}} F_c \tag{2.17}$$

where:

ε – strain from the initial height h_o of the sample to the height h_c;
F_c – compression force;
V – sample volume.

A disadvantage of the compression method is the relatively low deformation rate, so that the results may not be applicable to commercial processes, which utilize much higher shear rates. Besides, it is difficult to prevent the solid–liquid segregation. A friction between the sample and plates also contributes to the inhomogeneity in the stress–strain field.

2.4.3 Drop Forge Viscometer

The drop forge viscometer was designed based on the parallel plate compression viscometer with the difference that the upper platen is allowed to fall under the influence of its own gravity [20]. The movement of the upper platen is analyzed

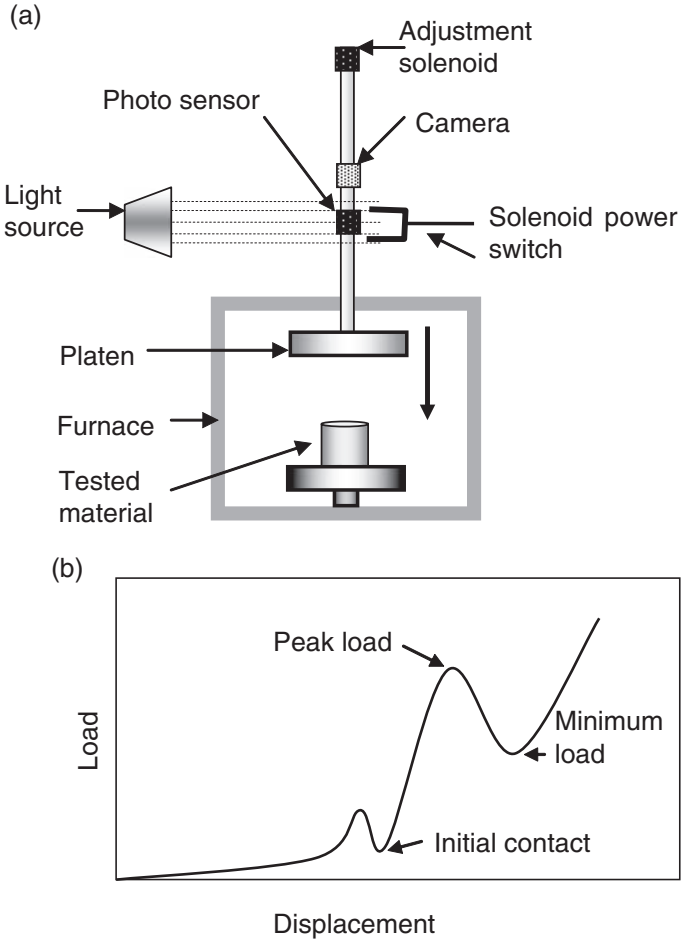

Fig. 2.12 Schematic diagram of the drop forge viscometer **a** [20] and typical response of a semisolid slurry to the fast compression **b** [59]

by a high speed camera (Fig. 2.12a). The force is determined from the second derivative of displacement data allowing calculation of viscosities at shear rates exceeding 1000 s^{-1}. Total duration of a test can be less than 10 ms. Besides, the drop forge viscometer can be operated like a conventional parallel-plate viscometer, attaining shear rates as low as 10^{-5} s^{-1}. A unique feature of this instrument is that the typical experiment yields instantaneous, volume averaged viscosity first under rapidly increasing and then under rapidly decreasing shear rate. Separation of solid and liquid is negligible for experiments shorter than 10 ms. For low compression velocities, segregation takes place. The drop forge viscometer allows the characterization of slurry with solid fractions as high as 0.7. A diagram of force versus ram displacement is the source of information required for

viscosity assessment (Fig. 2.12b). It is believed that the peak is associated with breaking up the solid skeleton, created during the rest period. Based on this design, the peak stress is calculated from the peak load and the minimum load is used to calculate the flow stress.

2.4.4 Back Extrusion Viscometer

The hardware setup used for viscosity measurements based on back extrusion is shown in Fig. 2.13a [21, 22]. The cylindrical sample is placed within the graphite cup and after preheating to achieve a required solid fraction, is extruded at a constant ram speed around the stationary plunger (Fig. 2.13b). The ram displacement and extrusion force are recorded using a data acquisition system of the tensile machine that represents the essential part of the setup (Fig. 2.13c).

The viscosity η is derived based on the plot of the force versus ram displacement, in particular its linear portion [19]:

$$\eta = \frac{1}{2\pi\lambda C_1 V_p}\frac{dF}{dt} \tag{2.18}$$

where:

dF/dt is the slope of the applied force versus time, measured from the plot's stationary region;
λ is the extrusion ratio calculated as

$$\lambda = \frac{R_s^{\,2}}{R_s^{\,2} - R_p^{\,2}} \tag{2.19}$$

where:

R_s and R_p are the radius of the sample and plunger, respectively (see Fig. 2.13b);
V_p is the plunger's velocity;
C_1 and C_2 are constants that may be calculated from R_s, R_p and V_p:

$$C_1 = \left(\ln\frac{R_p}{R_s}\right)^{-1}\left(C_2\left(R_s^{\,2} - R_p^{\,2}\right) - V_p\right) \tag{2.20}$$

$$C_2 = \frac{V_p\left(2\ln\dfrac{R_s}{R_s} - 1\right)}{\left(R_s^{\,2} + R_p^{\,2}\right)\ln\dfrac{R_s}{R_p} - \left(R_s^{\,2} - R_p^{\,2}\right)} \tag{2.21}$$

The mean value of shear rate between the container and plunger is described by [19]:

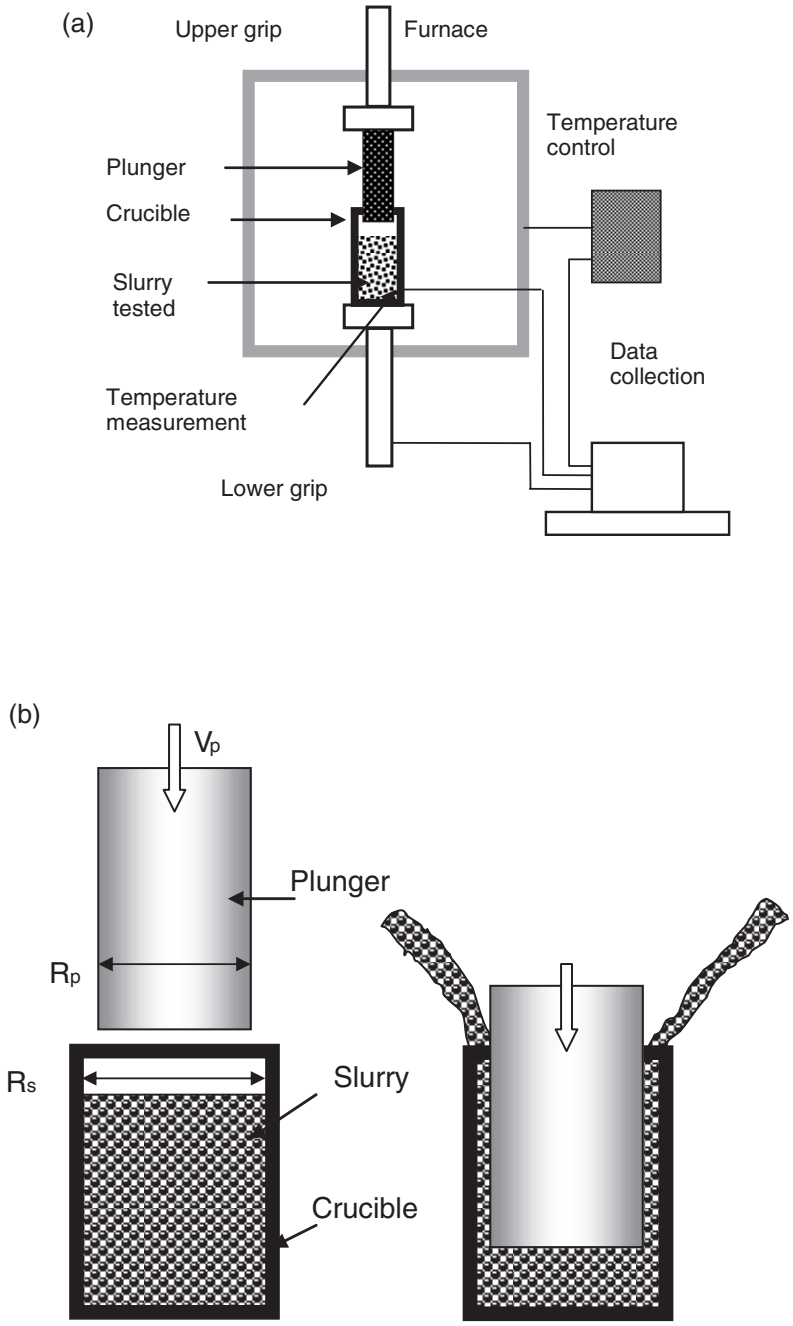

Fig. 2.13 The viscosity measurement based on back extrusion: **a** experimental setup; **b** magnified view of the sample extruded;

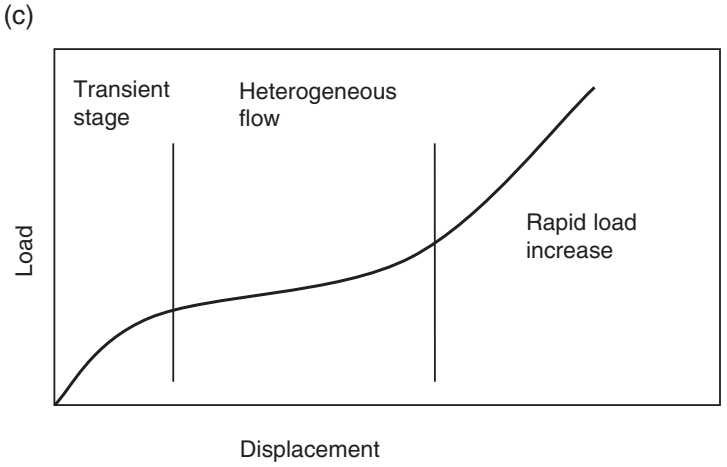

Fig. 2.13 (continued) **c** a diagram of force versus ram displacement

$$\dot{\gamma} = \frac{1}{R_s - R_p}\left[C_1\left(\ln\left(-\frac{C_1}{2C_2R_sR_p}\right)-1\right)-C_2\left(R_s^{\,2}+R_p^{\,2}\right)\right] \tag{2.22}$$

In back extrusion technique, the apparent viscosity is dependent on the extrusion ratio. In particular, the value calculated from the linear portion of the force versus ram displacement graph decreases as the extrusion ratio increases. This phenomenon is caused by a variation in the solid fraction under the plunger during extrusion. In particular, the amount of liquid removed into extruded product is higher than in the original non-extruded sample.

2.5 Rheological Measurements for Semisolid Magnesium Alloys

Rheological data for magnesium slurries was collected using the Couette, Searle and parallel plate methods. To properly interpret viscosity values the conditions of measurements should be taken into account. In addition, the method of generation of semisolid alloy is of importance. So far, rheological data for Mg alloys is limited to AZ91 and AM50 grades.

2.5.1 Isothermal Holding Measurements

During evaluation of thixotropic properties of the slurry at steady state by isothermal holding experiments the apparent viscosity is measured as a function of shear rate at a constant solid fraction, i.e., constant temperature.

The Searle type viscometer measurements for both AZ91 and AM50 at a constant temperature and the shear rate revealed that the apparent viscosity decreases with time until it reaches a steady state value [23]. The time required to reach the steady state value is inversely proportional to the shear rate. Similarly the steady state viscosity at constant temperature is also proportional to shear rate. For isothermally held alloys, the apparent viscosity follows the power–law relationship with the shear rate, given by equation 2.2. For the shear rate range between $100\,s^{-1}$ and $500\,s^{-1}$, the power–law constant n equals −0.85 for AZ91 and −0.98 for AM50.

Compression and backward extrusion measurements [19] of AZ91 alloy over a wide range of shear rate from 10^{-3} to $10^{3}\ s^{-1}$ revealed the shear thinning behavior with the average exponent factor in equation 2.2 of −0.87. The low shear rate range 10^{-3} to $10\,s^{-1}$, tested by compression, shows the power–law exponent of −0.65 while for the high shear rate up to $10^{3}\ s^{-1}$, the exponent was −0.95. Literature data is summarized in Fig. 2.14.

2.5.2 *Continuous Cooling Measurements*

During this type of experiment the apparent viscosity is measured for the continuously cooled slurry under constant cooling rate and at constant shear rates. Literature data is summarized in Fig. 2.15a,b.

At a constant shear rate with decreasing temperature, i.e., increasing the solid fraction, the apparent viscosity, initially up to f_s=0.3, increases slowly. For higher solid fractions, especially above 0.4, it increases more rapidly, presumably as interactions between

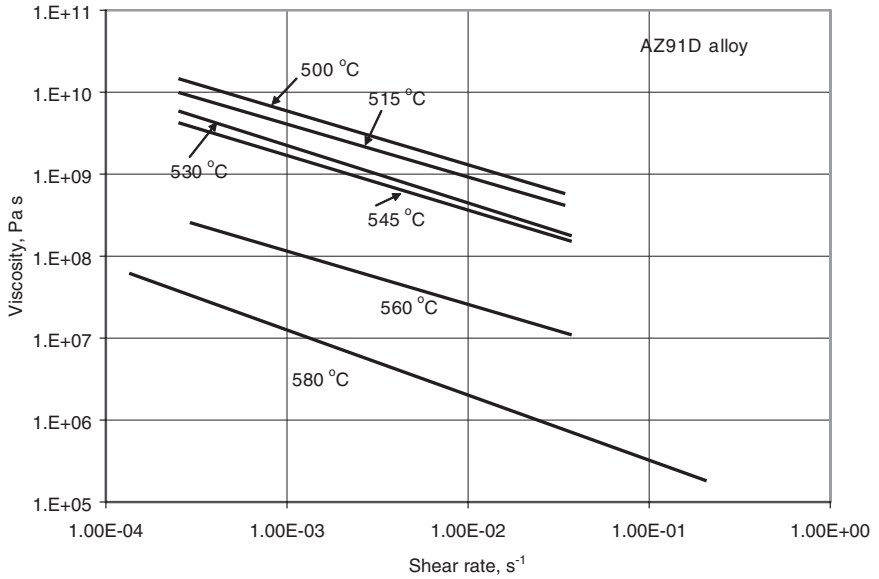

Fig. 2.14 The viscosity as a function of shear rate for AZ91D alloy [19]

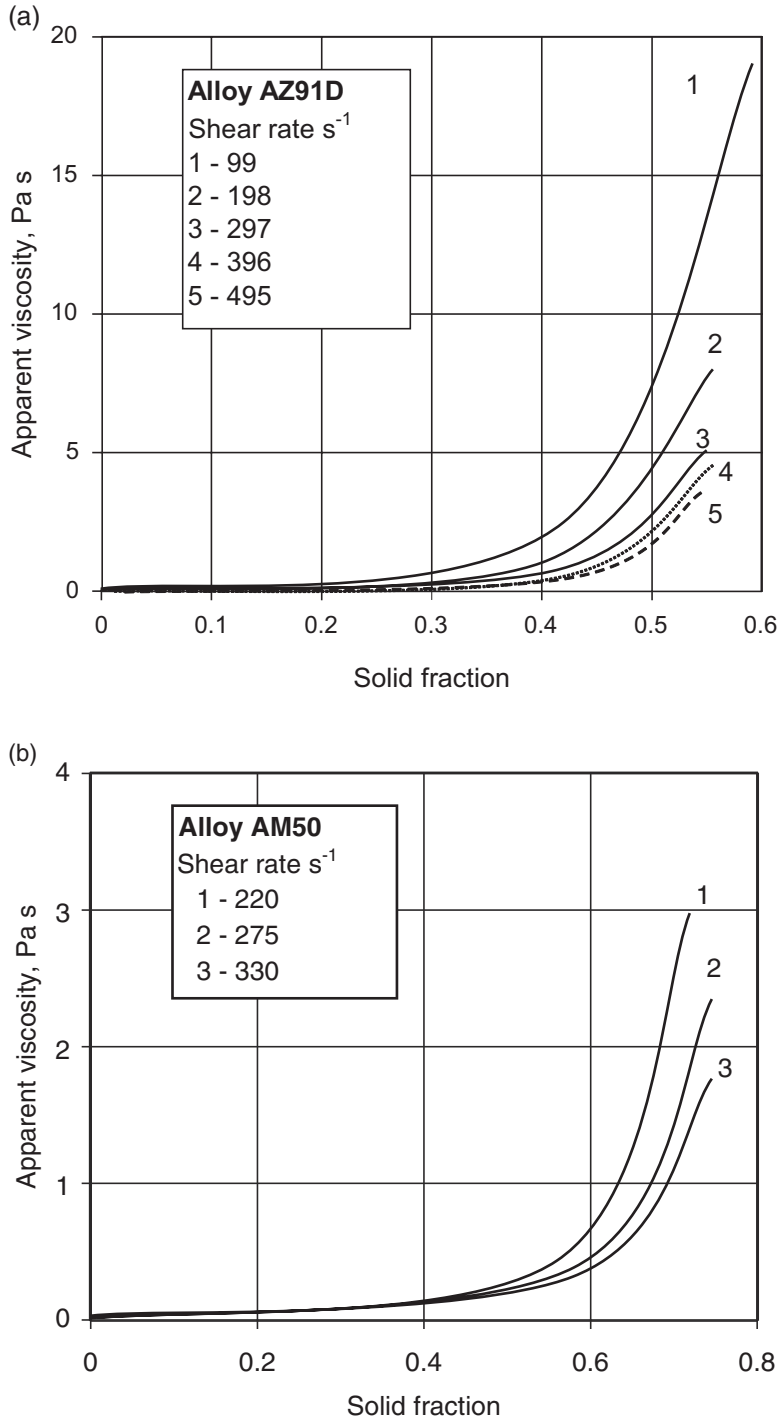

Fig. 2.15 The viscosity as a function of the solid fraction for AZ91D **a** and AM50 **b** alloys [23]

particles become significant. At any solid fraction, viscosity is inversely proportional to shear rate as is the case for the isothermal experiments. There is a difference between viscosity values obtained from continuous cooling and isothermal measurements, with the latter being lower. The difference is caused by the fact that the continuously cooled slurry does not have time to reach the steady state, resulting in higher values.

For AZ91 alloy and the shear rate of 5×10^{-3} s^{-1}, the dependence of viscosity η on the solid fraction is described by the relationship [19]:

$$\eta = A\exp\left(Bf_s\right) \tag{2.23}$$

where: A - material constant;
B equals 15 for a solid fraction from 0.55 to 0.95.

2.5.3 Influence of Rest Time on Viscosity

The behavior of AZ91D slurry under different rest conditions was studied using the Couette method [18]. Data is summarized in Fig. 2.16. The properties are charac-

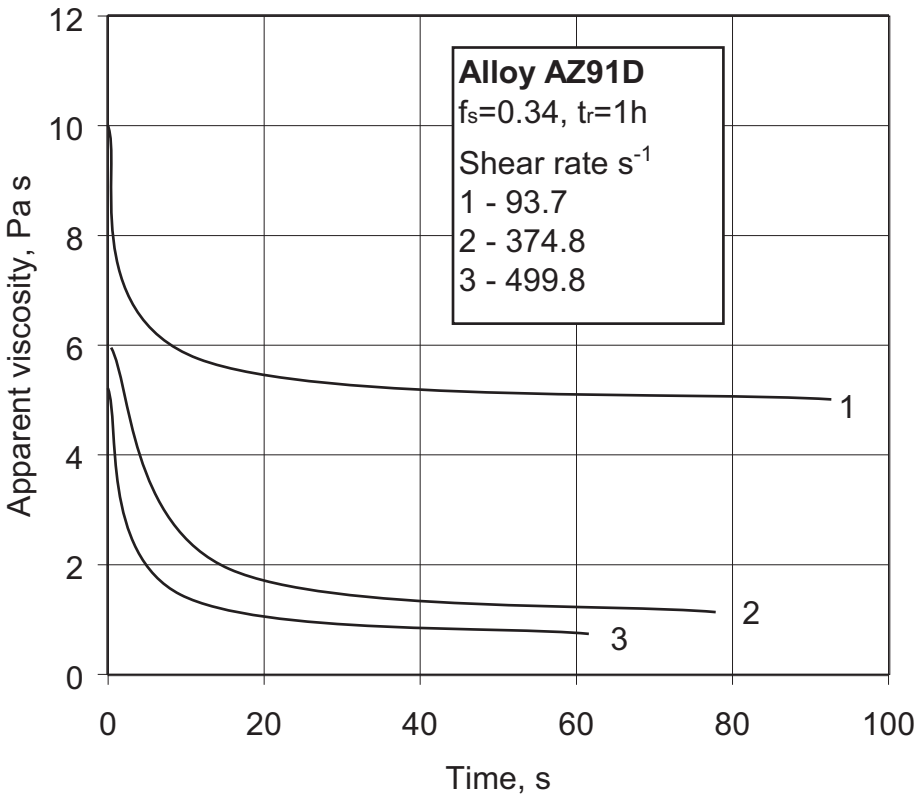

Fig. 2.16 The effect of rest time on viscosity of AZ91magnesium alloy [18]

teristic of other thixotropic materials described earlier. In general, the AZ91D alloy exhibits shear thinning behavior and the apparent viscosity increases during rest time but falls down again to the steady state when subjected to shearing. At the constant shear rate, increasing the rest time leads to an increase in steady state apparent viscosity. For higher solid contents, the time of reaching steady state is longer. While continuously increasing shear it is easier to reach the steady state, and the viscosity, measured at the steady state, is getting higher.

2.6 Techniques of Generating Globular Structures

Semisolid processing consists of two or three stages. First, a globular structure within the semisolid alloy is created. Then the semisolid slurry is used either directly for applications that require slurry (rheocasting) to form a component with near-net shape or be solidified as billets for later reheating during thixocasting. The techniques applied to generate globular structures since the invention of semisolid processing until today are described below.

2.6.1 Melt Stirring/Agitation

This historically first finding was that agitating or stirring solidifying alloys produces shear rates sufficient to break up the dendritic network formed and obtain a slurry comprising solid spheroids dispersed in a liquid.

2.6.1.1 Mechanical Stirring

The technique originated from a batch process and was adapted later to a continuous casting. The simple solution consists of a metal rod inserted into a cylindrical tube or chamber containing the solidifying alloy (Fig. 2.17). In order to produce the necessary shear rates and break up the dendritic network when mechanically stirred, two parameters are critical. First, to create the high shear rate around the stirring rod, the rod rotation speed must be of the order of 1000 rpm. Then, the minimum critical size of the gap between the rod and the cylinder wall should be maintained since the shear diminishes as a function of this distance. Fulfilling these requirements leads to extensive wear and erosion of both the rod and cylinder, as well as low volumetric throughput. In order to combine the rapid heat extraction and vigorous melt agitation, different sizes and shapes of rods, rotating at different velocities, are used. Solutions involve melt agitation by augers, impellers or other multi-paddle mixers, mounted on a rotating shaft.

In general, the technique has limited industrial importance [24]. Despite this, there are examples showing its effectiveness. According to recent findings [25], an agitation of partially solidified Al–10% Cu alloy for 60 s by means of a screw-shaped

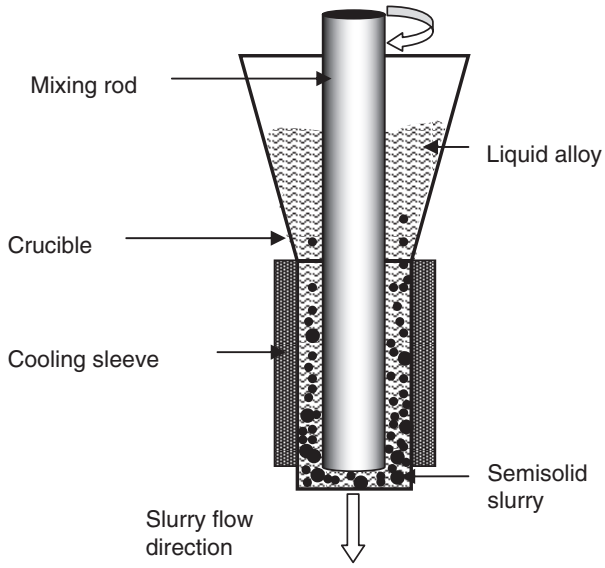

Fig. 2.17 The mechanical mixing arrangement to produce non-dendritic structures in a continuous mode

stirring rod at 800–1000 rpm resulted in grain size as small as 10 μm. A twin screw extruder with closely intermeshing, self-wiping and co-rotating screws is found to be an effective exploitation of another present method of mechanical stirring [26]. The fluid flow within the apparatus is characterized by high shear rate, high intensity of turbulence and cyclic variation in shear rate. Such a shear variation takes place because of continuous change of the gap between the screw and the barrel. The alloy fed to the extruder, being usually overheated 50 °C above the liquidus, is intensively sheared and cooled into the interval of liquidus and solidus. Typical agitation is expressed by the shear of 225 s^{-1} applied for 30 s. A velocity profile in the twin screw extruder is complex and principal forces of compression, rupture and shear are acting on the alloy between two screws and between screws and barrel.

2.6.1.2 Magnetohydrodynamic Agitation (MHD)

This method induces a turbulent motion within the melt during solidification by electromagnetic or electrodynamic techniques under controlled temperature (Fig. 2.18). As a result, it creates degenerate dendrites comprising solid spheroids suspended in the liquid. The vibration and stirring of the molten metals is achieved by either an induced alternative current (AC), electromagnetic field or the use of a pulsed direct current (DC) within an applied magnetic field. When using the AC electromagnetic current, the molten metal is fed to and held in an AC induction coil. For the AC induction coil, in addition to the coil geometry, the primary control parameter is the frequency, which affects the depth of penetration, and the current,

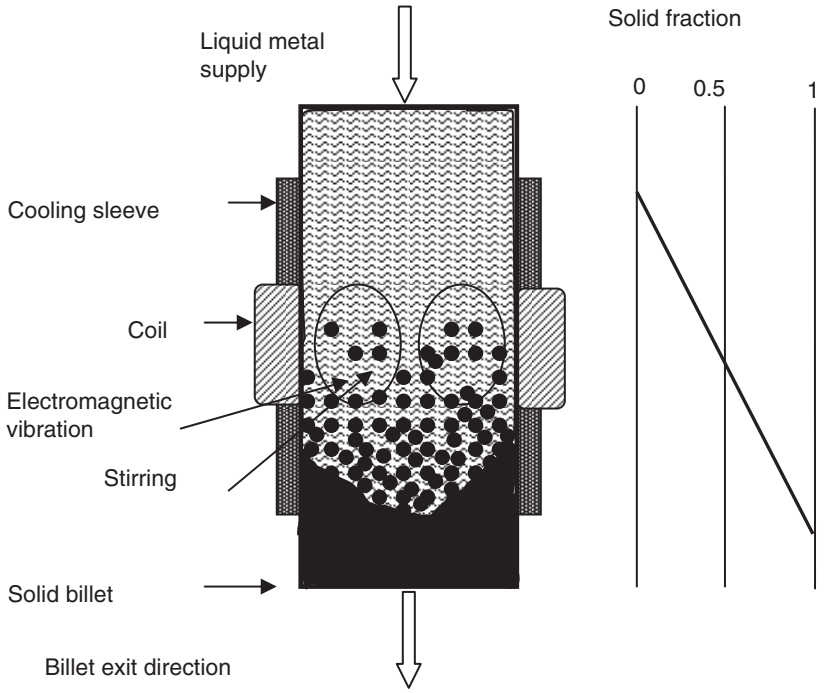

Fig. 2.18 The magnetohyrodynamic agitation arrangement to produce non-dendritic structures during solidification. Graph on the right shows a change of the solid fraction within the apparatus

which controls the force imposed. The typical frequency ranges from 60 Hz to 10,000 Hz and current from 500 A to 10,000 A. In another method, a pulsed DC current is used within an applied magnetic field. The magnitude of the DC current and magnetic field control the shear force and typical values are 100 A to 5,000 A and 0.6 Webers/cm^2 to 30 Webers/cm^2.

Vibrating molten metal by electromagnetic means offers advantages over mechanical stirring solutions. First, the use of electromagnetic force to effect vibration is much more effective. Flow of the slurry from the vibrating chamber is controlled by electromagnetic techniques and may be continuous or semi-continuous [27]. The electromagnetic technique does not require chambers with critical gap sizes, so it is not limited by the throughput. Besides, there are no moving components, so wear and erosion are suppressed.

2.6.1.3 Ultrasonic Agitation

In this technique, the high power ultrasonic vibration with intensities of the order of 7–20 W/cm^2 is applied to the solidifying alloy, leading to fine and non-dendritic microstructures. Thus, the growth of columnar grains is suppressed and a more homogeneous structure is formed. The mechanism explaining microstructural

changes is based on cavitation and acoustic streaming. Cavitation causes the formation, growth and collapsing of small bubbles inside the melt. The high compression rate of bubbles generates hydraulic waves resulting in the creation of nucleation sites. Moreover, the shock waves during the collapse of cavitation bubbles cause crystal breakage at the solidification front. It is also claimed that cavitation activates solid particles of oxides and intermetallics as nucleation sites [28]. The ultrasonic vibration affects also the temperature distribution within the solidification front. During the expansion half-period the bubbles rapidly increase in size, causing evaporation of liquid [29]. As an accompanying phenomenon, a reduction in bubble temperature is experienced, which leads to undercooling of the melt at the bubble surface and formation of nuclei. A fine grain structure is enhanced by the fact that ultrasound prevents agglomeration of individual bubbles during their growth in the semisolid state.

2.6.2 Chemical Grain Refinement

Grain refinement (Chap. 1), combined with a low pouring temperature, results in rosette-like grains that evolve into small globules during subsequent reheating and short holding. Semisolid slurries of fine and spherical particles in a broad range of solid fractions can also be obtained directly from the liquid state through control of nucleation and growth by a powerful grain refiner. A procedure for the production of thixotropic magnesium alloy is based on adding a grain refiner combined with controlled rapid solidification followed by re-heating to the two-phase area. It is essential that solidification takes place at such speed that growth of dendrites is avoided. According to some sources [30], the solidification rate should be higher than 10 deg/s. The size of the globules is dependent on the temperature and the holding time within the semisolid range and typical values quoted are below 100 μm. The formation of spherical primary magnesium particles is attributed to the combined effect of both dissolved and undissolved grain refiner particles of suitable sizes. Both forms cause the high nucleation rate and a slight undercooling in magnesium alloys [31].

2.6.3 Swirl Enthalpy Equilibration

The process consists of two steps:

(i) rapid extraction of a controlled quantity of heat from the molten metal charge in order to generate a liquid/solid slurry and
(ii) draining away the excess liquid, leaving a compact self-supporting slug which can then be handled and formed under pressure [32].

The draining step eliminates a need for precise control of temperature, which allows processing of alloys with a narrow melting range. The concept is shown in Fig. 2.19. At the beginning, the molten alloy is transferred to a vessel with large

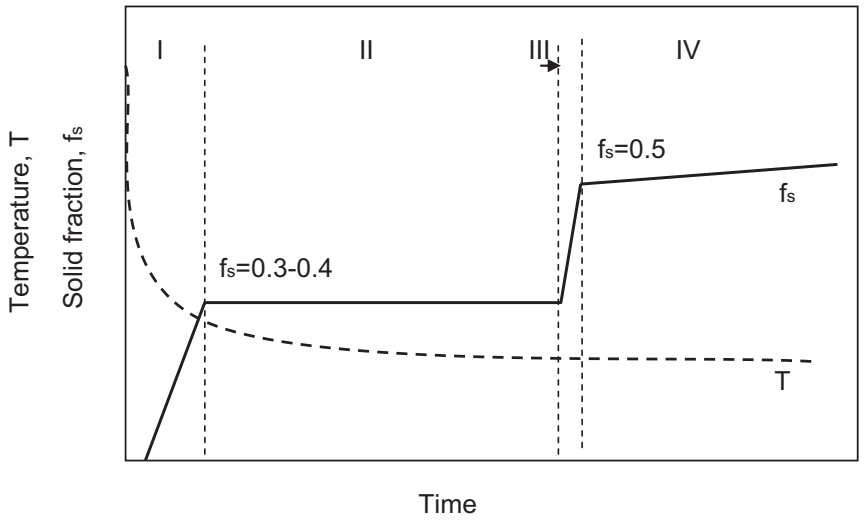

Fig. 2.19 Schematic diagram showing changes of temperature and solid fraction during a single cycle of the swirl enthalpy equilibriation process of Alcan International: I – crash cooling to solid fraction of 0.3-0.4; II – isothermal holding; III – draining the excess liquid; IV – transfer to die-casting machine. Based on [32]

thermal mass, sufficient to cool its content to 30–40% solid. When cooled, the alloy is swirled at 200 rpm to achieve the uniform distribution of solid at the walls. During the second stage the swirling motion is stopped and excess liquid is removed through the bottom opening within the vessel. The amount of liquid drained could be up to 30%. After draining is completed, the slug is removed and transferred to the forming machine.

2.6.4 Continuous Rheo-Conversion Process (CRP)

During the CRP process, two liquids, held at a certain level of superheat, are passively mixed within a reactor [33]. The reactor provides heat extraction and sufficient forced convection to effectively mix the melt streams during the initial stage of solidification (Fig. 2.20). The convection and turbulence experienced by the slurry during mold filling also play a role in formation of the globular structures. Very high density of nuclei within the slurry indicates copious nucleation. The particle size is dependent on cooling rates, and slower cooling rates within the semisolid range create structures having larger particles. The solid fraction can be quickly adjusted before forming. The high nucleation rates, combined with turbulence and forced convection, lead to

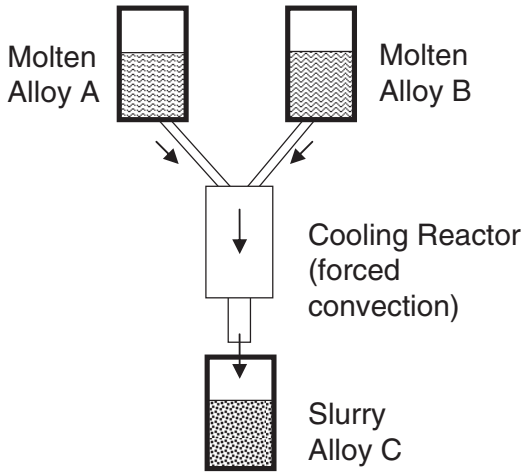

Fig. 2.20 A concept of the continuous rheo-convertion process: **A, B** overheated alloys used for mixing; **C** resultant alloy in semisolid state [33]

(i) copious nucleation of the of the primary phase;
(ii) uniform distribution of nuclei throughout the liquid;
(iii) survival of nuclei due to uniform temperature distribution.

2.6.5 Liquidus/Sub-Liquidus Casting/Pouring

The essence of these processes is the melt temperature in the vicinity of the liquidus. The melt with such a temperature is poured or injected and followed by solidification. It is known that reducing the pouring temperature inhibits growth of columnar forms and enhances growth of equiaxed grains. The technique is attractive for both direct forming and manufacturing feedstock for further semisolid forming [34]. Details of this method are presented in Chap. 12.

2.6.6 Rapid Slug Cooling

The rapid slug cooling technology (RSCT) explores a cooling control during solidification to produce a fine and homogeneous microstructure of globular dendrites suitable for thixoforming [35, 36]. No melt agitation is involved. The rapid solidification, where circulating water around the mold with an average temperature of 120 °C was the medium removing heat, led to formation in AM70 alloy of globular particles with a size over 250 μm. It was also established that a melt temperature of 30 °C above the liquidus creates the optimum conditions.

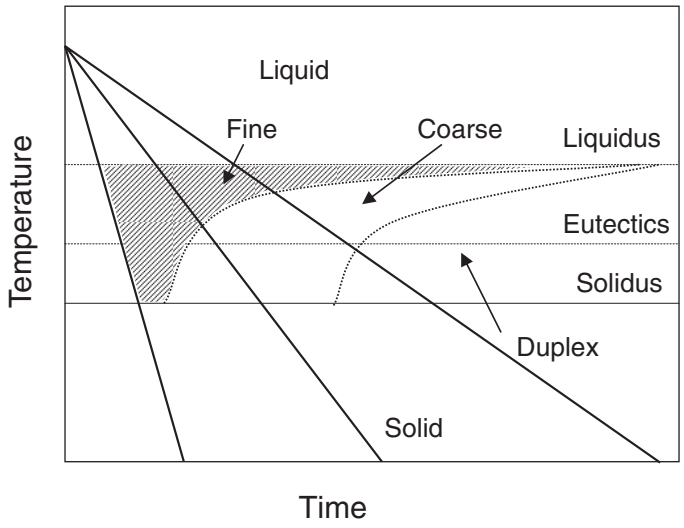

Fig. 2.21 Morphologies obtained during solidification as a function of cooling rate [37]

While the higher temperature results in coarse grains, lower temperatures produce cold spots inside the billet.

2.6.7 Controlled Slow Cooling

As opposed to rapid slug cooling, this method benefits from solidification rates (Fig. 2.21). The process does not require stirring or grain refining and its effectiveness is confirmed for A357 AlSiMg alloys [37]. Of the entire alloy volume, heated above the liquidus temperature in a furnace, a portion is transferred to an intermediate vessel with controlled temperature. The temperature of the melt is then adjusted to the required level and melt is transferred to the mold where solidification takes place. The transfer temperature is between 3 and 15 °C above the liquidus and the flow during mold filling is non-turbulent. The essential feature of this method is the slow cooling rate, not exceeding 0.5 °C/s. As a result, the microstructure consists of spheroidal particles suspended in a liquid matrix, which for A357 alloy stay below 50 μm.

2.6.8 Spray forming

Spray forming by the Osprey route explores atomization of a liquid metal by a high velocity jet of inert gas into small droplets (Fig. 2.22). As a result, liquid

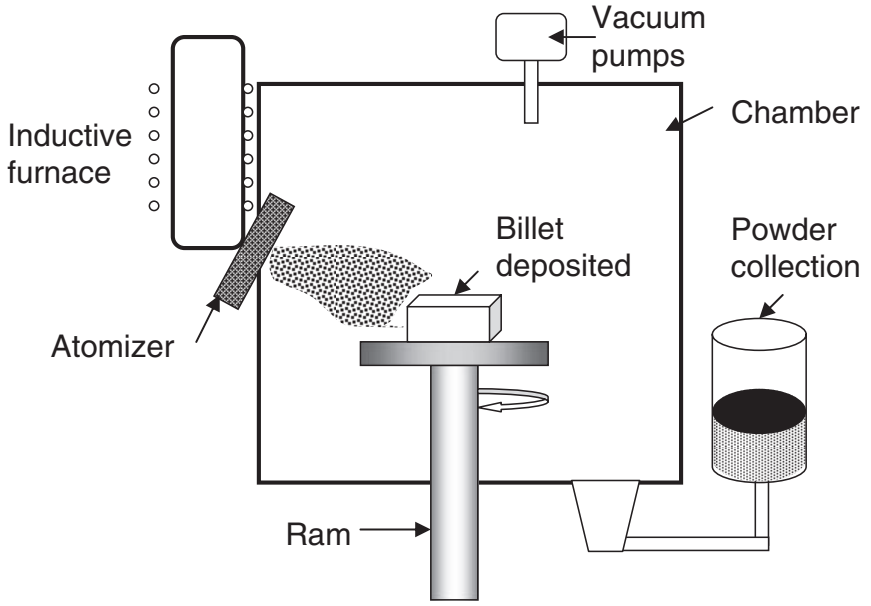

Fig. 2.22 Schematic diagram of the spray forming process

metal solidifies at a rate of 10^2 °C/s to 10^3 °C/s, forming a condensed product with fine equiaxed grains and low segregation. The semisolid nature of this method arises from the fact that solidification takes place both during atomization and deposition stages. The first stage of rapid solidification takes place while droplets travel at high speed towards the substrate. Then, solidification is continued at a lower rate after semisolid droplets reach the substrate. In general, the deposited layer contains initially over 60% solid and solidifies further at a rate as slow as 0.3 °C/s [38]. Thus, spray forming belongs to semisolid processing and shares similarities with techniques such as liquid phase sintering and rheocasting [39]. Fundamental differences exist, however, between spray forming and other semisolid techniques [40]. Since there is no equilibrium within the semisolid slurry during deposition, rapidly solidified droplets have the same chemistry, which prevents chemical segregation. As a result of spray forming, unique microstructure is achieved with fine equiaxed grains and low solute segregation.

For some alloys an additional step of semisolid forming is used as a way to improve properties after spray forming. For as-sprayed Al–Si alloys with high Si content, a large amount of hard Si particles limits deformation, and semisolid forming improves formability [41]. During reheating, however, the solid phase coarsens rapidly, deteriorating overall properties.

2.6.9 Liquid Phase Sintering (LPS)

Liquid phase sintering (LPS) is a subclass of the sintering processes, involving particulate solid along with a coexisting liquid during some parts of the thermal cycle [42]. A starting material is a powder, but during the process three phases coexist: vapor, liquid and solid. The presence of liquid during sintering creates an advantage of LPS over other methods of sintering. The liquid flows between the powder particles, filling pores and causing densification by a capillary action and through the provision of the fast diffusion pathway. The capillary attraction due to wetting liquid provides rapid compact densification without the need of an external force. The liquid phase can form directly from the chemical elements when the sintering temperature is between the melting point of the matrix and the additive. It is created by the melting of eutectic phase mixtures, which form by diffusion or by incipient melting.

2.6.10 Stress Induced Melt Activation (SIMA)

As opposed to the techniques described above that explore liquid-state changes, the stress induced melt activation relies on microstructural modifications introduced in the solid state. The SIMA cycle starts from the conventionally cast ingot, which is further subjected to hot or warm deformation by rolling or extrusion [43]. After hot work, the strain is introduced by means of cold work, including drawing, swaging, rolling or compression [44]. Then the alloy is reheated into the semisolid state. The strain level introduced should be such that upon reheating, the mixture comprises uniform discrete solid particles. After forming, the alloy is solidified to achieve the final microstructure. Due to difficulties with introducing sufficient cold work to large sections, the practical SIMA solutions are restricted to small diameters of the order of several centimeters.

2.7 Benefits of Semisolid Processing

The key feature of semisolid processing is the reduced temperature when compared to the casting of superheated melts. The generally accepted advantages of hardware performance and energy economy, achieved due to reduced operating temperatures, are universally positive for all alloys. The classic benefits are as follows:

(i) lower energy consumption;
(ii) increased die life;
(iii) no handling liquid metal;
(iv) less solidification shrinkage;
(v) near net shape capabilities;
(vi) less prone to gas entrapment;

(vii) better yield from the raw material due to lower oxidation, evaporation and fewer other losses related to melt overheating.

The alloy, subjected to forming in semisolid state exhibits essential differences as compared to overheated melts, used in conventional casting. Typical features include:

(i) lower heat content than in liquid;
(ii) reduced liquid content through the presence of solid;
(iii) higher and better controllable viscosity than in liquid;
(iv) flow stress lower than in solid.

It is considered that semisolid processing is competitive when the following features are required:

(i) intricate design often combining thin and thick sections;
(ii) net or near-net shape with opportunities to substantially reduce or eliminate machining;
(iii) high integrity for structural components to achieve high mechanical properties or pressure tightness purpose for other applications.

For general applications, when requirement of integrity is low, semisolid processing may not show sufficient economic advantage over conventional casting. When parts are simple or relatively massive, forging and squeeze casting may be competitive.

2.7.1 Structural Implications of Reduced Temperature

In addition to improved hardware performance and energy economy, the reduced processing temperature exerts an effect on alloy microstructure. First, it replaces a molten alloy with a semisolid slurry. Then, further reduction in temperature below the liquidus changes the solid to liquid ratio and slurry properties, which affect the final product, not only in terms of its internal integrity, but also its microstructure. The present literature, while assessing the improvement in properties, does not distinguish between the microstructure and the component's integrity.

As depicted in Fig. 2.23, the influence of the semisolid slurry on the component's integrity is complex. The common assumption that the benefits of semisolid processing arise exclusively from the flow behavior of the partially solidified metal is, apparently, a simplification. In general, the slurry affects product integrity through a reduction in porosity. The turbulent flow of a liquid alloy into a mold can result in the entrapment of air and mold gases into the melt, which in turn may translate into micro and macro porosity (voids or oxides). Smooth flow of the semisolid slurry allows for minimizing these defects. Similarly, a lower liquid content within the semisolid slurry reduces shrinkage porosity. Both the flow behavior and solidification shrinkage are improved with a reduction in liquid content, i.e., the alloy's temperature. The temperature cannot

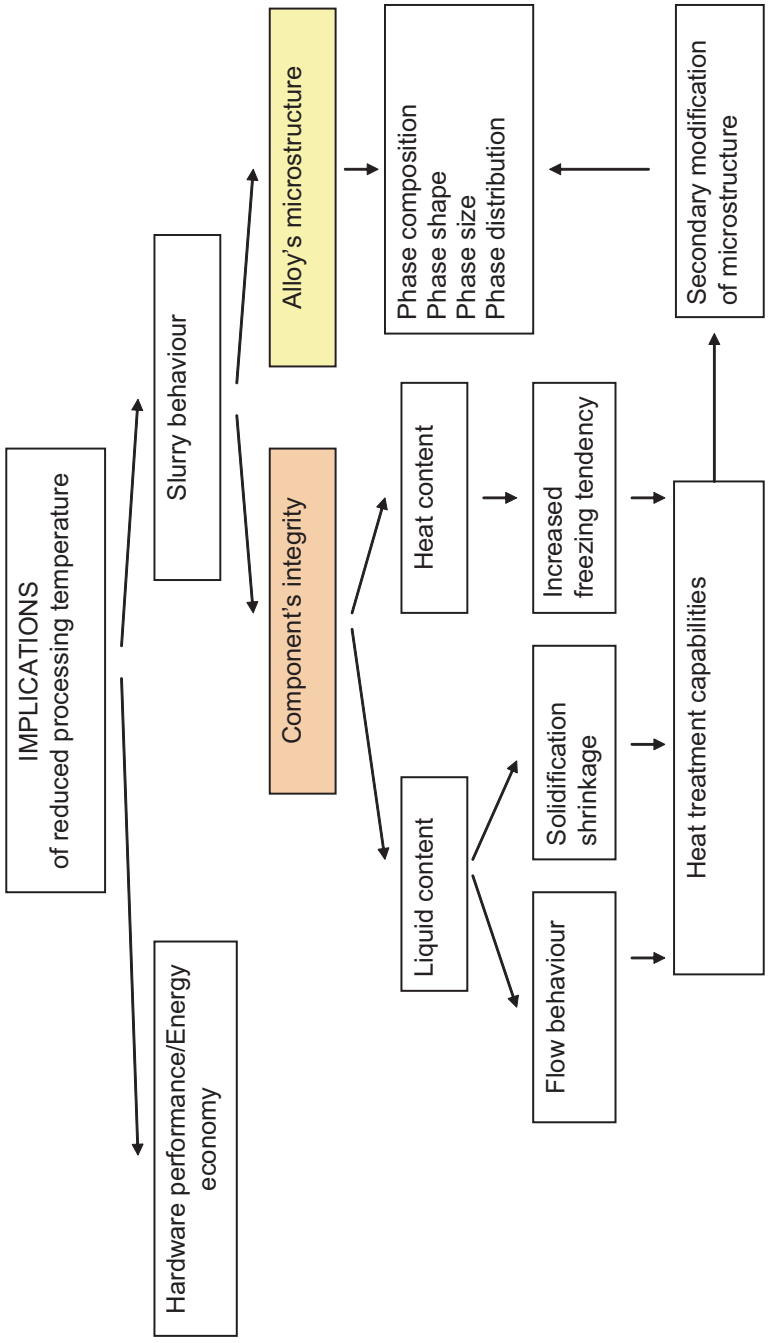

Fig. 2.23 The influence of reduced temperature during semisolid processing on hardware performance and behavior of components [60]

be reduced indefinitely since it simultaneously lowers the heat content and increases tendency of freezing, which adversely affects the mold filling and potentially the product's integrity.

As was the case for the benefits regarding hardware performance, the enhanced component's integrity has a universally positive effect for all alloys. The improvement in a component's integrity not only increases the material properties and allows achieving near-net shape capabilities but also makes it heat treatable. This is in contrast to superheated melt castings where heat treatment is, in most cases, not possible due to blistering. The heat treatment allows for an engineering of the microstructure that represents a path parallel to the component's integrity control.

2.7.2 Component's Integrity and Microstructure

In order to distinguish between a component's integrity and microstructure, differences were schematically emphasized in Fig. 2.24. The key microstructural change, observed after a slurry's solidification, is a replacement of dendritic forms

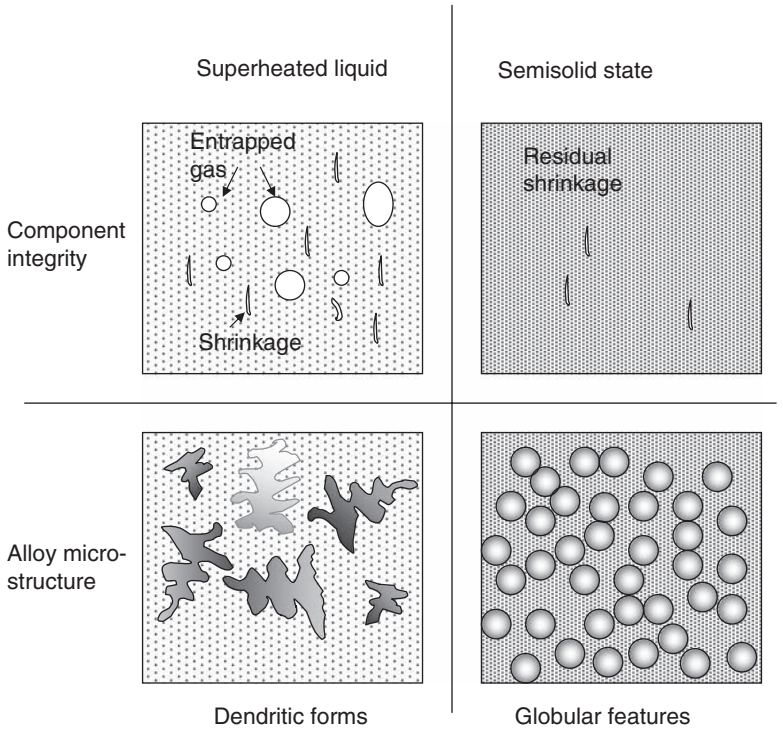

Fig. 2.24 Schematics emphasizing two different factors affecting a component's properties during semisolid processing: **(top)** an improvement in component's integrity, universally positive for all alloys; **(bottom)** a change in alloy's microstructure, an improvement or deterioration in properties which may accompany this change, depends on the particular alloy system [60]

by globular morphologies. The new features, unmelted globules with a size less than 0.1 mm, are surrounded by the solidification product of the remaining liquid fraction. Their presence leads to reduced segregation, typical for coarse dendrites, but also the selective partition of chemical elements between solid and liquid, which affects the phases and microstructural components. A magnitude of latter changes depends on the particular alloy and its phase diagram: The higher solid fraction causes the larger change in the chemistry of the remaining liquid. The enrichment of a liquid alloy in certain chemical elements can lead to increased precipitation of phases and modifications in their distribution pattern. In extreme cases, the phases not present during complete liquid casting may be formed. If the phases are of a brittle nature, their location at boundaries between the primary solid and matrix or secondary Mg grains may lead to a reduction in an alloy's ductility. Thus, excluding the macro segregation factor, the influence of globular solids on the direction of changes of alloy properties is not universally positive and should be evaluated for individual alloy chemistry. An advantage of the component's integrity, which allows for heat treatment, may be used to dissolve brittle phases, thus improving properties. The effectiveness of heat treatment depends, however, on the particular alloy system. It is generally known that heat treatment is more efficient for Al based face cubic centered structures than for alloys with an Mg–based hexagonal close packed matrix. Understanding the difference between the integrity and microstructure is not only of importance for the proper selection of the processing parameters to achieve the maximum with existing alloys, but also for the development of new alloys designed specifically for semisolid techniques.

2.7.3 Present Limitations

Current thixocasting methods represent batch operations, where only a small volume of slurry is produced at a time. A continuous process would eliminate this inconvenience. Although thixocasting eliminates the need for melting equipment within the final forming operation, feedstock has to be purchased at a premium price. The process control for thixocasting is difficult due to non-homogeneous properties of the billet resulting in differences in viscosity and flow behavior. This is due to the difficulty of achieving uniform distribution of solids. There is always a temperature gradient and especially for the narrow range between solidus and liquidus, this leads to differences in melting progress. A major drawback of emerging rheoforming routes are problems with availability of modern machinery and alloys designed for this purpose.

2.8 Suitability Criteria of Alloys for Semisolid Processing

The nature of transformations experienced by alloys subjected to semisolid forming indicates that the optimum results would be achieved using alloys designed especially for this way of processing. So far, alloy chemistry has not been optimized and

modern semisolid processes implement alloys designed many decades ago for conventional casting.

At present, a variety of alloys are tested for the possibility of utilizing semisolid routes: Zn-based, Al-based and Cu-based to high temperature alloys as stainless and high-speed cutting steels, cobalt alloys such as Stellite 21, titanium alloys such as Ti–20Co, and Ti–2Cu. The technical feasibility and success of commercial semisolid processing are, so far, almost entirely confined to aluminum alloys, mainly alloy A357 (Al–7Si–0.5 Mg) or A356 (Al–7Si–0.3 Mg) in automotive applications. According to year 2000 data, of a total 14,000 tonnes of alloys processed by thixocasting, A356 accounted for 2,100 tonnes and A357 for 11,200 tonnes. This leaves around 700 tonnes for other alloys.

2.8.1 Solidification Range

The temperature interval between solidus and liquidus defines the range of semisolid processing. Therefore pure metals and eutectic alloys cannot be subjected to semisolid routes. The general rule would be the wider the solidification range, the easier the control of solid fraction. At the same time, the wider the solidification range, the higher the tendency to hot tearing. For semisolid processing the solidification range is narrower and should rather be re-defined as the difference between the actual processing temperature and solidus. As it can be deduced from schematics in Fig. 2.25, the chemistry of liquid fraction and the solidification interval are essentially different from the same characteristics for the completely molten alloy.

2.8.2 Temperature Sensitivity of Solid Fraction

During semisolid processing, the residence time in a two phase region and the fraction solid as a function of temperature are the two key parameters. The alloy composition and the sequence of phases that precipitate during solidification are of importance. In order to achieve the uniform rheological behavior of the slurry, its solid fraction should be constant over the entire alloy volume. Since it is rather difficult to achieve the homogeneous temperature within the alloy volume where usually a gradient from the heat source is present, the alloy should exhibit low sensitivity of the solid fraction on temperature.

Temperature sensitivity of the solid fraction is defined as the absolute value of
the slope of the solid fraction f_s versus temperature T curve $\left|\frac{df_s}{dT}\right|$. The reliability of the process requires small values for $\left|\frac{df_s}{dT}\right|$. Otherwise, sophisticated heating and temperature control systems have to be employed.

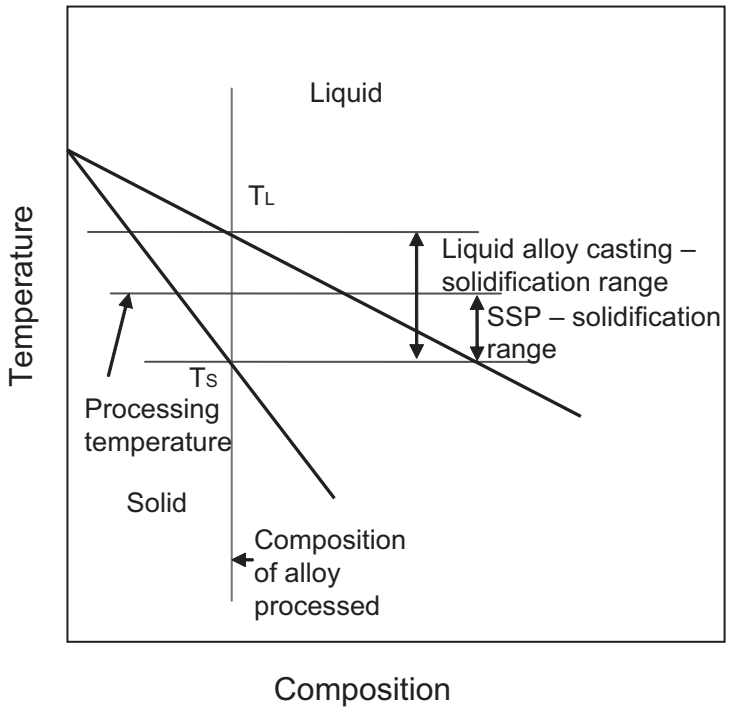

Fig. 2.25 A difference in the solidification range between casting of fully liquid alloy and semi-solid processing

2.8.3 Thermodynamic Characteristics of Alloys for Semisolid Processing

Analysis of the differential scanning calorimetry (DSC) curve and the fraction solid curve indicates the following parameters are important for semisolid processing (Fig. 2.26) [45].

(i) the temperature at which the slurry contains 50% liquid, $T_{1;}$

(ii) the slope of the curve at fraction liquid f_L=50%, $\frac{df}{dT(T_3)}$; to minimize the reheating temperature sensitivity, this slope should be as flat as possible;

(iii) the temperature of the beginning of α solution melting, T_2; at this point the eutectic melting is completed and the α solution grains start to dissolve; the difference $T_1 - T_2 \geq 2$ determines the kinetics of dendrite spheroidization during reheating;

(iv) the slope of the curve in the region where the solidification process is completed, $\frac{df}{dT(T_3)}$; this slope should be relatively flat to avoid hot shortness problems.

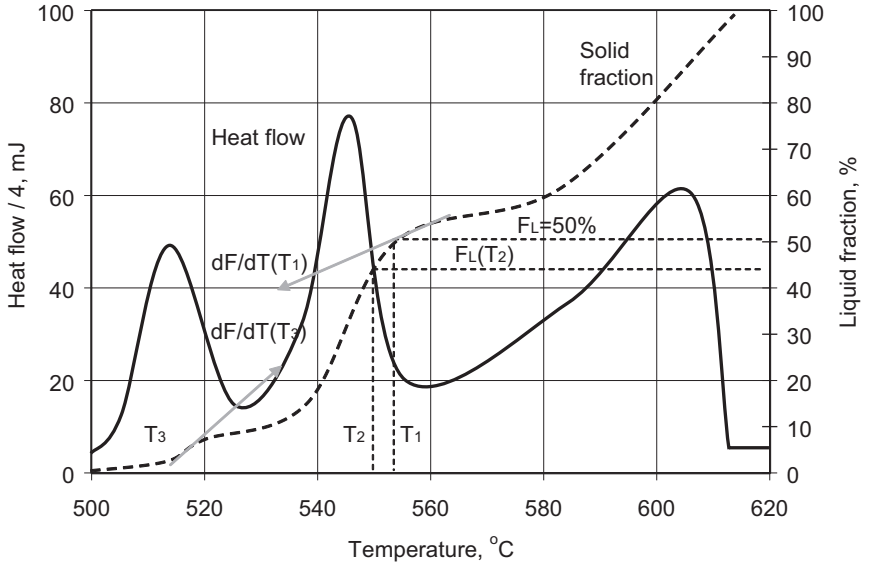

Fig. 2.26 The graph showing important parameters during semisolid processing: results of the differential scanning calorimetry [61]

2.8.4 Morphological and Rheological Characteristics of the Slurry

The alloy, designed for semisolid processing, should generate slurry that has certain behavior during flow into the mold and microstructure after solidification. To achieve this, the following parameters are of importance:

(i) morphology of the solid;
(ii) interconnectivity of the solid;
(iii) viscosity of the liquid;
(iv) interconnectivity of the liquid.

The alloy suitable for semisolid processing should exhibit at temperatures between liquidus and solidus a mixture of fine solid particles surrounded by the liquid matrix. The importance of this factor is emphasized throughout this volume. In addition, there should be a low tendency to particle agglomeration and coarsening, since this will affect the viscosity and flow behavior. Rheological properties are substantially influenced by the tendency to particle agglomeration. Any departure from uniform distribution leads to an increase in viscosity.

2.8.5 Applicability of Semisolid Processing for Magnesium Alloys

Despite extensive efforts, magnesium has not been able to compare with applications of aluminum alloys.

2.8.5.1 Applicability of Processing Techniques

The reactivity of magnesium requires special protection during processing to avoid oxidation and ignition. When combined with other unique features of magnesium it means that semisolid techniques, commercialized for aluminum, cannot automatically be adopted for magnesium. So far, there are limited applications of thixocasting, fed by pre-cast billet. Some attempts were made to produce the billet by the rapid slug cooling method. On an experimental scale, the twin screw process is being tested [46]. Thus, injection molding is at present the dominant commercial technique of semisolid processing of magnesium alloys. Since other techniques have a batch type operation, injection molding is also the only technique providing a continuous production cycle.

2.8.5.2 Suitability of Alloy Composition

At present, there is no single magnesium based alloy designed specifically for semisolid processing. For both commercial applications and research, alloys designed originally for die casting are used. An attempt was made to use thermodynamics to select chemistries of alloys suitable for semisolid technologies [47]. Three factors were considered during thermodynamic based qualifications: (i) temperature sensitivity of solid fraction, (ii) solidification range and (iii) proportion of $Mg_{17}Al_{12}$, γ phase. It is clear that at this stage the results of computational thermodynamics should be used as the preliminary guidance before entering experimental verification.

The thermodynamic approach applied to the Mg rich corner of the Mg–Al and Mg–Al–M (M=Zn, Mn, Si) selected compositions with potential improvement in both the semisolid processing behavior and resultant mechanical properties. The chemistry ranges selected based on operation at solid fraction f_s=0.3 are shown in Fig. 2.27 [47]. Compared with binary Mg-Al alloys, additions of Zn reduce $\frac{df_s}{dT}$, widen $\Delta T_{s\text{-}ss}$ and explain the formation of $Mg_{17}Al_{12}$, γ phase based on equilibrium calculations. In contrast, additions of manganese to binary Mg-Al alloys increase $\frac{df_s}{dT}$, decrease $\Delta T_{s\text{-}ss}$, and reduce the tendency to $Mg_{17}Al_{12}$, γ phase formation. Additions of silicon have little effect on $\frac{df_s}{dT}$ but a slightly increased tendency to $Mg_{17}Al_{12}$, γ phase formation. Scheil model calculations predict that non-equilibrium solidification involves smaller $\frac{df_s}{dT}$, wider $\Delta T_{s\text{-}ss}$ and larger $Mg_{17}Al_{12}$, γ phase proportions at the solidus irrespective of binary Mg-Al or ternary Mg-Al-M systems.

It should be mentioned that alloy development for semisolid processing should also focus on certain parameters affecting processing behavior that are not necessarily predictable through computational thermodynamics.

2.9 Industrial Implementations of Major Semisolid Concepts

A number of technologies have been developed over last three decades, mainly in a laboratory environment, to take advantage of the unique behavior of semisolid slurries. The progress in the commercialization of many of them seems to indicate the beginning of large-scale acceptance of semisolid processing by major industries.

2.9.1 Rheo- and Thixo- Processing Routes

All the technologies can be divided into two fundamentally different basic routes: the rheo-route and the thixo-route. When implementing rheo-route, the initially fully molten precursor is pre-solidified under controlled conditions and then transferred into the mold. This single-step process is called *rheocasting*. In a majority of applications, a slurry-on-demand concept dominates, where a single dose of slurry is separately prepared for each shot.

All existing thixo technologies are based on the unique combination of solid-like and liquid-like behavior. As a solid the material maintains its structural integrity,

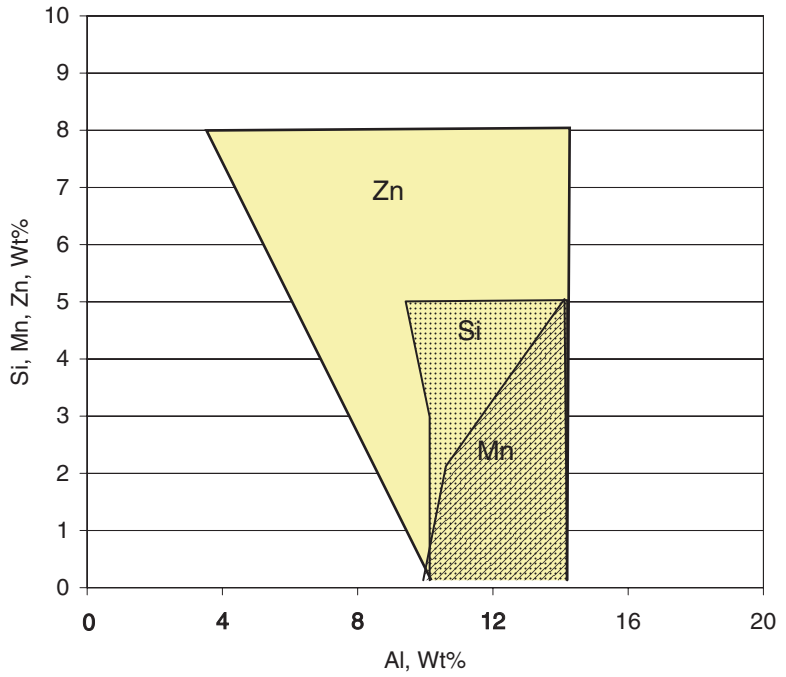

Fig. 2.27 The alloy compositions from Mg rich corner of Mg–Al and Mg–Al–M (M=Zn, Mn, Si) diagrams selected based on thermodynamic modeling for solid fraction f_s=0.3 as suitable for semisolid processing. The satisfaction criteria are indicated [47]

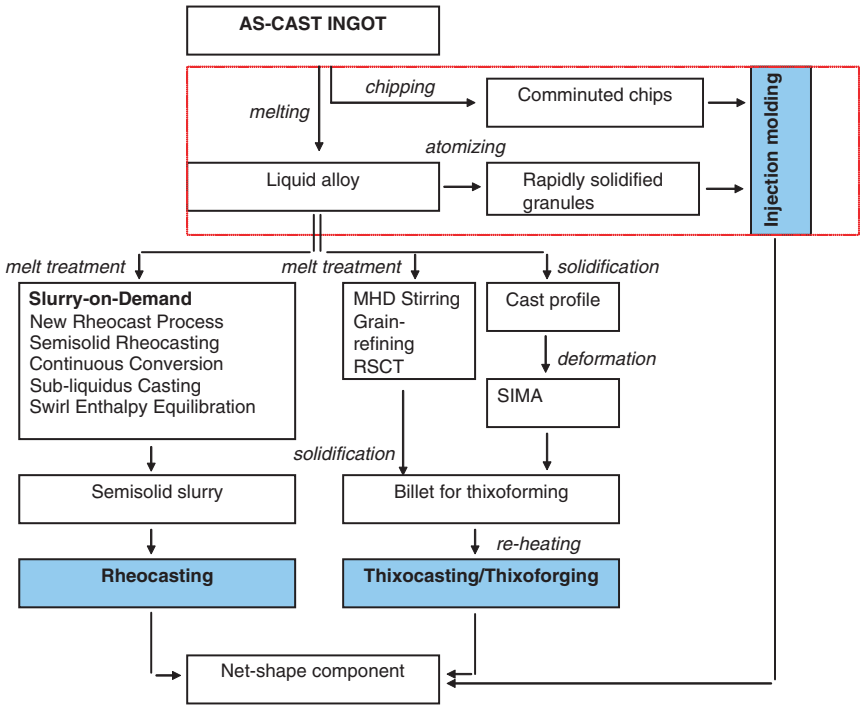

Fig. 2.28 The material's flow from the feedstock to final component during present technologies of semisolid processing of metallic alloys. Acronyms used: MHD – magneto hydrodynamic; SIMA – stress induced melt activation; RSCT – rapid slug cooling technology. Some terms may represent registered trademarks [60]

Table 2.2 Typical shear rates of generally known processes with the superimposed range experienced during semisolid processing [62]

Shear rate, s^{-1}	10^{-5}	10^{-4}	10^{-3}	10^{-2}	10^{-1}	10^{0}	10^{1}	10^{2}	10^{3}	10^{4}	10^{5}	10^{6}	10^{7}
Conventional processes			Superplastic forming		Isothermal forging		Stirring	Stamping, Gravity casting		Pressure die casting	Engine lubrication		
Semisolid forming							Semisolid forming						

and before processing it can be handled like a solid. As a liquid, the material flows with relative ease and due to high viscosity fills the cavity in progressive fashion in mostly laminar flow. The thixo route involves two stages: (i) billet preparation, which consists, in fact, of a portion of the rheo-route; and (ii) billet re-heating and component forming. If the forming process is conducted in a closed die, it is called *thixocasting*. When a die is open during this operation, the process is considered *thixoforging*. The purpose of preheating the previously prepared billet prior to forming is to provide the material with the precisely controlled solid fraction of fine spherical particles, uniformly distributed in a liquid matrix, having a lower melting temperature. Both conventional and induction heating methods are used with success. Although historically, rheocasting was discovered first, thixoforming methods were the first to be implemented commercially. However, due to cost disadvantage, they are recently being replaced by rheocasting with several modifications. The material flow from the feedstock to the final components during various semisolid processing methods is shown in Fig. 2.28. The comparison of shear rates generated during selected processes is listed in Table 2.2.

2.9.2 Thixocasting

The most common process of billet manufacturing is based on magneto hydrodynamic stirring during semi-continuous casting. Another alternative is applying special grain refining techniques to generate a fine-grained rosette-like structure. Electromagnetic stirring and rapid solidification combined with grain refinement account for most of present production. According to the stress induced melt activation idea, a conventionally cast billet of generally limited sizes is cold or warm deformed by, e.g., extrusion. The reheating stage involves an induction method, increasingly in the horizontal alignment design. Horizontal die casting machines equipped with a stronger shot end than conventional ones, and with a closed-loop real-time shot control system, are the standard equipment.

2.9.3 New Rheocasting (NRC)

This method was developed and commercialized by UBE Industries Ltd. of Japan. A liquid metal is poured into a crucible-receiver the size of a billet and then cooled into a semisolid state temperature before transfer to the shot tube. The cycle sequence is shown in Fig. 2.29. The alloy is held within the insulated container and cooled to a temperature corresponding to the required solid fraction. During this period a large number of spheroidal primary crystals are generated. The temperature of the cooling vessel creates a chill zone on the outer slug's surface, which is removed by induction preheating during the next stage. Afterward a slurry is directed into a shot sleeve and formed under pressure. The distribution of the solid within the crucible is uniform, which is essential for production of high quality parts.

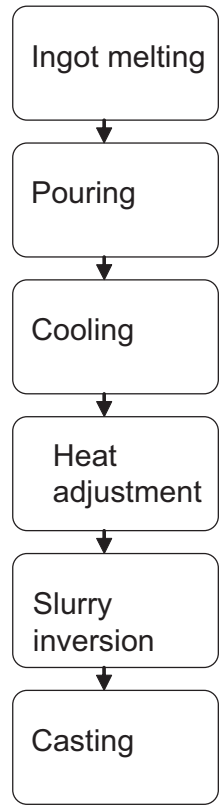

Fig. 2.29 The concept of new rheocasting process (NRC)

2.9.4 Semisolid Rheocasting (SSR)

This process was developed at MIT, USA, and commercialized by Idra Prince Inc. [48, 49]. It utilizes a graphite agitator as functional equivalent to conventional metal rod agitators. The purpose is to rapidly cool and apply convection from within the melt to create the globular microstructure. The critical factor for formation of thixotropic slurry in SSR is the combination of rapid cooling and convection while crossing the liquidus temperature. After a small fraction of solid is created, further agitation is not necessary to continue globular growth.

A superheated alloy is initially agitated and cooled for roughly 5–20 s. Then the rotating rod is removed and the quiescent melt is cooled to the desired forming temperature (Fig. 2.30). The process is implemented using a rheocasting machine, designed based on technology of existing die casting machines. During a cycle, a ladle cup of molten metal is brought to the station by a robot. The station cycle is designed to be less than the cycle of the die casting. It is claimed that this technique exhibits a number of advantages as compared to other rheocasting methods. Many of them are attributed to the way of cooling/agitation: (i) heat removal

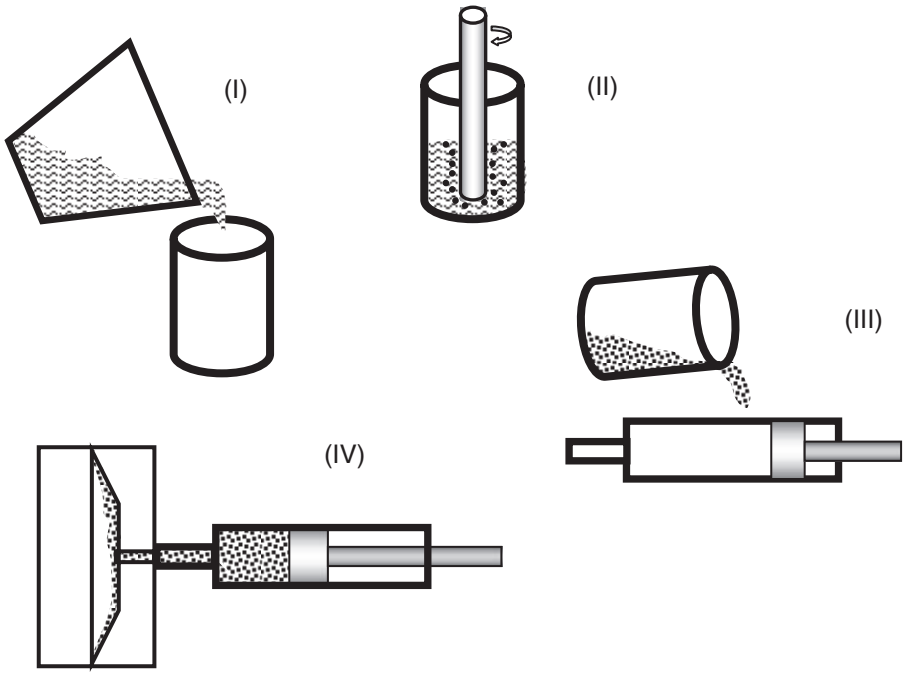

Fig. 2.30 The concept of semisolid rheocasting (SSR)

outside of the machine reduces the cycle time; (ii) a spinning rod ensures uniform cooling within the alloy volume; (iii) the rapid cooling/stirring combination creates fine microstructure which does not require a long time to transform into globular forms.

2.9.5 Sub-Liquidus Casting (SLC)

The process was developed by THT Presses Inc., USA [50-52], and explores a phenomenon of grain refinement accompanied by proper control of melt temperature and cooling rate. In fact, the successful process cycle can only be implemented if good grain refinement is achieved in the molten alloy supplied to the machine. The grain refined material is poured into the shot sleeve at temperatures just above liquidus and cooled to a semisolid state before transfer to the mold. For practical reasons, a superheat of 5–10 °C is used to compensate for heat losses during alloy transfer from the furnace to the shot sleeve. The slurry is developed within the shot sleeve, which means that no slurry processing equipment is required outside of the casting machine (Fig. 2.31). For aluminum alloy A356 the temperature in the chamber

before injection is between 570 °C and 590 °C. For proper grain refinement, fine rosettes transform into globules within seconds while coarse dendrites in poorly refined alloy would require more time to transform into globular features.

Although the machine features alone do not constitute the entire process, the specific features allow its proper implementation. They include large and shallow shot diameter and short stroke as well as a unique gate plate. The shot piston and sleeve wall temperatures are controlled to extract the heat primarily through the piston and less through the shot sleeve walls. The melt is transferred to the die cavity at very low velocity of the order of 1 m/s–2 m/s through a gate plate with multiple gates.

2.9.6 Other Semisolid Techniques

In addition to distinct technologies with advanced commercialization, there are a number of processes at the developmental stage or commercially implemented at lower scale. Two examples are described below.

A technique, called *Advanced Thixotropic Metallurgy* [53] is based on a semisolid feed system producing improvements in the fill pattern and part integrity. It uses small runners and gates with no overflows. As a result, the metal flow system provides a control flow of velocities during filling of the mold cavity, leading to the generation of semisolid slurry. Thus the mold filling takes place through the progressive semisolid front. The flow of metal through a runner takes place through at least one controlled expansion region where the metal is able to spread laterally to its injection direction which results of reduction in its flow velocity relative to the runner.

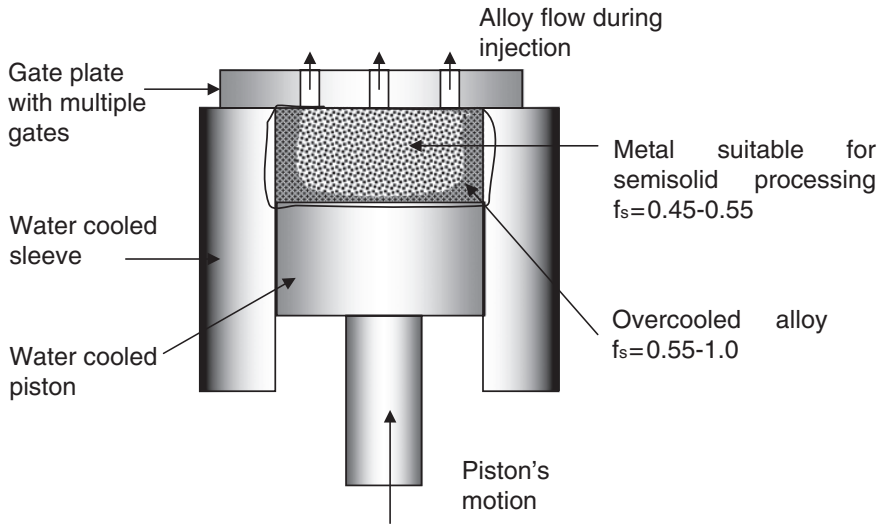

Fig. 2.31 The concept of sub-liquidus casting (SLC) developed by THT Presses Inc.

Another process, called *Direct Semisolid Forming* [54, 55] can be divided into three steps: formation of semisolid alloy, maintenance of the slurry suspension and transport of the slurry to the die casting machine. The slurry is generated by an agitation of the melt by an impeller with inclined rotating blades that force the flow of material upward in the melt. The final mixing is conducted by an anchor-shaped rotor with vertical shearing rods located proximal to the furnace walls. The original mixing arrangement is the main difference as compared to conventional rheocasting. During the final step the slurry is transferred to the shot sleeve within the die casting machine. It is claimed that the process has a number of advantages over conventional semisolid techniques: less energy and capital cost as compared to the billet route, and reduced scrap cost through the possibility of recycling.

2.10 Origin and Progress of Magnesium Molding

Metal injection molding represents a hybrid, combining features of both fundamental routes (see the classification in Fig. 2.28). Similar to the rheo-route, it consists of a single step, but as with the thixo-route it starts from a solid feedstock. The one-step processing is possible due to the specific structure of a coarse particulate feedstock, called chips, granules or pellets, created during their manufacturing. The cold-deformed structure of mechanically comminuted chips is of the same nature as that reported for a thixoforming billet, produced by the stress induced melt activation (SIMA). Similarly, the structure of rapidly solidified granules with fine dendritic forms is the same as that created in thixoforming billets by magneto hydrodynamic (MHD) stirring or grain refining. As a result of the unique microstructure, the particulates transform into thixotropic slurries under the sole influence of heat. It is of interest that the microstructure, deliberately created during the manufacturing of billets for thixoforming, is obtained here as a side-effect of comminuting bulk ingots into small particulates. Although injection molding belongs to the family of semisolid technology, some phenomena that take place during processing at high temperatures are unique, and mechanisms necessary for their explanation cannot be directly adopted from other semisolid techniques.

In addition to benefits common for the semisolid family, injection molding offers advantages unique to this technique: environmental friendliness with no SF_6 requirement, no melt loss due to a closed processing system, an ability to mold thinner parts and more complex shapes, and the capability to apply the unique ways of slurry distribution to the mold.

2.10.1 Technology Origin

Injection molding of magnesium was initiated by Dow Chemical Company, Midland, MI, USA, in 1979. A direct impact on the research was the invention of semisolid processing, which took place in the early 1970s at Massachusetts

Table 2.3 The key dates in development and commercialization of semisolid metal processing and magnesium molding

Year	Name	Country	Milestone	Reference
1923	E. Schalek & A. Szegvari	Germany	Discovery of thixotropy phenomenon	[1]
1927	T. Peterfi	Germany	Introduction of term of *thixotropy*	[2]
1971	M. Flemings and co-workers, Massachusetts Institute of Technology, Cambridge, Mass	USA	Invention of semisolid processing of metallic alloys	[5, 62]
1979	The Dow Chemical Company, Midland, MI	USA	Research initiation on magnesium injection molding	[63-65]
1987	The Dow Chemical Company, Midland, MI	USA	First hybrid machine for magnesium molding built	
1990	Thixomat Inc., Ann Arbor, MI	USA	Thixomat Inc. was established and acquired the technology from Dow Chemical Company	
1991	HPM Corp.	USA	HPM is granted a license and starts building machines	
1992	Japan Steel Works	Japan	JSW is granted a license and starts building machines	
1997	HPM Corp.	USA	HPM stops building machines	
1997	Husky Injection Molding Systems Ltd.	Canada	Husky IMS is granted a license and starts development of magnesium molding machinery	

Institute of Technology, USA (Table 2.3). Since Dow at that time dominated the world magnesium market as a supplier of the primary metal, incorporating novel processing techniques was a natural direction for the market's expansion. The early experiments at Dow were conducted using a conventional plastics molding machine. The only difference was a barrel assembly, designed to accommodate liquid magnesium. After over a decade of Dow's research, the technology was acquired by Thixomat, Inc., MI, USA, established in 1990, and licensed worldwide. Since 1992 the technology has been marketed under the trade name of Thixomolding® (Thixomolding® is a registered trademark of Thixomat Inc).

Two machine builders, HPM Corporation in the USA, with a die casting machinery profile, and Japan Steel Works (JSW) in Japan, with the steelmaking and injection molding machinery portfolio, started selling commercial machines in the early 1990s. When HPM, after building only several units, left the magnesium

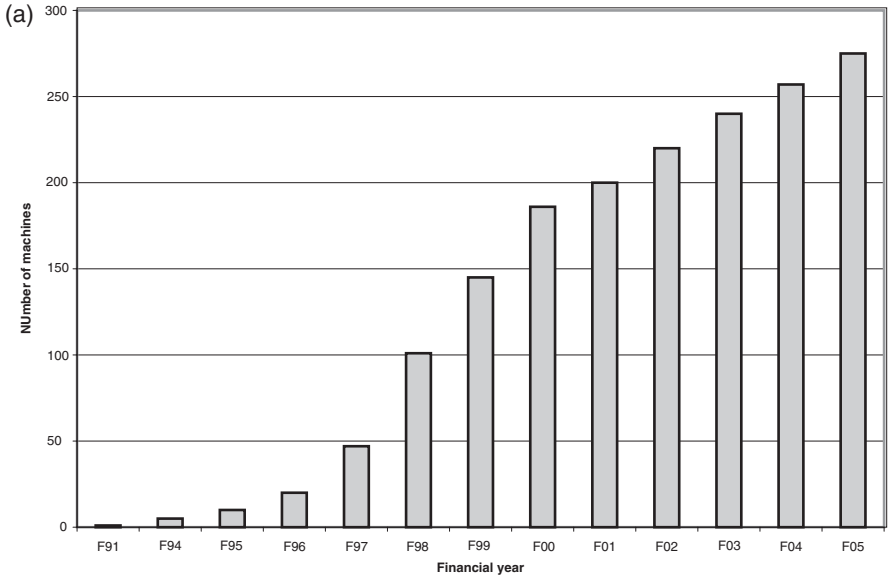

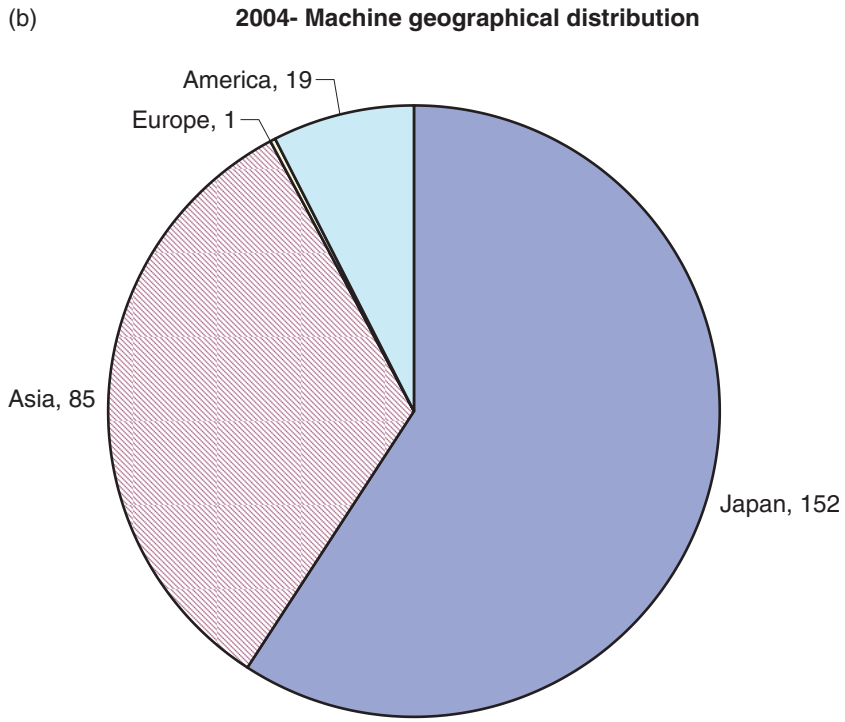

Fig. 2.32 The progress in commercialization of magnesium molding: **a** number of processing systems installed worldwide 1991-2005; **b** geographical distribution of machines in 2004

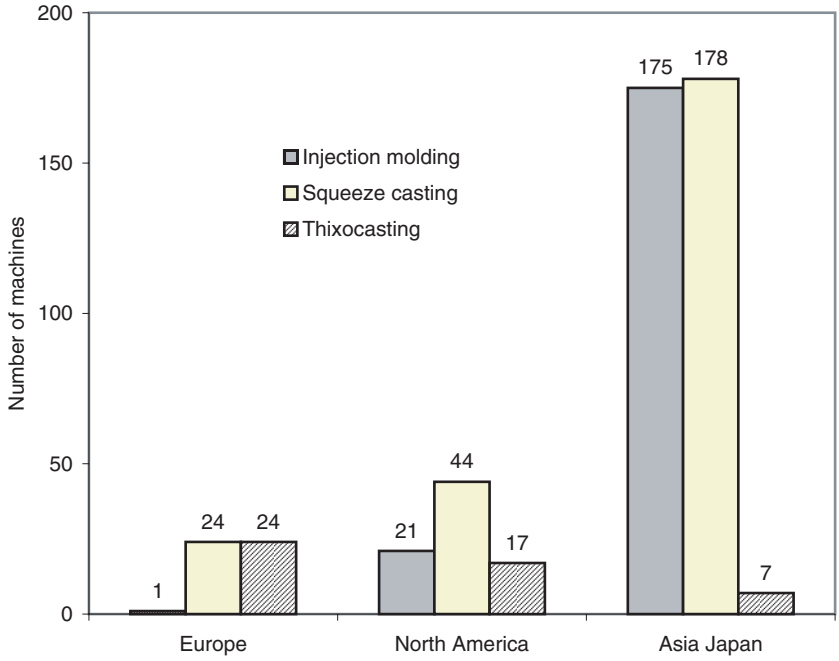

Fig. 2.33 Comparison of numbers of squeeze casting and thixocasting machines [56] along with injection molding units (2000)

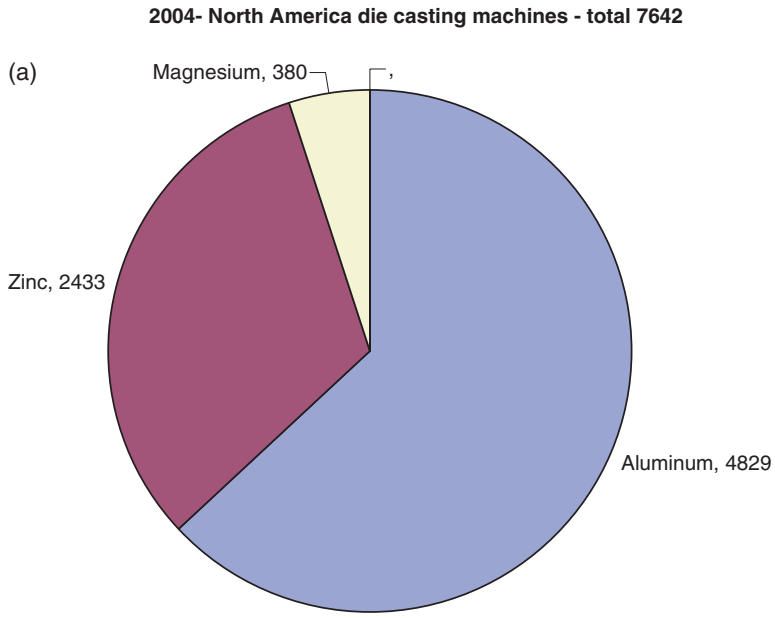

Fig. 2.34 The structure of die casting market in North America (NADCA data): **a** distribution of machines for different metals; **b** distribution of machines used for magnesium in regards to their size

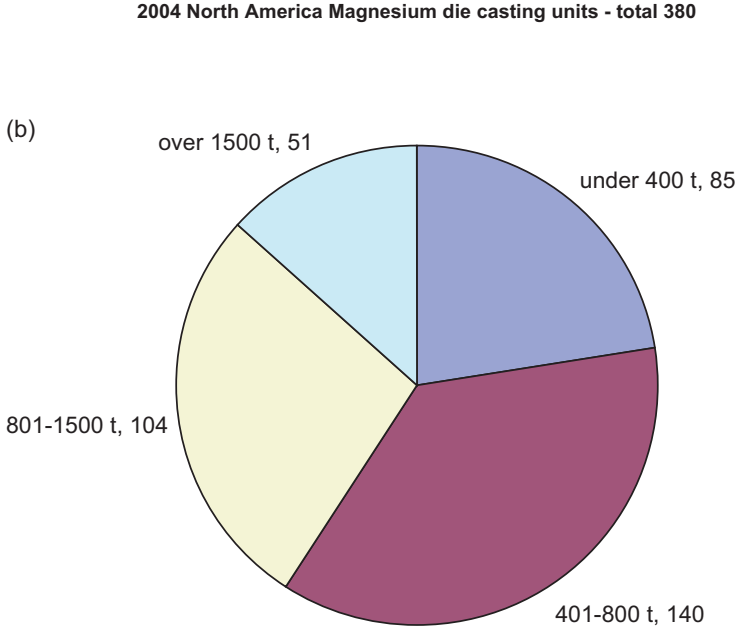

Fig. 2.34 (continued)

market in 1997, JSW was the sole supplier of machines for almost a decade. Husky Injection Molding Systems Ltd., Ontario, Canada, the builder of plastics injection molding machines, entered the market in 1999 and after intensive development emerged in 2005 as the global supplier of this modern machinery.

2.10.2 Commercialization Progress

The dynamics of the machine building market is shown in Fig. 2.32a. Although 52 end users (2004) are distributed in 10 countries across Asia, North America and Europe, the majority of machines are located in 3 countries of Asia: Japan, China and Taiwan (Fig. 2.32b).

The JSW machines are characterized by the following clamping tonnage: 75, 220, 280, 450, 650 and 850 tonnes. The present sizes of Husky machines include 400, 500, 650 and 1000 tonnes. In 2000 the number of machines with clamping tonnage below 450 tonnes and higher was roughly equal. In recent years the contribution of smaller machines has increased and in 2004, the 220-tonne to 280 tonne-systems represented around two-thirds of the entire market.

As compared to conventional casting, the number of machines is still low (Fig. 2.33a) [56]. At the world stage, however, the number of injection molding systems dominates the equipment for semisolid processing of both aluminum and magnesium (Fig. 2.34a). Among all die casting machines in North America, only 5% or 380 units, are used for magnesium. As shown in Fig. 2.34b, the majority of machines are within the range 400-tonnes to 1500 tonnes.

2.11 Present Applications and Future Opportunities for Magnesium Molding

The potential applications of injection molding cover all areas specified in Chap. 1 and associated with benefits related to magnesium: automotive, aerospace, consumer electronics as well as general purpose equipment. So far, mainly due to machine sizes available commercially, technology is focused on two latter markets with domination in the consumer electronics area. This section provides general characteristics of the market, products, manufacturing challenges and solutions offered by injection molding.

2.11.1 Consumer Electronics

Digitalization and the need for portability result in a rapid increase in the use of magnesium for housings of information and communication technology devices. During the last decade, the electronics market has emerged as an important player among non-automotive applications of magnesium castings. Sony first introduced magnesium for its digital video camera DCR-VX1000, benefiting from a reduction in noise and vibration, prevention of heat built-up inside the instrument, electromagnetic noise shielding and increased strength allowing for smaller size. At

Table 2.4 The major applications of the 3C housing market (Thixomat Inc. data)

Application	Companies
PC Notebook	Toshiba, NEC, Mitsubishi, Panasonic, Compaq, Sony, Sharp, Epson, Gateway, Casio, Fujitsu, Hitachi, JVC, Dell
Digital VCR	Sony, Sharp, Canon
Minidisks	Sony, Panasonic
Digital Cameras	Fuji Film, Nikon, Sony
Cell Phones	NEC, Ericcson, Panasonic, NTT, Pioneer, Casio
TV Cameras	Sony
TV Consoles	Panasonic
Digital Projectors	Sony, Texas Instruments, Epson, Sanyo, Compaq
Control Panels	Hewlett Packard

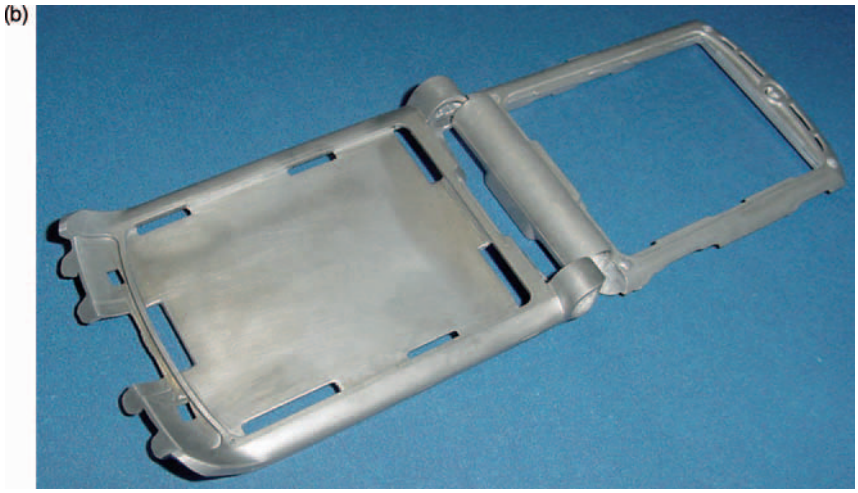

Fig. 2.35 Examples of consumer electronics components, manufactured using injection molding: **a** housings of various communication devices; **b** two-piece housing of a cell phone, weights of bottom and top parts—6.2 g and 4.6 g, respectively; **c** camera housing, weight–98 g;

Fig. 2.35 (continued) **d** 12 inch tablet casing after painting; **e** 17 inch laptop casing showing a quality requirement for the outer surface;

present, magnesium is applied extensively by all leading companies within the electronic industry with products covering computers, communications and cellular phones (3C), including notebook PCs, mobile phones, mini-disc players, and cameras as well as other handheld devices (Table 2.4). For some components, annual volume reaches hundreds of millions of pieces and annual growth exceeds 25%. The market demand is additionally magnified by continuous device replacements, triggered by model changes, for some of them as frequent as twice a year. Some examples of 3C components are shown in Fig. 2.35a-f.

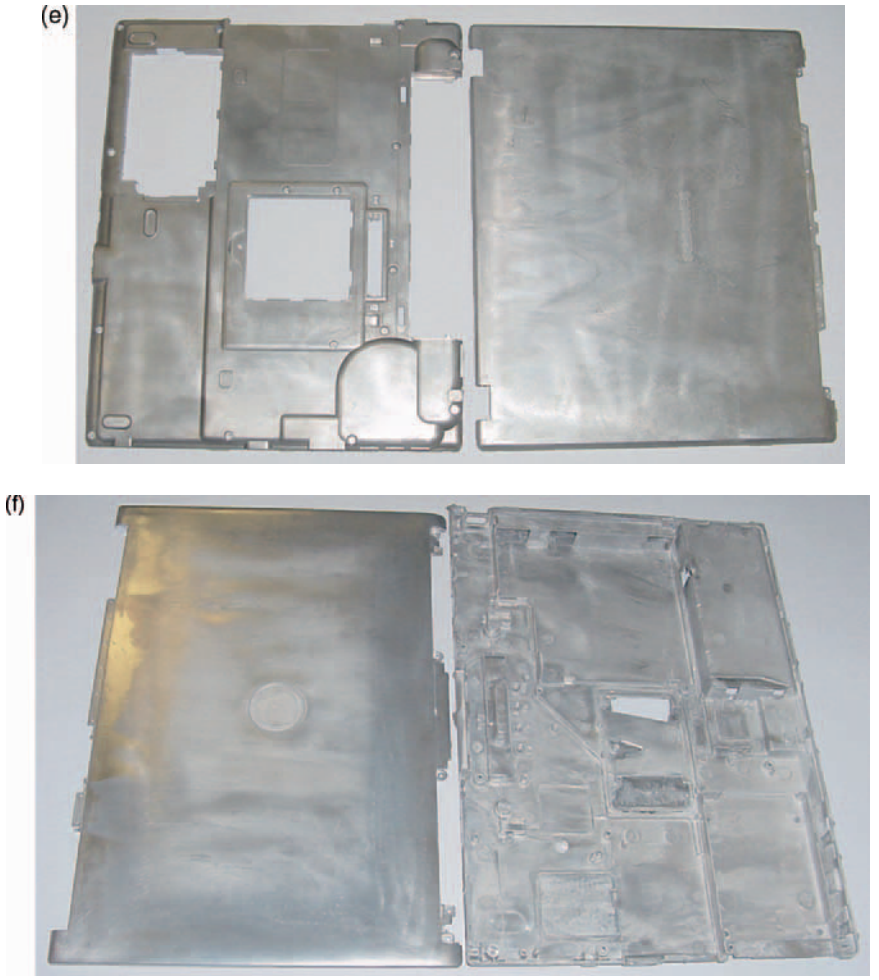

Fig. 2.35 (continued) **f** 17 inch laptop casing showing a complexity of internal details

2.11.1.1 Manufacturing Challenges

A tendency towards minimizing weight is important for complex-shaped cases and frames, providing strength, heat dissipation and protection against electromagnetic-interference. Thinner and lighter components, combined with the requirements for outstanding surface quality, which is suitable for fashionable finishes, create manufacturing challenges for conventional casting techniques. Injection molding with its precise control of the melt's temperature and flow into the mold is well suited for manufacturing 3C housings where wall thicknesses in the range of 0.5 mm are frequently accompanied by intricate shapes and long flow distances.

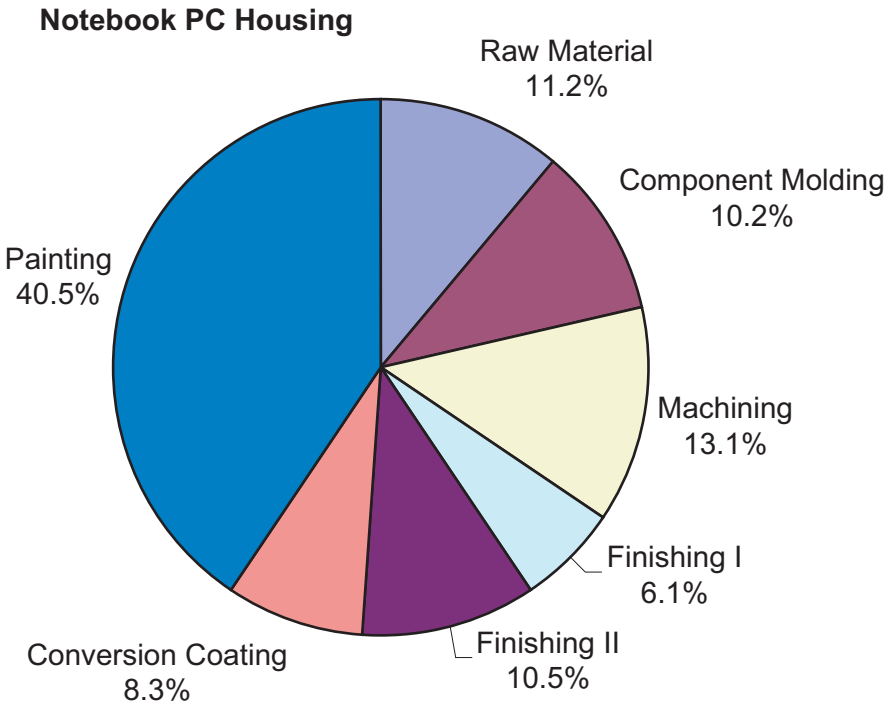

Fig. 2.36 The cost structure of 3C components, emphasizing the importance of surface finishing [57]

There is a substantial difference in the requirements between structural automotive parts and 3C housings. For the majority of structural automotive components, the key requirements are mechanical properties that are controlled by alloy chemistry, structure and internal integrity. While for 3C housings, mechanical properties are still important, the primary concern is shifted toward surface finish. To achieve a high quality surface, a number of surface modification steps are included in the manufacturing process. A typical production sequence of magnesium 3C painted products consists of the following steps [57]:

(i) injection molding;
(ii) trimming where runners and overflows are removed;
(iii) machining with tapping threads and polishing;
(iv) step one of surface finishing involving shot blasting and vibratory polishing;
(v) step two of surface finishing involving buffing and fine grinding;
(vi) deposition of chemical conversion coatings;
(vii) painting with solvent base or powder coating;
(viii) printing.

It is clear that the multi-step surface preparation, passivation and coating affect the final cost structure (Fig. 2.36). As a result, cost related to surface modifications

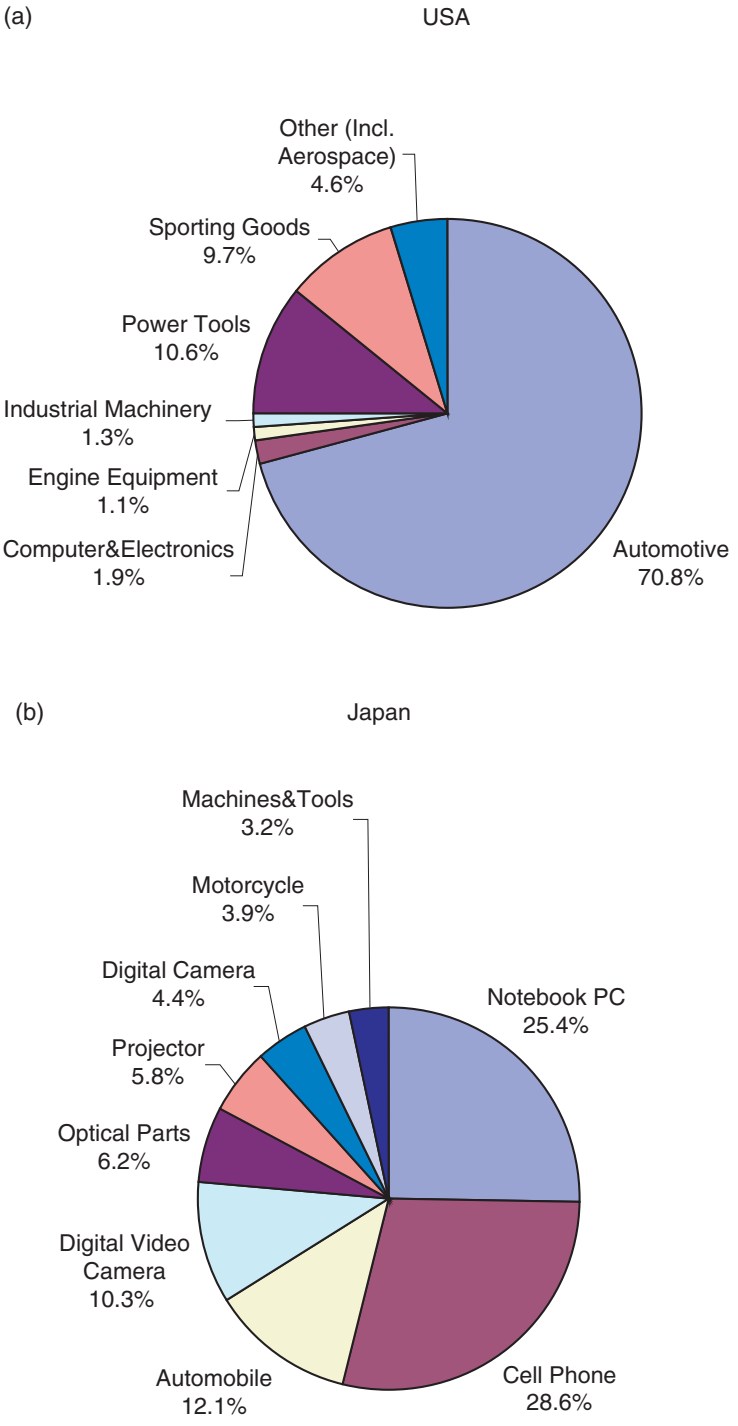

Fig. 2.37 The difference in structure of the magnesium die casting market between North America **a** [58] and Japan **b** (2004)

(a)

(b)

(continued)

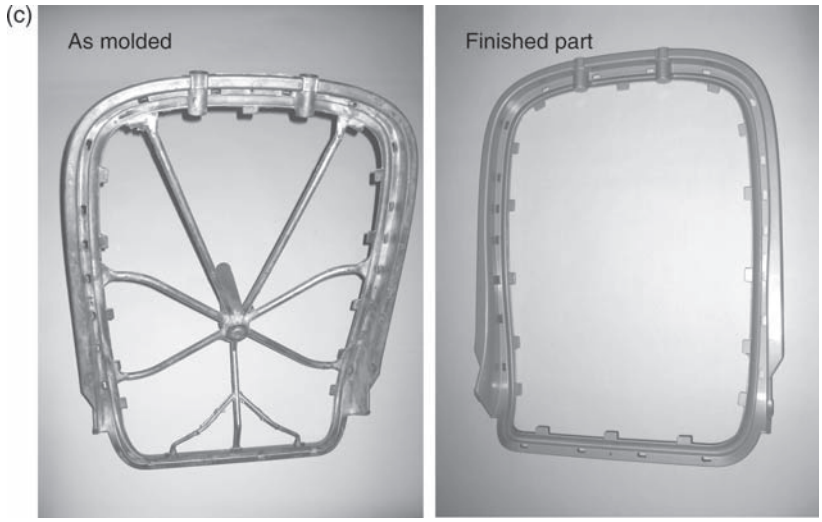

Fig. 2.38 Examples of automotive parts, produced by injection molding: **a** motorcycle wheel, diameter–40 cm, shot weight–1.8 kg; **b** car steering wheel, weight 560 g; **c** car seat frame, shot weight1.95 kg, part weight–1.25 kg

represents over 80%, and the cost of molding or casting itself accounts for less than 10%. Among other factors, the alloy's fluidity, which directly affects surface quality and capabilities of surface finishing, are seen as the key feature of a successful alloy for thin-wall molding.

2.11.1.2 Market Geography and Structure

Since its origin, manufacturing of housings for the 3C market has been concentrated in Asia. As seen in Fig. 2.37a,b, there is a drastic difference in magnesium-casting trends between North America or Europe and Asia. In North America, the largest and fastest growing market for magnesium castings is the automotive segment, mainly due to the increased interest in lightweight components that can improve fuel efficiency [58]. The computers and other electronics represent only around 2%, based on the volume shipped. In Asia, the market of magnesium products is focused on the electronic industry, and the automotive segment covers slightly above 12%. Notebooks and cellular phones represent over 50% of the entire volume of magnesium castings.

2.11.2 Automotive

Automotive applications represent the largest volume of injection molding opportunities. The potential components include:

Fig. 2.39 Examples of general-purpose components, produced by injection molding: **a** household equipment; **b** leisure and sport components

(i) interior parts—seat elements, instrument panel, steering wheel columns and armatures, air bag housings, gear and hand brake assemblies;
(ii) body and exterior parts—sunroof elements, luggage racks, bumper reinforcements, tire rims, headlight housings;
(iii) power train and drive train parts—oil pans, valve covers, cylinder heads, clutch and transmission housings, intake manifold, oil pump housings, engine accessory brackets, brake elements.

Although practically all components will be targeted in the future, the machine sizes available at present favor medium and smaller parts. After the hot runner system is commercialized, large components with long flow distances will also be molded. The examples of motorcycle wheel, car steering wheel and car seat frame are shown in Fig. 2.38a-c.

A special opportunity of injection molding is in processing of high temperature automotive alloys. Since during conventional casting, relatively high overheating up to 100 °C above the liquidus, is required, injection molding offers not only energy savings but also better stability in the alloy's chemistry. The alloy composition, containing reactive elements, may change during high temperature exposure. The benefits also arise from faster cycle time, a larger number of mold cavities, better repeatability and higher yield. The better quality parts with tight dimensional tolerances reduce a need for post molding operations such as machining and allow for net shape design. Integration with other manufacturing steps is likely by incorporating inserts into molded parts.

2.11.3 General Purpose Equipment

This market covers sporting goods, as well as household and office equipment, and is extensively used by injection molding. Examples are shown in Fig. 2.39a,b. In this area not only conversions from steel and aluminum but also from plastics are common. This is because for a number of hand tools, thermal loads are getting too high for plastics. The main driving force is the fact that magnesium molding improves strength and wear resistance, reducing wall thickness and allowing for design flexibility. For example, drills benefit from injection molding due to stiff and lightweight gear cases. Flatness and tight tolerances, achievable by injection molding, allow for consolidation of parts, replacing a number of processing steps required in other manufacturing methods.

2.12 Summary

After over three decades since its invention, semisolid processing of metallic alloys has established itself as a viable manufacturing method. Despite tremendous progress made, the technique is currently under intensive development, and a critical breakthrough is still expected. A number of technologies have been

developed and industrially implemented to take advantage of the unique behavior of semisolid slurries. Understanding the difference between the component's integrity and the material's microstructure is of key importance for the proper selection of the processing parameters to achieve the maximum properties with existing alloys. The detailed description and understanding of thixotropic microstructures will also be crucial for the development of a new generation of alloys, designed specifically for semisolid processing.

References

1. Schalek E, Szegvari A (1923) Kolloid Z 32:318
2. Peterfi T (1927) Arch. Entwicklungmech. Organ. 112:680
3. Barnes H (1997) Thixotropy—a review. Journal of Non-Newtonian Fluid Mechanics 70:1–33
4. Spencer DB, Mehrabian R, Flemings MC (1972) Rheological behavior of Sn-15%Pb in the crystallization range. Metallurgical Transactions A 3:1925–1932
5. Mehrabian R, Flemings MC Metal composition and methods for preparing liquid-solid alloy metal compositions and for testing the metal compositions. US Patent 3,951,651
6. Pryce-Jones J (1934) JOCCA 17:305
7. Joly P, Mehrabian R (1976) The rheology of partially solid alloy. Journal of Materials Science 11:1393–1418
8. Quaak CJ (1996) Rheology of partially solidified aluminium alloys and composites. Technische Univ., Delft, The Netherlands
9. Llorens J, Rude E, Mans C (1996) Structural models to describe thixotropic behaviour. Progress in Colloid Polymer Science 100:252–258
10. Denny DA, Brodkey RS (1962) Journal of Applied Physics 33:2269
11. Cross MM (1965) J. Colloidal Science 20:417
12. Mewis J, Schryvers J (1996) International Fine Particle Research Institute Report, Unpublished, 1996
13. Kristensen PG, Jensen CTB, Nguyen QD (1996) In A Ait-Kadi (ed) Proceedings of XIIth Congress on Rheology, Laval University, Quebec City, 1996, p 471
14. Alexandrou A, Duc E, Entov VJ (2001) Non-Newtonian Fluid Mechanics 96:383–403
15. Alexandrou A (2001) Rheology and numerical simulations of flow of semisolid suspensions. In AM De Figueredo (ed) Science and technology of semi-solid metal processing, Worcester Polytechnic Institute, Worcester, MA, pp 5.1–5.28
16. Lohmuller A et al (2003) Injection molding of magnesium alloys. In KU Kainer (ed) Proc. of the 6th international conference on magnesium alloys and their applications, Wolfsburg, Germany, Wiley-VCH, pp 738–743
17. Modigell M, Koke J (1999) Time dependent rheological properties of semisolid metal alloys. Mechanics of Time-Dependent Materials 3:15–30
18. Mao WM et al (2004) Thixotropic behaviour of semisolid AZ91D magnesium alloy. Transactions Nonferrous Met. Society, China 14(2):297–301
19. Gebelin JC, Suery M, Favier D (1999) Characterization of the rheological behaviour in the semisolid state of grain refined AZ91 magnesium alloy. Materials Science and Engineering A 272:134–144
20. Yurko JA, Flemings MC (2002) Rheology and microstructure of semisolid aluminum alloys compressed in the drop-forge viscometer. Metallurgical and Materials Transactions A 33:2737–2746
21. Loue WR, Suery M, Qyerbes JL (1992) In SD Brown, MC Flemings (ed) Proc. 2nd international conference on semisolid processing of alloys and composites, TMS, Warrendale, PA, pp 266–275

22. Basner T, Pehlke R, Sachdev A (2000) Thin-wall back extrusion of partially remelted semisolid slurry. Metallurgical and Materials Transactions A, 31:57–62
23. Ghosh D, Fan R, VanSchilt C (1994) Thixotropic properties of semisolid magnesium alloys AZ91 and AM50. In Proc. of the 3rd international conference of semisolid processing of alloys and composites, Tokyo, 1994, pp 85–94
24. Li DN et al (2002) Study on the semisolid rheocasting of magnesium alloy by mechanical stirring. Journal of Materials Processing Technology 129:431–434
25. Ichikawa K, Katoh M (1999) Method of manufacturing metallic materials with extremely fine crystal grains. US Patent 5,901,778, 11 May 1999
26. Ji S, Fan Z, Bevis MJ (2001) Semisolid processing of engineering alloys by a twin-screw rheomoulding process. Materials Science and Engineering A 299:210–217
27. Winter J, Tyler DE, Pryor MJ (1980) Method for the preparation of thixotropic slurries. US Patent 4,229,210, 21 Oct 1980
28. Abramov VO et al (1997) Hypereutectic Al-Si based alloys with the thixotropic microstructure produced by ultrasonic treatment. Materials and Design 18(4–6):323–326
29. Kapustina OA (1970) The physical principles of ultrasonic manufacturing. Nauka, Moscow
30. Gjestland H, Westengen H (1996) Procedure for the production of thixotropic magnesium alloys. US Patent 5,501,748, 26 Mar 1996
31. Qian M (2006) Creation of semisolid slurries containing fine and spherical particles by grain refinement based on the Mullins–Sekerka stability criterion. Acta Materialia 54:2241–2252
32. Doutre D, Hay G, Wales P (2002) Semi-solid concentration processing of metallic alloys. US Patent 6,428,636 B2, 6 Aug 2002
33. Apelian D, Pan, QY, Findon M (2004) Low cost and energy efficient methods for the manufacture of semisolid feedstock. Die Casting Engineer 48:22–28
34. Tausing G, Xia K (2001) Semisolid metal processing. US Patent 6,311,759 B1, 6 Nov 2001
35. Fehlbier M, Aguilar J, Sahm PR (2001) Rapid slug cooling technology (RSCT): A new approach for the production of thixocasting prematerial billets. International Journal of Cast Metals Research 14:71–78
36. Aguilar J (2005) Verarbeitung von Magnesium Legirungen im teilflussigen Zustand und deren Eigenschaften. Shaker Verlag, Aachen
37. Winterbottom WL et al (2004) Apparatus for and method of producing slurry material without stirring for application in semisolid forming. US Patent 6,742,567 B2, 1 June 2004
38. Mingard KP et al (1998) Acta Materialia 37:429
39. Annavarapu S, Doherty D (1992) Inter. Journal of Powder Metallurgy 29:331
40. Fuxiao Y et al (2001) Fundamental differences between spray forming and other semisolid processes. Materials Science and Engineering A 304–306:621–626
41. Tsao YA, Chiang CH (2005) Si coarsening of spray-formed high loading hypereutectic Al-Si alloys in the semisolid state. Materials Science and Engineering A 396(1–2):263–270
42. German RM (1985) Liquid Phase Sintering, Plenum Press, New York
43. Kirkwood DH (1994) Semisolid metal processing. International Materials Reviews 39(5):173–189
44. Young KP, Kyonka CP, Courtois JA (1983) Fine grained metal composition, US Patent 4,415,374, 15 Nov 1983
45. Kazakov AA (2000) Alloy compositions for semisolid forming. Advanced Materials and Processes (3):31–34
46. Fan Z (2002) Semisolid metal processing. International Materials Reviews 47(2):49–85
47. Liu YQ, Das A, Fan Z (2004) Thermodynamic predictions of Mg-Al-M (M=Zn, Mn, Si) alloy compositions ammenable to semisolid metal processing. Materials Science and Technology 20:35–41
48. Yurko JA et al (2004) Process and apparatus for preparing a metal alloy. US Patent Application 2004/0173337 A1
49. Yurko, JA, Flemings MC, Martinez RA (2004) Semisolid rheocasting (SSR)—increasing the capabilities of die casting. Die Casting Engineer 48(1):50–52

50. Kamm JR, Jorstad JL (2004) Semisolid molding method—2. US Patent 6,808,004 B2, 26 Oct 2004
51. Kamm JR, Jorstad JL (2003) Semi-solid molding method. US Patent Application 2003/0141033 A1, 31 July 2003
52. Jorstad JL (2004) Semisolid metal processing; the high integrity die casting process. Die Casting Engineer 48(1):42–48
53. O'Donnel R (2005) Advanced thixotropic metallurgy, revolution in casting technology. Die Casting Engineer 49(1):43–47
54. Rice CS, Mendez PF (2001) Slurry-based semisolid die casting. Advanced Materials and Processes (10):49–52
55. Brown SB et al (1999) Apparatus and method for semisolid material production. US Patent 5,887,640, 30 Mar 1999
56. Chiarmetta G (2000) Why thixo? In 6th international conference semisolid processing of alloys and composites, Turin, Italy, 2000
57. Nakatsugawa I, Tsukeda T, Kitamura K (2002) Latest developments in magnesium use for thixomolding in Asia. In 59th annual world magnesium conference, Montreal, International Magnesium Association, 2002, pp 11–14
58. Magnesium Casting Industry Technology Roadmap (2005) American Foundary Society
59. Liu TY et al (2003) Rapid compression of aluminum alloys and its relationship to thixoformability. Metallurgical and Materials Transactions A 34:1545–1554
60. Czerwinski F (2006) The basics of modern semisolid metal processing. Journal of Metals 57(6):17–20
61. Kazakov AA (2007) St. Petersburg State Technical University, private communication, 2007
62. Flemings M.C, Behaviour of metal alloys in the semisolid state, Metallurgical Transactions A, 1991, **22,** 957–981
63. Busk R. Method for making thixotropic materials-1, US Patent 4,694,882, September 22, 1987
64. Busk R. Method for making thixotropic materials-2, US Patent 4,694,881, September 22, 1987
65. Bradley NL, Wieland RD, Schafer WJ, and Niemi AN Method and apparatus for the injection molding of metal alloys, US Patent 5,040,589, August 20, 1991

3
Basic and Auxiliary Hardware

3.1 Introduction

In order to implement magnesium molding, highly sophisticated machines were designed and built, exploring the existing processing knowledge. Sharing most features with standard injection molding systems for plastics, they can easily be incorporated into injection molding facilities. The machine is a part of the integrated cell, which includes additionally, a high-speed robot for part removal and die-lubricant application, feedstock loading equipment, a part cooling conveyor and mist filtration, as well as mold lubricant mixing and distribution.

In this chapter, all elements of the magnesium molding system are described. Since the magnesium molding solutions are often considered as hybrids between plastics injection molding and metal die casting, a reference to both technologies is used.

3.2 Machine

The injection molding machine consists of two major sub-systems: clamp and injection unit (Fig. 3.1a). In a production environment, the machine is installed together with auxiliary equipment, indicated in Fig. 3.1b. The modern magnesium molding unit with a clamp force of 500 tonnes is shown in Fig. 3.2.

3.2.1 Clamp

Within the clamp portion, a mold is mounted on supporting platens and the clamps allow the mold to be opened and closed in a precisely controlled way. During the injection cycle, when a melt fills the mold cavity, the clamps keep the mold closed under high force, ranging from tens to thousands of tonnes. The methods of generating the clamping force include:

F. Czerwinski, *Magnesium Injection Molding*.

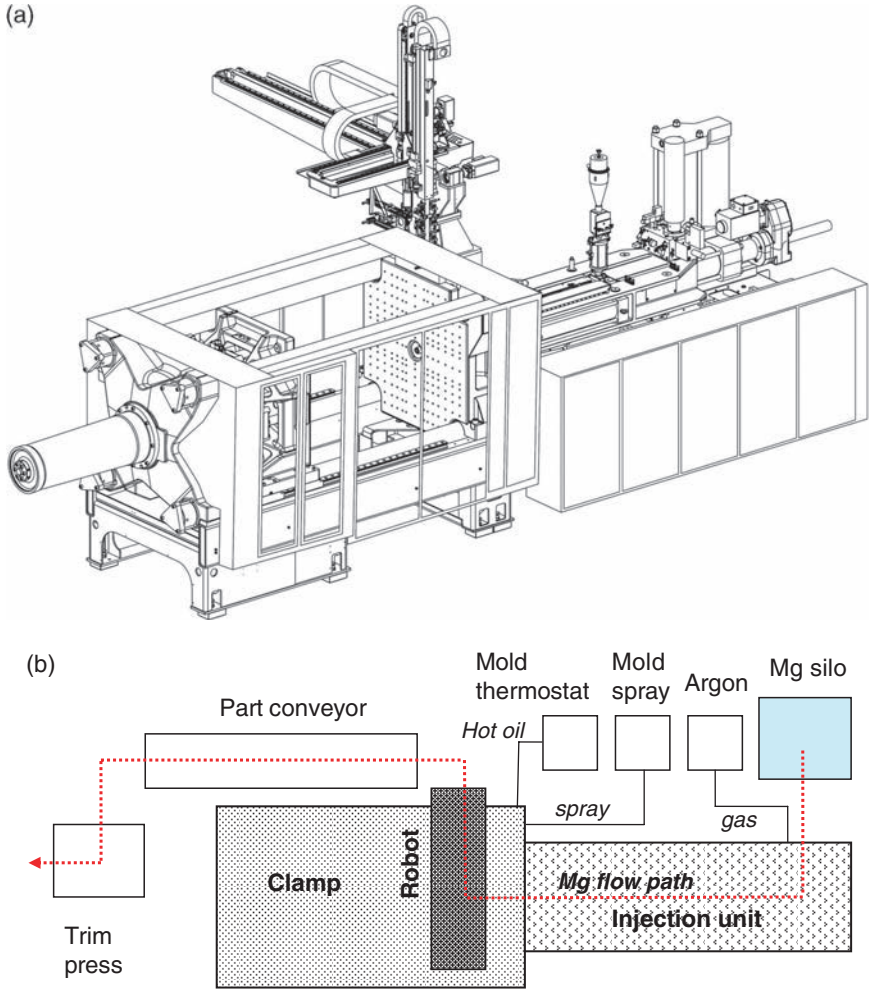

Fig. 3.1 The schematics of an injection molding machine with its basic parts of clamp (left side) and injection unit (right side) and top-entry robot **a**. A location of the machine within the integrated cell is shown in **b**

(i) mechanical (toggle);
(ii) hydraulic;
(iii) hydro-mechanical;
(iv) electro-hydraulic.

The comparison of their key characteristic features is given in Table 3.1. High pressure die casting is dominated by toggle clamps where no substantial changes were made during the last two decades (Fig. 3.3). According to designers of die casting machinery the linkage and toggle systems have many inherent advantages in that application: the proven ability to generate large tonnage forces on a die, rapid cycle

Fig. 3.2 The HyMet™ magnesium molding machine with a clamp force of 500 tonnes

time as well as a simple and repeatable operation. The linkage style clamp end does have economic and operational limitations. Very recent solutions allow generating tonnage using hydraulic locking tie bar nuts and only two platens, offering advantages of consistent force on the die from cycle to cycle, reduced floor space requirements, reduced machine maintenance because of the elimination of the linkage and reduced cycle time due to optimizing the die open stroke [1]. It is anticipated that the toggle clamp will remain in the near future as the dominant solution in die casting.

The new generation molding equipment is built to run on the hydro-electric machine platform (Fig. 3.4a). It features special platens to improve tonnage utilization and reduce mold wear as well as wide tie bar spacing for mounting oversized tools. The hydro-mechanical clamp design decouples stroke and clamp-up using cylinders optimized for speed. A clamp accumulator efficiently provides peak oil requirements when needed for faster mold stroke and clamp-up. The moving platen rides on low-friction

Table 3.1 The comparison of characteristic features for three different clamp technologies

	Toggle	Hydraulic	Hylectric
Fast cycle times	X		X
Good mold protection		X	X
Good force distribution		X	X
Energy efficient	X		X
Tonnage accuracy		X	X
Heavy mold support		X	X
Wide tiebar spacing		X	X
Clean molding area			X

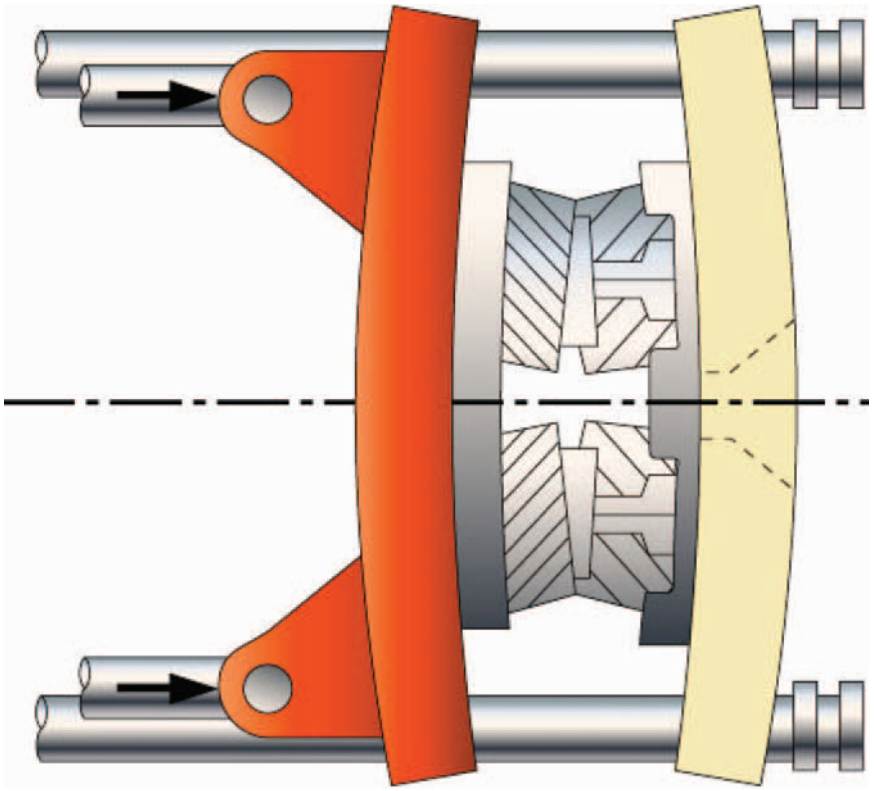

Fig. 3.3 The schematics of mechanical (toggle) clamp, showing deficiencies in a uniform force distribution

bearings, minimizing the power and time for acceleration. A regenerative mold stroke circuit results in efficient, high-speed injection. As emphasized in Fig. 3.4b, clamping force is directed to the molding area by the central clamp column and then redistributed evenly across the entire mold face by the platens. Mold protection sensing occurs under

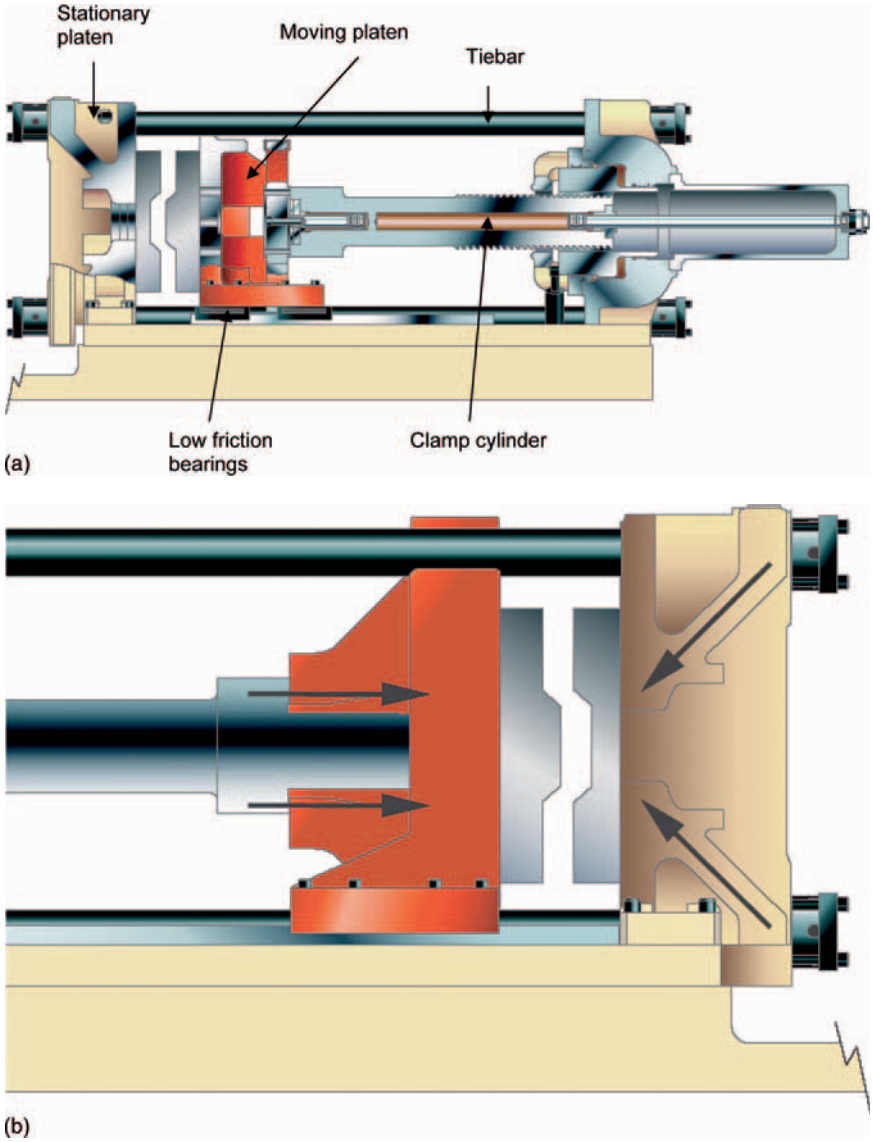

Fig. 3.4 The Hylectric™ clamp with major components **a** and uniform distribution of force within the Reflex™ platen **b**

mold stroke force at only a small percenage of full tonnage, compared to near maximum tonnage on toggle machines. The clamp design delivers true closed loop tonnage control to minimize cycle variations and over-tonnage or flush during start-up. Placing the clamp beams outside the tiebars increases clamp stiffness, improving support for heavy molds and reducing mold wear.

3.2.2 Injection Unit

Four major types of injection units were historically developed for plastics processing [2]. In the *single-stage plunger* solution, the plunger forces the material over the spreader. The *two-stage plunger* uses a single-stage plunger to prepare the material and the second plunger to shoot the material into the mold. In a *two-stage screw-plunger* design, the first stage of material preparation is conducted using a screw; however, the injection step is executed with a plunger. Finally, the most popular present solution of *reciprocating screw* uses a single screw to prepare the melt and to inject it into a mold cavity.

The modern injection unit is designed for challenging processing demands of metal molding (Fig. 3.5). Injecting magnesium requires significantly higher injection speeds and pressures than conventional plastics molding. A large cradle that supports the extruder barrel eliminates the transmission of injection forces through the barrel wall. This allows the use of a barrel design that enhances throughput capacity. The traditional approach used in plastics molding supports the injection barrel at its low-pressure end, and loads are transmitted along the walls of the barrel and through the mold sprue (Fig. 3.6a). The magnesium injection unit explores a support of the barrel at its high-pressure end, taking the high injection load off the barrel itself. Carriage force potential is 1.5 times static injection potential. Loads are transmitted directly into the stationary platen through the support cradle and the platen rather than through

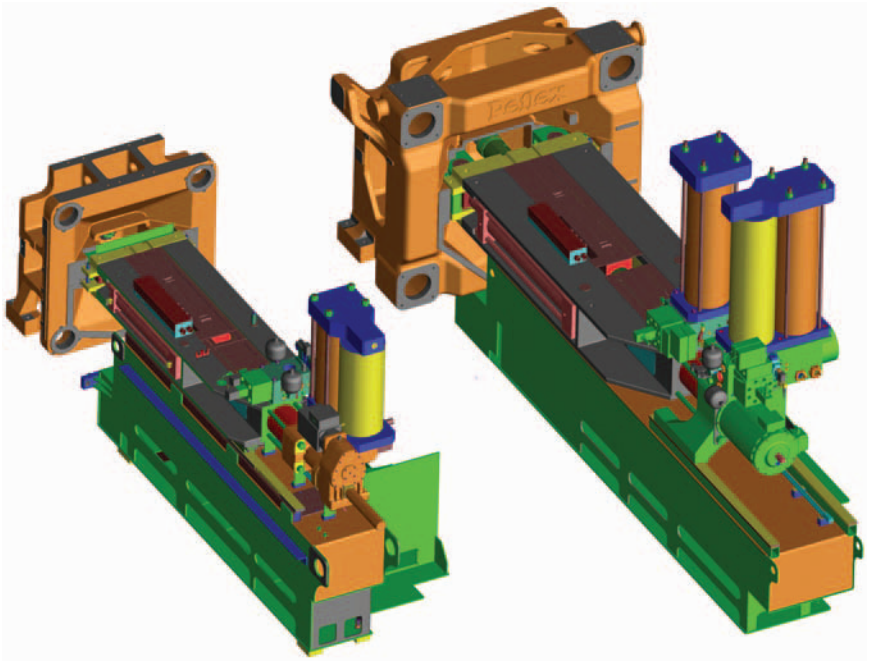

Fig. 3.5 The injection units of 500-tonne and 1000-tonne HyMet™ magnesium molding machines

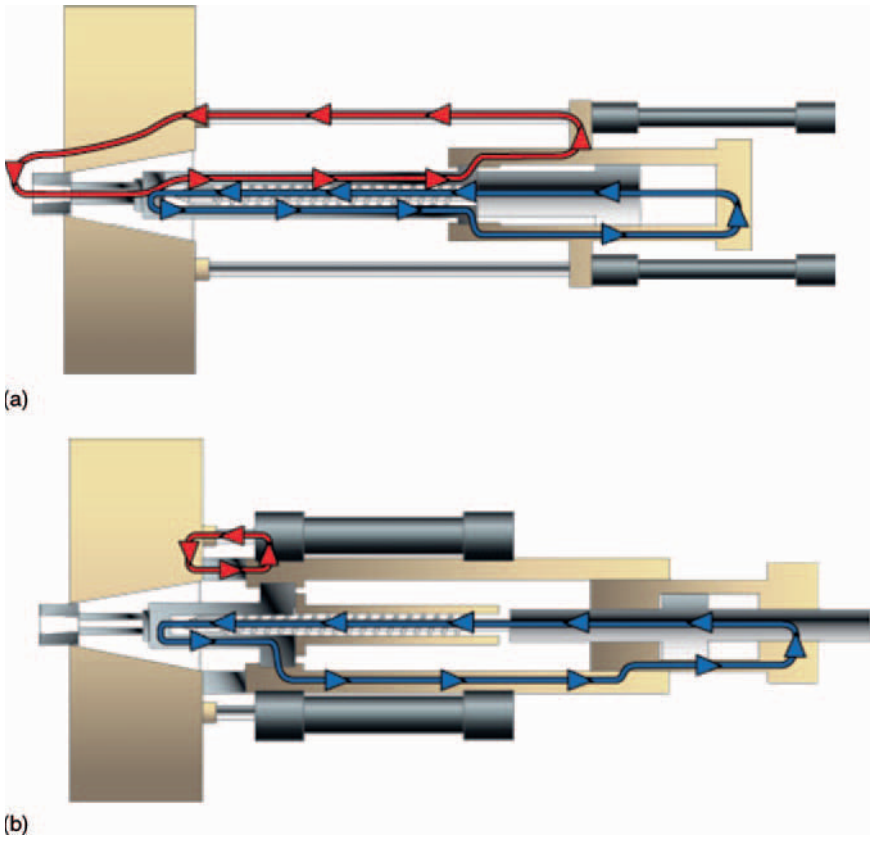

Fig. 3.6 The distribution of forces in traditional **a** and metal molding specific **b** injection units

the mold sprue (Fig. 3.6b). Effectively managing the injection loads eliminates the damaging effect of shock and vibration due to recoil, which results in smooth processing. A high performance hydraulic system, featuring a 1:1 injection cylinder with meter-out control, allows for executing the required cycle: high acceleration at the beginning and hydraulically controlled deceleration at the shot's end.

A front view of the injection unit is shown in Fig. 3.7. The components, as they are during processing in direct contact with magnesium, are described in more detail below.

3.2.3 Machine Barrel Assembly

3.2.3.1 Barrel and Barrel Head

The key feature of injection molding is that the feedstock melting and slurry preparation is performed inside the machine barrel, called also the cylinder. Thus, the barrel replaces the furnace and shot sleeve of the cold chamber or the furnace and gooseneck

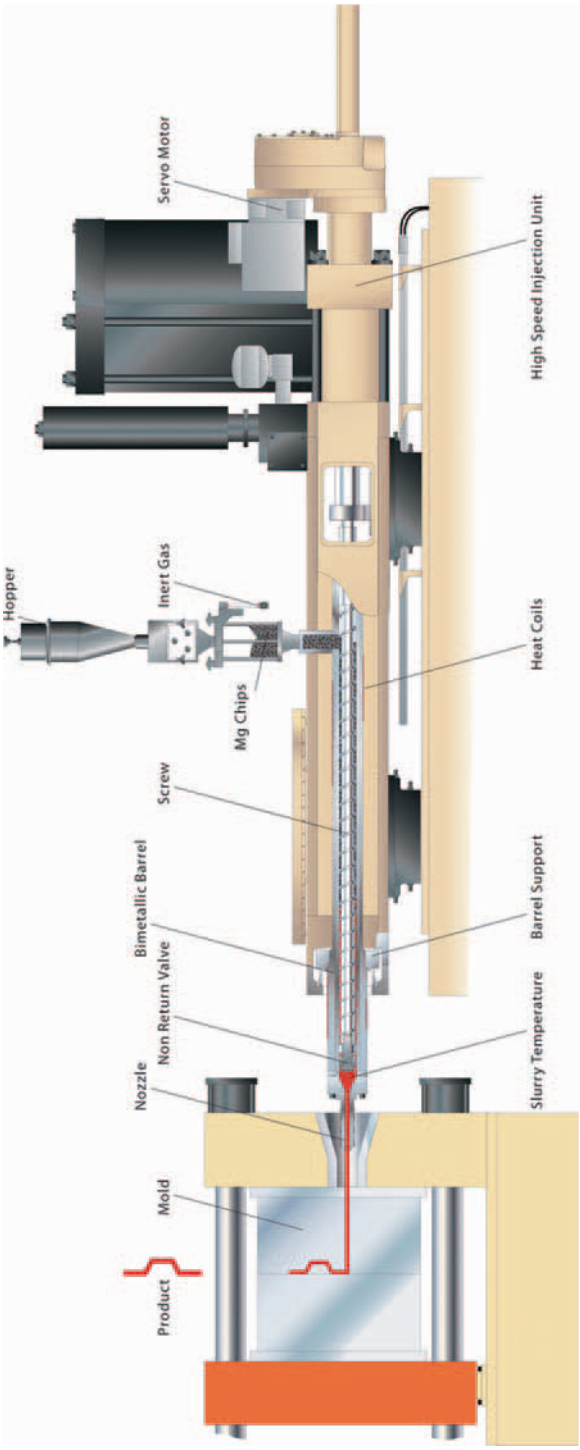

Fig. 3.7 The injection unit of the magnesium molding machine with indicated major components

of the hot chamber die casting machines. The barrel size depends on the clamp tonnage: For a clamp range of 500 tonnes to 1000 tonnes, the barrel inner diameter is between 70 mm and 85 mm. The barrel length is correlated with its diameter and equals approximately 2 m. As opposed to the simple cylinder in early designs, the present barrels have a complex external shape where the melt preparation and melt accumulation zones are separated. The thin wall of the initial zones, which represents the feeding section, allows for high heating rates and helps to avoid creating large temperature gradients across the wall thickness. An increased wall thickness of the barrel exit section allows the management of the high injection pressures.

3.2.3.2 Injection Nozzle

At the end of the barrel head, an injection nozzle is attached to allow a flow of the alloy slurry from the barrel to the mold. The key difference between various solutions offered is in the shape of the connection with the sprue (Fig. 3.8a,b). In early designs, as with plastics molding, it was assumed that the carriage cylinders could apply sufficient pressure to the nozzle to prevent it from losing contact with the sprue bushing. Therefore, the mating geometry between the faces of the nozzle and the sprue bushing were designed to withstand the positive forces applied by the

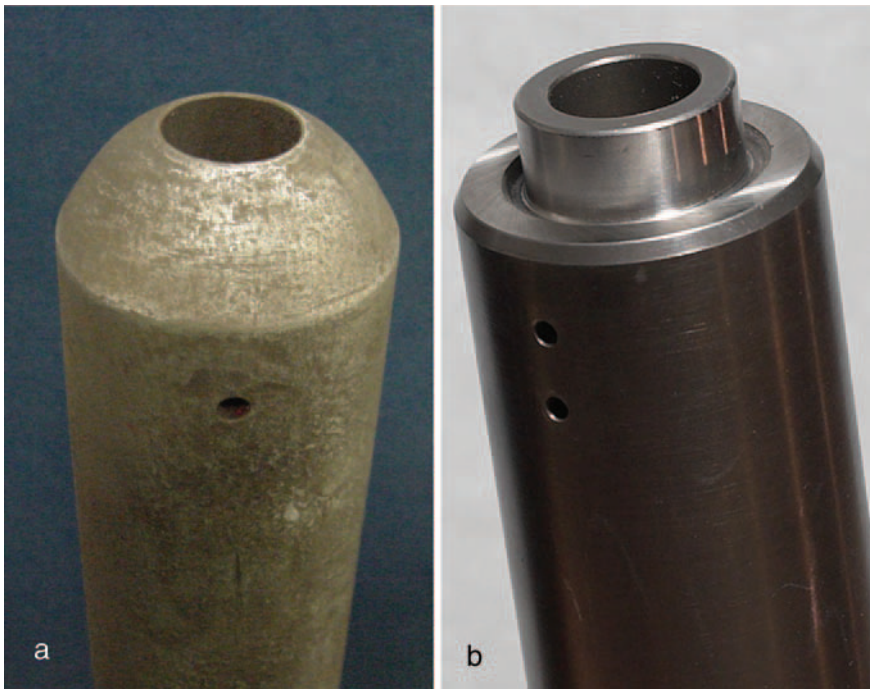

Fig. 3.8 The injection nozzles with different shapes of interfaces with a sprue: **a** conical interface; **b** spigot interface

carriage cylinders and to remain in a positive sealing contact throughout the complete processing cycle. The mating surfaces of the nozzle and the sprue bushing might be flat, spherical, conical or any other geometric shape that would provide an acceptable area of positive contact pressure. Unfortunately, the reactionary and dynamic forces of a large magnitude during injection cause separation between the nozzle and sprue bushing, which results in magnesium leakage. A novel concept provides an improved seal where the bushing has a cylindrical surface and the nozzle an annular portion (Fig. 3.9a) [3]. The annular portion fits within the cylindrical surface to provide a sealing engagement between the nozzle and bushing (Fig. 3.9b). The surface and the annular portion are of sufficient length to permit limited axial movement without loss of sealing.

3.2.4 Heating Systems for Barrel Assembly Components

All elements of the barrel assembly require a high reliability heating to operate under very demanding conditions. First, operating temperatures up to 650 °C exceed significantly the level of 350 °C used in plastics. Second—the higher injection speeds impose on heaters a higher shock and vibration.

3.2.4.1 Electric Resistance Heaters

The electric resistance heating solutions include band, tubular (cable), cartridge and cast-in heaters. The two first types are applied for heating the barrel assembly. The *ceramic heater bands* have unique heating capability similar to that of an electric furnace. The built in insulation on the ceramic band heaters acts to minimize unwanted temperature changes along the barrel. Despite the high cost, this type of heating is popular since it provides long service life, power efficiencies or large-area coverage. The *mica band heaters* are manufactured by enclosing a precision wound nickel–chromium resistance ribbon inside a specially treated steel sheath (Fig. 3.10a). In order to insulate the resistance ribbon from shorting out against the outer sheath, the outer sheath is made of mineral mica, which is known for its excellent dielectric properties and its ability to withstand voltage spikes or moisture. This type of heater is designed for contact heating as opposed to radiant heating of ceramic bands, and, therefore, it has to be tightly installed. A lack of contact results in poorer heat transfer, shorter heater life, heat loss and low heating efficiency. The alternative type of band heaters uses a special mineral insulation with higher thermal conductivity than the mica, e.g., high purity magnesium oxide. A thin layer of the mineral compound is applied to electrically insulate the element wire from the inside diameter of the metal sheath. A thick layer of low thermal conductivity compound backs up the resistive wire, directing the heat towards the part that is being heated.

The *cable (tubular) heater* consists of a resistance wire inside a tube of steel, filled with isolative powder (3.10b). Depending on the wall thickness of the tube

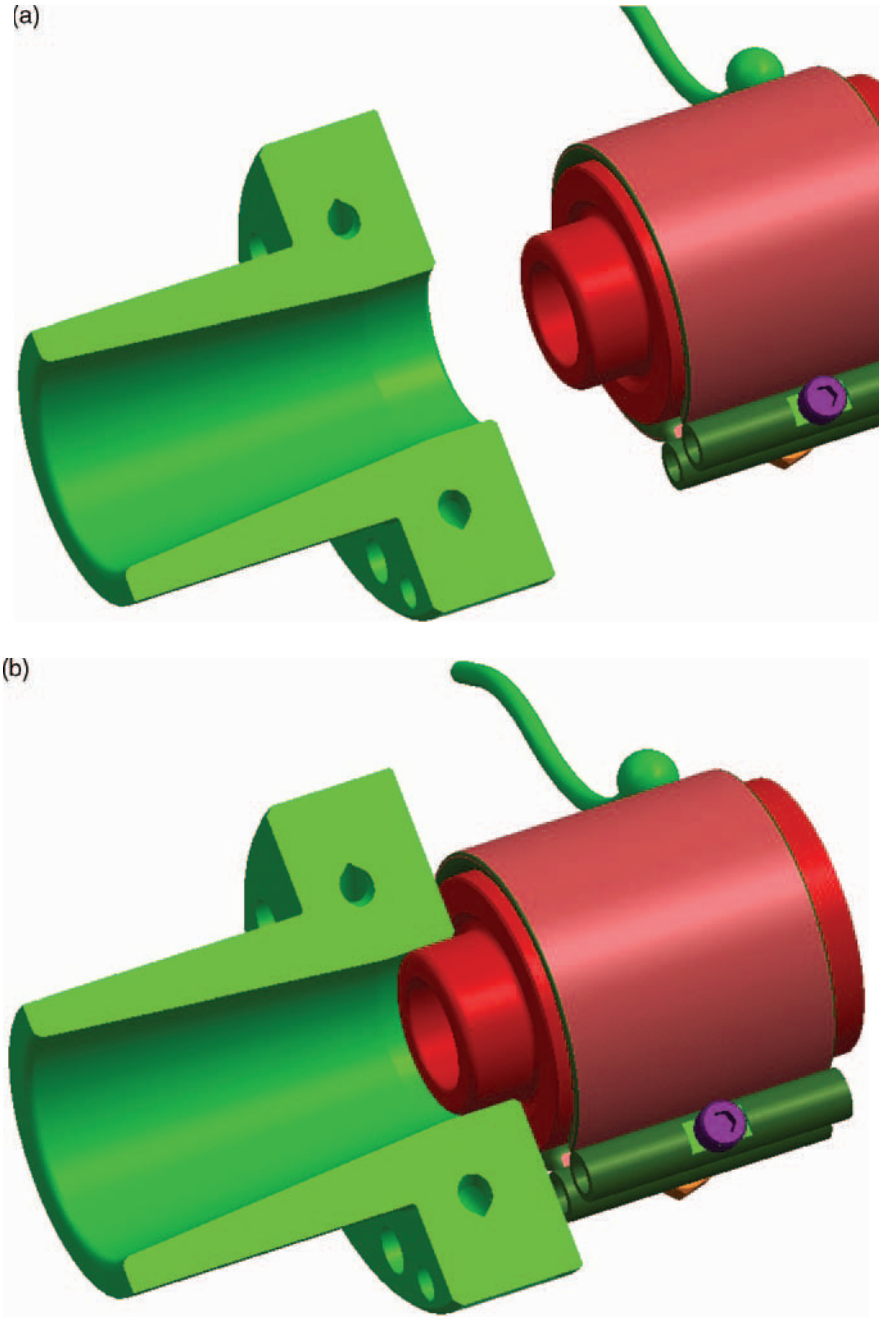

Fig. 3.9 The concept of spigot-type connection and sealing during service: **a** disengaged position; **b** engaged position

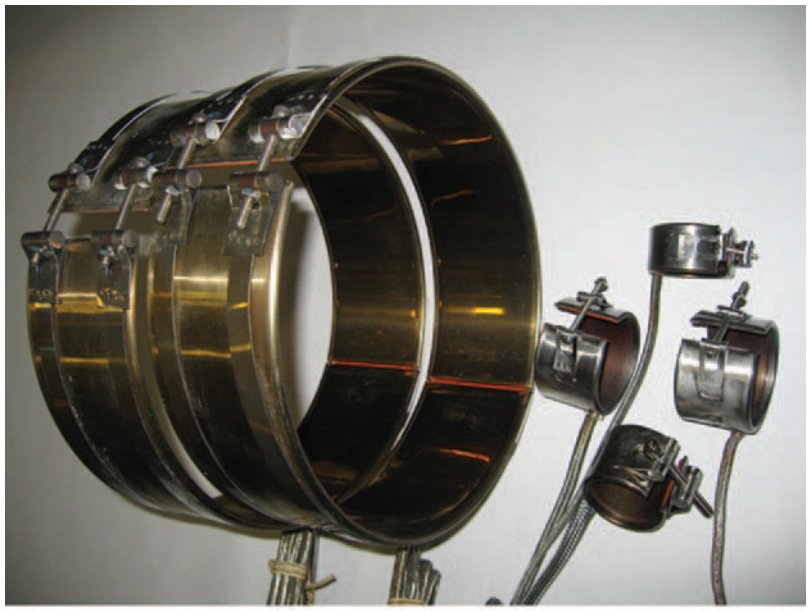

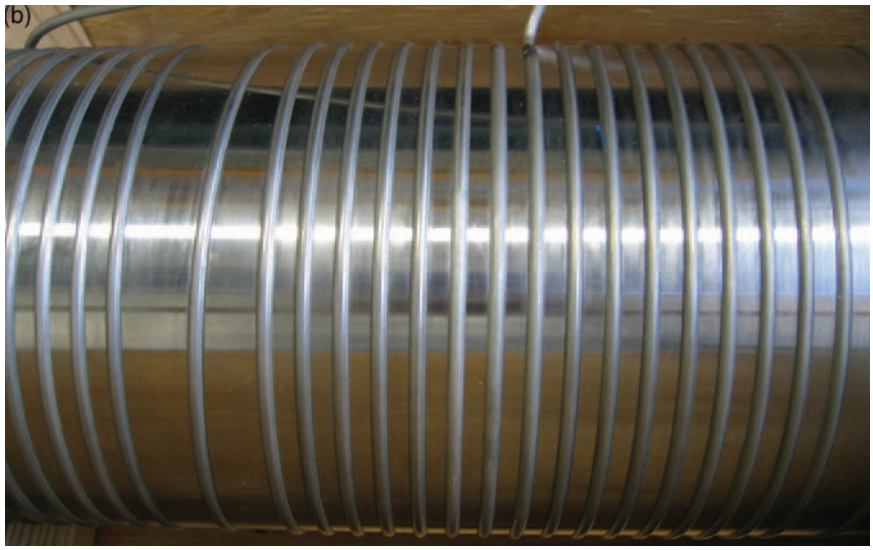

Fig. 3.10 Examples of heaters that can be used for magnesium melting: **a** mica band heaters; (Watlow) **b** cable heater placed within a groove on the barrel; **c** cross section showing the tubular heater's elements and an intimate contact of the heater with the substrate

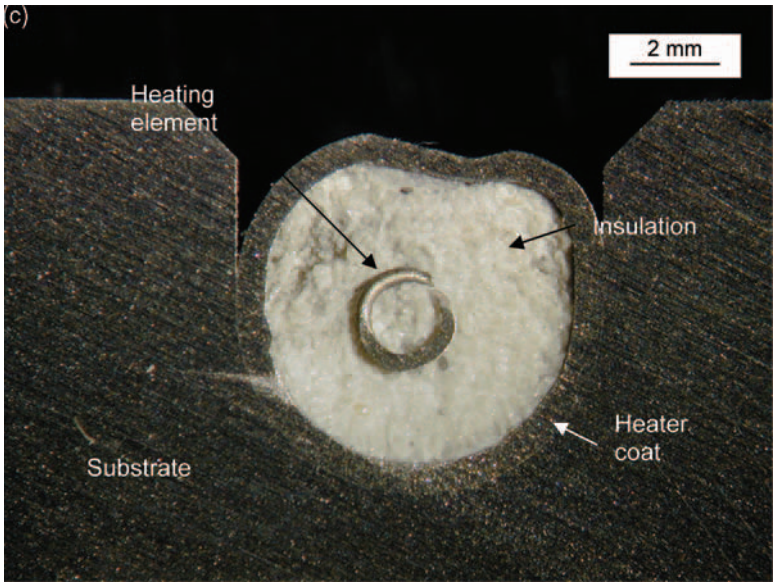

Fig. 3.10 (continued)

the heater can be either rigid or flexible. The benefit of cable heaters is their ability to form into a variety of shapes as required by applications with heat dissipation from a few watts to several tens of kilowatts. The heater can be formed into coiled shapes and installed into grooves on the nozzle or barrel heater, supplying a full 360 degrees of heat with uniformly distributed power. The mineral insulation heaters can work continuously to 650 °C or with intermittent operating periods up to 820 °C. Special solutions exist with long term heating up to 1000 °C. In all cases the cold ends, where the heater is connected to the power supply cable, are limited to 600 °C. The low mass of cable heaters allows for quick response to both heating and cooling. Their high efficiency is improved by an intimate contact with the heated substrate (Fig. 3.10c). They are suitable for use in air, under vacuum or high pressures in any corrosive environment compatible with the sheath metal.

3.2.4.2 Inductive Heaters

A different class of heaters, with capabilities for application to magnesium processing, utilizes an electromagnetic induction phenomenon. The induction heating makes use of the capability of the magnetic field to transmit energy without direct contact as was a case for resistance heating. Eddy currents, internally generated on the component by an alternating magnetic field, cause the heating effect. The following characteristics of inductive technique are usually quoted: rapid heating, non-contacting, clean operating conditions, high power densities, accurate location of the heated area, accurate time and temperature control and minimal stand-by power.

A typical induction heating system consists of the power supply, an induction heating coil and water-cooling systems to cool the coil and some power-supply components. The heat penetration depth is affected by the frequency of the alternating current. Low frequencies of 5 kHz to 30 kHz are effective for thicker penetration; high frequencies of 100 kHz to 400 kHz are effective for shallow penetration. High frequency is more efficient, but requires longer heating time for conduction to the center. The induction heating is characterized by high heating rates; its power transmission is 10^4 W/cm^2 as compared to 20 W/cm^2 for thermal conduction typical for mica or mineral insulation heaters and 10 W/cm^2 by radiation typical for ceramic band heaters.

3.2.4.3 Comparison of Heaters

In addition to cost, two major factors are of importance during the design of a heating system: heating technique and the heater's power. Applying a uniform heat to even simple geometries seldom results in a uniform temperature distribution. Therefore, achieving uniformity in temperature distribution requires a finite element analysis, which determines conduction, radiation and convection dynamics and helps to select the optimal location of heaters. At present, the resistance heaters dominate commercial molding equipment. The ceramic bands and mineral insulation cable heaters are used for the barrel, where outside diameters are up to 200 mm. For small diameters, usually below 50 mm, the mineral insulation bands are the most frequently used. Induction heating of the machine barrel is also examined and there are experimental units in testing. The coil dimensions are much larger than for resistance heaters and appropriate space is required. The machine barrel, however, has an excess of space, which helps to solve problems of cooling the induction coils. For applications with dimensional restrictions, new induction heating techniques are available, where induction coils do not require water cooling.

The initial step in selecting the heater's power is to calculate the required power density. It is determined by dividing the total power by heated area. For contact heaters, in this calculation, area with no contact should be subtracted. Then, characteristics of specific heaters should be examined to determine the maximum allowable power. For all heaters, for a given size the allowable power density depends on the part temperature: The higher the service temperature the lower the power density available (Fig. 3.11) [4].

3.2.4.4 Process Monitoring Systems

In order to control processing, the transformations of the alloy conveyed and melted inside the barrel should be monitored. At present, the barrel temperature is the only parameter measured. It is clear, therefore, that the control of heating requires accurate temperature measurement. The temperature of the barrel assembly components is measured with thermocouples. They are equipped with a spring loaded bayonet, fitting the tip closely to the metallic surface at the bottom, thus for proper temperature reading, good contact is required. Besides that, due to an air gap, temperature reading may be

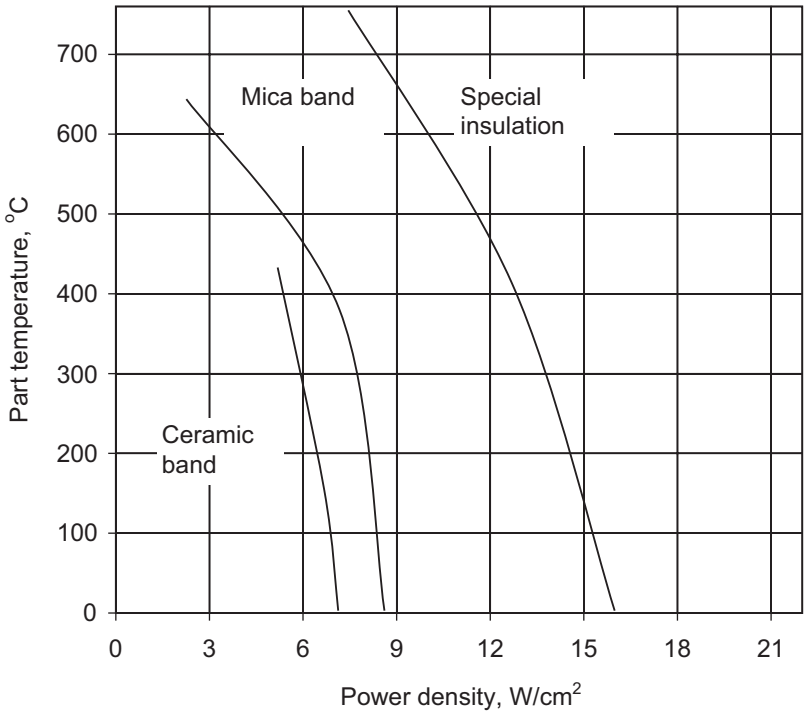

Fig. 3.11 Schematics of a relationship between the heater power and the temperature for three different heater types (Fast Heat Inc.)

distorted by a presence of insulating oxide scales. To control the melt temperature, the thermocouple should be located as close to the melt channel as possible. For thick-wall components, heated to high temperatures, thermocouples are placed at different wall thicknesses to additionally monitor the temperature gradient to avoid thermal shock.

The presently used systems rely on the correlation between the temperature of the barrel and the temperature of its content. The task is complex because the material changes are dynamic and difficult to attain at a steady state. It is a practical observation on a lack of equilibrium between those two, and a faster conveyance rate is accompanied by a larger difference. For smooth processing a good correlation is therefore required. In conclusion, using a sole temperature input leads to slow response and reduced repeatability. Employing pressure sensors to provide additional feedback to control transformations inside the barrel is difficult due to corrosive aggressiveness of molten magnesium.

There are attempts to use the computerized ultrasonic technology for accurate, non-intrusive and non-destructive monitoring of the injection barrel contents. Instead of temperature measurements, the solid to liquid ratio could potentially be directly accessed to provide the direct processing input (Fig. 3.12). The technique does not disturb the processing conditions or the quality of the final product.

Ultrasonic techniques are based on the fact that the ultrasonic waves lose some energy when impinging the boundary between two different media so the portion of energy is

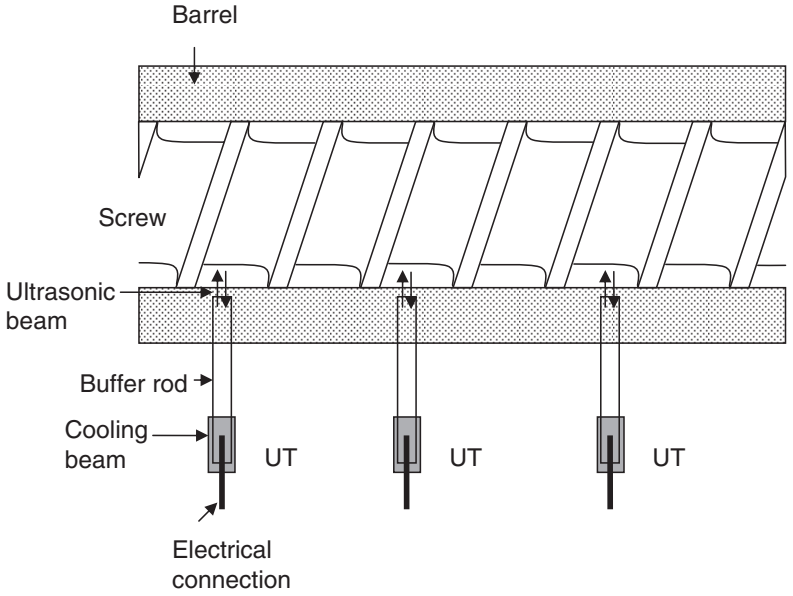

Fig. 3.12 The concept of ultrasound monitoring of the injection molding process. UT means the ultrasound transducer (NRC, Montreal, Canada)

reflected and the remaining fraction is transmitted. Pulse-echo ultrasonic measurements can be done in reflection or transmission modes. While in the transmission mode the signal is sent by one ultrasonic transducer and received by another one. In reflection mode both functions are performed by the same transducer. Experiments performed using metallic materials look promising. For example, the ultrasonic pulse-echo technique was successful in detecting, with high spatial resolution, the iron based inclusions in molten Zn at 600 °C [5]. The backscattered echoes had very low noise to signal ratio.

3.2.5 Injection Screw Assembly

3.2.5.1 Injection Screw

The injection screw along with the non-return valve represent unique features of injection molding that do not have an equivalent in die casting. The screw is connected by a thread or spline with a drive, which transfers power. There are two commonly used screw drives: hydraulic and electric. In a *hydraulic drive*, the screw is connected to a non-variable speed reducing coupling, driven by a hydraulic motor. A variety of different displacement pumps and motors are available to provide the required torque, horsepower and speed operating characteristics. The hydraulic system has continuous speed control of the screw. In an *electric drive* the

screw is attached to an electric motor through a speed-reducing gear train with different speed ranges. Usually, the electric drives do not have independent speed and torque controls. The speed is changed by trains. Because of the power preservation rule, a change in either speed or torque will inversely affect the other. There are also combined *hydro-electric drives* where typically the screw rotation is powered by electric drive while the injection is powered hydraulically. The screw geometry and its functions during processing are described in Chap. 5.

3.2.5.2 Non-Return Valve

For decades, different types of non-return valves, also called check valves, were developed in plastics injection molding. The most common designs include:

(i) sliding ring valve;
(ii) ball non-return valve with either side or front discharge;
(iii) poppet type valve with several modifications.

In plastics molding, the valve selection depends on the type of resin processed. Thus, the sliding-ring valves are used primarily with high viscosity, shear sensitive materials. Ball check valves are used mainly with low viscosity and shear-forgiving materials. The poppet valve is the least popular with limited applications. The major variables that play a role in the valve operation include viscosity of the resin, quality of the melt, the amount of the back pressure used, the amount of screw decompression used during the cycle, barrel size and injection speed.

Magnesium processing implements the sliding ring concept with several modifications. The valve tip does not usually have the conical tip profile which is required in plastics to preserve uniform flow of the high viscosity melt. It is also assumed that the conical tip allows holding the screw uniformly inside the barrel. In magnesium application, various shapes are used, mainly to improve the disassembling of the valve from the injection screw during maintenance (Fig. 3.13). The major change applies, however, to the slide ring, which similarly as in a die casting piston, contains seal rings. In the concept of a single-cut ring, one or several rings of different width are placed within a sliding ring outside diameter. The two-cut ring with a sub-ring is another solution. The sub-ring, which is a two piece semi-circular assembly, is installed directly on the sliding ring [6]. The overlapping gaps are in the opposite direction of the outside ring gaps. The seal concept relies on melt pressure that comes through the pressurized holes and expands the sub-ring, which in turn pressures the outside seal ring against the barrel walls (Fig. 3.14). At present, the single-cut ring, with or without subring, is used predominantly.

The new concept valve, called a spigot valve, has the slide ring inner diameter fitted with the tip outer diameter. Thus the seal surface is not limited to the ring-sit interface but is primarily shifted to the slide ring inner diameter–tip outer diameter. The major task of the seal ring is to generate a friction between the barrel walls and the slide ring that prevents inertia of the slide ring during the injection act, which separates the seat and slide ring [7].

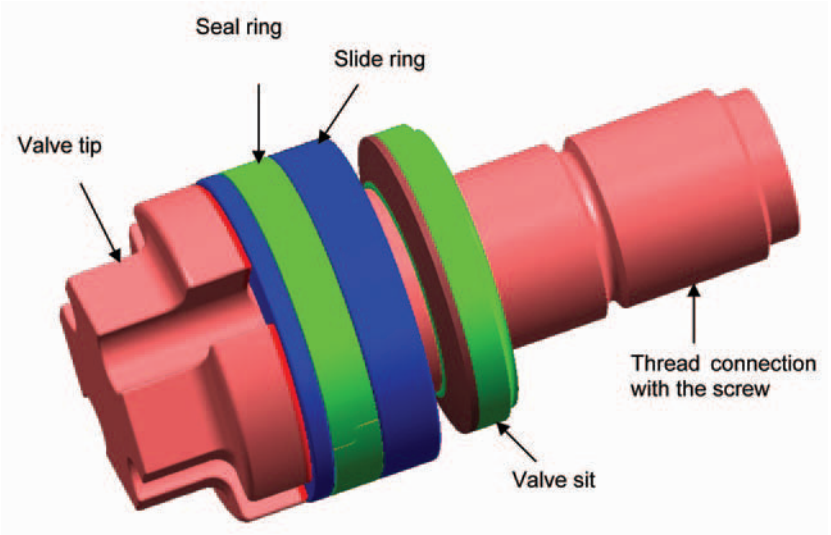

Fig. 3.13 The components of a typical non-return valve used in injection molding

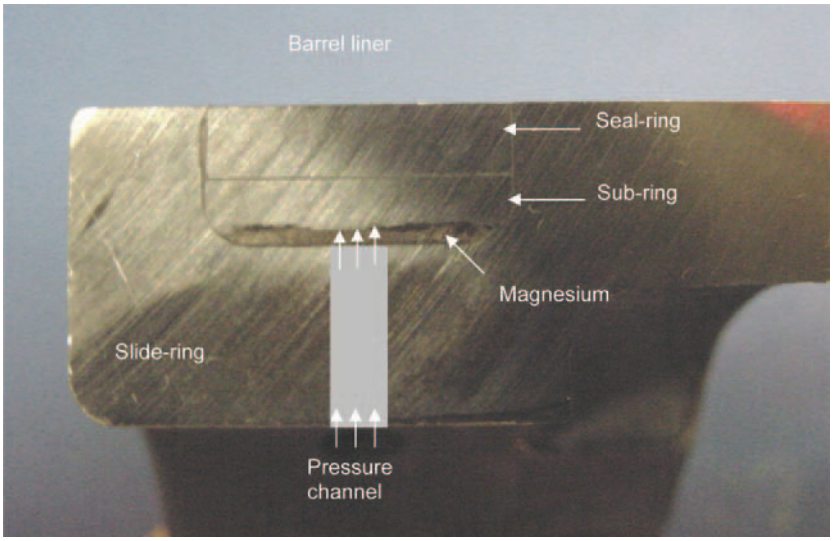

Fig. 3.14 The concept of sealing the non-return valve against the machine barrel wall

3.2.6 Feedstock Loading Devices

The particulate feedstock is stored in specialized containers and through a flexible hose is transported to the hopper, installed above the barrel feedthrow (Fig. 3.15). There are two distinct techniques and devices to supply the feedstock particulates

Fig. 3.15 The feeder used to supply the chipped feedstock to the injection molding machine

to the injection barrel. The first one, predominantly used at present, is called a *flood feeding*. In this technique, excess of material is provided to the barrel feedthrow, and only the injection screw controls the amount of material conveyed further (Fig. 3.16a). In this case, the feeding device is less complex. An alternative method represents a *starve feeding* where the quantity of feedstock supplied to the screw surface is determined by the feeding device. The appropriate feeding devices are equipped in auger feeder/motor or vibration-based mechanisms, which measure the amount of material that is being supplied to the screw (Fig. 3.16b).

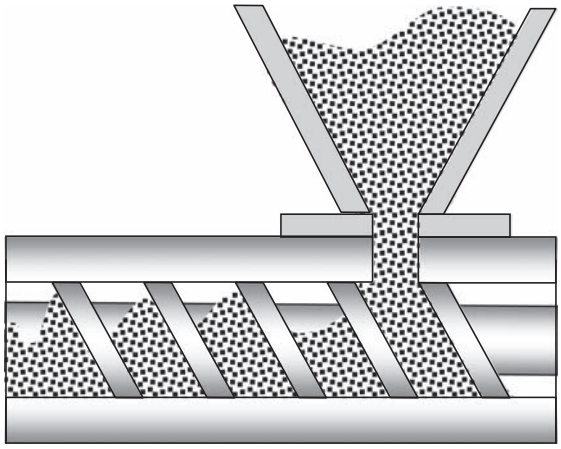

(a)

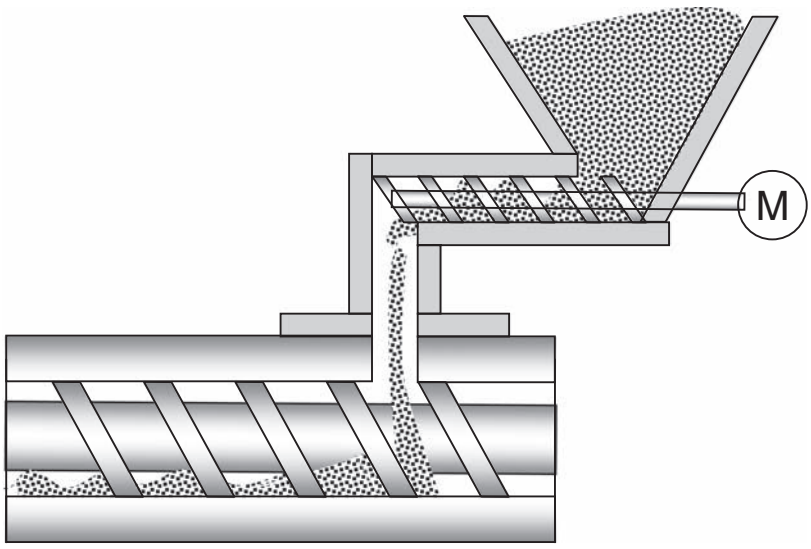

(b)

Fig. 3.16 The feeding techniques used in magnesium molding: **a** concept of uncontrolled dosing of the feedstock—flood feeding; **b** concept of controlled dosing of the feedstock—starve feeding

3.2.7 Feedstock Drying and Preheating Devices

In order to remove moisture accumulated within the particulate feedstock, and increase its temperature before entering the machine barrel, additional preheating devices can be installed between the feedstock container and the machine feeder. An experimental solution

represents a conical shaped device, added on the top of the hopper with metallic walls, being covered with cartridge heaters. As a result of heat conduction, temperature of the feedstock is increased to the required level, typically from 100 °C to 150 °C.

3.2.8 Protective Gas Supply to the Barrel

The tight nature of the barrel makes it relatively easy to protect the magnesium against contact with air and oxidation. This is achieved by introducing argon gas into the barrel. The gas supply chain consists of a gas container, pressure reducer, connecting hoses and dosing apparatus. After being introduced into the feedthrow, the gas spreads through the barrel, creating overpressure, hence helping to prevent air from entering the barrel from the nozzle direction.

3.2.9 Mist Filtration Devices

Spraying the hot mold with lubricants generates a large volume of vapor. To preserve air quality, vapor leaving the clamp area should be filtered. A design of the clamp gating with an open top to allow an access by the robot makes it difficult to direct vapors into a filtration system. Once vapor is removed from the clamp area, one possibility of cleaning it is by applying modular air filtration systems. The unit contains several filter stages, forcing contaminants through the filter elements and preventing contaminants from leaking past the filters. Vertical orientation allows filter units to drain, preventing liquid from re-entering the clean air stream. The blower has an adjustment of rotational speed for varying air volume requirements.

3.2.10 Robots

The robots employed for injection molding have dual functionality with component extraction and die lubricant application. These requirements are generally the same as in die casting. Robots can be floor mounted, wall mounted or suspended from the ceiling. Die casting uses six axis, floor mounted robots, integrated into a casting cell. The standard programs include extraction by biscuit gripper and checking for completeness, component cooling in the cooling bath and depositing in the press and/or discharge to the chute. The cast components are extracted using a rugged biscuit gripper that can be applied for different diameters. If required, special contour grippers are available. The robust construction and minimal use of parts contribute to high reliability and long intervals between maintenance.

An injection molding machine allows the installation of a top-entry robot that has some benefits (see previous figs 3.1a, 3.2). It allows for a design that separates part extraction and die application functions; thus, the part can be removed from the contamination area before

spray commences. Then it removes all sensitive mechanical components from the contamination zone. The top-entry robot allows using standard clamp gating so the machine maintains a minimum footprint. An installation on the clamp top allows using standard high speed robot modules, and with two Y-axes the cycle time can be minimized.

3.2.11 Barrel and Screw Maintenance Stations

In order to keep a smooth molding operation, the time of screw replacement should be minimized. This is accomplished by a replacement of the entire barrel assembly, which, in turn, is maintained outside the machine. The removal of the screw from the barrel is performed using the screw removal station (Fig. 3.17). First, the barrel is preheated to temperatures for melting magnesium, and after the barrel head disassembly, the screw is pushed out by a hydraulic device. During heating, argon gas is supplied to the barrel to prevent oxidation.

Although the common practice during screw removal is purging the metal from the barrel, there is still some metal remaining that occludes the screw root. In practice it is not possible to completely clean the screw by mechanical methods such as chipping away with a chisel or brushing. The only thorough cleaning method is a removal by dissolving it in an acid. In order to safely and efficiently remove magnesium from metallic surfaces, a special cleaning station is used [8]. The magnesium-covered component is immersed in a continuously flowing aqueous bath with additions of acids (Fig. 3.18). The reaction of magnesium with an acid is accompanied by an evolution of hydrogen, which should not be allowed to accumulate. Therefore, a purging gas flows over the surface of the bath so that the build-up of hazardous explosive conditions can be avoided. Moreover, the oxidation-reduction reaction is exothermic and liberates a large amount of energy. Thus the bath

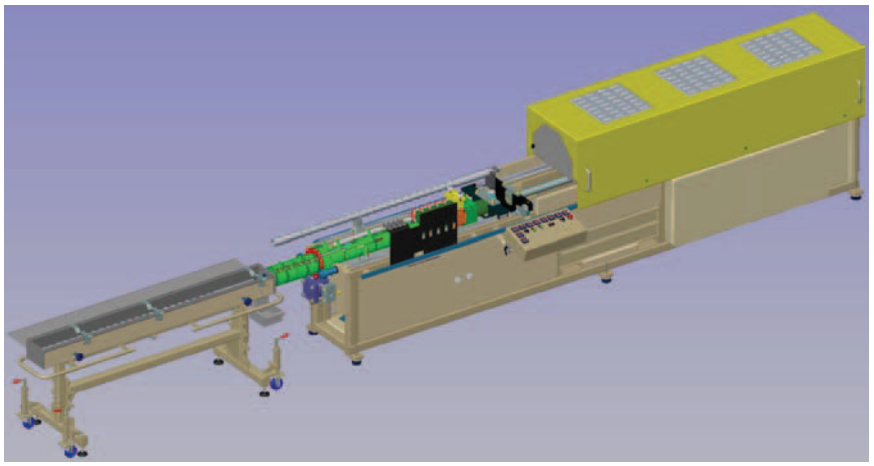

Fig. 3.17 The screw and barrel maintenance station used for automatic removal of the screw from the barrel and mechanical cleaning of both components

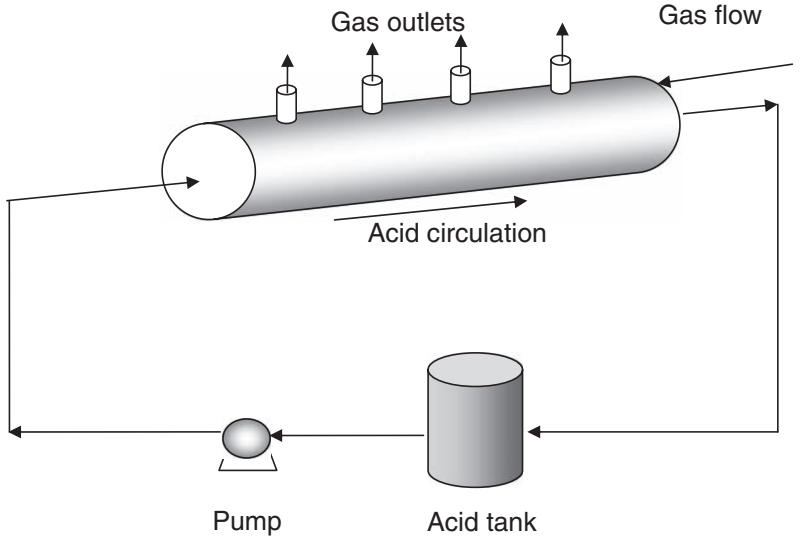

Fig. 3.18 The system used for removal of magnesium from the screw by a chemical reaction

temperature has to be controlled in order to prevent a drastic increase in the reaction rate. The solution chemistry is selected to aggressively dissolve magnesium and at the same time to not react with the steel base. Among common acids, hydrochloric acid reacts effectively with magnesium. At the same time it is too aggressive for steel substrates. In practice, a bath with around 25 wt% of phosphoric acid was found to be effective. Another detrimental factor is hydrogen ingress into the steel base. Although additions of inhibitors may reduce hydrogen ingress, potentially high stress areas should be masked.

3.3 Slurry Distribution Systems

3.3.1 Cold Sprue

The sprue provides a smooth transition from the barrel nozzle to the mold and promotes high heat extraction after injection is completed. In addition to the sprue, the metal feeding and distribution system includes the main and gate runners, gates and overflows. Because of the low heat capacity of magnesium alloys, large runners and gates are traditionally used in die casting to prevent premature freezing of the molten alloy.

There is an essential difference between sprue used in injection molding and in die casting. In cold chamber die casting, the shot sleeve extends through the machine platen, die covers and ends at the parting line of the die. The biscuit is formed partially by a cavity in the ejector die with the diameter of the plunger. By contrast, in hot chamber die casting, the molten metal delivery system allows using a sprue rather than an inserted shot sleeve. In this case, the sprue is a tapered hole extending from the mounting surface

through the cover die to the die parting surface. The molten metal flows through the hole to the runners. The sprue is usually formed in a water-cooled bushing insert and has protruding extensions of the ejector die that partially fill the sprue hole. In die casting, the spherical radius of the sprue bushing is slightly larger than the corresponding radius of the nozzle. The result is a line contact that seals the molten metal in the system. Because of the different radii, the seating surfaces outside the circle of line contact are spaced apart, and that space retards heat flow into the bushing [9]. The sprue uses a standard bushing, but the spreader is made to completely fill the bushing except for a flash clearance to accommodate manufacturing tolerances and mold shift.

The sprue used in magnesium molding is similar to solutions used in plastics molding. The major correction is made due to the larger thermal conductivity of magnesium. In order to provide a smooth flow the smallest cross section of the sprue should exceed the cross-section sum of runners leaving the sprue. Thus the sprue size is affected by the machine nozzle size, which is usually standardized by the machine manufacturer.

3.3.2 Hot Sprue

The hot sprue represents an extension of the machine nozzle, which allows the transport of alloy slurry or melt to the mold cavity. To maintain the required melt temperature, the sprue is heated. An example shows two designs for the straight (Fig. 3.19a) and the offset (Fig. 3.19b) devices. In general no cooling media, like air or oil, are required and a lower temperature of the flange zone is achieved by settings of heaters of neighboring zones. The offset device allows changing the injection axis from direct extension of the machine nozzle. For certain molds, the offset sprue may compensate for the requirement of a machine that has an offset of the injection unit.

In general it is possible to convert a mold with a cold sprue bushing to the hot sprue with a minimal rework. The only changes required represent a space for the connecting cables to heaters and thermocouples. The hot sprue is usually made to be interchangeable with the cold sprue (Fig. 3.20). This allows operating the same mold either with cold or hot sprue solutions.

3.3.3 Hot Runner

While molding with a cold or hot sprue, the cold runner carries the flowing metal further to the mold gate. Typical cold runners are round or nearly trapezoidal in a cross section to minimize surface area and heat loss. As the next stage of improvement, beyond the hot sprue, not only the sprue but also runners are eliminated and the molten or semisolid alloy is injected directly into a mold cavity. Designing hot runners for transferring molten metals is very challenging due to high temperature, high loads, thermal expansion and corrosive attack of molten alloys. Thermal expansion is managed by modules joined together and sealed by temperature control in the spigot-type connection region. For components requir-

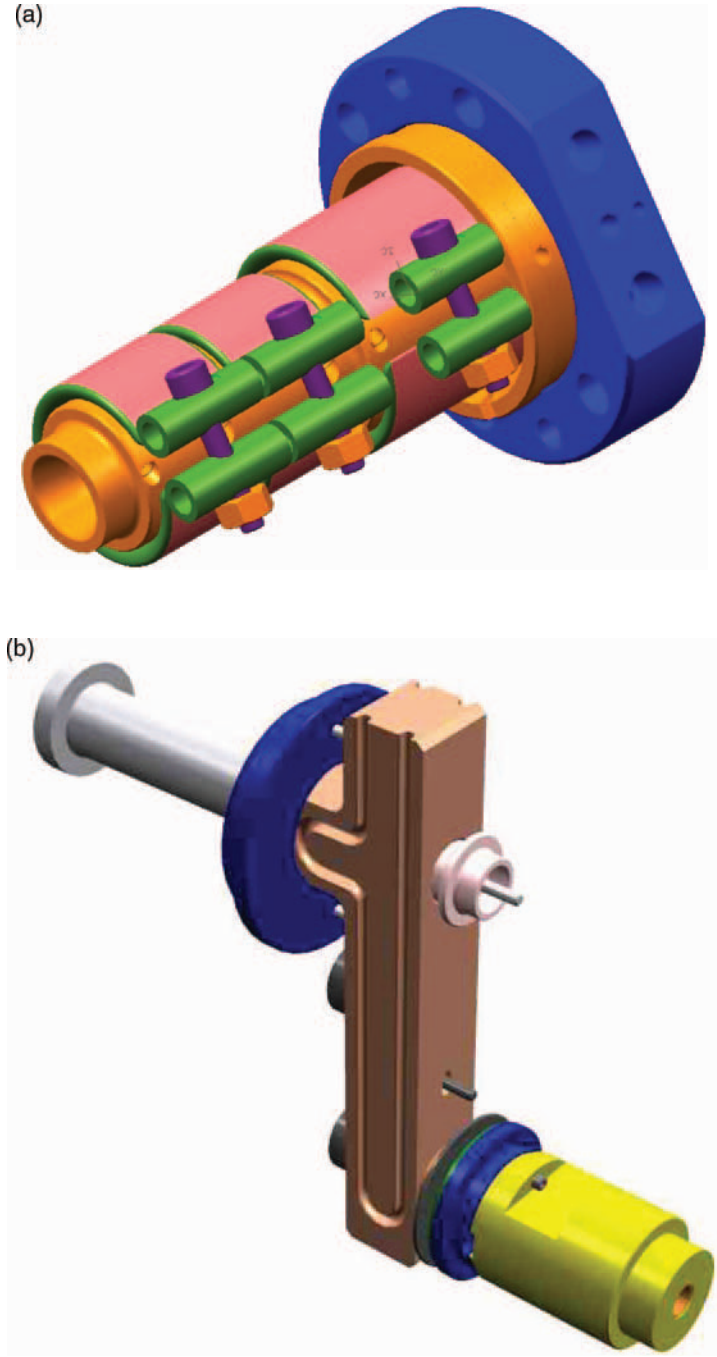

Fig. 3.19 The virtual model of the hot sprue: **a** straight design allowing alloy transfer along the machine nozzle axis; **b** offset design allowing change of the alloy transfer level

Fig. 3.20 The typical cold sprue inserts used in die casting along with the hot sprue solution for magnesium molding (shown in the center)

ing multiple injection spots, the appropriate hot runners with a geometry allowing certain injection are designed. An example of the four-drop hot runner is shown in Fig. 3.21.

Although in designs described above conventional electric resistance heaters are used, there are solutions using a controller with a high-powered electromagnetic induction heating system. Due to limited space, in both the hot sprue and hot runner, application of conventional induction coils, cooled with water, is not possible. There are, however, solutions that do not require coil cooling.

3.4 Mold

3.4.1 General Features

The mold represents a complex tool with many mechanisms and features, designed to fulfill multiple functions:

(i) define the net or near net geometry of a molded component that is repeatable over time;
(ii) create the optimum characteristics of mold cavity filling with a molten or semisolid alloy;

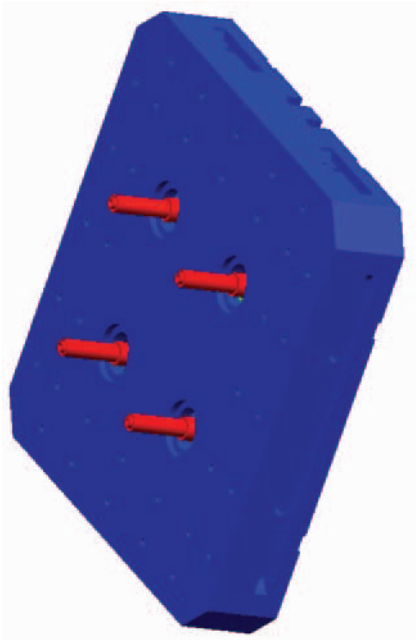

Fig. 3.21 The virtual model of the hot runner used for magnesium distribution into the part (4-drop solution)

(iii) create the optimum conditions for heat removal during the alloy solidification stage;
(iv) allow easy ejection of a component after its solidification is completed.

The cross section of a mold with names of all major components is given in Fig. 3.22. Since a mold is subjected to direct contact with the molten magnesium, there are similarities with design solutions used in die casting. First, the mold has to function at high temperatures and with significant temperature differences between its components. Then, the mold has to withstand the high impact transmitted through the melt from the injection unit. Such a strong impact requires high rigidity. Also, the design has to take into consideration that any magnesium flash trapped inside the mold could prevent it from normal operation. At the same time, as with plastics molds, metal molding allows for higher complexity features to be incorporated into the mold design. This is possible due to reduced temperature of the melt or slurry, which is less susceptible to flow through unwanted gaps, as is experienced during die casting.

3.4.2 Mold Heating–Cooling Systems

Temperature of the mold is the critical factor in removing heat from the molten metal. It allows proper filling of the mold cavity and solidification of the injected

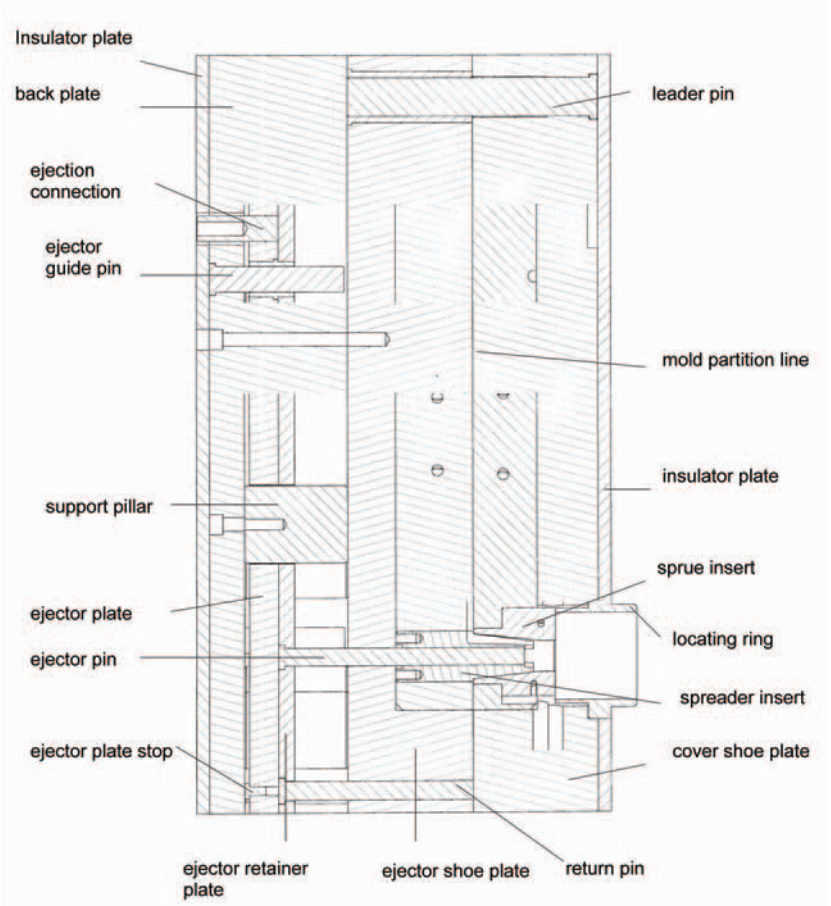

Fig. 3.22 The schematics of the mold in cross section describing all major components

alloy. Additional advantages of using temperature control include the longer service life of the mold, higher production yield and finally the lower component cost.

In order to maintain the part quality, the mold should exhibit a temperature distribution that is repeatable for each shot. The mold is initially preheated before molding, but during each shot heat is transferred to the mold, leading to nonuniform temperature distribution. Although there is a substantial heat dissipation to the atmosphere by mold volume, to eliminate areas with extremely high temperature, called hot spots, a certain amount of heat has to be redistributed before the next shot.

The mold temperature is maintained by oil circulated along channels within the mold and external thermolators that heat the oil using electric heaters. There are concepts to apply induction technology to heat the mold surface directly. At present, the following methods are used industrially to control the mold temperature in die casting:

(i) control of the fluid temperature, which is the most commonly used and sufficient in most cases;
(ii) control of the mold temperature, which utilizes a temperature sensor in the mold; this type of control is necessary for cases requiring a high degree of temperature stability in the mold and fully automated operation;
(iii) the cascade control, which is a combination of both of the above methods; the temperature of both the fluid and the mold is simultaneously controlled, providing superior stability of the mold temperature.

For die casting of Mg–Al–Zn alloys the typical mold operating temperature is between 200 °C and 240 °C, but for special chemistries this requirement may be as high as 350 °C. This task is divided between an internal cooling–heating system and external cooling with a spray, described in the next section and in Chap. 5. During die casting of Al, drilled water channels or water lines are key features of thermal control. Since the heat capacity of Mg is substantially lower than Al, the amount of heat transferred is much lower and, instead of cooling, some heating may be required.

3.4.3 Mold Spray Equipment

Lubrication of the mold surface with a mist of various compounds is a standard practice performed using automated lubrication systems. An example used in magnesium molding is shown in Fig. 3.23. The presently used systems include:

(i) needle-type shutoff nozzles—these nozzles incorporate a unique one piece piston assembly for low maintenance. When normal maintenance is needed, the entire inner assembly can be removed and replaced at the machine without tools. The one piece piston serves as both the liquid shutoff and the liquid metering needle.
(ii) spool type poppet shutoff— the internal spool valve is designed to assure sharp cutoff with no wasteful, damaging drip between applications. With this design, higher liquid pressures generate higher shutoff pressure, making a more effective seal. Outstanding engineering design incorporates a secondary O-ring seal backing up the metal-to-metal seal of the poppet shank and insert.

The principle of all types of spraying is essentially the same. The differences lie in the equipment used to obtain the desired spray and the desired liquid volume. The process of lubricant application is of critical importance. The most important parameters that affect characteristics of spray, heat transfer and film formation on the mold surface are:

(i) hardware type;
(ii) spraying time;
(iii) spray pressure;

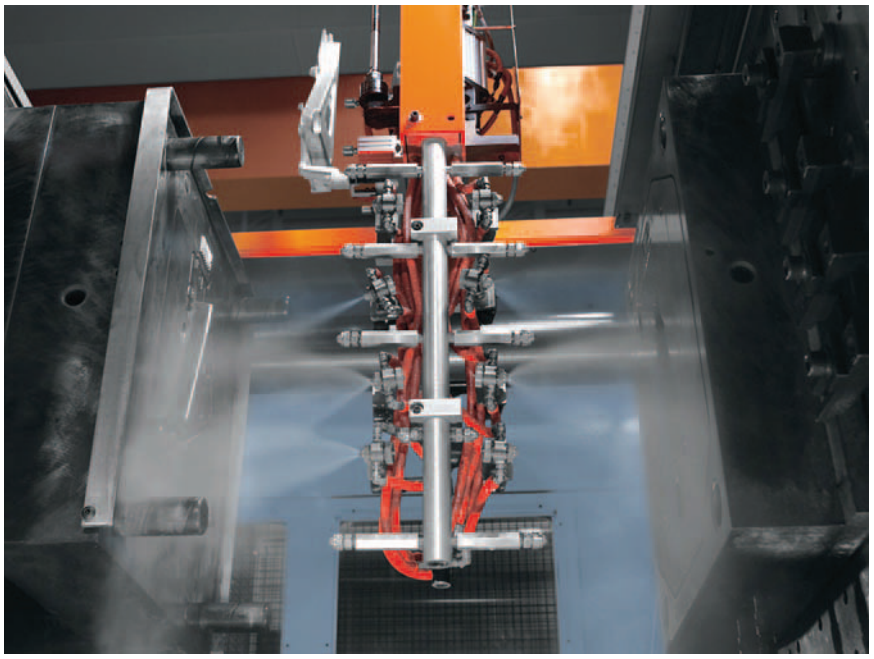

Fig. 3.23 The spray head for mold lubricant distribution during magnesium molding

(iv) lubricant flow rate;
(v) spray distance;
(vi) spray angle.

The mold spraying equipment is designed to adjust all the above parameters.

3.4.4 Mold Vacuum Systems

The purpose of vacuum molding is to improve the part integrity by minimizing the volume of entrapped gases. This is achieved by extracting gases from the mold cavity and the runner system. While considering gases in a mold cavity, the following origins are distinguished:

(i) external air entrapped in a cavity volume;
(ii) gas generated from decomposition of mold lubricants;
(iii) gases removed by liquid alloy during solidification.

It is considered that air and gases created in the mold cavity cannot escape fast enough, in particular from molds of complex shape containing blind regions; thus, a vacuum provides some assistance. Another advantage of vacuum is the ability to remove excess spray from the mold surface, a feature that leads to an improvement in surface quality of the components.

Vacuum molding is conducted by connecting a mold with a vacuum system. The system includes a vacuum pump, a shut-off valve to prevent liquid metal from entering the vacuum pump, and a control device. There are two types of valves: static and dynamic. A static valve utilizes a thermal gradient to protect the vacuum system. In static solution, chill block allows gases to pass through the vent while liquid metal solidifies before reaching the vacuum system (Fig. 3.24a,b).

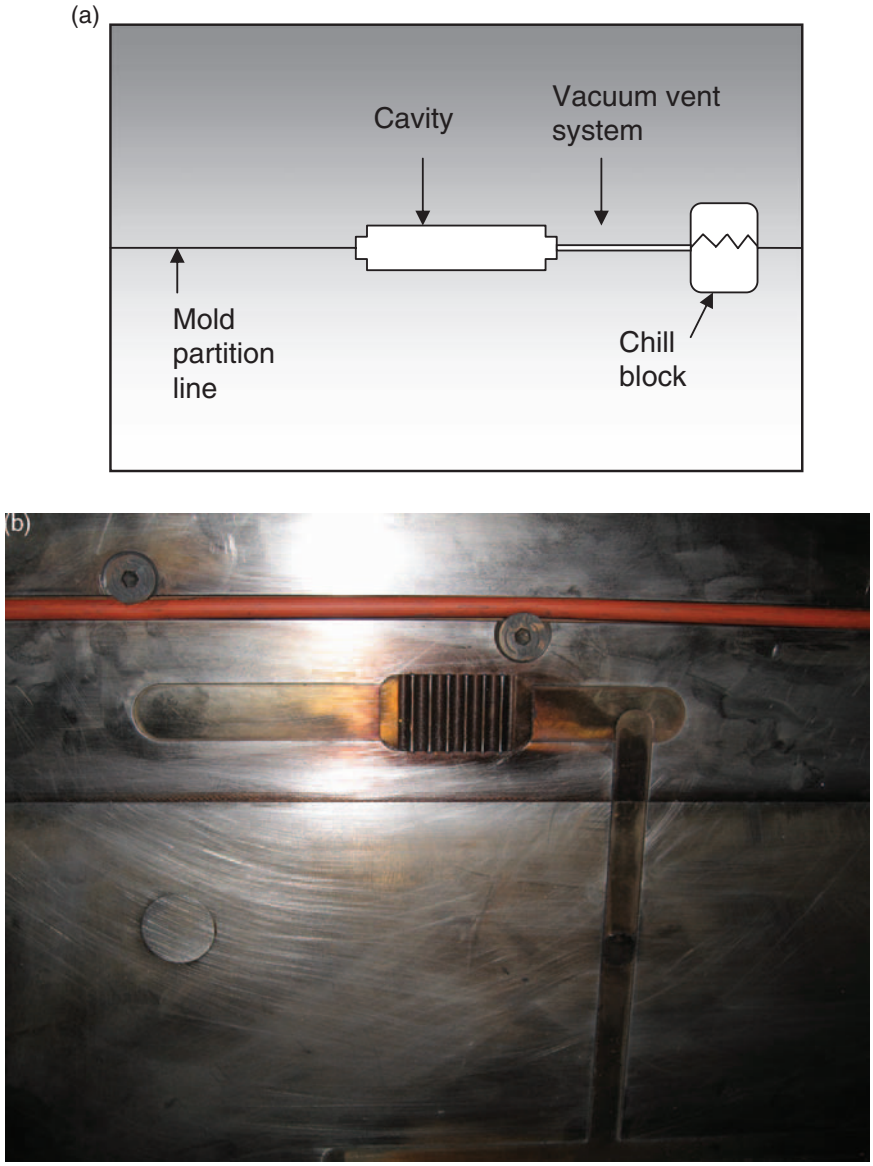

Fig. 3.24 The concept **a** and practical implementation **b** of the static vacuum valve based on chill blocks

In dynamic valves, the mechanical solution is the simplest. When the mold is closed, a valve is open. As the liquid metal fills the mold cavity, the cavity pressure generated is used to close the valve. There are also dynamic solutions that utilize the electronic control of the valve opening and closing.

3.5 Summary

Although the injection molding hardware used for magnesium processing is built based on a machine platform used for plastics molding, the changes introduced make it unique. The key changes, which represent the alloy flow path from the hopper to the nozzle, are imposed by the high melting temperature along with the reactive and corrosive behavior of magnesium alloys. In addition, the nature of injection imposes changes on the machine control system in order to support all requirements of the preparation of magnesium alloy slurry and its transfer into the mold cavity. The injection molding hardware provides more accurate control of the processing parameters as compared to conventional casting equipment.

References

1. Rubin II (1972) Injection Molding—Theory and Practice. John Wiley & Sons, New York
2. Rosato DV, Rosato D, Rosato MG (eds) (2000) Injection Molding Handbook. Kluwer Academic Publishers, Boston
3. Kestle M R, Manda JM (2002) Injection nozzle for a metallic material injection molding machine. US Patent 6,357,511 B1, 19 Mar 2002
4. Fast Heat Inc. (2002) Heating elements and Sensors, p.47
5. Moisan JF et al (2001) Ultrasonic sensor and technique for in-line monitoring of die casting process. Measurement Science and Technology 12:1956–1963
6. Kilbert RK (1997) Apparatus for the injection molding of a metal alloy: Sub-ring concept. US Patent 5,680,894, 28 Oct 1997
7. Manda JM, Weir S, Pinet JP (2005) Non-return valve for use in a molding system. US Patent 200502330020, 20 Oct 2005
8. O'Keefe WK, Pinet PJ (2003) Acid bath for removing contaminants from a metallic article. US Patent 6,544,342 B1, 8 Apr 2003
9. Herman, EA (1992) Designing Die Casting Dies. NADCA, Rosemont, Illinois

4
Thermal and Corrosive Aspects of Processing Molten Magnesium

4.1 Introduction

Molten or semisolid metallic alloys exert detrimental effects on materials they contact. Material degradation results from two factors: (i) corrosive attack and (ii) thermal effects due to high temperatures. Corrosion, caused by a liquid metal, is expressed most often by chemical dissolution, metal-to-metal alloying, embrittlement and cracking. A simple containment of a molten alloy during such operations as melting, recycling or conveyance involves mainly corrosion. However, die casting, injection molding and other processing techniques involve also cyclic pressurizing of the melt, which generates stress and activates mechanisms of structural changes at high temperatures. In an industrial environment both factors act simultaneously, causing multiple and complex mechanisms of material degradation. Moreover, corrosion and wear of hardware result in a contamination of the melt and reduction of product quality. For example, the resistance of magnesium alloys to atmospheric corrosion is sensitive to tiny contents of certain metallic impurities.

Magnesium, which exhibits a high reactivity in a molten state, is also corrosive with respect to other engineering materials. Although additions of alloying elements reduce the melting range and temperature requirements during processing, at the same time they generally strengthen the corrosive nature of alloys. This is particularly true for Al, acting as a universal solvent while in contact with the majority of metallic alloys. Since the simultaneous corrosive and thermal issues cannot always be solved using a single alloy, the material combinations are required as an effective alternative. Despite this, some limits on the process may be imposed to preserve materials used for the equipment. It is clear that the successful use of materials at high temperatures in a corrosive environment of liquid magnesium alloys is an integral part of magnesium processing.

This chapter contains a description of major degradation mechanisms associated with thermal and corrosive effects of molten magnesium, supported by examples of an impact on materials potentially applicable in this environment.

F. Czerwinski, *Magnesium Injection Molding*.

4.2 High Temperature Effect of Molten Magnesium Alloys on Other Materials

Tensile properties of most engineering materials at room temperatures do not practically change with time. By contrast, at elevated temperatures the strength becomes very dependent on both strain rate and time of exposure. A temperature factor will also modify the fatigue resistance and introduce new failure mechanisms, e.g., creep or oxidation.

4.2.1 Property Degradation Due to Structural Changes

There are two aspects of the influence of high temperatures on material properties which should be considered during magnesium processing. The first one relates to a modification of properties caused by an increased service temperature. The second aspect represents a potential deterioration of properties, experienced with the exposure time at high temperatures. The high temperature causes microstructural evolutions due to diffusion of chemical elements; thus, phases, which control properties, become unstable. Hence, in addition to their morphology and size, the chemistry and crystallography are also altered.

4.2.1.1 Alloy Steels

High temperature grades of steel are used predominantly in a hardened and tempered state. In order to preserve their properties over a long time, the service temperature should be substantially lower than the tempering level. An assessment of temperatures required for magnesium alloy molding indicates that it is difficult to fulfill the above condition. In extreme cases, short time exposures may be very close or may even exceed the tempering values. Hence, there will be a gradual deterioration of properties caused by the temperature factor. In steels, transformations of carbides and changes in distribution of alloying elements depend on both the time and temperature. For engineering practice, the tempering effect can be estimated using the Holomon and Jaffe parameter M:

$$M = T (C + \log t) \tag{4.1}$$

Where:

T – the temperature;
t – the exposure time;
C – a constant.

The formula shows that tempering is mainly controlled by temperature and less by time. For example, 100 times longer exposure has the same effect as an increase of temperature by 0.1.

The resistance to tempering depends on the steel chemistry and several examples are shown in Fig. 4.1. The steel chemistry is listed in Table 4.1. The range of stable

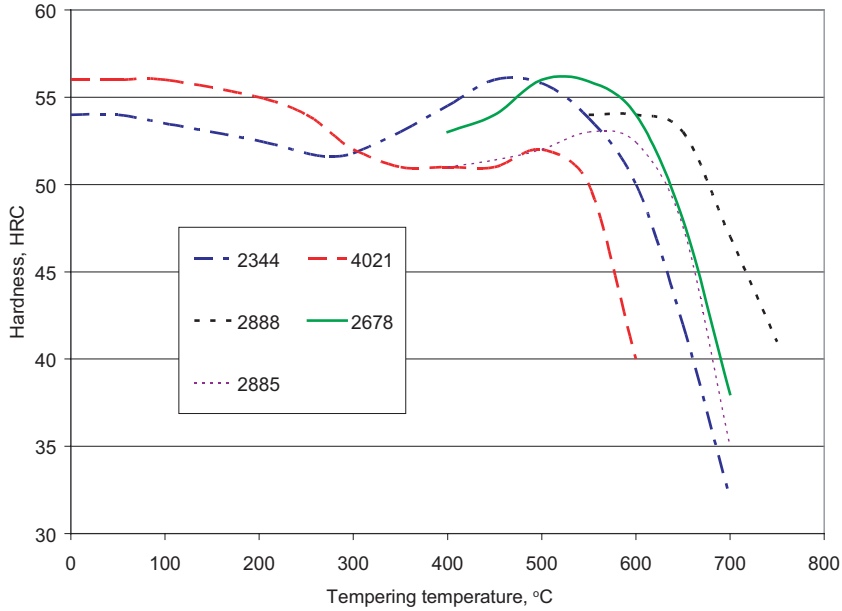

Fig. 4.1 The capability of selected steels for high temperature applications, portrayed by the tempering curves. The steel designations are given by their DIN numbers: 1.2344, 1.2888, 1.2885, 1.4021, 1.2678 (based on Thyssen, Kind & Co data)

Table 4.1 Selected grades of alloy steels applicable for direct contact with liquid magnesium. Nominal values in weight %. The applicability limit is determined as approximately 25 °C below the temperature of rapid hardness reduction

Germany	United States	C	Mn	Si	Cr	Co	Mo	W	V	Applicability limit, °C
DIN 1.2343	AISI H11	0.4	0.3	1.0	5.0		1.3		0.5	500
DIN 1.2344	AISI H13	0.4	0.3	1.0	5.0		1.4		1.0	500
DIN 1.2678	AISI H19	0.4	0.4	0.4	4.3	4.0	0.4	4.0	2.0	550
DIN 1.2581	AISI H21	0.3	0.3	0.3	3.5		0.4	9.0	0.5	580
DIN 1.2886		0.2	0.2	0.2	10	10	5		0.5	590
DIN 1.2885		0.3	0.4	0.4	3.0	3.0	2.8		0.6	550
DIN 1.2888		0.2	0.5	0.3	10	10	2	5.5		610
DIN 1.4021	AISI 420	Min 0.15	1.0	1.0	12					500

hardness determines the steel's applicability for high temperature service. Changes in microstructure of DIN 1.2888 steel with high resistance to tempering are shown in Fig. 4.2. A structure of martensite (Fig. 4.2a) changes after triple tempering (Fig. 4.2b). After overheating, the material shows coarse carbides, precipitated particularly at grain boundaries of former austenite (Fig. 4.2c). This microstructure leads not only to reduced tensile strength but also to low toughness. Another indicator of a capability for high temperature service is maintaining strength at high temperature, also called *red hardness*. An example of the influence of temperature on tensile properties of two high temperature steels is summarized in Fig. 4.3. It is seen that the

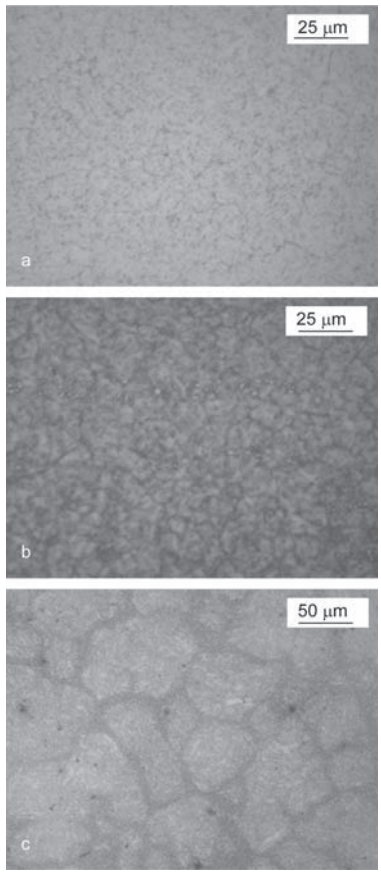

Fig. 4.2 The microstructure of DIN 1.2888 steel: **a** as hardened—50 HRC; **b** after tempering—45 HRC; **c** after long term exposure at 610 °C—30 HRC

reduction in tensile strength or yield strength is substantial even for the DIN 1.2888 special steel, and at temperatures close to 600 °C may reach 50%. It should be noticed that during short-term exposure at temperatures below 400 °C, differences in properties are rather low. The differences between low alloyed H13 and high alloyed 1.2888 steels increase during exposures at high temperatures, especially above 650 °C.

4.2.1.2 Ni Based Superalloys

Similar characteristics of tensile properties at different temperatures for Ni-based Inconel 718 are shown in Fig. 4.4. The chemistry of some Ni-based superalloys is listed in Table 4.2. Although the temperature deteriorates properties of the superalloy, the range of steep reduction in properties is shifted to higher temperatures as compared to steels. In this and previous figures, short time

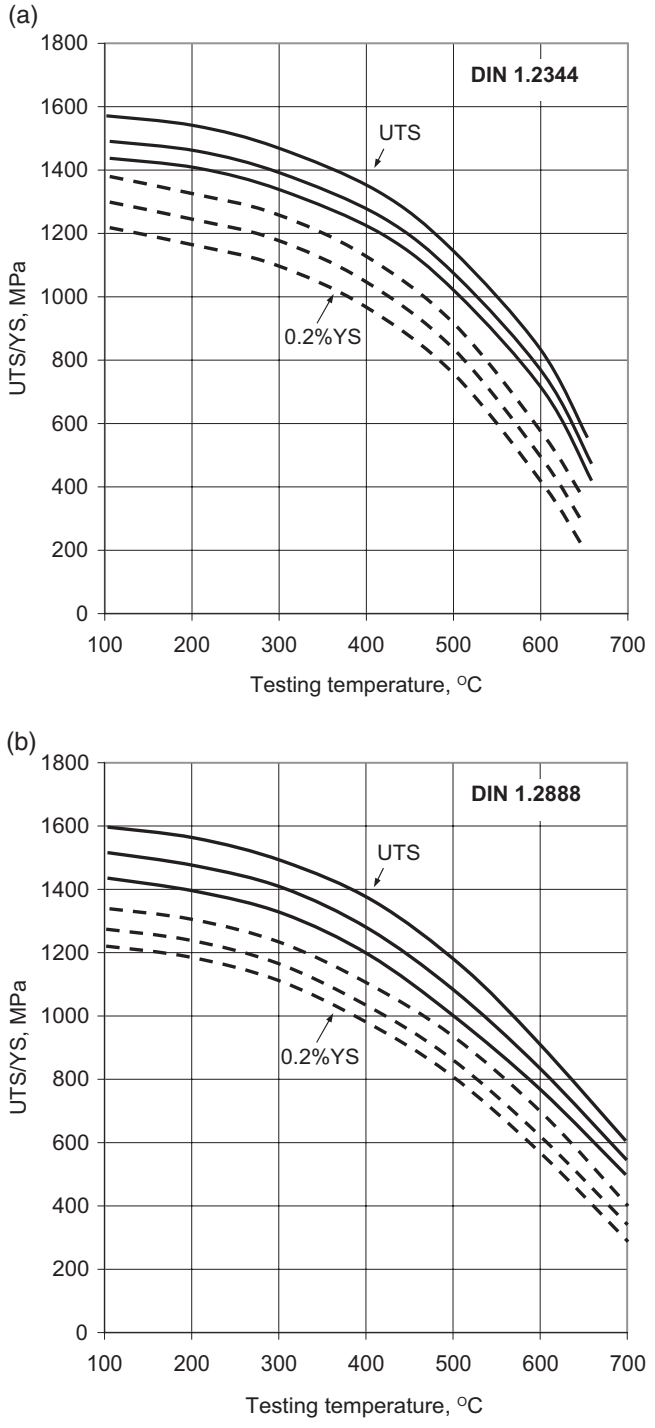

Fig. 4.3 The tensile properties of two steels at elevated temperatures, depending on the initial hardness: **a** DIN 1.2344; **b** DIN 1.2888 (based on Thyssen, Kind & Co data)

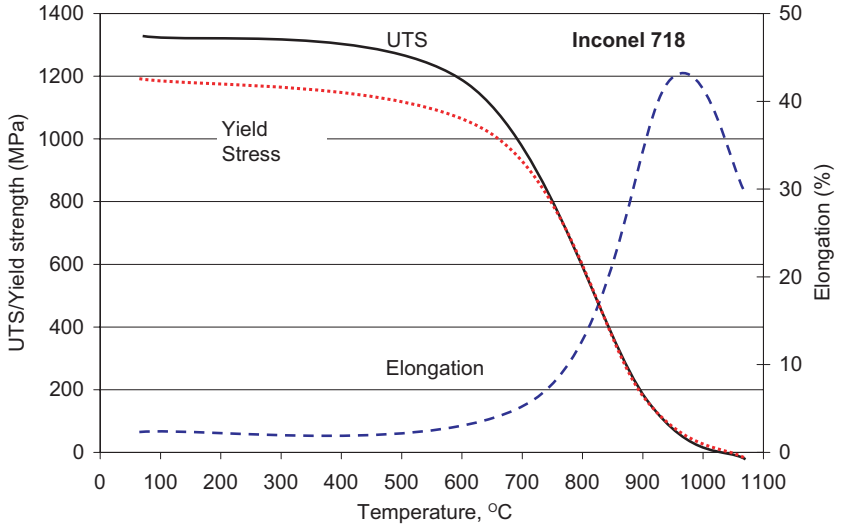

Fig. 4.4 The tensile properties of Alloy 718 at elevated temperatures (INCO)

exposures were used and the temperature was the only factor changed. In order to emphasize both the temperature and time, Inconel 718 alloy and high-alloy special steel 1.2888 were subjected to high-temperature exposures. As a parameter indicating degradation of mechanical properties, the alloy hardness was measured. The results for a temperature range of 650 °C to 750 °C and maximum exposure time of 160 h are summarized in a semi-logarithmic plot in Fig. 4.5. The 1.2888 steel, with an ultra-high resistance to tempering, experienced a reduction in hardness at temperatures of moderate overheating above 650 °C. At temperatures higher than 650 °C, a drastic loss of hardness occurred after several hours of exposure. The Alloy 718 exhibited substantially better resistance to degradation by heat and preserved its initial hardness at temperatures up to 700 °C. There are many structural changes when Alloy 718 alloy is subjected to high loads at high temperatures. A comparison shows the increase in grain size and modification of internal structure during stress load at room and high temperatures (Fig. 4.6a,b). In addition, high temperature exposure results in the increased volume of δ phase (Fig. 4.6c,d).

4.2.1.3 Co Based Superalloys

Co based cast superalloys are generally described as wear-, corrosion- and heat-resistant. The most important for Mg processing are Stellites: 21, 6 and 12, characterized by different carbon and tungsten (Mo in case of Stelite 21) content (Table 4.2). Stellite 21 with low carbon is the most ductile while Stellite 12 has the lowest toughness with the highest wear resistance. Their structure, which contains

Table 4.2 Selected grades of Ni-based and Co-based superalloys applicable for processing of liquid magnesium based on high temperature strength and oxidation resistance in air. Nominal values in weight % (Inco, SPS Technologies, Mattec, Deloro Stellite, Haynes Inter.)

	C	Cr	Ni	Mo	Co	Al	Ti	Nb	W	Fe	Other	Solidus Liquidus °C	Contact with Liquid Mg
Inconel 718	0.04	19	52	3		0.5	0.9	5		18.5		1260 1336	No
Udimet 720	0.03	18	55	3	15	2.5	5.0		1.5		0.03B 0.03Zr	1210 1340	No
Waspaloy	0.08	19.5	58	4	13.5	1.3	3.0				0.006B	1330 1360	No
Aerex 350	0.025 Max	17	Bal	3	25	1.1	2.2	1.1	2		4 Ta 0.025 B	1293 1364	No
Tribocor 532							30	50	20			approx 2100	Yes
Stellite 21	0.25	27	2.5	5.5	bal					Max 3		1338 1366	Yes
Stellite 6	1.2	28	Max 2.5		bal				5	Max 2.5		1260 1355	Yes
Stellite 6B	1.1	30	Max 3.0	1.5	bal				4.5	Max 3.0		1265 1354	Yes
Stellite 12	1.85	29	Max 2		bal				9	Max 2.5		1240 1310	Yes

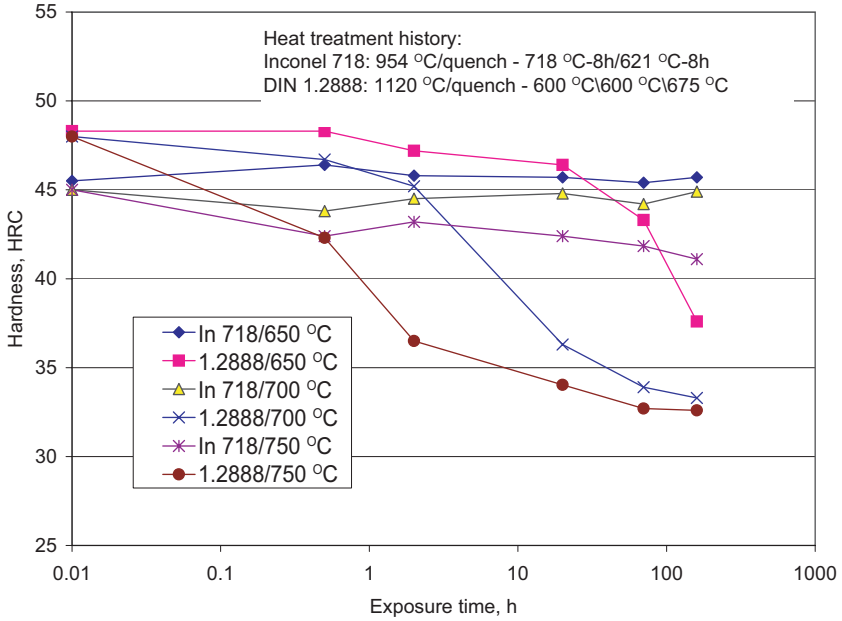

Fig. 4.5 The influence of exposure time at selected temperatures on room temperature hardness of DIN 1.2888 steel and Alloy 718.

hard carbides of chromium and tungsten (molybdenum), exhibits relatively high red hardness (Fig. 4.7). At operating temperature, however, some aging will occur, raising the strength of the alloy (Fig. 4.8). Although the strength gain is accompanied by some loss of ductility, impact strength is maintained at a fairly high level.

4.2.2 High Temperature Fatigue

In general, there are three basic factors required to cause fatigue failure [1]:

(i) a maximum of tensile stress with a high value;
(ii) a sufficiently large stress variation; and
(iii) a large number of cycles of the applied stress.

In addition, there are a number of secondary factors which change the conditions for fatigue, and service temperature is one of them. The fatigue phenomenon is of importance at temperatures roughly lower than half the *homologous temperature*. The homologous temperature is defined as a ratio of the service temperature to the melting temperature expressed in absolute temperature units. At higher temperatures fatigue is replaced by creep. At the microscopic level, the transient is accompanied by a replacement of the transcrystalline fracture, typical for fatigue (Fig. 4.9), with the intercrystalline type, being typical for creep.

The microstructural factors that lead to good high-temperature fatigue resistance do not necessarily produce satisfactory fatigue behavior. While considering the grain size, requirements are contradictory: Fine grain is beneficial for fatigue, but coarse grain enhances creep resistance.

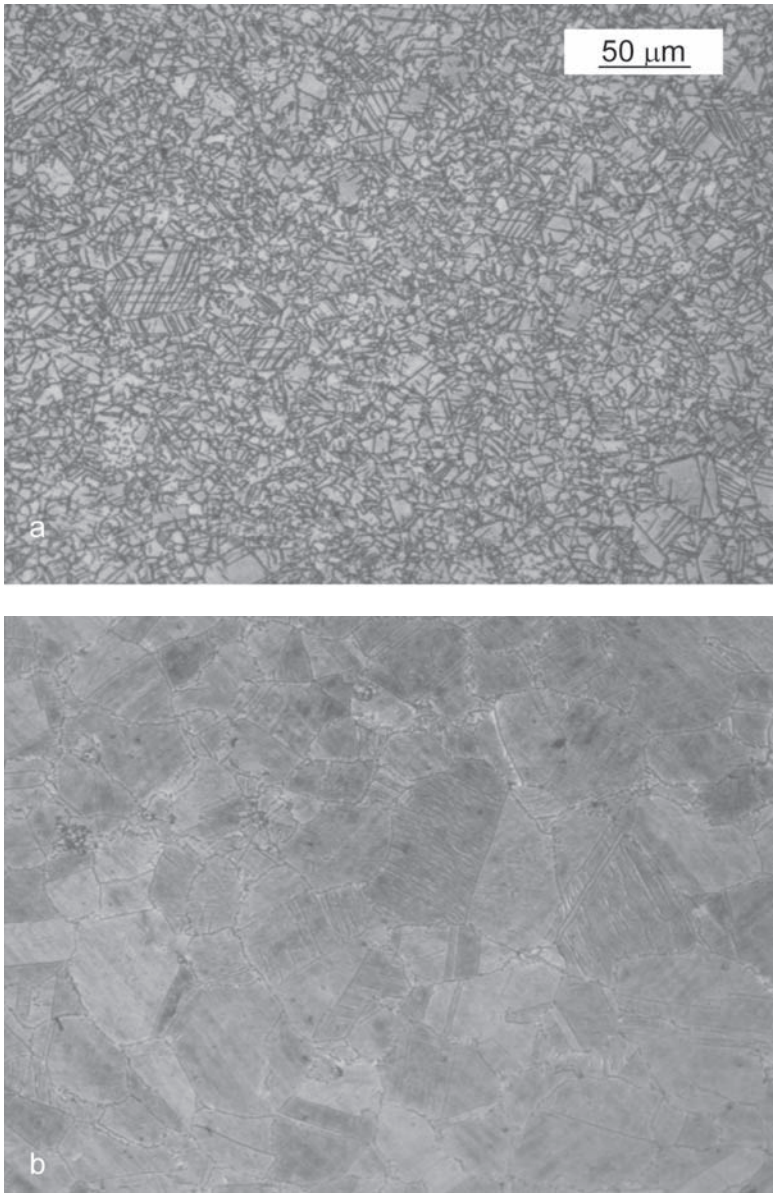

Fig. 4.6 The microstructure of Alloy 718 subjected to high loads of complex nature for long time periods: **a** exposure at temperatures below 200 °C; **b** exposure at 600 °C; **c** exposure at 600 °C—etching to reveal arrangement of δ phase; **d** exposure at 600 °C—morphology of δ phase

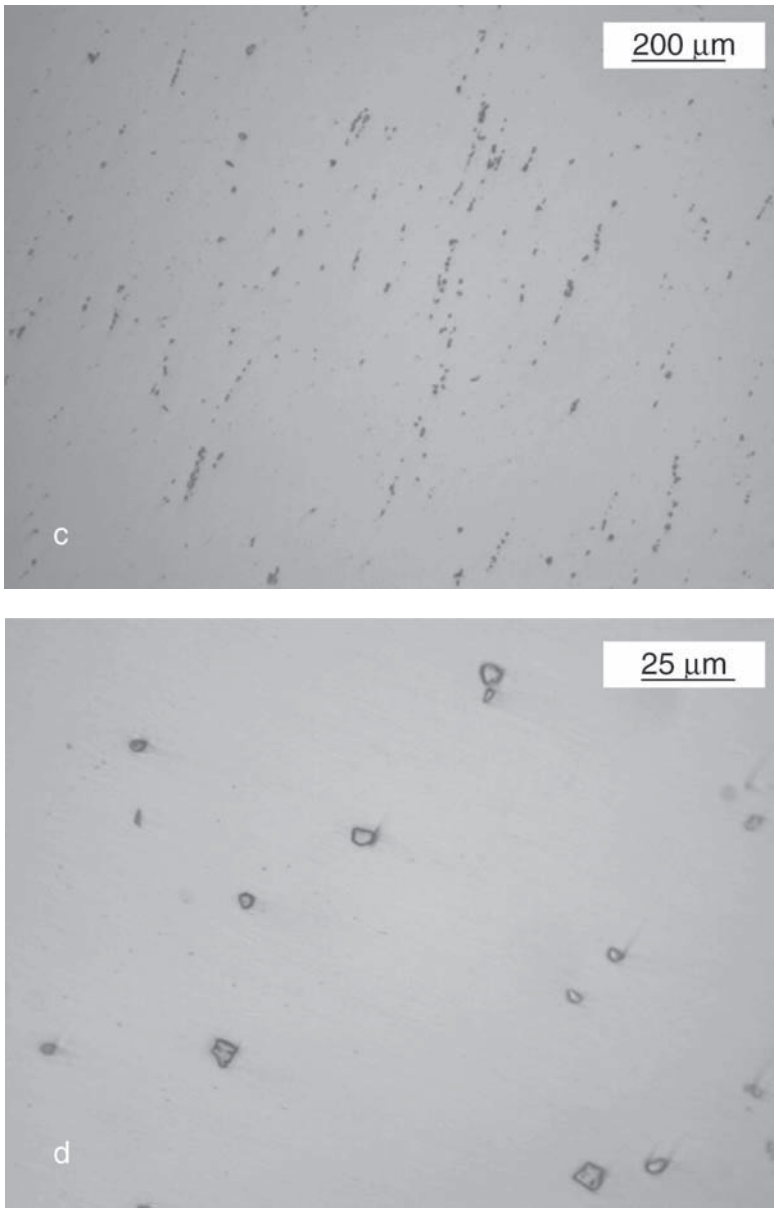

Fig. 4.6 (continued)

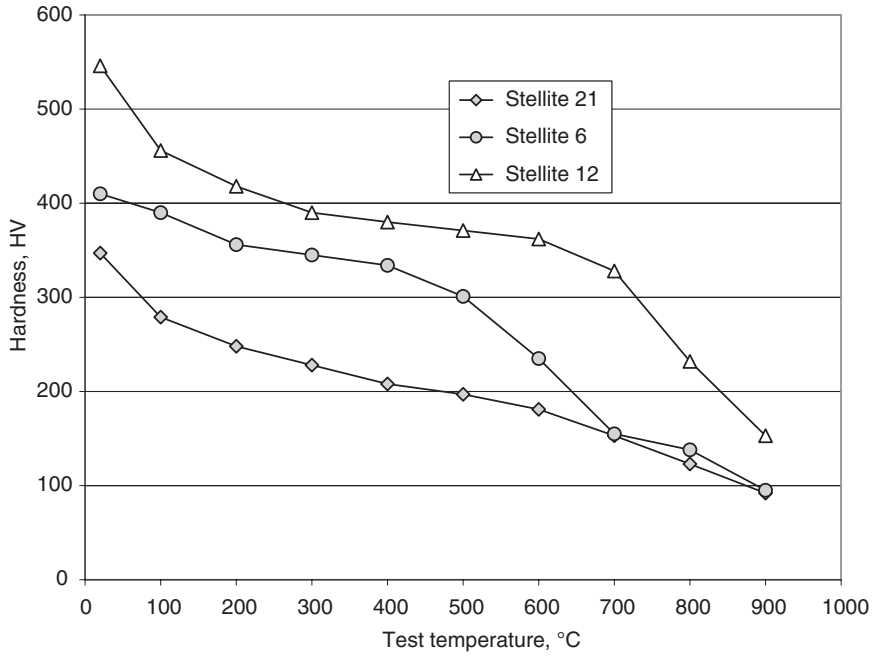

Fig. 4.7 The hot hardness of Co-based Stellite alloys (Deloro Stellite)

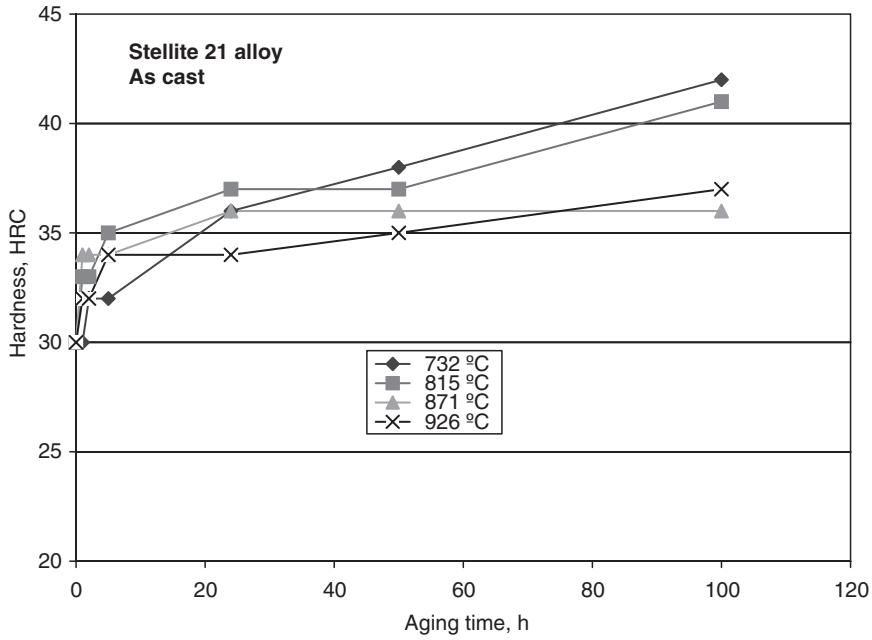

Fig. 4.8 The influence of exposure time at selected temperatures on room temperature hardness of as cast Stellite 21 superalloy (Deloro Stellite data)

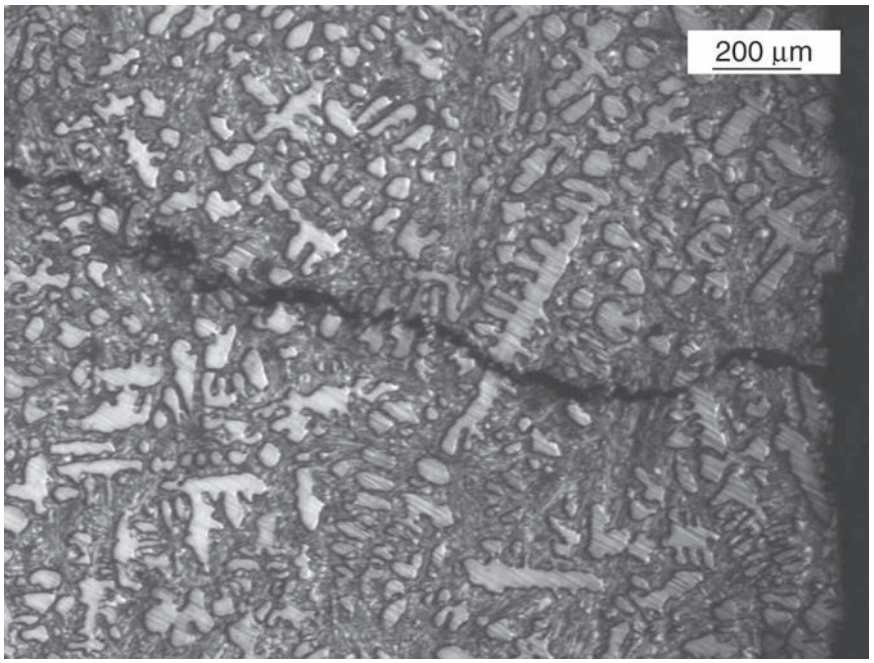

Fig. 4.9 The fatigue crack within Stellite 12 superalloy after it was subjected to long term stress at temperatures exceeding 600 °C

4.2.3 Thermal Fatigue

Thermal fatigue is the premature failure resulting from cyclic stresses due to temperature fluctuations. The stress is induced due to nonuniform contraction and expansion of a material. Usually, the initiation and growth of cracks is gradual and requires a certain number of cycles. In an extreme case, however, the failure can occur after a single action of thermal stress, and this condition is known as *thermal shock*.

An example of the failure of H13 steel, experimentally exposed by induction heating to a large number of cycles with the maximum temperature exceeding 750 °C, is shown in Fig. 4.10a. The most typical with regard to thermal fatigue are molds. Cyclic cooling and heating of the mold results in alternating compressive and tensile stress on its surface. The magnitude of thermal gradient and stress on the mold surface is affected by the mold temperature directly before injection. The high temperature of the molten alloy generates high compressive stress on the mold surface during injection. During the component's solidification and shrinkage a contact is lost, and the heat transfer is reduced. Then applying spray after the component's ejection generates a tensile stress in the mold surface. The formation of cracks due to such a mechanism is called *heat checking*. An additional degradation factor is a corrosive attack by molten

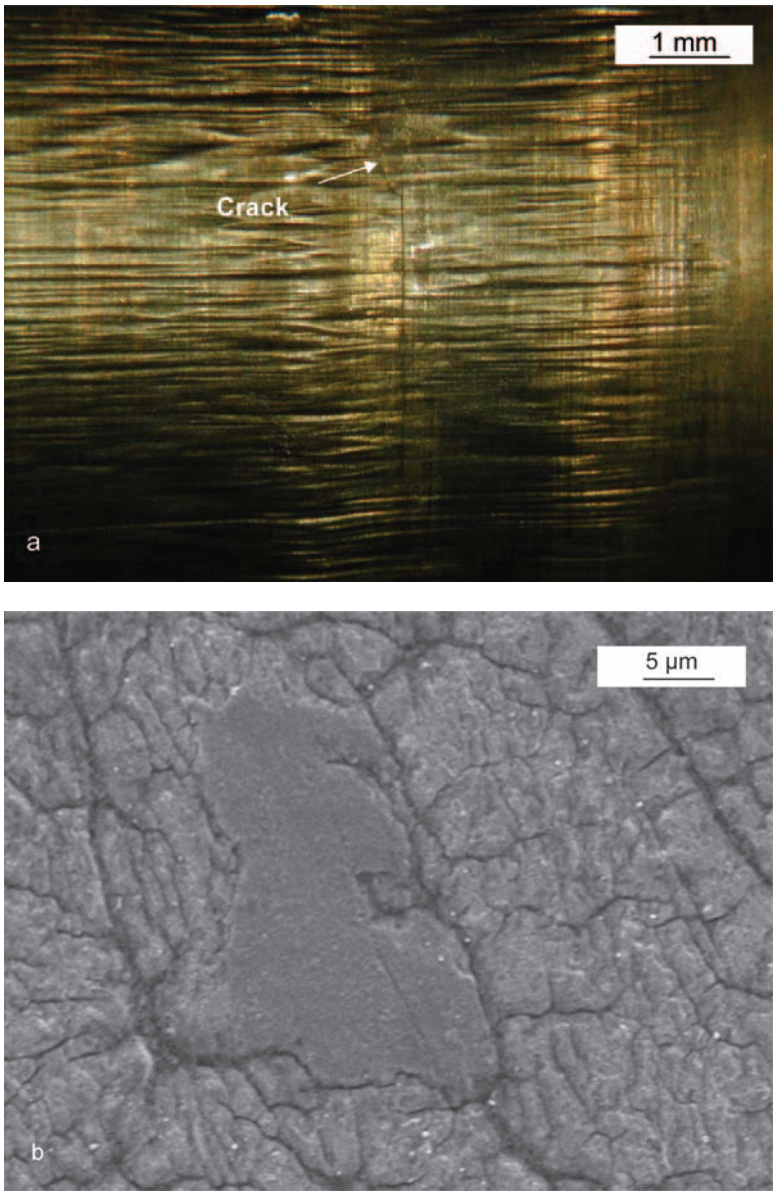

Fig. 4.10 The thermal fatigue of H13 (DIN 1.2344) hot work tool steel: **a** exclusive thermal effect of a large number of cycles with a maximum temperature exceeding 750 °C; **b** surface of a mold used for magnesium casting, subjected to a combination of thermal effect of large number of cycles and corrosive attack by molten magnesium

magnesium. An example of H13 steel with a surface initially polished, after long-term service is shown in Fig. 4.10b.

The service parameters are the major factors controlling thermal fatigue but material properties also play an important role. The coefficient, indicating a resistance of the material to thermal fatigue A, is expressed as:

$$A = \sigma k / E\alpha \tag{4.2}$$

Where:

σ – fatigue strength at a certain temperature;
k – thermal conductivity;
E – elastic modulus and α is the coefficient of thermal expansion.

The higher value of A shows a higher resistance to thermal fatigue. This property is also structure sensitive and, for example, a distribution of carbides in steel influences its thermal fatigue behavior [2].

4.2.4 Corrosion Fatigue

Corrosion fatigue is defined as the simultaneous action of cyclic stress and chemical attack. Corrosion fatigue should not be confused with stress corrosion where the crack initiation and growth takes place under a sustained load or residual stress. At a microscopic scale, there is a distinct difference: Stress corrosion occurs along grain boundaries, while corrosion fatigue exhibits a predominantly transcrystalline crack propagation path. Moreover, while only certain materials are susceptible to stress corrosion, corrosion fatigue can take place in all materials. Of engineering importance for metal injection molding are environments of gas and liquid metal. The existing failure mechanism due to corrosion fatigue relates to room temperatures and aqueous media. During injection molding, the molten magnesium alloy plays the role of a corrosive agent.

Examples of Ni-based superalloy surface exposed to liquid Mg and welded joint between Ni-based superalloy and Co-based superalloy are shown in Fig. 4.11a and 4.11b, respectively. It is assumed that the liquid metal corrosion may contribute first to crack initiation by creation of a pit acting as the stress riser on the material surface. After the crack is formed, liquid metal fills the crack area and, under cyclic opening and closing, the crack acts as a pump attracting liquid metal into a freshly formed fracture surface.

4.2.5 Creep and Stress Rupture

Creep is defined as the progressive deformation of a material at constant stress. Creep becomes of significance at a homologous temperature greater than 0.5 and represents

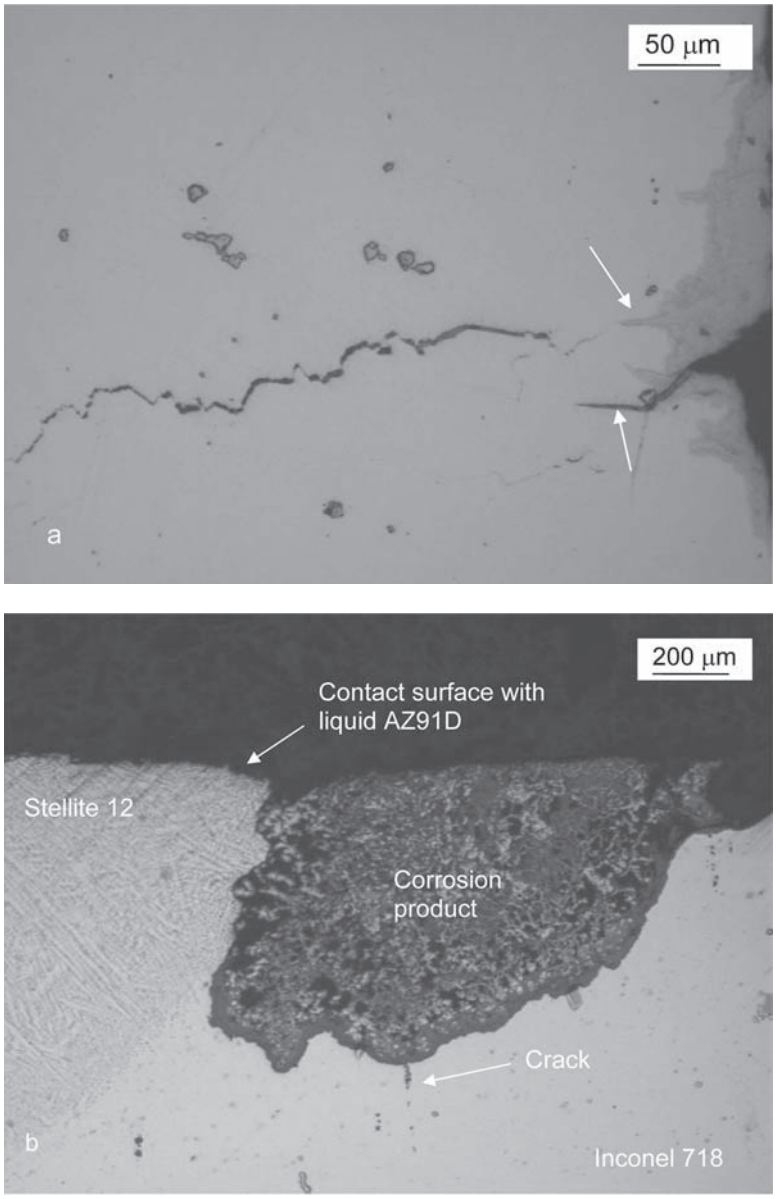

Fig. 4.11 The example of fatigue failure initiated by molten magnesium corrosion: **a** surface of Alloy 718 splashed with molted magnesium alloy; **b** Alloy 718—Stellite 12 welded joint, exposed to molten Mg–9Al–1Zn alloy

the major cause of failure. In addition to measurement of strain to determine the minimum creep rate, stress rupture characteristics are evaluated. To measure stress rupture, a test is continued until the material fails. The key information derived from a stress rupture test is the time to failure at a constant stress and temperature. The results are important for applications where creep deformation can be tolerated, but fracture must be prevented. Elements of creep theory are presented in Chap. 14.

The creep crack growth in nickel-based superalloys can be significantly increased by external environments. For alloys such as Inconel 718, Rene 95 and X750 this increase may reach up to three orders of magnitude [3]. Two mechanisms were proposed to explain the role of an environment in creep. The first one is based on the grain boundary structure and chemistry and assumes that grain boundaries oxidize, leading to embrittlement [4]. According to the second mechanism, the formation of nickel, iron or chromium oxides inhibits the crack growth [5]. For Alloy 718, it is suggested that the enrichment and segregation of niobium at grain boundaries is critical. The creep mechanism involves a formation and fracture of niobium oxide film along grain boundaries as a result of oxidation and decomposition of NbC and Ni_3Nb precipitates [6]. The creep crack growth and microstructural changes within Inconel 718 subjected to long-term stress effect at temperatures of approximately 600 °C are shown in Fig. 4.12a,b.

4.2.6 Oxidation

An important factor affecting high temperature properties is the interaction of a metal with an environment. It is clear that the catastrophic oxidation and intergranular penetration of oxide may represent a single cause of failure and must be avoided. The processing hardware components are heated using electric resistive or inductive heaters. In some furnaces, surfaces may still be heated by a gas flame. Some parts are heated by molten magnesium on one side while their other side is exposed to air atmosphere. Frequent changes of temperature aggravate the detrimental effect since they cause scale spallation, cyclically exposing bare metal. In addition to surface oxidation causing uniform degradation of a material, an internal oxidation may also be active. This is the process by which oxygen diffuses into an alloy and causes sub-surface precipitation of oxides of one or more alloying elements. Oxidation may damage a part independently or may initiate other failure mechanisms, e.g., fatigue. Scale also decreases efficiency of heating.

The resistance to high temperature oxidation requires the development and maintenance of an oxide barrier, which separates an environment from the substrate. A comparison of data in Table 4.3 and experimental observations show that energy of oxide formation does not characterize the metal oxidation resistance. Based on the value of energy released in the oxidation process, Al should oxidize 2.5 times faster than Fe, which is opposite to experimental observation. This is due to spalling and cracking, which reduce the protective properties of the oxide. There are two major sources of stress in oxide layers: thermal stress that arises due to difference in thermal expansion/contraction of substrate and oxide,

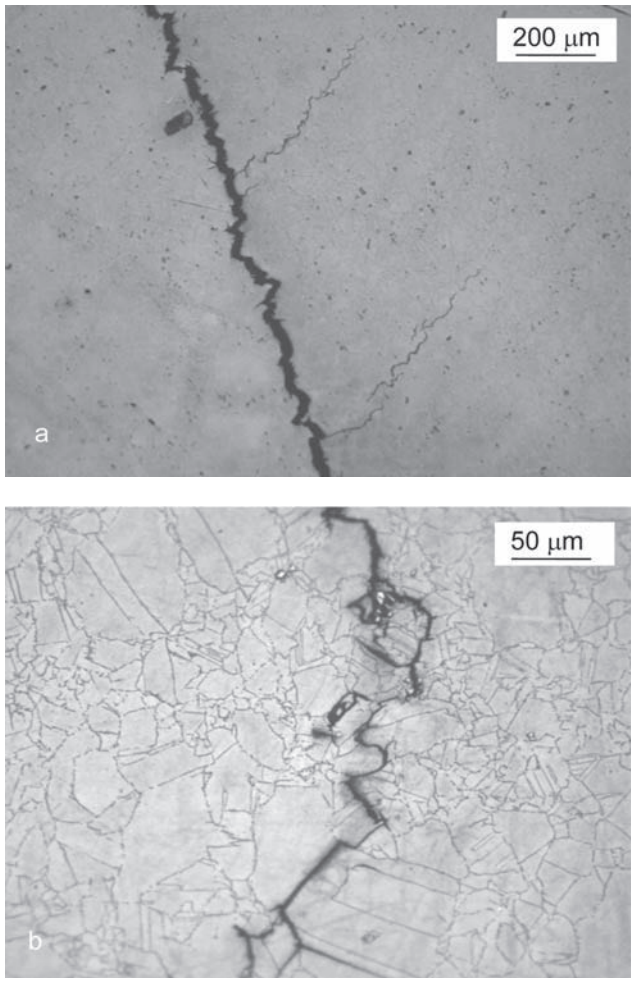

Fig. 4.12 The creep crack propagation within Alloy 718 after long term stress around 600 °C: **a** unetched surface, showing the major and secondary cracks; **b** etched surface, showing intercrystalline nature of the crack propagation path

Table 4.3 Energies of oxide formation at 20 °C and the oxide-to-metal-volume ratios for metals applicable in magnesium processing. Selected from [6, 7]

Metal	Oxide	Energy kJ/mol of oxygen O2	Oxide/metal volume ratio
Mg	MgO	– 1162	0.81
Al	Al_2O_3	– 1045	1.28
Cr	Cr_2O_3	– 701	2.07
W	WO_3	– 510	3.30
Fe	Fe_3O_4	– 508	1.68 FeO 2.10 Fe_3O_4 2.14 Fe_2O_3
Ni	NiO	– 439	1.65
Co	CoO	– 422	1.86

and growth stresses developed during isothermal oxide growth. Of several causes of growth stresses, volume difference between the oxide and the metal is important. The volumetric change is characterized by the Pilling–Bedworth ratio (PBR):

$$\text{PBR} = \text{volume of oxide/volume of metal} \tag{4.3}$$

Values of PBR for major oxides are listed in Table 4.3. If PBR is greater than 1, oxide develops compressive stresses; in the opposite case the oxide is in tension. It should be emphasized that although the PBR is the cause of growth stresses, other mechanisms are also valid in many systems, including epitaxial stress, compositional gradients, point defect stress, oxide formation within the scale, oxide recrystallization and component geometry.

4.2.6.1 Oxidation Features of Fe-Cr Alloys

The oxidation resistance of steels depends on their chemistry, particularly on the content of chromium. At low Cr content both Cr-rich and Fe-rich oxides form on the surface. Some Cr enters the solution in the FeO phase. At 5% Cr, the oxidation rate is fast and typical for pure Fe. The scale consists of thin Fe_2O_3, then thicker Fe_3O_4 and the thickest FeO with internal precipitates of $FeCr_2O_4$ near the alloy surface. Increasing Cr content leads to the scale of mixed spinel and oxidation rate reduction. The scale consists of Fe_2O_3 followed by layers of $FeCr_2O_4$ and $Fe(Fe, Cr)_2O_4$ adjacent to the metal [7].

The resistance to oxidation at high temperatures is not equivalent to resistance to wet corrosion at room temperatures. Materials designed for high temperature service contain more than 20% Cr, which leads to growth of a protective Cr_2O_3 scale. In general, a Fe-Cr system is not efficient for high temperature oxidation since even at high Cr, Fe ions diffuse rapidly through Cr_2O_3, destroying its protective nature. Moreover, at high Cr, brittle phases are formed within the substrate and additional alloying is required.

4.2.6.2 Oxidation Features of Ni-Based Superalloys

Ni-Cr alloys with low Cr content exhibit internal oxidation with Cr_2O_3 islands within a matrix of almost pure Ni [7]. The outer scale consists of NiO followed by NiO with precipitates of spinel $NiCr_2O_4$ while moving towards the metal. As the Cr content is increased, the mode of oxidation changes and a Cr_2O_3 layer is formed. Oxidation resistance of Ni-Cr alloys requires at least 18-20% Cr.

Ni-based superalloys, similar to Inconel 718, have good resistance to oxidation at temperatures throughout their operating range, but oxidize and scale appreciably at higher temperatures. During oxidation in air at 800 °C to 1000 °C, the initial oxide film consists of Cr_2O_3 with two nickel spinels, $NiCr_2O_4$ and $NiFe_{2-x}Cr_xO_4$

($0 < x < 1$). Iron is present as Fe_2O_3 and a mixture of its other oxides. Exposures at 1000 °C produce a thick Cr_2O_3 film [8]. As a result of the diffusion of oxygen along grain boundaries, creep crack growth and fatigue crack growth rates for Inconel 718 and other superalloys at elevated temperatures are faster in the air than in inert atmospheres. Under fatigue conditions, this detrimental effect of air environment becomes more pronounced with decreasing cycle frequency [8].

4.3 Corrosive Behavior of Molten Magnesium Alloys

It is known that there are metallurgical problems with handling molten magnesium alloys since they attack many metals. Not only does corrosion damage equipment, but metals soluble in magnesium can contaminate its alloys, making them unsuitable for specific applications. Corrosion of solid metals by liquid metals proceeds usually by a solution reaction at the interface followed by product diffusion into the liquid phase volume. The compounds, which may form in the liquid phase, do not affect the reaction rate. Instead, the reaction rate is controlled by a diffusion of the solute from the reaction zone. This is in contrast to aqueous corrosion, where the dissolving metal is oxidized to its positive ion and later frequently enters the chemical reaction on the interface.

4.3.1 Reactivity with Iron and Steel

4.3.1.1 Pure Magnesium

Iron exhibits an excellent chemical inertness with liquid magnesium at temperatures below 750 °C. This beneficial situation is caused by the mutual solubility of both metals: The solubility of Mg in solid Fe at 750 °C is negligible; the solubility of Fe in liquid Mg is about 0.04%. As seen in Fig. 4.13, no intermetallic compound exists in the Fe–Mg binary system [9]. The excellent compatibility between Fe and Mg is changed by trace volumes of impurities or by certain additions. Silicon and aluminum are two impurities of technical magnesium that are the most chemically active towards iron. According to [10], Al or Si, present in Mg at a level of 0.02%, reacts at 770 °C with iron forming the solid solution α–Fe (Al, Si). A first morphological change is the backward movement and roughening of the steel surface due to the dissolution without reaction of iron in the liquid phase. The quaternary compound of Fe_2 (Al, Mg) C is also identified after a contact with steel containing 0.17% carbon. Both phases are formed not only by the solid-state diffusion but also by a dissolution-precipitation, which involves the migration of iron within the liquid. These reaction processes could contribute to intergranular corrosion and grain coarsening on the iron surface that is in contact with molten magnesium.

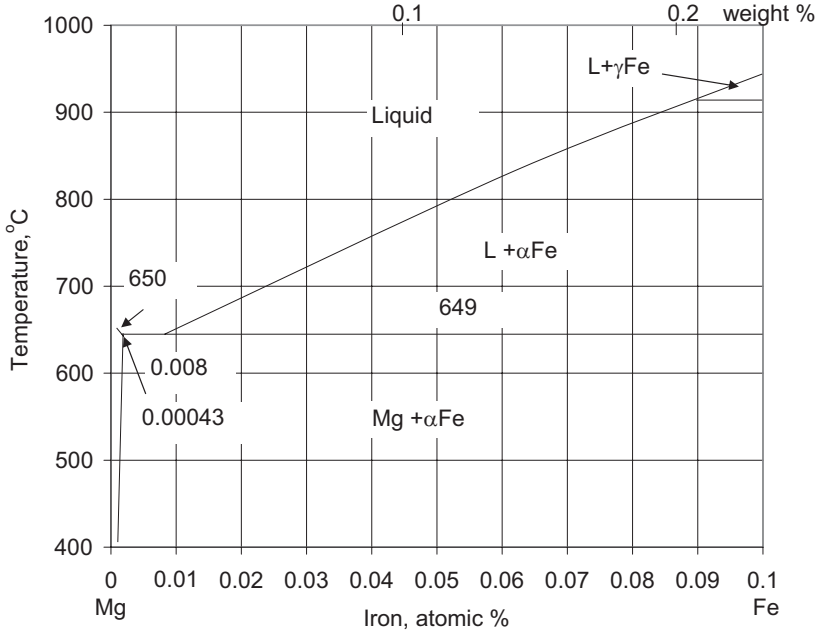

Fig. 4.13 The equilibrium phase diagram of Mg–Fe [9]

4.3.1.2 Magnesium Alloys

Aluminum is the major element affecting chemical reactivity of magnesium alloys (Fig. 4.14). The Mg–Al alloys react with steels first by a nucleation of the orthorhombic Fe_2Al_5 phase at the interface between Mg alloy and the steel [11]. Some of the iron atoms are replaced by Mn and the phase becomes $(Fe,Mn)_2Al_5$. The outer layer represents the $Mn_{23}Al_{77}$ compound. Growth rate of a corrosion product is linear. No impeding effect of Si is recorded, as is the case in Al alloys. In Al alloys, Si accumulates along the interface of the intermetallic layer with the melt, which impedes the diffusion processes. A thin scale formed after reaction between Mg–9Al–1Zn alloy and 1.2888 steel is shown in Fig. 4.15. Due to poor adherence, after solidification the scale is separated from the steel and remains on the Mg side. According to X-ray diffraction pattern, the layer contains: 30% of Mg, 5% of $Mg_{17}Al_{12}$, 20% of Al_2Fe_5, 20% of $Al_{77}Mn_{23}$ and 25% of Al_8Mn_5 (Fig. 4.16).

The corrosive attack intensifies with increases in Al content. For Al content of 11% the reaction front becomes highly nonuniform (Fig. 4.17a). Narrow channels are formed and molten alloy penetrates along them (Fig. 4.17b). There is no obvious influence of grain boundaries and the corrosion propagation has a rather transcrystalline character (Fig. 4.17c). It is likely that some contribution of stress may affect the cracking path in this case. The distribution of major alloying elements across the compact scale is shown in Fig. 4. 18a-c. Both Al and Mg are

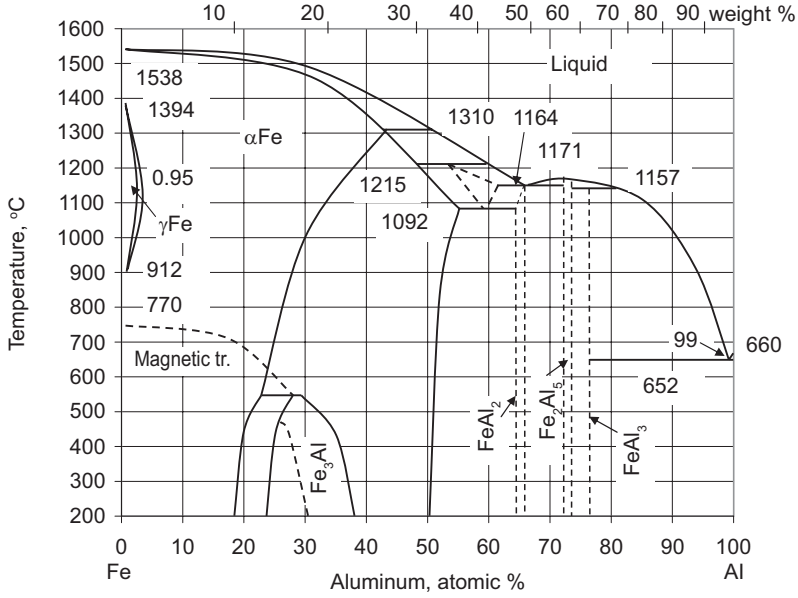

Fig. 4.14 The equilibrium phase diagram of Al–Fe [9]

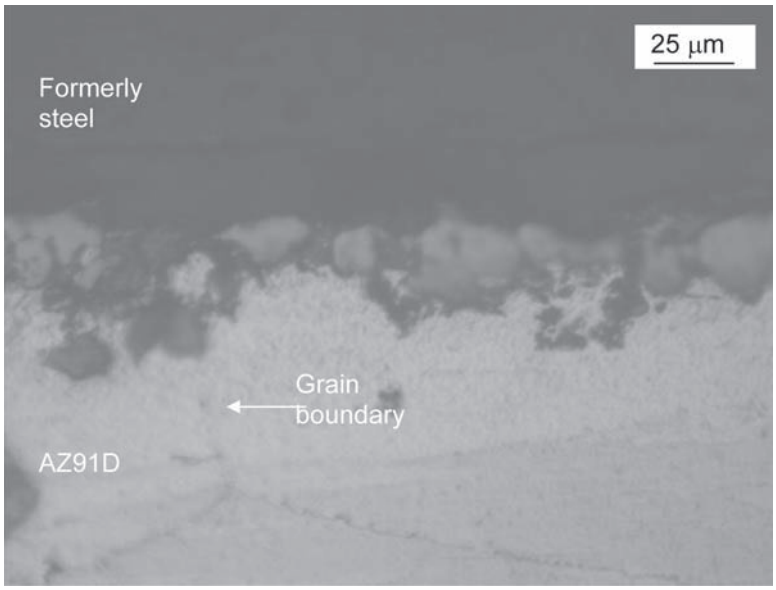

Fig. 4.15 The product of reaction between molten magnesium alloy Mg–9Al–1Zn and the DIN 1.2888 steel at 600 °C

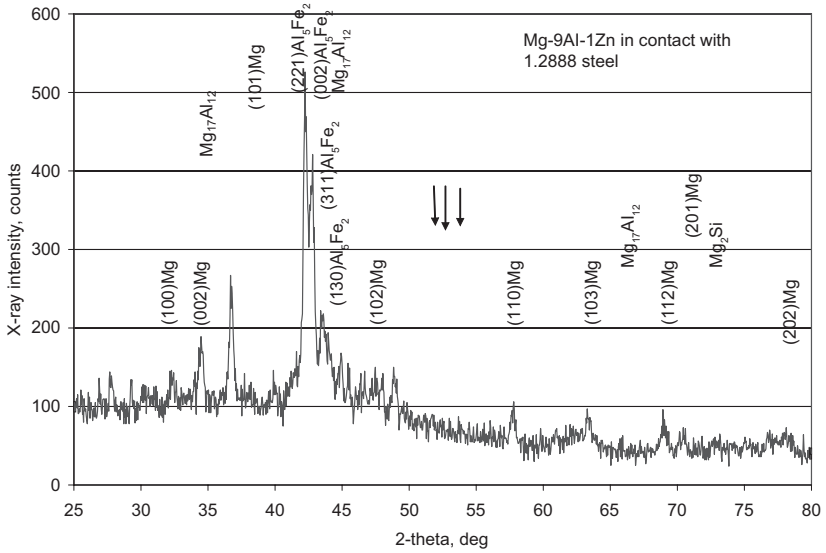

Fig. 4.16 The identification of phases present in a scale formed after interaction between molten alloy Mg–9Al–1Zn and DIN 1.2888 steel (X-ray diffraction pattern using $Cu_{K\alpha}$ radiation)

present in the scale. While Mg content is comparable to its average content in the melt, Al content exceeds 20%, which is more than double its level in the molten alloy. A contribution of Fe and Cr is lower than in steel but Co is at a similar level. Surprisingly, the content of Mn in the scale exceeds 20 times the content in both the Mg alloy melt and the steel. It is clear that such high volume arrived from the molten Mg alloy.

For Al base alloys, there are two mechanisms of soldering of die casting dies. According to the first one, soldering comprises a series of steps involving erosive wear, corrosive wear, dissolution of the die material and formation of intermetallic phases. There are cases in which soldering develops without any existence of erosive wear. According to the second mechanism, soldering is caused by corrosive wear as a result of the high affinity of aluminum to iron [11]. In this case, die material reacts with Al, forming complex intermetallic phases.

4.3.2 Reactivity with Ni-Containing Alloys

As seen from the equilibrium phase diagram, Mg dissolves in Ni (Fig. 4.19). This also applies to Ni containing alloys, and for engineering practice, alloys with more than 3% of Ni are considered to be reactive. As a result, Ni based superalloys cannot remain in contact with liquid magnesium. The situation worsens for alloys containing Al due to the reactivity of Al with Ni (Fig. 4.20).

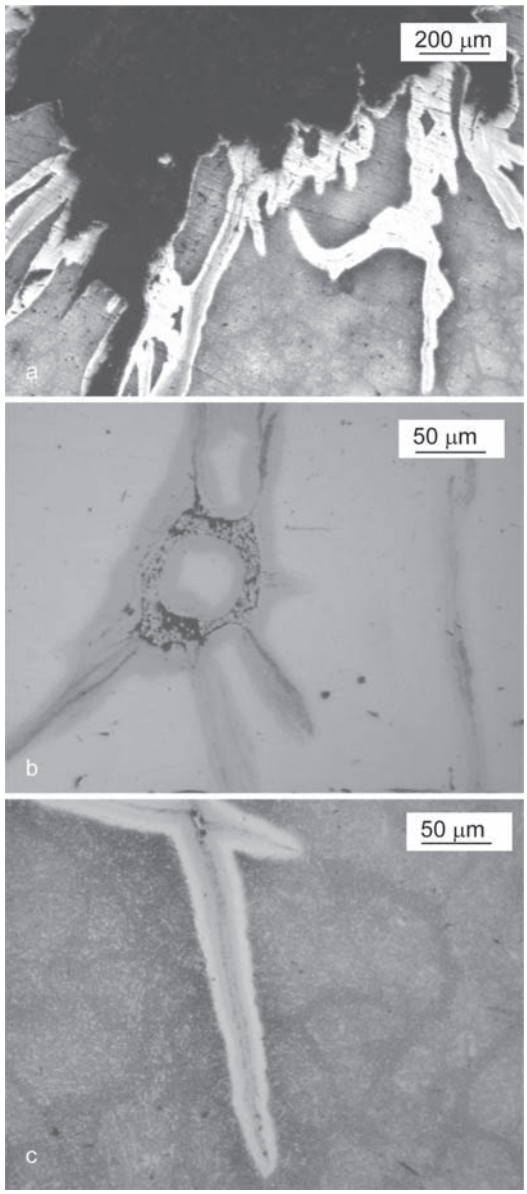

Fig. 4.17 The progress of reaction between the DIN 1.2888 steel and molten magnesium alloy Mg–11Al–1Zn with increased Al content: **a** interface between steel and molten magnesium alloy; **b** unetched surface showing the reaction front; **c** etched surface showing transcrystalline penetration of the reaction front

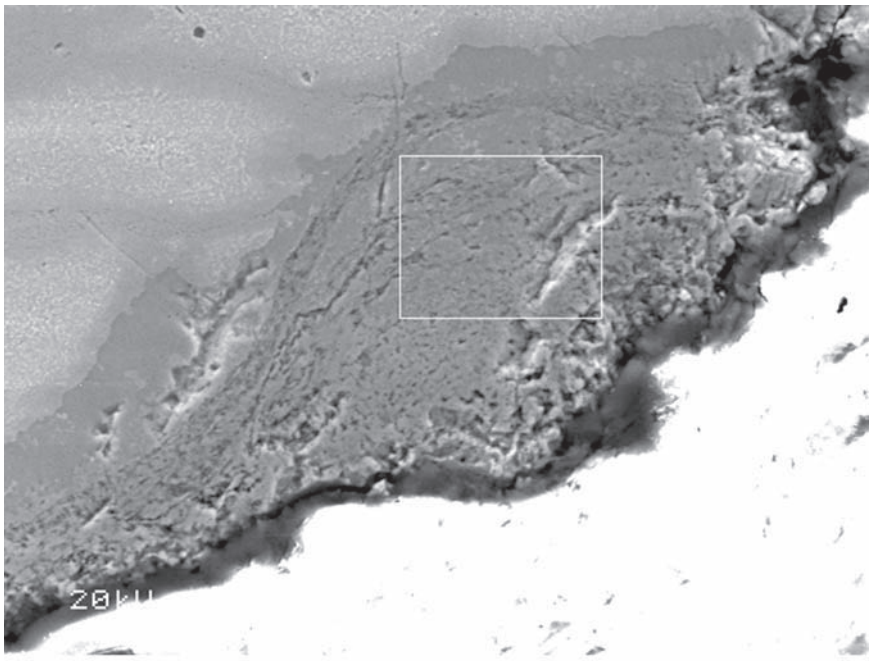
20kV

(a)

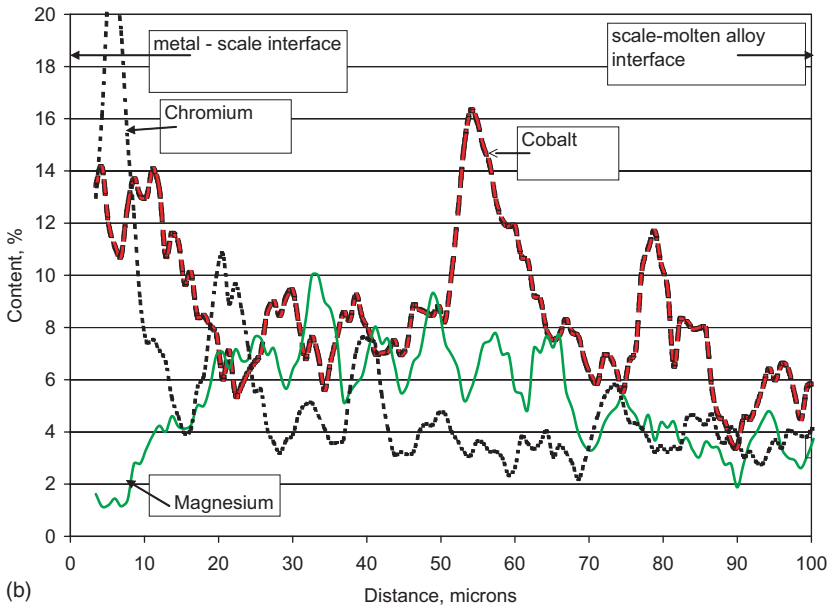
metal - scale interface
scale-molten alloy interface
Chromium
Cobalt
Magnesium
Content, %
Distance, microns
0
2
4
6
8
10
12
14
16
18
20
0
10
20
30
40
50
60
70
80
90
100

(b)

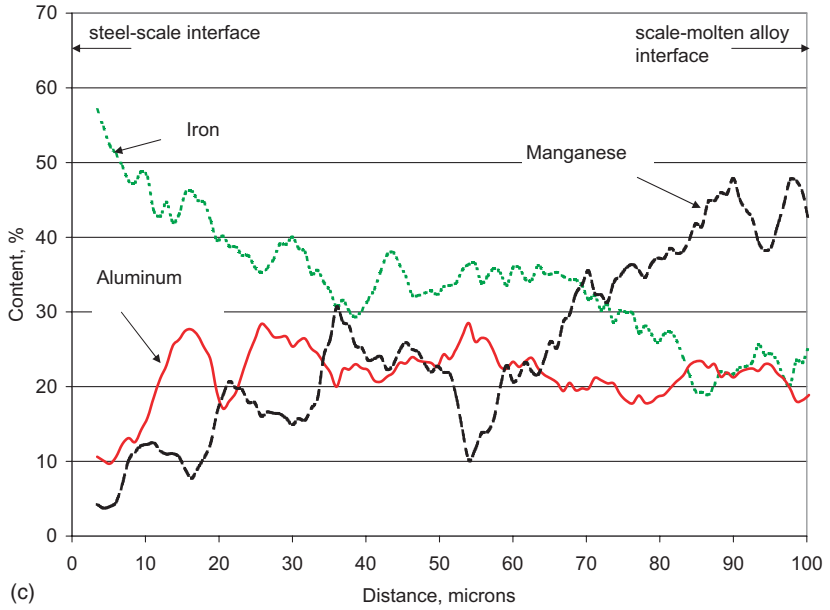

Fig. 4.18 Distribution of major alloying elements across the scale, formed after reaction between DIN 1.2888 steel and magnesium alloy Mg–11Al–1Zn (SEM–EDAX): **a** area analyzed: **b** distribution of Mg, Cr and Co; **c** distribution of Fe, Mn and Al

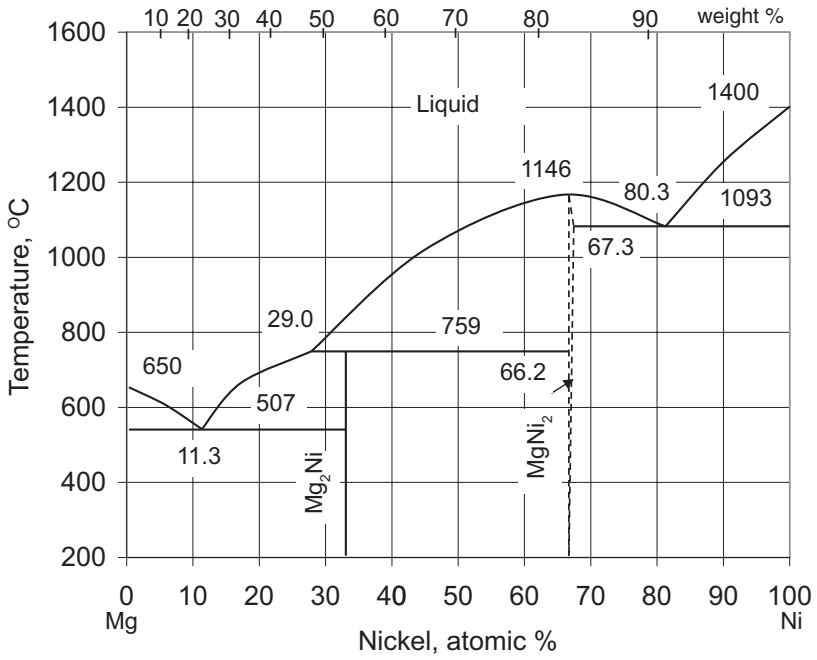

Fig. 4.19 The equilibrium phase diagram of Ni–Mg [12,13]

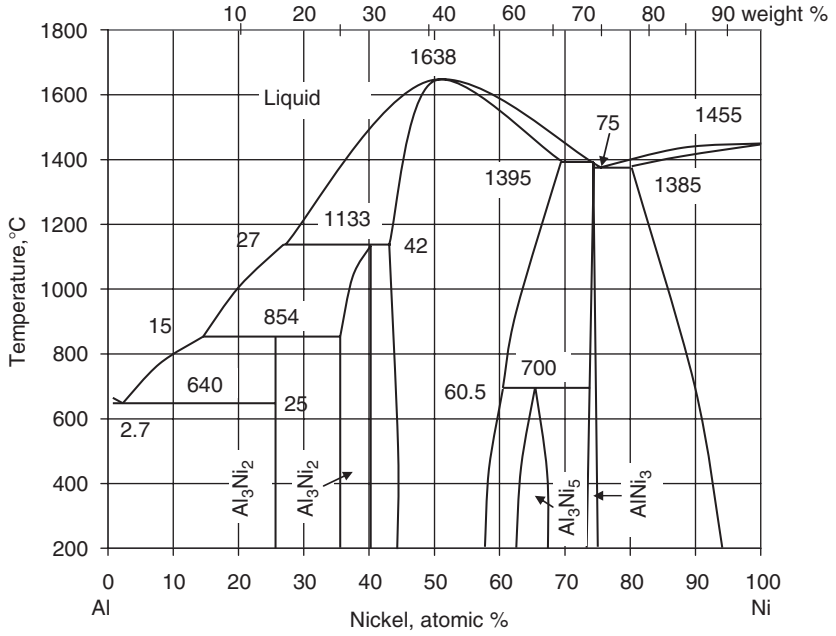

Fig. 4.20 The equilibrium phase diagram of Ni–Al [14]

Early stages of reaction between Alloy 718 and Mg–9Al–1Zn are shown in Fig. 4.21a-c. Such a reaction can occur during a splash of hot metal component with a molten magnesium alloy. From the very beginning, the growth front is non-uniform; however, the overall growth anisotropy within the thin film range is relatively low. As scale thickness increases, there is a tendency to develop cracks. For thicker scales, the reaction front at the interface between the scale and the metal is clearly seen.

The chemical composition of the scale at early stages is shown in Fig. 4.22a-b. Enrichment in Cr and Fe is observed with contents of both elements higher than in the bulk alloy. Also the Nb level is higher than in the alloy. By contrast, the content of Ni is lower than in the alloy. The same general tendency is observed during scale growth, but for well-developed thicker scales, the quantitative assessment of their chemistry is more accurate. As seen in Fig 4.23, the contents of Cr and Fe are 1.5 times higher than in the alloy. Also Nb content is twice that in the alloy. At the same time, Ni level is reduced almost three times. The content of Mg in the scale is half of that in the melt of AZ91 alloy. For both thin and thick films, Al shows very high enrichment at the interface between melt and the scale. At the same time, however, its content within the scale was very small, well below its average content in the Mg–9Al–1Zn melt.

The extent of corrosion of Alloy 718 alloy after 10 hours of exposure to Mg–9Al–1Zn slurry is shown in Fig. 4.24a,b. The temperature of the slurry during

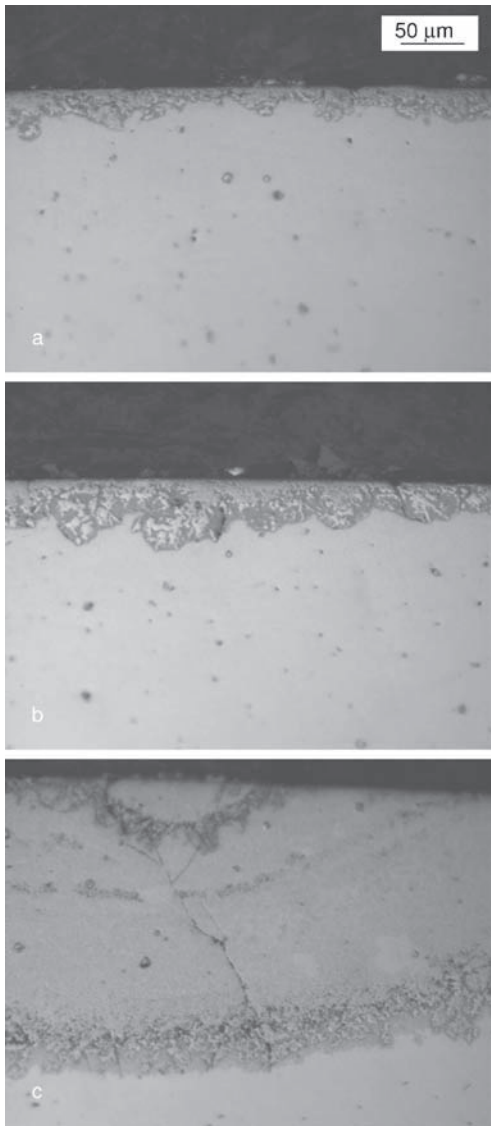

Fig. 4.21 The early stage corrosion between molten Mg–9Al–1Zn alloy and Alloy 718: **a** thin scale; **b** selective progress of the reaction front; **c** well-developed scale with through-thickness cracks

running periods was approximately 600 °C. The flow channel of the bushing is extensively corroded with both the uniform and preferential attacks. The nature of the corroded layer with an average thickness of the order of 1 mm is shown in 4.24c-e. The progress of corrosion was very fast with a clearly intergranular reaction front at the interface with a base metal. The attack is of chemical corrosive nature with the intergranular reaction front leading to a disintegration of the grain boundary network.

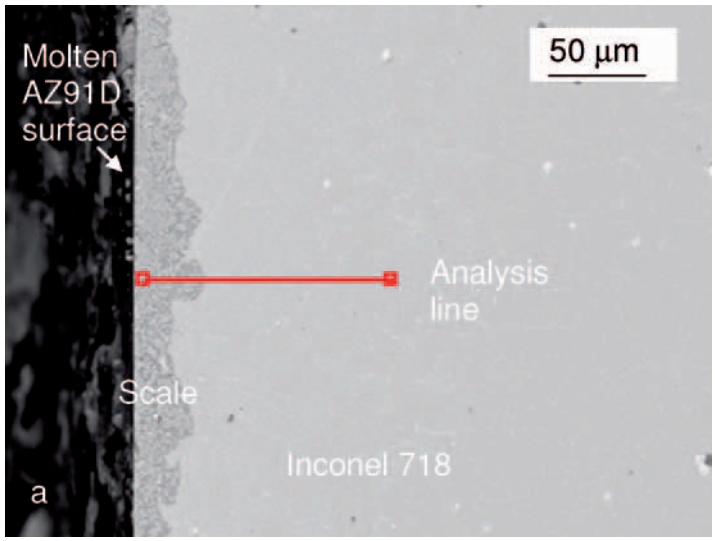

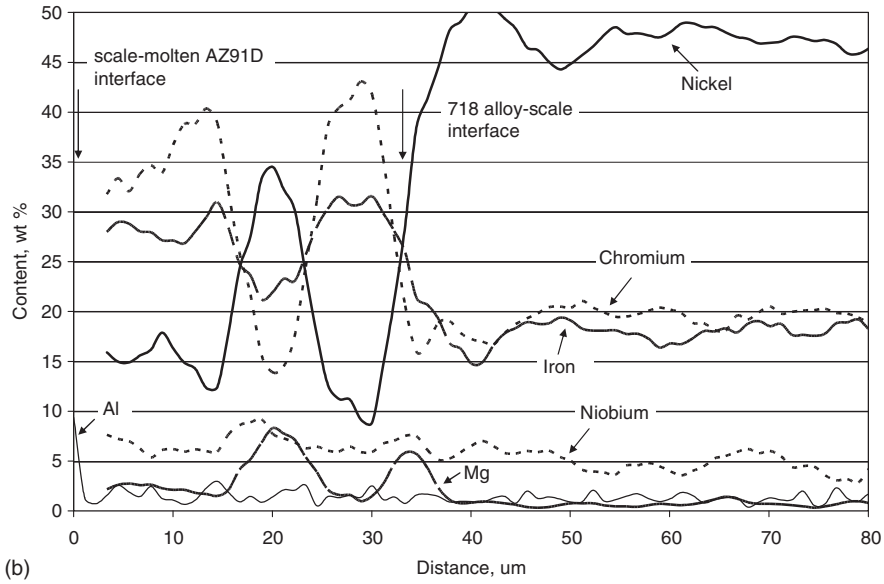

Fig. 4.22 The distribution of major alloying elements across the thin film, formed after reaction between molten Mg–9Al–1Zn alloy and Alloy 718: **a** SEM image of the scale; **b** EDAX line analysis

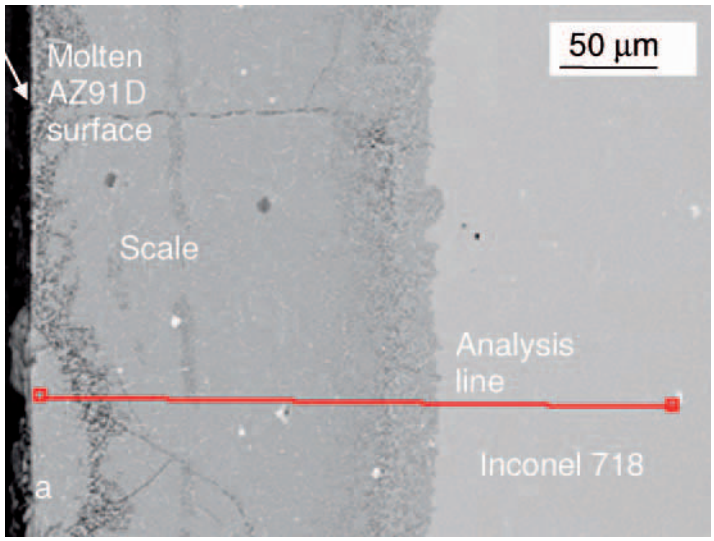

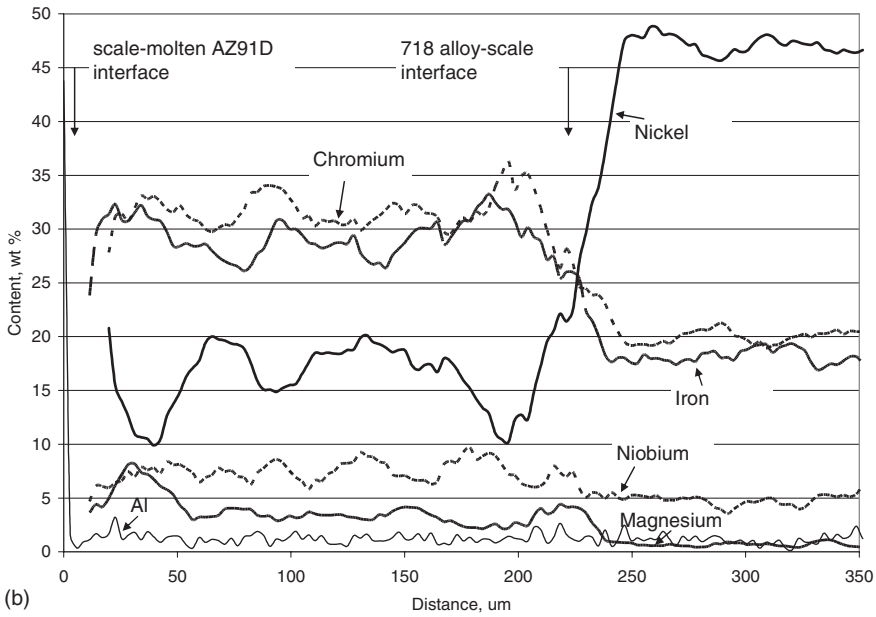

Fig. 4.23 The distribution of major alloying elements across the thick film formed after reaction between molten Mg–9Al–1Zn alloy and Alloy 718: **a** SEM image of the scale; **b** EDAX line analysis

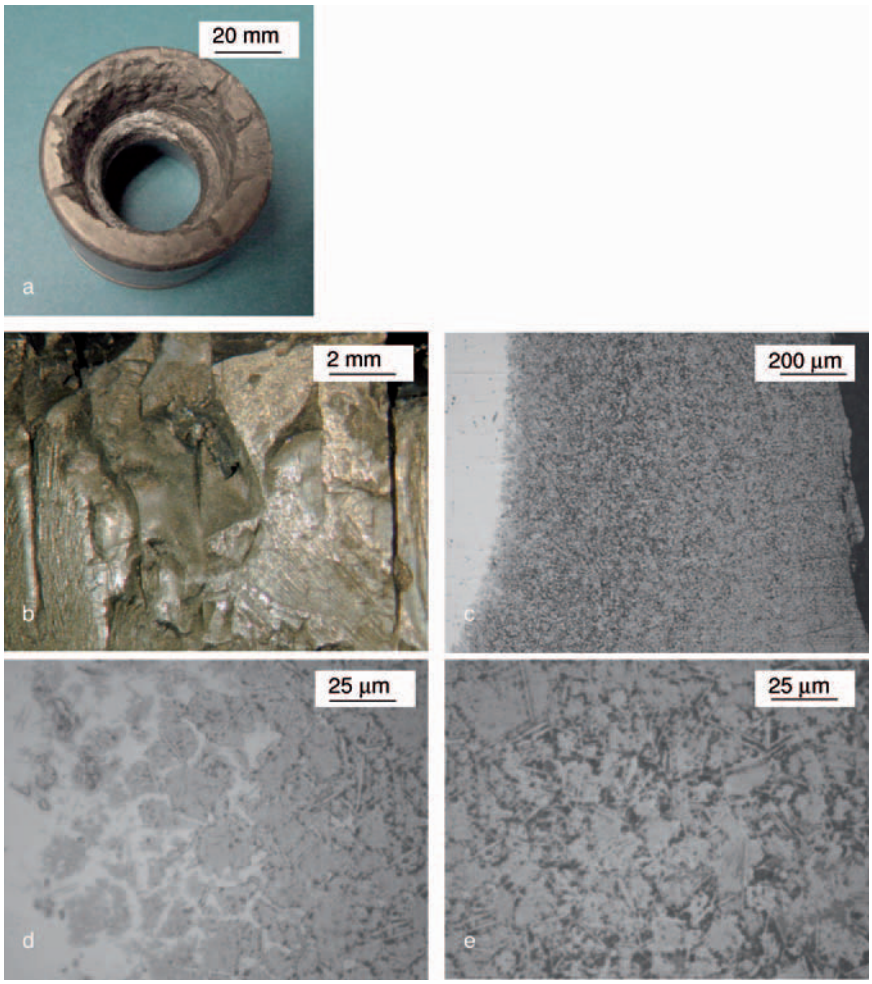

Fig. 4.24 The advanced stage corrosion between molten Mg–9Al–1Zn alloy and Alloy 718 (10 h, 600 °C): **a** bushing used as a flow channel for molten magnesium; **b** macro image of internal surface of the bushing; **c** cross section of the entire scale thickness; **d** magnified view of the metal-scale interface region; **e** magnified view, close to the outer scale surface

4.3.3 Simultaneous Corrosion and Wear

The high-speed flow of molten or semisolid metal causes surface damage resulting in a progressive loss of material, i.e., wear. In general, while classifying wear mechanisms, the following categories are distinguished:

(i) abrasive wear, caused by rubs-in contact with surfaces that have abrasive particles between them;

(ii) adhesive wear, caused by sliding surfaces when some areas adhere to each other;
(iii) fretting wear, caused by vibration and rotational stress resulting in microscopical pitting and failure;
(iv) erosive wear, occurring from solid particles present in gas or liquid striking the surface at high velocity;
(v) impact wear, caused by cyclic separation and closure of two surfaces;
(vi) cavitation wear, caused by fluids through the repeated formation and collapse of bubbles. This phenomenon generates high hydrodynamic stresses that cause deformation and erosion of the surface in proximity of the collapsing bubbles. It occurs when a fluid at high pressure and velocity contacts a surface, transmitting hydraulic shock.

An example in Fig. 4.25a shows the mold cavity, made of AISI H13 steel, extensively worn after several days of contact with flowing magnesium alloy. The reason was inappropriate venting, which does not allow for the mold gases to leave the mold cavity. Thus, the highly compressed gas leads to cavitation wear. The abrasive wear due to interaction with molten alloy is the most severe in mold gates where the material speed may reach up to 100 m/s. When conditions are formed for liquid Mg to flow at a high speed, erosion occurs. The material, worn under such conditions, includes Stellite 12, the alloy with excellent wear resistance (Fig. 4.25b). The wear pattern forms a network of not-always-interconnected grooves. The structural features of the material may contribute to the initiation of grooves. At a later stage, wear is controlled by existing grooves which represent easy channels for a flow, thus accumulating high flow intensity and wear. The erosive wear is often combined with an impact wear, as is the case for seal surfaces within valves. At high

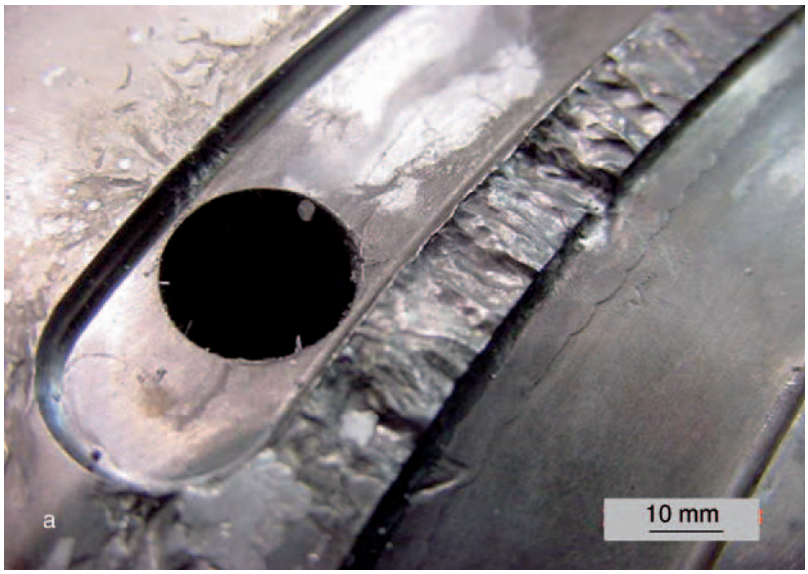

(continued)

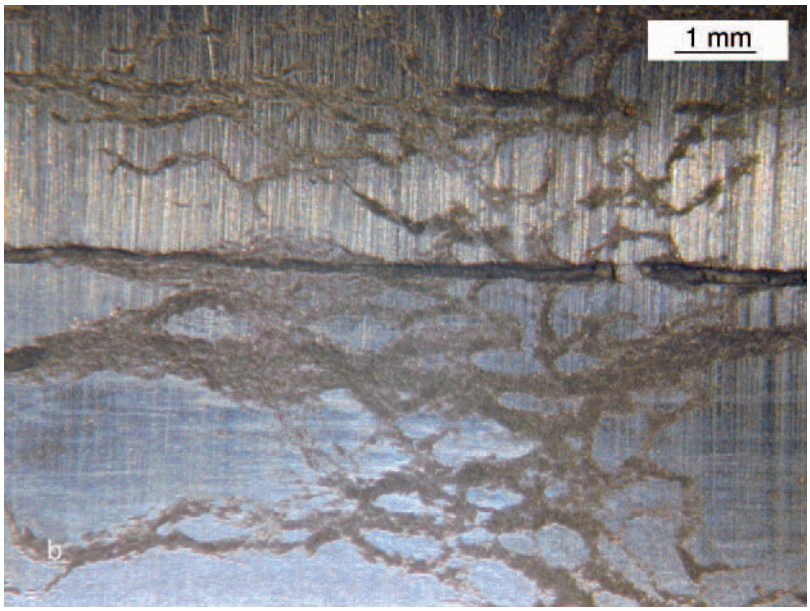

Fig. 4.25 (continued) The nature of wear, caused by liquid magnesium alloys flowing at high velocities: **a** cavitation wear of H13 steel preheated to 250 °C; **b** erosive wear of Stellite 12 at 600 °C

temperatures, hard particles, which get between contact surfaces, form dents (Fig. 4.26a) superimposed on an erosive wear pattern (Fig. 4.26b).

4.4 Summary

The high temperature and corrosive attack by molten magnesium alloys impose detrimental effects on engineering materials used for their containment and processing. As a result, the capabilities of materials being in contact with magnesium should be taken into account during selection of processing parameters. Although modern metallurgy satisfies general requirements, some limits may still exist. Therefore, research continues to develop alloys capable of increasing the service temperatures and extending the service life time of hardware used for magnesium processing.

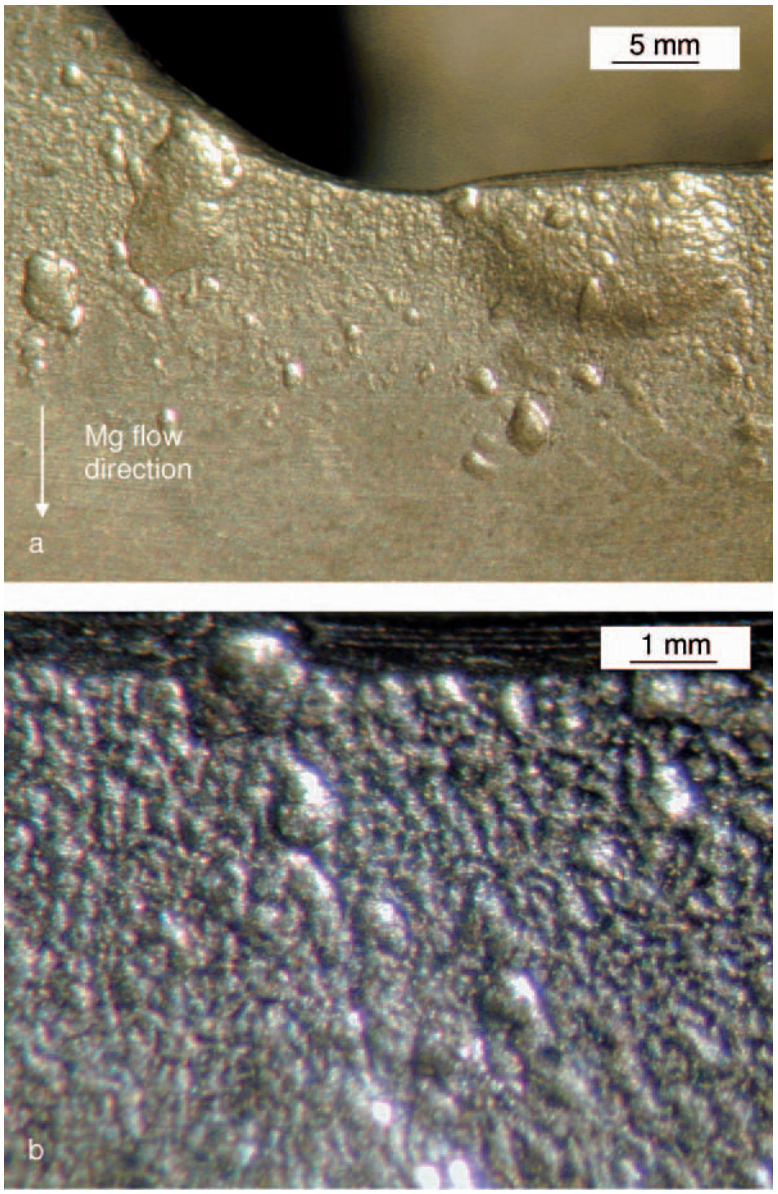

Fig. 4.26 The erosive wear superimposed on impact wear of the DIN 1.2888 steel in an environment of molten magnesium alloy of Mg–9Al–1Zn: **a** macro image showing the impact related dents; **b** micro image emphasizing the erosive wear caused by a high velocity flow of molten alloy

References

1. Dieter CE (1976) Mechanical Metallurgy. McGraw-Hill, New York
2. Kim CK et al (2004) Metall. & Mater. Trans. A 35: 481
3. Gao M, Dwyer DJ, Wei RP (1995) Scripta Metallurgica et Materialia 32 (8):1169–1174
4. Woodford DA, Briknell RH (1983) Treatise on Materials Science and Technology. Academic Press, New York, pp 157–199
5. Diboine A, Pineau A (1987) Fatigue, Fracture of Engineering Materials and Structure 10:141–151
6. Ashby MF, Johnes DRH (1982) Engineering Materials. Pergamon, Oxford
7. Birks N, Meier GH (1983) Introduction to High Temperature Oxidation of Metals, Edward Arnold Publishers, London
8. Lenglet M et al (1990) Materials Research Bulletin 25 (6):715–722
9. Massalski TB (1986) Binary Alloy Phase Diagrams, ASM, Metals Park, Ohio
10. Viala JC et al (1999) Chemical interaction processes at the interface between mild steel and liquid magnesium of technical grade. Scripta Materialia 40: 1185–1190
11. Tang C, Jahedi MZ, Brandt M (2002) In J Bergstrom (ed) The use of tool steels: experience and research. Karlstad University, Karlstad, Sweden, pp 137–146
12. Zeng K et al (1999) Thermodynamic analysis of the hydriding process of Mg-Ni alloys. Journal of Alloys and Compounds 283:213–224
13. Jacobs, MHG and Spencer, PJ(1993) J Chim. Physics, 90, 167
14. Metals Handbook (1990) 10th ed. vol. 1. ASM International, Materials Park, OH, p. 952

5
Process Theory and Practice

5.1 Introduction

Injection molding is generally known for highly effective process control. For polymer extrusion a significant amount of knowledge has been accumulated, describing both the melt preparation and injection stages. Some mechanisms, acting during the polymer melt preparation, are applicable for metal molding. However, a replacement of polymer, having low thermal conductivity and high viscosity, with highly conductive magnesium with a viscosity up to 50 times lower, introduces essential differences (Table 5.1). The stage of injection and mold processing differs completely from polymer molding and exhibits, rather, similarities to die casting. However, change from an overheated molten metal used in die casting to the semisolid slurry or melt with accurately controlled temperature creates differences at this stage as well.

This chapter is intended to provide an overall understanding of the processing features of magnesium injection molding. The critical elements of the process are explained along with operating parameters of the hardware and its functions at various stages. Theoretical analysis of the processing phenomena is supported by a description of practical aspects of molding components from magnesium alloys.

5.2 Key Processing Parameters

There are a number of machine settings that allow the control of all steps of slurry or melt preparation, injection into a mold cavity and subsequent solidification. The most important of them are described in this section.

5.2.1 Injection Molding Sequence

During injection molding the cycles of the clamp and injection unit are highly synchronized. While the injection cycle controls the slurry preparation, the clamp cycle controls various stages of mold processing. The key elements of both the clamp and

F. Czerwinski, *Magnesium Injection Molding*.

Table 5.1 The comparison of major properties of magnesium alloys, aluminum alloys and plastics Tg-glass transition temperature

Property	Unit	Magnesium alloys	Aluminum alloy 380	ABS Polyacrylobutadiene styrene	PC Polycarbonate
Melting temperatures	°C	550–650	538–593	90 (Tg)	160 (Tg)
Density	g/cm^3	1.7–1.9	2.7	1.03	1.23
Thermal conductivity	W/m K	51–84	110	0.2	0.2
Viscosity	Pa s	2–10	1.3	> 100	>1000
Enthalpy of fusion per unit mass	kJ/kg	368	397		
Enthalpy of fusion per unit volume	MJ/m^3	592	1012		
Heat diffusion rate	cm^2/s	0.290	0.244		
Young's modulus	GPa	45	71	2.1	6.7
Tensile strength	MPa	150–340	320	35	105
Yield stress	MPa	80–260	160	n/a	n/a
Elongation	%	2–17	3	40	3

injection cycles are shown schematically in Fig. 5.1. The time required to cycle the clamp is affected by mold stroke distance, clamp engagement, clamp-up where tonnage is applied, unclamping where tonnage is removed and clamp disengagement. On the clamp side, when the mold is opened and the part is ejected from the mold cavity the robot enters the mold space to remove the part. The second task of the robot, which follows directly the part removal, is to spray the open mold cavities. In parallel to the clamp cycling, the injection unit follows the steps of slurry preparation. Melt injection and pressure holding is followed by recovery, alloy melting and post recovery pullback. The major auxiliary device of the injection unit, i.e., the alloy supply system, forwards a fresh portion of chips from an external container.

The flow path of magnesium alloy through the injection unit components is shown in Fig. 5.2. A hopper (1) is filled with cold chips, which are heated and conveyed by a screw (2) powered by an motor (3) within the machine barrel (4) while protected against oxidation by argon gas. Upon accumulating the required shot size in the front of the non-return valve (5), the screw is accelerated forward, injecting the alloy through the sprue and gates (6) into the mold cavity to produce the net-shape component (7). Details of the alloy flow path after leaving the machine nozzle, starting from the sprue and ending within the part, along with the basic terminology, are shown in Fig. 5.3. The geometry, size and location arrangement of certain elements may change from mold to mold, but the general rules remain the same.

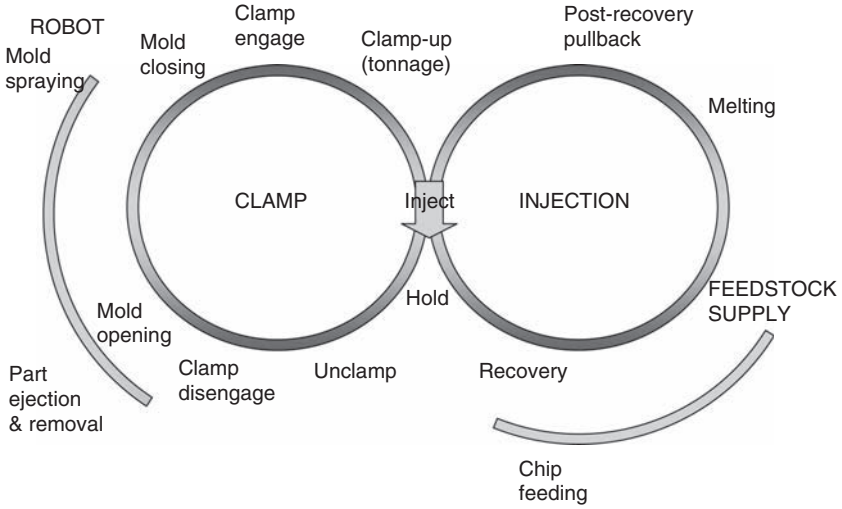

Fig. 5.1 The schematics showing various stages of the injection molding process performed by the clamp unit with a robot and the injection unit with a feedstock supply system

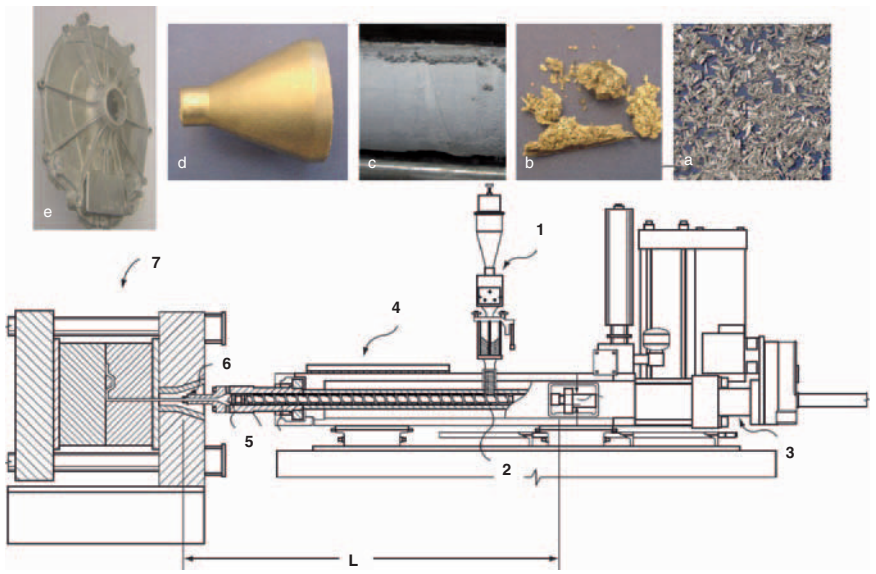

Fig. 5.2 The flow path of chipped alloy from the hopper to the mold: **a** chips before feeding into the machine; **b** feedstock partially processed; **c** end section of the screw; **d** alloy filling the barrel head; **e** molded component

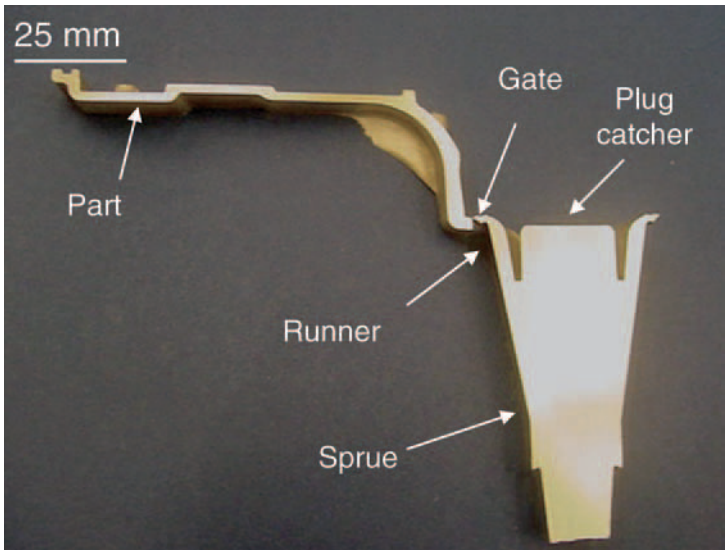

Fig. 5.3 The elements of alloy flow path after leaving the machine nozzle and related terminology

5.2.2 Barrel Temperature Profile

The barrel temperature profile is of key importance in controlling smooth processing by preventing bridging and slugging. In order to prepare the slurry so that it is suitable for injection, the total length of the magnesium flow path is divided into several zones where each of them has a different function in supplying heat. An example of a heating arrangement along the alloy flow path from the hopper to the nozzle exit is shown in Fig. 5.4.

5.2.2.1 Preheat Zones

The purpose of two initial zones is to supply energy sufficient for heating the feedstock below the melting range. Assuming that the feedstock is not preheated before entering the hopper, this will lead to a temperature increase from ambient to roughly 500 °C. In order to maintain proper feeding, it is crucial to prevent the feedstock's melting in this region. While it exceeds the melting range, feeding will be disturbed due to increased possibilities of bridging the feedthrow. The bridging occurs when a liquid metal reaches the cold feedthrow housing, resulting in its immediate solidification, which blocks the barrel entrance and prevents the screw from rotation and any axial movement. In practice, there are several scenarios leading to bridging. The first one is when the melt's flow through the barrel is blocked by unmelted or oxidized alloy sticking to the screw. The same will happen when the nozzle is blocked and the melt leaks backward through the non-return valve.

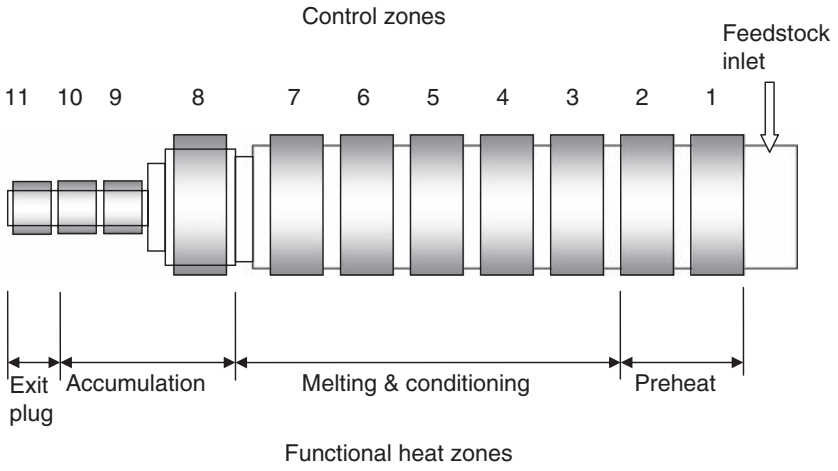

Fig. 5.4 The arrangement of control and functional heat zones along the magnesium flow path through the machine barrel and nozzle

Another scenario is likely when the screw filled with molten alloy is moved to a cold section of the barrel, causing its solidification.

5.2.2.2 Melting and Conditioning Zones

The melting and conditioning region covers zones from 3 to 7 in Fig. 5.4. Their purpose is to supply the amount of energy sufficient to transform the solid chips into semisolid slurry and achieve the desired solid to liquid ratio within it. Although the temperature is the primary factor, the slurry structure is also affected by its flow rate through the barrel. There are various thermal profiles that can be exercised. The most common is a continuous growth of the temperature followed by a plateau. Other variants include continuous growth or an exclusive plateau throughout the entire zone. For a processing technique of partial melting (thixo-route), the only exception is a negative gradient, where a drop in temperature is taking place after entering the melting range. The reduced temperature could lead to re-solidification of a portion of the liquid fraction formed in the preceding sections of the barrel. For a processing mode with a complete melting followed by partial re-solidification (rheo-route), a negative temperature gradient is required to generate a designed solid fraction.

5.2.2.3 Accumulation Zone

The accumulation zone covers the region in front of the non-return valve, including the barrel head and nozzle (zones 8 to 10 in Fig. 5.4). The material's residency time in this area depends on the cycle time and the part size, and is typically of the order of 20-40 s. However, during molding of small parts using large diameter barrels the

material volume in front of the non-return valve may equal several shots, thus increasing substantially the residency time. For a machine operated in a partial melting mode, there is no gradient in axial temperature settings within the short accumulation zone, and the temperature values usually match the last settings from the preceding conditioning zone. While exercising the rheo-processing, i.e., when complete melting is followed by partial solidification, a plateau will follow the negative gradient from a portion of the melting and conditioning zone.

5.2.3 Shot Size

The first step in calculating the shot size requires knowledge of the part volume (V_p) expanded by overflows (V_{ov}), sprue (V_{sp}) and runners (V_r). To determine the position (L_t) of the screw inside the barrel with a diameter D_b, a leakage and *cushion* (V_c) should also be included. All these ingredients are incorporated into the following formula:

$$L_t = \frac{4}{\pi D_b^{\,2}}\left(V_p + V_{ov} + V_{sp} + V_r + V_c\right)C_r \tag{5.1}$$

The main purpose of the cushion is to transfer the pressure entirely to the melt that fills the mold cavity and runners. A presence of cushion also prevents a bottoming out when the screw would be moved forward to the point that the non-return valve is in intimate contact with the barrelhead. The typical cushion size is from several to tens of millimeters. The leakage volume depends directly on the efficiency of the non-return valve, described later in this chapter. Another correction that should be considered is that the slurry accumulated in front of the valve is not fully dense but contains some gas entrapments. The approximate value of this correction, marked as C_r in Formula 5.1, is 10%, i.e. $C_r = 1.1$.

5.2.4 Injection Profile

The typical phases of a die casting cycle, plotted for the piston (plunger) displacement and injection pressure, are shown in Fig. 5.5. The low velocity of the piston at the beginning allows the reduction of gas content in the molten metal, residing in front of the piston. During the filling stage, the piston accelerates rapidly to achieve the required speed. When the cavity is almost entirely filled, the high pressure is applied for a certain time to increase the part integrity. At the end of the cycle, the part is ejected and the piston returns to its starting position for the next shot. For magnesium casting, due to the low heat content, the pre-fill and fill steps are rather quick to avoid premature freezing.

The ideal injection molding profile allows the distinguishing of three stages (Fig. 5.6). The first stage aims at blowing the plug, initiating the filling of sprue and

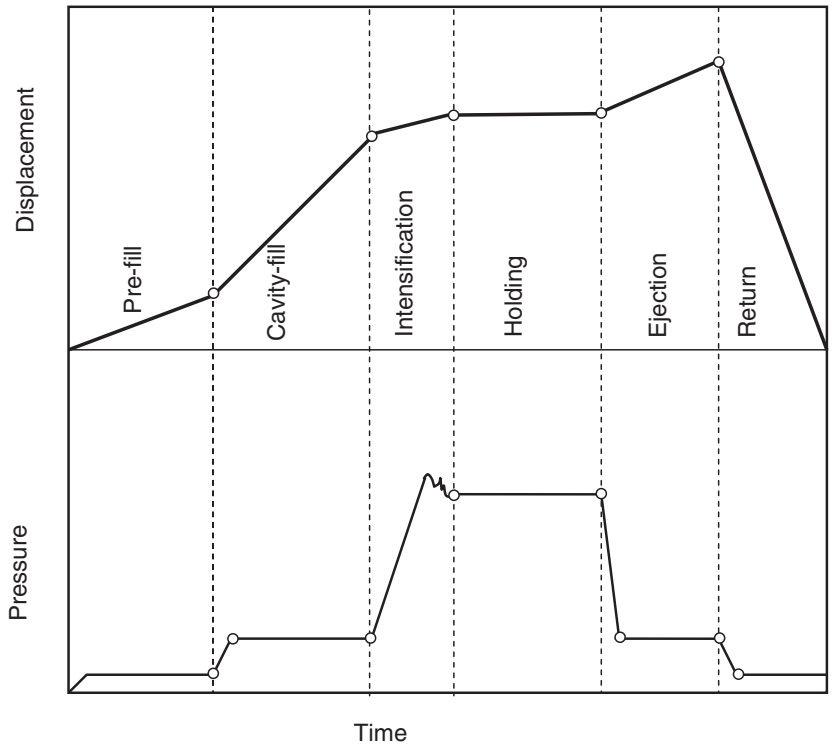

Fig. 5.5 The stages of the shot profile for die casting process showing changes of melt pressure and plunger displacement versus time during various stages of the casting cycle [14]

runners. During this stage the pressure reaches the first maximum and the screw velocity increases. According to principles of semisolid processing, the screw velocity during the first stage should remain low to avoid slurry turbulence. The second stage is designed to fill the cavity: The screw velocity increases until it reaches its maximum just prior to the material approaching the gate. As a result of reaching the gate and the back pressure created by an increasingly filled mold, the velocity starts to diminish. The third stage, called packing, is designed to exert high pressure while the cavity is full but the alloy is still in liquid or semisolid state. During this stage the pressure reaches its maximum. Since screw movement occurs only due to the alloy shrinkage and eventual reduction in gas porosity, its velocity is very low. After the maximum pressure is reached, it falls quickly to the lower holding level. Injection profiles, observed in industrial applications, have the individual stages less pronounced.

5.2.4.1 Transition Position

The transition position should be set right before the part has filled out. There are several types of inputs used to determine when to switch over from injection to

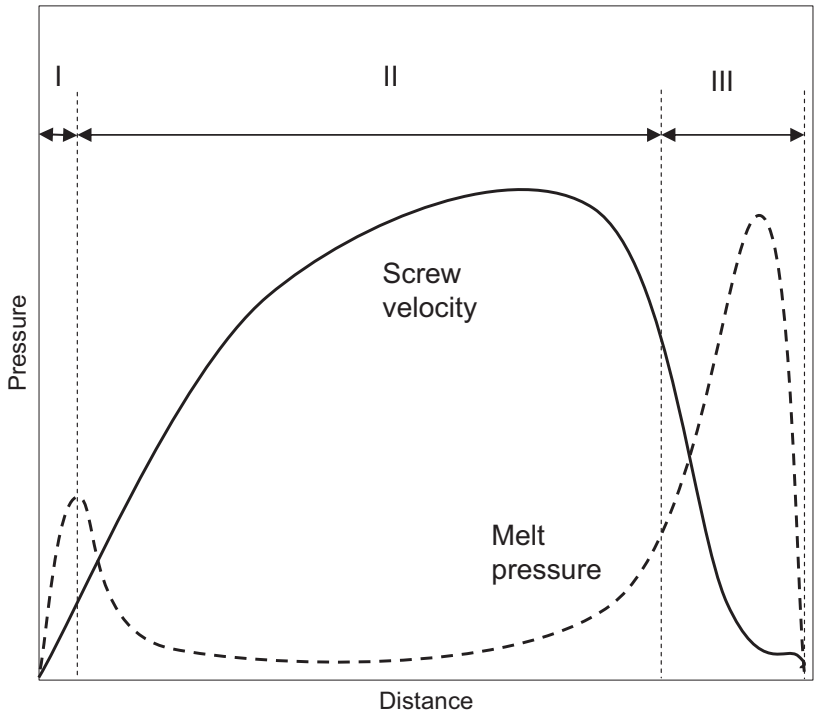

Fig. 5.6 The melt velocity and pressure as a function of the displacement of injection screw during injection molding: ideal graph with three distinct stages

holding pressure. Some delay is assumed due to control system inertia. While a set up that is too late leads to a pressure spike during injection, setting up too early results in a short shot and an incomplete filling of the cavity.

5.2.4.2 Holding Pressure

The purpose of the holding pressure is to allow the component's densification. It is assumed that after injection, the part still contains a certain volume of entrapped gases. In addition, solidification creates shrinkage porosity due to the alloy's volume reduction. Thus applying a pressure during early stages of solidification removes gases and increases the part integrity. While for thick-wall components and alloys with high heat capacity this approach is very effective, for magnesium alloys with low heat content and especially for thin-wall parts, the effectiveness of packing is limited. Thus, in engineering practice the holding pressure set up depends on the part's wall thickness. While increasing the wall thickness from 0.5 mm to 3 mm, the solidification time of magnesium alloys is increased from 5 ms to 100 ms. A typical setting of the hold time for magnesium molding is between 0.25 s and 1 s.

5.2.5 Recovery

When the injection cycle is completed, the screw is moved to its start position before the next shot. This cycle segment is called recovery, and it depends on the method of barrel feeding. For the flood feeding that is used predominantly, the screw speed is correlated with the rate of feedstock volume being supplied by the hopper system. If the screw rotation speed is too high, the hopper will not be able to supply enough feedstock. Back pressure retards the backward movement, assuring that the accumulation zone in front of the non-return valve is compacted, thus reducing the possibility of a short shot. A pullback is used to re-track the screw after recovery in order to decompress the accumulation zone. Moving the screw back prevents the nozzle plug from being unexpectedly released. The recovery rate is independent of the slurry quality and is measured by shot size divided by the screw run time (g/s). The recovery affects the melt quality, and it can contribute to excessive air entrapment inside the feedstock and then the molten alloy.

5.3 Functions of the Injection Screw

During polymer molding, the injection screw is the most important component, which directly affects the process performance, machine productivity and product quality. Although the screw is also an essential part of the metal molding machine, some of its functions differ from that for polymers. The general expectations for the injection screw performance are high throughput, low noise level, no tendency to slugging, low rotation pressure, easy retraction and consistent recovery time. The typical geometry of a screw with main functional zones is shown in Fig. 5.7a. The elements of the screw's geometry are given in Fig. 5.7b

5.3.1 Feedstock Conveying

Feedstock conveying represents forwarding of metallic particulates within the barrel in an axial direction towards the nozzle. Using an analogy with polymers, the major stages of conveying include [1]:

(i) initial forwarding;
(ii) compaction;
(iii) solid-bed conveying.

The process starts when particulates leave the hopper and enter the screw section through the feed throw. A requirement of uniform feeding in polymers is the resin sticking to the barrel and slippage on the screw (Fig. 5.8a). If the opposite is true and polymer sticks to the screw, the slug is developed with no output. In that case, as a possible improvement, barrel grooving is usually recommended. For magnesium particulates, the friction difference is not likely to be achieved due to a difference

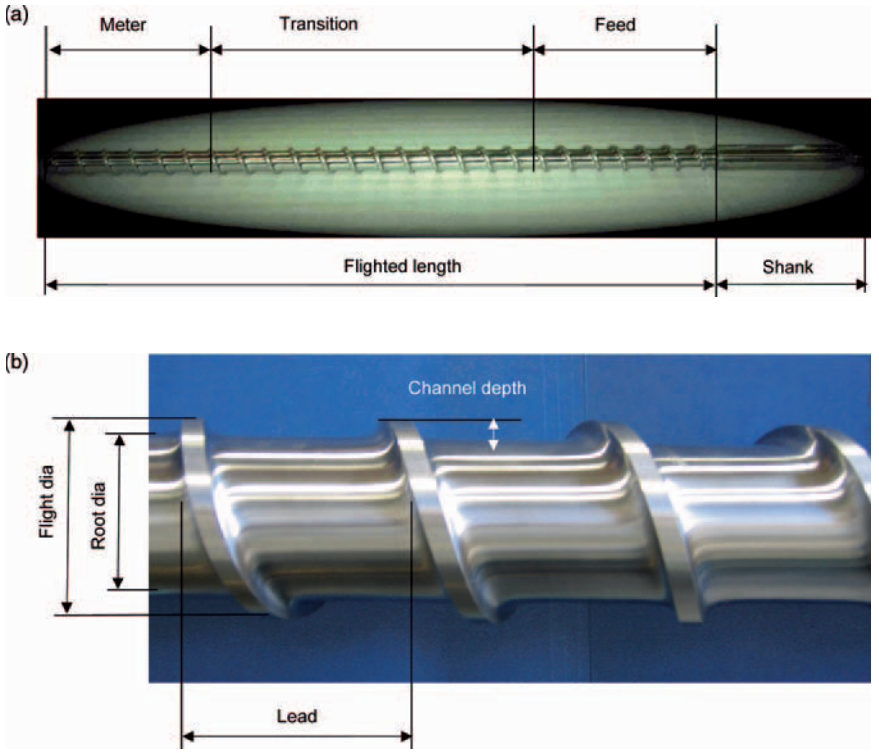

Fig. 5.7 The injection screw used in metal molding: **a** entire screw length with its functional zones; **b** screw section with geometry details

in physical properties between the magnesium alloy, barrel and screw (Fig. 5.8b). In fact, clean metallic surfaces exist during the first hours run of a new barrel/screw assembly, and soon after they are covered with oxide layers. For mechanically comminuted particulates, the internal friction is created by irregular shape and rough surface. The role of the feedstock's surface morphology is not clear, because the rapidly solidified granules with smooth surfaces and apparently lower internal friction exhibit good conveyance characteristics as well. The role of temperature difference between barrel and screw as a factor controlling friction is not clear either. Although the high thermal conductivity of Mg should equalize the temperature of both components, the continuous flow of cold particulates to the screw surface reduces the screw's temperature in the feeding zone.

During the compaction stage in polymers, the screw channels become increasingly filled with feedstock particulates. High internal friction between the particulates improves a torque transfer from the screw to compact plastic pellets into so-called solid bed. In this process the particulate hardness and shape also play a role, and softer particulates with irregular shape are easier to compact. Hence, the internal friction within irregular mechanically chipped Mg feedstock should help compaction. Due to much higher hardness of Mg feedstock as compared to polymers, a solid bed

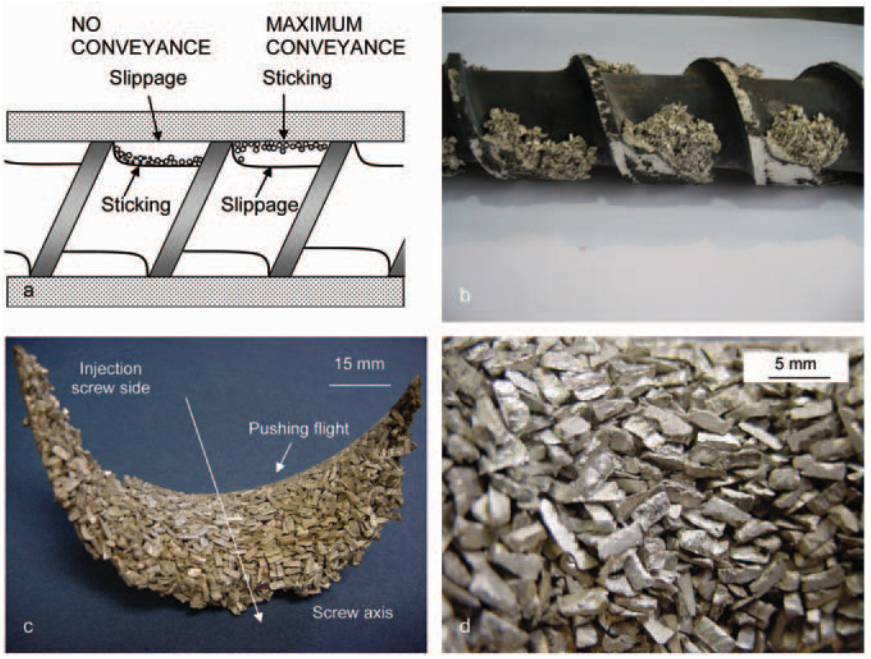

Fig. 5.8 The conveying and compaction mechanism of plastics and magnesium inside the barrel: **a** a principle of conveying plastics inside the injection barrel: Sticking to the screw results in no output while sticking to the barrel wall leads to the maximum output; **b** initial forwarding chips by the screw; **c** a partial rings of compacted solid chips removed from the screw; **d** a view of the chips/screw surface showing degree of compaction

cannot be achieved by compacting solid particulates. Although chips are rather highly packed, there is still a free space between them (Fig. 5.8c,d). In the case of Mg feedstock, the formation of a solid bed is possible after exceeding the solidus temperature when solid converts into a mushy state. Thus the semisolid bed for magnesium molding would represent an equivalent to the solid bed for polymers.

The solid bed conveyance for polymers relies on a difference in friction between the solid bed and the barrel on one side and the screw on another side. The higher friction with the barrel generates a breaking force, which contributes to a sliding of the solid bed on the screw. A difference in rotational speeds between the solid bed and screw results in the solid conveyance rate. Based on the polymer analogy, during magnesium molding, the semisolid bed conveyance is an appropriate equivalent.

5.3.2 Feedstock Melting

There is a fundamental difference in melting characteristics between polymers and magnesium alloys. As a result of very low thermal conductivity of polymers, the solid bed melts very slowly. For polymers two melting mechanisms were proposed [1]:

(i) dissipative melting of the solid bed on the hot barrel surface;
(ii) conduction melting of broken solid bed pieces mixed in the hot melt.

The key feature of dissipative melting is that the solid bed melts after contacting the barrel surface. The molten film is then scraped off and collected in a melt pool by the advancing screw flight. Since polymer melts have high viscosity, a large amount of heat is generated by dissipating the mechanical energy. The conduction melting becomes dominant where the solid bed disappears, and only solid pieces are surrounded by the hot melt. At this stage, the barrel temperature has a small effect on melting because of the low thermal conductivity of polymers.

The conductivity of magnesium alloys, which is three orders of magnitude higher than numbers for polymers, changes the melting mechanism. There is no evidence of a substantial influence of shear imposed on the solid feedstock by the barrel on melting. If there might be a contribution from shear at very high solid fractions it disappears as melting progresses. The reason is a reduction in the melt's viscosity. Thus the feedstock melting is controlled by external heat, and the contribution of shear should be neglected. Since heat is supplied from outside, and the barrel has a higher temperature than the screw, melting from the barrel direction dominates (Fig. 5.9a). It is documented in Figs 5.9b-d where molten alloy on the barrel side coexists with solid chips on the screw side. Structural transformations taking place during melting are described in Chap. 9.

5.3.3 Alloy Metering

The major function of the metering section of the screw is pumping the molten material. After the material becomes molten, its transport mechanism along the screw changes. At this stage, two types of flow are distinguished [2]. During the so-called pressure or Poiseuille flow, the velocity field is generated due to external pressure while the boundaries are stationary. During the so-called drag or Couette flow, the flow field is created by the boundary movements. The melt, which adheres to the screw, is moved with it at this stage while the melt adhering to the barrel is prevented from advancing forward. Thus, there are three major components that control the material flow, and, in general, the metering rate is calculated by subtracting from the drag flow rate the pressure flow rate and the leakage flow rate.

For metal molding, the screw's metering function depends on the solid—liquid ratio within the slurry as the solid fraction affects the viscosity. At high solid content, however, the viscosity of magnesium alloy slurry is only a fraction of that observed for polymers (Table 5.1). Hence, during metal molding the screw's pumping effectiveness, dependant on an alloy's viscosity, is suspected to be lower than for polymers. Several views of the metering zone are shown in Fig. 5.10. The cross section through the barrel exhibits uniform filling a space around the screw (Fig. 5.10b). Moreover, high integrity of the alloy with no air pockets is seen after sectioning of the alloy removed from the screw after freezing experiment (Fig. 5.10a,c).

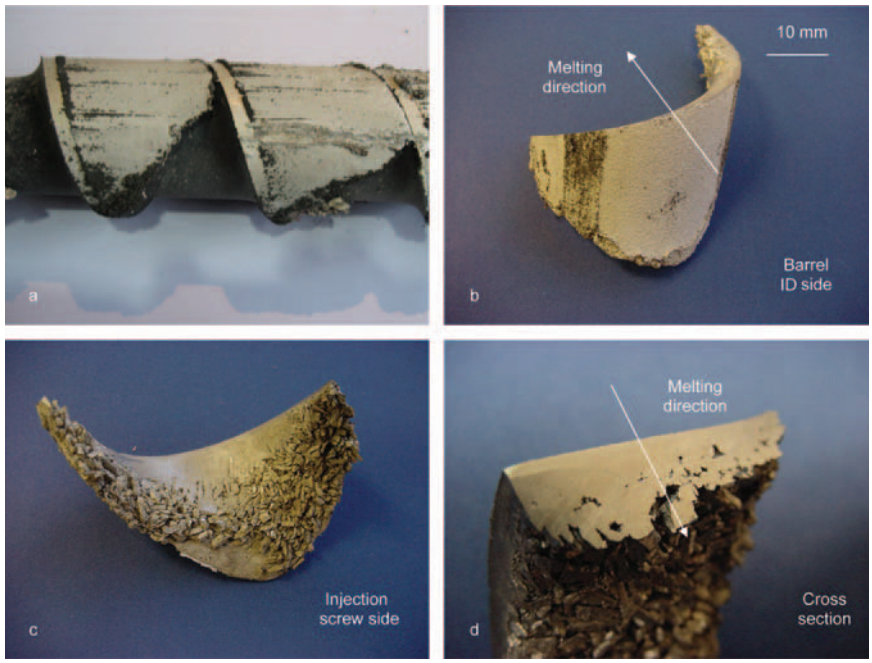

Fig. 5.9 The melting mechanism of magnesium alloys inside the machine barrel: **a** partially melted feedstock on the screw; **b** alloy removed from the screw showing the melting progress from the barrel walls; **c** screw side showing still not melted chips; **d** cross section through the alloy removed showing a progress of melting

5.3.4 Output of Injection Screw

The output of the screw is frequently seen as equivalent to machine throughput and is affected by a number of factors. More precisely, the machine throughput is dependent on the slurry quality and is measured by shot weight divided by cycle time, so it is a function of residence time. It can be predicted based on the following assumptions [2]:

(i) the output is the same as the metering rate of the metering section;
(ii) the sum of the mass solid conveying rate and the mass metering rate is constant and equal to the output rate at all cross sections along the screw;
(iii) the output cannot exceed the total melting capacity of the screw or the solid conveying rate of the feeding section.

The volumetric metering rate Q is obtained by integrating the Z component of the melt velocity (v_z) over the cross-sectional area of the screw channel (Fig. 5.11).

$$Q = \int_0^H \int_0^W v_z \cdot dx \cdot dy \tag{5.2}$$

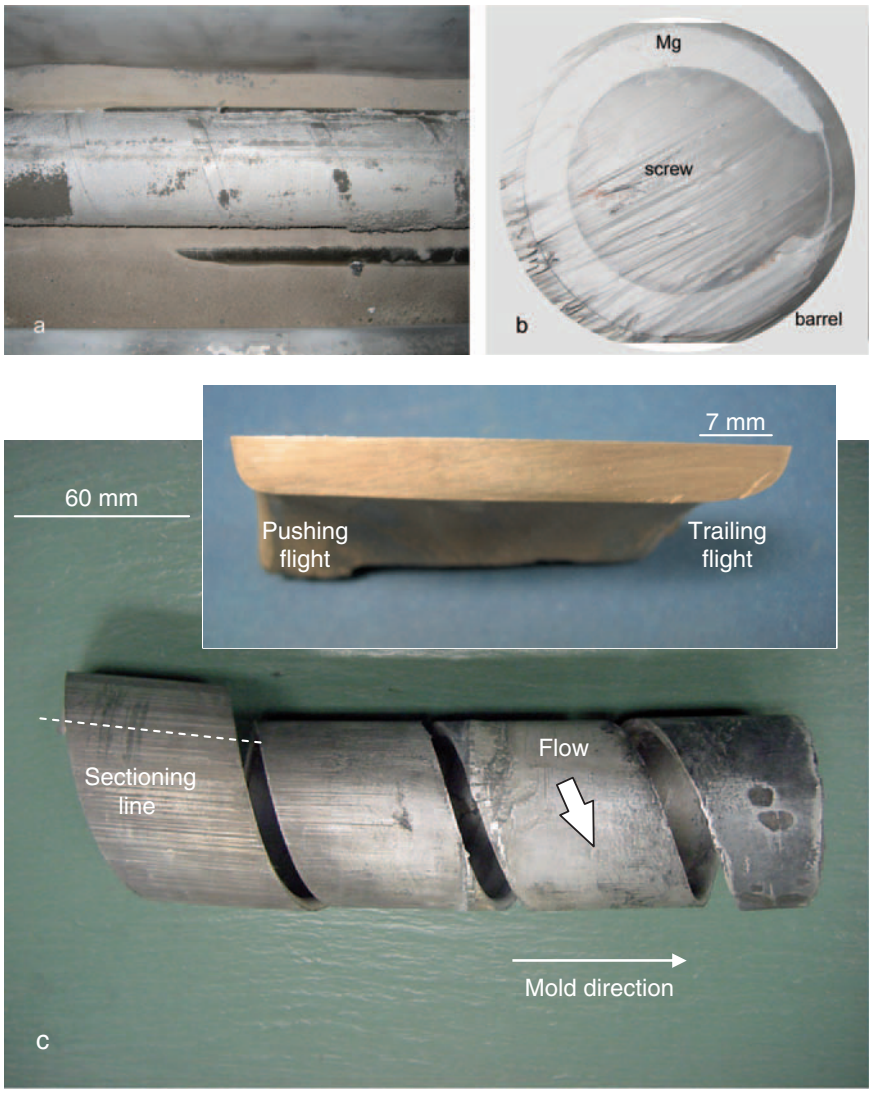

Fig. 5.10 The conveying molten alloy by the screw: **a** molten alloy with the screw; **b** barrel cross section perpendicular to the screw axis showing filling space between the screw and barrel; **c** alloy removed from the metering section of the screw during screw freezing experiment; (inset) cross section along the line marked showing geometry and integrity of the alloy filling the screw channel depth

Under assumptions of constant geometry of the screw channel and melt temperature, negligible clearance between the flight and barrel and the Newtonian behavior of the melt, a simplified model for calculating the metering rate was developed. The volumetric flow rate (Q) is the difference between the drag flow and the pressure flow; under an assumption of Newtonian fluid with a constant viscosity, independent of the shear rate [1]:

$$Q = Q_d - Q_p = \frac{1}{2} v_{BZ} WH - \frac{WH^3}{12\mu} \frac{\Delta P}{\Delta Z} \tag{5.3}$$

Where:

Q_d – drag flow rate;
Q_p – pressure flow rate;
v_{BZ} – melt velocity down the screw channel;
W – channel width perpendicular to the flight;
H – channel depth from the screw root to the barrel;
μ – Newtonian viscosity;
$\Delta P / \Delta Z$ – pressure gradient in Z direction down the screw channel.

The drag flow rate is proportional to the channel depth and the screw speed. It equals one half of the channel volume since one half of the fluid in the screw channel is dragged by the moving barrel if there is no pressure drop. The pressure drop is proportional to the pressure gradient and inversely proportional to the viscosity. It strongly depends on the channel's depth. Although the screw speed is not included to describe the pressure flow rate, Q_p increases with increasing the screw speed because the viscosity decreases with increasing screw speed. Although a number of simplifications that have been introduced reduce its accuracy, the equation (5.3) is useful in predicting the metering rate well, especially where the pressure flow rate is small in comparison to the drag flow rate.

5.3.5 Shear Function of an Injection Screw

There are two functions of the injection screw, sometimes referred to as the secondary ones, which include shearing and mixing. Both functions are of importance for melt quality and stability during metal semisolid molding.

5.3.5.1 Role of Shear in Polymer and Metal Molding

An essential difference exists between the role of shear in polymers and metal molding. Most of the energy from the screw is transferred to the polymer by a shear mechanism; hence, shear plays a key role in polymer melting and mixing. Too low shear causes poor mixing, low melt temperature and unmelted material. By contrast, excessive shear generates too high temperature, causing the burning of some materials.

The essential difference of the melt viscosity between polymer and metal questions the direct applicability of screw shear theories developed for polymers to metal processing. The screw shear function has a special meaning for semisolid metal processing due to its influence on the formation mechanisms of thixotropic structures and solidification mechanisms of agitated liquids. For injection molding, however, the formation of thixotropic structure is controlled by the nature of feedstock, which under the sole influence of heat transforms to spheroidal particles suspended in the liquid matrix (Chap. 9).

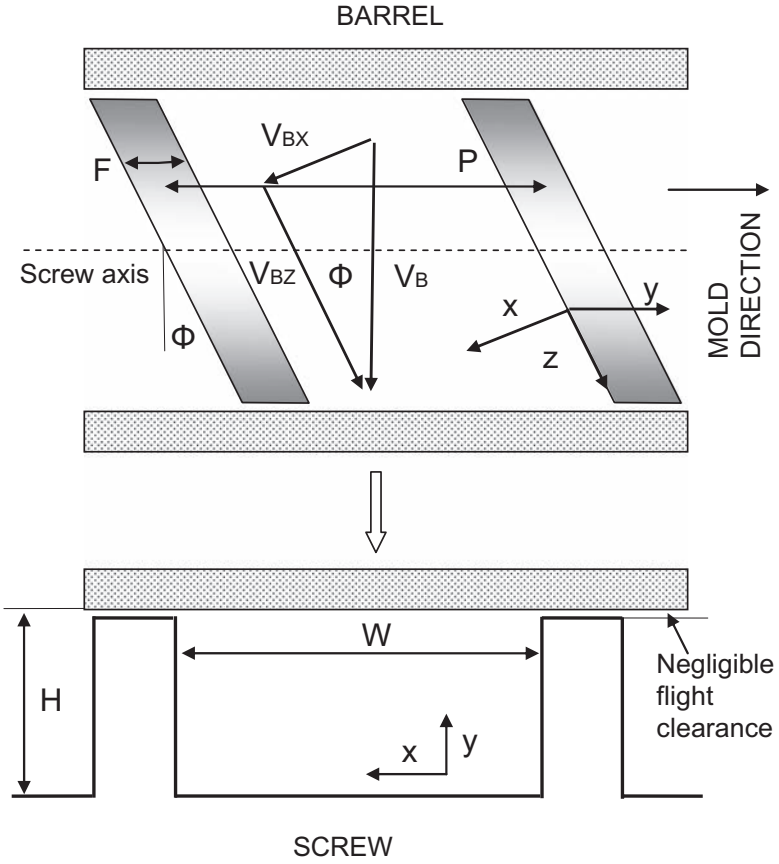

Fig. 5.11 The schematics of the longitudinal cross section of the barrel screw with coordinates of stationary screw channel and moving barrel [1]

5.3.5.2 Shear's Quantification for a Single-Screw Case

When liquid fills the area between two solid surfaces that are in relative movement, like a stationary barrel and rotating injection screw, it is subjected to shear. Since liquid layers adhere to the solid surface, intervening layers of liquid move with a velocity that varies as a function of the distance from the stationary surface of the barrel. The velocity gradient is understood as a deformation of the liquid and is called shear. The shear strain $\dot{\gamma}$ when using parameters specified in Fig. 5.12a is defined as:

$$\dot{\gamma} = \underset{\Delta y \to 0}{Lim} \frac{v}{\Delta y} = \frac{dv(y)}{dy} \tag{5.4}$$

For Newtonian liquids the shear stress is proportional to strain. The constant of proportionality that relates the shear stress to the velocity gradient is viscosity.

During injection molding the processed material is sheared at two contact interfaces in a relative movement to each other: screw surface and inner diameter of the barrel (Fig. 5.12b). The shear rate depends on the relative speed of two moving surfaces and the force acting between them. Shear rate within the screw channel is calculated based

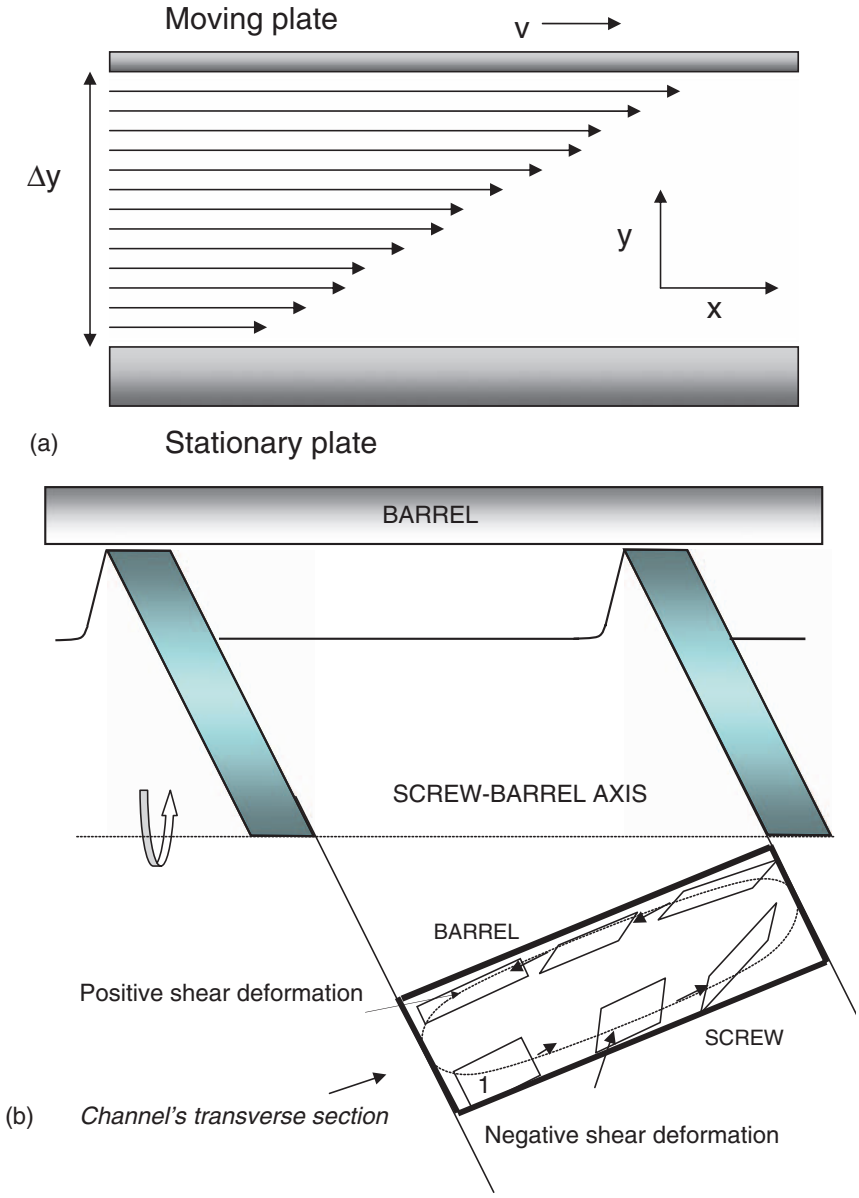

Fig. 5.12 The schematics to understand the shear **a** and cross channel flow and resulting shear deformation **b** (b-based on [3])

on the assumption that a screw extruder is similar to two coaxial cylinders. Assuming further that the screw root and barrel surface can be approximated by flat plates, the shear rate in the screw channel $\dot{\gamma}_{ch}$ is expressed by [3]:

$$\dot{\gamma}_{ch} = \frac{\pi(D-2H)N}{H} = \pi N(\frac{D}{H}-2) \tag{5.5}$$

Where:

D – the outer diameter of the screw;
N – the rotational speed of the screw in revolutions/s;
H – channel depth from the screw root to the barrel.

The shear rate in the screw channel consists of the down channel shear and cross channel shear. Both values are calculated by taking the first derivative of the melt velocity. According to [3], down-channel shear rate $\dot{\gamma}_{yz}$ is expressed by:

$$\dot{\gamma}_{yz} = \frac{dv_z}{dv} = \frac{\pi DN\cos\varphi}{H}\left(1-3r_d+6r_d\frac{y}{H}\right) \tag{5.6}$$

Where in addition to symbols defined in (5.5):

r_d – a ratio of pressure flow to drag flow;
y – the normal distance.

For a positive pressure gradient, the shear rates increase toward the barrel surface. For a negative pressure gradient the shear rate increases while moving away from the barrel surface. When the pressure is zero, the shear rate is constant and does not depend on a location.
The shear rate across the channel $\dot{\gamma}_{yx}$ is expressed by [3]:

$$\dot{\gamma}_{yx} = 2\frac{\pi DN\sin\varphi}{H}\left(-1+3\frac{y}{H}\right) \tag{5.7}$$

According to, e.g., (5.7) the fluid at the bottom of the channel is subjected to negative shear rates while at the channel's top the shear rates are positive.

5.3.6 Alloy Mixing

Mixing is important for a conventional semisolid molding of a single alloy since it affects the homogeneity of a thixotropic two-phase slurry of primary solid within the liquid matrix. It has, however, a particular importance during alloy generation by combining a number of semisolid slurries with different chemistries as well as during the composite formation by additions of re-enforcement particles to a semi-solid or molten matrix.

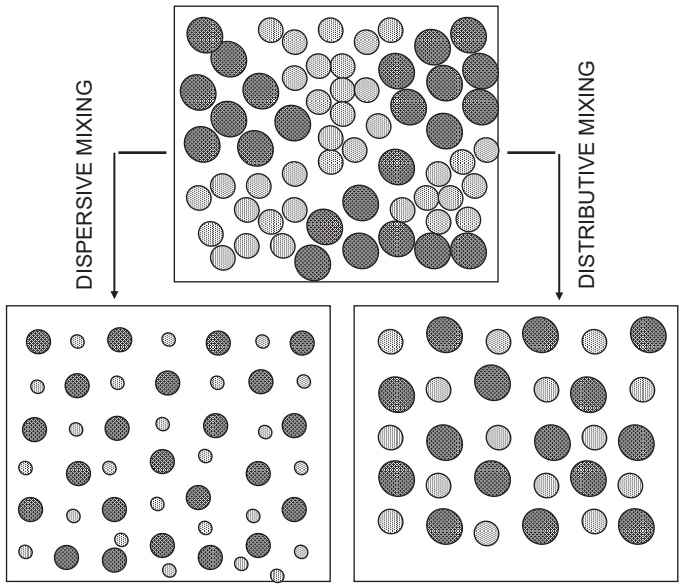

Fig. 5.13 The nature of mixing showing changes during dispersive and distributive mixing

5.3.6.1 Nature of Mixing

Mixing is defined as a process aimed at reducing non-uniformities or gradients in a composition or other properties of materials. When considering mixing results, two aspects are distinguished: distributive mixing and dispersive mixing (Fig. 5.13). While distributive mixing tends to achieve the material homogeneity, dispersive mixing aims at the refinement of structural components. In fact, both kinds of mixing are not physically separable. Dispersive mixing is always accompanied by distributive mixing. On the contrary, distributive mixing is only accompanied by dispersive mixing if there is a solid component, and acting stress exceeds the yielding point. It is understood that stress is required to break down a solid.

During mixing analysis at a general level an assumption is made that mixing takes place in a molten state and fluids exhibit the same viscosity. Granular mixing is essentially different from fluid mixing since during granular flow, collisions of grains are inelastic and friction between grains is able to support loads and distribute stresses. As a result, the granular motion has non-local properties. Contrary to fluid convection, the grains move faster and mix better near the walls of a container.

A thixotropic slurry of a metallic alloy imposes specific requirements on mixing. Thus general mechanisms developed for other materials including polymers are not fully applicable here. Major mechanisms involved are listed in Table 5.2.

Table 5.2 The role of mixing during semisolid injection molding

	Application			Mixing mechanism			
	Molding of a single alloy	Alloy generation	Composite molding	Diffusion	Distributive bulk convection	Extensive laminar	Intensive dispersive
Homogenization of a single alloy liquid matrix	×	×	×	×		×	×
Mixing of two or more liquid matrices		×	×		×	×	
Distribution of a single primary solid phase	×				×	×	
Distribution of two or more primary solid phases		×			×	×	
Distribution of re-enforcement particles within a semisolid slurry			×		×	×	

5.3.6.2 Mixing Quantification for a Single Screw

The mixing process for a screw is considered by determining the velocity profiles within the screw channel. Then the velocity profiles are used to calculate melt deformations. During analysis the common assumptions are that these are Newtonian fluids with components having the same flow properties and a two-dimensional flow pattern with the down-channel and cross-channel flow directions.

The mixing zone in the extruder starts from the plasticizing zone and extends to the screw end. The push side of the flight has greater pressure, and the trailing side of the flight has a reduced pressure. These pressure differences cause the circular flow of the material in the melt pool. According to shear rate distribution down the channel and across the channel, at the bottom the fluid travels in the direction of the barrel, while at the bottom of the channel the fluid travels across the channel (Fig. 5.14). It is expected that the significantly lower viscosity of Mg alloys reduces the mixing effectiveness of the injection screw.

The commonly used measure of mixing is the striation thickness. For a minor component introduced as randomly oriented cubes of height H and a volume fraction of φ the striation thickness *s* is expressed by [3]:

$$s = \frac{2H}{3\varphi\gamma} \tag{5.8}$$

According to equation 5.8, striation thickness is directly proportional to initial domain size of the minor component and inversely proportional to the volume fraction and total strain (γ). The striation thickness reduces rapidly with the shear strain because the orientation of the striation changes with shear strain. As the shear

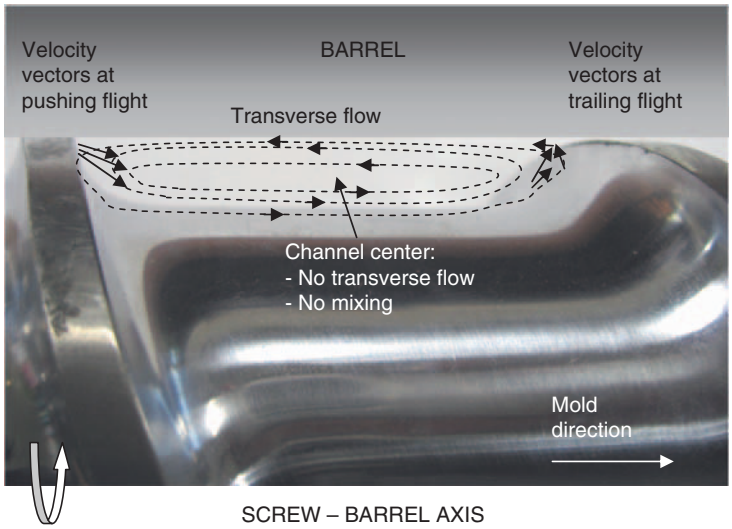

Fig. 5.14 The concept of mixing within the screw channels

increases, the striation orients itself in the flow direction. As a result, increasing mixing time does not substantially improve the mixing outcome.

In summary, non-uniform cross- and down-channel shear strain results in non-uniform mixing in the screw channel. Thus single screw extruders are characterized by poor mixing capabilities. In order to improve the mixing of plastics, special mixing sections are incorporated into the screw length or added at its front. So far, no additional mixers are used for magnesium molding.

5.3.6.3 Homogeneity Changes Beyond the Influence of Screw—Wall Slip Effect

A characteristic feature of metal molding is an injection rate that is substantially higher than that used in polymers. Thus the flow at high rate during the mold filling contributes markedly to the mixing. Since the semisolid alloy represents a two phase conglomerate with different specific gravities, its homogeneity is prone to modification by mechanisms acting after the alloy leaves the screw length. The most important influences are the high flow rate during mold filling, shape and size of flow channels, and the temperature gradient induced by relatively cold walls.

During flow of multiphase conglomerates, mixing is accompanied by segregation. One of several physical phenomena controlling segregation is induced by centrifugal force. When fluid streamlines are curved, heavier particles move out while lighter ones move in. The experimental verification is obtained by filling a spiral mold (Fig. 5.15). A cross section through the flow channel shows that the higher solid fraction is located along the outside ring wall (Fig. 5.16a-c). This behavior is explained by a difference in a specific gravity between solid (1.83 g/cm^3) versus liquid (1.65 g/cm^3) fractions of the AZ91D alloy.

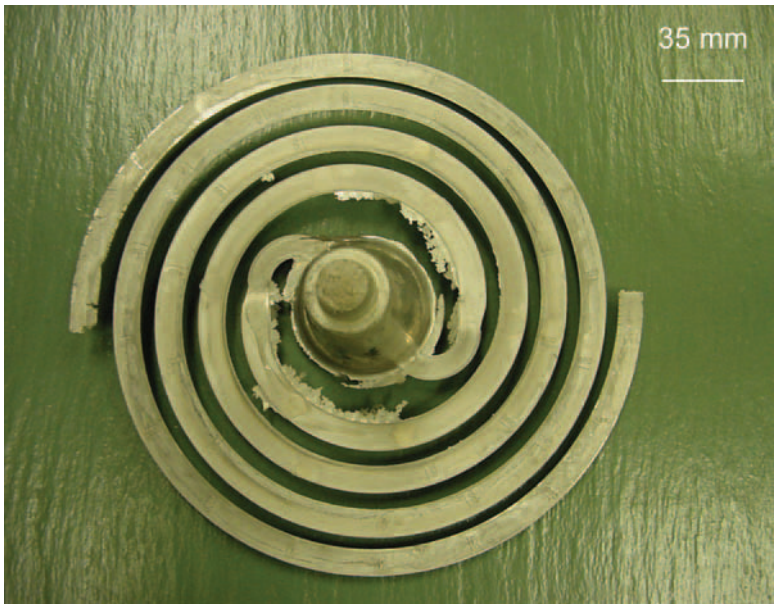

Fig. 5.15 The spiral mold for studying the flow behavior during injection molding and die casting

Another phenomenon, leading to segregation is the *wall slip effect*. It is based on the fact that a flow of dilute or concentrated suspensions through a channel is accompanied by an interaction with the solid walls leading to drastic changes in velocity profiles (Fig. 5.17). As a result a wall force is generated that acts to push the disperse phase away from the wall. Historically the migration and lift during flow were greatly influenced by observations in the 1960s. It was noticed in dilute suspensions of neutrally buoyant spheres, in pipe flows at Reynolds numbers between 2 and 700, that spheres migrated from the wall and centerline and accumulated at 0.6 of pipe radius [4]. The phenomenon was later extended on highly filled suspensions, up to 60% by volume.

The wall slip effect is of particular importance during flow of semisolid metallic slurries within narrow channels, as is the case during thin-wall molding. The wall slip effect during molding is more complex due to a temperature gradient across the flow channel. Namely, relatively cold walls cause instant freezing of the adjacent liquid metal. Even though the force is only active in a thin layer adjacent to the wall, continuous freezing may lead to macroscopic effects extending to thick layers.

A pattern of the solid's distribution is also present in molded parts with different shapes, including complex ones. An example of solid distribution within two thin-wall components with different solid contents is shown in Fig. 5.18a,b. It is clear that for both microstructures the solid particles are concentrated inside while the outer surfaces contain almost exclusively liquid (Fig. 5.19a). Another effect observed is the influence of particle size on their location across the wall thickness. While the larger particles stay near the center, the smaller ones travel closer to the wall surface (Fig. 5.19b). The influence of the particle size is especially evident for

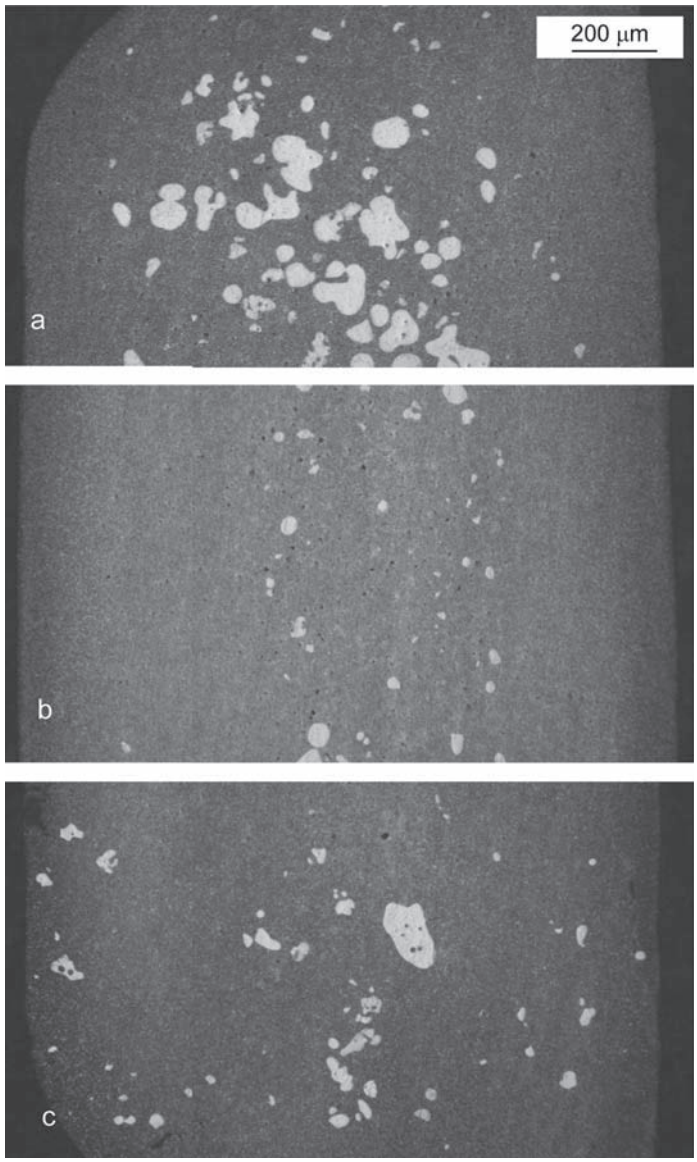

Fig. 5.16 The micrograph of solid distribution on the cross section of the flow channel of the spiral mold: **a** outside; **b** center; **c** inside diameter

slurries with solids having bimodal size distribution. As shown in Fig. 5.20, large particles of the unmelted primary solid are located in the middle of the wall thickness while small globules of the solid freshly precipitated from the melt are arranged closer to the walls. The above findings have engineering importance during the molding of composite materials.

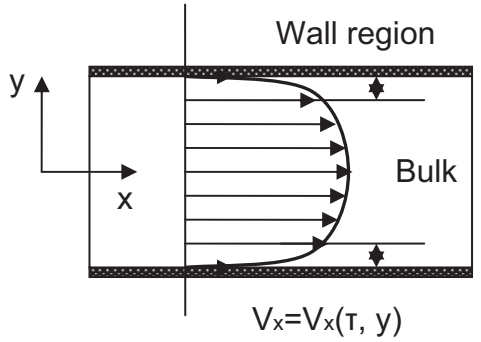

Fig. 5.17 The velocity profile of a slurry close to the wall at constant shear stress

5.3.6.4 Secondary Re-Solidification or Re-Melting

The changes in temperature of the region in front of the screw, i.e., in the barrel head and nozzle, lead to re-solidification or re-melting. Thus, depending on reduction or increase in temperature, precipitation or disappearance of solid particles will occur. Since these phenomena take place after the material leaves the screw, the freshly modified two-phase slurry cannot be mixed by the screw flights. If the reduced or increased temperature in front of the screw is present, the molded component will be filled with the slurry, which contains an accordingly higher or lower solid fraction than that prepared by the injection screw. For large shots and a temperature gradient, the component portions may be filled with slurries of gradually varying solid fractions.

5.4 Function of the Non-Return Valve

The presence of a non-return valve and screw instead of a plunger is one of the key processing differences between cold- or hot-chamber die casting and injection molding. The basic functions of the non-return valve or plunger, i.e., injecting the molten alloy into the mold cavity while preventing it from coming back, are the same for die casting and injection molding. There are, however, differences in how this task is executed in both technologies.

5.4.1 Role of Piston in Die Casting

Sealing the shot sleeve during the injection step is the major challenge of pressure casting methods. The piston is sealed against its sleeve using seal rings. The cold chamber is capable of achieving 30 MPa to 70 MPa pressure during injection. Since the wear degrades the seal, a portion of melt leaks back. To reduce wear, a lubricant is

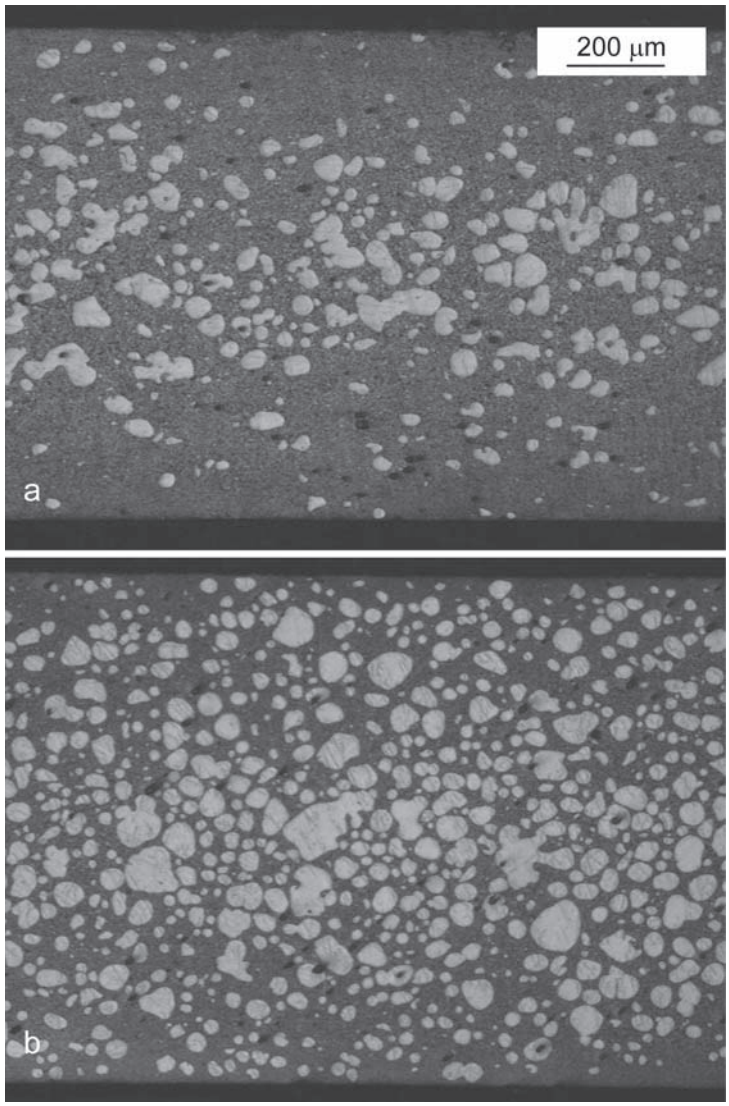

Fig. 5.18 The solid distribution across the wall thickness for low **a** and high **b** solid contents; Mg–9Al–1Zn alloy

applied that contributes to melt contamination. Since the shot sleeve is relatively cold, magnesium that leaks back solidifies instantly and is converted into scrap. The piston in a hot chamber die casting machine is more difficult to seal, which leads to much lower pressure, of the order of 20 MPa to 30 MPa. Injection molding should combine the capability of cold chamber pressure with processability exceeding that of

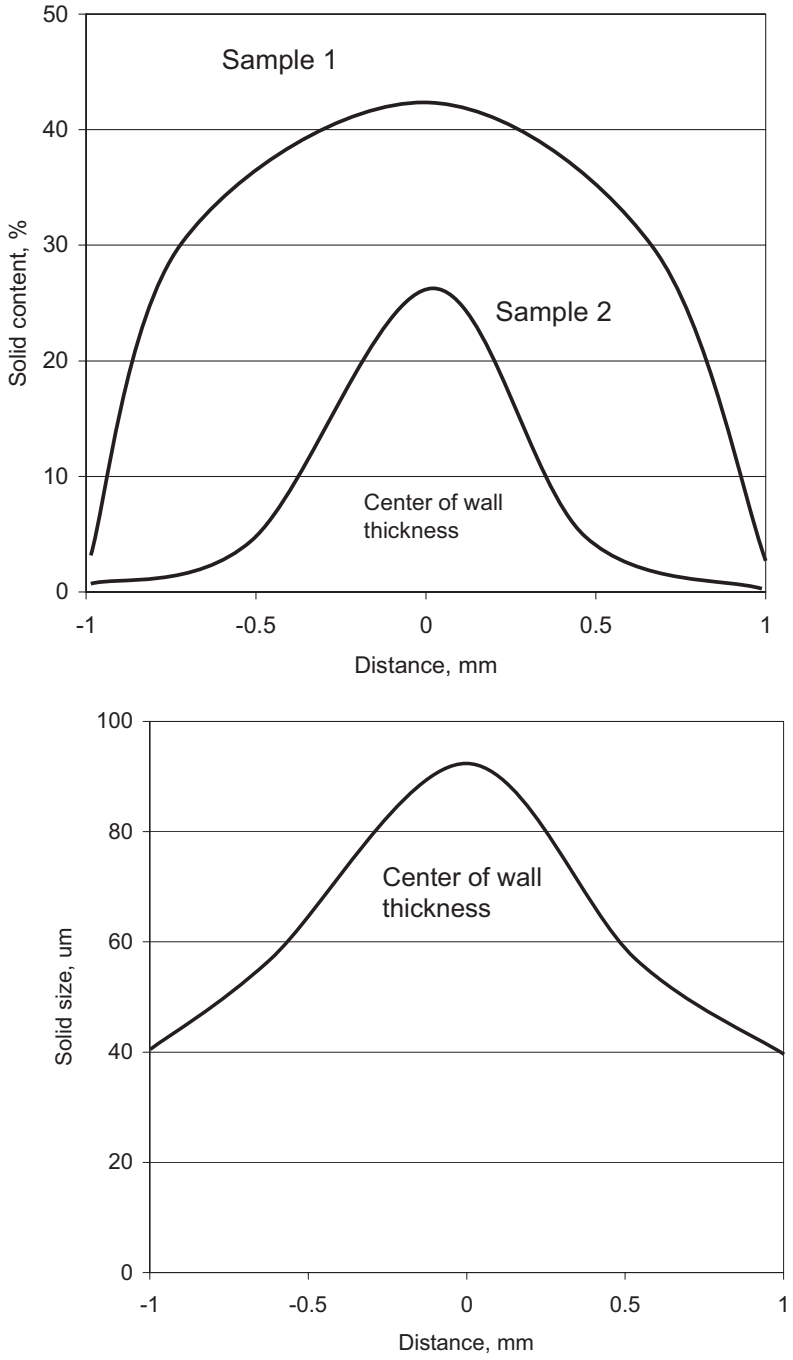

Fig. 5.19 The solid characteristics across the wall thickness: **a** concentration of particles for slurries with high (sample 1) and lower (sample 2) overall solid fraction; **b** solid size versus distance from component's walls for sample 1

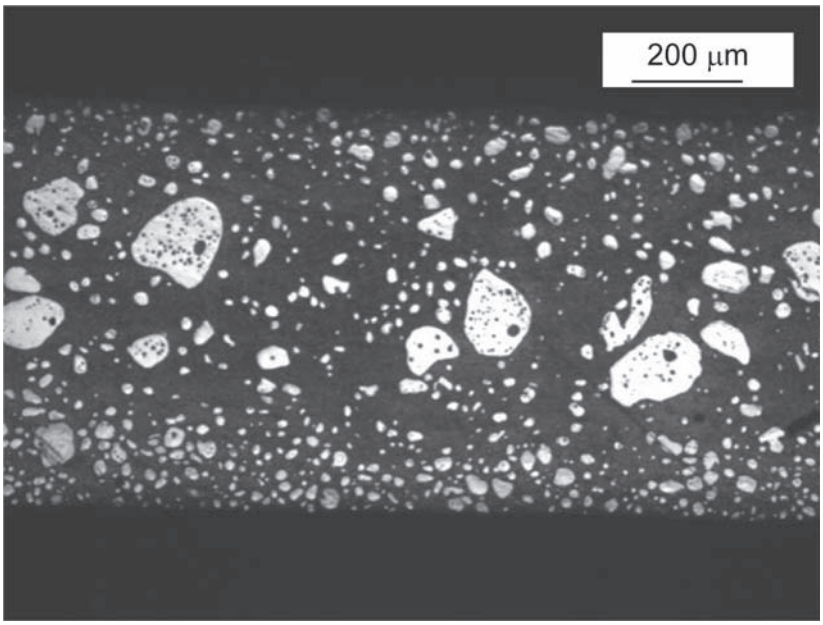

Fig. 5.20 The micrograph showing distribution of a solid across the wall thickness for an alloy with a solid of bimodal size (AM-lite alloy)

the hot chamber. Additional differences come from the semisolid nature of the alloy.

5.4.2 Role of the Non-Return Valve in Plastics Injection

During injection molding of polymers the valve closes the front of the barrel tightly and prevents the material from moving back. The best performance of the non-return valve is when it generates a high-pressure drop over a small cross section, which is closed quickly. The high pressure in front of the non-return valve should be maintained during the injection period. During recovery the opposite is true, and pressure in front of the check valve is lower than downstream of the screw. The high viscosity of plastics enhances the sealing function of the non-return valve.

5.4.3 Role of the Non-Return Valve in Magnesium Molding

Since the reciprocating screw plays the role of a plunger during an injection step, its end is equipped with a non-return valve as it is in plastics molding. The valve's

function is the same as in plastics molding: to allow the material to flow in front of it during the recovery stage. During the injection step, the basic function is to direct the alloy present in the accumulation zone into the mold while preventing it from flowing back into the barrel.

The substantially lower viscosity of a liquid metal does not allow for tight sealing, and some volume of metal flows back. The objective is to keep the leakage at a constant and fully predictable level. A valve back-leakage during magnesium molding has a different meaning than during die casting. Namely, the alloy leaked back is mixed with the hot alloy residing on the screw behind the valve. It does not degrade and is injected during the next shots.

5.5 Nozzle Plug—Principles of Thermal Gating

The nozzle plug acts as a thermal shut off valve, closing the barrel nozzle after injection is completed. It prevents the material's leakage and seals the barrel from the nozzle side to stop air ingress. Otherwise, a violent reaction of air with molten magnesium would occur. To form a plug, front nozzle extension heaters are used (zone 11 in Fig. 5.4). While too high temperature leads to Mg leakage (drooling), too low temperature requires high pressure to release the plug. This pressure reading, called the *plug-blow pressure*, is used, in fact, to tune the nozzle extension temperature.

5.5.1 Formation of the Nozzle Plug

Although the nozzle extension heater allows control of the external heat supplied, the primary factor that affects the plug formation is the intimate contact between the nozzle and the sprue insert. To solidify quickly the large alloy volume, the sprue may be cooled with a circulating medium. The alloy, solidified inside the mold and sprue, acts as a heat sink and removes heat fast through conduction, causing the content of the nozzle end to solidify too (Fig. 5.21). After a part's ejection and separation at the nozzle end, the heat sink through magnesium is not active any longer. Heat is, however, still transferred from the nozzle end to the sprue bushing. As a result, the temperature of the nozzle end increases. Hence, the nozzle heaters should be considered as one factor in a complex chain of the machine's heat management.

Information about the plug's internal structure at the time of injection may be deduced from *ex-situ* examinations of the nozzle core removed after a "freezing experiment." During component molding, the information about a plug's structure may be extracted from examination of the sprue-end. There are similarities between the structure of the sprue-end and the nozzle plug since before solidification they represented the same slurry. They both reside within the end-nozzle section, so their solidification conditions are similar. The only difference is that the plug resides at high temperatures until the next injection.

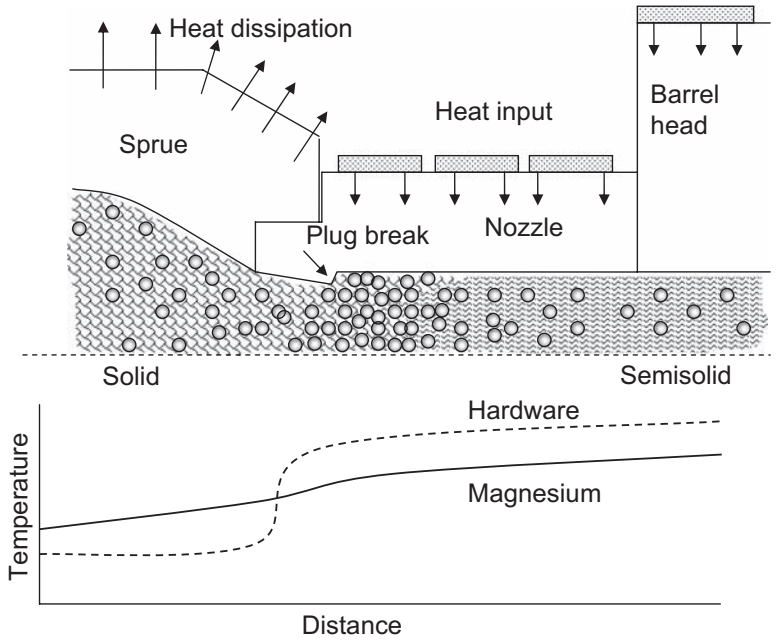

Fig. 5.21 The schematics showing the plug formation. A scenario directly before injection when the mold cavity is empty

The plug's temperature at the moment of the part's ejection is indicated by the fractured surface of the sprue (Fig. 5.22a). While assuring that the part was not ejected from the mold prematurely the sprue-end may be used as a source of information for the nozzle temperature settings. The fracture surface is formed as a result of the separation of the molded component from the plug, remaining inside the nozzle. The excessive temperature of the plug leads to sprue breakage while the material contains a high fraction of liquid (5.22b). Such a plug is unstable. A low temperature at the nozzle end results in a completely solid plug, which is difficult to inject. Therefore intermittent settings should be selected to obtain proper consistency of the plug with the fracture surface shown in Fig. 5.22c.

The plug's microstructure depends on the alloy's temperature before solidification. When an alloy's temperature is between the liquidus and solidus—the plug's structure is thixotropic. Different solidification conditions take place when an alloy reaching the plug region is superheated above its liquidus level. After solidification —the non-thixotropic structure is formed from such a liquid. A detailed description is presented in Chap. 9.

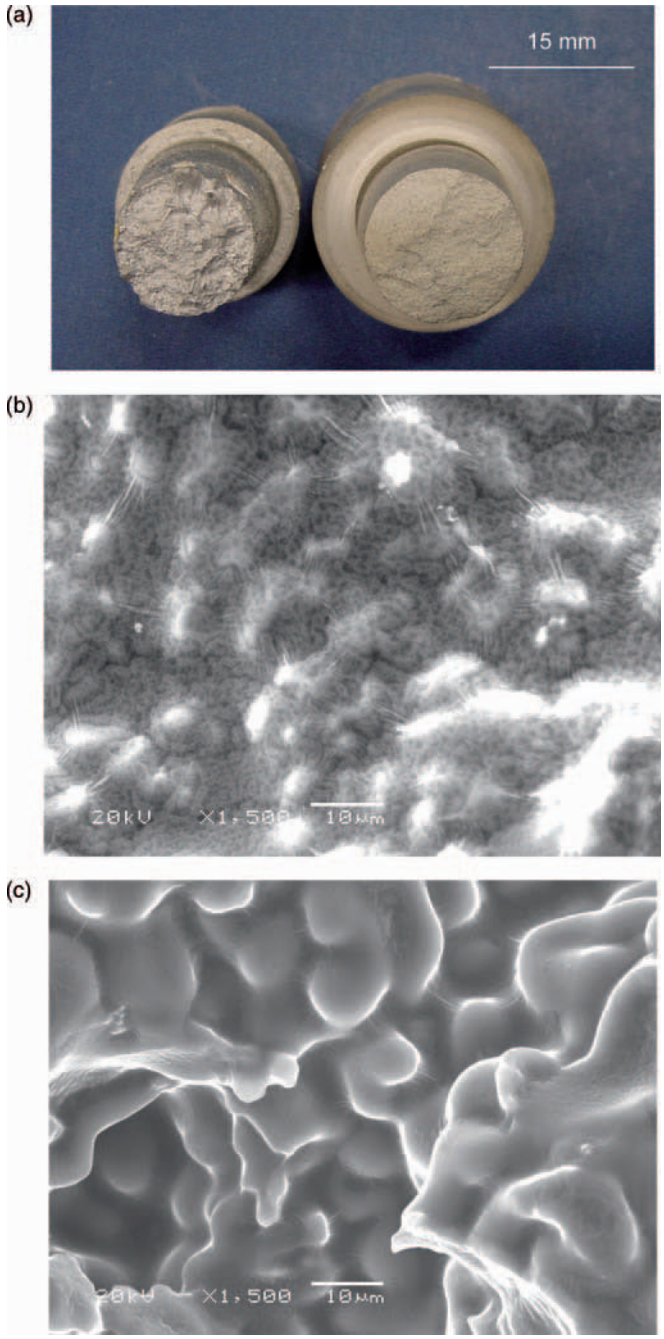

Fig. 5.22 The influence of the nozzle temperature during part release on the sprue fracture morphology: **a** top views of plugs with too high temperature (left) and correct temperature (right); **b** SEM image showing the fracture surface of plug with too high temperature; **c** SEM image of the plug with correct temperature

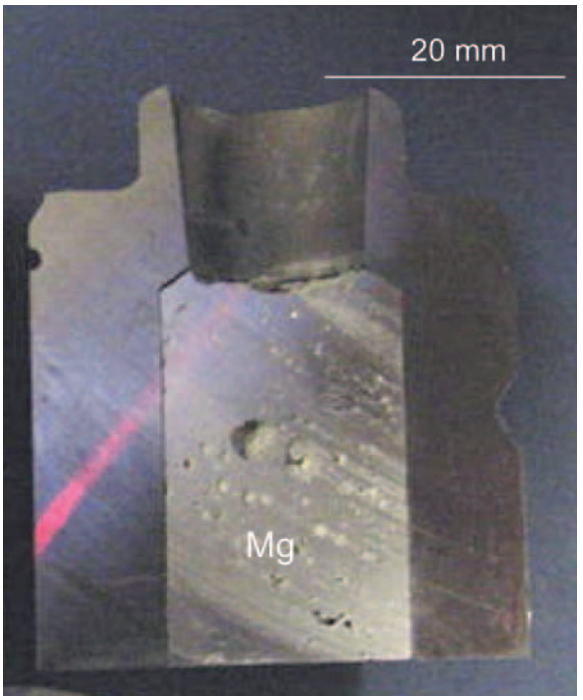

Fig. 5.23 A cross section through the machine nozzle showing the plug held by an undercut within the nozzle channel

5.5.2 Mechanism of the Plug's Release and Disintegration

Between injections, the plug is held by an undercut, made inside the nozzle channel near its exit, which assures that the plug is not released unexpectedly without applying pressure (Fig. 5.23). In order to execute injection, pressure is applied to the melt residing in front of the check-valve. The approximate values for the plug blow pressure are between 20 and 60 MPa. The structure of the plug affects its release behavior. Hence, a plug with a thixotropic structure is very easy to deform and pass through the undercut inside the nozzle after it is preheated to enter the semisolid range. To soften the plug with a non-thixotropic structure, substantial heating would be required to achieve the high liquid fraction that allows the alloy to flow. Usually, therefore, the plug is released as a solid with partially molten outer surface, which remains in contact with the nozzle walls.

5.5.3 Plug Nature During Induction Heating

There are concepts to explore induction heating to control the plug formation and release. According to the principle of induction heating, faster heat response should allow melting the plug to a greater extent within its volume by a direct heat transfer to the plug itself,

not through the nozzle material, as is the case for conventional heating. This effect is limited, however, due to the non-magnetic (diamagnetic) nature of magnesium. In practice, during induction heating as well, the plug is released before it is completely melted. Another challenge of induction heating is that the amount of heat transferred should be precisely controlled to prevent overheating or even melting the nozzle material.

5.5.4 Slurry Transfer to the Mold Using Hot Sprue

An injection molding system allows for significant improvement in the slurry transfer from the barrel to the mold gates by the application of hot sprue. The hot sprue conveys the melt to the gate during injection and maintains it at processing temperatures between injection cycles.

5.5.4.1 Thermal Gating During Molding with Hot Sprue

The hot sprue maintains the melt, which is ready for injection close to the mold. A presence of hot sprue leads to a smaller diameter of the nozzle exit channel and, in turn, a smaller plug diameter. In order to connect the hot sprue with the machine nozzle, an additional thermal seal is required, which is created inside the undercooling zone, thus forming an additional plug. It is clear that to execute injection and open the flow channel for the shot volume, both plugs have to be released.

The hot sprue introduces additional temperature control zones, as indicated by the control panel (Fig. 5.24). More accurate temperature tuning is therefore required to control the plug blow pressure. When replacing the conventional cold sprue with hot sprue, the size of the plug catcher is reduced (Fig. 5.25a,b), which means that the plug volume it can accommodate is smaller. This is in response to the smaller diameter of the hot sprue bushing and exit channel. The importance of the plug's structure during molding using hot sprue with a plug catcher is similar to that discussed earlier for the conventional cold nozzle. During direct gating the plug catcher may be eliminated completely (Fig. 5.25c). In this case, all the melt flows through the mold gate so the plug has to disintegrate into tiny particles to prevent blocking the gate.

The plug existence and thermal gating are unique for injection molding. For hot chamber die casting, the melt is retracted during each cycle. For a cold chamber die casting machine there is no sprue, but an excess of ladled metal called "biscuit" remains in the shot sleeve after injection is completed. It is part of the shot, and after solidification is removed along with the casting, runners and overflows. An example of the cold chamber "biscuit" is shown in Fig. 5.25d.

5.5.4.2 Processing Benefits of Using Hot Sprue

The first benefit of hot sprue is a reduction of the flow distance between the melt or slurry and the mold gates, thus minimizing a drop in temperature. Preventing heat loss is of special importance for magnesium alloys, known for their low heat

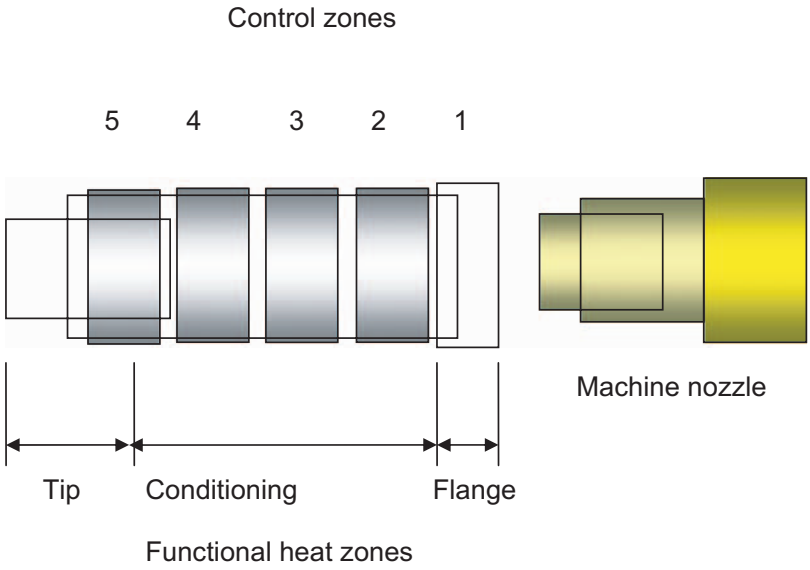

Fig. 5.24 The arrangement of control and functional heat zones along the magnesium flow path through the hot sprue

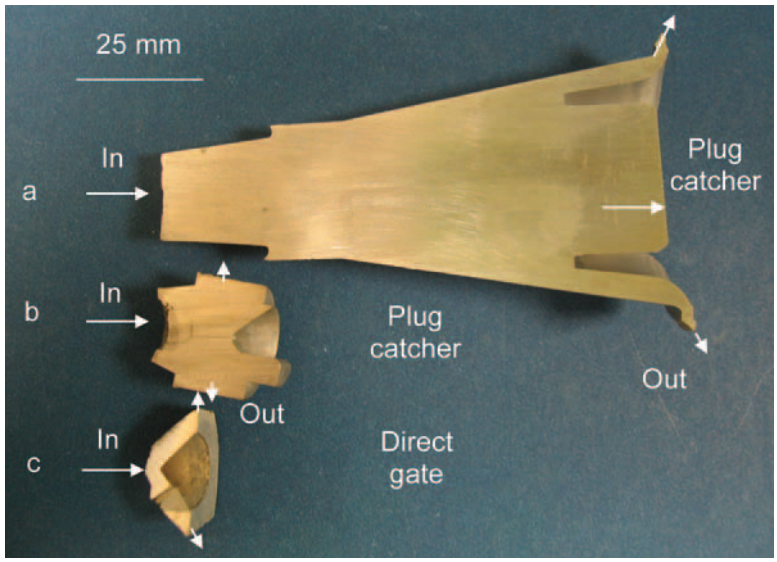

Fig. 5.25 The size of the plug catcher in injection molding: **a** cold sprue; **b** hot sprue with partly eliminated plug catcher; **c** hot sprue with completely eliminated plug catcher; **d** die casting "biscuit" with diameter of 63 mm and thickness of 20 mm—excess of ladled metal remaining in the shot sleeve of a cold chamber machine

Fig. 5.25 (continued)

capacity and tendency to quick solidification, which disrupts the complete filling of the mold. This factor is vital for semisolid processing, which requires a certain solid content and does not allow for the compensation of potential heat losses using melt overheating.

There are other processing benefits of hot sprue, including reduced shot size which, in addition to the lower alloy consumption, allows for a decrease in the clamp tonnage required. Further, the hot sprue reduces the recycling cost, and alloy re-heating energy, it shortens the cycle time, requires less die lubricant and improves the overall machine performance. Examples of parts manufactured with cold and hot sprue are shown in Fig. 5.26 along with benefits quantified in Table 5.3. It should be noted that after applying the hot sprue for a relatively large component with a rather small weight reduction, there are substantial savings caused by overall yield improvement.

A separate benefit of hot sprue is the possibility of *direct gating*. Although only one gate, located centrally or shifted from the injection nozzle line is allowed, the

Fig. 5.26 The examples of components, molded with cold and hot sprues: motorcycle bracket, snowboard boot binding, gear case cover and power tool housing

Table 5.3 Benefits of application of the hot sprue for molding of Mg–Al–Zn alloys

Part name	Weight reduction, %	Cycle improvement, %	Yield improvement, %
Motorcycle bracket	6	N/a	25–90
Snowboard binding	20	36	42
Gear cover	29	34	20
Power tool housing	22	42	23

improvement is substantial. Two examples of thin wall components are shown in Fig. 5.27 where the side gating and long runners were eliminated. Moreover, for the feature tool (Fig. 5.27a) the plug catcher was completely eliminated, and for the laptop case (Fig. 5.27b) highly minimized. The flow distance from the gate to the furthest point within components is reduced by a factor of at least two.

5.5.5 Slurry Distribution to the Mold Using Hot Runners

The purpose of hot runners is to inject molten metal directly into the part at multiple locations.

Fig. 5.27 The examples of thin wall components injection molded through direct gating with a hot sprue: **a** feature component, a concave shape beneath the sprue indicates no plug catcher (inset); **b** laptop housing, a flat area beneath the sprue indicates very small plug catcher (inset)

5.5.5.1 Exit Plug and Thermal Sealing in Hot-Runners

The role of the plug as a thermal gate changes substantially within a hot runner. Instead of one, there are multiple nozzles, each of them containing its own exit plug. To fill the mold uniformly, the release of plugs should be synchronized. In principle, there may be a small plug catcher for each drop. If the plug catcher cannot be placed because of the component's design, the released plug has to pass through the mold gate and flow into the part (earlier, Fig. 5.25c). It is obvious that under such conditions the semisolid nature of the plug, diluted by slurry that follows it, is required. The solid plug will block the mold's gate, leading to incomplete filling of the cavity.

As was the case for hot sprue, also within the hot runner there are multiple connections that require a thermal seal. After applying the injection pressure, seal plugs are released and displaced to hotter locations. From a heat management point of view, the hot runner with direct gating and modular connections based on thermal sealing represents a complex design system.

5.5.5.2 Processing Benefits Of Using Hot Runners

The processing benefits of a hot runner exceed those for hot sprue. The most important one is the capability of molding parts, which, due to the shape, size or combination of both, cannot be cast by conventional techniques. The multiple injection points shorten the alloy flow distances, thus allowing the molding of parts with larger dimensions. A first step in implementing the hot runner is injection from two directions through separate sprues and cold runners (Fig. 5.28a). Although this solution reduces the flow length there is no benefit of material saving. In fact, an additional sprue increases the material consumption. Both benefits are achieved while injecting directly into the part, and an example of an engine valve cover with a weight of 1 kg, molded with two-drop hot runners is shown in Fig. 5.28b. In this figure, the flow pattern of fully molten AZ91D alloy is also shown, as revealed by the flow simulation, performed using Flow-3D software (Flow Science).

The advanced application of the hot runner is shown in Fig. 5.28c (USCAR). An automotive component with a weight of 3 kg and a length of over 1 m is very challenging to manufacture using conventional casting. The single casting will replace the conventional multi-piece structure. An application of the hot runner allowed injection into four different locations, thus reducing the flow length and simplifying the geometry of the flow paths for the molten alloy.

5.6 Mold Processing

A distinct processing stage, which takes place inside the mold, covers the formation of net shape components using a metallic slurry or melt prepared within the barrel. It consists of filling the mold cavity, followed by the solidification and ejection of

the component. The key objective of mold processing is to fill the cavity completely before the metal solidifies. The mold processing is fully synchronized with the stage of slurry or melt preparation.

5.6.1 Fluidity of Molten Metals

Fluidity of a molten alloy is defined as its ability to flow along a channel before being stopped by solidification. It is an important property of an alloy since it affects the mold filling and resultant part quality. Two tests are commonly used to measure fluidity:

(i) the spiral mold test as an indicator of the flow distance;
(ii) the Ragone test as an indicator of metal pulled up by a tube attached to vacuum [5].

5.6.1.1 Role of Surface Tension

Factors affecting fluidity that relate to the molten alloy include:

(i) viscosity;
(ii) surface tension;

Fig. 5.28 The application of hot runners in magnesium molding: **a** an automotive bracket injected from two directions through cold sprues and cold runners

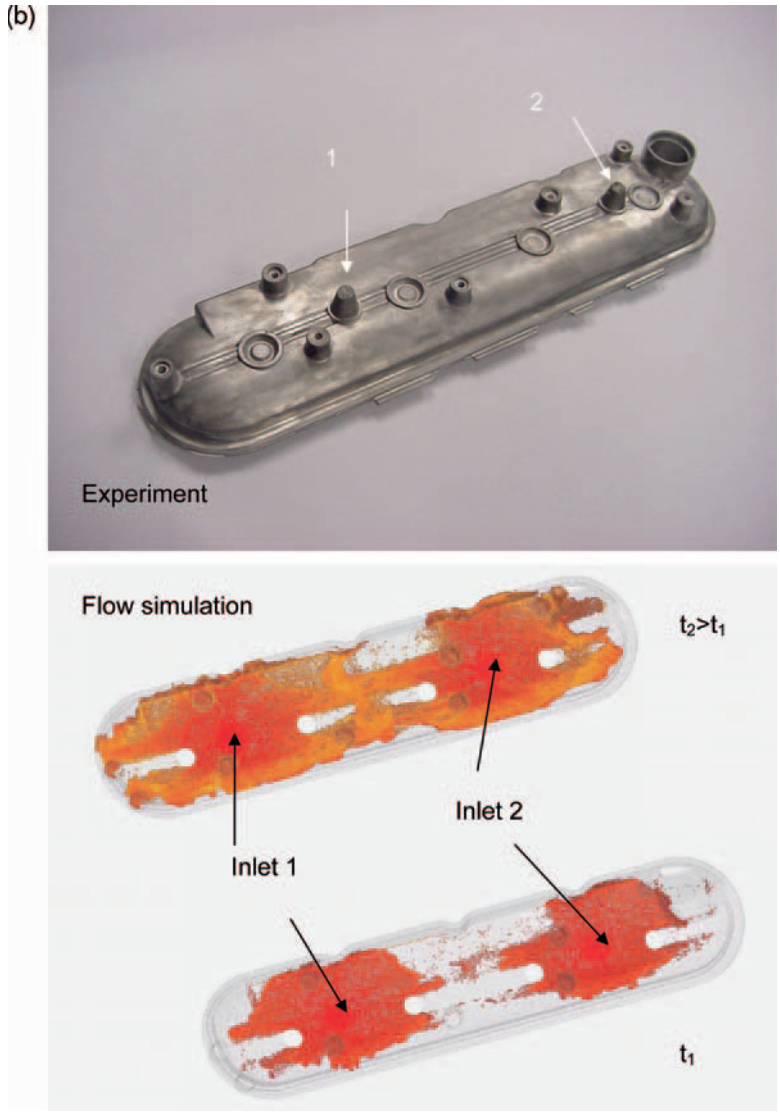

Fig. 5.28 (continued) **b** valve cover molded by direct injection using 2-drop hot runner along with a flow simulation of filling pattern with molten AZ91D; **c** automotive component molded by direct injection using 4-drop hot runner

(continued)

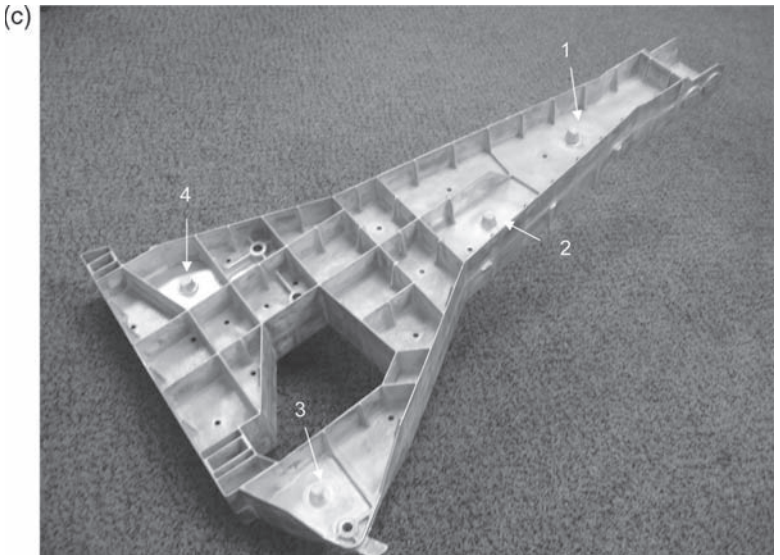

Fig. 5.28 (continued)

(iii) cleanliness;
(iv) solidification range of the alloy;
(v) latent heat of fusion;
(vi) thermal diffusivity.

The viscosity of metals is a multiple of that of water and the kinematic viscosity, understood as the viscosity divided by the mass density, is less than that of water. As a result, the influence of viscosity on metal fluidity is not very well pronounced. When a molten alloy does not wet a mold, filling condition is fulfilled when the pressure at the interface is higher than the resistance caused by surface tension [6, 7]:

$$p_i - p_e > \frac{\gamma}{r} \tag{5.9}$$

where:

γ – the surface tension;
r – half thickness of the mold cavity;
p_i – pressure inside the molten alloy as a sum of the metallostatic pressure and the atmospheric pressure;

p_c – cavity pressure as a sum of atmospheric pressure and the back pressure due to residual gases present inside the mold.

An analysis of the above equation indicates that gases generated within the mold increase back pressure and prevent metal from flowing. To improve mold filling characteristics, gases should be evacuated by appropriate venting.

Factors that reduce metal cleanliness, such as dissolved gases, intermetallic precipitates or non-metallic inclusions, reduce fluidity. Surface oxide films, representing a special kind of impurity, increase surface tension, also causing a reduction in fluidity. Surface tension of metals increases with the melting point and decreases with an increase in temperature. The influence of higher surface tension is to increase the pressure required to force a metal into the narrow channels. Fluidity is best for pure metals and eutectic compositions. For alloys, the fluidity is inversely proportional to the solidification interval. This finding, evaluated mainly for gravity casting, is questioned for die casting conditions where the opposite behavior is reported [7]. Namely, for a given superheat, fluidity increases with the decreasing solidus temperature. The reason for increased fluidity is that during high pressure die casting, an alloy can flow at high solid fractions, and flow stops at temperatures closer to the solidus level.

In addition to factors related to the cast alloy, fluidity is affected by casting parameters, including level of superheat, mold properties such as thermal conductivity and surface roughness.

5.6.1.2 Fluidity and Solidification Time

The influence of fluidity on solidification can be evaluated from the solidification time equation. For a pure metal, poured at its melting temperature, the solidification time t_f is expressed as [7, 8]:

$$t_f = S^2 \frac{\pi}{4} \left(\frac{\rho_s H_f}{T_M - T_o} \right)^2 \frac{1}{K_m \rho_m c_m} \tag{5.10}$$

Where:

S – solidified thickness;
ρ_S – density of solid metal;
H_f – enthalpy of fusion;
T_M – melting point;
T_0 – initial mold temperature;
K_m – thermal conductivity of the mold material;
ρ_m – density of the mold material;
c_m – specific heat of the mold material.

The above equation shows that fluidity increases with the solidification time. Solidification time is related to quantity of heat requiring removal during solidification, i.e., enthalpy of fusion. Moreover, a decrease in thermal conductivity, specific heat capacity or density of the mold material improves fluidity.

5.6.1.3 Fluidity of Magnesium Alloys

The general rules established for other metals are also effective for magnesium. Thus alloying elements reduce the fluidity and the best flow is observed for eutectic compositions. For Mg–Al alloys, fluidity is adversely proportional to the freezing range. During experimental verification of the filling capacity of a plaster mold using vacuum assistance, the influence of section thickness, position of casting in the mold, in addition to the mold and casting temperatures, were examined. A simple model led to the following relationship, expressing the flow length L_f [7]:

$$L_f = 14.25 D^{0.96} \frac{t^{0.80}}{d^{0.19}} \left(\frac{\Delta T_S}{T_C - T_M} \right)^{1.24} \tag{5.11}$$

where:

D – height of the metal head;
d – distance from the flask walls;
t – section thickness;
ΔT_S – superheat defined as T_C (temperature of the liquid metal) minus T_L (liquidus temperature);
T_M – initial mold temperature.

According to the above relation, increasing the metal head improves the mold filling. Also, higher temperatures of the poured alloy and mold retard solidification, thus improving cavity filling.

5.6.2 Mold Filling Time

The mold filling time provides a base for designing gating systems and establishing injection parameters, including the screw speed, mold temperature, spray and cycle time. It is defined as the time at which the molten metal arrives at the gate until the cavity and overflows are completely filled. The step of holding, which follows mold filling, is not included. A number of relationships were proposed for die casting to calculate the fill time for components with different wall thicknesses. All of them were derived from the basic principle that the liquid metal loses its heat during flow into the mold cavity. Accordingly, the amount of heat available within the metal, divided by the rate of heat transferred to the mold during its filling, gives the maximum filling time.

5.6.2.1 Gating Equation for Die Casting

The subject of calculation of the amount of heat available H_A, making up the first component of the gating equation, has been researched over the years. After a number of verifications, the following formula was established [9]:

$$H_A = \left\lfloor \left(T_i - T_f + SZ \right) C_p \right\rfloor M \tag{5.12}$$

Where:

T_i – alloy temperature at the gate;
C_p – specific heat of the alloy ;
M – mass of the casting;
T_f – minimum flow temperature;
S – solid content allowed in the alloy at the end of filling;
Z – coefficient of unit conversion from temperature to %.

The second component of the gating equation represents the rate of heat transfer from the molten metal to the mold (R_H) and is expressed by the following equation:

$$R_H = C_l A\left(T_i - T_d\right) \tag{5.13}$$

where:

T_i – alloy temperature at the gate;
T_d – mold surface temperature before alloy injection;
C_l – coefficient;
A – surface area of the mold.

According to [10], the metal is near the minimum flow temperature for much of the cavity filling time. First, the metal temperature drops to the liquidus almost instantly after the metal enters the die. Then, as it flows across the cold die, its temperature drops rather uniformly to the minimum flow temperature. For practical purposes, the minimum flow temperature is used for T_i in the equation (5.13). The die surface temperature is defined at the time when the metal reaches it. Therefore, the die temperature used in the equation (5.13) is considerably higher than that normally measured.

The basic assumption during an assessment of the mode of heat transfer is that the mold acts like an infinite heat sink [9]. It is further assumed that the heat from the center of the metal flow stream had to be conducted through one half the thickness of the casting to get to the die surface. The center of the flow stream preserves the molten metal ladling temperature. As a result, there is a temperature gradient from that center's temperature through the half thickness to a temperature near that of the die at the cavity surface. The above model assumes a laminar flow during mold filling. If a turbulent flow is developed the metal is at the same temperature at the cavity wall and at the center. The total resistance to heat flow is the sum of the convection coefficient, the lubricant–oxide layer conduction coefficient and the conduction coefficient of the die. Further, the effect of the convection coefficient is so small that it could be ignored. It was stated earlier that the conduction of the die was insignificant. That leaves the lubricant –oxide boundary conduction coefficient as the dominant resistance to heat flow.

After combining formulas (5.12) and (5.13) the final gating equation that specifies the maximum fill time t takes shape as follows [10]:

$$t = k\left(\frac{T_i - T_f + SZ}{T_f - T_d}\right)w \tag{5.14}$$

Where in addition to symbols explained in 5.12 and 5.13:

k – empirically derived constant in s/cm, related to the die material;
w – casting's wall thickness.

5.6.2.2 Application of Gating Equation for Semisolid Processing

The gating equation was originally developed for die casting overheated molten alloys. An attempt at its application to semisolid processing requires a correct interpretation of alloy temperature at the gate, T_i, minimum flow temperature, T_f, and solid content at the end of mold filling f_s. During semisolid molding, the temperature of the molten metal as it enters the mold is significantly lower than that used in die casting, which reduces T_i. At a minimum flow temperature, T_f, the alloy contains the primary solid introduced during injection and solid structures formed during solidification after flow through the mold gate. The early literature on magnesium molding portrayed the solidification of semisolid structures as rheocasting where the low minimum flow temperature was achieved by continuous agitation of the solidifying alloy. Such an approach does not resemble solidification conditions of injection molding where no agitation is applied after the semisolid slurry is injected into the mold. The term f_s will contain the primary solid present before injection, increased by the secondary solid formed during solidification inside the mold.

An example of a graph showing mold filling time versus component wall thickness is shown in Fig. 5.29. For solid contents of 30%, the reduction in filling time of a 2 mm thick section is almost 50%. It should be noted that a similar graph, created for a completely molten alloy shows a different tendency.

5.6.2.3 Gate Velocity

The gate velocity is understood as the speed at which molten metal moves through the gate opening. At optimum conditions atomized flow from the gate is required. For lower speeds a continuous jet or coarse particle flow takes place. According to [10] the fine atomized mist flow is achieved after:

$$D\rho v_g^{1.71} \geq J \tag{5.15}$$

Where:

D – gate parameter;
ρ – density of the molten metal;
v_g – gate velocity;
J – atomization value, J for Mg equals 360 for v_g = 42 m/s [10].

Typical values of v_g for Mg are 40–85 m/s, while for Al – v_g equals 25–40 m/s

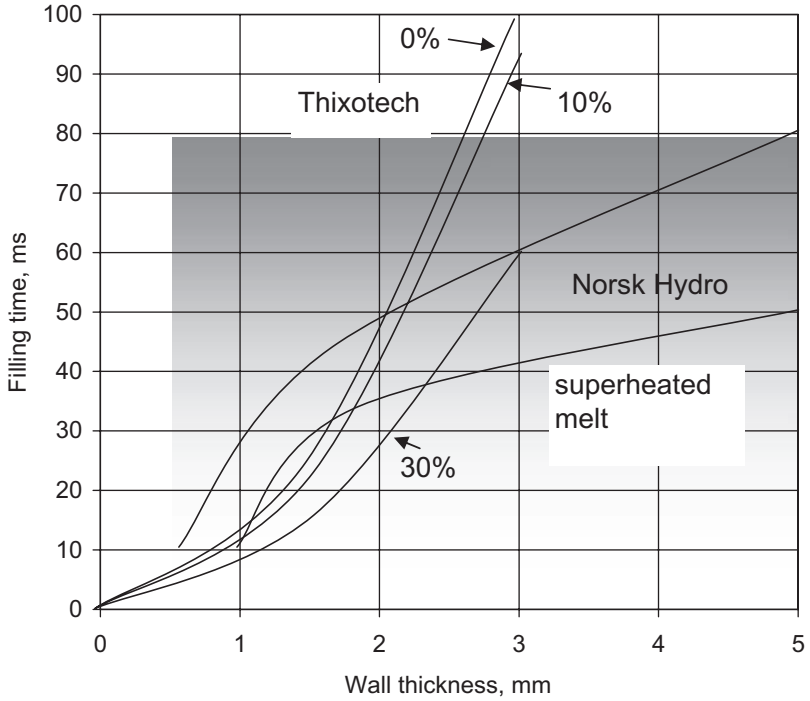

Fig. 5.29 Mold fill time during injection molding of magnesium alloys depending on wall thickness and initial solid content (Thixotech Inc. and Hydro Magnesium Inc.)

5.6.2.4 Flow Modes of Metals

The mode of fluid flow is affected by the velocity and its physical properties. Two types of flow are distinguished: laminar and turbulent. The criteria for their existence are controlled by the Reynold's number:

$$Re = \frac{Dv\rho}{\eta} \tag{5.16}$$

Where:

D – diameter of the cylinder through which the fluid is flowing or in general the geometry of the conduit;
v – mean linear velocity;
ρ – fluid's density;
η – viscosity of the fluid.

The Reynold's number measures the influence of inertial forces versus drag or viscosity forces. Small Reynold's numbers indicate that flow of fluid is dominated by viscous forces and is laminar. At very high Reynold's numbers (> 1000), inertial forces are more important and fluid flow becomes turbulent.

While estimating the influence of the flow mode on the mold filling behavior, two issues should be separated: the bulk flow mode and the geometry of the flow front. The difference was pointed out between them with the geometry of the flow front having a more pronounced effect on casting integrity [11]. It should be noted that the flow at the gate usually differs from the flow inside component with complex geometry.

5.6.2.5 Metal Injection Pressure

In order to push the molten metal through the gate, a certain pressure is required. The discharge pressure (p) is calculated using Bernoulli's equation:

$$p = \frac{\rho}{2g}\left(\frac{v_g}{c_d}\right)^2 \tag{5.17}$$

where:

ρ – metal density;
g – gravity constant;
v_g – gate velocity;
c_d – coefficient of discharge that covers losses from various sources and has values from 0.6 to 0.7 (no units).

The above equation is used to determine the pressure required for achieving the specific flow rate. The metal pressure is proportional to the gate velocity.

5.6.2.6 Process Operating Window

The capacity of an injection system in the die casting area is described using metal pressure versus flow—the so-called PQ^2 diagram. The PQ^2 diagram allows an adjustment of the process for machine-die (mold) combinations.

The pressure (p) on the metal and the hydraulic system is proportional to the square of the injection velocity and therefore the volume flow rate (Q). The machine power line is a straight line with one end representing static metal pressure and the other end showing the maximum machine performance, i.e., dry shot speed. The line with a positive slope is a measured relationship of pressure to flow rate for the particular casting and gate. The line movement, accompanying changes of certain parameters, is indicated in Fig. 5.30. The area on the PQ^2 diagram, located inside the calculated lines, is called a process window.

5.6.3 Mold Temperature

The mold temperature affects the cavity filling characteristics and solidification structures. A higher temperature delays solidification and thus increases the flow distance. It also improves filling, allowing a slower injection speed and extension of the

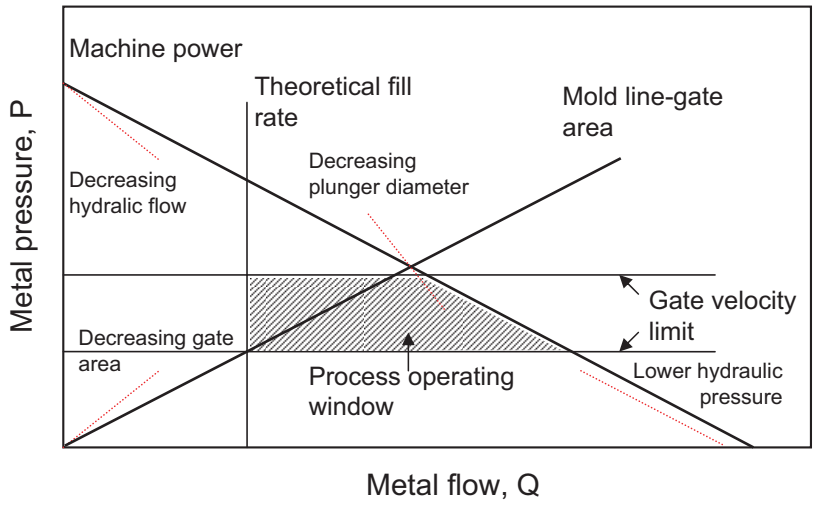

Fig. 5.30 The schematics of the PQ^2 diagram [10]

mold life. On the other hand, high mold temperature requires a longer cycle time, which reduces the production rate. The high mold temperature also reduces the solidification rate and phase transformations during cooling in the solid state. Thus the structures generated will have coarse features that generally reduce strength properties.

It is clear that the mold should be heated before molding begins. This is achieved by circulating heated oil through internal passages of the mold. During continuous molding, flowing metal heats up the mold, and the oil may play the role of coolant. The temperature distribution on the mold surface is further controlled by spraying functions, described below.

5.6.4 Mold Spraying Function

Mold spraying is the major difference between polymer and metal molding. When describing mold spraying, the functions of lubrication and cooling are only quoted. In practice, however, mold spraying is more complex and involves other functions as well:

(i) allowing the part release from the mold;
(ii) removing heat from the mold surface;
(iii) preventing soldering;
(iv) improving temperature uniformity on the mold surface;
(v) reducing thermal fatigue by insulating the steel surface;
(vi) enhancing metal flow and detail fill;
(vii) improving corrosion protection for mold, part and machine.

5.6.4.1 Types of Mold Lubricants

The mold lubricants are emulsions of petroleum or synthetic oils, fatty acids, soaps, glycols, sulfonates, silicones and surfactants dispersed in water. Mold spraying agents are diluted with water, which plays the role of lubricant carrier. After reaching the mold, the carrier evaporates, leaving the lubricant layer on the surface. The surfactans reduce the surface tension, allowing the agent to be spread uniformly over the mold surface and providing better wetting. To increase the adhesion of the deposited film and enhance its integrity a mineral or synthetic wax is added. The task for oils is to provide a molecular attraction of the film to the mold surface and, after burning, to generate isolative carbon film. Silicon is added to increase the heat resistance of the film up to 250 °C. After contacting molten metal, silicon decomposes, forming a film of silicon oxide with anti-sticking properties.

The lubricant's adhesion to the mold surface and the heat transfer coefficient are affected by a dilution ratio with water, spray mist density, spray pressure and mold temperature [12]. Of those factors, the mold temperature has a particular role. Too cold a mold surface does not lead to vaporization of water, which instead washes the mold surface, taking the lubricant with it. On the other hand, too high a temperature creates a vapor barrier that prevents spray from reaching the mold surface and depositing on it. Thus for proper lubrication, optimum mold temperature is required.

The cooling action of water contributes to the thermal fatigue of a surface layer of the mold material (Fig. 5.31). To eliminate this phenomenon, dry lubricants were developed. Since dry lubricants do not contain water, the internal mold cooling system must be re-designed. In the case of magnesium, however, the cooling action of the spray is not critical. Due to its low specific density, the heat transferred to a mold by magnesium is substantially lower than heat transferred during processing of Al. When combined with a further reduction of heat by a low temperature in the slurry, an opportunity is created for dry lubricants.

5.6.4.2 Mold Temperature Change During Spraying

During the spraying of the mold with water based lubricant, the higher liquid flux density results in a higher heat transfer coefficient (Fig. 5.32) [13]. For a given spray flux density, for surface temperatures below 250 °C, the heat transfer coefficient increases with an increase in the surface temperature. At temperatures above 300 °C, the heat transfer coefficient decreases with increasing surface temperature. This behavior is caused by a variation in the effectiveness of heat removal, which depends primarily on the temperature. In general, there are four modes of heat transfer during spray cooling. During the first mode, the liquid convective transfer occurs where heat flows away from the surface into the liquid. As the surface temperature exceeds the boiling point, bubbles form on the surface, resulting in increased heat transfer. Further increase in temperature intensifies the bubble formation and nucleation of the vapor film. This decreases the heat transfer. When the temperature is very high, a vapor film with insulative properties is present permanently, decreasing

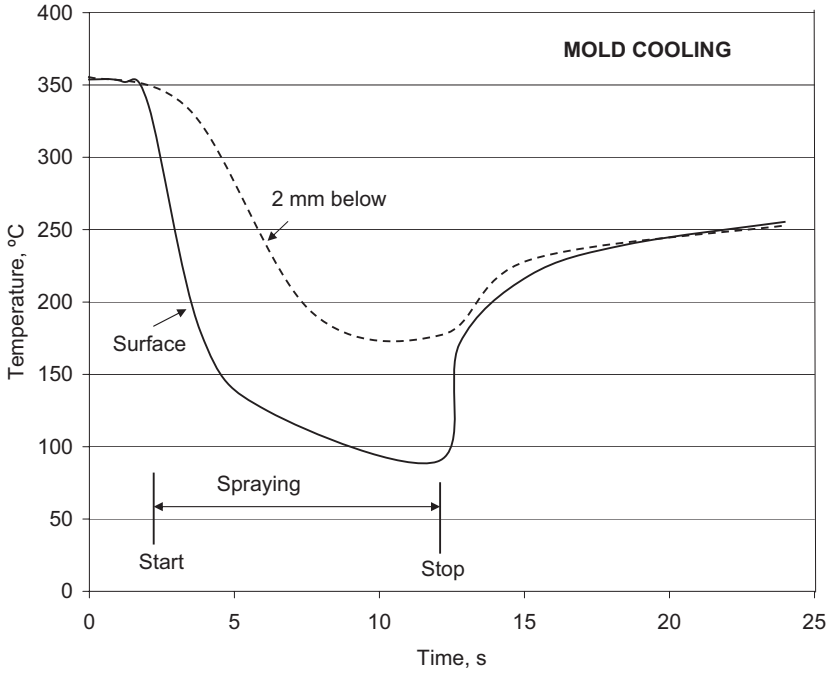

Fig. 5.31 The change of mold surface temperature during spraying [12]

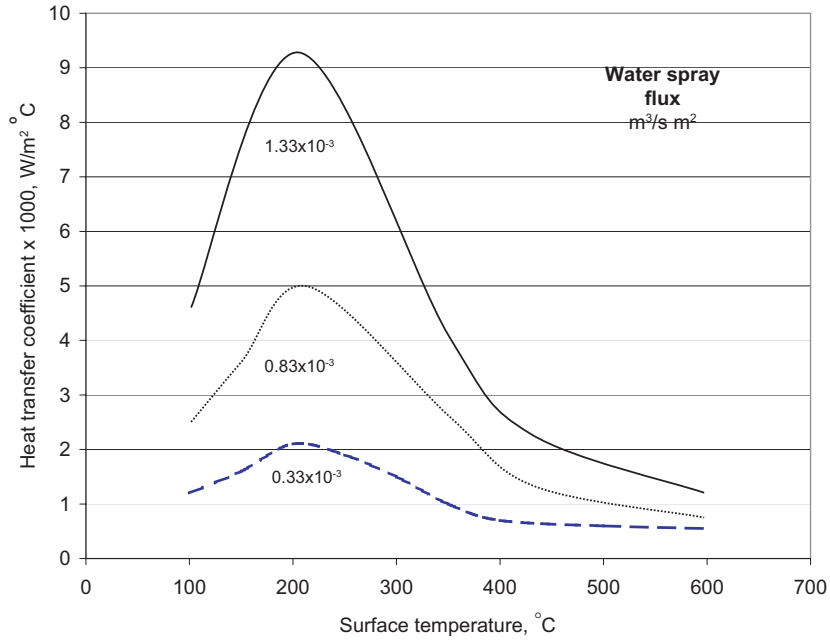

Fig. 5.32 Spray characteristics: heat transfer coefficient [13]

the heat flux to the minimum level. The steam blanket preventing film deposition is called the *Leidenfrost effect*.

An essential feature of a lubricant application is its atomization, which refers to a flow regime where a liquid jet of die lubricant disintegrates into a dispersion of liquid droplets suspended in a gas. Atomization affects not only the effective film deposition but also the heat transfer. Atomized liquids have orders of magnitude higher heat transfer properties.

5.6.5 Part Cooling After Ejection

The average temperature of the part leaving the mold is 200 °C to 300 °C. At this temperature the component is still prone to deformation. Its internal structure is also under development. An incorrect cooling rate after the part leaves the mold cavity may cause part distortion and undesired changes in internal microstructure. There are two ways to affect the cooling rate after the part is ejected: enforced air or water spray-baths.

5.7 Common Defects

Although the manufacturing objective are defect-free components, the industrial practice may generate defects. In addition to serious defects arising from errors in effective mold design and/or process engineering, there are also minor defects, inherent to casting and solidification of liquid metals. The first step in elimination of any defect is its proper identification.

5.7.1 Defect Classification and Characterization

The classification of major defects in injection molded parts is the same as for die casting. Some issues, however, are specific for semisolid processing and injection molding. Thus, the majority of defects can be divided into the following classes:

(i) Defects typical for conventional die casting or injection molding;

   a. Surface defects;
   b. Internal defects;
   c. Dimensional defects;

(ii) Defects specific to semisolid molding.

The particular defects commonly observed within the above groups are listed in Table 5.4 where, in addition to the defect name, its short description is also given. It should be noted that many defects, classified as surface related, may also extend deep into the component's volume. Defect examples, collected from die casting and injection molding practice are shown in figs. 5.33-5.40.

Table 5.4 The classification of defects common for die casting and semisolid molding. (*) Some defects detected on a surface may extend deep into the part's interior

Defect nature	Defect name	Description
Surface (*)	Cold shuts (flows)	Seams where two metal streams have come together but not fused
	Hot cracks (hot tearing)	Material fracture at temperatures where inter-dendritic regions are in a liquid state
	Stress cracks	Crack formed due to a stress typically of thermal origin
	Surface porosity	Any type of porosity exposed to the surface
	Solder	Tearing of the surface, formed during ejection and resulting from adherence to the mold
	Blister	Mottled area, formed by volatizing residual lubricant, reacting with molten surface
	Flash	Solidified metal which flew out from the cavity at the mold partition line
	Laminations	Cold flow where metal did not melt but adheres to the skin
	Short shot	Incompletely filled mold cavity
	Swirls	Circular paths, solidified before intensification step
	Drags (galling)	Scuffed or galled areas, resulting from difficulties with part release
	Heat check fins	Replica of mold cracks, created by thermal fatigue or shock
	Sinks	Depressions in the part surface, formed due to shrinkage of solidified metal
Internal	Contamination (oxide, lubricant, flux, dross etc)	Non-metallic inclusions of different morphology within the parent alloy
	Gas porosity	Discrete, separate holes with spheroidal or elongated shape, filled at high temperatures with a gas
	Shrinkage porosity	Series of interconnected holes, created by a lack of feed material at the end of solidification
	Knit line porosity	A form of gas porosity, created at a juncture of colliding metal fronts, being too cold to converge
	Segregation	Segregation of phases, e.g. eutectics, filling shrinkage-prone regions or separation the solid and liquid during semisolid processing
Dimensional	Bent cores	
	Warpage	Incorrect shape as a result of bending or twisting
	Distortion	

The shrinkage porosity results from a change in volume between liquid and solid state, not compensated by a compaction during solidification. For fully liquid alloys, the solidification shrinkage may have a form of uniformly distributed pores (Fig. 5.33a) or may be localized (Fig. 5.33b). In semisolid alloys, shrinkage porosity is frequently seen in regions between the solid and liquid, likely due to a structural weakness of interfaces between them. The shrinkage porosity may also occur for very high solid contents and is initiated by shrinkage of liquid film, filling gaps

between primary solid phase. Then it is magnified by the volumetric shrinkage during cooling to room temperature (Fig. 5.33c). As seen at high magnifications, the shrinkage porosity manifests by separated dendrites (5.33d,e).

Gas porosity is easily distinguishable from porosity caused by shrinkage. An extreme case is shown in Fig. 5.34a, where spherical shaped pores with a size up to 1 mm are

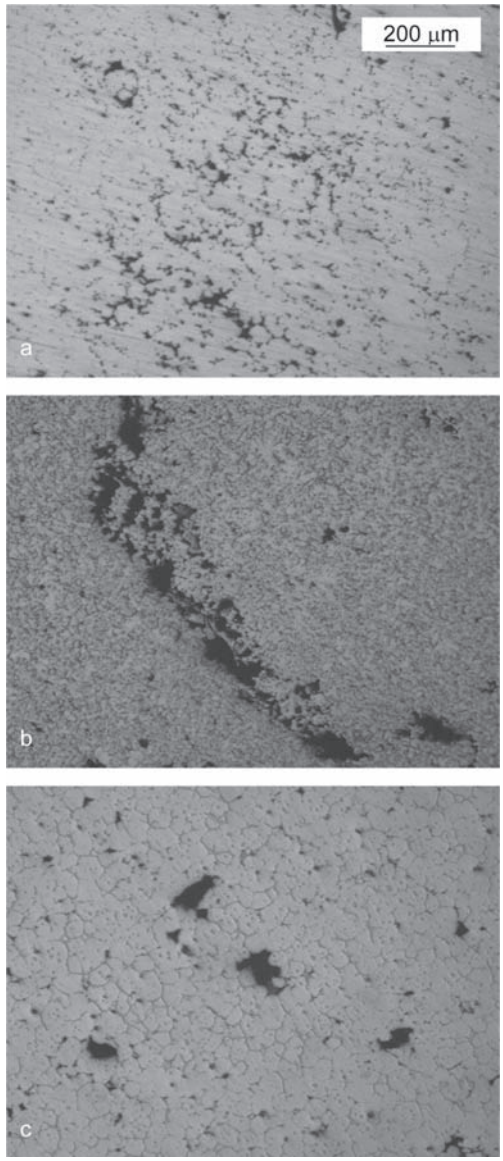

Fig. 5.33 Micro images of shrinkage porosity observed on metallographic sections: **a** dispersed—die casting; **b** localized—die casting; **c** localized—semisolid processing; **d** SEM image of shrinkage pores; **e** SEM image of neighboring dendrites, separated due to lack of liquid metal (AZ91D)

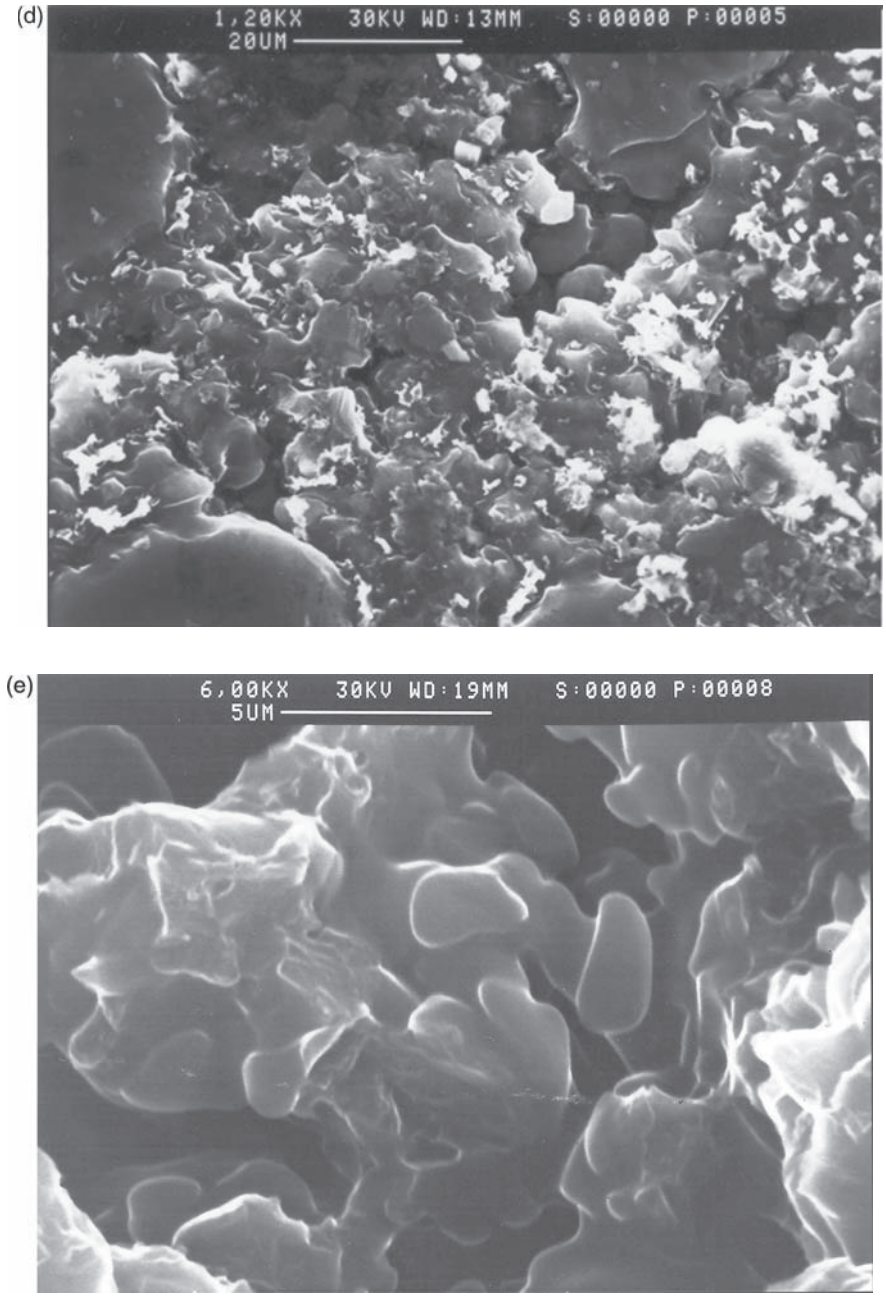

Fig. 5.33 (continued)

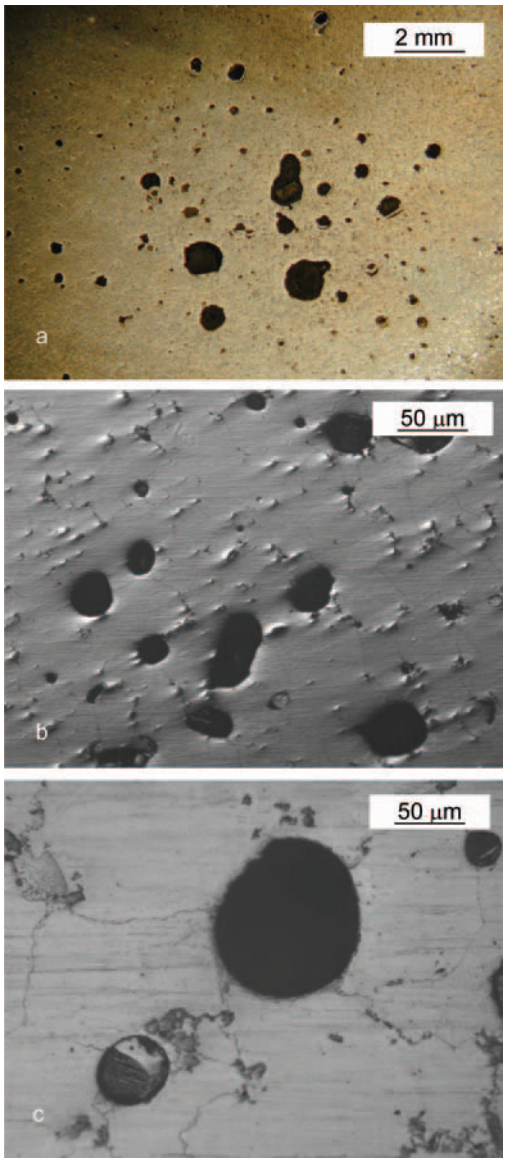

Fig. 5.34 Gas porosity observed on metallographic sections: **a** macro image showing a cluster of globular pores; **b** micro image; **c** detail view showing a pore location between Mg grains (AZ91D)

seen at the macroscopic scale. In addition, there are numerous pores of smaller size. At the microscopic level, pores reside at junctions between grains, and for very small pores the junction would be a triple point (Fig. 5.34b,c). Solidification leads to stress generation, which may cause part cracking. If the stress of solidified regions leads to cracking of neighbouring areas that are not yet fully solid and have strength disadvantage, the defect is called hot cracking (Fig. 5.35a). A similar implication will have flow lines although

the mechanism of their generation is completely different. Flow lines are formed when flow fronts do not mix together due to low temperature, and a lack of welding is seen (Fig. 5.35b). Two defects, shown in Fig. 5.36, arise from mold quality. The heat checking of the mold surface exerts an effect on the surface quality of the molded component, and an example of a crack network is shown in Fig. 5.36a. When the mold is damaged, it is prone to flashing when a large volume of liquid metal leaves the mold cavity (Fig. 5.36b). It should be noted that incorrect processing parameters also contribute to flashing. In extreme cases, they may be the sole cause of flashing.

In semisolid processing, it is expected that the solid fraction be uniformly distributed throughout the part. As discussed earlier during the mixing analysis, there are certain tendencies for solids to distribute following certain patterns, for example in the middle of the wall thickness. In addition to this, there may be an unpredictable arrangement of solid due to injection of non-homogeneous slurry, and this leads to unpredictable changes in properties (Fig. 5.37a). In some cases, the segregation may be caused by freezing of an alloy portion on the mold while the inner part is subsequently filled. An example in Fig. 5.37b shows not only the difference in solid fractions but also different morphology of solids near the surface and inside the part. In another defect two solids with similar morphology but different chemistry may be formed as shown in 5.37c. Differences in chemistry may be accompanied by pores at the interface with the matrix, created due to shrinkage (Fig. 5.37d).

Although the presence of semisolid alloy reduces solidification shrinkage, it does not eliminate it completely. An example of cracks for a roughly 20% solid is shown in Fig. 5.38a. The possible cause of this defect is insufficient injection pressure. The key role of injection pressure is supported by the coexistence of two defects: solidification shrinkage and gas porosity (Fig. 5.38b). As emphasized at high magnification, walls of the gas bubble and surrounding areas exhibit low integrity (Fig. 5.38c).

A special interpretation of defects is required for thin wall components with wall thickness below 1 mm. An entrapped gas creates blisters, seen on both sides of the part (Fig. 5.39a,b). Since the solidification time is very short, flow lines are readily detectable even when the welding of flow fronts is perfect (Fig. 5.39c). When welding does not occur and non metallic inclusions are involved, the defect is more severe (Fig. 5.39d). It should be noted that for thin wall components, the internal defects (Fig. 5.40a), surface defects (Fig. 5.40b) and subsurface defects (Fig. 5.40c) lead to component scrapping. This is because during surface preparation and finishing prior to coating, all of them translate to surface defects. It is frequently seen that some surface defects are revealed after coating is completed, which magnifies many times the losses.

5.7.2 Identifying Defect Causes

In order to eliminate a defect, it is imperative to identify its causes. The majority of causes, leading to defective parts, are related to the following issues [14]:

(i) mechanical problems of the mold;
(ii) metallurgical problems of the molten alloy;
(iii) interaction of heat flow and fluid flow.

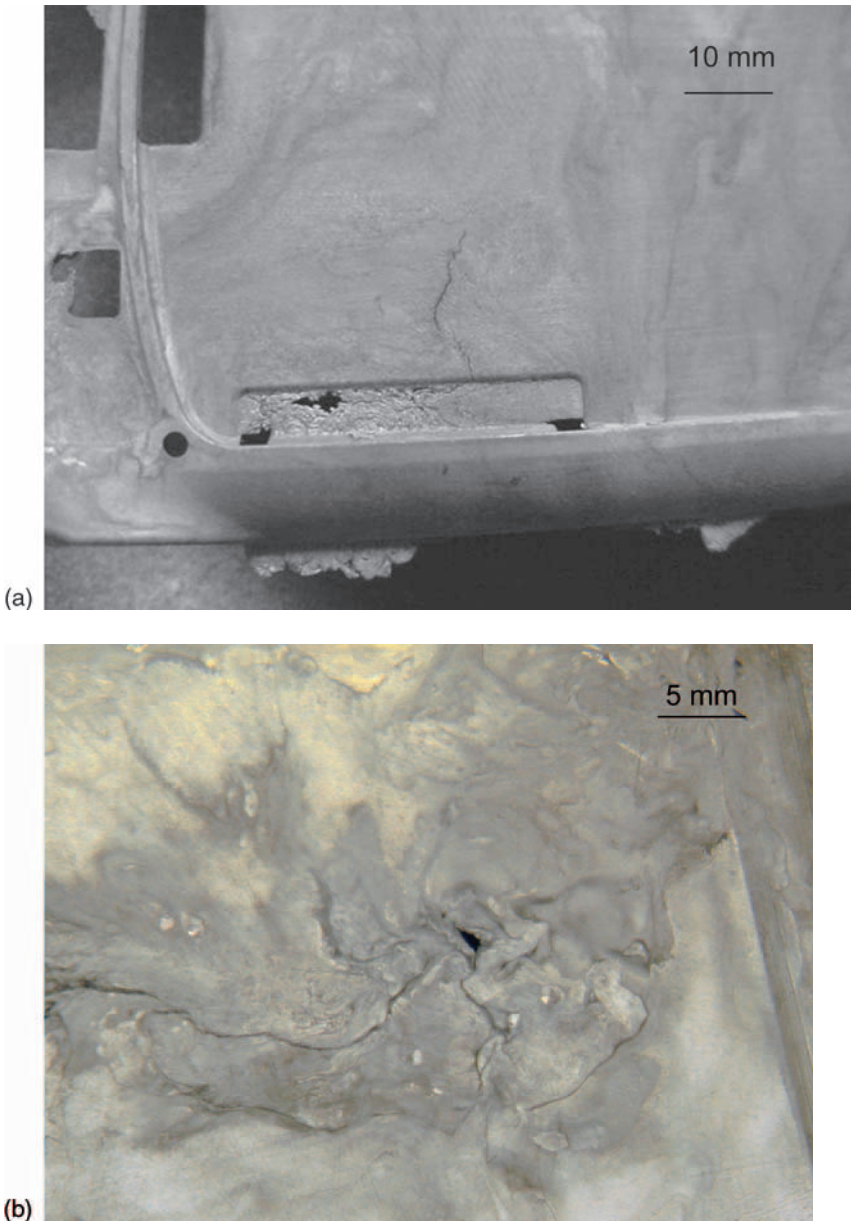

Fig. 5.35 Examples of simultaneous surface and internal defects: **a** hot crack; **b** cold shots (AZ91D)

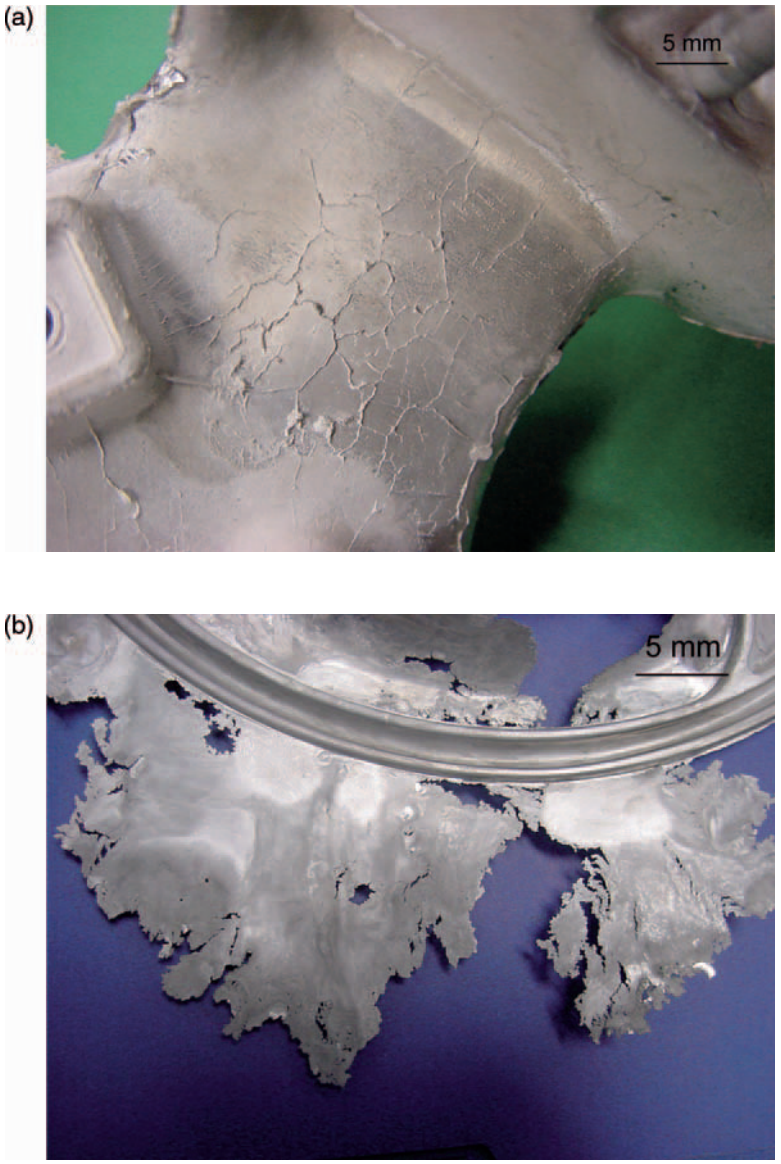

Fig. 5.36 The influence of tool quality on part defects: **a** surface cracks of the tool; **b** excessive overflow (AM60B)

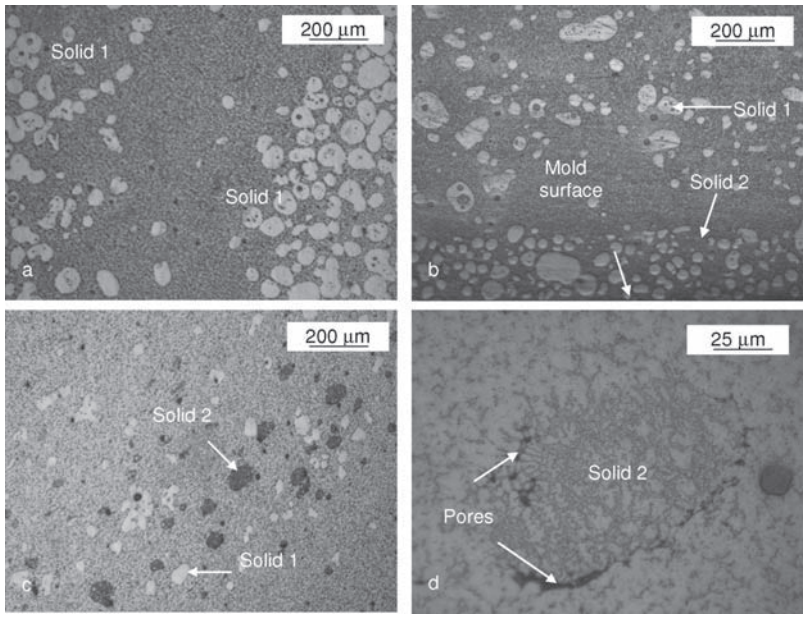

Fig. 5.37 Inhomogeneites in morphology, chemistry and distribution of solids within molded parts: **a** solids with the same morphology and chemistry, exhibiting heavy segregation in certain locations of a thick-wall part, molded from AM60B; **b** solids with slightly different chemistry and two morphologies - the partially melted, marked as solid 1, and re-solidified from the liquid marked as solid 2, with different content and location within a thin wall part of AZ91D; **c** two solids with similar morphologies but sharply different chemistries, marked as solid 1 and solid 2, mixed together and forming a separate band in a matrix of thick wall component of AZ91D; **d** detailed view of the solid 2 from figure (c), emphasizing differences in its phase composition and solidification behaviour, leading to a formating of shrinkage pores at an interface with the matrix.

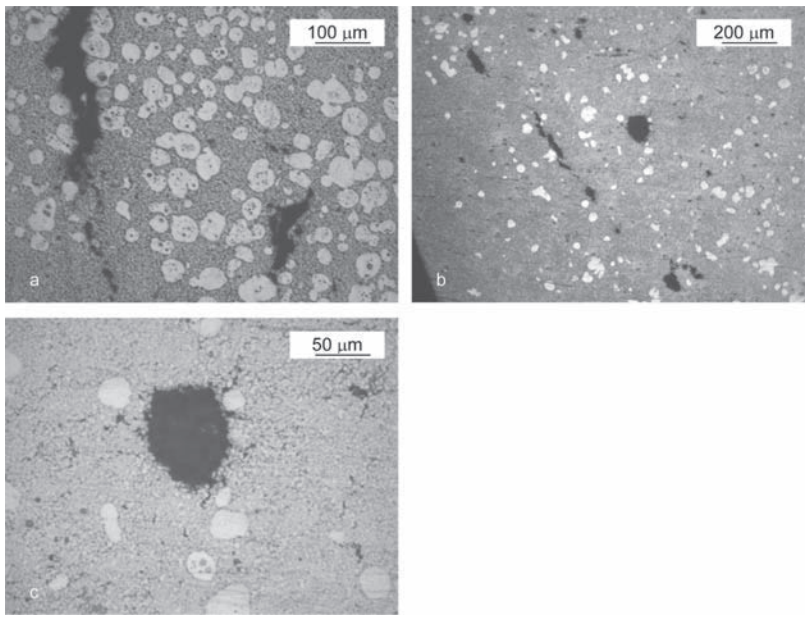

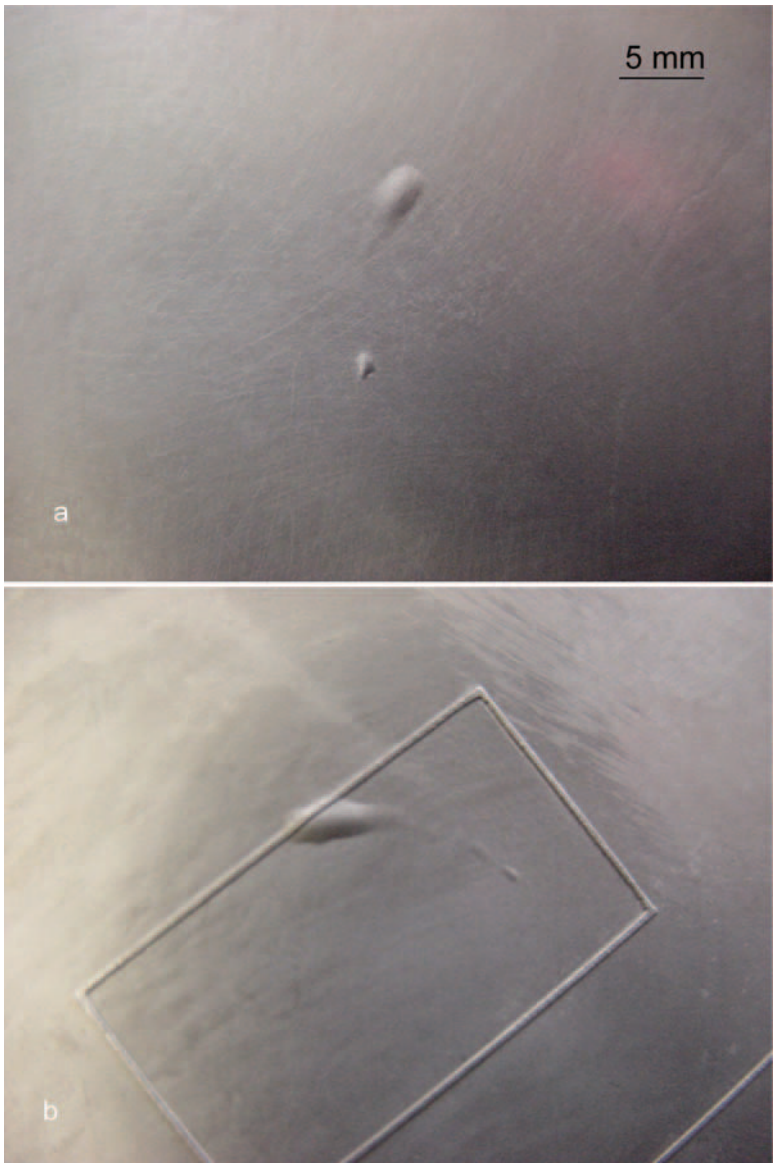

Fig. 5.39 Surface defects of thin wall components molded using AZ91D alloy with wall thickness of 0.6 mm: **a,b** blisters imaged on both sides of a plate; **c** flow lines; **d** premature freezing

Fig. 5.38 The shrinkage and gas porosity in semisolid structures; **a** crack caused by shrinkage porosity —AM60B 20% solid content; **b** a coexistence of solidification shrinkage and gas porosity—AZ91D 8% solid content; **c** a magnified view of Fig. c, emphasizing the shrinkage around the gas bubble

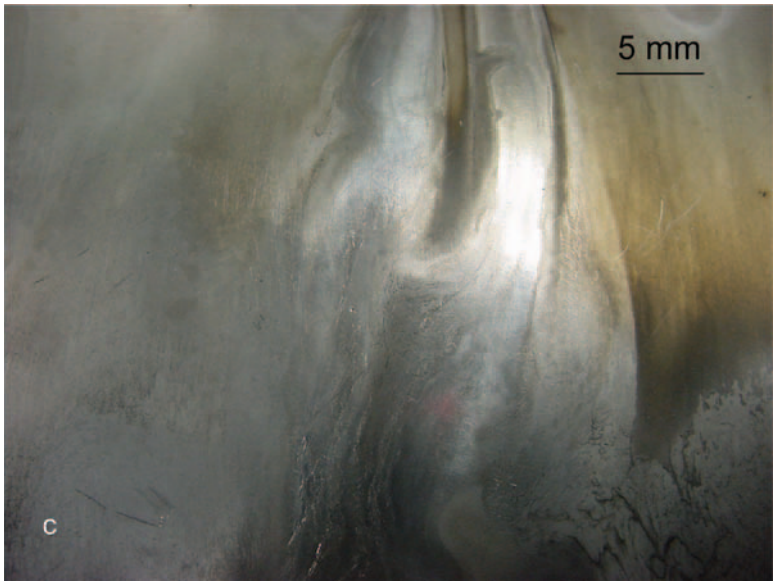

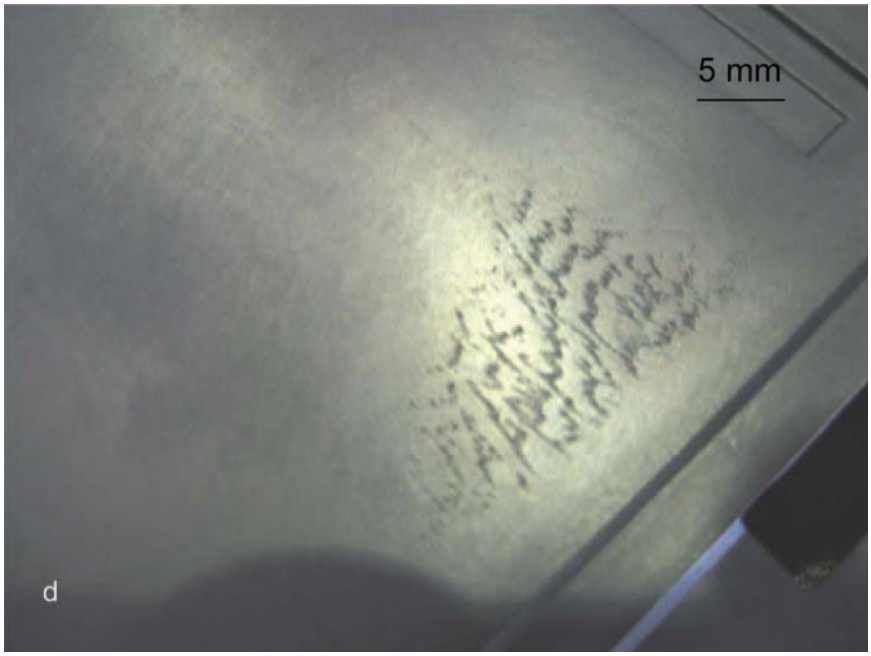

Fig. 5.39 (continued)

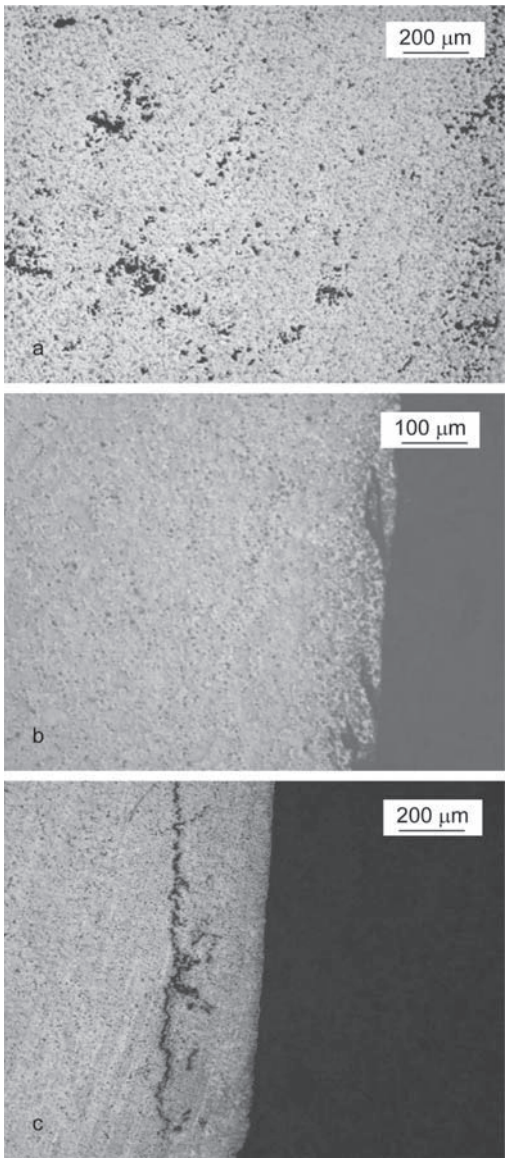

Fig. 5.40 The cross sectional images showing **a** internal defect; **b** surface defect; **c** sub-surface defect (AZ91D)

The mechanical problems of the mold include insufficient draft, tie bar issues leading to improper closing–opening of the mold and ejection system deficiencies. The metallurgical factors cover alloy chemistry, dissolved gases, solid impurities like oxides, flux dross or incorrect temperature. The last group consists of rapid fill time, complex part geometry and high heat-transfer rates. In practice, all major defects are related to several causes. In addition, many causes are interdependent

and affect each other to different extents. To help identify the appropriate cause, special diagrams were built, and an example is shown in Fig. 5.41a,b [15]. Such a graphical form is very useful during industrial practice and should be understood as the initial step in the analysis of a more fundamental root cause.

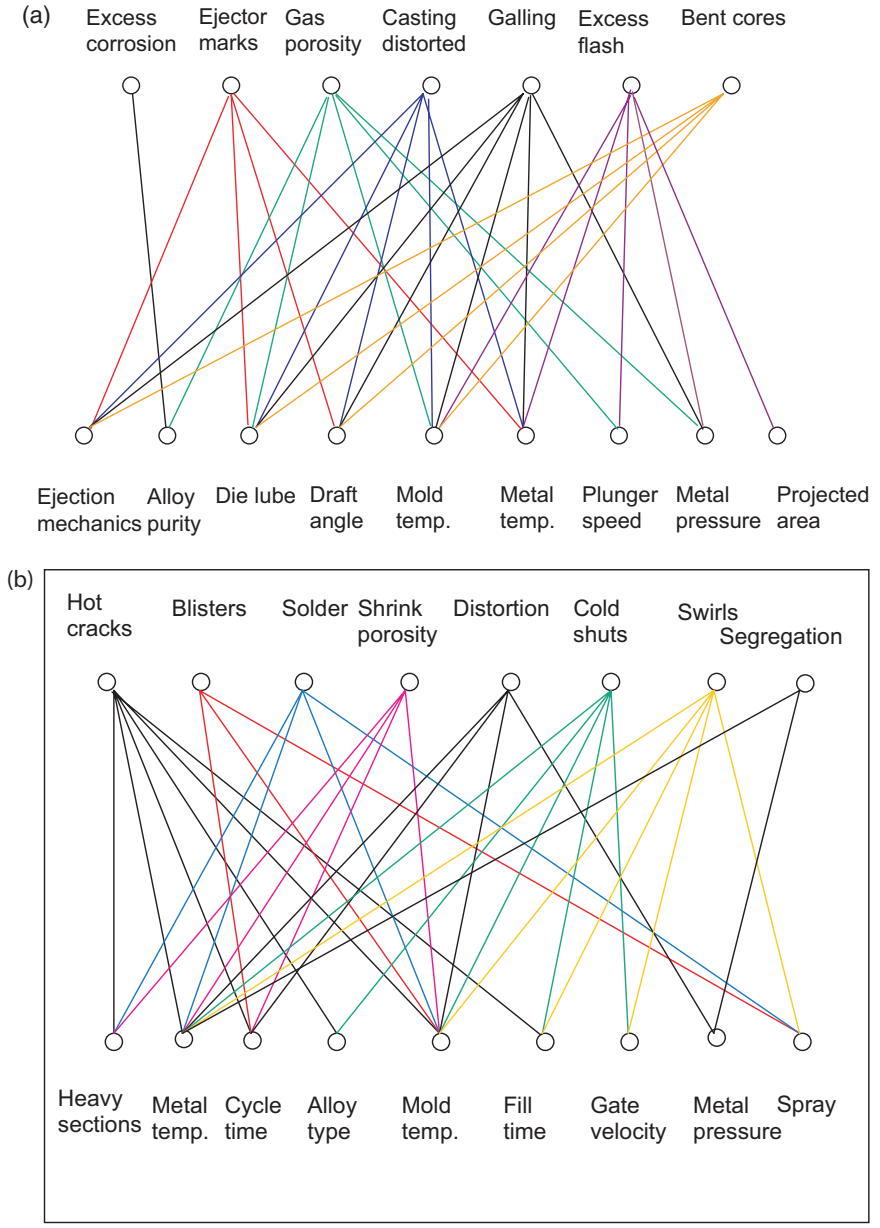

Fig. 5.41 Graphs correlating casting defects with their causes [15]: **a** mechanical; **b** thermal

5.7.3 Defect Prediction by Flow Modeling

Computer simulation represents a very convenient way to predict certain defects. It is used frequently to optimize the geometrical features of the mold at the design stage. An example in Fig. 5.42a shows a thin-wall component that consistently exhibited a serious defect of incomplete filling and cracks located above the window feature. Modeling predicts the front split caused by the window feature, located just above the gate leading to the defect at the same location (Fig. 5.42b). A comparison of the simulation and molded part indicates that the window feature represents the defect cause, and the mold geometry in that region should be modified.

5.8 Product Quality Control

In order to detect potential defects, a proper system of quality control should be in place. Both the surface and internal characteristics of molded components should routinely be examined.

5.8.1 Dimensional Accuracy and Surface Quality

Dimensional verification comprises a comparison of values achieved and drawing requirements. Surface defects, specified in Table 5.4, are easily revealed by visual assessment either directly or under low magnifications. In addition to defects, present exclusively on the component's surface, features should be identified that potentially extend deep into the component's volume. Depending on the part's application, surface defects and dimensional deviations are classified in terms of their relevance for service requirements.

5.8.2 Integrity of the Component

The internal integrity in a form of porosity, cracks, non-metallic inclusions, etc., is essential especially for structural components since it affects the mechanical properties. There are several techniques to test integrity of castings in a non-destructive way:

(i) ultrasound;
(ii) X-ray radiography;
(iii) X-ray tomography;
(iv) liquid penetrants;
(v) eddy current;
(vi) magnetic particles, etc.

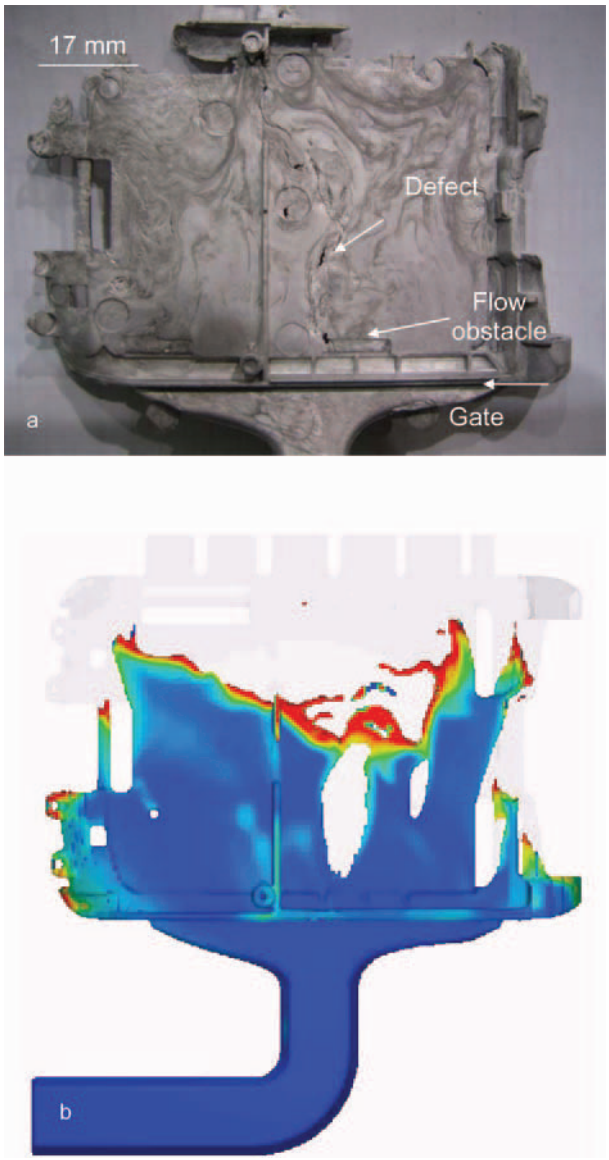

Fig. 5.42 Defect prediction by flow modeling: **a** component with a window feature, representing the flow restriction; **b** modeling showing flow front split during filling caused by the obstacle feature

Technical details of individual techniques can be found in the specific literature. X-ray radiography is based on the gray level being a function of composition and thickness. An example in Fig. 5.43 shows a part with a surface free of defects (Fig. 5.43a) and an X-ray with a dark region suggesting an internal defect (Fig. 5.43b).

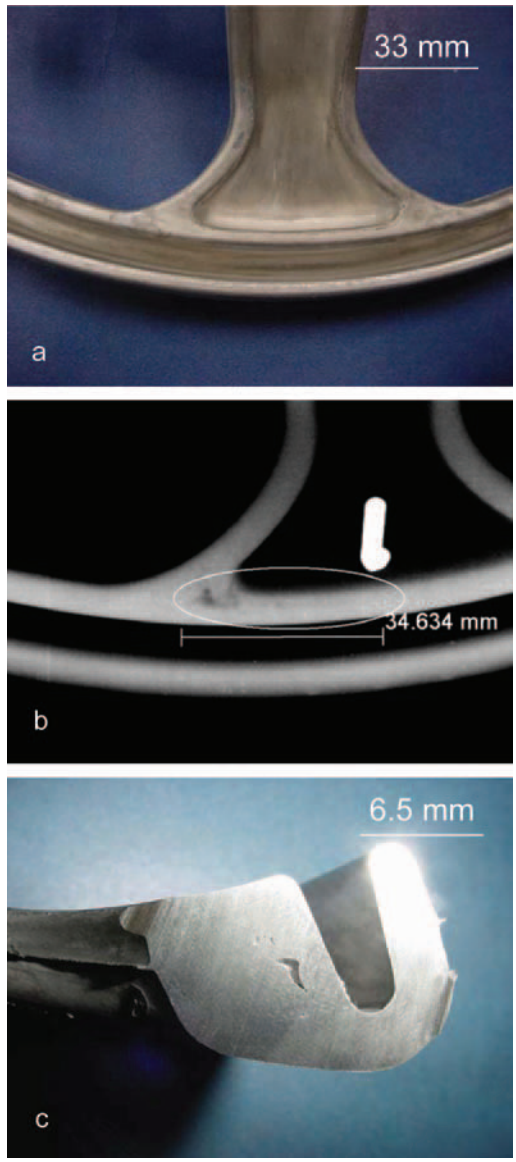

Fig. 5.43 X-ray detection of internal defects: **a** image of the defect zone; **b** X-ray radiograph revealing defect; **c** cross section revealing the defect geometry

After sectioning of the suspected region it was revealed that the defect represents the shrinkage porosity (Fig. 5.43c). Although X-ray allows both two and three dimensional imaging, it is difficult to quantify. The fluorescent penetrant is applicable to surface-related defects and gives only qualitative data. The complex shape and surface roughness may complicate application of ultrasound and magnetic techniques. For some defects more than one technique should be used to achieve a

satisfactory confidence level. A disadvantage of the above techniques is that practically all of them provide only qualitative results.

As an alternative, there is the quantitative metallographic analysis. This technique is, however, destructive and time consuming. For selected samples the porosity should be re-examined by metallography at least on two differently oriented sections. The small size of pores and their similarity to other microstructural features create special problems. In order to detect polishing artifacts, a very high quality surface is required. An advantage is that additional information may be obtained from the test to describe a type of porosity, geometry and distribution within the part.

5.8.2.1 Porosity Measurement by X-Ray Tomography

X-ray tomography generates a three-dimensional image of the interior of a material, including different phases, inclusions, cracks and pores [16]. During measurements, the intensity of X-rays is provided by a strong polychromatic source and transmitted through the component tested, rotated by small increments. On the opposite side, the X-rays are recorded by the solid state detector and used to calculate the local X-ray attenuation coefficient through the material using the Beer-Lambert law [17]. If pores are present within the material, the attenuation coefficient is very low (Fig. 5.44). Depending on the device used, defects of tens of microns may be detected within magnesium with thickness up to several millimeters.

5.8.2.2 Porosity Measurement By Archimedes Method

A quantification of porosity can be determined by a measurement of the material density. However, since molded parts have a rather high density it is difficult to find a reliable technique of measurement. Of two techniques available, the Archimedes

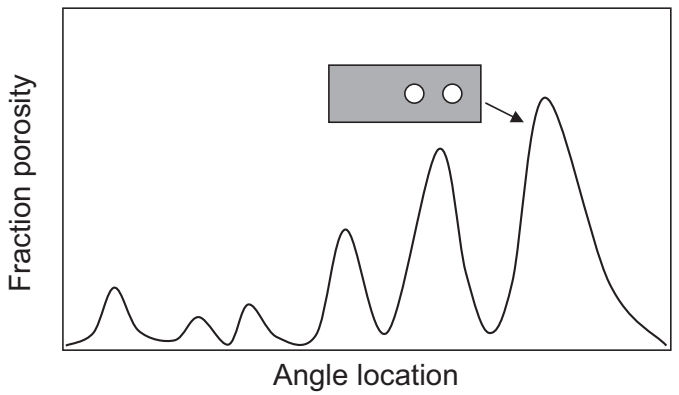

Fig. 5.44 The concept of porosity measurements by X-ray tomography

method and Helium pycnometry, the first one is simpler and can give a measure of total porosity in a sample. By contrast, the Helium pycnometry gives a measure of surface area of the connected porosity in a part.

Despite all concerns the Archimedes test is commonly used by the die casting industry. Among standards controlling testing there is ASTM D792–91—a document designed for plastics—and ASTM B328-96, which is designed for sintered metal structural parts and oil-impregnated bearings. The schematics of an experimental set-up are shown in Fig. 5.45. The weight of a molded component is determined first in air then in water. The porosity is then calculated based on the formula:

$$Porosity(\%) = 100\frac{1 - W_a\rho_w}{(W_a - W_w)\rho_{Mg}} \tag{5.18}$$

Where:

W_a – weight of the part in air;
W_w – weight of the part in water;
ρ_{Mg} – density of magnesium;
ρ_w – density of water.

Beyond density measurement accuracy, the effect of sample chemistry on the estimated theoretical density is of importance. For magnesium alloys, a change in theoretical density from 1.82 to 1.80 g/cm^3 results in a 1.1% difference in calculated porosity. Thus for the porosity range targeted during semisolid processing, being around 1% and below, the Archimedes method may be unreliable in terms of its accuracy and reproducibility.

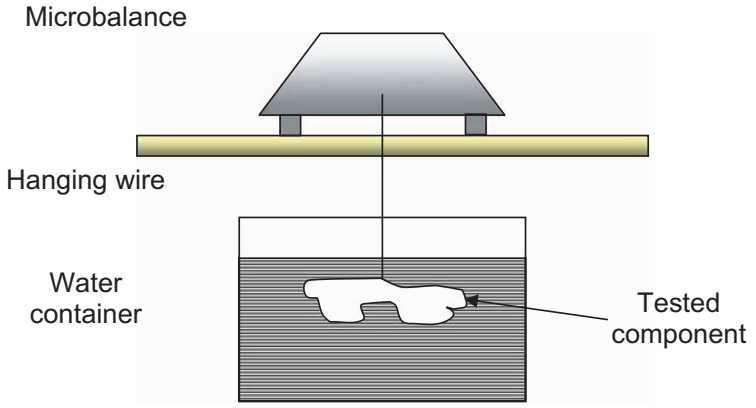

Fig. 5.45 The experimental set-up for porosity measurements based on Archimedes method

5.8.3 Chemistry

There are many reasons that chemistry of the casting may differ from the ingot precursor: evaporation of certain elements, segregation of alloys within the reheating furnace, contamination by products of reactions with hardware materials, etc. For injection molding, deviation possibilities are reduced. First, the lower processing temperature and closed barrel environment prevent volatile elements, such as zinc or magnesium, from evaporation. Moreover, chipping contributes to homogenization of chemistry since chips originating from a number of ingots are mixed. Among routine tests used for chemistry analysis the ASTM E1097–97 with some modifications or E1479–99 give satisfactory results.

5.8.4 Metallography

A detailed microstructural examination involves primarily different levels of microscopy: optical, scanning electron and scanning probe microscope (atomic force instrument), and transmission electron microscopy. For industrial purposes, the metallographic characterization with an optical microscope is usually sufficient. The routine analysis involves an assessment of morphology and volume fraction of the solid phase. A complete stereological characterization requires a description of the size, shape and distribution.

The polished flat section with structural features revealed by chemical or electrolytic etching methods is subjected to metallographic examination and measurement by software for quantitative image analysis. The preparation of polished sections of magnesium and its alloys is difficult due to its soft nature and high reactivity. As a result, it is difficult to eliminate scratches and generate sufficient relief between phases to create clear contrast during microscopy imaging. Their easy reaction with water restricts many suspensions and polishing agents. The etching chemicals for magnesium and its alloys are relatively simple in composition (Table 5.5). Practically all mineral and organic acids exhibit sufficient attack. The etchants developed are based on nital or picral with additions of various solvents. There are some special etchants for the selective attack of individual phases.

5.9 Summary

The processing phenomena of magnesium injection molding should be seen as a combination between the plastics molding in terms of melt preparation and die casting in terms of filling the mold cavity and melt solidification. While for some processing steps there are good similarities, for others the phenomena and mechanisms involved are different and unique.

Table 5.5 The etching chemicals for magnesium and its alloys [18, 19]

Composition	Applicable alloys	Effect	Method of use
1 ml HNO_3 75 ml diethylene glycol 25 mm water	Mg, Mg–Al, Mg–Al–Zn, Mg–Zn–Zr, Mg–Th–Zr	General structure	Swab 3–5 s
1 ml HNO_3 60 ml diethylene glycol 20 ml acetic acid 25 ml water	Mg, Mg–Al, Mg–Al–Zn, Mg–Zn–Zr	General structure	Swab 1–3 s
1-10 ml HNO_3 100 ml ethanol or methanol	All alloys	General structure	Swab or immerse for few seconds to a minute
0.7 ml H_3PO_4 4 g picric acid 100 ml ethanol or methanol	Mg, Mg–Al, Mg–Al–Zn, Mg–Th–Zr, Mg–RE	General structure, Phase identification in Mg–Th–Zr, Mg–RE	Immerse with gentle agitation 10–30 s
2 g oxalic acid 100 ml water	Mg, Mg–Al, Mg–Al–Zn, Mg–Mn, Mg–Zn–Zr	General structure	Swab
60 ml H_3PO_4 100 ml ethanol	Mg, Mg–Al, Mg–Al–Zn,	General structure	Electrolytic, stainless steel cathode, approx 3V, DC
5 ml acetic acid 10 ml water 6 g picric acid 100 ml ethanol or ethanol	Mg–Mn, Mg–Al, Mg–Al–Zn, Mg–Zn–Zr	General microstructure	Immerse with gentle agitation 10–60 s
2-10 g citric acid 100 ml ethanol	All alloys	General microstructure	Immerse for up to 30 s
2 ml HCl 100 ml ethanol	All alloys	General microstructure	Immerse for up to 10 s
5 ml acetic acid 95 ml water	Mg, Mg–Al alloys	General microstructure	Swab 3–5 s

References

1. Chung CI (2000) Extrusion of Polymers, Theory and Practice. Munich, Hanser Publishers, Munich
2. Middleman S (1977) Fundamentals of Polymer Processing, McGraw-Hill, New York
3. Rauwendaal C (2001) Polymer Extrusion, 4th ed. Hanser Publishers, Munich
4. Segre G, Silderberg A (1961) Radial Poiseeulle flow of suspension. Nature 189:209
5. Floreen S, Ragone DV (1957) The fluidity of some Al alloys. AFS Transactions 65:391–393
6. Campbell J (1993) Castings. Butterworth-Heinemann, Oxford
7. Lun Sin S, Dube D (2004) Influence of process parameters on fluidity of investment-cast AZ91D magnesium alloy. Materials Science and Engineering A A386(1-2):34–42
8. Flemings MC (1974) Solidification Processes. McGraw-Hill, New York
9. Herman EA (1988) Gating die casting dies. Society of Casting Engineers
10 Wronkiewicz J, Cox M, Fish R (1998) PQ2, NADCA, Chicago
11. Vinarcik EJ (2002) High integrity die casting processes. John Wiley & Sons, Hoboken, NJ, USA
12. Lee IS et al (1989) Spray cooling of die casting dies. In Proceedings of the Australian Die Casting Association (ADCA) annual conference, Melbourne, Auatralia, pp 53–70

13. Sawamura M et al (2005) Estimation of spray lubrication and die temperature for die life prediction in hot forging. R&D Review of Toyota CRDL 40(1):50–52
14. Metals Handbook (1973) 8th ed. vol. 8. American Society for Metals, Metals Park, Ohio
15. Bennett FC DCRF recommended procedures, trouble shooting charts. NADCA, Rosemont, Illinois, USA
16. Weiler JP et al (2005) Relationship between internal porosity and fracture strength of die cast magnesum alloy AM60B. Materials Science and Engineering A 395:315–322
17. Feldkamp LA, Davis LC, Kress JW (1984) Journal Optical Society of America 1:612–619
18. Vander Voort GF (1999) Metallography—Principles and practice. ASM International, Materials Park, Ohio
19. Microetching (1977) LECO Corporation

6
Feedstock Selection

6.1 Introduction

The idea of using metal particulates for consolidation into useful product forms has been explored for ages, before furnaces were developed that could exceed the melting point of metals. A classical example is the sponge iron used by the Egyptians around 3000 B.C. for making tools. Since the beginning of modern powder metallurgy in the 19th century, initiated by producing compact platinum from platinum sponge powder, the role of metal powders has experienced a continuous increase. Today, powder metallurgy represents well-established industrial technology, providing not only high quality intricate shapes, but also unique material microstructures. As opposed to particulates with tens or hundreds of micrometers, required in powder metallurgy, relatively coarse ones with a size of the order of several millimeters have been used for decades in a variety of chemical, pharmaceutical, military and metallurgical applications. The latter type became a precursor of the feedstock for injection molding. The particulates are also called chips, granules or pellets, depending on their shape and manufacturing technique. So far, the material choice is restricted to low-melting point alloys—mainly to Mg-based, Zn-based and Al-based compositions.

On macroscopic scale, in order to be suitable for use as feedstock material, particulates should exhibit certain general features, including size uniformity, with a minimum of sub-micron fines, an oxide-free surface, smooth flow through the system and an acceptable manufacturing cost. As a result of the search for the optimum particulate, many combinations of morphology and size were manufactured worldwide on both a laboratory and commercial scale; the most typical of them are described in this chapter. In addition, features are defined that make the particulates useful for injection molding applications.

6.2 Techniques of Particulates Manufacturing

Two major techniques of particulates generation are available:

(i) in a solid state by mechanical comminution;
(ii) in a liquid state by rapid solidification.

F. Czerwinski, *Magnesium Injection Molding*.

Both techniques have several sub-solutions, as listed in Fig. 6.1. The mechanical comminution was historically the first, and it is still the major method of producing particulates of magnesium and its alloys. Most often, it involves lath turning, rasping, chipping, milling or grinding. In some cases, two techniques are combined, such as, for example, chipping and milling, to produce near-spheroidal shapes. Relatively coarse particulates, obtained by mechanical fragmentation and referred to as chips, represent the only commercially viable feedstock used presently in injection molding.

The continuous quest for high quality feedstock available for injection molding has catalyzed the development of alternatives to the presently explored technologies of mechanical comminution. In this search, particular attention is being paid to techniques based on the liquid precursor. It is anticipated that it will be possible to implement in the near future, direct manufacturing from the primary melt, omitting the ingot stage, thereby providing energy savings and reducing the final cost.

6.2.1 Mechanical Comminution

Solid-state mechanical comminution allows for the generation of particulates with a variety of shapes and sizes. Since injection molding requires relatively coarse particulates, it imposes some restrictions on the manufacturing stage, and not all methods explored for other applications are useful here. Although there are many manufacturing techniques, they fall into two major categories:

(i) fragmentation (cutting) of large ingots into small pieces;
(ii) generation of small particulates by extensive bulk forming.

6.2.1.1 Fragmentation, Chipping

The starting material for mechanical chipping is as-cast ingot (Fig. 6.2a). During this process the material passes through rolls with cutting teeth located around their surfaces. The chip shape is controlled by the chipping tool. The process is carried out at

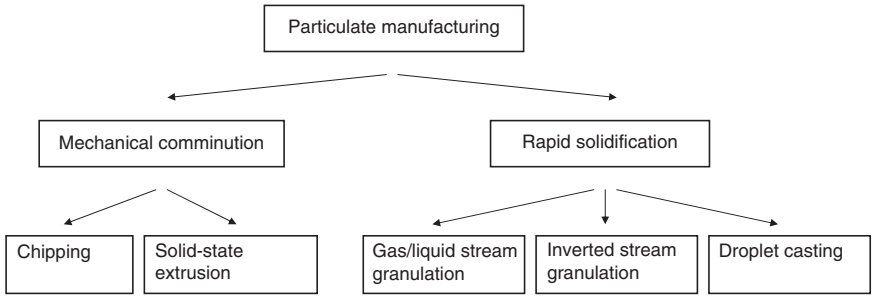

Fig. 6.1 Schematic diagram of techniques presently used for manufacturing coarse particulates [16]

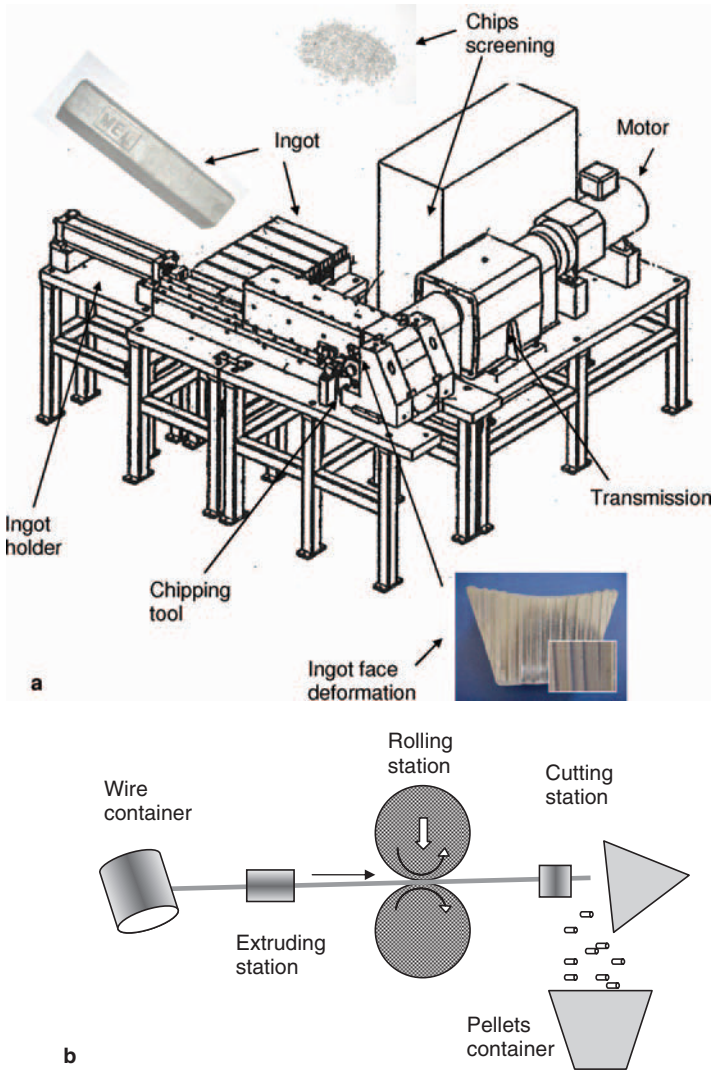

Fig. 6.2 Manufacturing of injection molding feedstock by mechanical cutting or forming in a solid state: **a** system for mechanical fragmentation designed by Metal Processors, Inc. MI, USA - insets portray an ingot precursor, ingot face deformation during chipping and chips as the final product; **b** schematics of particulate manufacturing by solid state extrusion followed by cutting

room temperature, but due to heat generation, the material experiences heating to 50 °C to 70 °C. After cutting, chips may be subjected to screening by sieving.

6.2.1.2 Solid-State Extrusion

This is essentially a two-step process where the cylindrical shape is first obtained by multi-pass extrusion [1]. Since the cross section reduction is large, the alloy is

preheated. The typical temperature of magnesium preheating is of the order of 300 °C. In order to obtain high surface quality, final passes are conducted at room, or slightly elevated temperatures. Subsequently the extruded alloy is cut into pellets with a length below 25 mm. During cutting, one or more extruded wires are directed to the multi-tooth cutter, shear cutting wheel or shearing ledge (Fig. 6.2b).

6.2.2 Techniques Based on Rapid Solidification

Rapid solidification is characterized by a very high cooling rate that ranges from 10^5 °C/s to 10^6 °C/s for convective heat transfer, to 10^6 °C/s to 10^8 °C/s for conductive heat transfer mechanisms. It has been used for many magnesium alloys to produce melt spun ribbons which, after mechanical comminuting into powders, were sealed in cans and extruded into bars [2]. In another application, the granules obtained by rapidly solidifying droplets of the molten alloy were subsequently compacted and extruded into various shapes [3]. Atomizing, i.e., disintegrating a liquid stream of magnesium into droplets, and freezing them into solid particulates of a spherical shape, is a method that utilizes the idea of rapid solidification. A different concept is used during the emulsification of globular salt-coated particulates, where liquid magnesium is first agitated in a boron-containing flux. On freezing, magnesium particulates with a size of 10–50 mesh, which emulsify as small spheres, are freed by grinding [4].

Although the idea of manufacturing particulates for injection molding is the same as that used for powder metallurgy, the significantly larger size required for the former imposes new challenges on the equipment and process. As a result, there is still no commercial scale manufacturing, and small quantities of the feedstock are generated at the laboratory level using prototype hardware. Depending on the final destination and particulate size, there are several modifications of atomization techniques widely used for the manufacturing of a large tonnage of powders. Since, for injection molding, relatively large particulates with a size typically over 0.5 mm are required, the technique is frequently referred to as granulation instead of atomization.

6.2.2.1 Granulation Using Inert Gas Apparatus

Conventional atomization methods allow the production of granules mostly in the size range of 0.2 mm to 1 mm, depending on the apparatus' height (Fig. 6.3a). In this technique the liquid stream of molten metal is fed vertically down to the nozzle which is located at the top of the tower [5]. As the metal stream exits the nozzle, it is struck by a high velocity stream of an atomizing medium, e.g., inert gas. As a result, the molten metal is disintegrated into fine droplets that solidify during the fall through the apparatus tower. Since inert gases such as helium or argon have poor cooling properties, the solidification time is long and a magnesium droplet of 1 mm requires a tower about 7 m high. For larger diameters, the problem is more severe, and a droplet with a diameter of 2 mm requires a tower with a height of 21 m.

Other frequently quoted disadvantages of using an inert gas are (i) the large volumes of gases required and the related cost; (ii) use of an inert gas enhances the evaporation of Mg from the alloy; (iii) and the reactivity of magnesium with gas impurities.

In order to overcome the above limitations, an apparatus based on the liquid quenching concept was developed [6]. The metal is fed under high pressure into the nozzle, which disintegrates it into small droplets, and the droplets are formed in argon, helium or other inert gases at a pressure of 0.1 MPa (1 atm) and very low oxygen and vapor concentrations. The droplets are subsequently solidified and cooled in an inert bath, e.g., a non-polar oil, continuously stirred, cooled externally and kept at a temperature of 5 °C to 200 °C. Alternatively, centrifugal force can be used to break up the liquid as it is removed from the nozzle of a rotating electrode or spinning disk.

6.2.2.2 Granulation Using Inverted Stream Apparatus

The unique feature of the inverted-stream apparatus is the positioning of a nozzle at the bottom of the cooling chamber [7]. During their upward trajectory, the streams break up into droplets that solidify substantially before landing on a collector plate at the base (Fig. 6.3b). Due to the parabolic trajectory of the droplets over a 2 m vertical displacement, it is approximately five times longer than a free fall, thus significantly increasing the cooling time (Fig. 6.3c). The prototype tower, built at the Alberta Research Council, Edmonton, Canada had dimensions of $6 \times 1.2 \times 1.2$ m and is capable of generating spherical granules up to about 4 mm in diameter at a rate of 15 kg/h with a yield of 97%-99%. Up to 50 kg of metal is melted in a resistance furnace located in the containment vessel on the bottom. The vessel is pressurized between 100 kPa and 200 kPa gauge, and at least one stream of a molten metal is generated upwards through a nozzle. The nozzle is vibrating at a high frequency transverse to the fluid stream to cause a periodic dispersion of the segmental droplet trajectory, preventing the droplets from impacting each other and coalescing. Most of the granules produced are immediately removed from the collector. At steady-state conditions, the inner temperature of the tower is as high as 100 °C. The tower is cooled due to heat radiation from the steel walls and also by recirculating gas through heat exchangers. There are a number of advantages to this process: It does not require SF_6 or corrosive protective gases such as SO_2, it does not require an oil quench and it has the possibility of using a recyclable argon atmosphere.

6.2.2.3 Casting of Large Droplets

There are techniques to produce relatively large granules with a size exceeding several millimeters by the mechanical break up of a liquid stream of Mg alloy into droplets. As a source of liquid alloy either furnaces or screw extruders are used. In these systems, the cooling towers are eliminated and large metal droplets are formed just above the quenching medium, most frequently a liquid. Alternatively, quenching may be conducted using a fluidized sand bed.

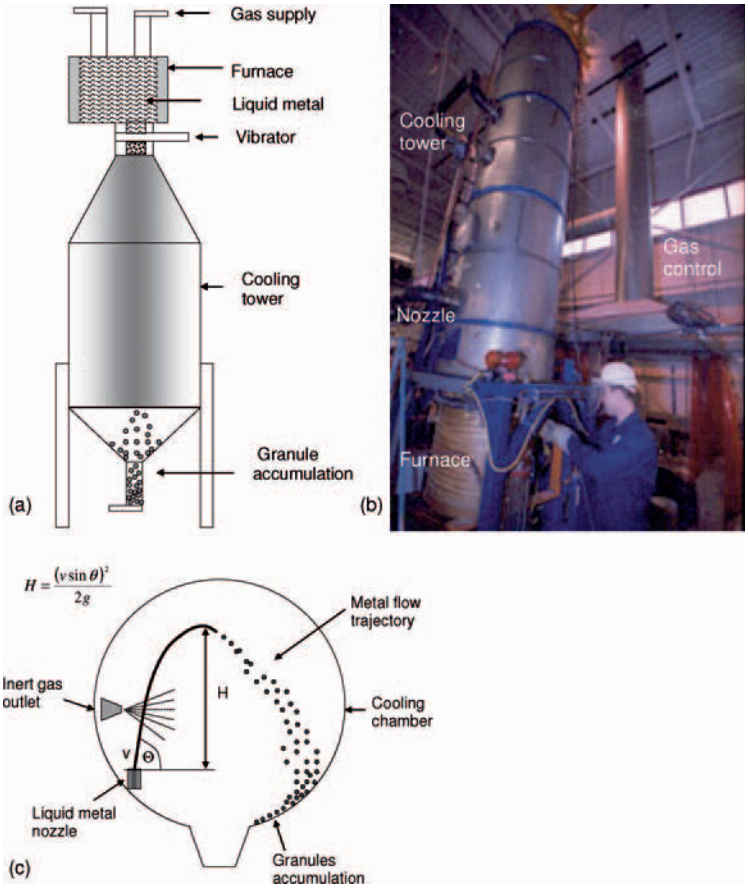

Fig. 6.3 Manufacturing of injection molding feedstock by rapid solidification: **a** conventional atomization system with solidification of granules occurring during falling down from the atomizer along the high cooling tower; **b** inverted stream system at Alberta Research Council (Canada) with a furnace and metal exit nozzle located beneath the cooling tower; **c** [7] a concept of the inverted stream apparatus with a metal flow trajectory, explaining a benefit of substantially lower cooling tower - maximum flow height is calculated as $H = \frac{(V\sin\theta)^2}{2g}$, where v is the initial melt velocity, Θ is the nozzle angle and g equals 9.81 m/s^2

6.3 Characterization of Particulates Manufactured by Mechanical Fragmentation

6.3.1 Morphological Features

A selection of particulate morphologies is presented in Fig. 6.4. The most widely used chips are those with an elongated shape, shown as C1 and C2 in Fig. 6.4a,b. Chips C3 in Fig. 6.4c have shape, resembling deformed hemispheres. Morphology C4 (Fig. 6.4d)

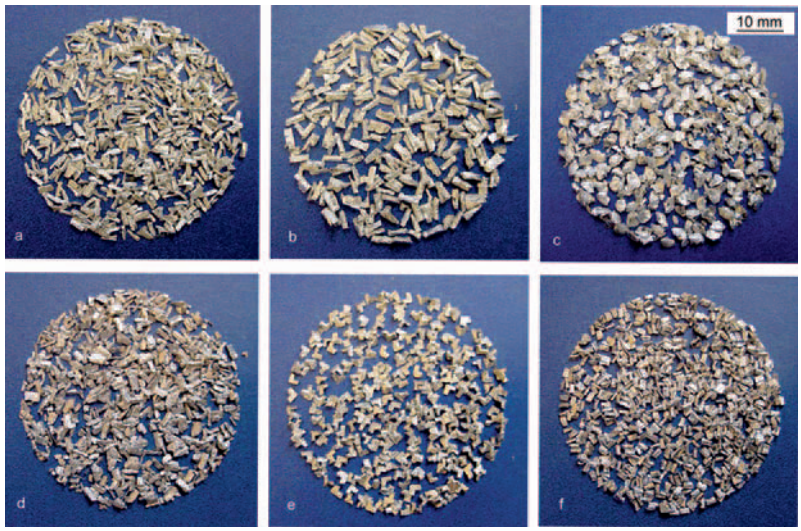

Fig. 6.4 Morphologies of AZ91D chips, obtained by mechanical fragmentation of as-cast ingot: **a** C1; **b** C2; **c** C3; **d** C4; **e** C5; **f** C6

is highly irregular and represents chips used in the past. Another type, marked as C5 (Fig. 6.4e), resembles the highly reproducible right angle shape. Also, the C6 shape in Fig. 6.4f shows high regularity and consistency: Its cross section is roughly square-like, but its length is significantly smaller than that seen for C1 or C2 chips.

Non-conventional morphologies are shown in Fig. 6.5. The shapes F1 and F2 in Fig. 6.5a,b remind us of flakes or short lathe-turnings. They are relatively thin with a large surface area, and the surface relief reflects their multiple bending during cutting. The pellets shown in Fig. 6.5c (P1) were obtained by a combination of extrusion and cutting. They have a cylindrical shape with a diameter of 2.5 mm and approximate length of 4 mm. The end faces are roughly perpendicular to the axis of the cylinder. According to [1], the maximum length of the cylinder should be less than 25 mm—most preferably 4 mm to 6 mm. At the same time, it is recommended that the maximum length to maximum diameter ratio should be about 0.8 to 1 up to 4 to 1. The positive feature of magnesium is its ability to be recycled, and this opportunity is explored during feedstock manufacturing. An example of the recycled feedstock, obtained by a cutting and ball-crushing of die-cast parts, is shown in Fig. 6.5d. Their size is generally larger than other particulates described in this chapter.

Morphological details were analyzed using particulates C2. It is seen in Fig. 6.6a that even for chips with a repeatable morphology, the cross section gives a wide range of shapes. Although irregular shapes are portrayed as generally detrimental, it is also claimed that they do not unduly affect the properties of the matter unless they are present in an unacceptably large amount. While magnified, the chip surface reveals its heavily deformed nature (Fig. 6.6b). On a macro scale, there is a difference in deformation between individual chips and also between different portions of each chip. The typical nature of chip deformation is shown in Fig. 6.6c where

Fig. 6.5 Non-conventional morphologies of particulates: **a** F1–MEZ flakes obtained by mechanical fragmentation of an ingot; **b** F2–AZ91 flakes; **c** P1–AZ91D pellets obtained by a combination of solid state extrusion and cutting; **d** R1–AZ91D recycled feedstock generated from fragmentation of die-cast components

two regions formed by cutting and fracturing can be distinguished. The strain in metal cutting takes place in a concentrated band of shear projecting from the tool tip towards the free surface. The inclination and width are affected by the rake angle, the depth of cut and the friction with the tool face [8]. The macro inhomogeneity is accompanied by micro features: It is known that the plastic deformation of polycrystalline Mg at room and elevated temperatures is inhomogeneous and dominated by the appearance of shear bands [9].

6.3.2 Sieve Analysis

A commonly accepted technique for particulate size determination is the sieve test, specified by ASTM E276-68. While applied to elongated shapes it has, however, some limitations, and the result refers only to the smaller cross section. A summary of the sieve analysis is given in Table 6.1 with plots of selected data compared in Fig. 6.7. The general observation is that not only the average size, but its distribution, are the features that characterize the differences. The majority of chips C1 were retained by sieves with openings of 0.6 and 1.4 μm, with one strong maximum for

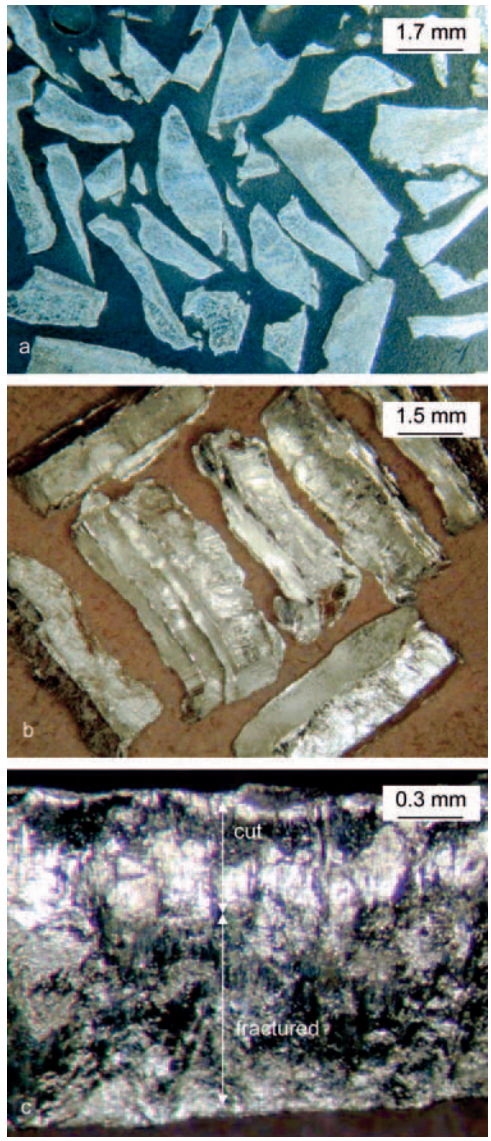

Fig. 6.6 Morphological details of mechanically comminuted chips C2: **a** cross-sectional view; **b** top view showing surface deformation; **c** chip surface with regions formed by cutting and fracturing

C1-AZ91D and two weaker for C1-AM60B and C1-AJ52. It suggests that the material properties affect, to some extent, the size distribution and shape of the particulates, manufactured using identical hardware. For shape type C2, the majority of chips were retained by the sieve with an opening of 1.4 µm. For coarser chips C3, a larger fraction was retained by the sieve 2.36 µm. For the highly reproducible morphology C5, almost equal fractions of chips were retained by sieves 0.60 µm and

Table 6.1 The size distribution of particulates manufactured by mechanical comminution as determined by the screen analysis according to ASTM specification E276–68. The table values represent fractions in weight % retained by sieves of given opening

Particulate type	Shape type	Alloy grade	Sieve opening, mm							Tap density
			4.75	3.35	2.36	2.00	1.40	0.60	0.00	g/cm^3
Chips	C1	AZ91D	0	0	0.6	1.4	7.9	89.6	0.5	0.896
	C1	AM60B	0	0.1	2.3	4.8	38.0	54.4	0.5	0.819
	C1	AJ52	0	0.3	7.8	9.9	42.0	40.0	0	0.844
	C2	AZ91D	0	0	1.9	8.4	70.4	15.1	0.2	1.002
	C3	AZ91D	0	0.3	16.1	20.8	60.2	2.3	0.3	1.045
	C4	AZ91D	0	0	2.5	8.9	80.9	7.6	0	0.999
	C5	AZ91D	0	0	1.1	4.5	45.4	47.3	1.6	1.004
	C6	AZ91D	0	0	0.5	0.9	19.5	78.9	0.2	1.016
Flakes	F1	MEZ	0	3.9	48.7	11.5	22.4	13.4	0.1	0.729
Pellets	P1	AZ91D		100						1.201

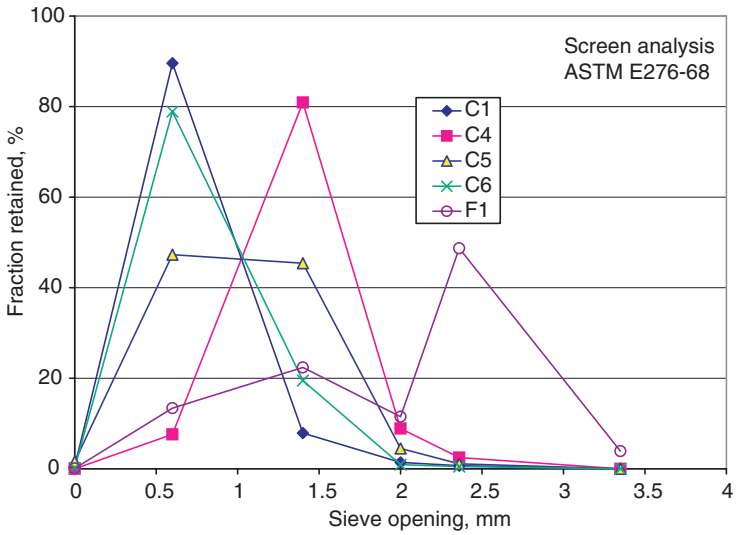

Fig. 6.7 Plots of size distribution of selected chips, determined by the sieve analysis following ASTM E276–68

1.4 µm. The size distribution of flake-like particulates F1 shows the maximum close to 50% retained by the sieve of 2.36 µm, with the rest spread between sieves of 3.35 µm and 0.00 µm (Table 6.1). In summary, chip size distributions exhibited either one strong or two weaker maximums which extend over one or two sieve openings.

To provide a perspective for interpretation of the sieve test results, the analysis should be extended by the direct measurement of the length and width of chips under magnification. The distribution plots, along with average data for chips C2, are summarized in Fig. 6.8. Average values of 4.78 mm and 1.62 mm were obtained for chip length

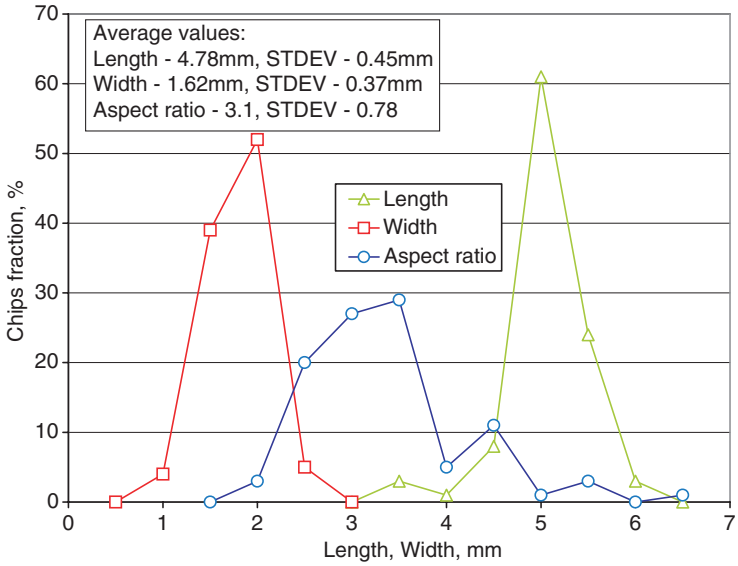

Fig. 6.8 Size distribution and aspect ratio of chips C2, determined by direct measurement of over 200 chips under magnification

and width, respectively, with the latter having a higher standard deviation. It is seen that the average width of 1.62 mm is close to a maximum of 70.4% for a sieve with an opening of 1.4 mm, obtained for the same morphology C2 from sieve analysis.

6.3.3 Bulk Density

Another parameter characterizing particulates is their tap density. It affects directly their delivery from a manufacturer, their conveyance within a processing system and their heating rate. As summarized in the last column of Table 6.1, the morphologies described here have tap density values between 0.729 g/cm^3 for flakes F1 and 1.201 g/cm^3 for pellets P1. For the commonly used chips C1-C6 the density is between 0.819 g/cm^3 and 1.016 g/cm^3. According to literature estimates, a value larger than half of the ingot density is required to achieve appropriate transport and heat transfer properties. The values of tap density for particulates examined here either exceed or are very close to this threshold.

6.3.4 External Defects

The major defects generated during mechanical comminution refer to the size and shape of particulates. The most frequent cases are shown in Fig. 6.9. When the

Fig. 6.9 A selection of defective feedstock occasionally generated during mechanical fragmentation: **a** large fractured pieces affecting melting homogeneity, CD1; **b** long laths prone to blocking a feeding system, CD2; **c** sub-micron fine prone to oxidation and ignition, CD3

ingot is not cut but rather fractured by chipping tools, relatively large chips (CD1) that are surrounded by pure fracture surfaces are generated (Fig. 6.9a). Since the volume of such a defective chip is significantly larger than a regular chip, they might not be completely melted while in a semisolid slurry, thus affecting the integrity of product microstructure. The material factor exerts some influence, and brittle alloys are more prone to generate such defective morphologies. On the other hand, alloys with high ductility exhibit difficulties in separating into individual pieces. The feedstock CD2, shown in Fig. 6.9b, has a form of long lathes with a cross-section similar to regular feedstock. These were created when a tool was turning an ingot rather than chipping it. A substantial contribution of this feedstock would negatively affect the feedstock flow behavior within the system. The sub-micron fines are considered highly detrimental when mixed with the regular feedstock (Fig. 6.9c). They create safety issues that may lead to ignition and explosion during feeding or even storage. When introduced into the machine barrel, the powder has a tendency to react with traces of oxygen occluding the powder surface which, after reaching the system, is mixed with argon. After conversion to the oxide in small volumes it contaminates the final product. While large volumes of an oxide are created, they may also adhere to the screw surface and barrel wall, thus increasing the mixing torque value required, which may ultimately lead to the jamming of the equipment.

6.3.5 Phase Composition and Microstructure

The chemistry of mechanically comminuted chips and its homogeneity are inherited entirely from as-cast ingots. The morphology and distribution of the major structural components of magnesium alloys, i.e., αMg size and intermetallic phases, depend on the chip location within an ingot. Thus each chip has its specific portion of the dendritic structure, as well as the content and morphology of intermetallics. The chips that originate from a skin layer exhibit

finer-grained structures. While for Mg–Al and Mg–Al–Zn alloys the $Mg_{17}Al_{12}$ compound is the major intermetallic phase, for alkaline or rare earth elements containing alloys, such as AJ52 or MEZ, the intermetallic phase structure is more complex. In summary, the consequence of comminuting large ingots into small particulates is the elimination of chemical and phase macrosegregation.

As a result of interaction with the chipping tool, alloys experience microstructural changes. For chips with a smaller size, deformation is severe, frequently accompanied by cracks originating at the interface between massive precipitates of intermetallics and αMg, or within the divorced eutectic and propagating further into the αMg matrix (Figs 6.10a,b). Details of microstructural changes depend on the type of alloy and its deformation behavior, but the same general features are present in Mg–Al–Sr (Figs 6.10b,c) and Mg–Zn–Re (Figs 10e,f) alloys. For chips of alloys with higher Al content, e.g., Mg–11Al–1Zn, cracking of the massive $Mg_{17}Al_{12}$, and a divorced eutectic with crack propagation into the matrix is more frequently observed than the presence of other deformation features within the αMg grains themselves (Fig. 6.10g,h). As suspected from macroscopic observations for all chips, thin surface films usually exhibited more extensive damage, while the deformation of inner portions is rather uniform.

The pellets manufactured by extrusion show substantially different microstructures. The cross-sectional view (Fig. 6.11a) indicates the equiaxed αMg grains with numerous precipitates of $Mg_{17}Al_{12}$. Occasionally single inclusions of metallurgical rectification origin are present with some of them having a size of the order of the matrix grains. The equiaxed character of the matrix is confirmed on the longitudinal section (Fig. 6.11b). Although no evident gradient along the through-thickness direction is detected, grain size is non-uniform with bands parallel to the extrusion direction. Moreover, the surface skin of a single-grain thickness has grains significantly smaller. At longitudinal sections, the intermetallic phase forms chain-like colonies of spheroidal particles and elongated stringers oriented along the extrusion direction, i.e., the pellet's axis.

6.4 Characterization of Rapidly Solidified Granules

6.4.1 Morphological Features

The application of injection molding requires relatively coarse particulates, and their diameter should be in the order of millimeters as opposed to micrometers, as is used in powder metallurgy. Several examples of granules manufactured using techniques described earlier are shown in Fig. 6.12. The granules with smaller sizes, shown in Figs. 6.12a-c (G1-G3), were obtained in granulation towers. The majority of them have a shiny metallic color, characteristic of the oxide-free surface. However, some particulates, especially among those in Fig. 6.12b, exhibit dark oxidized surfaces. A correlation exists between the particulate size and surface color, with larger particulates experiencing more surface oxidation. The significantly

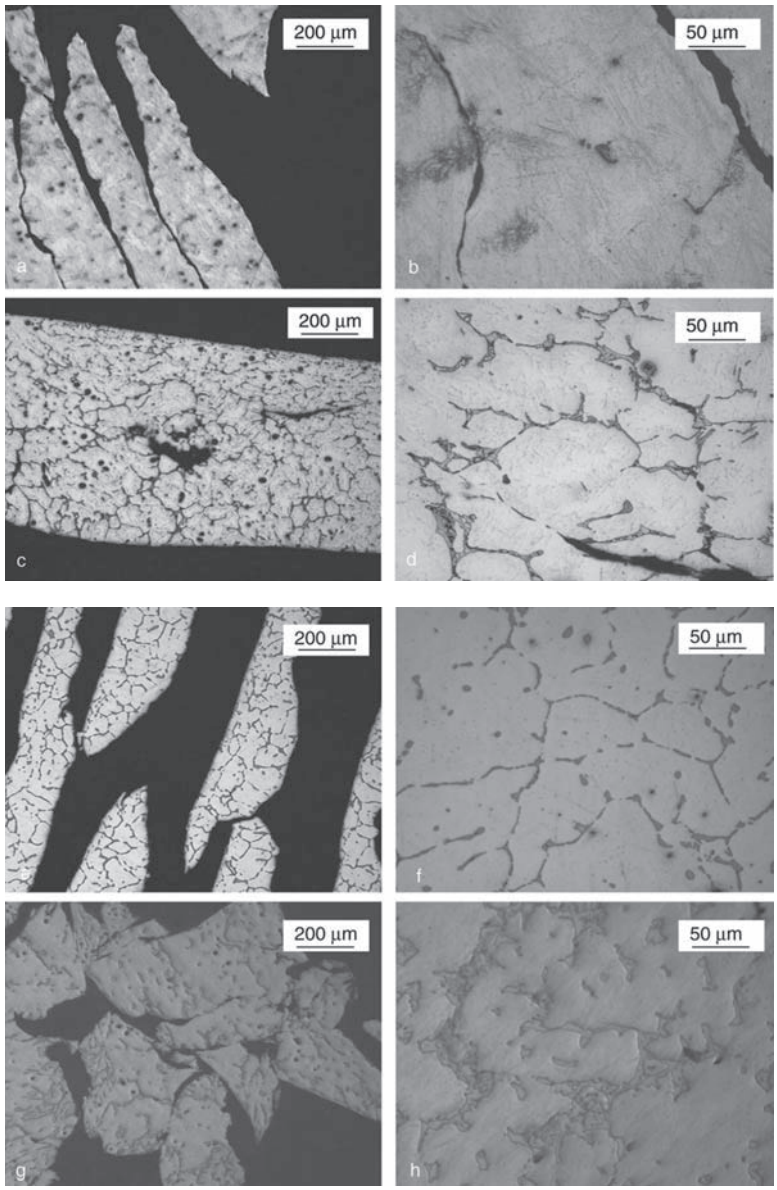

Fig. 6.10 Effect of alloy chemistry on morphology of chips manufactured by the same technique of mechanical fragmentation. Cross sectional images showing evidence of cold deformation: **a,b** AM60B; **c,d** AJ52; **e,f** MEZ; **g,h** AZ11-1

larger granules shown in Fig. 6.12d and 6.12e were obtained by direct casting of the alloy droplets followed by quenching using a liquid or gas (G4) and in a fluidized sand bed (G5). Recently, an experimental technique was developed by

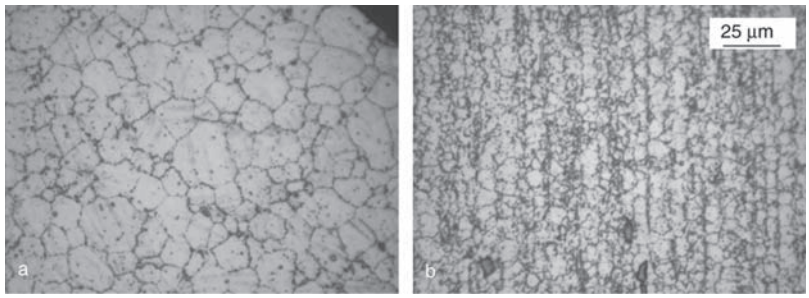

Fig. 6.11 Internal microstructure of extruded pellets P1-AZ91D: **a** transverse section; **b** longitudinal section

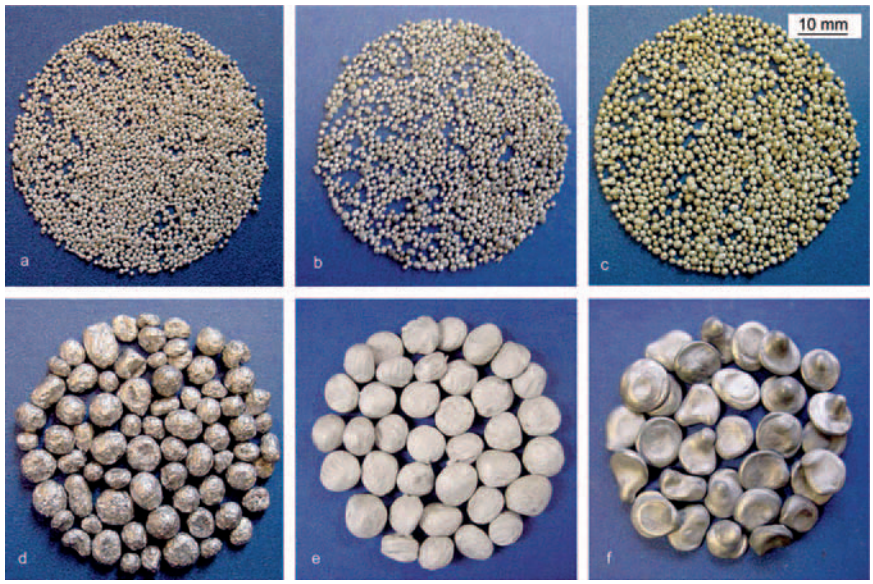

Fig. 6.12 The morphology of particulates obtained from a liquid precursor by various methods of atomization/granulation: **a** G1–inverted stream apparatus; **b** G2 – argon gas system; **c** G3–inverted stream apparatus; **d** G4– large droplets casting with a liquid or gas quench; **e** G5–large droplets casting with a quench in a fluidized sand bed; **f** ZA8 zinc tear-drop shape

Noranda Inc. for manufacturing tear-drop-like shape particulates from Zn based alloys. The process may generate different sizes from 2 to several millimeters, and the relatively large version (G6) is portrayed in Fig. 6.12f.

6.4.2 Dimensional Features

The major difference between granules examined here is their average size and size distribution. The summary of sieve analysis is given in Table 6.2 with plots

of selected granules compared in Fig. 6.13. For the smallest granules G1, a fraction of 90% was retained by the sieve with an opening of 0.6 mm. The remaining portion was retained on sieves with openings between 2.36 mm and completely solid. A different distribution was found for granules G2 where sizes were split almost equally between sieves of 0.6 mm and 1.3 mm. For granules G3, the maximum fraction was retained by the sieve of 1.4 mm with a very small portion held by the 2.36 mm opening. The sieve analysis did not provide full characterization of large granules G4 and G5. This is expressed by the plot in Fig. 6.13, where almost all G4 granules were retained by the largest sieve opening of 4.74 mm, i.e.,

Table 6.2 The size distribution of particulates manufactured by the rapid solidification, as determined by screen analysis according to ASTM specification E276–68. The table values represent fractions in weight % retained by sieves of given opening [17]

Particulate type	Shape type	Alloy grade	Sieve opening, mm							Tap density, g/cm^3
			4.75	3.35	2.36	2.00	1.40	0.60	0.00	
Granules	G1	AZ91D	0	0	0.5	0.9	7.0	90.0	1.6	1.078
	G2	AZ91D	0	0	0	0.1	41.8	58.1	0	1.020
	G3	AZ91D	0	0	0.8	8.1	67.7	23.4	0	1.127
	G4	AZ91D	76.1	23.5	0.2	0	0.1	0.1	0	1.008
	GD2	AZ91D	0	0	0	0	47.2	52.8	0	1.064
	GD3	AZ91D	0	0	1.8	8.3	50.6	39.3	0	0.911

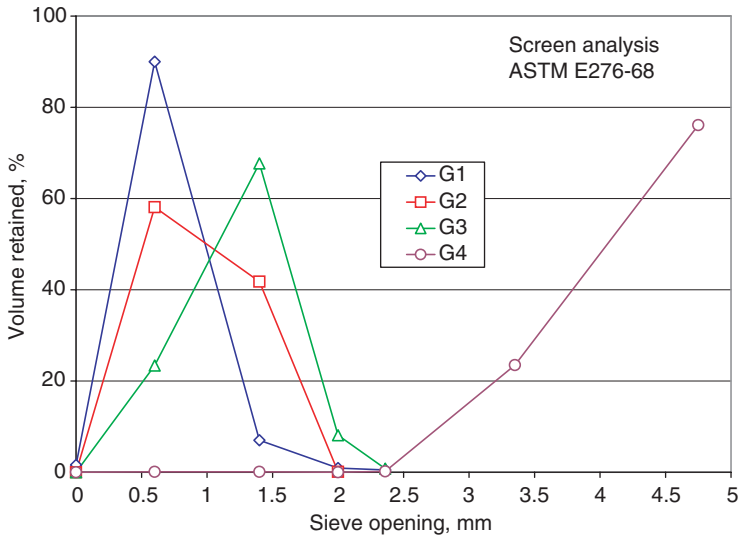

Fig. 6.13 The size distribution of particulates, as determined by the sieve analysis ASTM E276–68 [17]

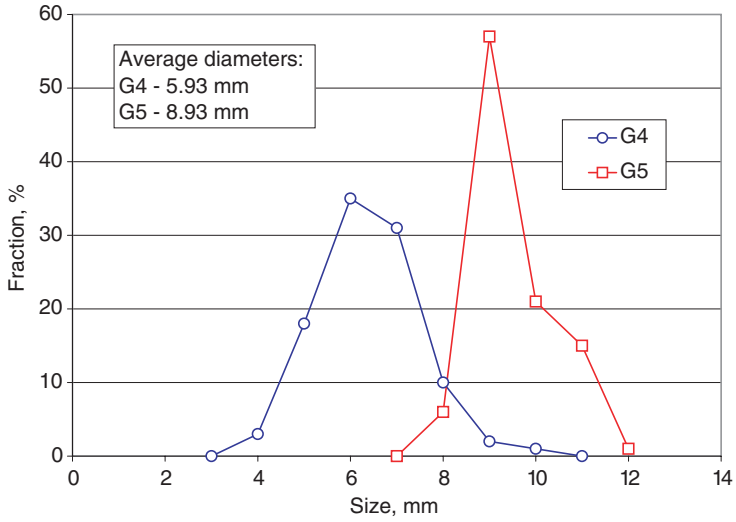

Fig. 6.14 The size distribution of granules G4 and G5 determined by a quantitative analysis under magnification [17]

they remained outside the sieve size employed. According to a direct measurement of over 200 granules, the average diameter of the G4 shape is 5.93 mm with a relatively wide distribution profile and a maximum of 35% around a diameter of 6 mm (Fig. 6.14). The visually larger G5 granules are characterized by an average diameter of 8.93 mm. Their distribution profile has a maximum of 57% at the location close to the average value.

6.4.3 Bulk Density

As explained in previous sections, the bulk density is of importance for the transportation of particulates, the feeding of the injection system, their conveyance along the machine barrel, as well as for heat transfer and melting rate. For all types of granules examined here, the tap density was between 1.008 and 1.127 g/cm^3 with no evident correlation with their size (Table 6.2). Since this is over 0.5 of the AZ91D alloy density of 1.81 g/cm^3, granules meet the condition of minimum density. The tap density of granules is generally larger than values exhibited by mechanically comminuted chips.

6.4.4 External Defects

There are numerous defects created at the manufacturing stage, and the most frequent of them include:

(i) spherical shape distortion;
(ii) agglomeration;
(iii) surface deterioration through reactions with impurities of the gases inside the granulation tower.

Because individual droplets spheroidize from a ligand shape as a result of the break up of a liquid stream, too fast solidification prior to spheroidization generates irregularly shaped particulates. In contrast, too slow solidification, combined with a lack of sufficient separation between particulates, causes their agglomeration. Shape deviations are seen within particulates which, according to visual assessment, appeared to be highly spheroidal (Fig. 6.15). An interaction was taking place between particulates that traveled in liquid and semisolid states during granulation. As a result, the particulates at the initial and well-advanced coalescence stages were occasionally observed. An extreme case of shape deviation is shown in Fig. 6.16a where particulates marked

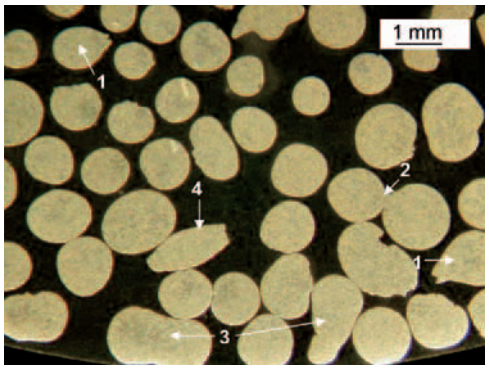

Fig. 6.15 The cross-sectional image of granules G1 with several shape deviations indicated: 1–tear-drop shape; 2–initial stage of coalescence; 3–advanced stage of coalescence; 4–ovoid shapes [17]

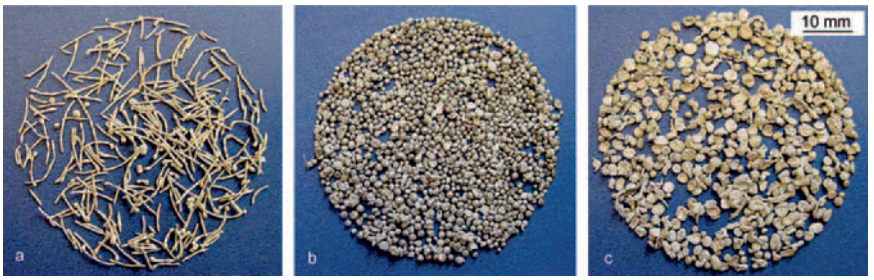

Fig. 6.16 A selection of granules with external defects: **a** long needles–complete deviation from globular shape, GD1; **b** granules containing fraction with irregular shape and partial oxidation, GD2; **c** particulates with heavily oxidized surface and irregular shape, GD3 [17]

as GD1 reached the form of whiskers with a diameter of 0.8-1 mm and a length up to 20 mm. Frequently the whiskers have a spherical particle attached to their end. Since their surfaces are shiny metallic, an oxidizing reaction is excluded as the key cause of shape defect. At this stage, the exact cause of their origin is not clear.

Prevention of surface deterioration during granulation is of particular importance for magnesium alloys, known for their high affinity to oxygen. There are reports that even for a granulation environment of high purity He, the oxygen potential was still high enough to cause a reaction, and for Al–Mg particulates with a size between 5 μm and 50 μm, an oxide layer with a thickness of 5 nm was formed. A moderate surface oxidation was experienced by particulates GD2 (Fig. 6.16b). For a fraction of granules GD2 with a spherical shape, the extent of oxidation was correlated with their size: While small granules had a shiny metallic surface, larger ones were matt and dark, indicating oxidation. There were also some particulates among GD2 with an irregular shape and a surface covered with an oxide. In an extreme case of a highly oxidizing atmosphere, the oxide layer can be thick enough to make spheroidization impossible. Under such conditions, the particles with an irregular shape and heavily oxidized surface were formed (Fig. 6.16c). Their size distribution, with roughly 50% of particulates retained by the sieve of 1.4 mm, is close to types designated as G1 and G3 (Table 6.2).

6.4.5 Stability of Chemical Composition

During granulation, a relatively large free surface of the liquid alloy is exposed to the gaseous atmosphere. Since certain chemical elements of magnesium alloys are known to have a very high evaporation rate, the chemistry of small droplets is prone to changes. Such a phenomenon was registered during the laser melting of an AZ91D alloy where the Al content was increased to 11%–12%, mainly due to the evaporation of Mg [10]. Zinc, present as a minor element in AZ91D alloy, is also affected by evaporation and its content was reduced to 0.68%–0.70%. Such a strong loss occurs because zinc has a vapor pressure one order of magnitude higher than magnesium in the molten state. The reduced content of Mg leads to a higher volume fraction of the $Mg_{17}Al_{12}$ phase—a phenomenon exactly opposite from what should be expected based on solidification conditions.

The chemical analysis of selected granules is summarized in Table 6.3. The measurement was conducted using an inductively coupled argon plasma mass spectrometer and following ASTM E1097-97 (modified) and E1479-99 standards. It is seen that the content of all elements tested, including Al and Zn, is within the range specified by the ASTM B94 standard. Moreover, there is no difference in chemistry between particulates of different sizes. Originally, it was suspected that due to a longer solidification time and exposure to the gas atmosphere, larger G3 granules might exhibit higher deviations in chemistry than G1 particulates with smaller size.

Table 6.3 Chemical compositions of selected granules as determined by inductive coupled plasma spectrometry according to ASTM E1097–97 (modified) and E1479–99. All values are in weight % [17]

	Al	Zn	Mn	Si	Cu	Ni	Fe	Mg
G1	8.58	0.79	0.18	0.02	<0.001	<0.001	<0.004	Bal
G3	8.74	0.79	0.17	0.01	<0.001	<0.001	<0.004	Bal
AZ91D Standard ASTM B94	8.3-9.7	0.35-1.0	0.15	0.10 Max	0.03 Max	0.002 Max	0.005 Max	Bal

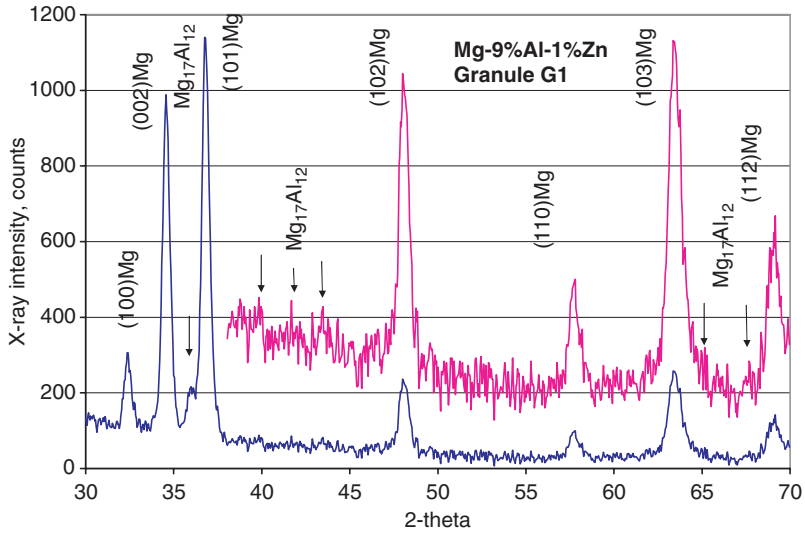

Fig. 6.17 The X-ray diffraction pattern of granules G1 with all major peaks of αMg phase and indicated angle locations, corresponding to peaks of $Mg_{17}Al_{12}$ intermetallic phase [17]

6.4.6 Phase Composition

The principal effect of a high cooling rate during solidification is a drastic slowdown, or sometimes even complete suppression, of movement or diffusion of atoms within an alloy. As a result, atoms are prevented from occupying the equilibrium crystal sites with the lowest energy. The solubility of a solute in solid and liquid under equilibrium conditions is usually different, and solute partitioning leads to segregation phenomena. However, if the solid/liquid interface advances rapidly, partitioning cannot follow and solute trapping occurs. Thus the solute content within the solid, growing from the melt, is higher than that predicted from the phase diagram. In extreme cases of very rapid solidification, there is no partitioning whatsoever and a solid forms with the same composition as the liquid.

The diffraction pattern of rapidly solidified granules contains all peaks typical for Mg with the strongest of (101) at 2-theta of 36.6 deg (Fig. 6.17). The major

difference, as compared to patterns collected previously from the same alloy in the as-cast state, is the significantly higher intensity of the (002) peak from the basal planes. According to the JCPDS standard, the intensity of this peak is 41% of that for the (101) peak. Another feature of this pattern is a lack of distinct peaks for the $Mg_{17}Al_{12}$ phase. In fact, the only peak that could be ascribed to this phase is the strongest one with I/Imax of 100% and located at 2-theta of 36.191 deg. Two remaining strong peaks with an equal intensity of 33%, located at 2-theta of 40.227 deg and 65.186 deg, are difficult to extract from the background noise. Based on a comparison with previously published diffraction patterns of the same alloy, it is concluded that the volume fraction of the $Mg_{17}Al_{12}$ phase within granules is lower than the 9% to 10% detected in the as-cast state. At this point, the exact extent of this reduction cannot be unambiguously defined. The reduction in content of the $Mg_{17}Al_{12}$ phase is consistent with the literature observations made during melt spinning and splat quenching [11, 12].

6.4.7 Internal Microstructure

Due to rapid solidification of a small volume of the alloy, the granules developed a fine microstructure of equiaxed dendrites which were constituted of the αMg phase, while the $Mg_{17}Al_{12}$ (γ) compound was distributed within the interdendritic zones. Content of the γ phase is equal across the granule cross section (Fig. 6.18a). For G1granules, the typical distance between the closest dendrite arms is of the order of 10 μm to 15 μm, and the arrangement of dendrites suggests their random crystallographic orientation (Fig. 6.18b).

The detailed morphology of the αMg and $Mg_{17}Al_{12}$ (γ) phases is shown in Fig. 6.19. The γ phase contrast in the scanning electron microscopy is bright—the reverse of that seen in optical microscopy (Fig. 6.19a). The massive precipitates of the intermetalic phase, observed under high magnification, are irregularly shaped while filling the interdendritic spaces. In the case of larger precipitates, there were internal voids, and some of them likely formed due to solidification shrinkage. Some of them could also be caused by etching during sample preparation (Fig. 6.19b). Since the intermetallic phase γ is distributed within interdendritic spaces, it separates αMg and very often forms a cellular structure (Fig. 6.19c). The particulates are essentially pore-free, though for larger sizes an irregular surface porosity could occasionally be seen (Fig. 6.19d). The general features discussed here for granules G1 were also valid for granules G2 and G3. The major difference was a tendency toward coarsening of αMg dendrites and an increased distance between the $Mg_{17}Al_{12}$ precipitates with dendritic arms. It is assumed that in all systems dendrites begin coarsening immediately after formation [13]. During the coarsening process the average length of the system and the dendrite shape evolve, resulting in a microstructure determined largely by the coarsening process. Therefore, it was suspected that substantial changes could be created in the case of the larger granules G4 and G5. In fact, after solidification in air, G4 granules exhibit a much

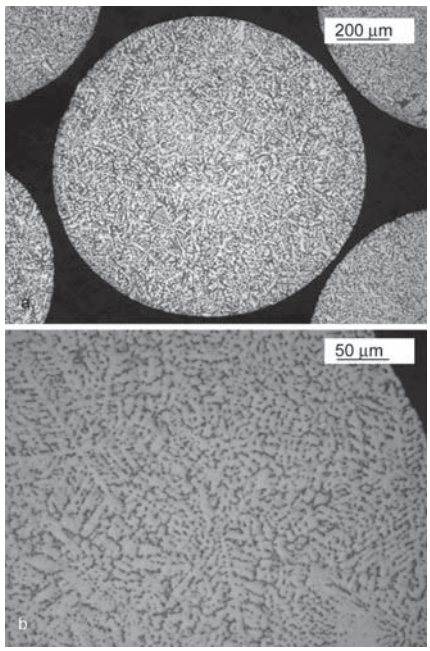

Fig. 6.18 Optical microscope images of internal microstructures of granules G1: **a** general view; **b** magnified image with an alignment of dendrites in near surface region [17]

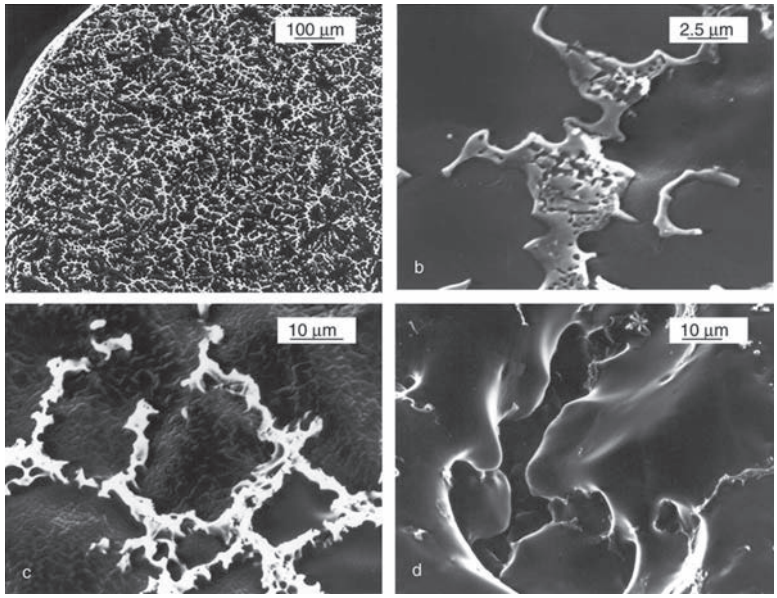

Fig. 6.19 SEM images of microstructural details within granules: **a** general view of distribution of intermetallic phase in granule G1; **b** a detailed morphology of $Mg_{17}Al_{12}$ phase in G1; **c** cellular arrangement of intermetallic $Mg_{17}Al_{12}$ phase in G1; **d** shrinkage porosity on the surface of granule G3 [17]

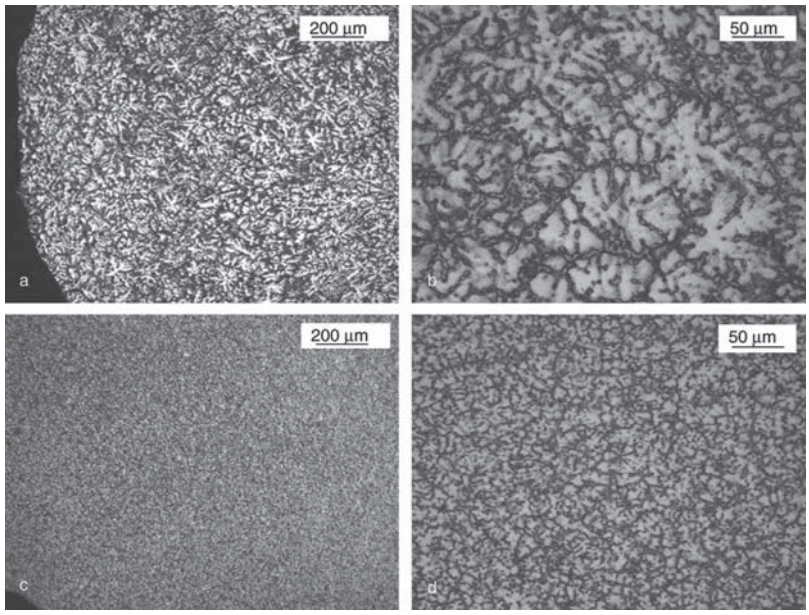

Fig. 6.20 The influence of quenching rate on the microstructure of large granules G4 obtained by casting of large droplets: **a** granule solidified in air; **b** details of dendrites morphology from **a**; **c** granule after solidification in a quenching liquid; **d** details of dendrite morphology from **c** [17]

coarser microstructure, and the αMg cell within the eutectics is of the order of 96 µm (Fig. 6.20a,b). Quenching in a liquid, however, for a similar size of granules, significantly refines their microstructure with the eutectic αMg cell size reduced to 11 µm (Fig. 6.20c,d). Thus by introducing more aggressive quenching media, granules with sizes up to 10 mm retain essentially the same microstructure as that observed for small granules typically below 1 mm in size.

6.4.8 Microstructure of Globules with External Defects

As revealed by cross-sectional analysis, external defects do not substantially affect the granule's internal microstructure, which in the case of the GD1 type, is slightly finer than that for the type G1 (Fig. 6.21a). In addition, there is some difference in the orientation of dendrites caused by the elongated shape of particulates, which affects directions of heat transfer during solidification (Fig. 6.21b). The shape distortion, observed for granules GD3, is most likely associated with their surface oxidation. Since the oxide blocks the heat transfer, some coarsening of internal structure was anticipated. However, even for an extensively oxidized surface such as that for granules GD3, the oxide layer is not seen as a separate phase but rather as the deterioration of the outer surface expressed by an increased roughness

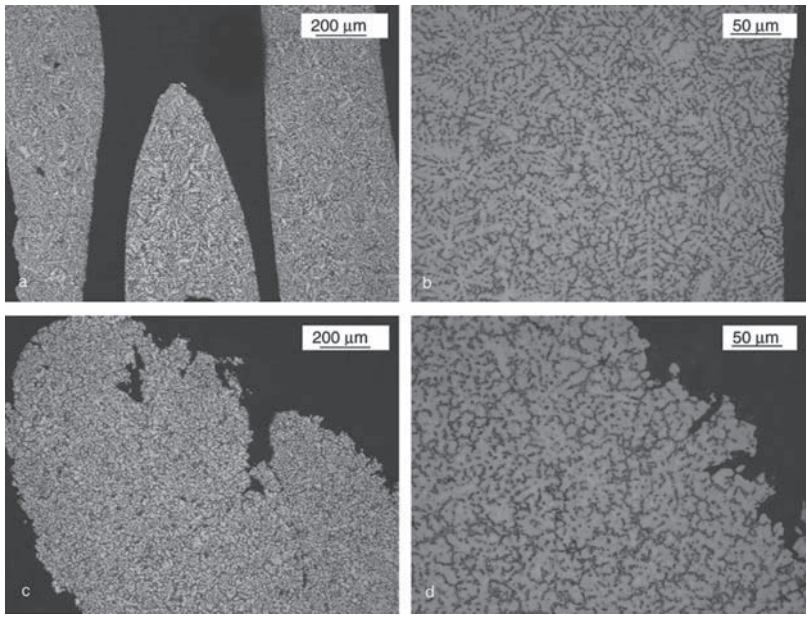

Fig. 6.21 The microstructure of granules with defective shape: **a** general view of thin whiskers GD1; **b** morphological details of dendrites in magnified GD1; **c** general view of heavily oxidized granules with irregular shape GD3; **d** details of surface roughness and morphology of dendrites in GD3 [17]

(Fig. 6.21c). Here, numerous protrusions and pits on the surface are seen under higher magnification (Fig. 6.21d). The internal microstructure is essentially the same as that observed for spheroidal granules. No noticeable coarsening of the microstructure is detected, which could be associated with a reduced cooling rate caused by a presence of the oxide film.

6.5 External Characteristics Affecting Injection Molding Applications

According to early predictions, the size of particulates was not thought to be critical, even though smaller sizes were preferred because of better heat transfer and handling capabilities. Similarly, the particulate shape was not seen as the key factor, and the initial feedstock was mostly irregular. Later experiments revealed that irregular feedstock is prone to blocking the system and does not exhibit good packing characteristics, causing difficulties in achieving a fast enough heat transfer from the barrel walls and the appropriate melting rates. Despite claims that spherical particulates represent the optimum shape, challenges from the mechanical comminution method prevent their commercial manufacture. Cylindrical pellets

still experience similar difficulties. As a result, elongated chips with a roughly trapezoid shape represent the major commercial product. The size of all particulates is within a several millimeter range. So far no extreme dimensions outside this range are explored.

6.5.1 Mechanically Fragmented Chips

As a result, later developments attempted to specify shape and size requirements. According to invention [14], a substantial proportion of particulates should be shaped such that the ratio of the length of the largest dimension to the effective diameter is in the range of 1 to 4, and that a substantial proportion of the particulates lies within the range of 0.5 mm to 5 mm. Preferably, the particles should be shaped such that the ratio of the length of the largest dimension of a particle to the effective diameter is in the range 1.2 to 3—preferably 1.2 to 2. As another indicator, the tap density of the mass of particles is used, and it is claimed [14] that it should be at least 50% of the theoretical density of the bulk alloy. Of the three distinct shapes considered—ovoid, teardrop and needle-like—the two former were preferred. It is emphasized that the spherical particles would provide an optimum profile for minimizing the foregoing problems, but the cost of their manufacture by mechanical comminuting is unacceptably high, and for magnesium alloys the process may be dangerous. Of concern is also the nature of the particulate surface. Although the particle should have a substantially smooth surface, it is appreciated that the particles will have a small degree of surface roughness.

In engineering practice, the selection of particulate size depends on the barrel diameter. The optimum size distribution for machines with barrel/screw diameters 70 mm to 85 mm is listed in Table 6.4. While there is obviously a limitation on the maximum size, the critical factor is an absence of the fine fraction.

6.5.2 Rapidly Solidified Granules

Experimental verifications confirmed that granules of AZ91D alloy, obtained by rapid solidification techniques, were successfully used as a feedstock in a barrel

Table 6.4 The requirement of chip size distribution during processing with barrel diameter 70 mm to 85 mm, as determined by screen analysis according to the ASTM E276–98 standard. The values represent fractions in weight %, retained by sieves of given opening

	Sieve opening, mm						
Particulate type	4.75	3.35	2.36	2.00	1.40	0.60	0.00
Chips	0	0	5 max	30-70	30-60	5 max	0

with diameter of 70 mm. The near spheroidal shape and consistent size of the granules were beneficial for both the feeding and flow characteristics inside the machine barrel. An important factor that affects the application of particulates is their shape. Literature data indicate that irregular particulates are prone to block feeding devices and do not show good packing characteristics. Their irregular shape inhibits heat transfer from the machine barrel walls, thus reducing effective melting rates. Of many particulate shapes studied, including ovoid, teardrop, needle-like and cylindrical, the spheroidal shape, such as that obtained after granulation from the liquid precursor, provided the best feeding, packing and heat transfer behavior. There is still no data on the optimum size required, and granules with diameters between 0.5 mm and roughly 5 mm are considered well processable in presently used systems. It is further anticipated that larger or differently designed systems will accommodate particulates as large as 10 mm in diameter. Instead, attention is paid to size uniformity, since too wide a size distribution profile negatively affects the homogeneity of their melting.

6.6 Global Manufacturing Market of Magnesium Particulates

The market for particulate feedstock was created in 1993 after commercialization of the first injection molding machine in Japan. According to source [15], the global consumption of magnesium feedstock in 2000 was approximately 7,600 tonnes. At that time, there were 199 molding machines worldwide, 143 of them in Japan. As the number of machines increased to 264 in 2003, according to proportional estimation, the world consumption of magnesium particulate feedstock should be close to 12,000 tonnes. Compared to 128,000 tonnes (2002) of magnesium alloys consumed by the die casting sector, molding represents over 9%.

There are a number of companies involved in particulate feedstock production worldwide, and most of them are listed in Table 6.5. The major volume is manufactured in China and Japan, partly because of the proximity to the consumers' market. The single manufacturer Taiyuan Corporation (China) shipped over 3,000 tonnes in 2003. The second largest: Nanjing Welbow Metals, produced 500 tonnes during the same time. The largest North American manufacturer, Magnesium Technology (formerly Rossborough Manufacturing Co), shipped about 500 tonnes in 2003, which is a decline from 1,000 tonnes in 2002. Two other American manufacturers, Reade and ESM II, stopped production due to insufficient demand. Similarly the large European manufacturer Ecka Granules, with two plants, Aluma and Non-Ferrum, having a total capacity of 12,000 tonnes, does not produce feedstock due to low demand.

Excluding China and Russia, the chipping companies are not associated with smelters of the primary magnesium metal. Instead, their major operation is grinding magnesium fines for desulfurization of steel. This sector represented 60,000 tonnes or 16% of magnesium shipments worldwide in 2002. The production of fine chips

Table 6.5 The major manufacturing and development centers of magnesium particulate feedstock for injection molding applications [18]. Xe–Laboratory trials, xn–Commercial scale equipment but no manufacturing at present

		Production level		Production method		
Country	Company name	Experimental	Commercial	Mechanical Chiping	Rapid Solid-ification	Solid State forming
Canada	Alberta Research Council, Edmonton, Alberta	x			x	
Canada	Intermag Technologies, Sainte-Foy, Quebec	x			x	
China	Taiyuan Inter. Economical and Technical Corporation, Taiyuan		x	x		
China	Nanjing Welbow Metals Co. Nanjing, Jiangsu		x	x		
France	MCP Technologies S.A., Romans, Drome		xn	x		
Germany Austria	Ecka Granules:- Aluma GmbH, Fridolfing- Non-Ferrum Metallpulver Geselschaft, St. Georgen, Saltzburg		xn	x		
Japan	Chuo-Kosan Co. Chuo-Ku, Tokyo		x	x		
Japan	Japan Steel Works, Chiyoda-ku, Tokyo		x	x		
Russia	Solikamsk Desulfurized Works, Solikamsk		x	x	xn	
USA	Magnesium Electron, Reade Manufacturing Co, Manchester, NJ		xn	x		
USA	Magnesium Technology (Rossborough Manufacturing Co.), Walkerton, Indiana		x	x		xe
USA	ESM II Inc., Valencia, PA		xn	x		
USA	The DOW Chemical Co., Midland, MI	x		x		

for desulfurization, along with the possibility of using the same equipment, are the major reasons that the techniques of the mechanical fragmentation of as-cast ingot are the only ones used at a commercial scale. Techniques of rapid solidification and solid state forming still remain on an experimental level. There are some attempts to recycle the molded scrap by direct mechanical fragmentation into chips. A clear advantage here is the low contamination of a scrap generated during molding, as compared to die cast standards. While at present a predominant portion of the feedstock is represented by the AZ91D grade, other alloys with more complex chemistry are also gradually introduced.

6.7 Summary

The coarse particulates represent a new type of feedstock, suitable for semisolid processing. Different sizes and shapes of magnesium alloy particulates are presently produced worldwide, at both laboratory and industrial levels, using mechanical comminution and rapid solidification techniques. The internal microstructure generated at the stage of manufacturing is essential for semisolid processing applications, since it leads to the generation of thixotropic slurries under the sole influence of heat. An increased demand for quality feedstock initiated extensive research to develop particulates with optimum dimensional and morphological features at a low cost. Manufacture of the particulate feedstock created a niche market with growing opportunities for the magnesium industry.

References

1. Hostetler D Metal injection molding. US Patent 6,350,328 B1, 26 Feb 2002
2. Das SK, Chang CF (1985) In SK Das, CM Kear, CM Adams (eds) Rapidly solidified metallic alloys, TMS, Warrendale, PA p 137
3. Avedesian MM, Baker H (eds) (1999) Magnesium and Magnesium Alloys. ASM International, Materials Park, OH
4. Busk Z (1984) In Metals Handbook. 9th ed. ASM International, Materials Park, OH, p 131
5. German RM (1994) Powder metallurgy science. MPIF, Princeton, NJ
6. Saxena S (1995) Apparatus for production of metal granules. US Patent 5,402,992, 4 Apr 1995
7. Ghosh DS, Olsen KP (2000) Apparatus and method for the formation of uniform spherical particles. US Patent 6,162,377, 19 Dec 2000
8. Turley DM, Doyle ED (1982) In RC Gifkins (ed) Strength of metals and alloys (ICSMA6). Pergamon Press, Oxford, pp 553–559
9. McQueen HJ, Blum W (2000) Dynamic recrystallization: Sufficient mechanism in the hot deformation of Al. Materials Science and Engineering A 290(1-2):95–107
10. Dube D et al (2001) Characterization and performance of laser melted AZ91D and AM60B. Materials Science and Engineering A 299(1):38–45
11. Heymann F et al (1989) Journal of Materials Science 24:2369

12. Koutsomichalis A, Seattas L, Badekas H (1994) Journal of Materials Science 29:6543
13. Ludwig A (2001) Comparison of dendrites of a pure material with thermal alloy dendrites: An experimental method to estimate the To temperature. Acta Materialia 49(1):165–168
14. Kjar A et al (1996) Particulate feedstock for injection molding. US Patent 5,777,546, 26 Nov 1996
15. Dworog A (2002) Grundlagen of Magnesiumspritzgiessens. Shaker Verlag, Aachen
16. Czerwinski F (2005) Coarse particulates—a new material precursor for net shape forming. International Journal of Powder Metallurgy 41(1):64–70
17. Czerwinski F (2004) Magnesium alloy particulates for thixomolding applications manufactured by rapid solidification. Materials Science and Engineering A 367:261–271
18. Czerwinski F (2005) Injection molding feedstock—a niche market for magnesium industry. Metall 59(6):376–381

7
Oxidation Behavior of the Feedstock

7.1 Introduction

An extremely high affinity of magnesium to oxygen, along with the highly developed surface area of magnesium alloy chips, used as a feedstock during injection molding, makes the system prone to oxidation. It is anticipated that alloy protection inside the machine barrel by an inert atmosphere of argon is essentially better than molten surface shielding by SF_6 gas during die casting. So far there is a lack of experimental verification, and existing data send a rather unclear message. First, the inertness of an argon atmosphere is sensitive to small amounts of entrapped air, and the growth rate of MgO on Al-based alloy at temperatures of 450 °C to 800 °C in a mixture of Ar+1%O_2 and Ar+5%O_2 equals 25% and 70%, respectively, of the oxidation rate in air [1]. Second, the final oxygen content in molded parts is still about one order of magnitude higher than that present in an initial feedstock [2]. A description of the alloy oxidation behavior is therefore of key importance for designing material feeding and Ar flow systems. It is also important for feedstock manufacturing in terms of morphology and its chemical modification against oxidation. In particular, it is helpful in verifying the necessity of beryllium additions routinely used in conventionally cast alloys.

The objective of this chapter is to identify factors controlling surface degradation of magnesium alloys at high temperatures, exposed to both reactive and inert atmospheres. Moreover, the techniques of molten metal protection during industrial processes are presented along with possible consequences of the protection perturbation.

7.2 Oxidation Kinetics

The progress of any oxidation reaction is most often controlled by a continuous monitoring of the weight change. Thermogravimetric measurements of AZ91D commercial alloy reveal the complex character of alloy weight changes versus time.

F. Czerwinski, *Magnesium Injection Molding*.

7.2.1 Initial Stage Reaction

The initial stage reactions typically cover the several first minutes after an alloy is exposed to high temperatures. A high affinity of magnesium to oxygen makes it difficult to preserve the oxide free metallic surfaces. A reaction with air at room temperature creates a thin passive film with an estimated thickness of 25 Å [3]. The film, preformed at room temperature, continues to grow first during heating up to the test conditions following kinetics represented by the thermogravimetric curves. As seen in Fig. 7.1a, the very initial stage of air exposure at temperatures in the range of 197 °C to 487 °C is characterized by rapid weight gain, similar for all samples. However, after a time interval of 2–4 min and a corresponding weight gain of 20–25 μg/cm^2, the further reaction kinetics depend on the temperature. While the alloys tested at 472 °C and 487 °C continued to increase their weight at a significantly lower rate, the alloy subjected to temperatures lower than 397 °C experienced a weight reduction. In general, the lower the test temperature, the faster and larger weight loss is observed.

The maximum oxide thicknessess achieved during preheating, as converted from weight gain data, are equal to 640 Å and 840 Å for 197 °C and 487 °C, respectively. This calculation is based on the assumption that at this stage the oxide is uniform in thickness and the weight gain of 1 μg/cm^2 corresponds to a 28 Å thick MgO film with a density of 3.58 g/cm^3. As pointed out in early studies by Pilling and Bedworth [4], due to the large difference in densities between the oxide and

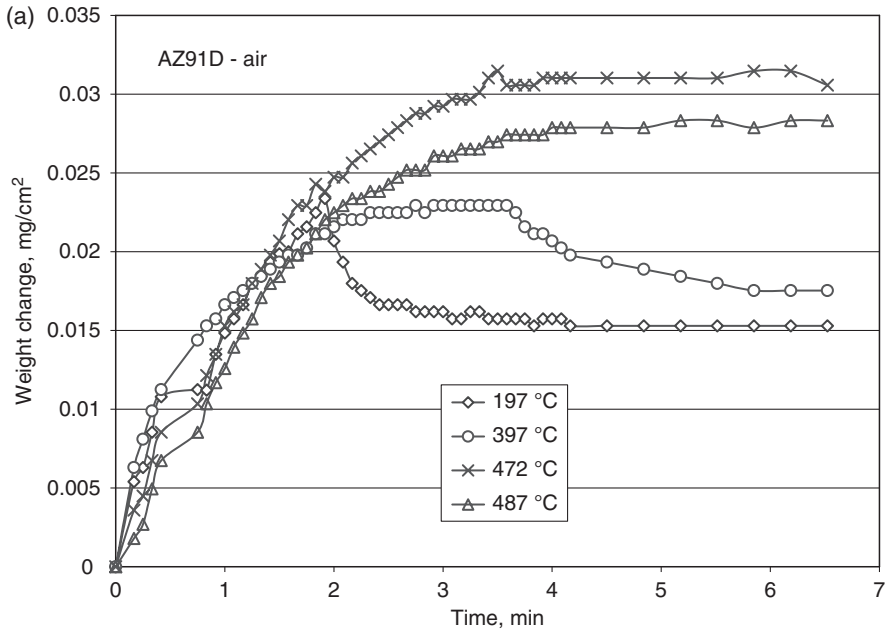

Fig. 7.1 Thermogravimetric measurements of weight change versus time for an as-cast AZ91D alloy in an air environment: **a** initial stage reaction at temperatures between 197 °C and 487 °C;

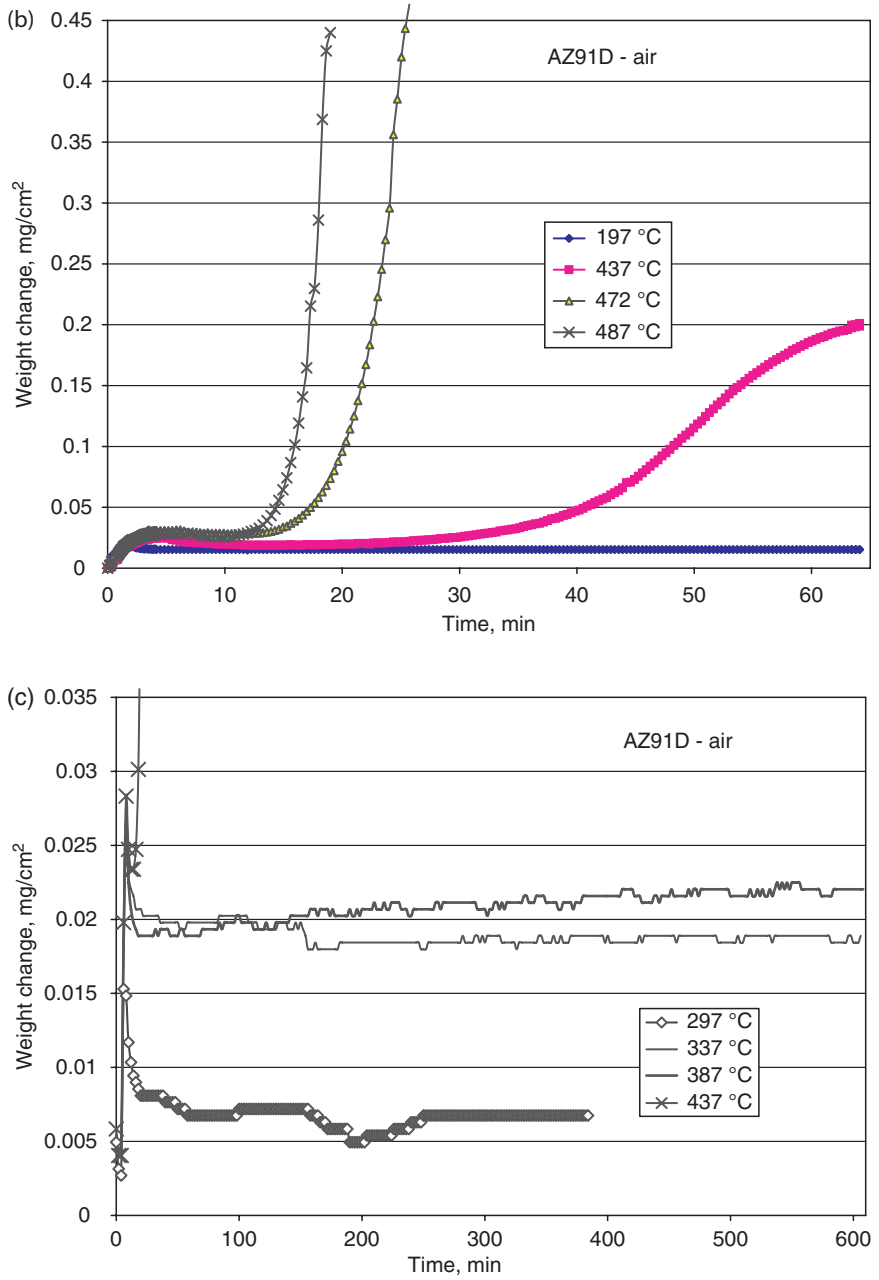

Fig. 7.1 (continued) **b** growth kinetics for a maximum time interval of 1 h showing the incubation period and non-protective oxidation; **c** long-term exposure curves at temperatures between 297 °C and 437 °C. The specimens were inserted into a chamber at room temperature and heated to the reaction temperature at a rate of 100 °C / min. Accuracy of measurements—1 µg. The alloy chemistry: 8.94% Al, 0.59% Zn, 0.34% Mn, 0.0005% Ni, 0.002% Fe, less than 0.005% Si, less than 0.001% Cu, less than 0.005% each of Zr, Sn, Pb, 5±0.15 ppm of Be and Mg balance [29]

metal expressed by the MgO to Mg volume ratio of 0.81, the scale should not form a compact layer. Observations show, however, no systematic spallation of the oxide in the thin film range where it exhibits highly protective behavior. The explanation might be the fact of the inherent strength of thin MgO film in which stress is operating in an essentially two-dimensional system so that the oxide can withstand the tensile stress necessary to adapt to the dimensions of the metal. The rupturing occurs only after the film exceeds a critical thickness, as suggested previously for metallic systems [5].

7.2.2 Transient and Steady Stage Reactions

The effect of test temperature on weight change curves is also evident during the transient stage. The transient stage is understood here as the time before an onset of accelerated oxidation, and some curves for a maximum time interval of 1 h are shown in Fig. 7.1b. The alloy tested at a temperature of 197 °C does not change its weight for up to 1 h. At the same time, the measurement conducted for the same alloy exposed at 437 °C reveals an accelerated weight gain after approximately 30 min of the reaction. An increase of the temperature up to 472 °C essentially changes the thermogravimetric curves, which show a rapid rise after the transient stage. The time of rapid weight gain is approximately 20 min and 15 min for reaction temperatures of 472 °C and 487 °C, respectively. Since the magnesium alloy exposed to air at temperatures higher than 437 °C exhibits a catastrophic oxidation relatively quickly, it is only possible to conduct the long-term thermogravimetric tests at lower temperatures. The weight change curves below 437 °C and time intervals up to 10 h are plotted in Fig. 7.1c. It is clear that at temperatures of 297 °C and 337 °C the sample weight remains practically constant over the whole range of time intervals examined. A slight but continuous weight increase is observed for the alloy tested at 387 °C. Such characteristics indicate so-called linear oxidation at a constant rate. The curve for the alloy exposed at 437 °C, which experiences a rapid weight gain, is shown for comparison in the left-hand part of the plot in Fig. 7.1c.

Thus, three distinct stages are revealed during the 10 h long oxidation of an AZ91D magnesium alloy in air at temperatures between 197 °C and 487 °C. The initial formation of the protective oxide, taking place mainly during preheating to the test temperature, is followed by an incubation period with negligible oxygen uptake. While at temperatures below approximately 337 °C, the second stage lasts at least 10 h; at 437 °C and 487 °C it is replaced within 30 min and 15 min, respectively, by non-protective oxidation with a rate sharply increasing over time. At intermediate temperatures the linear reaction with a constant rate occurs between the alloy and oxygen from air. The temperature of eutectics melting is of critical importance for an onset of non-protective oxidation, and with the increased content of the liquid phase the alloy exhibits a tendency to ignition and combustion.

7.3 Oxidation Surfaces

A simple visual assessment indicates that the morphology of the oxide growth surfaces depends both on the temperature and time of the reaction. At a test temperature of 387 °C, no significant differences are macroscopically detectable for exposure times as long as 10 h (Fig. 7.2a). A change of the surface color from bright metallic to matte gray suggests the formation of a macroscopically uniform layer of oxide, and this is essentially true for all temperatures below 437 °C. By increasing the temperature over 437 °C, the exposure time exerts a primary influence. There is initially an incubatory period of time after which the macroscopically uniform oxidation front is not stable and nodular growth is activated. An example of the morphology formed after 1h at 472 °C is shown in Fig. 7.2b, where numerous dark oxide nodules extend above the alloy surface. At temperatures higher than 472 °C,

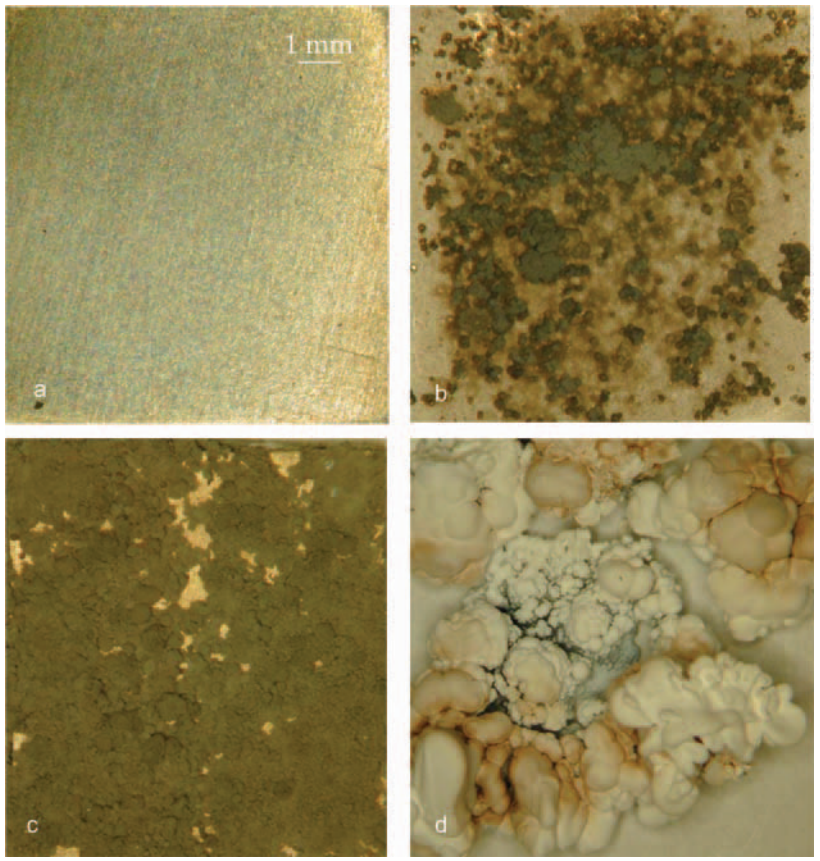

Fig. 7.2 Macroscopic images of AZ91D alloy surfaces after air exposures: **a** 387 °C, 10 h; **b** 472 °C, 1 h ; **c** 497 °C, 1 h; **d** 547 °C, 10 min [29]

nodular growth is the dominant oxidation mechanism, and after 1 h exposure at 497 °C, nodules coalesce into a continuous layer which almost covers the entire surface (Fig. 7.2c).

A further increase in the air temperature above 507 °C makes the alloy prone to ignition. At 547 °C the incubation time preceding ignition lasted between 10 min and 15 min. Usually, the ignition takes place simultaneously in several spots and spreads over the entire sample surface of approximately 200 mm^2. On a macroscopic scale the material exhibits inhomogeneity in terms of both the color and morphology, suggesting non-uniformity in distribution of combustion heat generated over the reaction area. As seen in Fig. 7.2d, it is still possible to distinguish the oxide formed before ignition as well as the products of direct metal combustion.

7.4 Oxide Growth Morphologies

7.4.1 Thin Films

An analysis of polished cross sections aimed to reveal the internal structure of the oxide, the interface between the oxide and metal, as well as the metallic substrate itself. As-cast alloy consists of dendritic grains with two phases of αMg and intermetallics. Morphologically, the massive intermetallics, the eutectics as a lamellar structure of intermetallics and αMg, or a mixture of both components, are distributed along the αMg grain boundaries (Fig. 7.3a). The image contrast shows that there are also some minor phases with the morphologies suggesting Al–Fe–Mn intermetallics and Mg_2Si inclusions, originating from a metallurgical rectification of the alloy. It should be noted that precipitates of minor phases, particularly that believed to be Mg_2Si, easily developed oxide films during sample preparation. The oxide films formed at temperatures lower than approximately 437 °C were too thin for cross-sectional imaging with the optical microscopy, and the main effect of the heat was expressed by microstructure changes within the substrate, especially clear after long-term exposures. Since at the reaction temperature all the alloy components were in solid state, the major change is a spheroidization of the intermetallic phase and its gradual dissolution within the matrix (Fig. 7.3b).

Observations of the planar alloy surface subjected to high temperatures allow the registration of the oxide growth under magnifications of optical microscopy. At the beginning, the oxide thickness does not depend clearly on the crystallographic orientation of the substrate grains. The first oxide nucleus forms on some specific microstructural features of the substrate well before it is possible to detect the continuous layer. The preferential sites for oxide growth are the intersections of some grain boundaries with the alloy surface. However, the most important feature causing oxidation anisotropy is the alloy phase composition. While at 433 °C areas surrounding the intermetallic phase act as sites for accelerated oxidation, at 517 °C the intermetallic phase itself is quickly transformed into the oxide. SEM examinations revealed that the macroscopically flat and smooth oxide scale formed during the

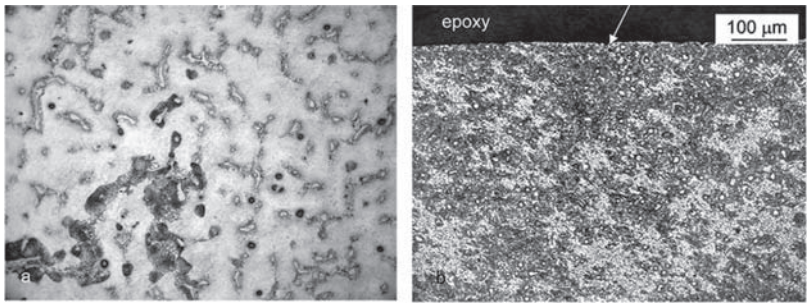

Fig. 7.3 Cross-sectional images of an AZ91D alloy and oxides grown after air exposure: **a** as cast alloy with arrows indicating precipitates covered with an oxide during polishing; **b** spheroidal precipitates in the alloy oxidized for 16 h at 420 °C; the arrow points out the oxidized surface

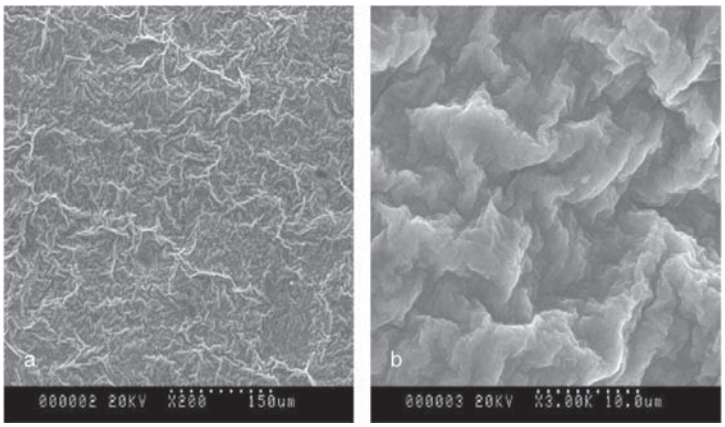

Fig. 7.4 Top-view morphology of the oxide formed on an AZ91D during the early stage reaction: **a** 487 °C, 1 min general view of oxide surface, SEM; **b** magnified part of the area between ridges of **a**, SEM [29]

transient period is, in fact, relatively rough, covered with nonuniform growth features (Fig. 7.4a). The protrusions, called "ridges," grow usually in the through-scale cracks. Although it is difficult to conclude oxide grain size from the surface morphology, the estimated oxide grain is around 5 µm to10 µm (Fig. 7.4b).

7.4.2 Nodular Features

The oxide nodules, imaged under the magnification of SEM, reveal their highly irregular shape (Fig. 7.5a). Each nodule contains numerous craters connecting the surface with the substrate alloy (Fig. 7.5b). The fresh oxide formed around craters is very fine

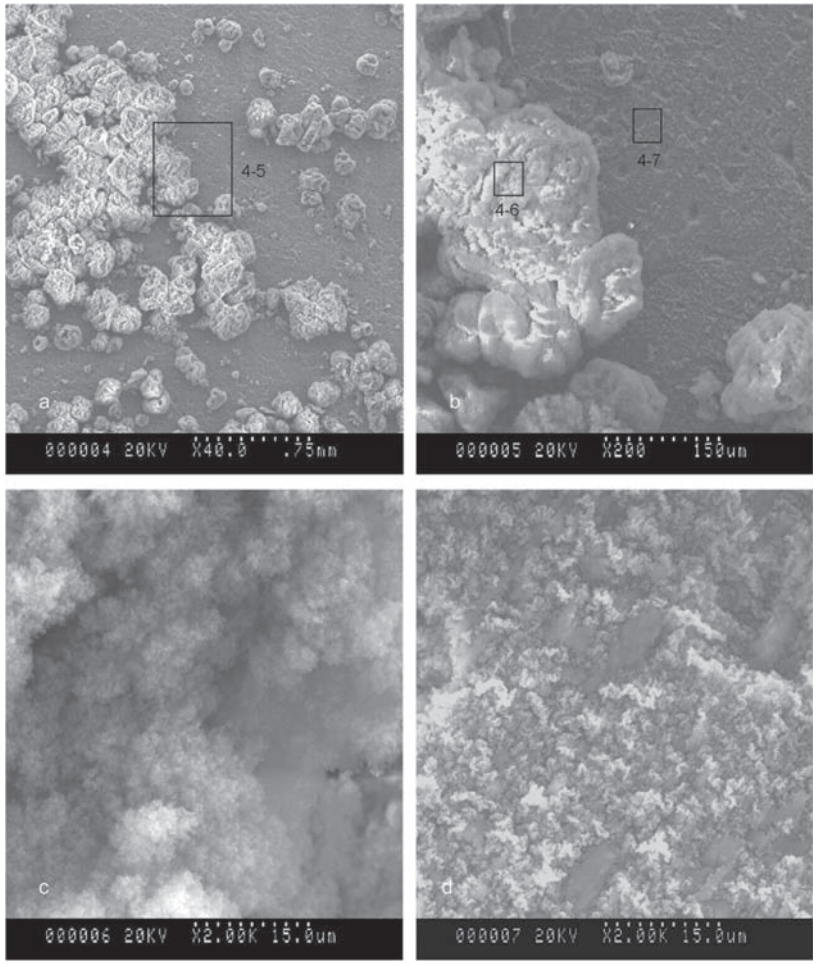

Fig. 7.5 SEM morphologies of the alloy surface after air exposure at 472 °C for 1 h: **a** general view; **b** magnified part of an image marked as 4–5 in **a; c** ultra-fine grain structure of the nodule marked as 4–6 in **b; d** flat area, marked as 4–7 in **b** [29]

grained and has an appearance of a relatively loose, powder-like nature (Fig. 7.5c). The macroscopically flat area surrounding nodules also contains microscopic growth features. As seen in Fig. 7.5d, the surface is covered with numerous small pits and patches of fresh oxide with a matrix exhibiting a quite compact structure. Since, according to the principle of image formation in SEM, bright areas indicate the gathering of electrons, the bright component should have a lower electrical conductivity, suggesting the possibility of a difference in phase composition. The bright component forms ridges on the top of the nodules as well as some irregular precipitates on flat areas.

SEM imaging of oxide growths reveals a thin metallic layer on the nodule/gas interface (Fig. 7.6a). The microchemical segregation over the oxide surface was

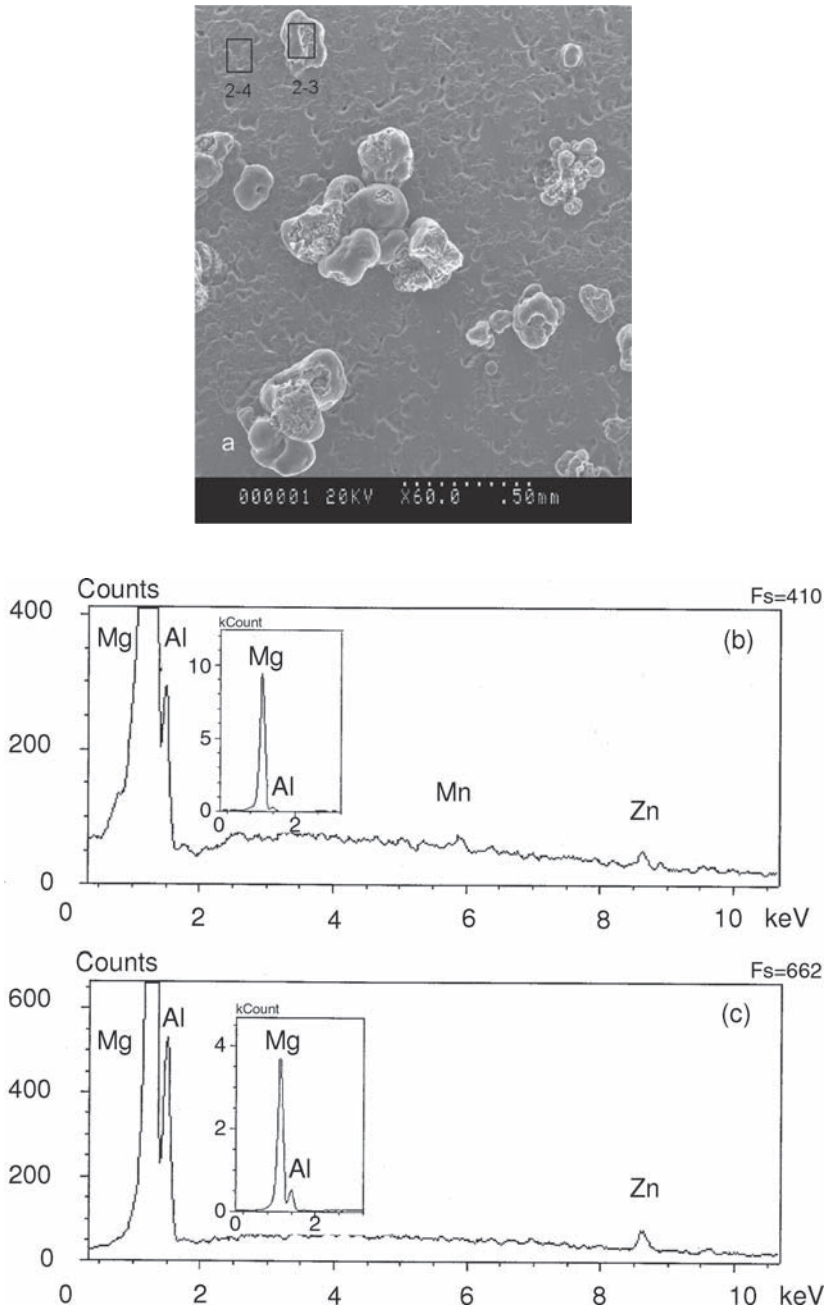

Fig. 7.6 SEM/EDAX analysis of the oxide formed after air exposure at 472 °C for 1 h: **a** surface morphology with nodules extended from the uniform oxide; **b** EDAX spectrum from the uniform oxide marked as 2–4 in **a**, the inset shows the full height of the Mg peak; **c** EDAX spectrum from the oxide nodule marked as 2–3 in **a**, the inset shows the full height of the Mg peak [29]

examined using the SEM/EDAX technique with a focus on the difference in chemical composition between the nodule and the surrounding area. A comparison of Al and Mg peak intensities from energy spectra reveals that the nodule area contains significantly more Al than the surrounding area (Fig. 7.6b,c). A low intensity Zn peak formed by its 0.59% addition makes it difficult to assess differences, and at least, for a first approximation, the concentrations are similar. Manganese, added in the quantity of 0.34% to transform the iron and other heavy-metal elements into relatively harmless intermetallic compounds, is in the area surrounding the nodules.

7.5 Internal Structure of Oxide Layers

The cross section of nodules reveals that they are composed of dark oxide and white inclusions, representing a metal (Fig. 7.7a). While metal particles of the order of micrometers are densely distributed within the oxide, large voids are present at the

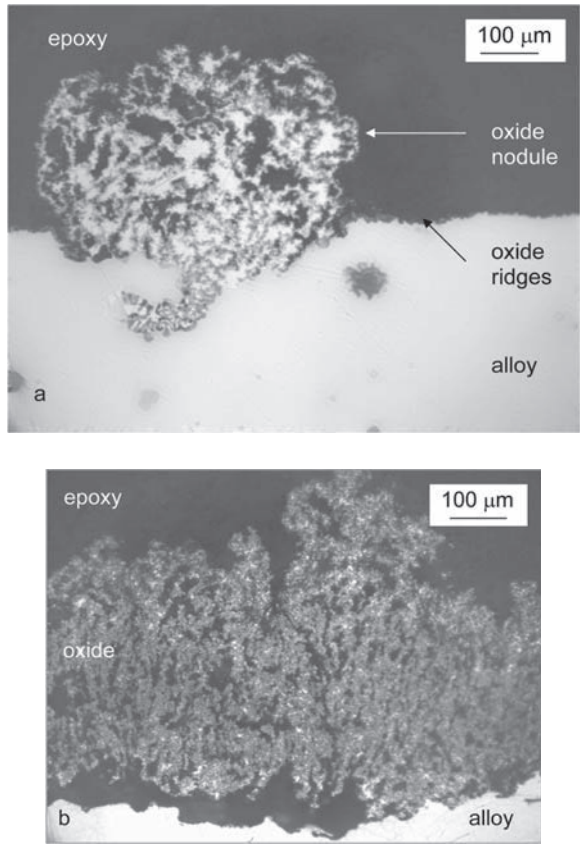

Fig. 7.7 Cross sectional images of oxide grown on AZ91D alloy: **a** individual nodule formed after 5 min at 527 °C, sample without etching; **b** oxide grown after 20 min at 495 °C, sample without etching [29]

substrate-nodule interface. Besides this, there are numerous channels oriented from the substrate towards the gas/oxide interface. Increasing the temperature to 527 °C influences the nodule microstructure, and the most noticeable change is the higher contribution of the metallic phase. Although the oxide/metal interface contains voids similar to those developed at 495 °C, the novel feature is the selective oxidation of the substrate with the oxide penetrating deep into the substrate material. Longer oxidation times enlarge the nodule size and lead to growth of loose structures as seen for 495 °C-20 min exposure in Fig. 7.7b.

The higher the reaction temperature, the deeper the penetration of the oxide into the substrate. After long-term exposures at 527 °C, the oxide forms a continuous layer with essentially the same microstructure as characterized above for individual nodules. A preferential oxidation of intermetallic phases is still the case (Fig. 7.8a,b). Since, in order to reveal the substrate microstructure, the sample is subjected to etching, the small metallic particles within the scale disappear. At 527 °C the alloy is in a semisolid state and the dark spherical shaped features correspond to the islands being liquid at the reaction temperature. As a result of selective oxidation the oxide/metal interface is serrated, showing numerous protrusions (Fig. 7.8c,d).

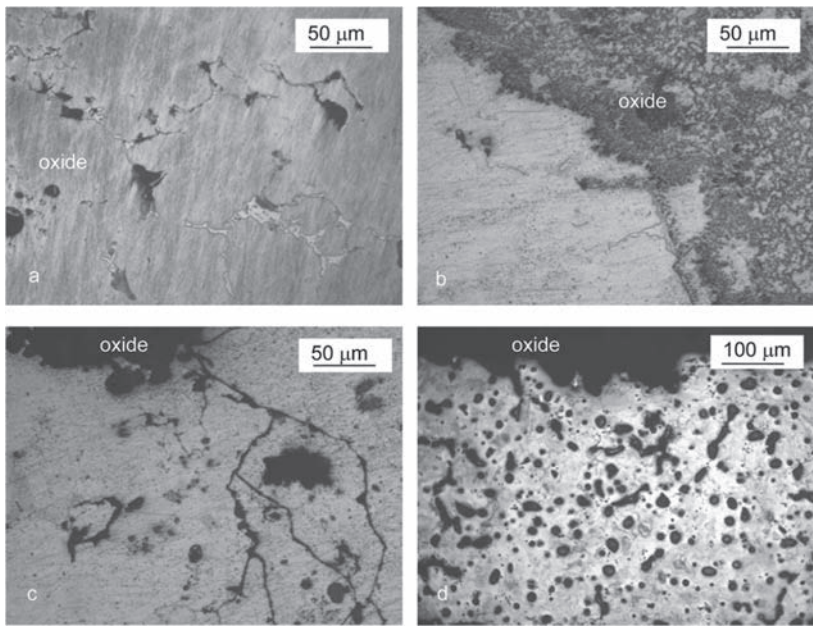

Fig. 7.8 Cross sectional images of magnesium oxide growth on AZ91D revealing the anisotropy: **a,b** preferential oxidation of the intermetallic phase; **c** oxidation penetration along grain boundaries presumably due to their enrichment in intermetallics; **d** oxide-metal interface showing a preferential reaction after oxidation for 17 min at 527 °C

7.6 Oxide Phase Composition

Several typical systems were selected for X-ray examination including a bare substrate, a substrate covered with thin oxide grown during early-stage reaction, a product of total oxidation of the metallic substrate and a product of combustion

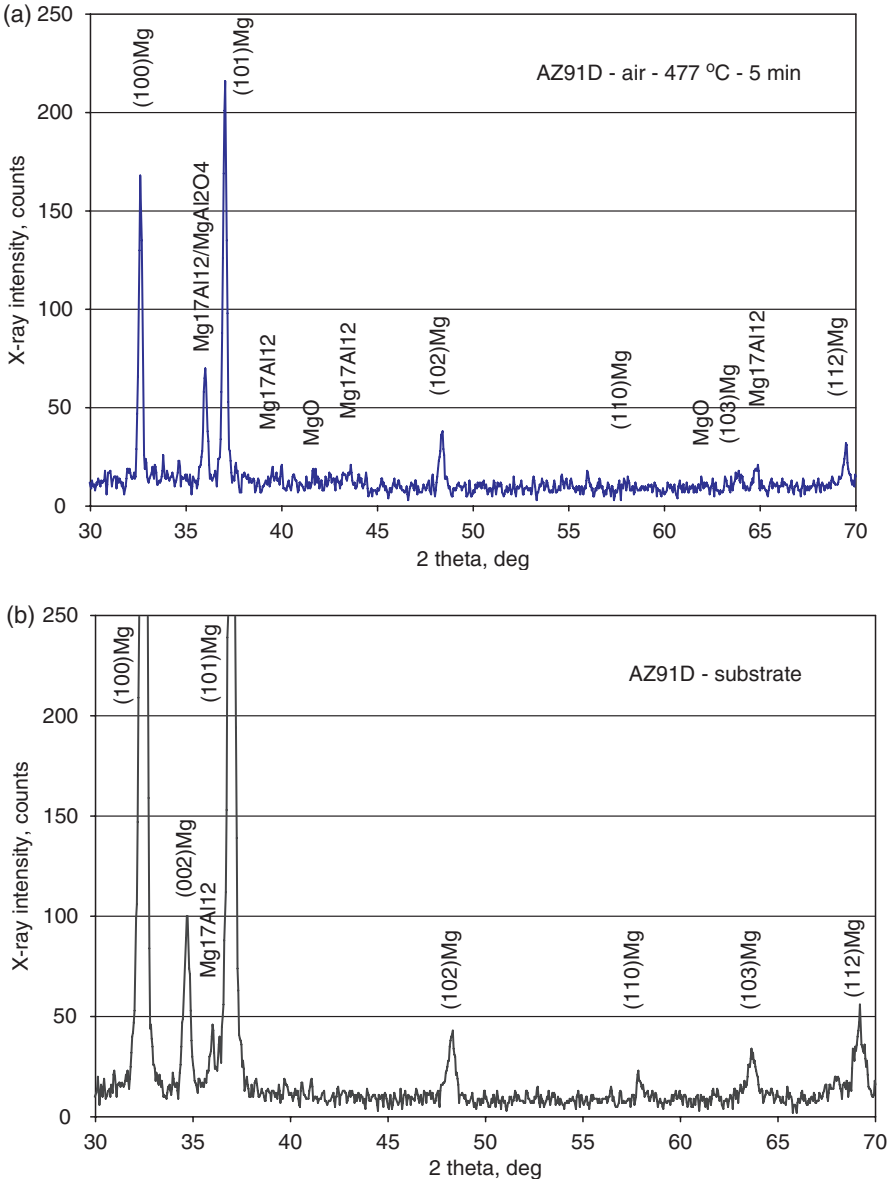

Fig. 7.9 X-ray diffraction patterns of oxides formed after the air exposure of AZ91D: **a** at 477 °C for 5 min; **b** as in **a** after removal of the oxide film

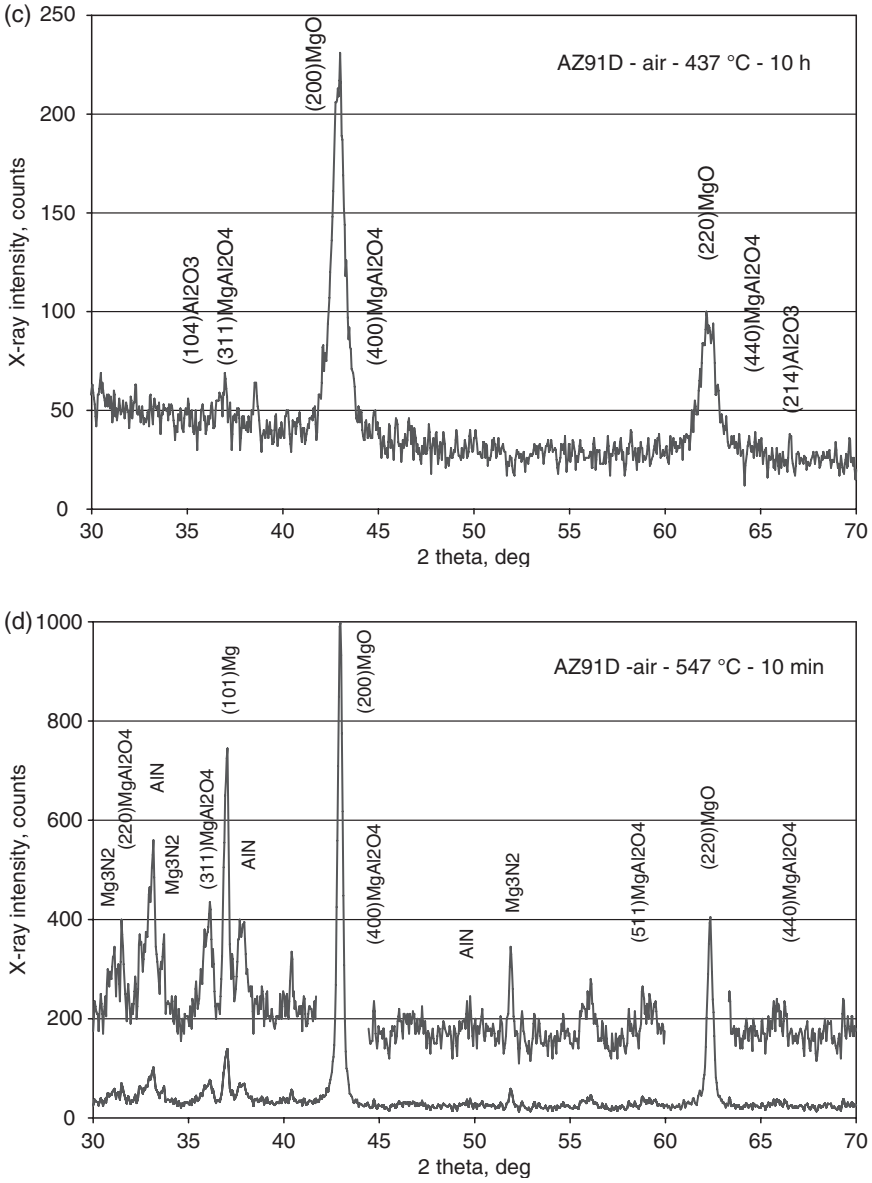

Fig. 7.9 (continued) **c** at 437 °C for 10 h; **d** at 547 °C for 10 min, which included an ignition and combustion [29]

of a partly oxidized alloy. Air exposure at 477 °C for 5 min produces a uniform oxide with the morphology described above. Surprisingly, X-ray diffraction analysis does not detect a crystallographic phase on the alloy surface (Fig. 7.9a). The diffraction pattern contains a majority of peaks characteristic for Mg and

three peaks that can be ascribed to the $Mg_{17}Al_{12}$ phase. It should be noted that the location of the strongest peak for $Mg_{17}Al_{12}$ at 2–theta of 36.191 deg is very close to the strongest peak of the $MgAl_2O_4$ spinel at 2–theta of 36.853 deg. In order to exclude the possible spinel contribution, the oxide was removed by mechanical polishing using sandpaper, and the substrate was subjected to X-ray re-examination. Results shown in Fig. 7.9b indicate that intensities of Mg peaks increased by one order of magnitude after the removal of the oxide absorbing the X-ray radiation. Some change in relative intensities of Mg peaks might be caused by the crystallographic texture introduced by the surface deformation. A diffraction peak at 2–theta of 36 deg is still present, though its intensity is low. A comparison of both spectras suggests that the sample oxidized at 477 °C for 5 min was either covered with an amorphous oxide, or the thickness of crystalline film was too small to produce a sufficient X-ray signal.

The major component of the reaction product formed after high temperature exposure of an AZ91D alloy was magnesium oxide MgO with a cubic structure and a lattice parameter of 4.21 Å. An example of an X-ray diffraction pattern, recorded from an oxide formed after 10 h at 437 °C, is shown in Fig. 7.9c. It consists of two major peaks corresponding to 200 and 220 crystallographic planes of MgO. An absence of Mg diffraction peaks indicates complete oxidation within the sample volume being penetrated by X-rays, and this finding coincides with macroscopic observations revealing an exclusively dark color oxide. A color difference as compared to gray oxide of the thin film range may be caused by a deficiency in Mg or O atoms within the MgO lattice. Both diffraction peaks exhibit evident broadening. Since the oxide is relatively soft and free of internal stress, it is reasonable to assume that the peak broadening was caused by an ultra fine grain. An estimation of oxide grain size was conducted using Scherrer's formula [6]. Based on the corrected broadening of the 200 peak of MgO, the calculated oxide grain size equals 9.5 nm. In addition to MgO, the X-ray diffraction scan detected the presence of magnesium aluminum oxide of $MgAl_2O_4$ spinel, having a cubic structure and a lattice parameter of 8.803 Å. The presence of Al_2O_3 alumina cannot be unambiguously proven since the suspected peaks have intensities slightly above the background noise (Fig. 7.9c).

An essentially different diffraction pattern was recorded after reaction at 547 °C. At this temperature, the initial oxidation was followed by combustion of the remaining Mg substrate (Fig. 7.9d). Due to the high temperature caused by the heat generated, the sintering and melting of the oxide formed prior to ignition took place. Although the 200 and 220 MgO peaks again dominate the diffraction scan, they have a relatively higher intensity and do not exhibit broadening. The contribution of $MgAl_2O_4$ spinel is higher than observed in Fig. 7.9a. The peaks which could be associated with the presence of alumina are missing. Instead there are new peaks which indicate magnesium nitride Mg_3N_2 and aluminum nitride AlN. Their presence indicates that during combustion, nitrogen also reacted with both major constituents of the alloy. The presence of Zn was not detected in the form of a separate oxide phase. Properties of the oxides detected are listed in Table. 7.1.

Table 7.1 Selected properties of oxides formed on an Mg–9%A1–1%Zn alloy and the alloy's substrate

Material	Chemical formula	Crystallographic structure	Density	Melting point	Thermal expansion coefficient	Thermal conductivity	Specific heat at 20 °C
			g/cm^3	°C	10^{-6}/°C	W/m °C	J/kg °C
Magnesia	MgO	Cubic	3.58	2800	8.0	40.6	837
Spinel	$MgAl_2O_4$	Cubic a=8.803	3.60	2130	7.45		
Alumina	γAl_2O_3		3.60	2100	8.0	21.0	880
Mg–9%Al–1% Zn substrate	αMg, $Mg_{17}Al_{12}$	Hexagonal close packed (αMg matrix)	1.81	470-595	27.2	56.2	800

7.7 Influence of Chemical Composition on Magnesium Oxidation

The oxidation behavior of magnesium alloys is affected by their chemistry, and the role of aluminum is discussed later in this chapter. There are, however, alloying additions that drastically inhibit oxidation kinetics, and the most frequently quoted are calcium, rare earths and beryllium (Be).

It is well established that Be additions provide a safety factor during the melting and casting of aluminum and magnesium alloys. Beryllium is one of the few elements that is more reactive to oxygen than magnesium, and it is known to getter iron and similar impurities from the melt, thus providing some degree of refinement in purity when needed. The film forming behavior of Be reduces moisture interaction and mold reactions. The oxidation curves for the AZ91D alloy with two Be contents of 5 ppm and 10 ppm are shown in Fig. 7.10. The initial stage up to roughly 10 min is quite similar for both alloys. During further exposure, additions of 10 ppm of Be significantly delay the onset of an accelerated oxidation stage, and differences are

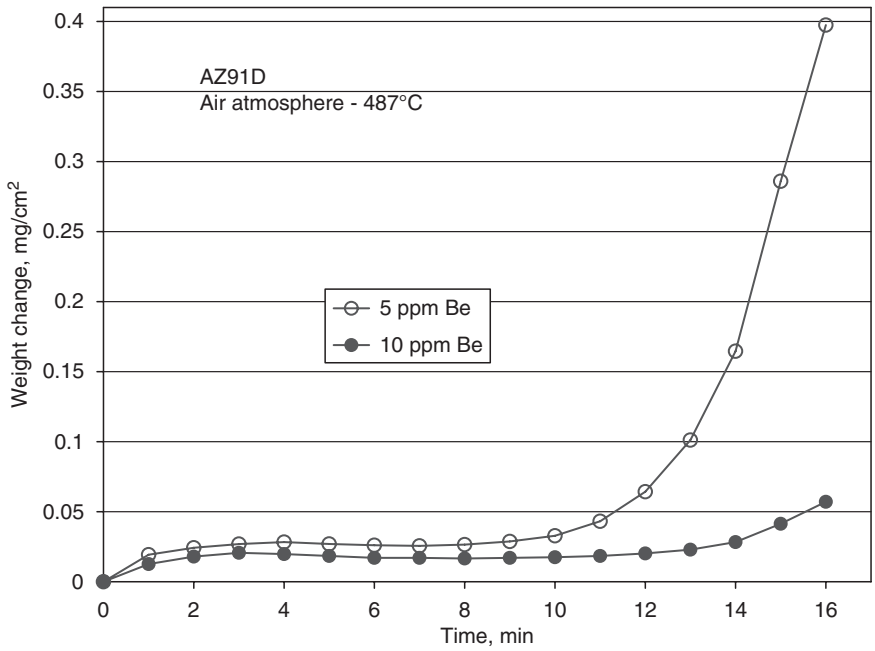

Fig. 7.10 The influence of beryllium content on oxidation kinetics of an AZ91D alloy in air. The alloy with increased Be content had the following composition: Al–9.24%, Zn–0.69%, Mn–0.25%, Si–0.012%, Ni–0.0006%, Cu–0.003%, Be–0.0010% and Mg balance [13]

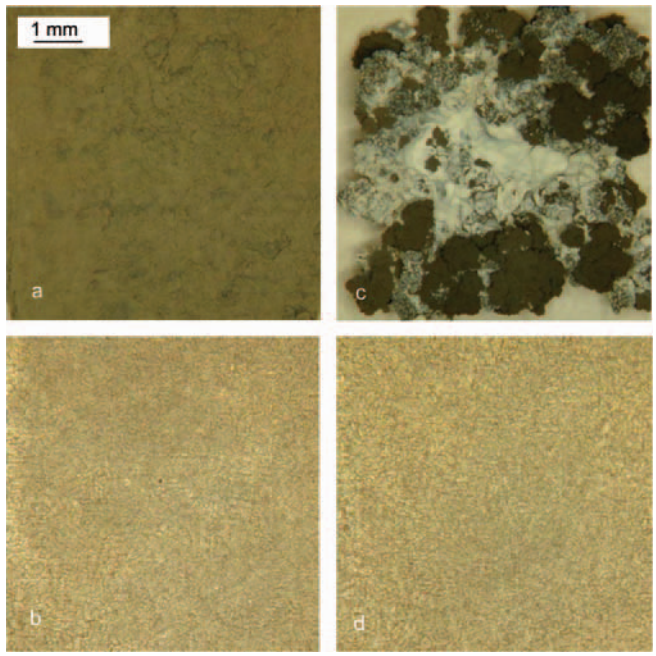

Fig. 7.11 Surface morphologies of an AZ91D alloy after high temperature exposures: **a** 5 ppm Be, 500 °C–1 h; **b** 10 ppm Be, 500 °C–1 h; **c** 5 ppm Be, 547 °C–10 min; **d** 10 ppm Be, 547 °C–10 min [13]

substantial after roughly 10 min of reaction. A more profound influence of beryllium is observed at higher temperatures, as proved by observations of growth morphologies. After 1 h exposure at 500 °C, the alloy with 5 ppm of Be is entirely covered by the oxide scale (Fig. 7.11a) while the alloy containing 10 ppm of Be is still free of the oxide (Fig. 7.11b). After roughly 10 min at 547 °C, the alloy with 5 ppm of Be experiences ignition and combustion (Fig.7.11c). An increase of Be content to 10 ppm delays not only ignition but also oxidation (Fig. 7.11d).

At present, there is no experimentally proven mechanism that would explain the role of Be. A similar tendency is observed for other elements with high affinity to oxygen, such as Ca, Sr or Zr. It is reported that elements with very high affinity to oxygen enhance the formation of a thin and uniform oxide layer and prevent the growth of thick nodular oxide features. It seems that the role of Be can be explained in terms of the so called “reactive element effect” documented for NiO, chromia or alumina formers [7]. According to recent theory, the reactive element ions diffuse to native oxide grain boundaries and block the outward diffusion of metal cations. As a result, an inward diffusion of oxygen ions is the only possibility for the oxidation to proceed. For Ni substrate and Ce dopants, a reduction in oxidation rate by roughly

two orders of magnitude was achieved [8]. It is likely that a similar mechanism can be active for the MgO growth. Since a certain concentration of reactive element ions at native oxide grain boundaries is required to impede diffusion, this would explain a change in oxidation rate between alloys containing 5 ppm and 10 ppm of Be.

7.8 Evaporation Characteristics

Magnesium is known to have high vapor pressure as compared to other metals (Table 7.2). A plot of the vapor pressure of magnesium versus temperature is shown in Fig. 7.12. When heated in an oxidizing environment this phenomenon is not clearly seen since evaporation is superimposed on oxidation. To separate these two processes, alloys should be exposed to high temperatures in an inert atmosphere, e.g. argon. The plot in Fig. 7.13 shows that during very initial stages,

Table 7.2 The comparison of vapor pressures for several metals

	Fe	Al	Mg	Zn
		Pa		
At melting temperature	2.3	10^{-6}	360	23
At 773 °C	0	1.2×10^{-5}	1360	12,000

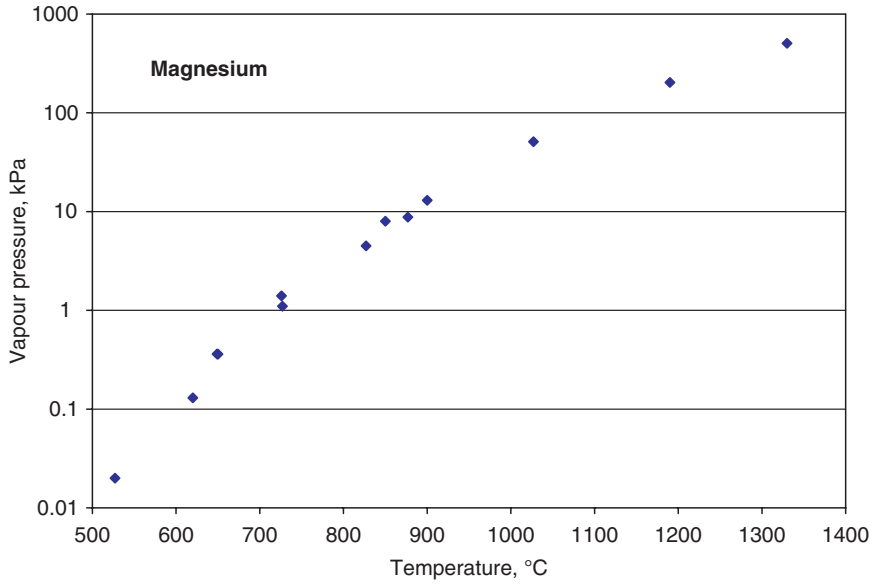

Fig. 7.12 The diagram of magnesium vapor pressure versus temperature (IMA data)

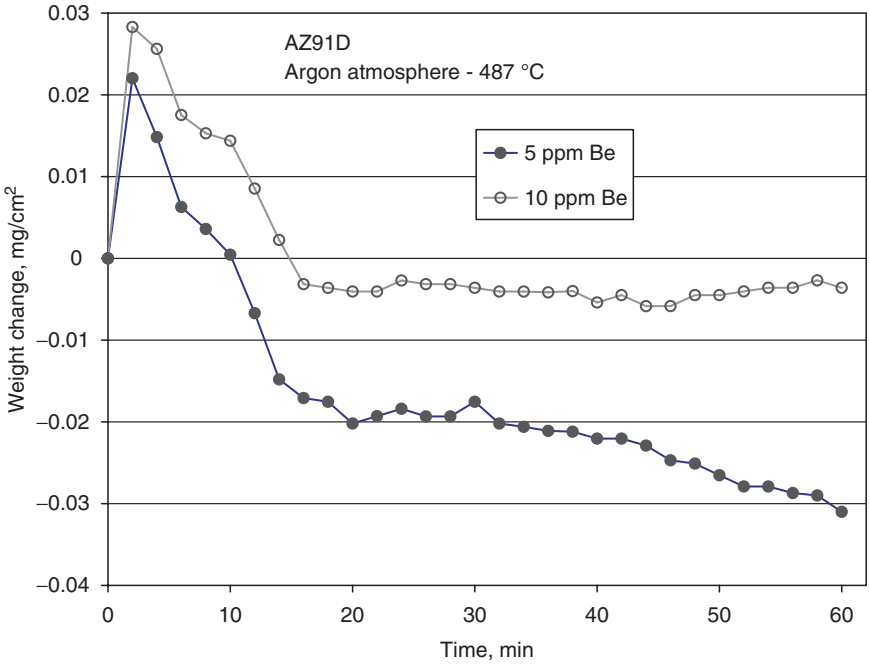

Fig. 7.13 The evaporation kinetics for AZ91D alloy containing 5 ppm and 10 ppm of beryllium [13]

alloys with 5 ppm and 10 ppm of Be experience similar weight gains, which could be interpreted as an uptake of oxygen impurities. Then, beryllium suppresses the magnesium evaporation rate.

The specific feature of Mg is the high vapor pressure, and for a vacuum environment its evaporation rate is described by the Arrhenius type relation [9]:

$$K_{evap} = 0.6 \exp\left(\frac{-25{,}000}{RT}\right) \text{ g/cm}^2\text{sec} \tag{7.1}$$

According to a simple calculation, an evaporation of 1 µg Mg/cm^2 translates to the removal of an approximately 55.3 Å thick metal layer. The higher the reaction temperature the more evaporation exceeds oxidation kinetically. For the Al–Mg alloy, at 500 °C the difference between evaporation and diffusion rate constants is over three orders of magnitude.

Assuming that magnesium evaporates from the metallic surface, according to equation (7.1) after 60 min at 487 °C, the sample weight reduction should be of the order of 100 µg/cm^2. The weight reduction, measured at this temperature by TGA is close to 50 µg/cm^2. The difference may be caused in part by experimental error and in part by a partial suppression of magnesium evaporation by a very thin oxide film, formed during the first 10 min of exposure in argon. Magnesium

may evaporate at an initial constant rate after the incubation period by two possible mechanisms: It may diffuse through the oxide film upon establishment of a concentration gradient or evaporate from the metal/vacuum interface if the compact oxide films breaks down to a porous layer. Experiments show that the protective oxide formed tends to block the evaporation of magnesium, while the loose high temperature oxide permits the evaporation to occur at a rate faster than that found at the beginning. The mechanism of evaporation suppression could be the same as explained in the previous section for the reactive element effect on the inhibition of oxidation.

7.9 Oxidation Mechanism

7.9.1 Initial Oxidation—Thin Film Stage

The initial stage morphology in magnesium oxide growth is uniform, as shown schematically in Fig. 7.14a. The physical interpretation of the incubation period is not straightforward. The X-ray measurements did not determine the nature of initial oxides. A suspicion of their amorphous character does not have strong proof in the literature and "in situ" TEM observations suggest rather a crystalline structure of the initial MgO films [10]. This is in contrast to γ–Al_2O_3 protective films grown on Al–Mg alloys, which tend to be amorphous at the beginning and then suffer discontinuous change of the structure [1]. It is generally accepted that the growth of compact MgO films is controlled by solid state diffusion through adherent oxide areas followed by the reaction with oxygen at the oxide/gas interface. Hence, a lack of easy paths for fast Mg transport, as found for other crystalline oxides [11], enforcing the lattice diffusion, could be a possible explanation of highly protective behavior. Since the diffusivity D of magnesium within the MgO lattice is expressed by [12]:

$$D = 1.0 \times 10^{-6} \exp\left(\frac{-150{,}000}{RT}\right) \quad \mathrm{m^2/s} \tag{7.2}$$

at 400 °C the value of D is as low as 2.24×10^{-18} m^2/s, explaining the negligible weight gains. The outward Mg^{2+} ion diffusion, leading to the inward vacancy flux, creates voids at the metal/oxide interface that not only act as channels for the transport of magnesium vapor, but also form the local stress risers contributing to film cracking.

7.9.2 Transient Stage—Oxide Ridges

The top view morphology of thin oxide films does not reveal the strong correlation between the surface oxide pattern and grain boundary alignment within the underlying

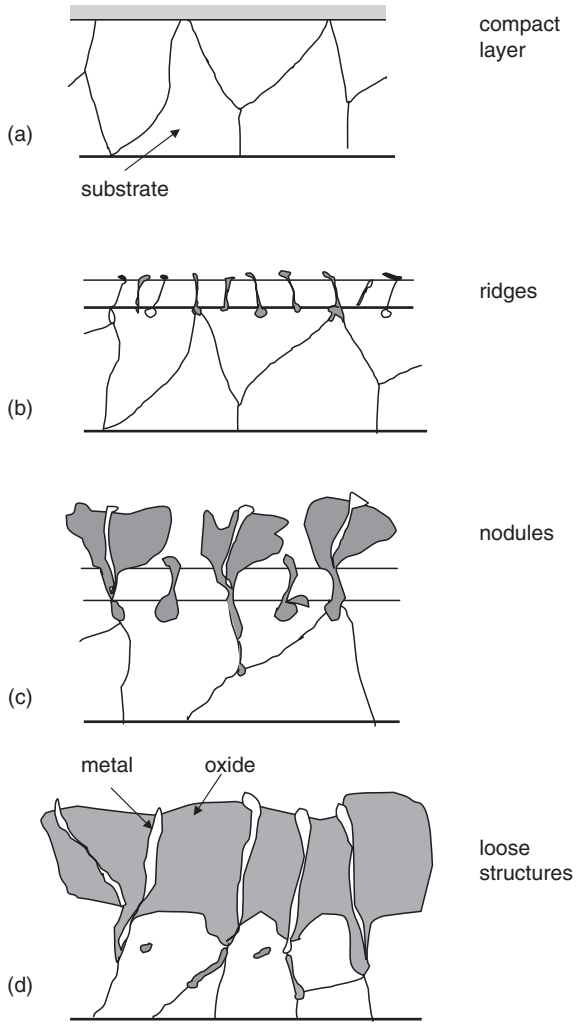

Fig. 7.14 Schematic representations showing development of MgO morphologies at various stages: **a** compact uniform layer; **b** transient to oxide ridges; **c** growth of oxide nodules; **d** loose scale structures [13]

metal. The anisotropy is mainly expressed by thicker oxide grown in the areas covered by the intermetallic phase, and it is particularly true during the transient stage between initial films and the ridges replacing them (Fig. 7.14b). In part, this supports conclusions drawn from observations of MgO growth on an Al–based alloy where oxide nucleation was not affected by the generation of slip traces, thermal grooves and grain boundaries [10]. While analyzing literature data, however, some ambiguity arises due to a lack of a precise description of surface finishing. Mechanical

polishing applied here causes the deformation of a thin layer of the material that suppresses the nucleation of epitaxially oriented oxide and for some cation-diffusing scales promotes the formation of randomly oriented structures over differently oriented substrate grains [13]. At present, there is no description of how this factor affects the evolution of MgO. Crystallographically, a comparison of peak intensities on the X-ray diffraction pattern to that on the JCPDS standard indicates the roughly random distribution of grain orientations within both the substrate and the oxide, which does not allow for the determination of the crystallographic relationship between both constituents.

The morphology of oxide ridges, which replaces initial-stage structures, is non-uniformly distributed over the alloy surface, and also does not show an obvious link with the substrate features. This type of structure indicates the formation of a fresh oxide at the oxide/metal interface within the oxide and at the outer oxide surface. It is considered that the morphology is formed by inward oxygen transport through the cracks, followed by the reaction of oxygen with the metal at the crack walls and an outward growth of ridges [14]. The relative contribution of these processes to the overall matter transport within the scale depends on the extent of cracks and on the stage of their healing by the freshly formed oxide.

7.9.3 Steady Stage Growth—Oxide Nodules

The growth of thick MgO scales is widely considered to be controlled by linear reaction [9, 15, 16]. In general, this type of oxidation is insensitive to the thickness of the scale, and it is assumed that oxygen can easily penetrate to the metal surface. The kinetic curve plots showed previously in Fig. 7.1a–c indicate that for AZ91D alloy, purely linear oxidation is only valid for a certain range of temperatures and then an increase in oxidation rate takes place. Further details of the interpretation of thermogravimetric kinetics are provided by microstructure observations. First, an onset of non-protective oxidation is associated with the growth of oxide nodules. Second, the nodular growth is activated by phase inhomogeneity and in particular the formation of liquid islands of the metal and a process of Mg evaporation. Although Mg can sublimate or evaporate at a constant rate after the incubation period, by diffusion through the oxide film upon establishment of the concentration gradient, of more importance is that at high temperatures there is the evaporation from the metal surface if the compact oxide film breaks down to a porous layer. The microscopic analysis shows that above 437 °C, the Mg evaporation rate is so high that the vapor not only saturates all the pores within the nodule but also reaches the nodule/oxygen interface where it forms a continuous film. It is suspected that for such a high evaporation rate, the reaction can even occur at a considerable distance from the surface, and the resultant product would be released as incandescent MgO gas. Such a possibility raises some concerns about the accuracy and interpretation of TGA measurements.

The open nodules continue to grow by the transfer of magnesium vapor through voids and simultaneous reaction with oxygen, forming a product with cauliflower-like morphology (Fig. 7.14c). It is clear that the mechanism proposed here, based on the saturation of scale pores by condensed metallic particles and their simultaneous reaction with oxygen, is also valid after the coalesced nodules form a continuous layer. The selective oxidation of magnesium results in the formation of the alloy depleted with respect to magnesium (i.e. rich in aluminum) as the oxide moves inward to fill the space of the consumed metal. As proved by X-ray measurements, the direct reaction between aluminum and oxygen occurs only during combustion. During gradual oxidation, aluminum reacts to form $MgAl_2O_4$spinel. Although the presence of dispersed spinel particles can serve as diffusion barriers in compact scales [17], their role within loose oxide structures is certainly limited. It is postulated that a sharp acceleration of the oxidation, with an exposure time recorded here for temperatures higher than 472 °C, is attributed to the increased volume of voids and cracks available for the vapor condensation within thicker scales which, in turn, increases the surface area of the metal exposed to oxygen. Further increase in the oxidation rate is caused by the selective oxidation of the alloy constituents leading to a serrated interface between the oxide and metal, which increases the surface area available for evaporation (Fig. 7.14d).

7.9.4 Role of Substrate Phases in Oxide Growth

The oxidation of an alloy is affected by its phase composition and the distribution of alloying elements between phases at the reaction temperature. At room temperatures, there is a significant difference in corrosion resistance between AZ91D constituents. For example, in an NaCl aqueous environment the $Mg_{17}Al_{12}$ phase exhibits a better resistance by nearly one order of magnitude than αMg [18]. At high temperatures, especially above 437 °C, the opposite behavior is observed and $Mg_{17}Al_{12}$ experiences accelerated degradation. An apparent difference in the high temperature process is the fact that the chemistry and relative volumes of phases change due to diffusion. Thus, the oxidation at the gas/metal interface is superimposed on structural transformations taking place within the alloy. It is of interest that in as-cast conditions the phase composition of an AZ91D alloy deviates from the state of equilibrium. This implies that the heating rate to the semisolid range affects the volume, composition and also the state of the phases present. For example, the high heating rates do not allow for diffusion and cause the incipient melting of the eutectics and intermetallics.

When the alloy is exposed to a temperature below that corresponding to eutectic transformation, the $Mg_{17}Al_{12}$ phase undergoes spheroidization and gradual dissolution within the Mg lattice to homogenize the alloying elements throughout the matrix. Of special interest for an AZ91D is Al because it is the major alloying element and has very different oxidation and evaporation characteristics than Mg. Although Al itself forms a highly protective γ-Al_2O_3 film [14], the Al additions over 1 at% accelerate

Mg oxidation, and there are proofs that for 10% Al the rate constant at 400 °C increased by over two orders of magnitude [15]. To emphasize complexity, it should be mentioned that for Al based alloys the exact opposite effect is registered and additions of Mg accelerate the oxidation process [19]. The effect of Al content within the alloy should particularly cause the oxidation difference if metal ion diffusion throughout the scale is not the rate controlling factor, but the reaction takes place at the scale/metal interface where oxygen has free access. In this case, the fact of gradual dissolution of Al should lead to an increase in the oxidation rate, as discussed above. Such expectation is not supported by experiments where the oxidation rate at 387 °C remains constant and no evident changes are detected at lower temperatures. Additions of Zn to the binary Mg–Al alloy reduce the solid solubility of Al in Mg. At high temperatures, Zn increases the Mg oxidation rate at least in part by the formation of pores within the oxide scale [15]; however, the influence of Zn is expected to be less due to its lower content.

7.10 Ignition Behavior

Magnesium ignition is directly related to its oxidation behavior. The formation of magnesium oxide MgO is a highly exothermic reaction. Thus, self-heating is an additional factor, contributing to ignition, especially at higher temperatures where the oxidation rate deviates from linear towards accelerated ones. Since the ignition temperature depends on a number of factors, such as heating conditions, heat loss and the nature of oxidation, as well as the alloy form, it is not an intrinsic parameter, and the value changes. There are two basic definitions of the ignition temperature related to the procedure developed to measure the ignition point:

(i) temperature defined as the lowest temperature associated with the observation of flames;
(ii) temperature defined as a sharp increase in the heating rate experienced by an alloy.

During ignition testing, two methods of measurements of the ignition temperature are practiced:

(i) continuous heating;
(ii) isothermal holding at a certain temperature level.

There are a number of experimental observations on ignition of magnesium alloys. For pure magnesium, ignition occurs at a temperature lower than the melting point. In general, bulk magnesium alloys do not ignite in air below 500 °C, but at the same time prolonged heating at temperatures as low as 427 °C leads to ignition. For Mg–Al alloys ignition occurs in the semisolid state, which implies that the liquid is required to cause burning. As it was described earlier in this chapter, at high temperatures, the rate of evaporation of magnesium is high enough that reaction between vapor and oxygen takes place at a distance from the surface, resulting in combustion.

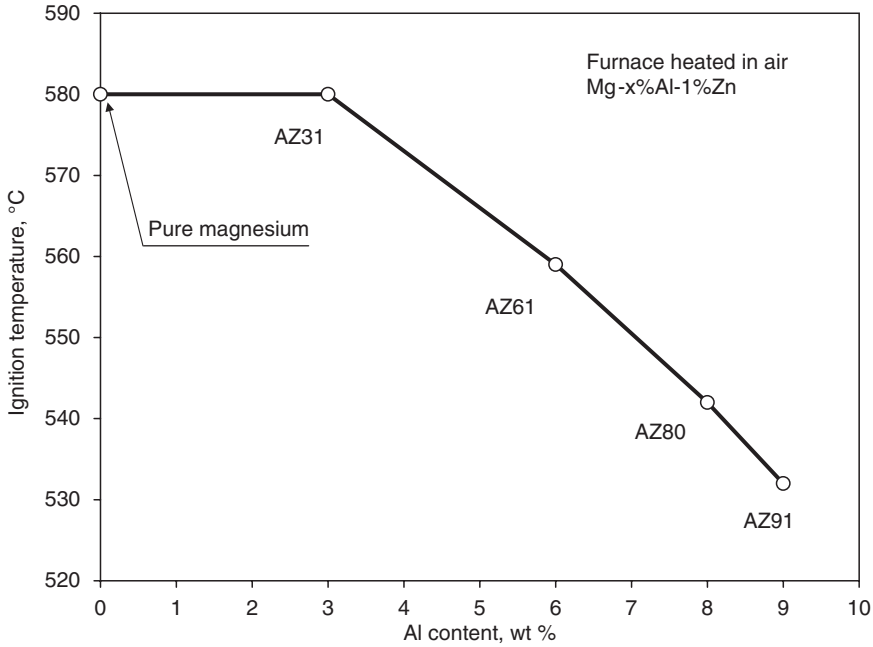

Fig. 7.15 The influence of Al content on ignition temperature of Mg–Al–Zn alloys

Similarly as with oxidation, ignition is influenced by the alloy's chemistry. The major alloying element, aluminum, reduces the ignition temperature first by reducing the liquidus level (Fig. 7.15). Another effect is associated with a presence of the $Mg_{17}Al_{12}$ phase. The solution-annealed state exhibits the highest ignition temperature. Both the size and the morphology of the intermetallic phase are important, and aged alloys ignite faster than as-cast structures. A doping with calcium, beryllium and yttrium leads to improvement in ignition resistance by the formation of a protective and continuous oxide layer which separates the alloy from oxygen. It is also reported that the presence of small quantities of sulphur compounds in the atmosphere increases the temperature of magnesium ignition.

7.11 Alloy Protection Against Oxidation and Ignition

Molten magnesium requires surface protection against oxidation. There are three major sectors where protection is essential:

(i) production of primary metal;
(ii) casting of components (die casting, gravity casting, permanent mold etc.);
(iii) recycling.

Several general concepts may be applied to protect liquid magnesium:

(i) covering the melt surface by melt-viscous salt or salt mixtures;
(ii) additions of passivating elements to the melt to trigger formation of a protective scale;
(iii) melt handling under an inert gas atmosphere;
(iv) melt handling under gas forming a protective scale;

The detrimental sides of using salt fluxes are the melt contamination, reducing its quality, and metal losses in sludge. Although doping a melt with some chemical elements, such as Be or Ca, reduces oxidation, it cannot, unfortunately, eliminate ignition. A protective blanket of inert gas such as argon or helium has only limited applications where magnesium vapor cannot accumulate. Confusion is frequently created in regard to the protective nature of nitrogen. It should be emphasized that at high temperatures, nitrogen reacts directly with molten magnesium to form Mg_3N_2. The product does not form a barrier layer and is not able to protect the melt. The reaction is exothermic and leads to an increase in temperature.

The method of melt handling under gas, which forms a protective scale, is most frequently applied commercially. The fluorine bearing gas atmospheres, capable of forming protective films on magnesium, were identified in the 1920's. In 1934 a US Patent names SF_6, SO_2 and BF_3, along with their recognized ability to protect magnesium [20]. Based on this discovery, a number of techniques for the protection of molten magnesium were developed historically.

7.11.1 Sulphur Hexafluoride SF_6

Research in the 1960's resulted in adoption of SF_6 over the salt based fluxes, BF_3 and SO_2, used earlier [21]. The fluxless melting by Batelle in 1977, exploring SF_6, was interpreted as the major advance in safe casting of molten magnesium. At present, SF_6 is widely applied by industry as the effective protection of magnesium melt against oxidation. SF_6 is a synthetic gas, heavier than air, odorless, colorless, non-toxic and non-flammable. It was first obtained in 1902, has high dielectric strength and is thermally stable up to 800 °C. At temperatures exceeding 600 °C it reacts with water vapor, forming HF, and therefore requires dry air for blending.

SF_6 is applied in low concentrations, below 1% in air or air with CO_2, to the space above the surface of molten magnesium in casting furnaces through a distribution tube with multiple nozzles. In die casting, the SF_6 concentration used is in the range 0.2%–0.3% by volume in air or in CO_2, which results in a consumption of 1 kg/tonne of metal. On a worldwide scale there are variations in SF_6 consumption by die casting, ranging from 0.1 kg/tonne to 11 kg/tonne of magnesium. Some recommendations suggest that concentrations as low as 0.04% by volume are fully sufficient.

7.11.1.1 Mechanism of Melt Protection by SF_6

When molten metal is covered with an SF_6 blanket, the reaction starts from a formation of an MgO layer as a result of the reaction between magnesium and oxygen (Fig. 7.16a). In the presence of SF_6, the contact angle between solid MgO and molten magnesium is reduced, resulting in the wetting of MgO by magnesium metal. The metal is drawn up between the MgO particles by capillary forces, pulling them together and forming a cohesive layer which separates liquid metal from air, thus preventing evaporation, oxidation and ignition (Fig. 7.16b). The decomposition of SF_6 provides fluorine for the formation of MgF_2. In an attempt to explain the melt protection mechanism, fluorine is often identified as the only gas controlling the protective properties of SF_6.

While observed in the solid state, the reaction film has the morphology of an interlocking irregular dendritic network that forms a dense and cohesive layer. The layer consists of solid MgO and MgF_2 with no traces of any sulphur-containing compounds [22]. Increasing the exposure time from 1 min to 100 min, for a specific level of SF_6 in the cover gas, has no significant effect on the relative concentration of oxygen, magnesium or fluorine in the surface film. At the same time, a direct relationship exists between the level of SF_6 in the cover gas and the concentration of fluorine in the film, and for three SF_6 concentrations examined, namely 0.1%, 0.3% and 1%, the highest level of fluor was detected for 1%. According to depth profiling, the concentration of each particular element remains constant from the

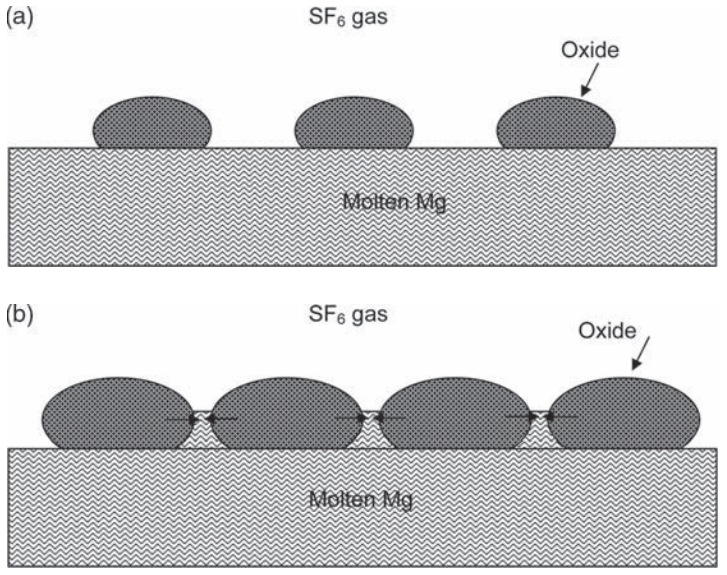

Fig. 7.16 The mechanism of magnesium melt protection by SF_6 blanket: **a** beginning of formation the surface layer; **b** well formed protective layer [23]

outer region of the film to the magnesium surface, excluding the depth segregation of specific elements during oxide growth.

In the absence of SF_6, there is a large contact angle, poor wetting of MgO by Mg metal and non adherent surface film [23]. The porous layer does not inhibit evaporation. The oxidation of magnesium in vapor state does not lead to formation of a protective layer, and the process continues, causing ignition. This behavior is probably related to a change in the surface tension of magnesium melts in the presence of different cover gas mixtures.

7.11.2 Sulphur Dioxide SO_2

Sulphur dioxide was for a long time used to protect magnesium melts. It is of interest that SO_2 gas was replaced in the 1970's by SF_6. The present environmental concerns with SF_6 shifted attention back to SO_2. Due to the progress made in equipment and methods of worker protection, as well as scrubbers to remove SO_2 from emissions, it is possible to use it more safely than previously.

The concentration required is approximately 1.5% in air. Frequently, SO_2 is diluted with nitrogen as a carrier gas with the content of SO_2 from 3 to 0.3 vol %. A negative side is its toxicity—the occupational exposure limit is 2 ppm per 8 hours. When combined with water vapor it forms an acid that corrodes steel equipment. Under certain conditions, reaction products and deposits form, which may cause metal eruptions from furnaces. Another obstacle is that SO_2 has to be stored as a compressed gas or liquid, thus in case of accidental release the volume is rather large. Moreover, quite a complex system for storage and distribution is required with appropriate safety precautions.

7.11.3 MagShield

The technology was developed by Hatch Inc., Mississauga, Ontario, in 1999, and is based on BF_3 gas, well known for its protective behavior. The gas is classified as highly toxic with a TLV level of 1 ppm. BF_3 is not a greenhouse gas, hence, fugitive emissions can be controlled. The major inconvenience with BF_3 is its storage as concentrated, highly compressed gas. In this form, it is potentially hazardous due to the risk of rupture, so storage under cool conditions is required. The novelty of the MagShield method is the *in situ* production of BF_3, which after mixing with air, is directly distributed to the magnesium melting equipment.

The schematics of the MagShield protection method are shown in Fig. 7.17. The main parts consist of a solids feeder, air dryer, decomposer and a scrubber assembly. To prevent issues of gas handling, storage and transportation, an in-line fluoride gas generation method is used. The small amounts of BF_3 in dilute concentrations are produced by the controlled thermal decomposition of fluoride compounds. During

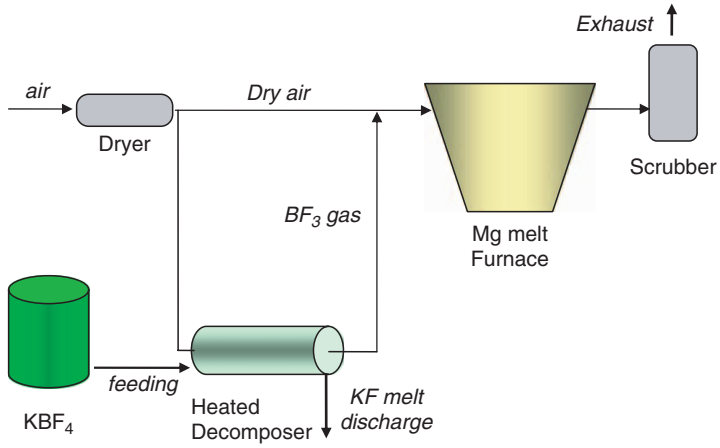

Fig. 7.17 The schematic diagram of the MagShield method of protectiing liquid magnesium, developed by Hatch Inc.

this process, KBF_4 decomposes *in situ* to generate the BF_3 gas and an inert glassy fluoride compound that is removed as solid or liquid. BF_3 generation begins roughly at 350 °C and increases with temperature. Liberated BF_3 is then carried from the furnace to a dryer and after dilution is ready for use. The control features include the feeding rate of the solid fluoroborate and the carrier gas dilution ratio. Also the use of heat is seen as protection against developing uncontrolled leakage.

The protection requires a concentration of 1.5% BF_3 in air. Industrial trials show a reduced volume consumption of BH_3 in comparison with SF_6 and less than half of the mass consumption, with an operating cost of 5%—10% of the former. The process generates no odor, fume or smoke, and there is no corrosive attack on the equipment.

7.11.4 Other Methods

In addition to the protective methods proven commercially there are numerous candidates that have been tested only in a laboratory environment. Some potential solutions are described below.

7.11.4.1 Fluorinated Ketones Fks

The fluorinated ketones represent a new class of chemicals, similar to hydrofluorocarbons. Gas mixtures from 0.024% to 1.3% in dry air or CO_2 are effective

in protecting magnesium melt [24]. During thermal degradation, which takes place at temperatures higher than 575 °C, CO is the first product found. Then, a reaction with oxygen generates a number of other chemicals, such as COF_2, CF_4, C_2F_6 and $C_3F_{8,}$ indicating that undesirable compounds can be created. At the same time, however, degradation reactions can be controlled by a selection of the proper carrier gas. Therefore, carrier gases other than oxygen are used to prevent degradation. The mechanism of protection is not clear, but it was noticed that surface films had a color from silvery, metallic, gray to dull, depending on concentrations. The scrubber analysis indicates that around 97% of the gas is consumed, i.e., incorporated in the melt.

7.11.4.2 Hydro-Fluorocarbons HFC

The protection mechanism by HFC is similar to that known for other fluorine bearing cover gas mixtures. A difference in composition of the surface film formed is observed, which for HFC-134a may contain up to 50% magnesium fluoride as compared to 13% found for SF_6 [25]. The gas itself is considered non-toxic. The required concentration depends on alloy grade, temperature, time and other design features of the furnace. Various mixtures were tested, including dry air, CO_2 and N_2. The consumption may be up to three times less than SF_6. At temperatures higher than 730 °C, SF_6 provided better protection.

7.11.4.3 Solid Or Gaseous CO_2

The version based on solid CO_2 relies on injecting the gas into the furnace chamber at high pressure by a nozzle where after expansion the solid CO_2 is created [26]. Then, the solid snow in the form of particle agglomerates precipitates at the bath surface, hence lowering bath temperature and a tendency of the molten alloy to evaporate. The cooling effect of CO_2, due to sublimation, is of 573 kJ/kg at 78 °C. The reduction in temperature takes place within a top layer of 5 mm to 10 mm thick. As a result of CO_2 sublimation and increased gas volume, oxygen is displaced from the bath surface. In general, 1 g of solid CO_2 transforms to about 0.541 of CO_2 gas.

The version based on gaseous CO_2 is also explored in a mixture with other gases [27]. The gaseous mixture is prepared by adding to the carbon dioxide an oxidizing gas, argon and xenon. As an example a mixture of 70% CO_2, 20% argon, 1% xenon and air, is quoted.

7.11.4.4 Inert Gases

The concept of using inert gases to replace reactive gases and suppress oxidation and ignition is effective for a number of metals. Due to the specific nature of

molten magnesium, however, this idea has limited applications. Although inert gases, such as argon or helium, do not react with magnesium, they do not suppress its extensive evaporation. An accumulation of a highly reactive magnesium vapor takes place above the melt surface. In the event of contact with air, it leads to an explosion.

Similarly, mixtures of Ar with N_2 do not form a protective layer on the melt surface. Instead, the layer, which consists of agglomeration of spherical particles, is not cohesive, exhibiting cracking and separation from the molten metal. In this case, both oxidation and evaporation are active.

In industrial practice, inert gas mixtures can protect magnesium during casting operations, but for melt holding furnaces, SF_6 is still required. There are attempts to design furnaces that prevent contact between magnesium vapor and air, thus allowing the application of inert gases.

7.11.5 Protective Atmospheres for Heat Treatment

Heat treatment is a process that exposes solid magnesium alloys to high temperatures, frequently for extended time periods. Of special concern is the procedure of solution annealing, conducted at temperatures exceeding 400 °C. It is considered that the bulk magnesium components do not ignite during typical heat treatment cycles in air. The ignition may, however, be triggered by a presence of machining fines or other mechanical damage. To prevent ignition, an atmosphere of nitrogen is recommended, containing less than 2% oxygen [28]. Thus no more expensive inert gases such as argon or helium, are required. Similarly, there is no need to use the sulphur-containing gases.

7.11.6 Environmental Impact

According to present tests, no significant conversion or destruction of SF_6 occurs during magnesium casting. A small fraction of SF_6 reacts with magnesium to form a protective layer. Very small concentrations of two reaction byproducts, identified as HF and SO_2, were detected. It is assumed, therefore, that all SF_6 used as cover gas is emitted to the atmosphere.

For a number of decades SF_6 was considered to be environmentally friendly. However, as discovered in the mid 1990's, SF_6 is the most potent greenhouse gas of all those defined under the Kyoto Protocol. The estimated atmospheric lifetime of SF_6 is 3,200 years, and a 100-year global warming potential is 23,900 times that of CO_2. It means that 1kg of SF_6 has the same effect as approximately 24 tonnes of CO_2.

In the United States, the magnesium industry accounts for roughly 3% of the total emissions from industrial processes. Tremendous pressure is being exerted

Table 7.3 The key characteristics of selected potent Greenhouse Gases

Name of gas	Chemical formula	Atmospheric lifetime (years if not specified)	Global Warming Potential (100 year time horizon)
Carbon dioxide	CO_2	-	1
Fluorinated ketons, FKs		3–5-days	≈1
Methane	CH_4	12	21
Perfluoromethane	CF_4	50,000	6,500
Perfluoroethane	C_2F_6	10,000	9,200
1,1,1,2–tetrafluoroethane, HFC–134a	CH_2FCF_3	13.6–14.6	1,300–1,600
HFC–23	CHF_3	264	11,700
Sulphur hexafluoride	SF_6	3,200	22,200–23,900

worldwide to eliminate SF_6 completely. As listed in Table 7.3, the possible replacements are not neutral and also have negative effects on greenhouse gases.

7.12 Implications for Injection Molding Practice

During injection molding, magnesium alloys in the form of solid chips, semisolid slurry or complete melt are conveyed inside the machine barrel while covered with argon. The processing environment creates conditions which allow a benefit from magnesium oxidation characteristics.

7.12.1 Advantages of Oxidation Kinetics and an Incubation Period

In a case where the protective atmosphere contains entrapped air, introduced by a feedstock, an oxidation reaction would occur. Thus at temperatures of semisolid range the processing time is of critical importance for reducing the progress of magnesium oxidation. The oxidation kinetics show that the incubation period, preceding the onset of catastrophic oxidation, favors quick processing. It is, therefore, reasonable to assume that injection molding, with a typical residency time of semisolid magnesium alloy shorter than 3 min, should result in particularly low oxygen uptake and high integrity of the final product.

The oxidation kinetics also favor preheating the particulate feedstock prior to feeding it to the machine. At temperatures recommended for preheating, typically below 150 °C, the incubation period is long, allowing drying and preheating outside the barrel.

7.12.2 No Accumulation of Magnesium Vapor—Protection by an Inert Gas

When magnesium melt is kept, magnesium vapors condense above it and are ready for explosion. During injection molding the alloy fills the machine barrel almost completely, leaving no room for accumulation of metal vapor. In addition, alloy is continuously conveyed through the barrel. This environment favors using an inert gas to prevent oxidation or ignition, and there is no need to involve SF_6.

7.12.3 Issues Caused by the Particulate Nature of the Feedstock

The particulate nature of the feedstock creates a large surface area for a possible reaction between metal and reactive gases. Such a reaction may take place during long-term storage in a high-humidity environment. Care should be taken to store chips in dry conditions.

The large surface area of chips can accumulate a large volume of air and introduce it into the barrel. During feeding, therefore, the method of argon flushing removes air, preventing it from entering the barrel. While chips are not completely dry, a potentially large volume of water vapor would also be introduced into the barrel. The best prevention is drying them prior to the feeding so any moisture is removed.

The small size and sharp edges of chips may create fine particles during transportation. A part of the processing issues they may create is that magnesium fines may ignite due to heat or electrostatic spark.

7.12.4 Advantage of a Small Volume of Molten Alloy

A potential of ignition and fire is a possible drawback of magnesium casting. This issue may have tragic consequences when large volumes of molten magnesium are kept in the casting area. In this regard, injection molding exhibits a unique advantage. The volume of alloy being molten or semisolid at a given time is rather small and corresponds to 2–7 kg.

7.13 Examples of Alloy Degradation from Injection Molding Practice

Although injection molding creates an environment allowing the minimization of alloy degradation due to oxidation, there are still challenges resulting mainly from eventual process perturbation or equipment maintenance.

7.13.1 Magnesium Evaporation

Protection from oxidation by the use of an inert gas, e.g., argon, does not eliminate the evaporation of magnesium. Therefore, the long breaks in processing accompanied by too high stand-by temperature and insufficient flow of argon create conditions for the build-up of magnesium vapor. Thus, because of limited volume of free space for vapor build up, magnesium degradation phenomena are seen in the barrel head and in the nozzle.

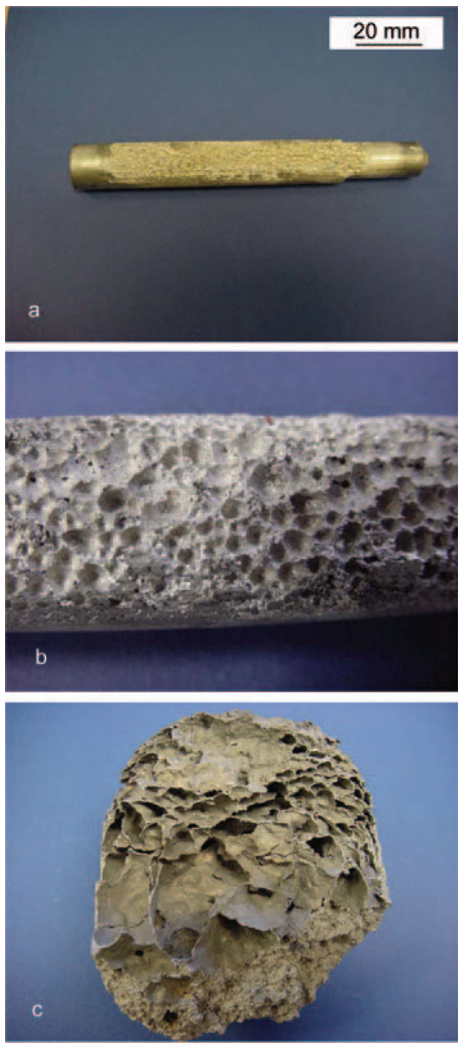

Fig. 7.18 The AZ91 alloy, solidified within a nozzle and barrel head, showing high density of bubbles generating a porous structure formed by magnesium vapor, subsequently reacting with air: **a** general view; **b** magnified image, revealing the foam morphology; **c** porous structure generated within the barrel head

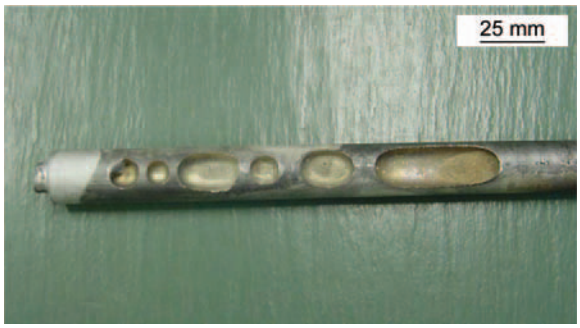

Fig. 7.19 The AZ91 alloy, solidified within a nozzle with surface bubbles formed by magnesium vapor

The formation of a sponge-like structure caused by magnesium vapor is shown in Fig. 7.18a-c. The process took place inside the nozzle and barrel head during stand-by. At the stage when the vapor bubbles were formed the alloy solidified, preserving the liquid foam morphology. Although the nozzle is closed relatively tight, traces of oxygen migrate from outside and after reacting with magnesium vapor causing micro explosions. When the alloy is kept for a longer time in liquid state the bubble vapor will coalesce, forming large features (Fig. 7.19). During a long stand-by period the build up of magnesium vapor pressure formed well-shaped features, apparently interacting with each other through separating liquid metal.

7.13.2 Oxidation Within a Machine Nozzle During Stand-By Periods

The nozzle plug does not seal the barrel volume completely. This is because the solidification shrinkage leaves a gap between the nozzle walls and the plug, allowing air ingress. During continuous processing the positive pressure of flowing argon and short residency time eliminate oxidation. However, long stand-by periods, low argon flow and too high temperature of the nozzle result in oxidation (Fig. 7.20). When the alloy within the nozzle is converted to oxide it will permanently block the barrel exit. Practice shows that even partial transformation of alloy into oxide will create an effective blockade, preventing further processing.

If a large volume of oxygen enters the barrel it may form bubbles interacting with molten alloy. While this kind of oxide is formed inside the barrel, it potentially disintegrates into micropieces and mixes with surrounding melt. If the oxygen bubbles are pushed into the nozzle, a characteristic yellowish discoloration is seen, indicating surface oxidation (Fig. 7.21a). If such a bubble is formed by the inert gas of argon, the surface is metallic and free of oxide (Fig. 7.21b,c). The microscopy reveals, however, that surfaces of argon filled bubbles show morphologies of initial oxidation (Fig. 7.21d).

Fig. 7.20 The formation of oxide on the free surface of molten magnesium alloy within the machine nozzle

7.13.3 Oxidation and Ignition During Equipment Maintenance

During maintenance and the screw replacement procedure, the screw that is partially filled with the alloy, having a temperature ranging from semisolid slurry to preheated chips is exposed to air. As shown in Fig. 7.22, depending on the alloy's temperature, a different level of degradation is observed. For flights with lower temperature, the reaction with air causes the formation of individual spots of oxide nodules (Fig. 7.22a). For flights with higher temperatures individual spots are replaced with entire colonies of nodules (Fig. 7.22b). A further increase in temperature not only increases the nodule density but also generates ignition spots (Fig. 7.22c). Finally,

Fig. 7.22 (continued) barrel: **a** individual nodules in colder zone; **b** colonies of oxide nodules with some of them experiencing ignition; **c** high density of nodules with high density of ignition sites; **d** surface morphology after burning of the alloy in hotter zone

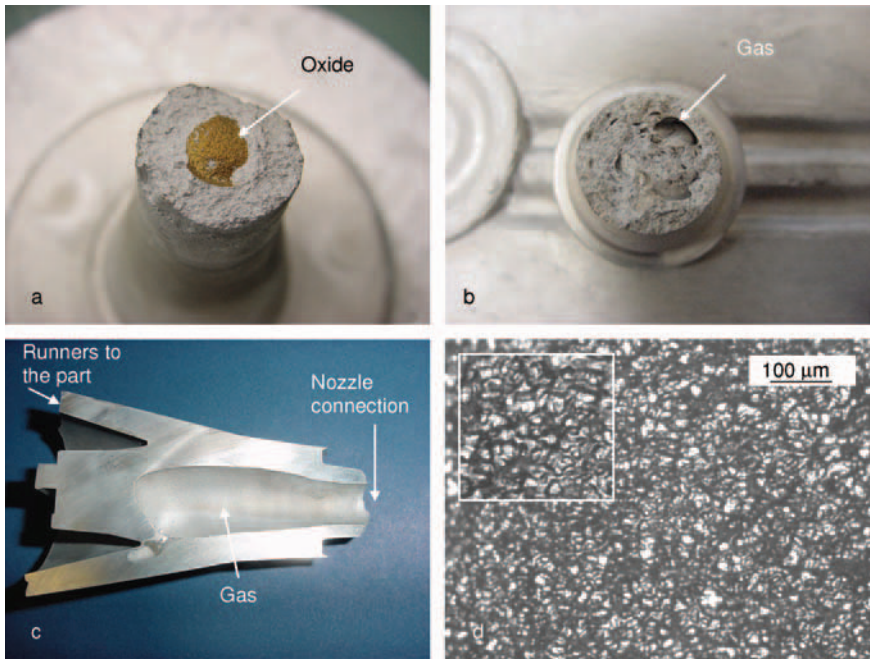

Fig. 7.21 The formation of oxide due to gas bubbles present inside the liquid magnesium prior to leaving the machine nozzle (AZ91D alloy): **a** Oxide with a different color contrast in the sprue - the oxidized surface was revealed after sprue fracturing; **b** high concentration of numerous gas bubbles inside the sprue; **c** high volume of a gas, forming a single bubble which fills almost the entire sprue - a difference in color contrast as compared to figure **a** suggests less intensive oxidation; **d** magnified view of gas bubble surface from figure **c** showing growth morphology of an oxide

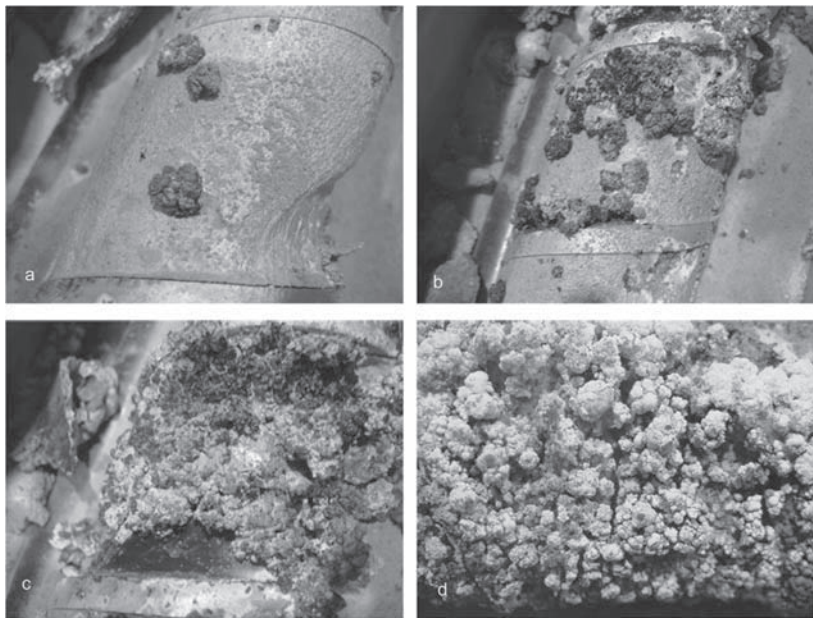

Fig. 7.22 The oxidation and ignition of AZ91 alloy on the injection screw, removed from the

ignition engulfs the entire surface and the combustion morphology covers the alloy surface (Fig. 7.22d).

7.14 Summary

The oxidation mechanism of magnesium alloys represents a complex process where structural changes within the substrate are accompanied by several surface reactions. The oxidation mechanism changes from protective to non-protective with linear or accelerated kinetics depending on the temperature and time of exposures. During reaction in an oxidizing environment, the addition of beryllium delays the onset of non-protective oxidation. It does not affect, however, the oxidation kinetics during very initial stages. During reaction in an inert atmosphere of argon, beryllium suppresses the magnesium evaporation. Although the alloy is highly reactive, the processing environment of injection molding creates conditions allowing a benefit from its oxidation characteristics. In addition, the processing environment makes simple protection by the inert gas argon sufficiently effective in oxidation and ignition prevention. As a result, no complex prevention techniques, which are inherent to conventional casting, are required here.

References

1. Tenorio JAS, Espinosa DCR (2000) High temperature oxidation of Al-Mg alloys. Oxidation of Metals 53(3–4):361–373
2. Walukas DM, Decker RF, Totten AW (2001) Effects of beryllium content in Thixomolding AZ91D. In J.N. Hryn (ed) Magnesium Technology 2001. TMS, New Orleans, LA, pp 95–98
3. Cohen MS (1960) Acta Metallurgica 8:356
4. Pilling NB, Bedworth RE (1923) Journal of Institute of Metals 28:534
5. Czerwinski F (1998) The microstructure and internal stress of Fe-Ni nanocrystalline alloys deposited without a stress reliever. Electrochemica Acta 44:667–675
6. Klug HP, Alexander LE (1974) X-ray diffraction procedures, John Wiley, New York
7. Czerwinski F (2000) On the use of the micro-marker technique for studying the growth mechanism of thin oxide films. Acta Materialia 48:721–733
8. Czerwinski F, Smeltzer WW (1993) The early-stage oxidation kinetics of CeO2 sol-coated nickel. Journal of the Electrochemical Society 140(9):2606–2615
9. Smeltzer WW (1958) Oxidation of an aluminum 3pct magnesium alloy in the temperature range 200–250 °C. Journal of the Electrochemical Society 105:67–71
10. Scamans GM, Butler EP (1975) In situ observations of crystalline oxide formation during aluminum and aluminum alloy oxidation. Metallurgical Transactions A 6:2055–2063
11. Czerwinski F, Szpunar JA (1998) The influence of the crystallographic orientation of nickel surface on oxidation inhibition by ceria coatings. Acta Materialia 46:1403–1417
12. Lea C, Molinari C (1984) Magnesium diffusion, surface segregation and oxidation in Al-Mg alloys. Journal of Materials Science 19:2336–2352
13. Czerwinski F (2003) The early stage oxidation and evaporation of Mg-9%Al-1%Zn alloy. Corrosion Science 46:377–386
14. Jedlinski J, Borchardt G (1991) Oxidation of Metals 36:317

15. Leontis TE, Rhines FN (1946) Rates of high-temperature oxidation of magnesium and magnesium alloys. Transactions of American Institute of Mining and Metallurgical Engineers 166:265–294
16. Gulbransen EA (1945) The oxidation and evaporation of magnesium at temperatures from 400 to 500 °C. Transactions of the Electrochemical Society 87:589–599
17. Zayan MH (1990) Model for non-protective oxidation of Al-Mg alloys. Oxidation of Metals 34:465–472
18. Song G, Atrens A, Dargusch M (1999) Corrosion Science 41:249
19. Hine RA, Guminski RD (1960) Journal of Institute of Metals 89:417
20. Reimers HA (1934) Method for inhibiting the oxidation of readily oxidizable metals. US Patent 1,972,317, 4 Sept 1934
21. Hanavalt JD (1972) Practical protective atmospheres for molten magnesium. Metal Engineering Quarterly 12(4)
22. Cashion SP, Rickettes NJ, Hayes PC (2002) Characterization of protective surface films formed on molten magnesium protected by air SF6 atmospheres. Journal of Light Metals 2:37–42
23. Cashion SP, Rickettes NJ, Hayes PC (2002) The mechanism of protection of molten magnesium by cover gas mixtures containing sulphur haxafluoride. Journal of Light Metals 2:43–47
24. Milbrath DS (2002) Fluorinated ketones as a new cover gas for protection of molten magnesium: A progress report. In 59th Annual World Magnesium Conference, Montreal, Canada, IMA, pp 66–71
25. Rickettes NJ, Cashion SP (2001) Hydro-fluorocarbons as a replacement for sulphur hexafluoride in magnesium processing. In JN Hryn (ed) Magnesium Technology 2001, pp 31–36
26. Bach FW et al (2005) Use of CO2-snow for protecting molten magnesium from oxidation. In NR Neelameggham, HI Kaplan, BR Powell (eds) Magnesium Technology 2005, TMS, pp 3–6
27. Peschaux M, Rhodon M (2002) Method for protecting a non-ferrous liquid metal from oxidation. US Patent 6,500,230, 31 Dec 2002
28. Stratton PF, Chang EK (2000) Protective atmospheres for the heat treatment of magnesium alloys. In HI Kaplan, JN Hryn (eds) Magnesium Technology 2000, pp 71–75
29. Czerwinski F (2002) The oxidation behaviour of an AZ91D magnesium alloy at high temperatures. Acta Materialia 50:2639–2654

8
Melting Behavior of the Feedstock

8.1 Introduction

There are many requirements imposed on the potential feedstock, including size uniformity with a minimum of submicron fines, an oxide-free surface, smooth flow through the system and acceptable manufacturing cost. The key feature that determines its use for semisolid processing is, however, the formation of spheroidal particles of the unmelted phase within the semisolid slurry. The melting characteristics are sometimes seen as independent of the feedstock nature, and it is claimed that the alloy turns thixotropic during its conveyance through an extruder, due to the combined effect of shear imposed by the injection screw and external heating. To explain this, a description of the microstructural evolution of an alloy during processing and an assessment of the individual contributions of shear and heat are required. In this description, the role that a specific nature of feedstock plays needs to be established. This knowledge is important in the design of machinery that will better meet the requirements of semisolid processing.

In this chapter, the sole influence of external heat on melting characteristics of the feedstock is considered. A variety of sizes and morphologies of magnesium-based particulates, manufactured by various techniques, were selected in order to analyze a wide range of microstructural and microchemical factors, believed to be of importance at high temperatures.

8.2 Factors Affecting Feedstock's Thermal Instability

Feedstock used for injection molding represents a specific type of material not only because of its particulate form but also due to its internal microstructure. The latter feature is created as a side effect during the stage of feedstock manufacturing.

8.2.1 Cold Deformation in Metals

The cold work is described as plastic deformation, which could not be relieved due to the temperature and time conditions under which it was imposed. To prevent

F. Czerwinski, *Magnesium Injection Molding*.

stress relief, the deformation temperature should be lower than that, causing recrystallization.

As a result of cold work, metals experience strain hardening, thus their tensile and other physical properties change. Almost all theories attempting to explain strain hardening are based on dislocation models. Accordingly, the relationship between the strain hardening as a flow stress σ_o and the structure is expressed by [1]:

$$\sigma_o = \sigma_i + \alpha G b \sqrt{\rho} \tag{8.1}$$

Where:

σ_i – friction stress opposing motion of dislocations;
α – numerical constant, generally between 0.3 and 0.6;
G – modulus of elasticity in shear;
b – magnitude of the Burgers vector of the lattice;
ρ – dislocation density.

Due to a presence of the single slip plane in hexagonal close-packed magnesium, i.e., the basal plane {0001}, the amount of strain hardening is anticipated to be limited. In a polycrystalline structure there is, however, extensive interference of neighboring grains, which activates multiple slip, thus creating an opportunity for substantial work hardening.

8.2.2 Cold Deformation of Magnesium

The hexagonal, close-packed lattice makes the plastic behavior of magnesium crystals highly anisotropic. At room temperature, typical for the chipping process, deformation in magnesium takes place almost entirely due to slip along the basal {0001} planes in the $\langle 11\bar{2}0\rangle$ direction. Although slip on the $\{10\bar{1}0\}\langle 11\bar{2}0\rangle$ prismatic and $\{10\bar{1}1\}\langle 11\bar{2}0\rangle$ pyramidal systems has been observed experimentally, the critical resolved shear stress is an order of magnitude higher than that for basal slip [2]. Thus, the limited number of slip systems available, adversely affecting the conditions of simultaneous deformation of differently oriented grains, results in restricted formability of the polycrystalline structure. When stress or strain concentration occurs, slip takes place locally on non-basal planes. The grain boundaries are an important region for this phenomenon, so that a cellular structure forms there long before it does in the central regions of the grains [3]. The presence of serrations in the grain boundaries is often confirmed during metallographic observations.

The deformation of a crystal results, typically, in the creation of deformation bands, and there are findings that shear bands dominate the plain-strain compression of pure magnesium at 100 °C where deformation reached a level of 70% [4]. At the same time, the microstructure remained highly inhomogeneous, supporting a speculation that, due to high local stress within shear bands, secondary deformation mechanisms, in the form of prismatic or pyramidal glide, were activated. According to another source [1], deformation bands are considered to be rarely

seen for the hexagonal close-packed type of lattice inherited by magnesium and its alloys. The latter finding seems to support our observations that, particularly for larger chips, cracking at the αMg/γ interface, and within the γ phase itself, is the major indicator of the chip's deformation.

For Mg alloys, formability is additionally reduced by the brittle γ phase. As a result, for Mg–Al and Mg–Al–Zn systems, the elongation values reported are of the order of 5% at room temperature and 18% at 180 °C. A possibility of larger deformation has been expected, due to the fact that, during chipping, the material is subjected to compressive stress. Although there are data [5] suggesting that magnesium can mechanically twin in compression, allowing for larger formability, the maximum deformation achieved in our research did not exceed 10% for Mg-9Al-1Zn. In addition to the low deformation, evident cold work features within the αMg matrix were clearly registered for a fraction of the smallest chips only.

8.2.3 Compression Deformation Of As-Cast Ingot

The structure of the as-cast ingot consists of dendritic grains with their shape and size being dependent on the distance from the ingot surface. As usually encountered, the skin layer contains very small equiaxed grains, the transient zone is characterized by columnar shape crystallites and the middle part has much larger equiaxed structures. The average distance between secondary dendrite arms is in the range of 200 μm to 300 μm, and the surface relief indicates the presence of chemical microsegregation inside the interdendritic cells.

The as-cast ingot subjected to uniaxial compression allowed for a maximum 8.3% deformation before fracture. After compression, external surfaces of the samples exhibited macroscopic protrusions that form a cellular pattern with an average cell size of 2 mm to 3 mm. Essentially, the same cellular structure is present within the whole sample volume, as revealed by deep etching (Fig. 8.1a). The cracks are initiated at interfaces between the intermetallic phase and αMg, as pointed out by the arrow in Fig. 8.1b. The dark contrast corresponds to the γ phase, being the intermetallic compound of $Mg_{17}Al_{12}$, while the white component represents the αMg matrix, a solid solution of Al and Zn in Mg. The majority of cell boundaries coincide with the massive intermetallics and divorced eutectic islands formed during casting and are interconnected by short bridges across the αMg phase. The deformation structure formed under controlled conditions of uniaxial compression represents the base for an analysis of deformation features obtained after mechanical chipping.

8.2.4 Deformation in Mechanically Cut Chips

The as-cast ingot precursor has a highly inhomogeneous microstructure, created by segregation phenomena during its relatively slow solidification. The factors affecting chip microstructure include:

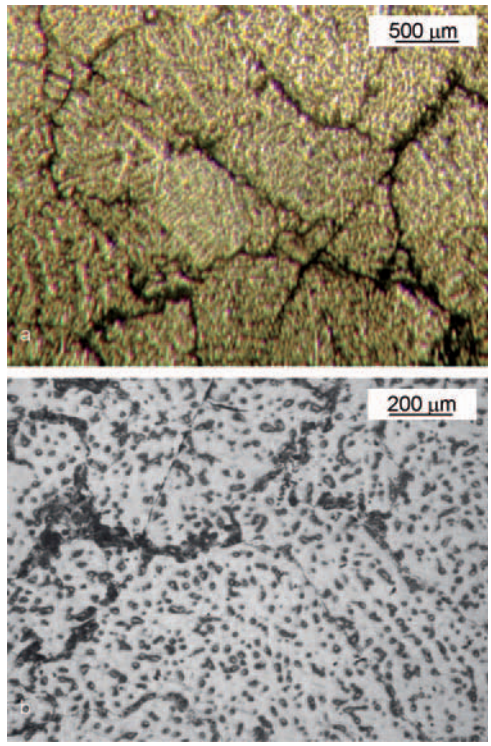

Fig. 8.1 The structural changes introduced during cold deformation by 8.3% under uniaxial compression of as-cast ingot of Mg–9Al–1Zn alloy: **a** surface after deep etching; **b** crack propagation paths

(i) a chip's place of origin within the ingot;
(ii) morphology and content of the intermetallic phase;
(iii) a chip's overall shape and size.

The major structural components, i.e. the morphology and distribution of the intermetallic phase, depend on the chip location with regard to the ingot surface. While chips that originated from a skin portion contain more fine-grained precipitates, chips cut at a distance from the surface inherit large dendrites. Thus, each chip has its specific portion of dendritic structure in terms of the content and morphology of the intermetallic phase.

Manufacturing chips by mechanical comminution involves mainly cutting. In general, the strain in metal cutting takes place in a concentrated band of shear projecting from the tool toward the free surface [3]. The inclination and width are affected by the rake angle, the depth of cut and the friction with the tool face. The size of the chip is variable depending on the presence of particles or segregates that initiate the cracking. As a result of a small volume of shear zone, the cell size is

much finer and the dislocation density is much greater. Therefore, in a shear zone of small volume the operation slip systems and other flow modes are activated, which are not commonly observed for bulk metals. The dislocation density is increased by friction with the cutting tool, which may locally increase the metal temperature. Thus fine subgrains with high misorientations are developed, suitable for intense nucleation during re-heating.

As anticipated, the chipping operation changes the alloy microstructure significantly. Due to relatively small chip size and a temperature of the order of 50 °C, the mechanical fragmentation causes cold work within their entire volume. The extent of chip deformation depends on the chip size as well as the content and morphology of the γ phase. The most evident cold work features are registered for chips with low contents of γ having globular morphology. In such cases, deformation bands are formed, indicating that homogeneous deformation is not possible and strain had to accumulate locally. Some inhomogeneity of deformation is also seen in the vicinity of the α/γ interfaces. Apparently, this is a result of differences in the mechanical properties of α and γ, expressed by a hardness of 60 HV for αMg as compared to 190 HV for the γ phase.

Although it is difficult to estimate quantitatively the extent of chip deformation, in general the internal structure exhibits all features typical of heavily deformed material. For some chips, particularly those with smaller size, deformation is severe, frequently accompanied by cracks originating at the interface between massive γ precipitates and αMg or within fine, divorced eutectic and propagating further into the αMg matrix (Fig. 8.2a,b). For all chips, thin surface films usually show more extensive damage, while deformation of inner portions is quite uniform (Fig. 8.2c). The large chips do not reveal, under magnification of optical microscopy, features that can support substantial deformation. Instead, their microstructure is similar to the ingot part from which they originate. In this case the cracking of massive precipitates of the intermetallic phase and a divorced eutectic with extension into the matrix is more frequent than the presence of other deformation features within the αMg grain itself. The cold work structure of chips is thermodynamically unstable and will evolve at elevated temperatures.

8.2.5 Deformation in Pellets Manufactured by Solid-State Extrusion

The manufacturing process of pellets by extrusion and cutting involves extensive deformation of the entire material's volume. Thus, feedstock created this way exhibits unique structural features, distinguishing it from the chips described above. The reproducibility of deformation conditions within extruded pellets make them more suitable for detailed microscopical analysis than the mechanically comminuted chips. The opportunity to employ electron microscopy allows for a better understanding of the role of the feedstock nature in generating thixotropic structures required for semisolid injection molding.

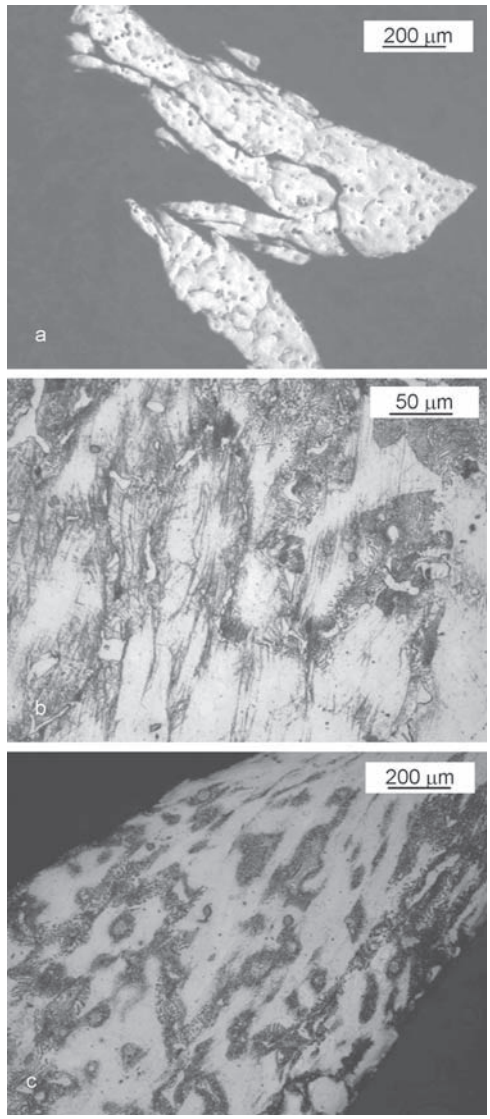

Fig. 8.2 The initial microstructure of mechanically comminuted chips of Mg-9Al-1Zn: **a** general view of mounted chips; **b** heavy plastic deformation within chip volume; **c** comparison of surface and volume deformation

8.2.5.1 Deformation Features of Magnesium Extrusion

To increase the formability of hcp magnesium structure, the material is preheated before extrusion. Since in addition to the external preheat, the temperature in the extrusion zone rises by several hundred degrees, the alloy experiences dynamic

recrystallization. In general, dynamic recrystallization occurs under certain conditions of hot or elevated temperature deformation in materials with low or medium stacking fault energy. During studies of an iron–nickel–chromium alloy 800H (21%Cr, 32%Ni, Fe–base) with fcc structure, a remarkable fraction of annealing twins was observed in the recrystallized regions [6]. It was concluded that even though the first recrystallized grains are formed at prior grain boundaries, the further progress of recrystallization twinning is an active mechanism of dynamic recrystallization. For Mg–5.8%Zn–0.65%Zr, substantial evidence was accumulated that the mechanisms of the nucleation during dynamic recrystallization and the mechanism controlling steady state deformation are similar [7]. The presence of twins in as-extruded structures points towards dynamic recrystallization, which is active during AZ91D alloy pellet extrusion. It is known that the original microstructure controls transformation kinetics and the recrystallized grain size [8]. An increase in the original grain size slows down the evolution of dynamic recrystallization, and for the same deformation conditions, transformation may not occur at all if the grain is coarse enough.

The presence of differently oriented twins after extrusion in AZ91 alloy proves that some grains were poorly oriented for basal slip, and twinning occurred on several sets of pyramidal planes. As a result of the stress concentration at twin boundaries, interfaces between twin colonies and twin-grain boundary intersections, a cellular structure develops that is further responsible for the alloy's thermal instability. There is another example in the literature of the non-equilibrium structure of equiaxed grains for AZ91D alloy, processed by equal channel angular extrusion. In that case, high resolution electron microscopy revealed that grain boundaries were mostly curved or wavy and corrugated with regular or irregular arrangements of facets and steps [9].

8.2.5.2 Microstructure Evolution During Extrusion of Pellets

For pellets with a diameter of approximately 4 mm, the as-extruded matrix comprises equiaxed αMg grains with differently oriented twins in their interiors. Fragmented particles of the $Mg_{17}Al_{12}$ compound of a submicron size are distributed at grain/subgrain boundaries and form stringers, oriented along the extrusion direction.

The optical micrographs of as-extruded alloy are shown in Fig. 8.3. The transverse section view (Fig. 8.3a) indicates the equiaxed αMg grains with numerous precipitates of the intermetallics. Occasionally, single inclusions that originated from metallurgical purification are present, with some of them having a size of the order of the matrix grains. The equiaxed character of the matrix is confirmed on the longitudinal section (Fig. 8.3b). Although no evident gradient along the through-thickness direction exists, the grain size is non-uniform with bands parallel to the extrusion direction. Moreover, the surface skin, with a thickness of several micrometers, has grains significantly smaller. The electrolytically etched surface makes the fragmented particles of the intermetallic compound easily visible with the SEM contrast,

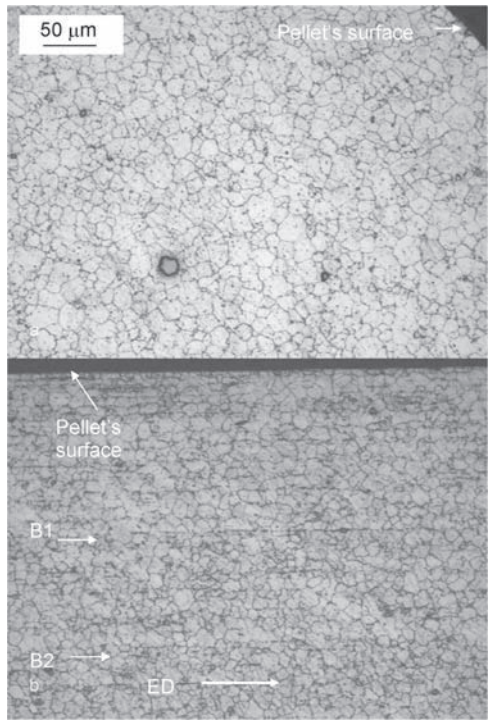

Fig. 8.3 The general microstructure of as-extruded Mg–8Al–2Zn alloy: **a** transverse section view; **b** longitudinal view. The optical micrograph of the surface etched with nital. Two bands B1 and B2 with $Mg_{17}Al_{12}$ stringers as well as extrusion direction (ED) are indicated

providing more details regarding their morphology and distribution. When viewed on a transverse section plane, the intermetallic phase with a volume fraction of approximately 11%, has a near-spheroidal shape and is distributed along well-etched grain boundaries (Fig. 8.4a). There is some correlation between the particle size and its location with larger precipitates occurring at high-angle grain boundaries and smaller ones accumulated rather at subgrains. At longitudinal sections, the intermetallic phase forms chain-like colonies of spheroidal particles and elongated stringers oriented along the extrusion direction, i.e., the pellet's axis (Fig. 8.4b). Their location coincides with the bands of finer αMg grains.

8.2.5.3 Thermal Instability of Extruded Pellets

The specific microstructure of extruded pellets, created during their manufacture, is the key factor that affects the pellet's transformation at high temperatures. Although the extrusion is conducted at elevated temperatures, and the equiaxed

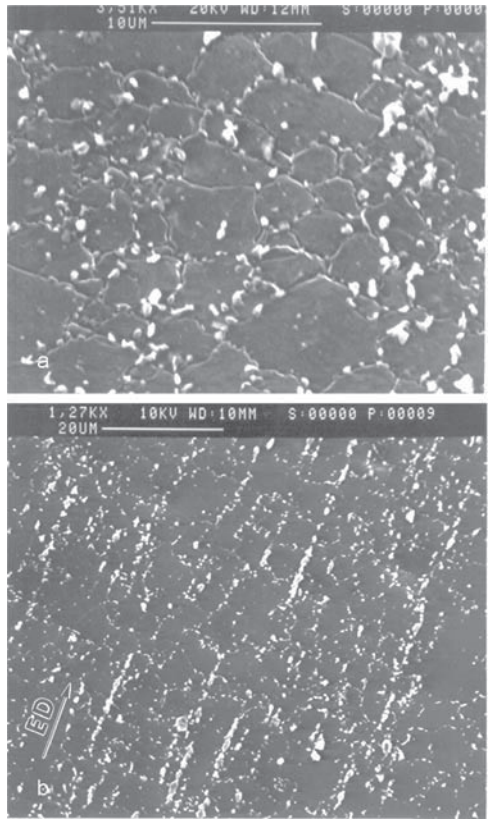

Fig. 8.4 SEM images emphasizing morphology and distribution of the intermetallic phase in as-extruded Mg–8%Al–2%Zn alloy: **a** transverse section view; **b** longitudinal view. Surfaces after electrolytic etching. ED indicates the extrusion direction [31]

grains, revealed by various imaging techniques after extrusion, suggest an equilibrium state, subsequent heating reaffirmed the alloy's thermal instability. The feature controlling this process is the twinning substructure that provides sites for uniform and intense nucleation. The origin of twins is traced to the magnesium deformation mechanism.

The intermetallic compound, distributed along the αMg grain boundary, was verified by electron diffraction as $Mg_{17}Al_{12}$. Its morphology, according to thin foils analyzed using transmission electron microscopy, is rather complex with numerous protrusions extended into the interiors of neighboring grains (Fig. 8.5a). Moreover, there are also individual $Mg_{17}Al_{12}$ precipitates of submicron size at some distance from the grain boundary. High-magnification imaging indicates that the equiaxed αMg grains exhibit a well-developed deformation substructure.

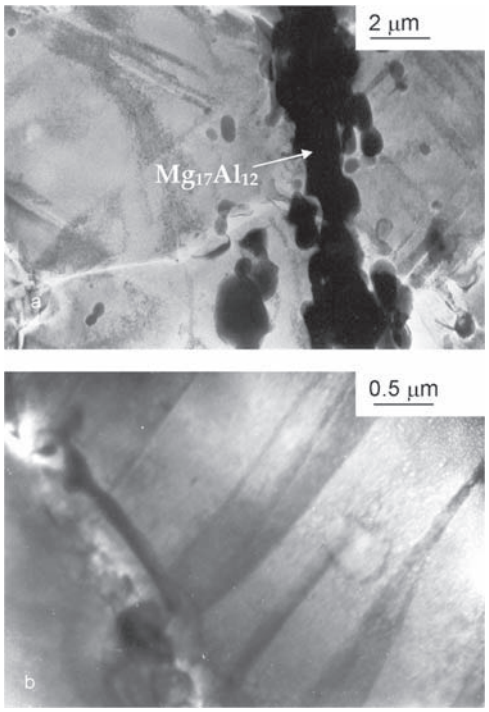

Fig. 8.5 TEM images showing microstructural details of as-extruded state of Mg-8Al-2Zn alloy: **a** the massive intermetallic phase at αMg grain boundary and smaller precipitates in grain boundary vicinity; **b** substructure of twins within the αMg grain [31]

It consists of multiple twins having at least two different orientations within each grain. The imaging indicates significant stress concentrations at the twin interfaces, and where twins intersected with previously formed twins or grain boundaries (Fig. 8.5b). These features determine the thermal instability of the pellets' microstructure.

8.3 Solid-State Transformation During Heating

Solid-state transformations within the two-phase system of αMg and $Mg_{17}Al_{12}$, are essential for the generation of spheroidal solid particles during partial melting. The grain boundary migration during recrystallization and grain growth create equiaxed structures with $Mg_{17}Al_{12}$ precipitates and augmented concentrations of alloying elements, located at triple junctions and grain boundaries.

8.3.1 Phenomena During Annealing of Cold-Deformed Metal

Although over 90% of the energy imposed during cold work is dissipated in the form of heat, the remaining 10%, which is stored in a metal, makes it thermodynamically unstable. Thus, during subsequent heating, the system will tend to return to the state of lower energy. Three separate processes can be distinguished during the heating of cold-deformed metal:

(i) recovery;
(ii) recrystallization;
(iii) grain growth.

The first stage of recovery is defined as restoration of some properties without noticeable changes in the microstructure. The properties of interest here are those controlled by point defects, e.g., electrical conductivity. An exception is a hexagonal close packed single crystal, where complete restoration of yield stress is possible.

The stage of recrystallization is understood as a replacement of the cold work structure by new, strain-free grains. In general, the recrystallization temperature (T_r) is a function of the melting temperature (T_m). While for pure metals T_r is defined as 0.4 T_m, for alloys the temperature required is higher, around 0.6 T_m. The major factors affecting the recrystallization rate include:

(i) deformation level;
(ii) temperature;
(iii) time;
(iv) initial grain size;
(v) chemical composition;
(vi) progress of recovery.

The recrystallization temperature depends on the amount of cold work: A higher amount of cold work translates to a lower temperature of recrystallization. There is, however, the minimum amount of work imposed, which is required to initiate structural transformations, and this threshold is called the critical deformation (Fig. 8.6). For deformations lower than the critical value, recrystallization will not occur. The activation energy of recrystallization depends on the cold work. At a given temperature, the recrystallization rate rises with an increasing amount of the cold work. Recrystallization of metals is affected by time and temperature, and at higher temperatures it takes a shorter time to complete structural changes (Fig. 8.7). Therefore, for practical reasons, the recrystallization temperature is defined as the temperature at which transformation of the entire material volume is completed within one hour.

After recrystallization is completed, further increasing temperature leads to grain growth. A driving force for this phenomenon is a reduction in surface energy of the system. At high temperatures the grain coarsening becomes rapid, and the process is described as secondary recrystallization.

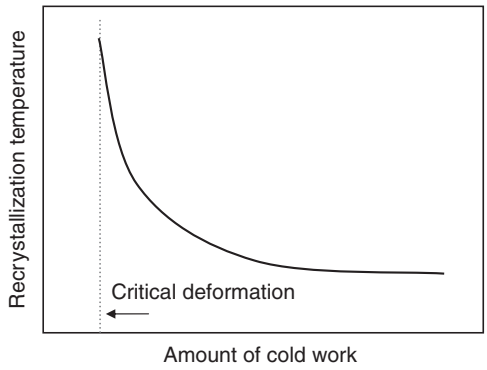

Fig. 8.6 The recrystallization temperature as a function of cold work. When the amount of cold work does not exceed the critical value, recrystallization does not occur

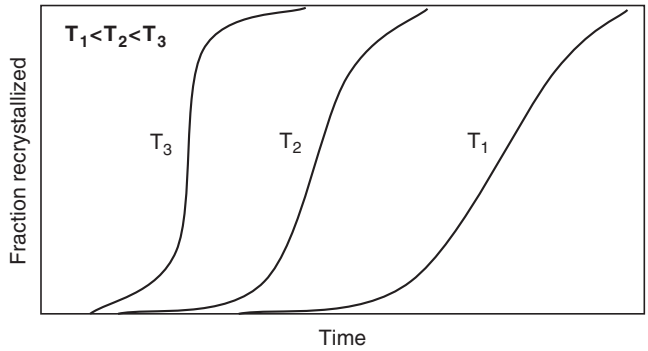

Fig. 8.7 The influence of temperature on the progress of recrystallization. For higher temperatures the incubation time is shortened, and the recrystallization progress is faster

8.3.2 Recrystallization Phenomena in Magnesium

Thermal stability of cold-worked magnesium depends on deformation parameters, and the literature gives a wide range of recrystallization temperatures. The homologous temperature for pure magnesium is 184 °C. There are reports, however, showing that during processing of an AZ91 alloy by equal channel angular extrusion, the recrystallization temperature was as low as 175 °C [9]. In that case, in spite of large straining, electron microscopy revealed the presence of high-angle grain boundaries and few dislocations in the grains' interior, indicating complete recrystallization. There are, however, data showing the stability of severely deformed AZ91 alloy with submicron and nano-size grains up to 425 °C. A specific structure with nano-size grains is credited for the high temperature stability.

8.3.3 Recrystallization of Cold-Deformed Ingot

The microstructure of as-cast undeformed ingot, subjected to a thermal cycle of 400 °C for 15 min is shown in Fig. 8.8a. Instead of a network of equiaxed grains, a deep etching reveals only the remains of the dendritic, as-cast structure, which partly disintegrated due to the short-term effect of heating. A common feature of undeformed ingots, annealed above approximately 400 °C, is a porosity that results from incipient melting. The irregular shaped pores, with a size of tens of micrometers, are mainly located at triple junctions.

The identical ingot, which was deformed under uniaxial compression and subjected to the thermal cycle of 400 °C for 15 min, experienced complete recrystallization (Fig. 8.8b). Apparently, the volume fraction of undissolved primary $Mg_{17}Al_{12}$ compound is relatively high and is accompanied by less visible fine precipitates along grain boundaries.

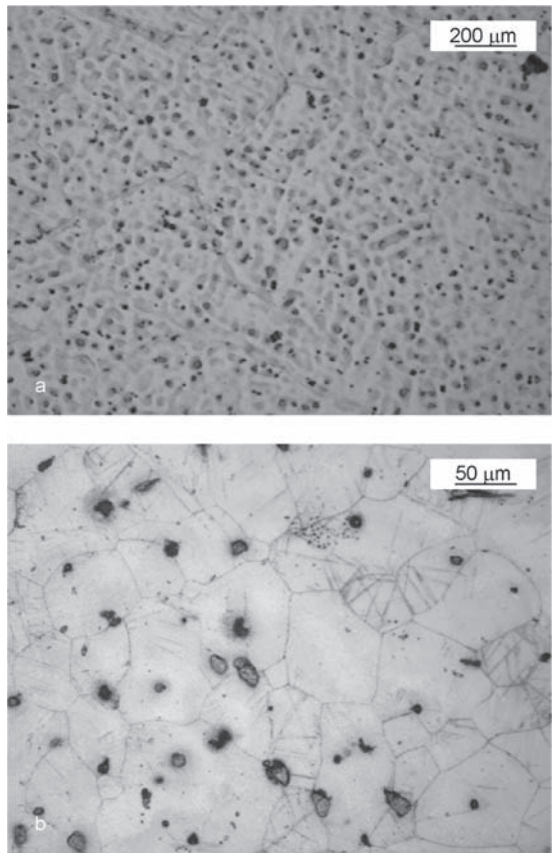

Fig. 8.8 The microstructure of as-cast Mg–9Al–1Zn ingot after annealing at 400 °C for 15 min followed by deep etching **a** and the same ingot deformed by 8.3% under uniaxial compression and annealed at 400 °C for 15 min **b**

8.3.4 Annealing Phenomena Within Mechanically Comminuted Chips

8.3.4.1 Recrystallization Microstructure

Heating of the mechanically chipped alloy leads to essential changes within its microstructure, expressed primarily by a replacement of cold-deformed structure by strain-free grains. A complete recrystallization, observed during annealing of all chips, provides proof that during manufacturing the material experienced cold deformation, exceeding the critical level required to initiate recrystallization. An example of recrystallized, equiaxed grains, developed within the chip exposed to 400 °C for 15 min, is shown in Fig. 8.9a. As viewed on the cross-section, grains with an average size of 42 µm are generally uniform and no special effect around the chip edge is recorded. Despite the small chip size and resultant high cooling rate, grain boundaries are decorated by discontinuous precipitates of the intermetallic phase.

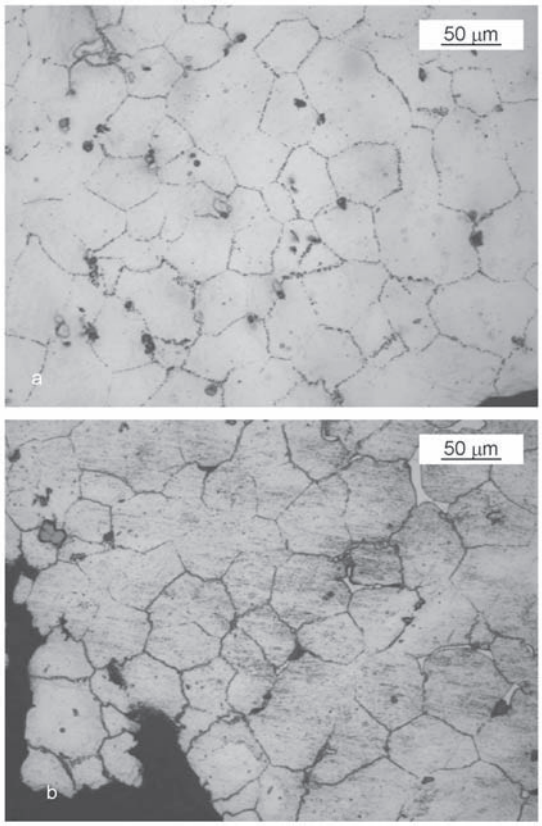

Fig. 8.9 The microstructure of mechanically fragmented chips after annealing at 400 °C for 15 min: **a** chip of regular size C1; **b** chip of large size C3 [32]

Although for larger chips, the deformation features are less evident during microscopic examinations, they also experience complete recrystallization and develop an equiaxed-grain structure. Size characterization of chips is specified in Chap. 6. The major difference, as compared to smaller chips, is expressed by a denser network of precipitates along grain boundaries. As seen in Fig. 8.9b, large islands of the primary $Mg_{17}Al_{12}$ phase, which originated from casting and did not dissolve under the conditions of heat treatment, remain at grain boundaries and triple junctions.

8.3.4.2 Grain Size—Chip Size Correlation

Differences in deformation conditions of chips raise a question about the influence of chip size on grain evolution during subsequent recrystallization. To build a correlation, as an indicator of chip size, its smaller cross sectional dimension, determined metallographically, was used. A summary of the recrystallized grain size, plotted as a function of the chip size for three chip types, is depicted in Fig. 8.10. In this graph, the grain size is represented by an average chord obtained from the measurement of approximately 200 grains. The plot indicates that, for all chip morphologies examined, the grain size is within a range of 30 μm to 80 μm. An increase in chip size is generally accompanied by grain coarsening. However, the differences in changes are specific for each chip type. The graph also includes the large chips, where cold work features of αMg matrix are rarely seen at magnifications of optical microscopy.

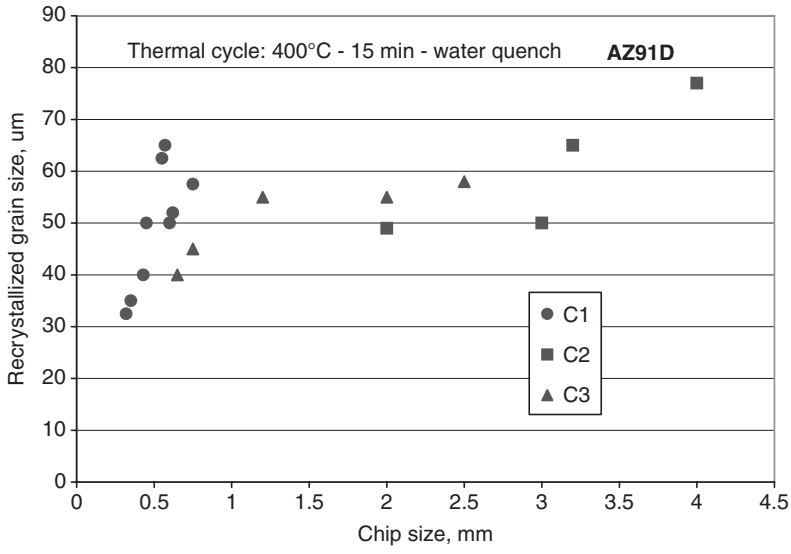

Fig. 8.10 The plot of grain size after recrystallization at 400 °C for 15 min as a function of chip size [32]

A specific feature of chips is their deformation inhomogeneity, inherited from mechanical comminuting. Since the grain's nucleation is related to the local strain energy, the recrystallization is expected to have a heterogeneous nature as well, and this should be particularly seen at intermediate stages. The final results, obtained after complete recrystallization and after partial melting, do not exhibit relevant differences within individual chips. The only difference is a reduction in the recrystallized grain size, which was registered for smaller chips. This points toward the larger deformation they experienced during manufacturing. Extending the annealing time up to two hours causes mainly a further dissolution and spheroidization of the primary intermetallics, while the αMg grains experience only limited growth. For an average chip size of 0.5 mm, the grain size reaches a value of 45 μm which is roughly 10% larger than that measured after 15 min of exposure.

8.3.5 Annealing Phenomena in Extruded Pellets

8.3.5.1 General Microstructure Development

While heating the extruded pellets at 200 °C, a significant refinement of grain size takes place within their volume, which proves the recrystallization (Fig. 8.11a). The deformation gradient across the pellet's cross section exerts influence during

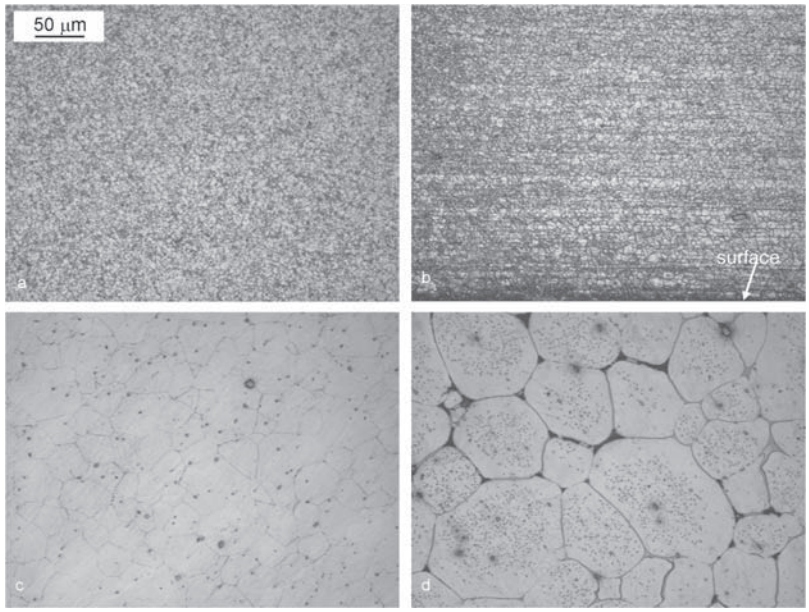

Fig. 8.11 Solid-state evolution of the Mg–8Al–2Zn alloy's microstructure during annealing for 15 min at: **a** 200 °C; **b** 330 °C; **c** 460 °C and **d** 480 °C. The extrusion direction is oriented horizontally [31]

the early stages of recrystallization. Increasing the temperature to 330 °C creates banding, which results from a chemical segregation and appears as dark streaks in the matrix. The bands have high intensity in the vicinity of the pellet's surface (bottom of Fig. 8.11b) and blend with the matrix when close to the pellet's center. In addition to smaller αMg grains within the segregation bands, there is a clear gradient in grain size along the through-thickness direction. The banding disappears gradually during a further increase in the temperature, but at 460 °C there are still individual dark precipitates aligned along the extrusion direction (Fig. 8.11c). There are also evident changes within grain interiors, expressed by the formation of numerous fine precipitates. Two features of the near-solidus structures are revealed by detailed metallography: (i) Near grain boundary regions are precipitation free and (ii) the precipitates exhibit alignment affected by the grain's orientation. It is suspected that some of these precipitates experienced melting at annealing temperatures. Around 480 °C the melting process is initiated at triple junctions and grain boundaries (Fig. 8.11d).

8.3.5.2 Changes of Intermetallic Phases

When the micro-alignment of secondary precipitates is linked to the grain's crystallographic orientation, the macro alignment of the primary fragmented particles is affected by the extrusion direction. The evident segregation bands, formed by the latter, are shown in Fig. 8.12a. In addition to the major precipitates of $Mg_{17}Al_{12,}$ there are also minor phases of different morphology and chemistry. The generally larger particles of rectangular shape were confirmed to be a manganese aluminum compound (Figs. 8.12b,c, particle 1). It is known that manganese added for metallurgical rectification, combines with aluminum to form $MnAl_4$ or $MnAl_6$. All precipitates seen as the gray-contrast phase on optical micrographs are typically contained in a single particle, with the ratio of Al to Mn increasing from the center to the surface of the particle [1]. Due to an increased Zn content of 2%, there are also Zn rich inclusions. Since Zn-containing phases have a low melting point, they easily experience spheroidization and then melting (Figs. 8.12b,d, particle 2).

The subtle details of the annealed structures are shown in Fig. 8.13. The matrix consists of freshly recrystallized αMg grains where all deformation features, observed after extrusion, are absent. The second major microstructural component, i.e., $Mg_{17}Al_{12}$, experienced substantial changes as well, and TEM allowed for distinguishing at least three different morphologies. The primary massive particles, which remained after extrusion within high-angle grain boundaries, experienced fragmentation and spheroidization (Fig. 8.13a). As seen under higher magnification in Fig. 8.13b, there are small particles of elongated shape distributed at certain grain boundaries, as well as other substructural features. Their morphology and size indicate fresh precipitation from the supersaturated αMg matrix. The third type of the $Mg_{17}Al_{12}$ phase represents precipitates within grain interiors. As depicted in Figs. 8.13c,d, these are the plate-shaped precipitates of continuous nature having the primary habit plane parallel to the basal plane of the matrix.

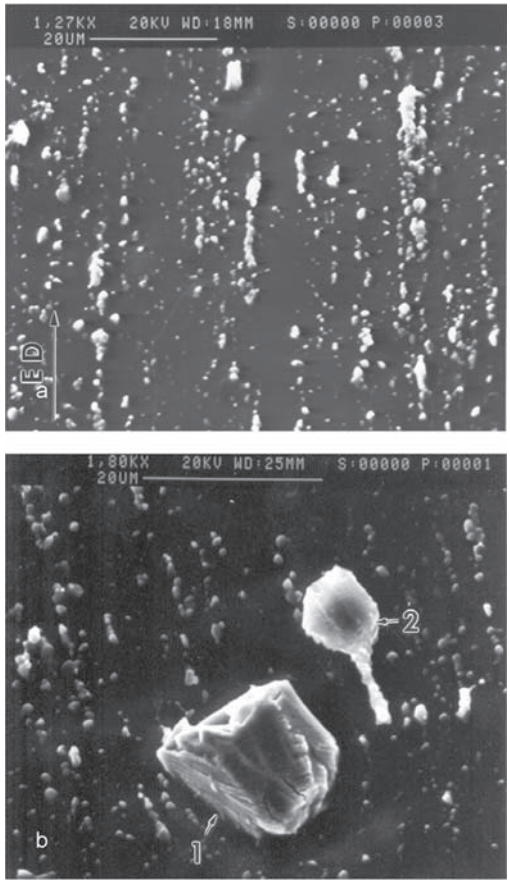

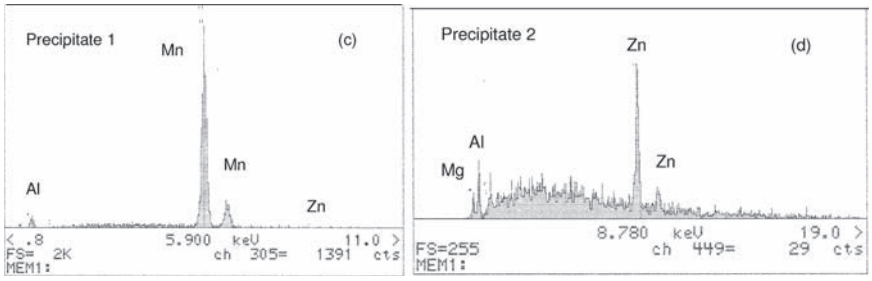

Fig. 8.12 SEM images of the Mg–8Al–2Zn alloy annealed at 330 °C for 15 min: **a** an alignment of the $Mg_{17}Al_{12}$ phase along the extrusion direction; **b** morphology of minor phases with the Mn-rich particle marked as 1 **c** and the Zn-rich particle marked as 2 **d** [31]

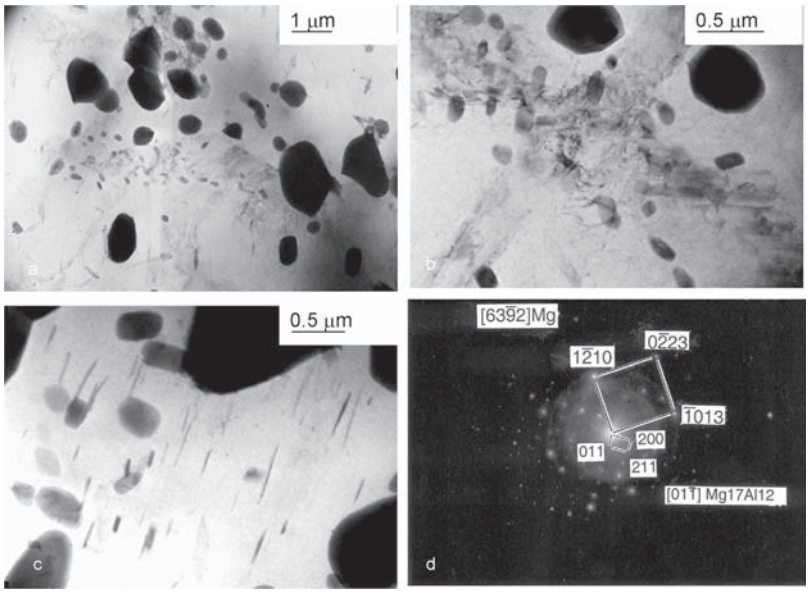

Fig. 8.13 TEM images and accompanying electron diffraction pattern of the Mg–8Al–2Zn pellet after annealing at 330 °C for 15 min: **a** large primary spheroidal particles at αMg grain boundary and its vicinity; **b** freshly precipitated $Mg_{17}Al_{12}$ laths along αMg grain boundary; **c** $Mg_{17}Al_{12}$ plates, freshly precipitated in grain interior; **d** SAD pattern identifying $Mg_{17}Al_{12}$ and αMg phases, the zone axis is indicated [31]

8.3.5.3 Quantitative Description of Grain Growth

The quantitative description of the changes in αMg grain size upon annealing is characterized by the histogram in Fig. 8.14. For the as-extruded state, the maximum frequency of αMg grain size was 10 μm, but there were also grains as large as 26 μm. After 15 min at 330 °C, the surface region of the pellets has the maximum grain-size frequency at 8 μm, with scatter similar to that after extrusion. The dominant pellet's volume has much smaller grains with a maximum frequency at 4 μm. The sharp edge of the histogram at 4 μm results from the resolution limit of the optical microscope used for grain detection. It is likely, therefore, that a certain fraction of finer grains is omitted in Fig. 8.14.

The evolution of the size and content of the intermetallic compound after annealing is summarized in Table 8.1. The stereological parameters were measured based on SEM micrographs, collected at magnifications significantly higher than those achievable by optical microscopy. An annealing at 330 °C for 15 min reduced the volume fraction of the $Mg_{17}Al_{12}$ phase from 11.3% to 8.2% and doubled its average size from 0.3 μm to 0.7 μm. Such a change in stereological parameters indicates the dissolution of small particles in the matrix. The additional data, which are included in Table 8.1 and obtained from analysis of optical micrographs,

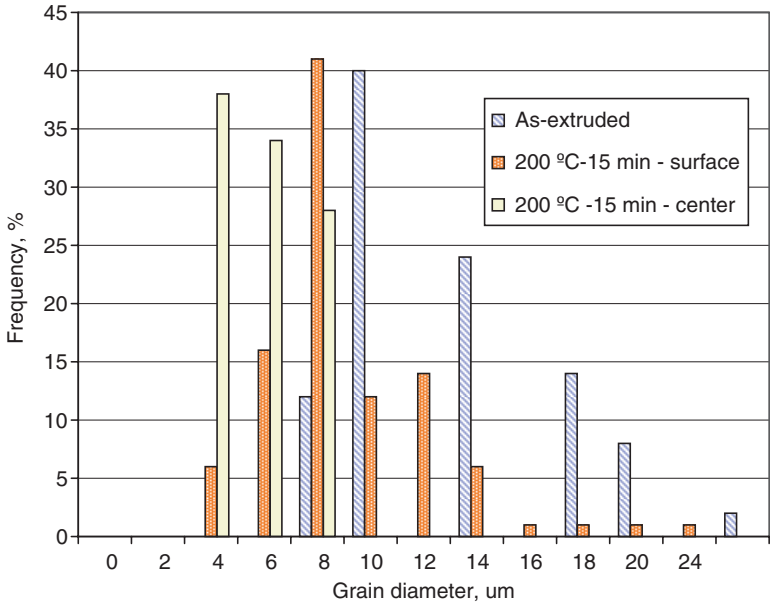

Fig. 8.14 The histogram of αMg grain sizes in as-extruded Mg–8Al–2Zn pellet and after annealing at 330 °C for 15 min. For annealed state the surface and interior of pellets were characterized [31]

Table 8.1 The comparative values of stereological parameters characterizing the pellet's microstructure in as-extruded state and after annealing at 330 °C for 15 min [31]

	Volume fraction of $Mg_{17}Al_{12}$	Diameter of $Mg_{17}Al_{12}$		Diameter of αMg	
	Average	Average	Standard deviation	Average	Standard deviation
Pellet's state	%	μm	μm	μm	μm
As-extruded	11.3	0.31	0.18	9.30	3.02
Annealed 330 °C–15 min	8.2	0.67	0.39	6.97	1.29

indicate that the average size of the αMg grain at 7 μm after annealing at 330 °C, was still smaller than that of 9.3 μm, detected directly after extrusion.

8.4 Microstructure Evolution During Feedstock Melting

Exceeding the solidus temperature activates an alloy's melting and transforms an equiaxed grain structure into semisolid slurry. During studies in the metallurgy of semisolid processing, key attention is paid to the solidification step since it generates a microstructure of the final product. For injection molding, a vital role is additionally

associated with the step of melting. Since the majority of precipitates represent intermetallic compounds that have a low melting point, a combination of the matrix recrystallization and chemical segregation along grain boundaries are the potential factors that control the feedstock's transformation during melting.

8.4.1 Nature of Non-Equilibrium Melting

When considering the melting of magnesium alloys, changes in phase composition are described based on the equilibrium phase diagrams. This approach introduces a simplification since the heating rates applied in practice are frequently too fast to lead to equilibrium. As a result, substantial differences in phase composition exist between commercially processed alloys and the equilibrium state.

Magnesium-aluminum alloys are known to solidify in a non-equilibrium state and, depending on the cooling rate, form various fractions of the eutectics. A typical location and morphology of the eutectics in Mg–9Al–1Zn alloy are shown in Fig. 8.15a and Fig. 8.15b, respectively. For 9%Al the amount of eutectic equals 12.4% [10]. A difference in the initial phase composition of non-equilibrium structures of chips and granules does not allow for absolutely correct estimations of their melting behavior. In addition to the segregation and a lack of equilibrium, complication also arises from an incipient melting, which for Mg–9%Al–1%Zn occurs around 420 °C. The pores observed after heat treatment indicate that the incipient melting temperature may be as low as 400 °C.

The influence of a solute segregation on melting progress is generally considered at macro and micro scales. For the majority of Mg alloys, the influence of Al solute represents the major factor. A variation in solute content over large dimensions, typically of the order of several millimeters, leads to the macro-inhomogeneity of melting. As a result, the melt from Al–rich areas is fed to Al–poor regions. It is believed that the movement is controlled by diffusion, caused by differences in solute distribution in the liquid phase. The microsegregation is understood as a chemistry gradient within a single Mg grain.

8.4.2 Melting by Liquid Penetration Along Grain Boundaries

Rapid penetration of a liquid phase along grain boundaries of a polycrystalline solid is a commonly observed phenomenon in many metallic systems. The thermodynamic driving force of the process is a difference between energies of the grain boundary γ_b and of the solid–liquid interface γ_{sl} expressed by $\gamma_b - \gamma_{sl}$. The driving force is independent of the thickness of the penetration layer, being of the order from a fraction to tens of micrometers. Although there are many mechanisms proposed, none of them fully satisfies experimental observations [11, 12].

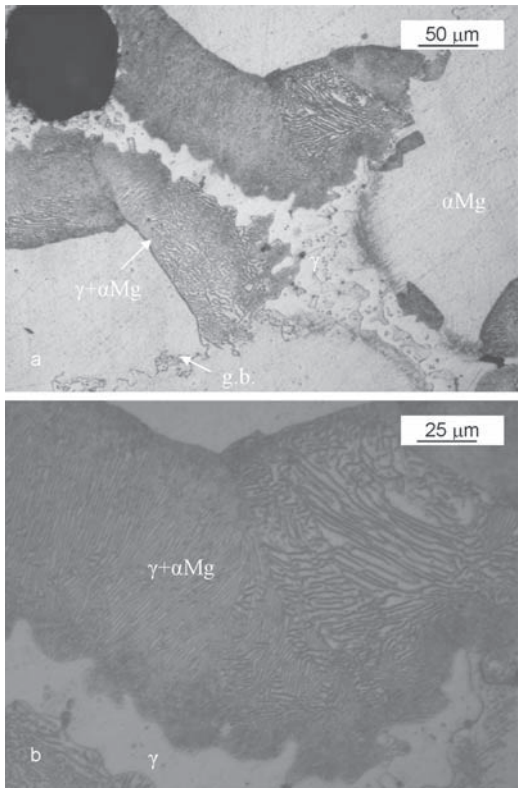

Fig. 8.15 The location **a** and detailed morphology **b** of eutectics αMg-γ in Mg–9Al–1Zn alloy

There are models emphasizing the key role of faceting of the solid–liquid interface in the penetration process [13]. They assume that the penetration of grain boundaries by a liquid requires an undersaturated solid to allow for a positive spreading coefficient of the liquid along some grain boundaries. The faceting itself is promoted by low temperatures and residual impurities in the liquid. Lower temperatures decrease the mobility of the facets, slow down the equilibriation rate of the grain boundary with impurities contained in the liquid, enhance faceting, and thus promote liquid penetration. Although it is believed that adsorption of certain impurities also enhances faceting, the evidence of this is not clear.

8.4.3 Assessment of The Solid to Liquid Ratio During Melting

The fraction solid versus temperature relationship provides the fundamental basis for the design of an alloy composition for semisolid technology. In order to describe the melting or solidification behavior of alloys, knowledge of melting or solidification

curves is required. Although there are many methods for investigating solidification and melting, not all of them are adequate for non-equilibrium processes, characteristic for magnesium alloys.

8.4.3.1 Differential Thermal Analysis (DTA) Method

Differential thermal analysis relies on heating or cooling an alloy and an inert reference material under identical conditions while recording the temperature difference between the alloy and the reference. Changes in the alloy, which lead to absorption or release of heat, can be detected relative to the inert reference. This is a standard method of determining transition temperatures and other properties of materials, e.g., latent heat or specific heat. Accuracy of measurements is affected by details of heat transfer within the experimental cell and by transformation kinetics. It was shown that the melting onset and peak temperatures depend on sample mass and heating rate [14]. Differences between thermodynamic points and features on the DTA curve are caused by heat flow limitations in the DTA. In addition, the DTA signal is influenced by diffusion kinetics within melting or solidifying alloys. Thus, methods should be developed to extract reliable melting information from DTA data. An example of the DTA curve for the Mg-9Al-1Zn alloy is shown in Fig. 8.16.

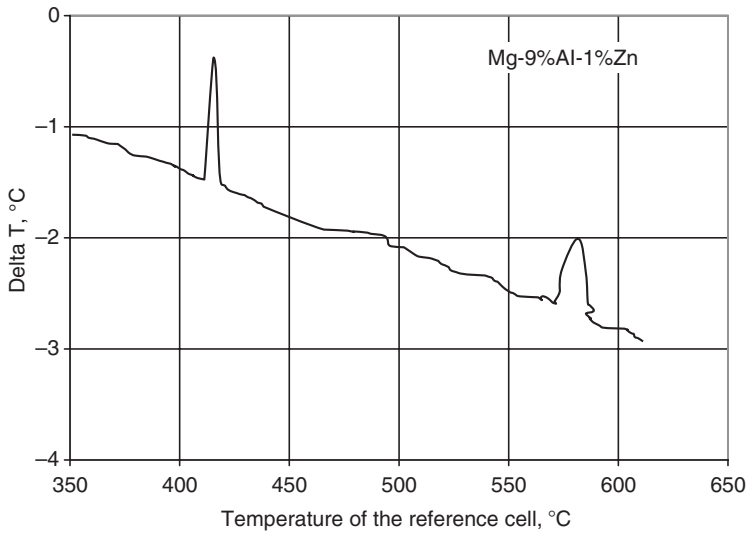

Fig. 8.16 The cooling curve of Mg–9Al–1Zn determined by DTA at a cooling rate of 1 deg/min [18]

8.4.3.2 Differential Scanning Calorimetry (DSC) Method

Differential scanning calorimetry is a technique for measuring the energy necessary to establish a nearly zero temperature difference between an alloy and an inert reference material while both samples are subjected to identical thermal cycles. The result can be achieved by the power compensation DSC or the heat-flux DSC. In the power compensation method, the temperatures of the alloy and reference are controlled independently using two heat sources. The energy required to equalize the temperature of both samples is a measure of the enthalpy changes in the alloy. The heat-flux method utilizes the single heat source, while the alloy and reference are connected by a low resistance heat-flow path. Enthalpy changes of the alloy lead to difference in its temperature relative to the reference. The major difference between DSC and DTA is that the DSC measures the heat input or heat removal required to keep the sample at a constant temperature. DSC is considered superior with regard to DTA or thermal analysis because of the quantitative heat flow measurement and the more stable baseline [15].

8.4.3.3 Metallographic Image Analysis

This method relies on experimental heating of a number of samples into the semisolid range, resembling different progressions of melting. After the equilibrium temperature is obtained, the sample is rapidly quenched in water or liquid nitrogen. It is assumed that the solid fraction, measured metallographically by quantitative image analysis at room temperature, corresponds to that which existed at high temperatures in the semisolid range. The solidification or melting curves are then built by plotting the solid fraction versus the corresponding temperature.

8.4.3.4 Cooling Curves Method

The experimental set up consists of thermal measurement and data collection equipment as well as software for data analysis (Fig. 8.17a). Thermocouples are placed in the molten alloy, which is cooled using different media (gas, water or natural air convection). The temperature change is recorded as a function of time and then analyzed to detect arrest points. To improve sensitivity in detecting events taking place within the alloy, the derivatives of the cooling curves are determined.

An example of the solidification curve for Mg-9Al-1Zn alloy is shown in Fig. 8.17b [16]. In this figure, calculations of ΔT and $\frac{dT}{dt}$ are also included. The start of solidification is defined when a $\frac{dT_w}{dt}$ curve first exhibits a rapid change from

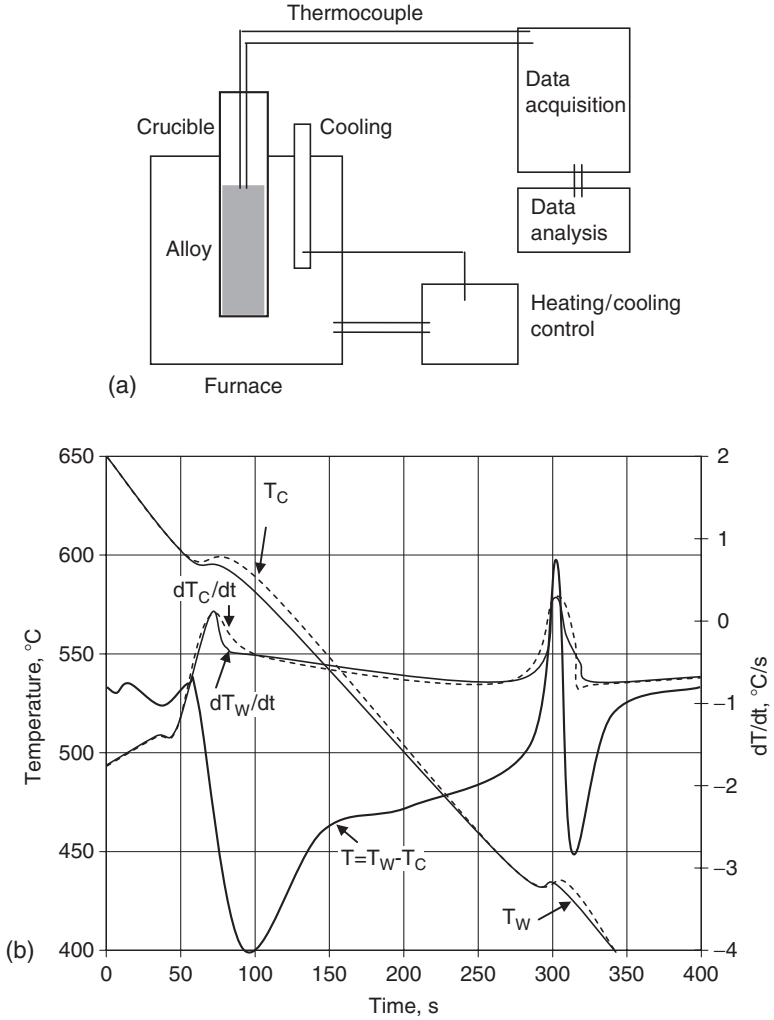

Fig. 8.17 The experimental setup for solidification analysis with a cooling curves method **a** and the solidification analysis of Mg–9Al–1Zn alloy using cooling curves method **b** [16]

the liquid cooling. The end of solidification is defined by extrapolating backwards the linear $\frac{dT_c}{dt}$ after solidification. Since the solidification starts at the crucible walls and ends at the crucible center, considering temperatures T_w and T_c provides an image of solidification for the entire ingot.

According to [17], the following equation can be used to determine the fraction solid-time based on cooling curves analysis:

$$f_s = \sum_n \frac{1}{\Delta H_{f(n)}} \sum_{t=0}^{tf} c_p(T) \cdot \Delta \frac{dT(t)}{dt} \tag{8.2}$$

Where:

f_s – solid fraction;
n – number of phases;
ΔH_f – excess enthalpy of formation;
$c_p(T)$ – specific heat capacity of entire system;

$\Delta \frac{dT(t)}{dt}$ – difference between $\frac{dT}{dt}$ and baseline curves

The technique involves a curve fitting the cooling rate of the liquid phase with the cooling rate of the solid phase. In order to isolate the heat transfer effects, characteristic for phase transformations, a so-called baseline must be assessed that estimates the heat transfer due to cooling effects only.

8.4.3.5 Combined DTA and Heat-Transfer Modeling

In this technique, the cooling curves of an alloy are determined by the differential thermal analysis (DTA) method [18]. This technique offers the advantages of simplicity, high reliability and no need of certain difficult knowledge needed to measure thermophysical properties. The last aspect is of importance since there are solidification models that cannot be applied due to the lack of certain thermophysical parameters.

According to the methodology developed in [18], the heat flow between the DTA cells and the furnace is described based on the thermal balance equation and Gray's theory [19]. The model assumes some simplifications: (i) The heat of solidification is constant; (ii) the heat transfer resistivities and heat capacities are the same for the reference cell and sample cell; (iii) the temperature inside cells is uniform. The equation derived is as follows:

$$\left(T_s - T_r\right) = RH \frac{df_s}{dt} + RC \frac{d\left(T_s - T_r\right)}{dt} \tag{8.3}$$

Where:

T_s – temperature of the sample cell;
T_r – temperature of the reference cell;
H – heat of solidification;

R – heat transfer resistivity;
C – heat capacity;
f_s – solid fraction.

Since there are difficulties in measuring R, H and C, all being dependant on the thermal properties of the DTA equipment and the alloy, they are calculated as two system parameters RH and RC based on the cooling curves.

8.4.3.6 Calculation of Solid Fraction

The solid fraction is described by two parameters:

(i) volume fraction of solid f_s^v;
(ii) weight fraction of solid f_s.

Both parameters are related by the formula:

$$f_s^v = \frac{f_s}{f_s + (1 - f_s)\frac{\rho_S}{\rho_L}} \tag{8.4}$$

Where: ρ_S and ρ_L are densities of solid and liquid phases, respectively. Both ρ_S and ρ_L depend on alloy's composition and temperature.

As the first order simplification, it is generally assumed that the volume fraction and weight fraction are identical, i.e., $f_s = f_s^v$. This implies that densities of solid and liquid are equal and do not depend on temperature and the alloy's composition.

Two different models are used to consider solidification of alloys:

(i) the equilibrium model;
(ii) the Scheil model.

They represent two extreme cases and the solidification observed in practice falls usually within the range specified by these two models.

8.4.3.7 Equilibrium Solidification Lever Rule

An assumption of equilibrium solidification is total mixing in both solid and liquid (Fig. 8.18a). In practice, this scenario is not achievable. The solid and liquid fractions for such solidification conditions and hypothetical phase diagram where the liquidus and solidus are straight lines (Fig. 8.18b) can be calculated based on the conservation of mass: Total solute equals the sum of solute in liquid and solid:

$$C_L f_L^{Eq} + C_S f_S^{Eq} = C_0 \tag{8.5}$$

Where:

C_0 – average composition of an alloy;
C_S, C_L – compositions of solid and liquid;
f_S^{Eq}, f_L^{Eq} – equilibrium fractions of solid and liquid.

Thus, during solidification, when a semisolid state is reached, the solid fraction is expressed by:

$$f_S^{Eq} = \frac{C_L - C_0}{C_L - C_S} \tag{8.6}$$

The equation (8.6) is known as the equilibrium solidification lever rule.

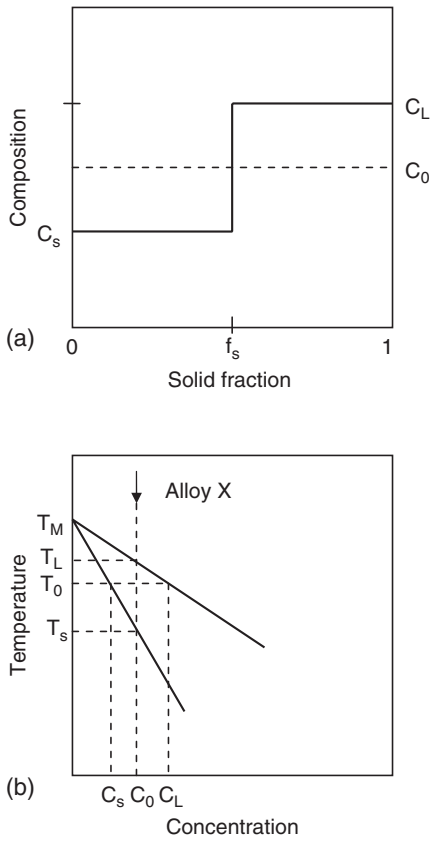

Fig. 8.18 The schematics of solidification under equilibrium conditions: **a** solute concentrations in solid and liquid phases; **b** a fragment of hypothetical phase diagram to understand the lever rule

8.4.3.8 Non-Equilibrium Solidification Lever Rule

For non-equilibrium solidification, the fraction of solid is different from that predicted by the phase diagram. For specific solidification conditions the solidification behavior is described by the Scheil equation [20]. These assumptions are as follows:

(i) there is perfect mixing in the liquid and uniform solute distribution resulting in a uniform concentration C_L;
(ii) no diffusion in the solid phase and solute concentration is C_S.

As explained in Fig. 8.19, during solidification the excess solute is rejected ahead of the moving front. The advancement of solidification results in movement of the solidification front, which requires:

$$\left(C_L - C_S\right) df_S^{Sch} = dC_L \cdot f_L S^{ch} \tag{8.7}$$

Where:

C_0 – the initial composition;
C_L – liquid composition at a given location;
f_S, f_L – solid and liquid fractions, respectively.

After introducing the partition coefficient, k, which defines how the solute is divided between the solid and liquid phases:

$$k = \frac{C_S}{C_L} \tag{8.8}$$

and several transformations, the equation (8.8) becomes:

$$C_S = kC_0\left(1 - f_S\right)^{k-1} \tag{8.9}$$

Thus for non-equilibrium solidification behavior is expressed by the relation of the weight fraction of the solid in the liquid zone, called Scheil's equation [20]:

$$f_S^{Sch} = 1 - \left(\frac{C_L}{C_o}\right)^{-\frac{1}{1-k}} \tag{8.10}$$

Since the alloy temperature T and the composition of the liquid C_L are related by the equilibrium liquidus line, the equation (8.10) can be expressed as:

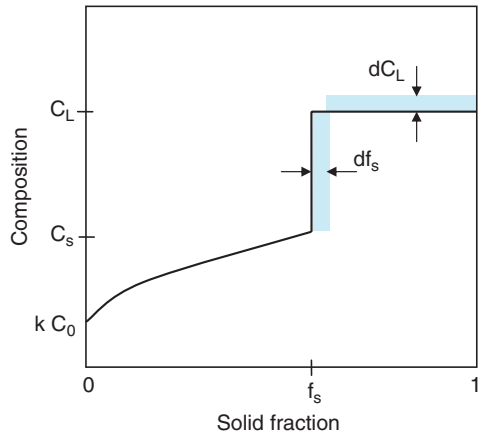

Fig. 8.19 The non-equilibrium solidification showing the concentration of solute in solid and liquid phase

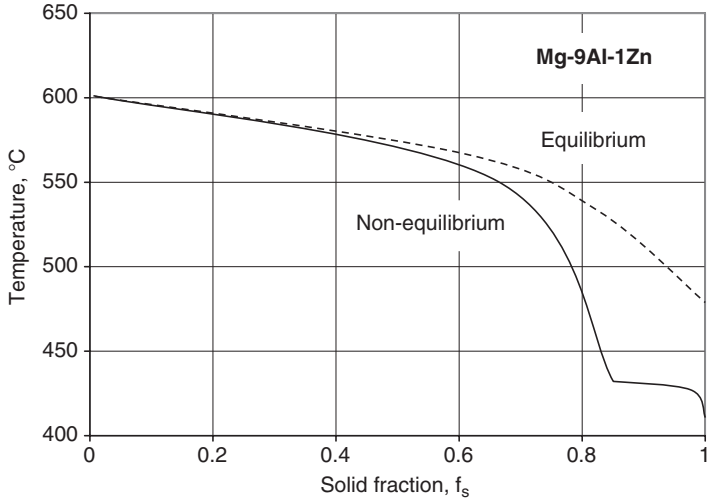

Fig. 8.20 The solid fraction versus temperature for Mg–9Al–1Zn alloy determined for equilibrium and non-equilibrium processes [16]

$$f_S^{Sch} = 1 - \left(\frac{T_M - T}{T_M - T_L} \right)^{-\frac{1}{1-k}} \tag{8.11}$$

Where:

T_M – melting point of the pure element;
T_L – liquidus temperature of the alloy;

k – partition coefficient of the alloy with composition C_o.

A comparison of the equilibrium and Scheil calculations for the Mg–9Al–1Zn alloy is shown in Fig. 8.20. For solid contents lower than 30% differences are nonexistent or negligible. For solid contents exceeding roughly 40% differences are significant, and the Scheil calculation provides lower solid content. At solid content exceeding 80%, curves obtained by both methods have a completely different shape.

8.4.3.9 Solid Fraction Versus Temperature Data for Magnesium Alloys

The solid fraction versus temperature data is essential to design the setting of a temperature gradient along the barrel. A selection of curves for several alloys is shown in Fig. 8.21.

8.4.4 Melting Mechanically Comminuted Chips

In order to include all the factors involved in the chips' transformation, the role of shear should be assessed. The potential effect of imposing shear could occur during solid- and semisolid-state conveyance inside the barrel. Given the high heating rate, the cold work would be instantly replaced by hot deformation followed by dynamic recrystallization. Such a hypothesis can be verified by melting the feedstock outside the injection machine.

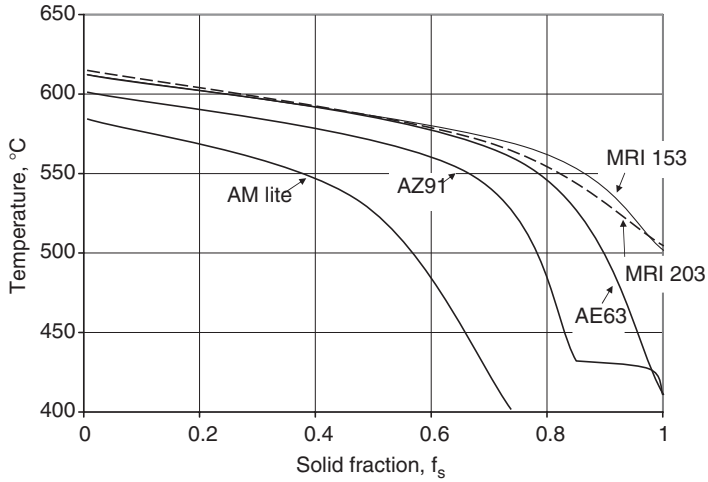

Fig. 8.21 The solid fraction versus temperature curves measured for several magnesium alloys. AM lite—data from AMT; MRI alloys—data from DSM; AE63-data from Hydro Magnesium

8.4.4.1 Melting Under Moderate Heating Rates

While exceeding the solidus temperature during heating of chips inside the furnace, the alloy is still in the form of individual chips with some of them being slightly deformed under the influence of weight of the crucible content (Fig. 8.22a). Microscopically, the chips have already started to create a bond between each other as a prerequisite for a bulk alloy. An example of partially bonded chips, marked as 1, 2 and 3, is depicted in Fig. 8.22b. In addition to a difference in the liquid fraction between chips 1, 2 and 3, there is also some variation within the same chip, e.g., the upper part of chip 2 contains more liquid than its lower part. During the very initial stage of alloy melting, as observed under high magnification, the network of grain boundaries is covered with the liquid phase, which at room temperature represents a practically pure $Mg_{17}Al_{12}$ compound (Fig. 8.22c). A thickness of the liquid film distributed along grain boundaries is not uniform, and the same is true for the range of its penetration toward selected grain interiors. In some areas, only triple junctions are molten and grain boundary wetting by penetrating liquid alloy is still in progress, e.g., the boundary between grains marked as 1 and 2 in Fig. 8.22c. As the temperature increases, the equiaxed grains transform to spherical solid particles,

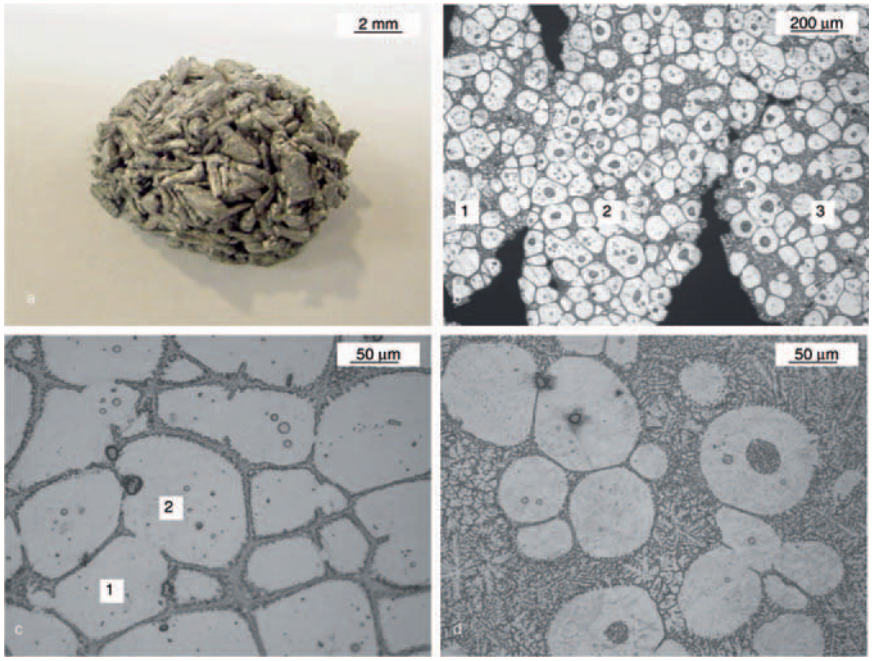

Fig. 8.22 The evolution of microstructure within chip C1 during melting: **a** macroscopic view of chips removed from a crucible; **b** equiaxed grain structure within partially bonded chips, marked as 1, 2 and 3; **c** the very initial stage of chip melting—equiaxed grain structure; **d** globular morphology of alloy containing 22% of solid [32]

surrounded by the liquid phase (Fig. 8.22d). Frequently, the particles exist as conglomerates of several, separated from their neighbors by a distinct boundary. Some of the boundaries are only partially penetrated by the liquid metal, in the same way as for particles in the right-hand part of Fig. 8.22d.

8.4.4.2 Melting Under High Heating Rates

High heating rates are achieved by the chip's immersion in a molten alloy of the same chemistry. During initial stages of melting, there is still a sharp interface between the solid chip and a molten component of the slurry (Fig. 8.23a). The equiaxed grains indicate that recrystallization resulted from cold work inherited from chipping. An average grain size of 100 μm is the same order of magnitude as the size of solid particles in the surrounding slurry. Hence, assuming an average volume of a single chip of 1.5 mm^3, one can deduce that the single chip disintegrated into 150–200 particles. An advanced stage of chips' melting is depicted in Fig. 8.23b. At that time, some of the alloy's grain boundaries melted and the individual grains started to separate from the chip, moving to the slurry and transforming into primary solid particles. A formation of equiaxed structure and melting are superimposed on chemistry changes within macro-segregation regions, reaching through a number of grains. An example of coexistence of the remaining skeleton of dendrites within the background of equiaxed grains is shown in Fig. 8.23c.

Thus, a combination of cold deformation introduced during chipping and recrystallization during subsequent heating controls the thermal decomposition of chips during melting. Heating experiments outside the machine prove that the cold-work energy stored during chipping is sufficient to initiate the recrystallization in all chips.

8.4.5 Melting of Extruded Pellets

At temperatures of the solidus–liquidus range, the equiaxed structure of pellets that develops after recrystallization and grain growth, transforms gradually into a mixture of spheroidal particles suspended in a liquid. The primary melted phase, obtained after exceeding 480 °C, is mainly distributed at triple junctions and selected grain boundaries. The presence of triple junctions with a black contrast suggests that the liquid alloy evaporated from these locations due to the small sample size and the vicinity of the free surface (earlier Fig. 8.11d).

Examples of more advanced melting with 63%, 22% and 3% solid, are depicted in figs. 8.24a, b and c, respectively. A simple comparison reaffirms that the shape of particles does not change within the wide range of the liquid content. The former liquid transforms into quasi eutectics and, due to rapid solidification after immersion of the crucible into water, the dendrite's size is rather small. The vast majority of the solid particles seen in Fig. 8.24 contain in their interiors the spherical pools of the former liquid. There are also smaller particles, consisting of the αMg phase only.

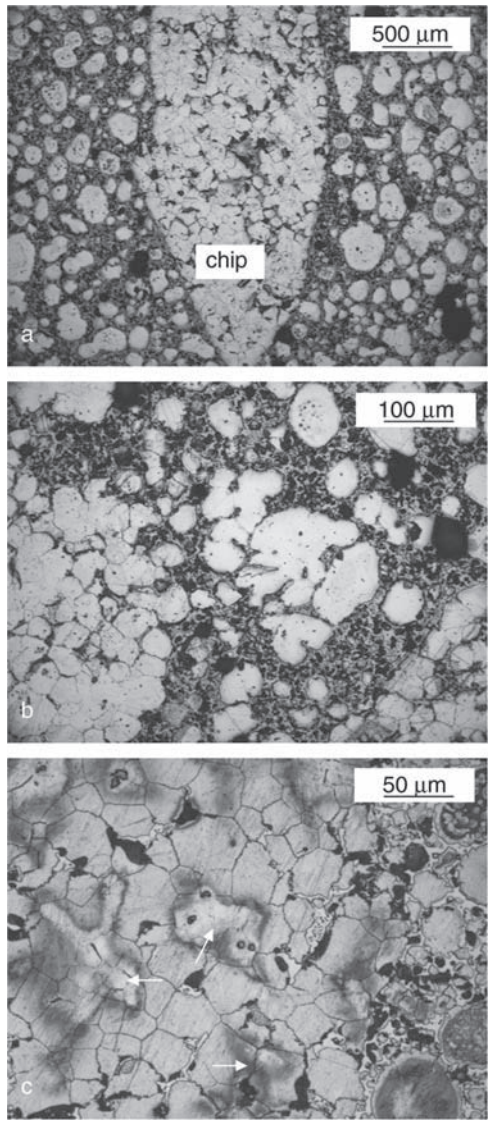

Fig. 8.23 The melting sequence of a mechanically comminuted chip of Mg–9Al–1Zn submerged in a semisolid alloy of the same chemistry: **a** general view of recrystallized chip structure; **b** advanced stage of chip melting; **c** chemical macro-segregation from former dendrites (marked by arrows) within fully recrystallized chip

It is expected that the single-phase structure results from a lack of chemical segregation within the particles. Some images, however, may represent artifacts of a random sectioning of larger particles in the region outside the entrapped liquid pools.

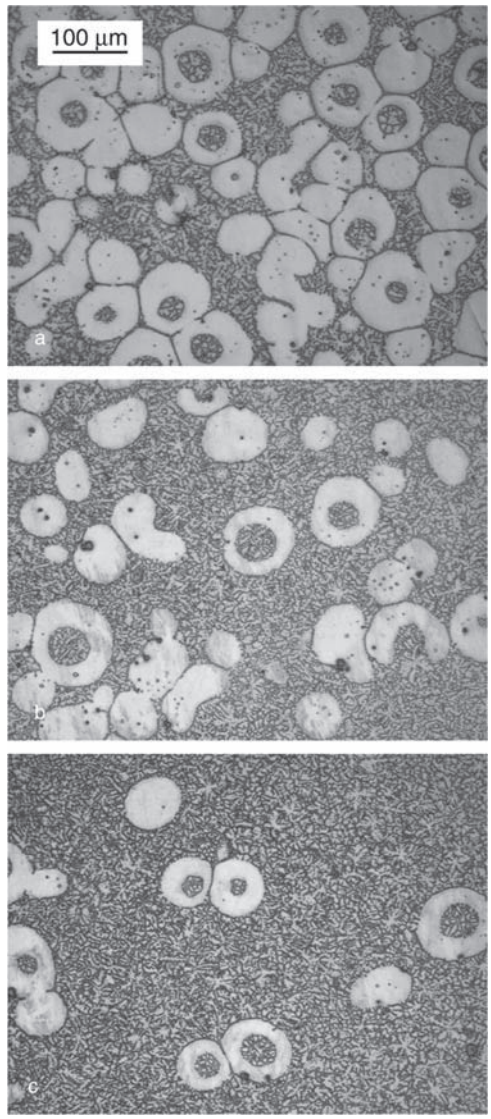

Fig. 8.24 The general view of the Mg–8Al–2Zn pellets' microstructure after partial melting: **a** 63% solid phase; **b** 22% solid phase; **c** 3% solid phase. Optical microscopy images after etching with nital [31]

The free surface of the single pellet after partial re-melting, examined with SEM, indicates some effect of the extrusion direction on the longitudinal alignment of the eutectics (Fig. 8.25a). The dark contrast features in Fig. 8.25a represent the solid particles, unmelted at high temperatures. At the pellet's cross section there is a

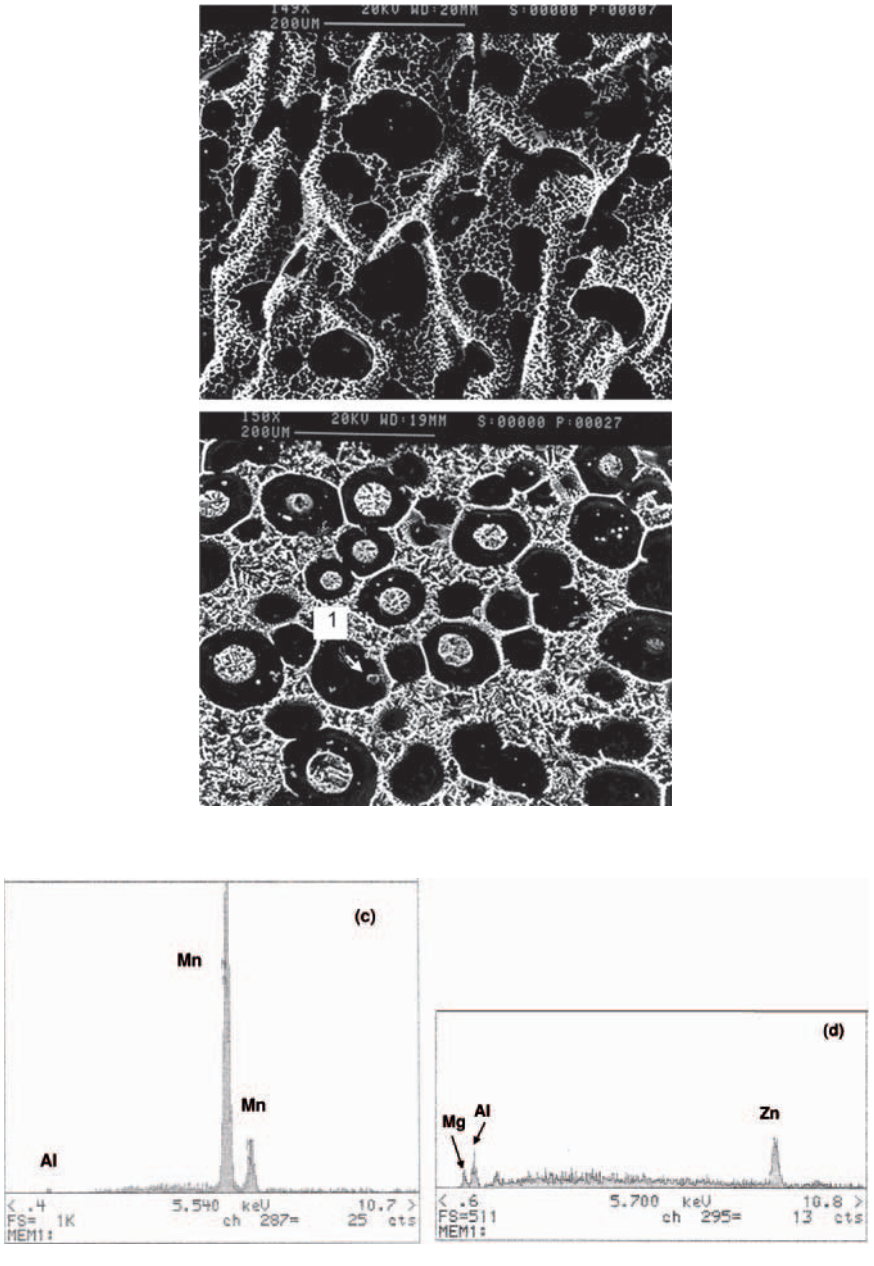

Fig. 8.25 SEM images of the partially remelted Mg–8%Al–2%Zn alloy: **a** pellet's surface; **b** pellet's interior with the Mn-rich precipitate marked as 1; **c** EDX analysis of Mn-rich particle; **d** EDX analysis of the matrix [31]

uniformity of size and distribution of primary particles surrounded by the eutectics (Fig. 8.25b). The Mn-rich inclusions, discussed separately, are distributed within both the former solid and liquid phases. Due to their high melting point, they preserved a rectangular shape at melting temperature of the Mg alloy. There is, however, a change in their chemical composition expressed by the depletion of Al content (Fig. 8.25c). The intermetallic phase contains all three major elements Mg, Al and Zn, with the EDAX spectrum indicating a higher Zn content than observed within a typical AZ91D alloy with 1% of Zn (Fig. 8.25d).

In addition to the change in proportion between the solids and quasi eutectics, there are also subtle differences in the internal microstructure of both constituents, particularly the unmelted αMg. The quasi eutectics comprise small αMg grains interconnected by the $Mg_{17}Al_{12}$ phase, and no evidence of precipitates inside αMg eutectic grains is registered (Fig. 8.26c,d). There are differences in the size of the αMg grains. Since the latter is affected not only by the liquid content, but also by the solidification rate, the details are not analyzed here. The internal structure of the primary solid for a low liquid fraction is shown in Fig. 8.26a,b. Similarly, as was the case for near-solidus temperatures, the plate-shaped continuous precipitates of $Mg_{17}Al_{12}$ are uniformly distributed within the grain interior. For higher liquid fractions, the precipitates are generally smaller and less densely distributed. As shown

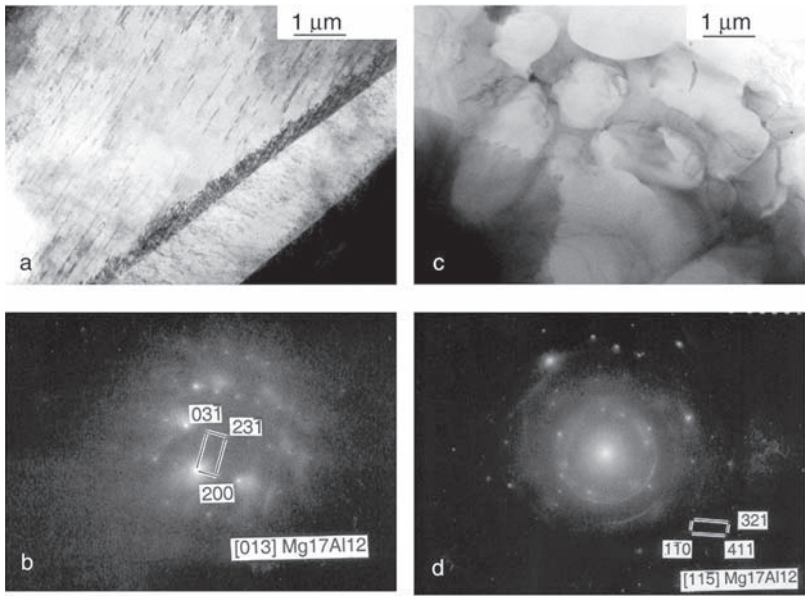

Fig. 8.26 TEM images of partially melted Mg–8%Al–2%Zn pellets: **a** plate-like precipitates within grain interior for the slurry with 58% solid; **b** SAD pattern from the region shown in **a**; **c** morphology of eutectics in the slurry with 32% solid with globular αMg grains interconnected by $Mg_{17}Al_{12}$ phase; **d** SAD pattern from the region shown in **c**; **e** lath-like precipitates within unmelted αMg phase for 12% of its content; **f** SAD pattern from the area shown in **e** [31]

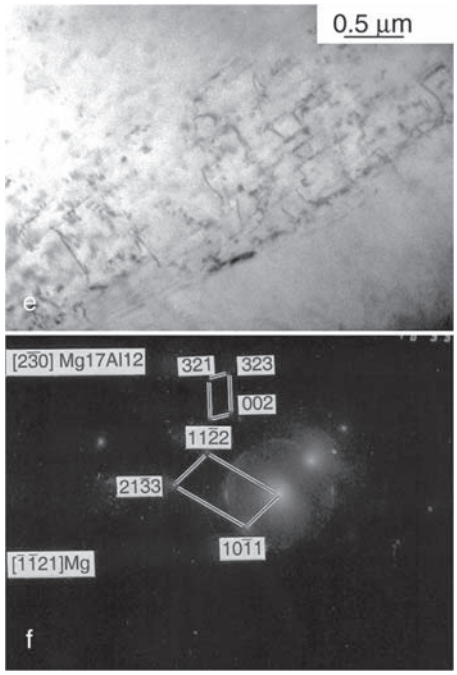

Fig. 8.26 (continued)

in Fig. 8.26e,f, their higher content is visible in the vicinity of grain boundaries. During the final stages of melting, the precipitates within the primary solid are small and, as concluded from their lath shape, rather randomly oriented within the αMg matrix. The shape of dislocations suggests that the latter precipitates are very effective in blocking their movement.

8.5 Melting of As-Cast Ingot

As-cast ingot, when re-melted without cold deformation, develops morphologies significantly different from those observed for chips and pellets. A primary feature is a lack of equiaxed structures, not only in the near solidus range, but also at higher temperatures, corresponding to less than 20% of unmelted fraction. The alloy shown in Fig. 8.27a contains in total 27% of the liquid phase, with 8% distributed along grain boundaries. An exception is represented by the skin layer of an ingot, with an approximate thickness of 1 mm, which developed equiaxed structures during the initial stages of remelting, as indicated in the left portion of Fig. 8.27b. The essential part of the ingot, however, during the advanced stages of melting, characterized by 37% of

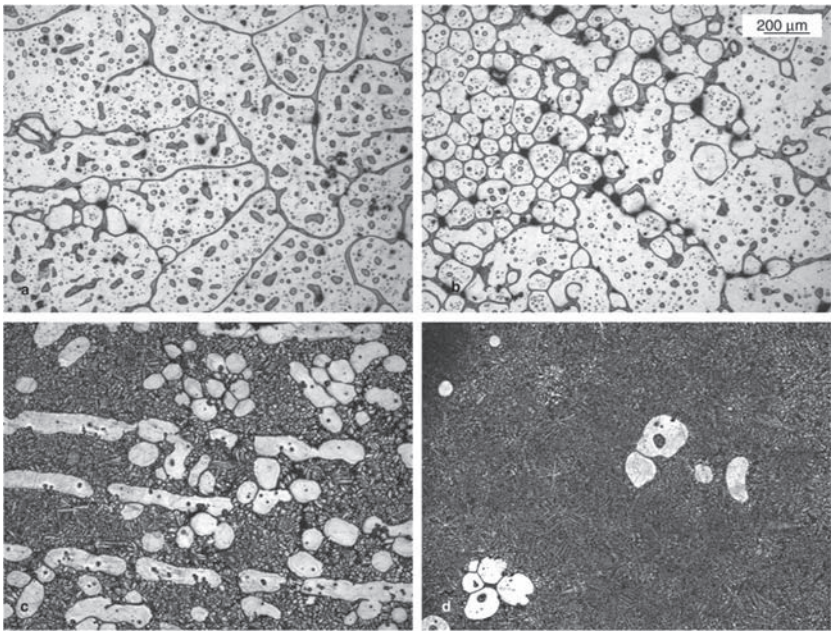

Fig. 8.27 The evolution of microstructure within as-cast (undeformed) ingot of Mg-9Al-1Zn re-melted: **a** the initial stage of melting with grain boundary liquid of 8% and total liquid fraction of 23.7%; **b** skin section after the same remelting as shown in **a**; **c** morphology for 37% of unmelted fraction; **d** morphology for 4.9% of unmelted fraction [32]

solid, contains still elongated particles with an alignment apparently related to former dendrites (Fig. 8.27c). Although the particles' sphericity is improved with an increase in temperature, the shape remains irregular for up to roughly 20% of their volume fraction. At the very end of melting, in close to 5% of the unmelted fraction, the solid particles are spheroidal, with some of them still attached to at least one of their neighbours (Fig. 8.27d).

In addition to the microsegregation within grains, an ingot of Mg–9Al–1Zn alloy exhibited chemical macrosegregation along large distances. Some implications of this phenomenon were seen during melting in the near liquidus range, where spheroidal particles coexisted with rosettes. Overheating of the alloy above the liquidus temperature resulted in the presence of numerous rosettes after subsequent quenching. An example in Fig. 8.28 shows how substantially the microstructure of irregular rosettes, quite common in die casting, is different than globular morphologies formed during the melting of chips and granules of the same alloy. Thus, the as-cast ingot develops, at the beginning of re-melting, the coarse, irregular morphologies associated with former dendrites, and spheroidal shapes evolve only during the advanced stages of melting, usually above 80% of the liquid fraction.

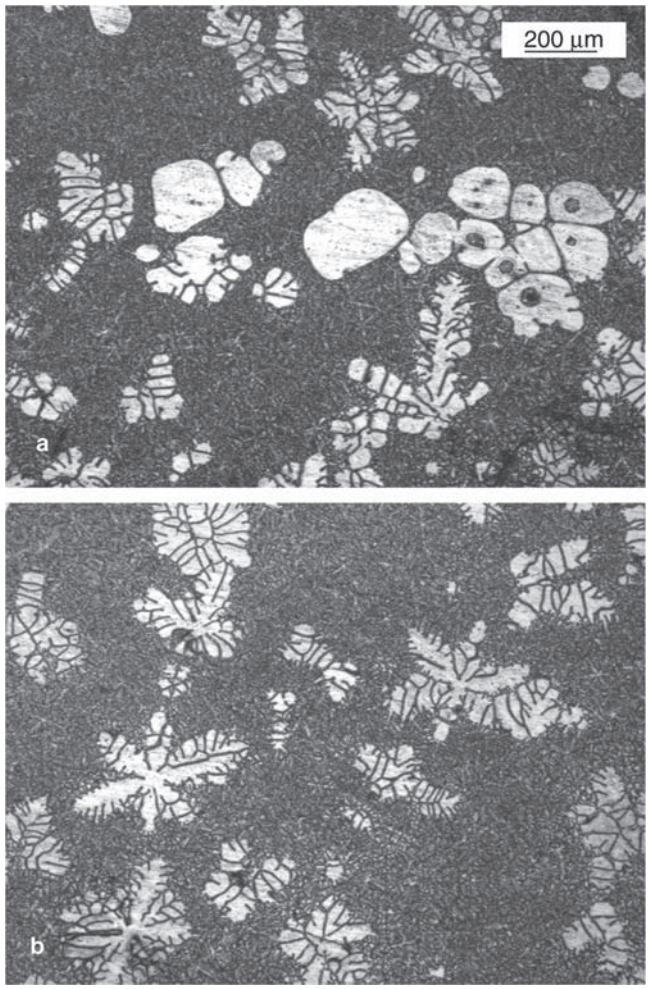

Fig. 8.28 The morphologies of as-cast ingot Mg-9Al-1Zn re-melted in near liquidus range: **a** at the liquidus temperature; **b** overheated by 20 °C above the liquidus temperature [32]

8.6 Phenomena During Heating of Rapidly Solidified Granules

Granules manufactured by rapid solidification do not exhibit cold deformation, which controls the melting of cut chips or extruded pellets. Thus, other features of the specific microstructure of a rapidly-solidified state lead to development of globular forms during subsequent re-melting.

8.6.1 Features of As-Solidified Microstructure

Due to rapid solidification of a small volume of an alloy, the granules exhibit an essentially different microstructure than the mechanically formed chips or pellets. A typical cross-section of a granule shows very small dendritic grains with massive type of intermetallic compound at the grain boundaries (Fig. 8.29a). The segregation is not clearly visible here, but high magnification imaging as well as behavior during the heat treatment, support its existence. The arrangement of dendrites suggests that they are, most likely, randomly oriented with respect to each other, due to

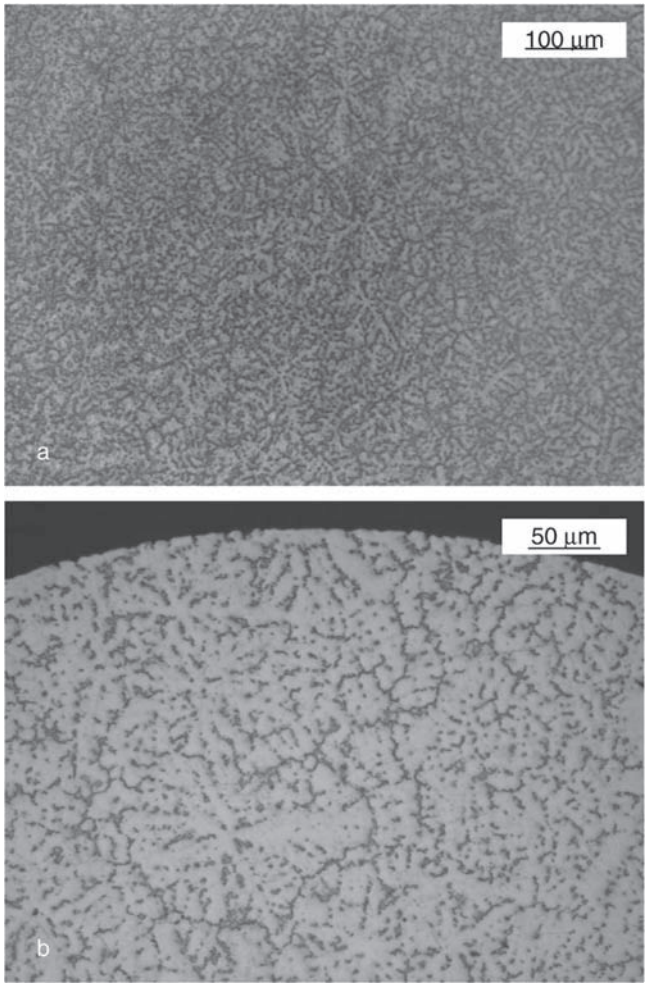

Fig. 8.29 The initial microstructure of rapidly solidified granules of Mg-9Al-1Zn: **a** general view in the granule center; **b** dendritic structure close to granule surface

independent nucleation (Fig. 8.29b). Although the intermetallic phase is distributed homogeneously throughout the granule, larger dendrites are occasionally present in central areas. The same description is valid for large granules, even though their dendritic grains are slightly coarser. It comprises coarse dendrites and, in some cases, is accompanied by large precipitates of the massive intermetallic compound. A novel feature of large granules is porosity, almost non-existent within the small granules.

8.6.2 Transformations During Heating in Solid State

The annealing of rapidly solidified granules does not create evident αMg grains, and the major change is the morphology of the intermetallic compound. A typical microstructure of granules, annealed at 400 °C for 15 min is shown in Fig. 8.30a. The precipitates of $Mg_{17}Al_{12}$ experience spheroidization, and in some areas are dissolved to saturate the matrix with Al, as one would expect from an equilibrium phase diagram [21]. The pattern of the intermetallic phase forms a fine, cellular network that surrounds αMg grains, as shown by the high magnification image in Fig. 8.30b. Due to segregation, some islands of $Mg_{17}Al_{12}$ are entrapped inside αMg grains.

8.6.3 Granule Melting

As observed previously for chips, at temperatures slightly exceeding the solidus, the granules are susceptible to deformation due to a load resulting from their weight (Fig. 8.31a). At this stage, the microstructure of individual granules consists of equiaxed grains surrounded by areas representing the liquid phase from the semisolid state (Fig. 8.31b). The volume fraction of the former molten alloy, entrapped inside grains, is larger than that recorded for chips, suggesting a stronger segregation effect. Although there are some exceptions within microregions, the liquid phase is uniformly distributed within the granule volume. Moreover, the liquid fraction within different granules, heated to the same temperature, is similar. Observations under high magnifications indicate that, in a semisolid state, selected boundaries are covered with a thick film of molten alloy while others are still not completely penetrated by the liquid (Fig. 8.31c). As the liquid fraction increases, the solid particles become spheroidal. At 26% of the unmelted fraction, the individual particles were suspended in the liquid phase, with some of them remaining within conglomerates, either fully or partially separated from their neighbors (Fig. 8.31d).

The unique microstructure, accompanied by chemical segregation, created within globules during rapid solidification, allows for the formation of equiaxed morphologies during the early stages of the alloy melting. The experiment with a

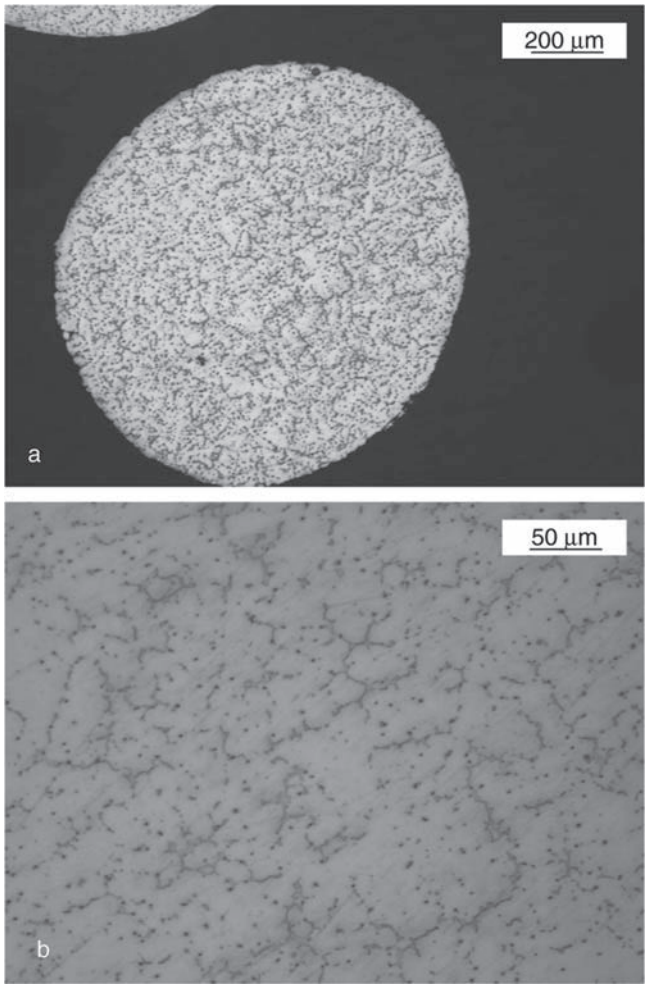

Fig. 8.30 The microstructure of granule G1 of Mg-9Al-1Zn annealed at 400 °C for 15 min: **a** general view; **b** area in the granule center with the intermetallic phase forming cellular structure

non-deformed ingot (Section 8.5) provides valuable evidence that supports this finding; a skin layer of the ingot, known to be of fine structures after solidification, exhibits equiaxed morphologies after remelting. Although the role of some structural components of as-cast alloy in the formation of equiaxed features during remelting is not yet fully understood, its benefits are explored in various alloy systems. For example, the low-temperature pouring (LTP) of an Al–Si–Mg alloy [22] or spray cast 7075 Al alloy [23] were successfully applied to produce, after partial remelting and isothermal holding, an equiaxed microstructure. There were also attempts to produce non-dendritic grains in Al alloys by so-called liquidus casting,

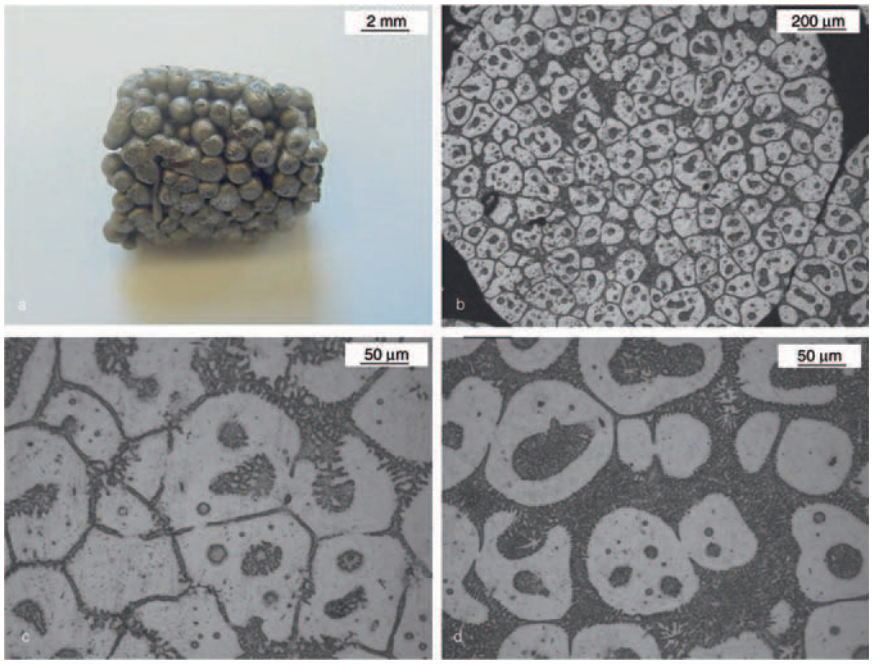

Fig. 8.31 The evolution of microstructure within granule G1 of Mg-9Al-1Zn during melting: **a** macroscopic view of granules removed from a crucible; **b** equiaxed grain structure within partially bonded granules; **c** equiaxed grain structure at the very initial stage of melting; **d** globular morphology of alloy containing 26% of unmelted fraction [32]

where high-rate nucleation is achieved within the entire volume of undercooled melt [24]. Thus, a lack of recrystallization and equiaxed grains within solid granules leaves chemical microsegregation as the key feature affecting their thermal decomposition during melting.

8.6.4 Common Melting Features of Particulate Feedstock

Of the major structural parameters within magnesium alloys, microchemical inhomogeneity and/or cold deformation were identified as critical in controlling remelting behavior. The chemical inhomogeneity of a particulate feedstock, expressed overall by the phase composition and microsegregation within the αMg matrix, is inherited from an ingot and does not change during chip manufacturing at room temperature. It has been proved here that the as-cast structure of an ingot alone does not lead directly to spheroidal particles in semisolid state. However, as a result of the mechanical interaction between an ingot and chipping tools, cold

deformation is introduced to the as-cast structure, essentially modifying its thermal decomposition characteristics.

In all types of particulate feedstock, the process of melting starts at grain boundaries. Since the solubility of Al in liquid is higher than in solid, the solid surrounding liquid will be depleted in Al. A reduction in Al content results in an increase in solidus temperature and slows down melting. For rapidly solidified granules a similar mechanism is effective: Pools of high Al content act as melting centers. In fact, the depleted zone is seen for all types of feedstock. Each pool of liquid exhibits this feature. It is also seen for undeformed ingots. The only requirement for as-cast alloys is the fine dendritic structure.

8.7 Microstructure Correlation Between the Solid and Semisolid State

A room temperature metallography identified several mechanisms acting in a semisolid state under the exclusive influence of heat. The Mg–9Al–1Zn alloy at temperatures ranging between the solidus and liquidus forms a two-phase system of a dispersed solid and a large amount of interfacial area. Due to coring, alloy melting is highly selective and directly controlled by Al content, even though the coring effect diminishes over time, due to diffusion and homogenization. It is surprising that the size of the solid does not essentially change during melting. This is so, despite the dramatic reduction in its content within the semisolid mixture.

A summary of solid particle size evolution during the melting of chips and particulates is presented in Fig. 8.32. The particle change, measured in re-melted undeformed ingot is also included in this figure. As a particle size, the average Feret's diameter is used. The experimental points show the reduction in the particle size from 120 μm to 80 μm, while decreasing their volume fraction from 95% to 12%. There is no substantial difference in the particle size between the particular types of chip or granule.

It is intriguing to see that the solid particle size obtained from the chip and granule precursor is quite similar. Of the same order of magnitude are solids in injection molded AZ91D alloy: A reduction in solid fraction from 58% to 4% corresponds to a reduction in particle size from 67 μm to 35 μm [25]. Similar numbers are reported for other systems: For example, for Al alloys and the solid range between 5% and 60%, the particle size was between 80 μm and 120 μm [26], which is quite similar to the results for as-cast ingot. Since the solid size plays a role in the apparent viscosity of the slurry, there is engineering interest in its control. According to some suggestions, the relative energies of the solid–solid and solid–liquid interfaces may be altered by adding a dopant to the alloy. Changing the crystallographic texture may also alter the number of grain boundaries as described for other systems. Heating rate is another possibility, although an additional effect might be expected during heating at high rates, since the coarsening is affected by the temperature gradient, and the volume fraction of particles decreases in the warmer regions and increases

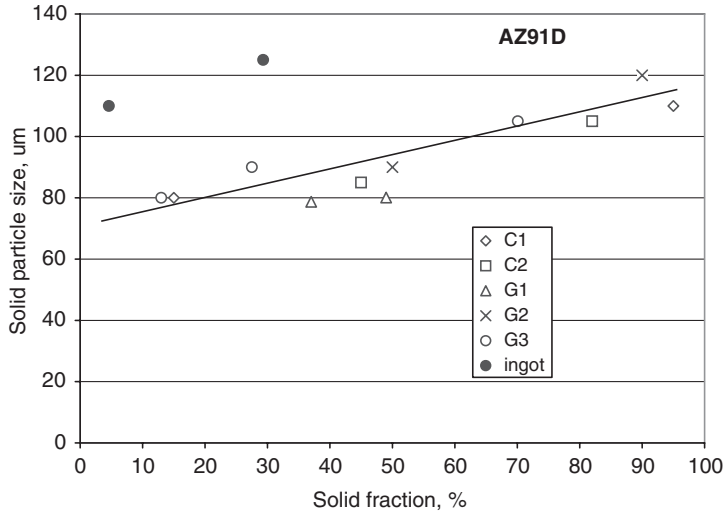

Fig. 8.32 The plot of solid particle size achieved after melting of particulates and an ingot as a function of unmelted fraction. Fit line: y = 0.48x + 69.75, R = 0.88. [32]

in the cooler regions [27]. This is in addition to externally applied shear, which is not considered here. A selection of appropriate parameters will allow for better control of the solid phase morphology during semisolid processing.

8.7.1 Solid-State Grain Versus Semisolid-State Solid Globule

The summary of solid size evolution upon heating is plotted in Fig. 8.33. Due to the recrystallization described earlier, an annealing at 200 °C refines the initial grain size of 11.3 µm to approximately 4 µm. Annealing at higher temperatures, particularly above 400 °C, leads to grain growth. An interesting observation is that substantial grain/particle growth takes place during the initial stages of melting: A reduction in solid content from 98% to 65% is accompanied by an increase in the solid size from 88 µm to 130 µm. During a further increase in temperature, the solid particle size diminishes, achieving 89 µm at the end of melting (3% solid). Thus during the total melting process the solid particle size practically does not change. The size of solid particles present during the final stage of melting corresponds to the grain size within the solid state at the solidus temperature.

At the early stages of melting the formation of solid particles with a size approximately equal to the αMg grains beneath solidus temperature can be linked to the multiple grains' nucleation at large segregated particles, which located them at triple junctions. The process starts by the melting of the γ phase at triple junctions

and selected grain boundaries, followed by wetting the remaining grain boundaries by the spreading liquid. The low melting point of grain-boundary regions is due to the fact that migrating boundaries of new grains collect and drag augmented concentrations of dissolved alloying elements, and the boundaries also tend to come to rest on small particles. Excluding some perturbations in the vicinity of the free surface (pellet's outer diameter), the melting within the pellet's volume is macroscopically homogeneous. It is clear that the melting of equiaxed grains leads to the generation of highly spheroidal particles. Since the majority of precipitates represent the γ compound with a low melting point, a combination of the recrystallization and chemical segregation along grain boundaries should be considered as factors controlling pellet transformation during melting, similar to what was found previously for mechanically fragmented chips and rapidly solidified granules. These results reaffirm that solid-state transformation exerts a crucial effect on the generation of thixotropic structures during subsequent melting.

8.7.2 Size-Evolution of Solid Phase Within the Slurry

The size of globular morphologies at the beginning and at the end of melting does not indicate substantial refinement. When comparing data points in Fig. 8.33 it should be understood that evolution in particle size was caused by two simultaneously acting mechanisms: coarsening and melting. Under such circumstances, an increase in the

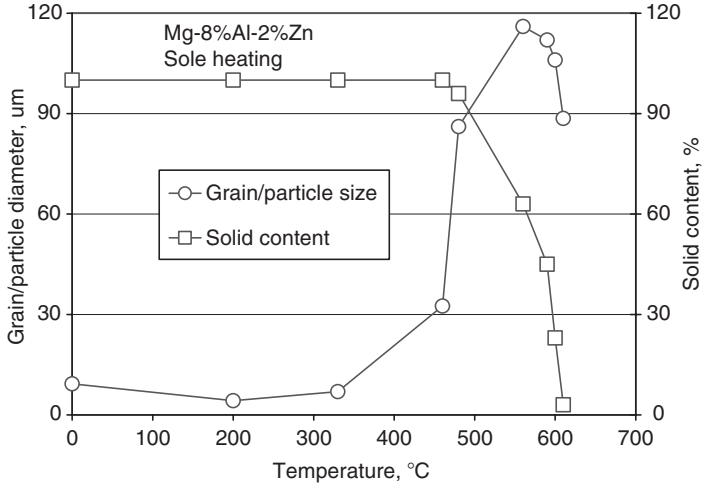

Fig. 8.33 The diameters of grains (solid state) and unmelted particles (semisolid slurry) as a function of temperature for extruded pellets. For comparison, the changes in solid content are also included [31]

liquid fraction could be achieved by the selective melting of some particles while others could only slightly change their size, and the chemical segregation of alloying elements is the potential cause of the latter behavior. It is well established that the system reduces energy by the elimination of the interfaces of high curvature, and two mechanisms are generally considered to control particle coarsening: coalescence and Ostwald ripening.

Such a finding suggests that, during heating and the relatively short isothermal holding period, the solid fraction reduction due to melting is superimposed on the coarsening due to coalescence and Ostwald ripening. It appears that the conglomerates of particles shown in earlier Figs. 8.22, and 8.24 remained from casting rather than being formed as a result of particle migration within the liquid. The only external force would be gravity-induced buoyancy, originating from a difference in density between the solid and liquid and expressed by microstructure sedimentation. Although in the Mg–9Al–1Zn alloy, a difference in density between the solid and liquid may increase, due to higher Al content in the liquid, it is generally small. The relative contribution of Ostwald ripening and coalescence to particle coarsening also remains a matter of controversy. Previous theories on the requirement of particle rotation to minimize grain boundary energy before coalescence are not entirely supported. According to a recent finding [28], particles do not rotate into low energy configurations to minimize the grain boundary energy and coalescence is not prevalent. Instead, Ostwald ripening was found to be the primary mechanism for coarsening in semisolid mixtures. It is also unclear which mechanisms prevail under the conditions of the experiment. However, the short residency time of the slurry, which limits the role of diffusional processes, seems to support the coalescence.

An interesting finding of the present stereological analysis is that rapid particle growth occurs during the early stages of melting, as estimated from experimental points in Fig. 8.33, up to approximately 40% liquid. This specific behavior of coarsening kinetics at ultra high solid contents is recognized by published research. In general, the theories of Ostwald ripening (Chap. 9) predict that during diffusion, controlled coarsening of the average particle size should increase in time according to a power law. However, the basic assumption of a low-volume fraction of the coarsening phase cannot be justified for high solid fractions. Results of computer simulations show that the kinetic coefficient in the equation describing coarsening increases particularly strongly above solid fractions of 0.7 [29]. Another study that examined the coarsening of higher solid fractions in terms of the migration of grain boundary liquid film concluded that the coarsening rate of semisolid alloys should increase continuously with an increase of the solid fraction [30]. The experiments with a number of spray-formed alloys revealed that grain coarsening increases with a higher solid fraction up to a range of 0.70–0.75, but the exact value seemed to be dependant on the alloy, and in particular, the dihedral angle between two solid grains in contact with the liquid. Above this value the opposite behavior was recorded, and the grain boundary film model was modified to accommodate experimental findings.

8.7.3 Internal Changes of the Globular Solid

The internal microstructure of primary solid particles was identified as the major change during the melting progress expressed by the solid/liquid ratio. In fact, the solid fraction of the slurry was subjected to heating and, depending on temperature, it experienced either aging or solution annealing. The heat effect also causes changes in microchemistry since an increase in temperature results in the melting of the Al-rich compound; thus, the remaining solid particles exhibit a diminishing Al content. The above changes may represent a strengthening mechanism of the primary solid. This is particularly critical since each particle represents a single crystal, and the overall structure is coarse-grained.

8.8 Summary

Both the mechanically comminuted chips and rapidly solidified granules possess unique microstructural features that allow them to transform into thixotropic slurry under the exclusive influence of heat. This mechanism, leading to the origin of thixotropic structures within mechanically comminuted chips, comprises two stages where, at first, the equiaxed grains nucleate and grow in a solid state, due to recrystallization. A cold deformation introduced during the mechanical fragmentation of chips and chemical microsegregation inherited from a rapid solidification by granules represent key features that allow the alloy to transform into fine, equiaxed structures during the very initial stages of melting under the sole influence of external heat. The process is subsequently continued by the melting of the intermetallic phase at triple junctions and selected αMg/αMg grain boundaries, the wetting of the remaining grain boundaries by an Al-rich alloy and their final dissolution. The generation of equiaxed structures within rapidly solidified granules is initiated by the melting of the intermetallic compound, distributed between fine dendritic grains and followed by a migration of the melt front toward the grains' interiors.

A direct link exists between the size of equiaxed αMg grains in a solid state and the unmelted particles in the semisolid slurry. Under the sole influence of heat, particle coarsening is especially active during the early stages of melting, and up to approximately 40% liquid, the average particle size exhibits growth, in spite of a reduction in the solid fraction. There is no major change in the shape of unmelted particles as melting progresses. The difference is expressed in their internal microstructure where $Mg_{17}Al_{12}$ precipitates have a morphology and habit plane dependent on the liquid/solid ratio. For high solid contents, the continuous plate-shape precipitates with the primary habit plane parallel to the basal plane of the matrix, are frequently seen. By contrast, the lath-like precipitates of submicron size and random orientation dominate at low solid contents.

References

1. Dieter GE (1976) Mechanical Metallurgy. McGraw-Hill, New York
2. Partidge PG (1967) Metals Review 12:167
3. McQueen HJ (2003) Comments on "On the generation of thixotropic structures during melting of Mg-9Al-1Zn alloy" by F Czerwinski. Scripta Materialia 49(8):917–920
4. Gehrman R, Gottstein G (1999) In ICOTOM 12, Montreal, 1999, NSERC Press, Ottawa, Canada pp 665–670
5. Roberts CS (1960) Magnesium and Its Alloys. John Wiley & Sons, New York
6. Wang X, Brunger E, Gottstein G (2002) The role of twinning during dynamic recrystallization in alloy 800H. Scripta Materialia 46(12):875–880
7. Galiev A, Kaibyshev R, Gottstein G (2001) Correlation of plastic deformation and dynamic recrystallization in magnesium alloy ZK60. Acta Materialia 49(7):1199–1207
8. Kaibyshev R, Galiev A, Sokolov BK (1994) Physics of Metals and Metallography 78:209
9. Mabuchi M et al (1999) Low temperature superplasticity of AZ91 magnesium alloy with non-equilibrium grain boundaries. Acta Materialia 47(7):2047–2057
10. Uggowitzer PJ, Wahlen A (2000) On the formation of eutectic phase in magnesium alloys during cooling from the semisolid state. In 6th conference on semisolid processing of alloys and composites, Turin, Italy, 2000. 429–435
11. Glickman EE, Nathan M (1999) Journal of Applied Physics 85:3185
12. Rabkin E et al (2000) Diffusion-induced grain boundary porosity in NiAl. Scripta Materialia 42(11):1031–1037
13. Chatain D et al (2001) Role of the solid liquid interface faceting in rapid penetration of a liquid phase along grain boundaries. Acta Materialia 49:1123–1128
14. Boettinger WJ, Kattner UR (2002) On DTA curves for the melting and freezing of alloys. Metallurgical Materials Transactions A 33:1779–1794
15. Mirkovic D, Grobner J, Schmid-Fetzer R (2004) Determination of solidification curves based on DSC experiments with improved heat-transfer model. In DM Herlach (ed) Solidification and Crystallization. Wiley-VCH, Weinheim, pp 95–102
16. Riddle YW, Makhlouf M (2003) Characterizing solidification by non-equilibrium thermal analysis. In HI Kaplan (ed) Magnesium Technology 2003, TMS, Warrendale, PA, pp 101–205
17. Tamminen J (1988) Thermal analysis for investigation of solidification mechanisms in metals and alloys. PhD Thesis, University of Stockholm, Sweden
18. Mirkovic D, Grobner J, Schmid-Fetzer R (2000) An approach to determine solidification curves of commercial magnesium alloys. In KU Kainer (ed) Magnesium alloys and their applications. DGM Wiley-VCH, Weinheim, pp 783–788
19. Gray AP (1968) Analytical Calorimetry. Plenum Press, New York
20. Flemings MC (1974) Solidification Processes. McGraw-Hill, New York
21. Okamoto H (1998) Journal of Phase Equilibria 19:598
22. Wang H et al (2000) Materials Science Forum 329–330:449
23. Wang JL, Su YH, Tsao CYA (1997) Structural evolution of conventional cast dendritic and spray-cast non-dendritic structures during isothermal holding in the semisolid state. Scripta Materialia 37(12):2003–2007
24. Xia K, Tausing G (1998) Liquidus casting of a wrought alloy 2618 for thixoforming. Materials Science and Engineering A 246(1–2):1–10
25. Czerwinski F et al (2001) Correlating the microstructure and tensile properties of thixomolded AZ91 magnesium alloy. Acta Materialia 49(7):1225–1235
26. Zavaliangos A, Lin JC, Yin M (2000) In Sixth conference on semisolid processing of alloys and composites, Turin, Italy, 2000, pp 463
27. Snyder VA et al (1999) The influence of temperature gradient on Ostwald ripening. Metallurgical and Materials Transactions 30A(9):2343–2348
28. Wolfsdorf Brenner TL, Voorhees W, Sutliff, J (1999) Metallurgical and Materials Transactions 30A:1995

29. Fan D et al (2002) Phase-field simulation of 2-D Ostwald ripening in the high volume fraction regime. Acta Materialia 50(8):1895–1907
30. Annavarapu S, Doherty RS (1995) Inhibited coarsening of solid-liquid microstructure in spray casting of high volume fraction of solid. Acta Metallurgica and Materialia 43(8):3207–3230
31. Czerwinski F, Zielinska-Lipiec A (2003) The melting behaviour of extruded Mg-8Al-2Zn alloy. Acta Materialia 51(11):3319–3332
32. Czerwinski F (2002) On the generation of thixotropic structures during melting of Mg-9Al-1Zn alloy. Acta Materialia 50(12):3265–3281

9
Alloy Transformations During Molding

9.1 Introduction

The unique microstructure of injection molded alloys is created as a result of multiple transformations that take place during the flow of material through the machine barrel, followed by injection into the mold cavity and final solidification. While for die casting and some semisolid technologies the microstructure evolution is quite well described, for semisolid molding, the role of processing parameters is still being researched. In particular, the contribution of shear imposed by the injection screw remained for a long time a matter of controversy. This is in part due to the uniqueness of injection molding, which does not allow for the direct adoption of phenomena and mechanisms common for other semisolid techniques. First, as opposed to the majority of semisolid processes, which rely on the formation of the thixotropic structure during solidification, during injection molding the globular features are predominantly created at the stage of melting. Second, the feedstock represents a specific form of an alloy whose microstructure is modified during conversion into small particulates by mechanical or thermal methods.

The objective of this chapter is to characterize the generation of the thixotropic slurry within the injection molding system and its solidification behavior. *Ex-situ* analysis of material samples, extracted from the machine barrel at different processing stages, is intended to provide an insight into processes that happen at high temperatures and cannot be observed directly.

9.2 Factors Controlling Microstructure Evolution

A consideration of microstructure evolutions during implementation of various routes of semisolid processing involves three general parameters:

(i) temperature;
(ii) time;
(iii) external agitation.

F. Czerwinski, *Magnesium Injection Molding*.

The alloy microstructure affects the overall properties of molded parts, which also include a surface quality and internal integrity.

9.2.1 Slurry Generation

The transformation of the feedstock in solid and semisolid states is a combination of thermal and mechanical effects (Fig. 9.1). The thermal effect, in turn, is expressed by temperature and time. When considering the injection molding process, three technological variables are primary:

(i) barrel temperature profile;
(ii) shot size;
(iii) cycle time.

The shot size and cycle time affect the exposure of an alloy to the heat supplied from outside. The alloy melting within the injection molding system is essentially different from that within a furnace, used during all types of casting. As a result of the very short residency time, no temperature equilibrium is reached between the barrel and the alloy. For example, for parts with a weight between 250 g and 550 g, a barrel with diameter of 70 mm, and a cycle time between 20 and 40 seconds, an average residency time ranges from 100 to 300 seconds. Thus, the amount of heat transferred to the feedstock depends on its conveyance rate and will increase with the smaller shot size and with longer cycle time. The short residency time does not equilibrate the microstructure of the magnesium chipped feedstock, which is known for macro and micro segregation phenomena, including coring. The latter is expressed in the increasing aluminum content from the grain center to the grain boundary.

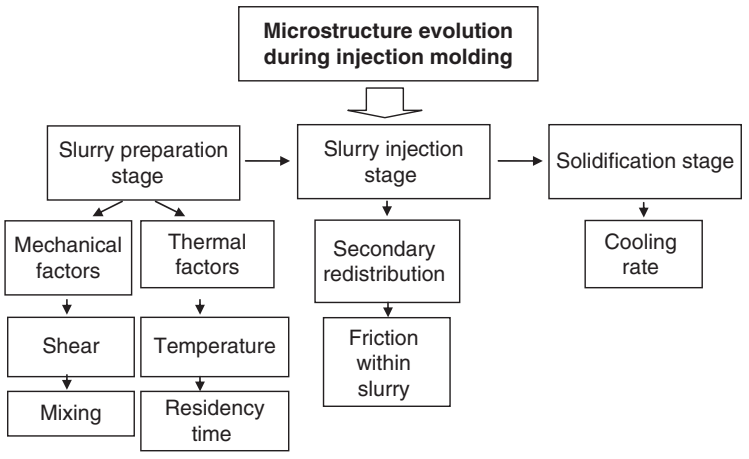

Fig. 9.1 Factors controlling the microstructure development at various stages of injection molding

Prior to injection, the melt leaves the screw and accumulates in front of the non-return valve. While for conventional cold sprue and large components the accumulation time is low and close to the cycle time, for hot sprue or complex hot runner systems and small parts, the melt resides substantially longer after leaving the screw prior to injection. Depending on the initial melt temperature and the temperature gradient inside runners, the melt may experience fundamental modifications.

The mechanical effect imposed on the feedstock by the screw is expressed by shear and mixing. The corresponding processing parameters include:

(i) screw rotation speed;
(ii) screw geometry;
(iii) screw and barrel tolerances.

9.2.2 Secondary Changes During Injection

The secondary changes during injection involve mainly redistribution of the primary solid within the component. Structural evolutions may also occur when variations in temperature take place. The only phenomenon important for engineering practice is the generation of heat due to friction between solid particles that are in intimate contact with each other. According to practical observations, it is only effective for ultra high solid contents and leads to particle melting, e.g., during the short time of flow into the mold cavity.

9.2.3 Solidification Conditions

The final solidification takes place inside the mold, preheated typically from 200 °C to 250 °C. The solidification time varies depending on the wall thickness and size of the component. For thin-wall parts the solidification time is extremely short, of the order of 20–30 ms. For thick-wall parts it takes longer to reach the solidus within the entire volume. In addition, the cooling time following solidification, when the part is inside the mold and then after it is ejected, may be long enough for structural changes to occur. Although all parameters described above affect the product quality, the temperature distribution along the alloy flow path in the barrel and the residency time are of critical importance because of their profound effect on the feedstock's transformations.

9.3 Solid-State Transformations During Initial Conveyance

The solid-state transformations within the machine barrel involve similar mechanisms as described in Chap. 8 for feedstock decomposition under the sole influence of heat. They take place after initial periods of heating within the first 4–5

flights, which cover about 20% of the screw length (Fig. 9.2a). At this stage, the feedstock remains in the form of individual chips that preserved their original shape (Fig. 9.2b). The cross section reveals equiaxed grains that occupy the entire chip's volume (Fig. 9.2c). The equiaxed grains of completely recrystallized alloy

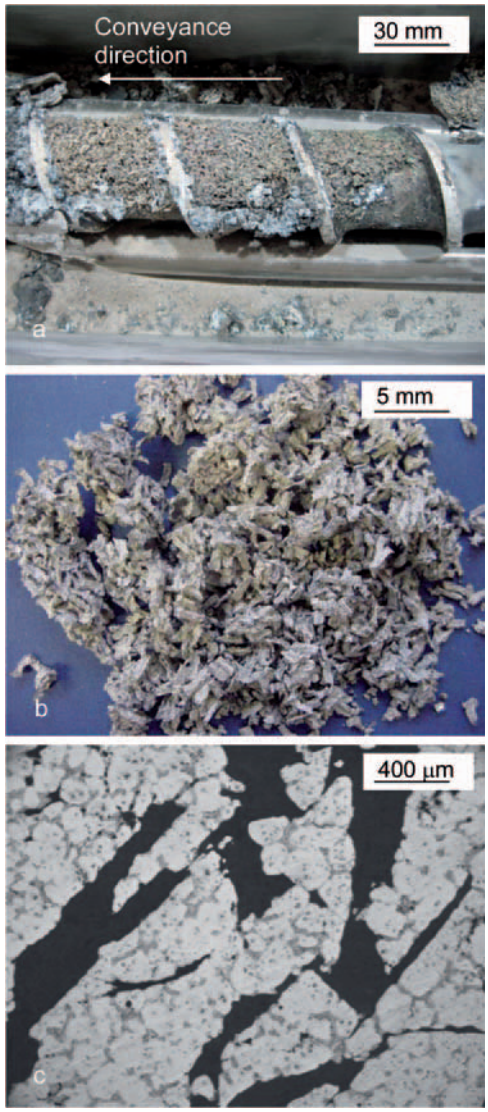

Fig. 9.2 The solid-state transformations during initial conveyance of the feedstock within the barrel: **a** distribution of chips within the screw flights; **b** morphology of chips removed from the screw; **c** cross section of several chips showing recrystallization of cold deformed structure; black areas represent a mounting resin connecting chips (alloy AZ91D)

contain precipitates of the massive intermetallic phase, located at grain boundaries and at triple junctions. Due to the low cooling rate of the alloy inside the barrel, the $Mg_{17}Al_{12}$ phase is also present at some distance from grain boundaries as discontinuous lamellar precipitates within the αMg matrix.

While some of the boundaries in the recrystallized alloy coincide with the α/γ interface, others separate the single-phase αMg regions, forming bridges between the γ precipitates (Fig. 9.3a). Their high-angle character can be deduced by assuming that recrystallization consists of a nucleation of the strain-free region whose boundaries can transform the cold-worked matrix into strain-free material as they move along the temperature gradient. This requires that the migrating boundary be a high-angle type so that there is a high degree of misfit to accommodate dislocations. Since the grains' nuclei appear at grain boundaries, twin boundaries, inclusions or second phase particles, and the migrating grain boundary has to resist the pinning forces usually offered by triple junctions, impurity atoms and second phase precipitates, the recrystallized microstructure is initially fine-grained. Then growth occurs, leading to the grain size observed after removal of

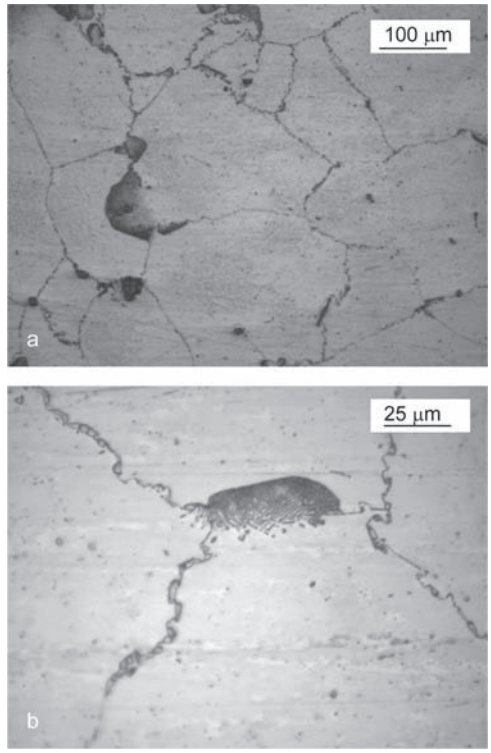

Fig. 9.3 The recrystallization details of chips: **a** general view of fully recrystallized structure; **b** magnified image of the serrated grain boundary, dragged at high temperatures by matrix inclusions (AZ91D)

the material from the barrel. It is important for the melting that even in the single-phase αMg matrix the grain boundary contains a low melt fraction of precipitates (Fig. 9.3b). No significant differences were recorded in the recrystallization mechanism between conveyance inside the machine barrel and being heated outside the machine, as described in Chap. 8.

9.4 Semisolid-State Transformations Within the Machine Barrel

In general, the melting process of an alloy starts during heating, when the solidus temperature is exceeded. However, due to the chemical segregation in magnesium alloys the evaluation of this temperature from an equilibrium phase diagram is not straightforward. The reduction in Al content, while moving from the γ phase towards the central regions of the αMg matrix, results in a gradual increase of the local melting range. Since magnesium feedstock coming into contact with the hot barrel walls and screw surface is subjected to a high heating rate, the alloy cannot reach its equilibrium phase composition, and the first portion melted could be close to the eutectic one.

The initial stage of melting and formation of the thixotropic slurry is depicted in Fig. 9.4a. The right hand part of the micrograph indicates the alloy portion, which was still unmelted, while the rest covers particles, partly separated by the liquid, filled with a mounting resin on the polished cross section. As shown in Fig. 9.4b, the melting starts at triple junctions and grain boundaries, being preferable locations for the γ phase. After the Al-rich liquid penetrates along the αMg/αMg grain boundaries within the one-phase region, it causes their wetting and dissolution. The process is enhanced by the fact that even in a single-phase αMg matrix the grain boundary contains a low melt fraction of precipitates (see previous Fig. 9.3b).

The material extracted from the barrel after an advanced stage of melting does not allow tracking back the transformations it experienced. Although the volume and cross-sectional dimensions of the alloy are relatively small, the cooling rate is very low due to the massive injection screw it covered. The major information obtained is that the as-solidified slurry did not develop dendritic forms but entirely equiaxed structures. However, the coarse spherical grains do not allow identification of the grain's portion, which remained solid at the processing temperature. To distinguish the primary solid phase, the polished section was immersed in hot water to enhance the growth of a thin oxide layer. The morphological differences of surface oxide delineate the primary solid island from the surrounding area, which is in a liquid state during residency in the barrel (Fig. 9.4c). Thus, the high fraction of unmelted solid acted as a nucleation site within the liquid during solidification and the final grain morphology was created by thickening of the initial substrate. The practical implication of this mechanism is that the presence of globular particles in the semisolid slurry should inhibit independent nucleation and the growth of dendritic structures. As will be seen later,

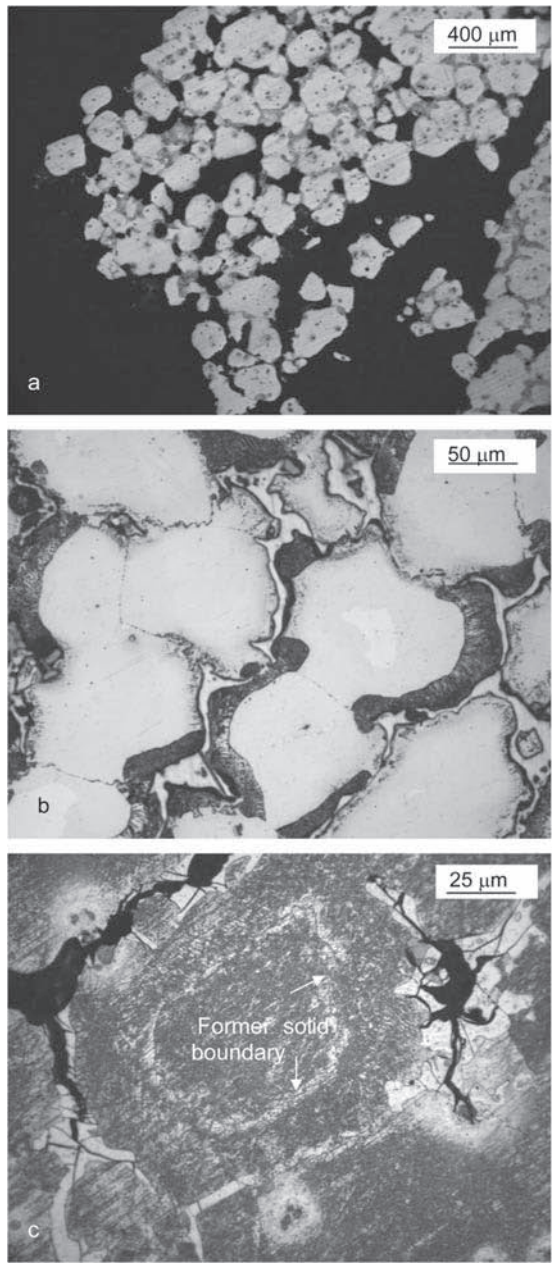

Fig. 9.4 The formation of the semisolid slurry within the machine barrel: **a** solid particles at the advanced stage of separation from each other; **b** detailed image emphasizing the mechanism of the penetration of Al-rich molten alloy along single phase grain boundaries; **c** structure obtained after slow solidification of semisolid slurry, the center shows the original primary solid particle, a difference in surface morphology of the oxide film deliberately grown to reveal the interface; black areas in **a** represent a mounting resin (AZ91D) [16]

this finding does not apply to faster cooling rates observed during industrial molding.

In order to take advantage of semisolid processing, the thixotropic slurry with primary solids of spherical shape should be obtained directly before injection into the mold cavity. Based on the temperature profile, an injection molding system allows the implementation of several routes for processing magnesium alloys. In this section, we consider only the role of the temperature profile along the machine barrel under the assumption that the other processing parameters remain constant.

9.4.1 Transformations Under a Regime of Partial Melting

The essential method of generating a thixotropic slurry during injection molding relies on partial melting. The partial melting can be achieved by exploring a variety of temperature profiles (Fig. 9.5). The most practical one is a continuous increase followed by isothermal soaking (curve 2). A profile with a continuous increase only (curve 1) may lead to the required results too, but the alloy structure may be shifted further from the equilibrium. The profiles with a maximum are rather reserved for special processes when re-solidification is required. When the maximum within the semisolid range is reached, the cooling that follows occurs within the screw length (curve 3), or the alloy may be cooled beyond the screw length (curve 4).

Examples of microstructures generated during molding after preheating to temperatures between the liquidus and solidus are shown in Fig. 9.6a–d. The primary solid particles are near-globular and no obvious changes were recorded for a wide range of unmelted fractions. A typical feature for the majority of alloys is that the

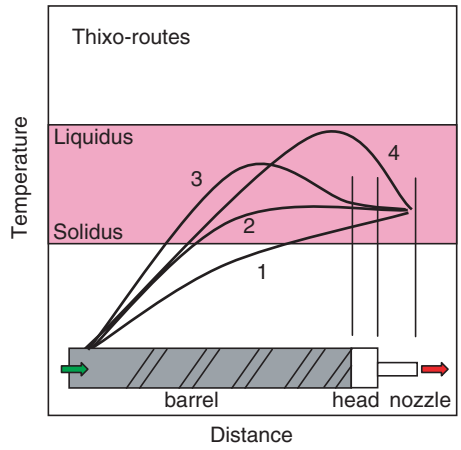

Fig. 9.5 The schematics of thermal profiles along the magnesium flow path during processing, relying on partial melting of the feedstock

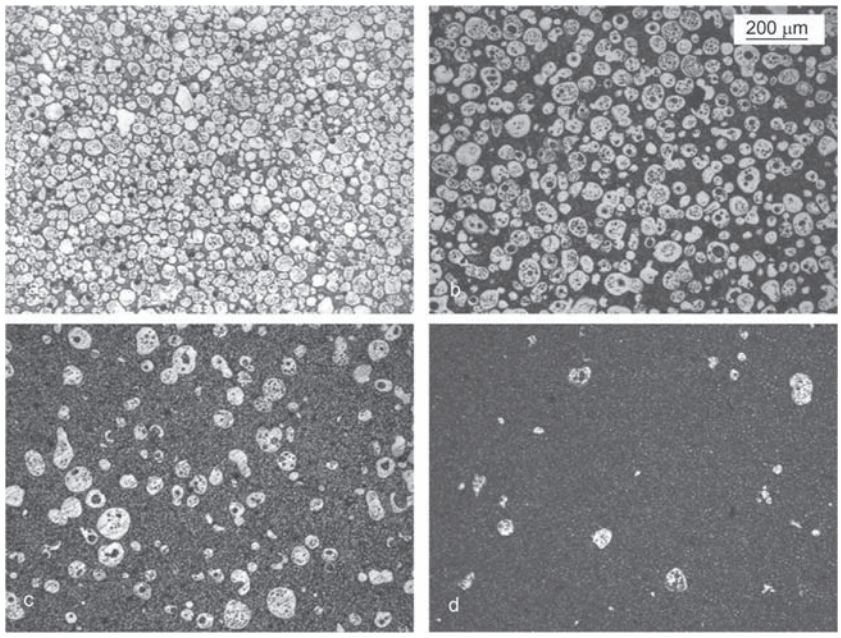

Fig. 9.6 The microstructures of injection molded alloy, processed following a regime of partial melting. The solid fraction is as follows: **a** 78%; **b** 50.2%; **c** 12.9%; **d** 2.2% (AZ91D) [8]

particles exhibit in their interior the entrapped liquid. Details of the thixotropic microstructure are described in Chap. 10.

A substantial difference in transformations occurs when the temperature increase is followed by a reduction since it leads to partial re-solidification. In engineering practice, this type of temperature profile within the barrel occurs due to a perturbation rather than deliberate selection. However, cooling always takes place within the nozzle as a condition required for the seal-plug formation. Thus, this phenomenon is of importance for small components molded with low mold cavity numbers.

A partial cooling of semisolid slurry leads to a generation of bimodal structures. Although the existing primary solid particles represent the easy crystallization substrates, the practice of fast cooling conditions shows that they do not experience preferable growth. Instead, nucleation within the melt volume occurs and new particles are formed. The structure created has, therefore, two kinds of solids: (i) particles that remained from a solid state, usually having larger size with features of entrapped liquid and (ii) freshly re-precipitated, of generally a smaller size (Fig. 9.7). In some cases, especially when operating close to the liquidus, the size of both phases may be similar, and a lack of entrapped liquid is the first feature, allowing the distinction of the freshly grown particles from existing ones. This rule does not apply, however, to all alloys, since for some of them the entrapped liquid phenomenon does not occur at all.

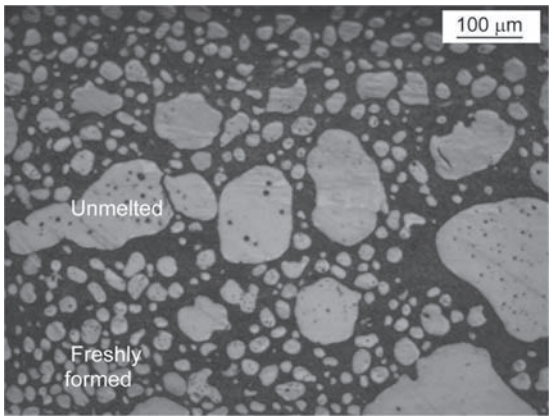

Fig. 9.7 The bimodal microstructure, obtained after partial solidification of the semisolid slurry. The large particles remained unmelted from the feedstock while the fine fraction precipitated during undercooling within the semisolid range (AM-lite)

9.4.2 Transformations Under a Regime of Complete Melting and Partial Re-Solidification

The alternative processing route relies on complete melting and partial re-solidification before injection into the mold cavity. According to the commonly accepted terminology, this method represents rheomolding. In principle, the completely molten alloy could also be injected directly into a mold, assuming the influence of a thermal plug is reduced to the negligible level. From an engineering standpoint, processing with a thermal profile exceeding the liquidus level does not provide the benefits of energy savings, which are achieved in partial melting. Besides, an additional effort is required to create the globular structure.

There are two key features of a thermal profile with potential implications for alloy transformation:

(i) location of the sub-liquidus cooling range within the barrel;
(ii) level of overheating above the liquidus.

9.4.2.1 Location of the Sub-Liquidus Cooling Range Within the Barrel

The partial solidification of overheated melt before injection can take place within the screw length or outside it, within the barrel head or nozzle (Fig. 9.8). Thus, the location of sub-liquidus range within the thermal profile specifies where the solidification takes place. Although the partial solidification can be stopped within the screw length (curve 1), in practice, it is continued in front of it (curves 2 and 3).

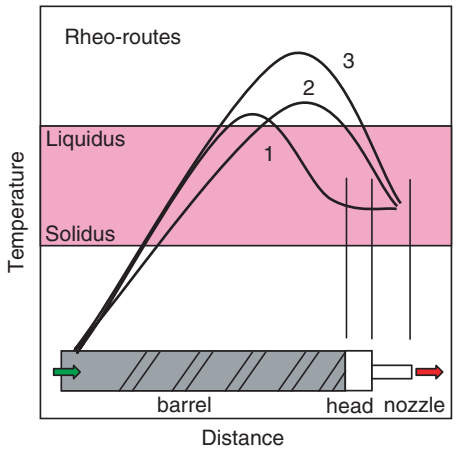

Fig. 9.8 The schematics of thermal profiles along the magnesium flow path during processing, following the route of complete melting and partial re-solidification prior to alloy injection into the mold

The typical microstructures obtained after complete melting and partial re-solidification are shown in Fig. 9.9a–d. The primary solid particles, significantly smaller than those obtained after partial re-melting, are spherical in shape and their internal structure does not reveal the presence of entrapped liquid. In reducing the temperature, the volume fraction of solid particles increases but their size does not change significantly.

The location of the sub-liquidus range within the barrel determines the influence of screw shear on the alloy solidification. Early research indicated that only the solidification within the screw length leads to globular forms. Although it is true, new results seem to add also the overheating level above the liquidus as the more important factor.

9.4.2.2 Overheating Level Above the Liquidus

The overheating range of the alloy above the liquidus has a detrimental effect on formation of globular forms (profiles 2 and 3 in Fig. 9.8). Although there is no quantitative data, experiments show that the high overheating leads to formation of rosette-like structures (Fig. 9.10a). In general, while solidification is superimposed on the shear, globular forms are generated. For injection molding, this seems to be true for higher solid contents. For low solid fractions, the presence of rosettes or dendrites in molded structures points towards limited effectiveness of the screw shear.

There is, however, substantial evidence accumulated that after low overheating above liquidus, partial solidification within a nozzle or hot runner before injection, generated spheroidal morphology. It is still not clear if the history of previous shearing by the screw has an effect. At present, the low overheating above the liquidus is seen to be the key factor contributing to the formation of this kind of thixotropic structures.

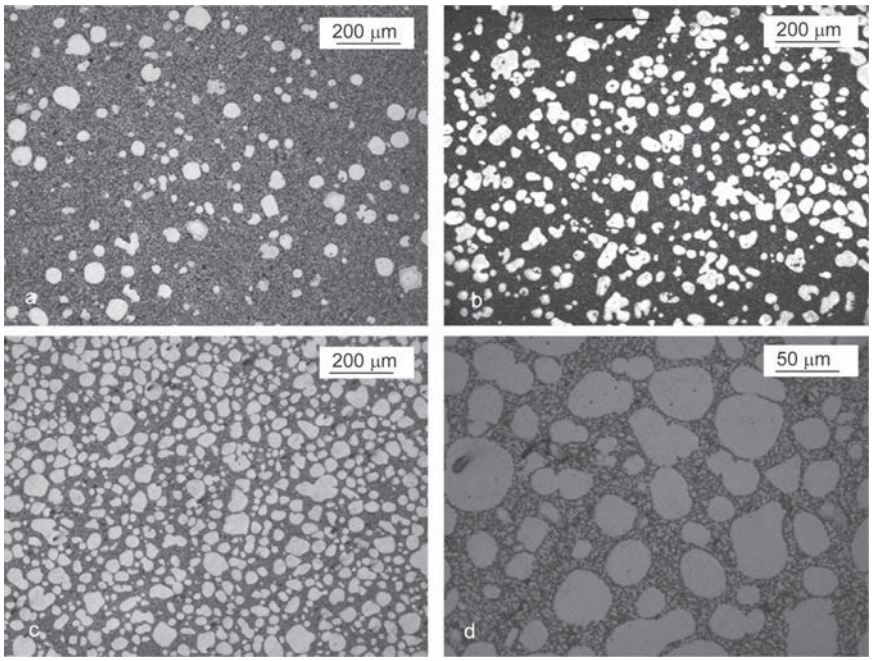

Fig. 9.9 The microstructure of injection molded alloy processed following a regime of complete melting followed by partial re-solidification: **a** 9% of the primary solid; **b** 19% of the primary solid; **c** 46% of the primary solid; **d** magnified image of **c**, showing details of the alloy's matrix (AZ91D)

9.4.2.3 Residency Time in Front of the Screw

It is a general concern that residency of thixotropic slurry in the accumulation zone of the barrel head and nozzle will cause agglomeration of particles, resulting in subsequent clogging of the exit. This concern is not supported by industrial practice. The role of residency time in front of the screw creates a noticeable difference when the time is longer than roughly 10 min. After prolonged residency in a semisolid state, some spheroidization of rosettes and dendrites occurs (Fig. 9.10b). This may be valid for stand-by situations or to a lesser extent for molding small parts with hot runners of large internal volume. For continuous production a slight increase in residency time of the injection-ready slurry as a result of increasing the caution, i.e., the material remaining in front of the check valve after injection is completed, has negligible effect.

9.4.3 Effectiveness of Shear During Mold Filling

The high velocity flow into the mold generates shear. As seen in molded structures (Fig. 9.10a,b) for low solid fractions, however, this shear is not able to

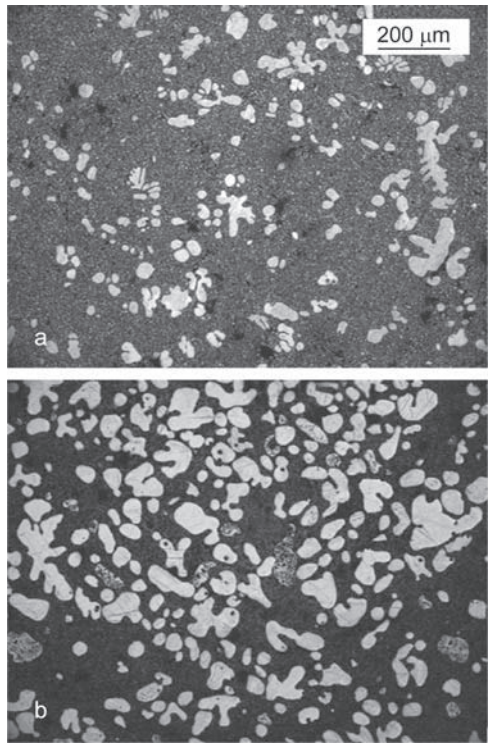

Fig. 9.10 The influence of residency time in front of the screw on morphology evolution: **a** initial morphology of rosettes; **b** ripened rosettes after 30 min holding (AZ91D)

eliminate rosettes or dendrites. The same observation is valid for die casting, where pre-solidified dendritic features do not disintegrate during injection at gate velocities of 50–70 m/s but are present in cast parts. The practice of semi-solid extrusion molding (Chap. 11) suggests that to achieve effective shear, ultra-high solid content within the slurry is required, where particles are in direct contact with each other.

9.4.4 Transformations During Non-Conventional Processing

In addition to thermal profiles along the magnesium flow path, covered in this chapter and typical for conventional processing, there are special profiles to control novel processing routes. Examples include near-liquidus molding and semisolid extrusion molding, as described in separate chapters.

9.5 Transformations Associated with the Seal Plug

After the alloy reaches the nozzle exit it is subjected to additional transformations, caused by the temperature gradient, which first allows the formation of a plug to seal the barrel. Then the temperature profile is modified to allow the plug's release before injection. Thus, the alloy is subjected first to cooling then to re-heating.

9.5.1 Role of Alloy Temperature in the Plug's Microstructure

The plug's microstructure depends on the temperature of the melt arriving at the nozzle plug zone (Fig. 9.11). When the alloy's temperature is initially between the liquidus and solidus, the plug's structure consists of globular forms. This is expressed by curves 1 and 2 for solid and mushy plugs, respectively. Different solidification conditions occur when an alloy reaching the plug zone is overheated above its liquidus level (curve 3). After solidification—the non-thixotropic structure is formed from such a liquid.

9.5.2 Changes During Reheating, Preceding the Plug's Release

The structure of the plug affects its release behavior. The plug with a thixotropic structure, after it is preheated to enter the semisolid range, deforms easily and passes through the undercut inside the nozzle (Fig. 9.12a). To soften the

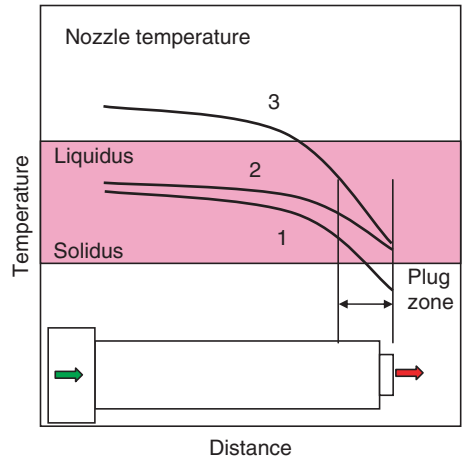

Fig. 9.11 The temperature profiles within the barrel nozzle. The approximate zone of the plug formation is indicated

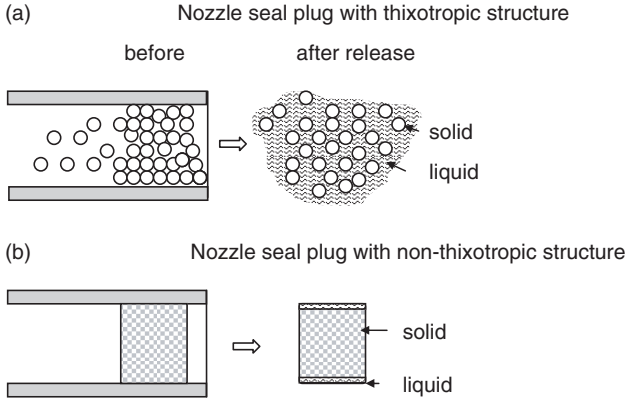

Fig. 9.12 The schematics showing differences in release behavior of nozzle plugs with thixotropic **a** and non-thixotropic microstructures **b**

plug with dendritic structure, a substantial heating is required to achieve sufficient fluidity at a high liquid fraction. Usually, therefore, it is released as a solid with a partially molten outer surface, being in contact with the nozzle walls (Fig. 9.12b).

9.5.3 Effect of Microstructure on Plug's Disintegration

A common question, asked during an analysis of the thermal gating mechanism, is what happens to the plug after it leaves the nozzle. It was found that in addition to the release characteristics, the plug's decomposition behavior also depends on the type of microstructure it developed during solidification.

The plug with thixotropic structure decomposes into globular solid and liquid phases (Fig. 9.13). While processing at high solid contents, the released plug contains more liquid than an average for the entire shot. The plug, diluted with the liquid alloy, is subsequently accumulated inside the plug catcher (Fig. 9.13a–c). Excluding the slightly higher liquid fraction, no other differences, as compared with the remaining portion of the sprue, are seen (Fig. 9.13d).

A different scenario is active when the plug is formed after the solidification of an overheated melt. In this case, the plug is injected in a solid state (Fig. 9.14). After injection and impact with the plug catcher walls, the solid fractures and disintegrates into irregular blocky shaped particles. As seen in Fig. 9.14a, b, the fractured pieces, with an approximate volume of 6.2 cm^3, occupy the plug catcher. The solid plug is followed by a mixture of liquid and rosette-like morphologies, formed from an overheated liquid (Fig. 9.14c, d).

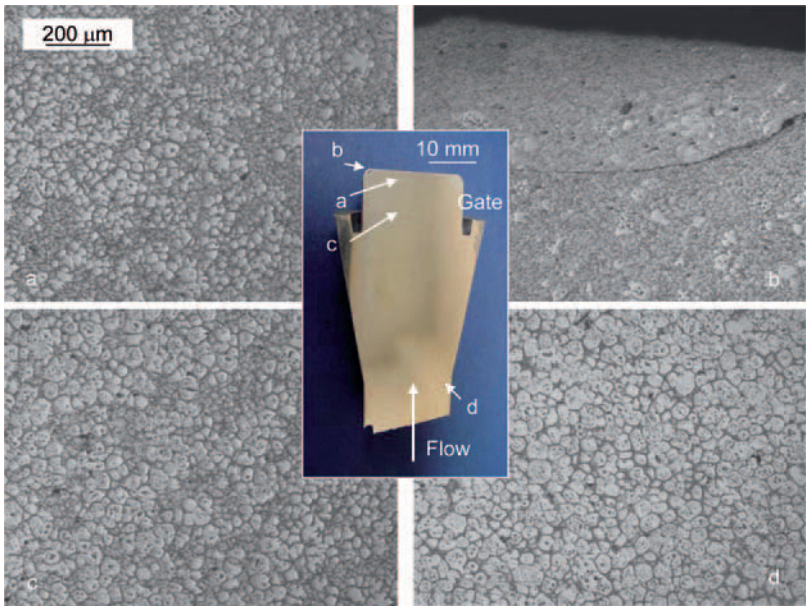

Fig. 9.13 The nozzle seal plug, formed after solidification of semisolid slurry: **a–c** microstuctures of various regions of the plug catcher as indicated in the inset; **d** microstructure of the initial slurry. The macro-view of the sprue is shown in the inset (AZ91D)

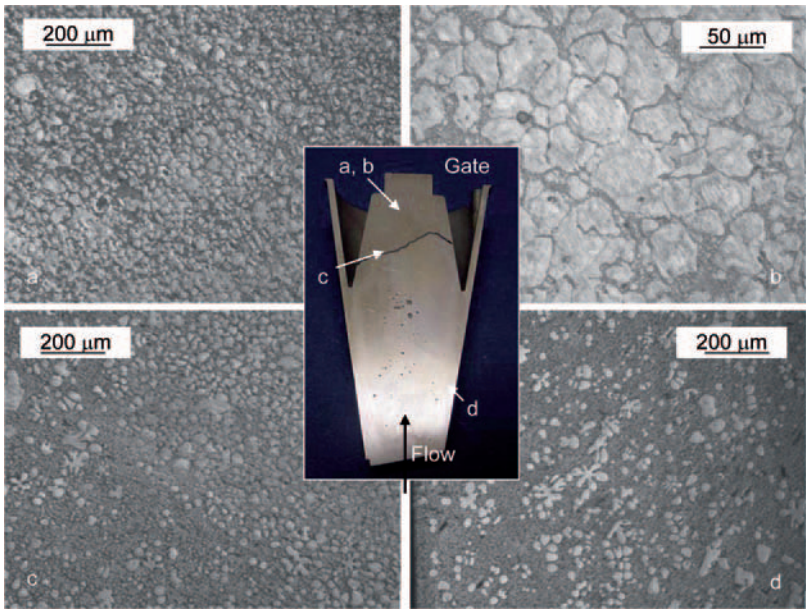

Fig. 9.14 The nozzle seal plug, formed after solidification of an overheated liquid alloy: **a–c** microstuctures of various regions of the plug catcher as indicated in the inset; **d** microstructure of the initial slurry. The macro-view of the sprue is shown in the center (AZ91D)

9.5.4 *Effect of Microstructure on Plug Flow Behavior Through the Mold Gate*

It is frequently assumed that the plug after release is contained by the plug catcher. In practice, however, a portion of the plug usually flows through the gate into the part. Thus, the flow behavior of the disintegrated plug directly affects the mold filling by the essential volume of alloy that follows the plug. The solid particles with dendritic or irregular shape show a tendency to block the gate, preventing the cavity from filling. The planar section through the gate of the same thin-wall component is shown in Fig. 9.15. The blocky shaped particles, which originate from the decomposed solid plug, are concentrated in front of the part gate (Fig. 9.15a–c). The slurry which follows the plug contains solid particles with rosette-like morphology (Fig. 9.15d). As explained earlier, this kind of morphology is generated after solidification of an overheated liquid. The issue of gate blocking is especially valid for thin-wall parts with tiny gates, acting as flow obstacles (Fig. 9.16a). In that case the solid particles with large size and a morphology indicating an origin from the solid plug, may show a tendency to block the flow through the gate (Fig. 9.16b,c).

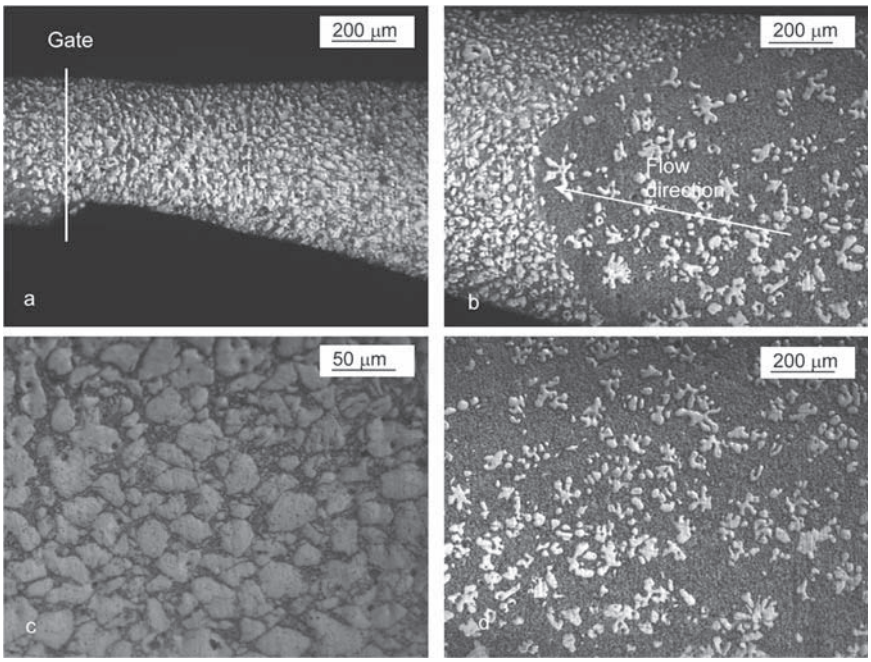

Fig. 9.15 The concentration of blocky shape solid in front of the mold gate; **a** the gate line; **b** interface between irregular-shape particles followed by rosettes; **c** morphology of blocky particles; **d** morphology of the essential portion of the alloy injected. AZ91D

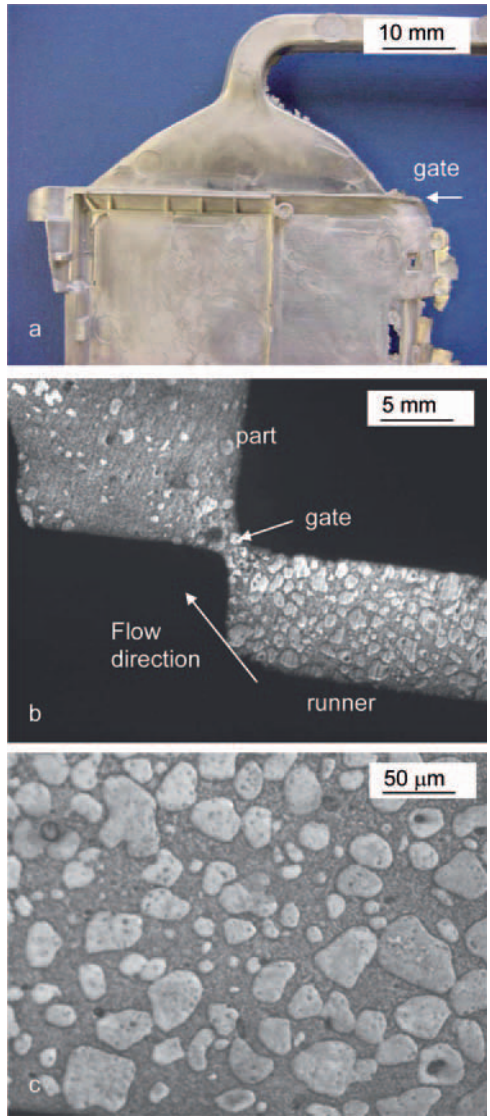

Fig. 9.16 The blockage of the tight gate by the irregular-shape solid particles present within the component after decomposition of solid plug with non-thixotropic structure: **a** the component fragment with the runner and gate; **b** gate with flow blockage; **c** morphology of the irregular-shape solids. AZ91D

9.6 Theories of the Formation of Globular Structures During Melting and Solidification

9.6.1 Morphology of the Crystallization Front

The morphology of the crystallization front is controlled by the temperature gradient within the liquid. As seen in Fig. 9.17a, rejection of the solute from the solidification front leads to change in the local liquidus temperature. When the temperature gradient is shallow (Fig. 9.17b) the temperature of the liquid is lower than the liquidus, a condition called constitutional undercooling. In that case, when a protrusion on the solidification front is created, it reaches the region of higher undercooling, and its growth is accelerated. As a result, growth morphology becomes dendritic. The steeper gradient reduces the effective undercooling and transforms dendrites into cellural morphology. When the gradient is steep enough to reach the condition shown in Fig. 9.17c, the temperature of the liquid exceeds liquidus. Any protrusion generated at the crystallization front finds unfavourable growth conditions and is melted down. As a result the crystallization proceeds with a planar and stable front.

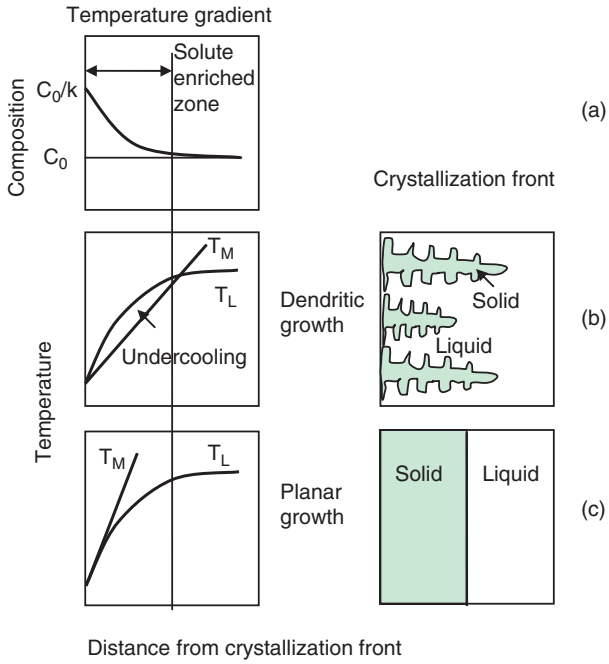

Fig. 9.17 The correlation between the temperature gradient within the molten alloy and the morphology of the solidification front: **a** solute enrichment zone in front of the solidification front; **b** shallow temperature gradient leading to constitutional undercooling and dendritic front; **c** steep temperature gradient leading to planar solidification front. T_L-local liquidus temperature; T_M-molten alloy temperature

The dendritic growth of crystals into an undercooled liquid is a very common form of virtually all solidification processes. The dendrites formed are initially separated by the melt, and they can move freely. At a certain stage, dendrites start to impinge upon one another, creating a solid network. This stage, called a dendrite coherency, leads to a change of properties characteristic for a solid. The formation of the solid network leads also to variations in further solidification since feeding of the melt is possible only within interdendritic spaces. The solid fraction at which the cohesive network is formed depends on dendrite size and morphology, with typical values quoted as 0.1% to 0.2%. Factors reducing a tendency to the formation of dendrites include:

(i) high number of nucleation sites;
(ii) small inter-nuclei distance;
(iii) slow cooling rate.

9.6.2 Dendrite Description

Dendrites represent tree-like and topologically complex structures, frequently forming a connected solid skeleton within the entire region subjected to a transformation. In practice the only parameter characterizing dendrite is the secondary dendrite arm spacing (DAS). Since the formation temperature of a dendrite is high, it is subjected to instant coarsening. The driving force is a reduction in surface energy through reducing the surface area. The process is controlled by the diffusion rate of a solute in the liquid, and as a result the larger arms grow at the expense of smaller ones, causing an increase in DAS. Since the mechanical properties depend on DAS, it is beneficial to reduce the DAS as far as possible. A number of neighboring dendrites with the same crystallographic orientation form a grain. In cast structures the grain boundary is created where two dendrite colonies with different crystallographic orientations meet.

The dendrite morphology and its evolution are difficult to describe in a three-dimensional system. A recent attempt explores a serial sectioning where the solidified dendrites are cut and reconstructed using a computer [1]. Then for each point of the surface the mean and Gaussian curvatures are determined numerically. Finally, the dendrite morphology is completely characterized by the curvature tensor along the dendrite surface.

9.6.3 Segregation in Cast Structures

Cast structures are characterized by segregation, understood as a nonuniformity in chemical composition. Based on a criterion of the distance between regions of chemistry perturbation, the micro- and macrosegregations are distinguished [2]. Microsegregation is a consequence of the removal of solutes by the solid into interdendritic liquid. Its negative effect can be eliminated by thermal or thermo-

mechanical treatment of castings. Macrosegregation is caused by movements of microscopic regions exhibiting microsegregations over macro distances. It occurs due to the movement of liquid alloy and free solid crystals.

In the interdenritic liquid the positive microsegregation occurs due to solute rejection from the solidifying dendrites. Thus the composition of a dendrite is not uniform. The type of segregation mentioned earlier as coring is when the core, solidifying first, is the purest. Further solidification leads to continuous enrichment of the interdendritic liquid with solutes. Consequently, there is a continuous increase of solute content in the dendrite from the core to its periphery. For Mg–Al alloys, Al plays the role of solute. In practice, many complex segregation features are created and an example for Mg–9Al–1Zn alloy is shown in Fig. 9.18a,b.

9.6.4 Globular Growth Due to Fragmentation of Dendrites

The assumption of dendritic structure as a starting morphology of the thixotropic slurry implies that during the initial stage of residency, the dendrites are fragmented into smaller particles, and the shearing and abrasion among them lead to a more

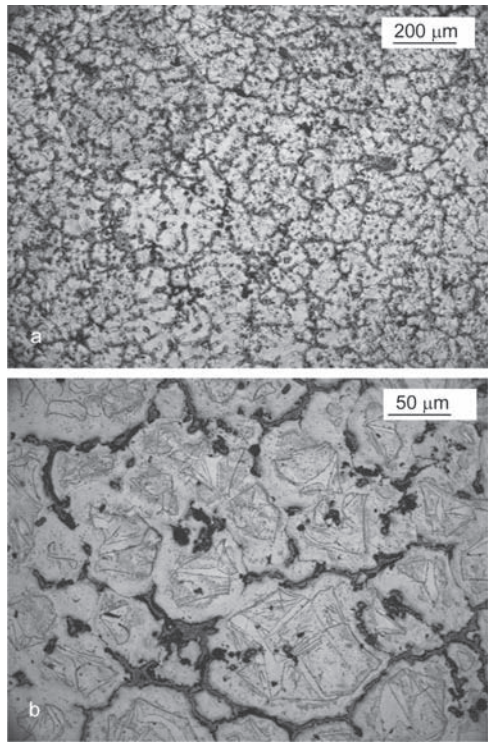

Fig. 9.18 The segregation of Mg-9Al-1Zn alloy after solidification from an overheated melt: **a** general view; **b** details of the grain interior

equiaxed structure. The mechanisms of dendrite fragmentation and the deformation of dendritic structures provided by the early literature on magnesium molding were adopted from a description of solidification under an external shear, developed originally for rheocasting. According to this mechanism, the higher shear rate leads to a more equiaxed structure with smaller particles and primary rosettes which may form due to bending and the plastic deformation of dendrites.

There is evidence for arm bending of partially solidified dendrites due to externally applied stress of high value [3]. The mechanism of dendrite fragmentation, developed for stir-casting, involves the dendrite arm bending, causing recrystallization followed by liquid wetting of high angle grain boundaries. During spray forming, dendrite arm bending occurs due to the high velocity impact of partially solidified dendritic droplets on the solid substrate, leading to the fine structure. At the same time there are studies claiming the opposite. According to one of them the solidification during conventional casting found the likelihood of dendrite damage due to the flow of a melt as a remote [4]. This is because the conditions would require high flow velocities and fine dendrites to initiate damage.

9.6.5 Development of Globular Forms During Melting

Two major factors affect the transformation of the semisolid slurry during its conveyance along the machine barrel: heat supplied from the external source and the shearing force imposed by the injection screw. The key finding affecting the generation of thixotropic structures is that the solid phase within the slurry has at the very beginning of melting, a non-dendritic morphology. Therefore, the transformation of such morphology should be considered instead. Four mechanisms are proposed to control deformation of non-dendritic structures in a semisolid state [5].

Two mechanisms are dominant when the solid particles are surrounded by the liquid phase:

(i) liquid flow mechanism and
(ii) flow of liquid incorporating the solid particle mechanism.

Two other mechanisms are dominant when the solid particles have been in contact with each other. They involve:

(i) sliding between solid particles;
(ii) plastic deformation of solid particles.

The interaction between particles of the solid phase leads to structure breakdown due to shearing and collision, as well as to structure agglomeration due to bond formation among particles caused by impingement and reaction. It was postulated for aluminum semisolid processing that there is a critical shearing time below which the particle size decreases. A further increase in shearing will cause the coarsening of particles [6]. A secondary rosette structure may form due to the particle coalescence when the agglomeration mechanism dominates.

9.6.6 Solidification of Remnant Liquid

Apart from the globular solid, the microstructure of components after semisolid processing contains the remaining liquid. Its volume fraction usually exceeds 40%, and in many cases represents a predominant portion of the alloy, being as high as 90-95%. The solidification microstructure of the liquid fraction depends on:

(i) alloy heating history above the liquidus;
(ii) solidification rate.

In the majority of applications, the remnant liquid is subjected to rapid solidification, which leads to fine structures. Although the detailed microstructure depends also on the previous heating history, the heating rate is essential.

The heating history is more pronounced during slow solidification. While the alloy's history involves partial melting, subsequent slow cooling leads to spheroidal forms of bimodal size distribution, as shown previously in Fig. 9.7. While the alloy's history involves complete melting, the structural evolutions follow a path discussed earlier in this chapter. During processing using the twin-screw rheocaster it was observed that following a long shearing time at a high shear rate, the remaining liquid solidified as spheroidal particles [7]. The growth of existing solid particles was restricted, whereas nucleation and growth of fresh particles took place. The nucleation throughout the melt was favored by a uniform temperature distribution created by turbulence resulting from high shear. Reduction in shear time and shear rate resulted in the growth of fine rosettes and dendrites. The resting time before solidification led to coarse rosettes and dendrites, similar to those forms during conventional casting.

9.7 Evolution of the Primary Solid Phase During Molding

The key feature that characterizes the primary solid particles is their shape. A distinction is made in the literature between dendritic and globular solids in terms of their influence on the flow characteristics of the semisolid slurry, with well-documented advantages of the latter. It is further anticipated that the size of globular solid particles plays a significant role in the permeability of the solid skeleton, the ability to flow in narrow channels and the residual porosity.

9.7.1 Characteristics of the Primary Solid After Various Processing Routes

The characteristics of solid particles obtained after different routes of injection molding and after partial melting under the sole influence of heat are listed in Table 9.1. An analysis of the particle size reveals two findings. First, there is no

substantial difference between the solid particle size for the alloy partially re-melted inside a furnace and that processed within the injection molding system. Second, the reduction in particle size that accompanied processing in both environments is rather small and not proportional to values anticipated from a reduction in its volume fraction.

A visual assessment of molded microstructures shows that there is no essential change in the shape of particles, with the reduction in their volume fraction. Moreover, there is no drastic difference between the shape of particles generated within the injection molding system and those created under the sole influence of heat. This means that for alloys processed in the semisolid range following partial melting the screw shear does not essentially affect the shape of the primary solid phase.

9.7.2 Particle Size Versus Solid Volume Fraction

Statistical analysis of the size variation of primary solid particles during melting is shown in Fig. 9.19 [8]. Each data point is collected during a separate experiment, performed under individual settings of the injection molding system used in a partial melting regime. The liquid content covers a range between 22% and 95% liquid, but for a comparison, a data point for 0% liquid is included as well. This is in fact the grain size of the fully recrystallized structure of the mechanically comminuted chip directly before melting. The recrystallization took place when chips were immersed in the semisolid slurry of the same magnesium alloy. The plot in Fig. 9.19 reveals that the solid particle size at low liquid fractions, which represents the begin-

Table 9.1 The stereological parameters describing primary solid particles in microstructures obtained after different processing routes. Numbers in brackets represent standard deviations from measurement of over 500 particles [16]. a) calculated according to the formula (10.2)

Processing route			Volume fraction	Feret horizontal diameter	Feret vertical diameter	Feret average diameter	Shape factor SF [a)]
			%	µm	µm	µm	
Molding machine	Partially melted		50.2	62.4 (29)	61.2 (28)	62.4 (27)	0.64
			12.9	57.5 (23.7)	60.4 (30.1)	59.9 (25.6)	0.59
			2.2	56.4 (24.2)	61.2 (39.9)	59.1 (29.8)	0.56
	Completely melted	Partially re-solidified to globules	4.2	18.6 (12.6)	18.2 (13.0)	19.0 (12.9)	0.75
		Partially re-solidified to rosettes	5.4	49.6 (30.1)	49.2 (26.4)	51.0 (27.0)	0.44
Furnace	Partially melted		60.9	81.1 (43.4)	77.5 (42.6)	80.1 (41.1)	0.65
			34.2	70.2 (31.4)	65.8 (30.9)	69.1 (29.5)	0.67

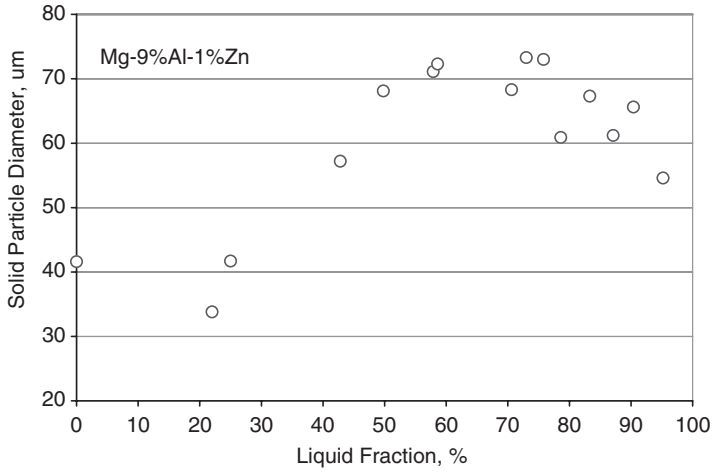

Fig. 9.19 The solid particle size plotted as a function of the liquid fraction within Mg–9Al–1Zn slurry [8]

ning of melting, is comparable to the recrystallized grain of the chipped feedstock. As the liquid content increases, the size of particles increases rapidly, reaching the value of 70 µm to 80 µm for 60%–70% of liquid. It is of interest to note that a further increase in the processing temperature causes a rather small reduction in the particle size. As a result, the solid particles in almost complete liquid alloy (95% liquid) are comparable to those present in the slurry with a liquid content of 45%.

Additional information regarding the size evolution of solid particles within the slurry is provided by the particle-size distribution. Examples of histograms are shown in Fig. 9.20. The particles within the slurry with the lowest liquid content tested, i.e., 22%, exhibit a sharp maximum around 30 µm. The distribution profile is generally similar to that of the recrystallized grains within chips, and the major difference is expressed by a 10% fraction of grains above 70 µm in the recrystallized structure. The slurry with a content of 50% liquid exhibits a broad scatter of particle sizes between 20 µm and 150 µm. As seen from the histogram for 95.2% liquid, particles with a size of 150 µm are still present at the end of melting. The lower average size of the particles within the alloy slurry having 95.2% liquid results from the higher fraction of smaller particles, generally of the order of 40 µm.

9.7.3 Mechanisms Controlling the Solid Particle Evolution

The stereological examinations revealed that the relationship between the size of the unmelted phase and its volume fraction is complex. As described previously [7],

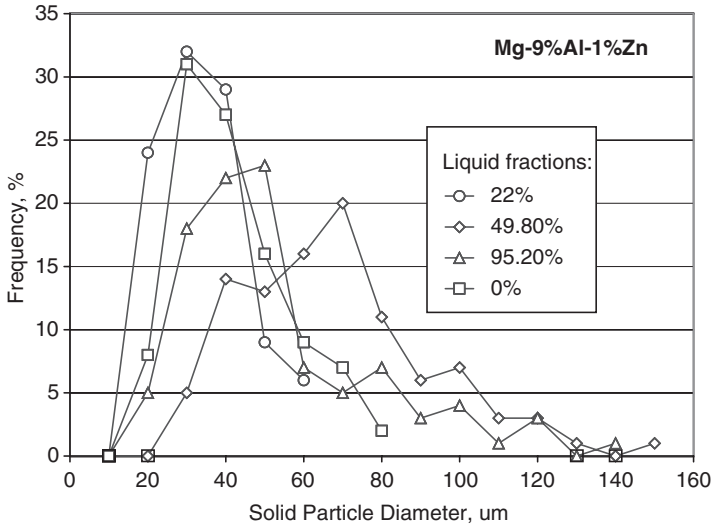

Fig. 9.20 The histogram of solid particle diameter for selected liquid fractions within Mg–9Al–1Zn alloy. The data point for 0% liquid represents the recrystallized structure of the chipped feedstock, directly before melting [8]

the initial morphology of the semisolid slurry, which is formed during injection molding, is of an equiaxed nature. Such a structure is created by recrystallization of the plastically deformed feedstock and its further disintegration by grain boundary melting. As can be deduced from previous Fig. 9.6a, at ultra-high solid contents the alloy represents a deformable, semi-cohesive granular solid, saturated with liquid. The solid grains are partially interconnected by unwetted grain boundaries, and liquid fills the intergranular spaces. When subjected to external stress resulting from screw action or flow under high pressure into the mold cavity, the alloy will respond by disagglomeration of partially bonded grains. The macroscopic deformation of such structures is accommodated by [9]:

(i) elastic-plastic deformation at grain contacts;
(ii) bulk grain deformation or fragmentation;
(iii) grain rearrangement by sliding or rolling.

A comparison of the primary solid size for 0% and 22% liquid shows no evidence of substantial refining. Since the response of the alloy also includes structure agglomeration due to bond formation among particles caused by impingement and reaction [10], the external stress effect should be interpreted as a potential for prevention of particle coarsening.

In addition to structure breakdown and agglomeration, caused by external strain, the reduction of interfacial energy between the particles and liquid provides the driving force for morphological and dimensional changes. Two potential contributors include:

(i) Ostwald ripening;
(ii) coalescence ripening.

It is postulated that at very high solid fractions, the particle–particle interaction resulting from the external shear is the effective mechanism that preserves the fine structure inherited from the recrystallized feedstock. The effectiveness of this mechanism during further melting is reduced by the presence of higher volume fractions of the liquid alloy. At higher liquid fractions the mechanisms of coalescence, Ostwald ripening or selective melting, control the size of solid particles.

9.7.3.1 Ostwald Ripening

Ostwald ripening is governed by the Gibbs–Thompson effect, which alters the concentration at the particle-matrix interface, depending on the curvature of the interface, thus creating the concentration gradient for the diffusional transport of the material [12].

Moreover, solutes diffuse from small particles to larger ones, resulting in the coarsening phenomenon. Since a higher shear rate enhances the solute diffusion, it accelerates the coarsening, promoting a larger particle size. Through Ostwald ripening, the system may reduce its interfacial area, and thus, its energy. The concentration at the particle-matrix interface depends on the curvature of the interface and is expressed by [10]:

$$C_A(R) - C_A(\infty) = \frac{\alpha}{R} \tag{9.1}$$

Where:

$C_A(R)$—composition of the matrix phase A outside of a particle with radius R;
$C_A(\infty)$—composition of the matrix phase A at equilibrium where the interface is flat;
α—constant, proportional to the specific interfacial energy.

Thus, large particles tend to grow at the expense of small ones, the average particle size increases and the total number of particles decreases. Both the higher shear rate, i.e., liquid mixing, and the higher temperature increase the diffusion rate and lead to larger particles.

The classical interpretation of the Ostwald ripening was developed by Lifshitz and Slyozov [11] and Wagner [12] (LSW) during examination of coarsening in a system where globular particles are indefinitely separated. According to this theory, under steady-state conditions the cube of the average particle radius increases linearly with time:

$$\bar{R}(t)^3 - \bar{R}(0)^3 = K_{LSW}t \tag{9.2}$$

Where:

R(0) and R(t) – the average radius at time t= 0 and t=t, respectively;
K_{LSW} – coarsening rate constant.

In LSW theory the diffusional interactions between particles are neglected so the mechanism is applicable in a negligible fraction of the coarsening phase.

9.7.3.2 Coalescence Ripening

Coalescence is usually defined as the nearly instantaneous formation of one large particle upon contact of two smaller ones. After particles coalesce, they are first interconnected by a necking region (Fig. 9.21). Then a spheroidization takes place due to a mass transport exclusively in the necking area. Several coalescence ripening theories were developed, essentially based on the diffusion of the solute atoms

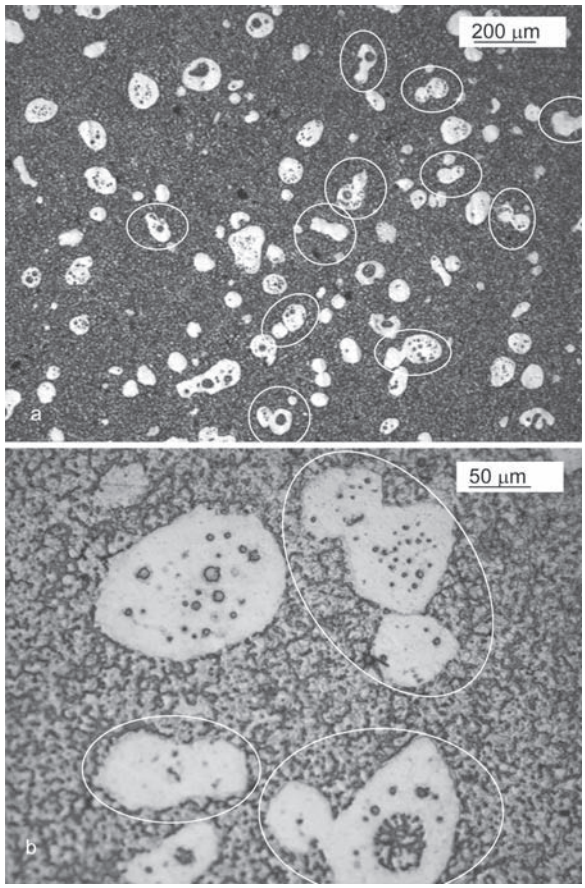

Fig. 9.21 The coalescence of solid particles during injection molding: **a** general view showing about 11 pairs of total 85 particles involved in coalescence ripening; **b** detail image showing morphological transformations after the coalescence event

in the liquid [13]. Although growth is controlled by the cubic law, similar to (Equation 9.2), it is observed that an active coalescence mechanism broadens the particle distribution as compared to the pure Ostwald ripening.

9.7.3.3 Coarsening Theory for High Solid Fractions

Coarsening at high solid fractions was described using the model of migration of grain boundary liquid films [14]. In contrast to the LSW theory, which considers only diffusion fields around isolated solid particles, this mechanism better describes coarsening behavior for solid fractions higher that 0.5. The model assumes that the spherical solid particles are separated by the spherical liquid film and the coarsening controlled by diffusion of solute through the liquid film. The cubic coarsening rate K is not constant as in LSW theory (Equation 9.2) but changes as a function of the solid fraction f_S [14]:

$$K = \frac{3DC_L(\infty)\sigma V_m}{2RT\left(C_L(\infty) - C_S\right)\left(f_s^{-1/3} - 1\right)} \tag{9.3}$$

Where:

D – diffusion coefficient of solute in the liquid;
$C_L(\infty)$– molar composition of the liquid in equilibrium with solid particles of infinite radius;
σ – solid/liquid interfacial energy;
V_m – molar volume;
R – universal gas constant;
T – absolute temperature;
C_S – molar composition of the solid.

The theory concludes that the coarsening rate increases steadily with a solid fraction up to 0.75. For solid fractions exceeding 0.75, the coarsening rate decreases due to reduction of liquid film when particles approach and meet each other.

9.7.3.4 Influence of Temperature Gradient on Particle Coarsening

During injection molding the coarsening is frequently superimposed on an alloy's melting. If the system is not isothermal, the temperature gradients may activate flow of mass or heat. As opposed to isothermal coarsening caused by mass flow due to concentration gradients caused by capillarity, a temperature gradient results in differences in interfacial composition [15]. This, in turn, generates concentration gradients and mass flow from warmer to cooler regions. Thus both processes will compete with each other.

While increasing temperature it is likely that instead of uniform melting of all particles, the preferential melting of some particles occurs. The observation of

continuous melting indicates that there is a critical fraction of liquid at which the particle size starts to decline. It is surprising that the solid size does not significantly reduce during advanced stages of melting. This is so, despite the large reduction in solid content.

The particle coarsening, particularly intense between 20% and 50% of the liquid fraction, indicates that the effectiveness of the mechanism that preserved the particle size is diminished by increasing liquid content. It seems that the particle coarsening in this range of molten fraction should be understood as a competition between the shear and coalescence effects. Shear forces between particles, which may be carried only by the solid phase, are reduced since they can easily separate within the surrounding liquid. At the same time, the inter-particle distances are short, so particles can meet each other to coalesce. A preferential melting of particles with smaller size is a possibility.

At temperatures approaching liquidus the coalescence is less active because at higher liquid contents the probability that particles will come in contact with each other is reduced. On the other hand, the role of Ostwald ripening is expected to be greater because of faster diffusion at high temperatures.

9.8 Engineering Microstructure for Commercial Applications

The universal nature of the injection molding system, and the capability of creating different microstructures, raises the question of how to select the proper manufacturing process for particular components. Before such a decision is made, many factors that affect the processing route selection should be considered. The component size, its geometry and wall thicknesses, define requirements regarding mold-filling conditions. The particular properties required define the microstructure after molding. In some cases, the alloy's chemistry and its melting behavior will impose special adjustments. Moreover, there is a factor of energy economy pointing towards lower temperatures.

Thus, an optimum between these factors is a key for the selection of the appropriate method of manufacturing components with a minimum porosity and satisfactory properties. The ultimate goal is the same as that for semisolid processing in general—to manufacture parts with sound structural integrity and properties comparable to wrought products at a low cost similar to castings. Among processing parameters, the temperature that controls the solid fraction is fundamental. For a given alloy, the component wall thickness affects the solid fraction required.

9.8.1 Thick Wall Components

For components with wall thicknesses exceeding approximately 2 mm, the higher solid content is beneficial. From the processing side it is easy to fill components

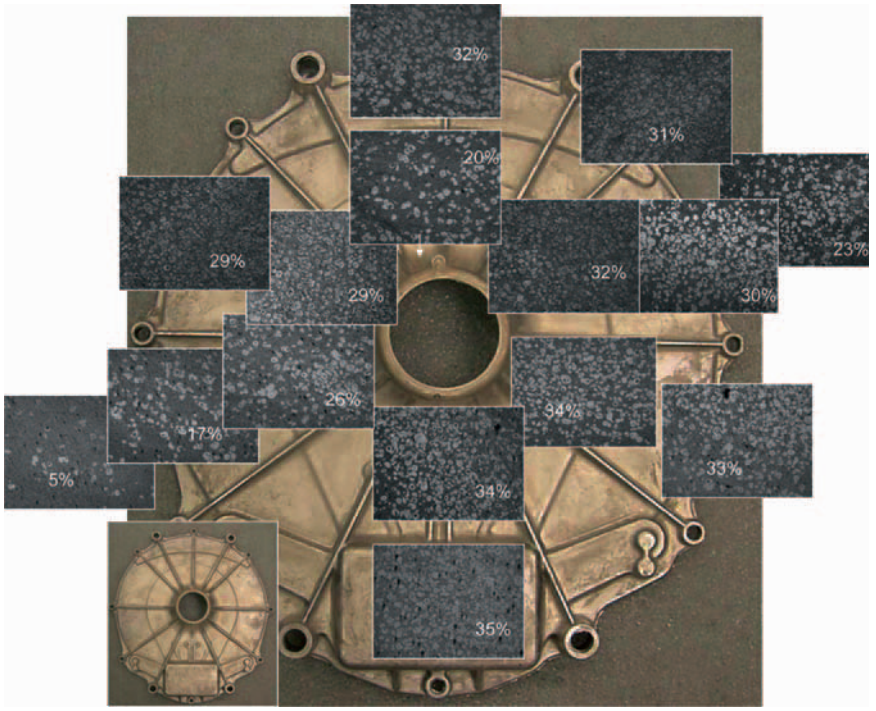

Fig. 9.22 The microstructural characterization of the thick wall component molded at high solid fraction. A spacial distribution of solid fraction shows some differences caused by the influence of the nozzle seal plug

with even a very complex shape. An example of solid distribution within the part with outer diameter of 270 mm, wall thickness of 3 mm to 4 mm and weight close to 600 g is shown in Fig. 9.22. The fan gate is located in the center of the part. While operating at high solid contents, reheating the plug introduces a certain volume with reduced solid content. After injection the higher liquid fraction ends up in certain regions of the component. Thus, the bottom-left regions contain a lower solid fraction as compared to the remaining area of the part.

9.8.2 Thin Wall Components

Although thin-wall casting is generally associated with consumer electronics, other markets utilize it as well. The definition of thin and thick wall casting is rather arbitrary with dividing values of wall thicknesses being characteristic for the particular market. With technology development, the minimum wall thickness, achievable for specific shape and size, is continuously reduced. For consumer electronics, the wall thickness of 1 mm, being typical several years ago, is recently as low as 0.6-0.5 mm.

Thin-wall components, with the wall being below 1 mm, represent the specific application where the solid content is kept to be rather low. The major reason for the low solid fraction is to maximize the flow length. Depending on the size of the seal plug,

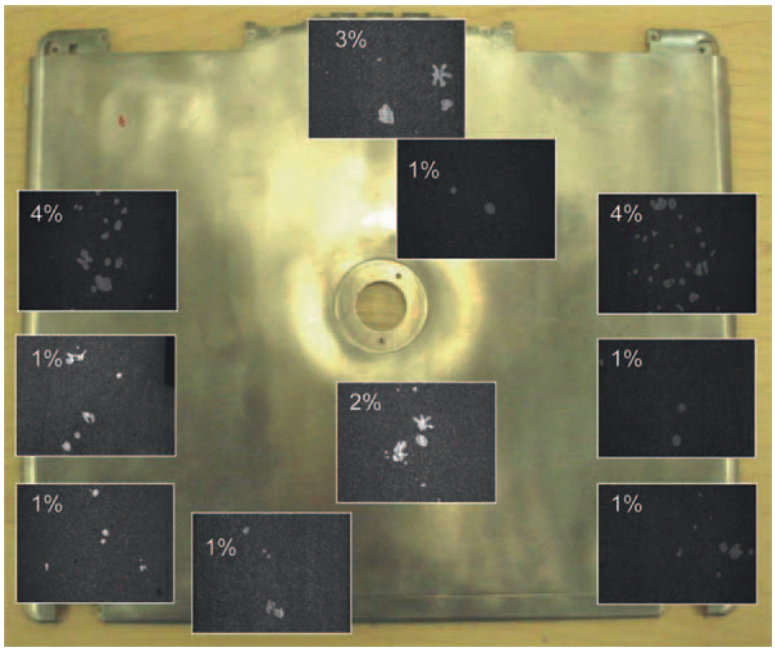

Fig. 9.23 The distribution of solid content within the thin-wall component of a medium size, injection molded using low solid content

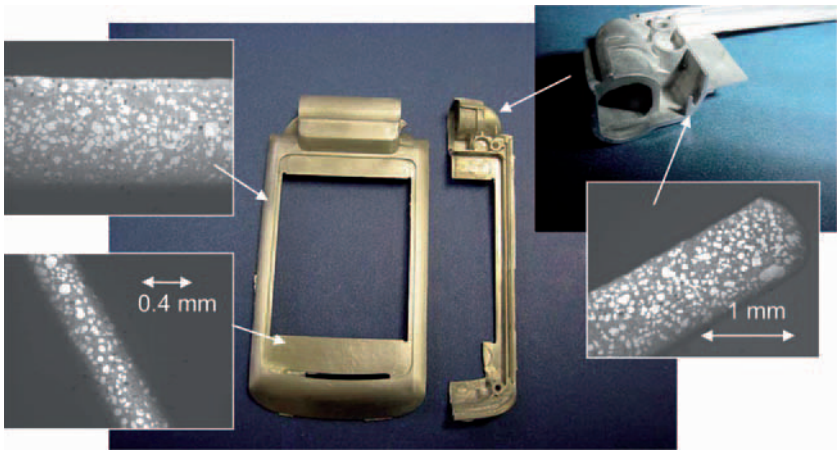

Fig. 9.24 The distribution of solid content within the thin-wall component of small size, injection molded using solid content with an average of 35%

plug catcher, runners and overflows, the solid particles from the plug may end up within the component. As a result, although the predominant area of the component contains a low solid fraction, there may be regions with higher solids (Fig. 9.23). There are also attempts to mold thin wall components with high solid content. An example of a cell phone housing containing about 35% of the solid fraction is shown in Fig. 9.24. The component contains sections with a wall thickness of 0.4 mm and a number of tiny details. As indicated by insets, all elements were perfectly reproduced by a semisolid slurry of AZ91D alloy.

9.9 Summary

Ex-situ microstructural analysis is a useful tool to assess the high temperature transformations of an alloy within the injection molding system. The role of heat and shear in the microstructural evolution of the magnesium alloy and potential mechanisms involved, depends on the temperature profile along the injection-machine barrel. For partially melted chips, the shear imposed by the injection screw does not essentially change the size or spheroidal shape of the primary solid particles. Although shear plays a role during molding of the alloy, which was completely melted and partially re-solidified before injection, the temperature role is crucial. A substantial overheating above the liquidus level leads to the generation of dendritic or rosette-like morphologies, believed to be detrimental for the flow characteristics of the slurry and the properties of injection molded products.

The size of the unmelted phase within a magnesium alloy depends on the liquid fraction within the semisolid slurry. The initially small particles, being of the same order as the grain of the recrystallized feedstock before melting, experience significant coarsening in the range of the liquid fraction between 20% and 50%. Although a further increase in the liquid content caused some particle refinement, changes are significantly lower than those expected from the reduction in a solid volume fraction. Since the particle size affects the slurry flow mode and properties of the final component, its control is of engineering importance. The role of the screw may have some contribution only at very high solid contents. While the liquid fraction is higher, the influence of the injection screw disappears.

References

1. Alkemper J, Voorhees PW (2001) Three-dimensional characterization of dendritic microstructures. Acta Materialia 49:897–902
2. Ghosh A (2001) Segregation in cast products, Sadhana (India) 26(1–2):5–24
3. Doherty RD (2003) Comments on “Mechanical deformation of dendrites by fluid flow during the solidification of undercooled melt.” Scripta Materialia 49:1219–1222
4. Dragnevski K et al (2002) Mechanical deformation of dendrites by fluid flow during the solidification of undercooled melts. Acta Materialia 50:3743–3755

5. Tsao CA, Chen CP (1997) Semisolid deformation of non-dendritic structures—I. Phenomenological behaviour. Acta Materialia 45:1955–1968
6. Yang YS, Tsao CA (1994) Thixotropic behaviour of structural evolution of A356 alloy in semisolid state. Acta Materialia 30:1541–1546
7. Ji S, Das A, Fan Z (2002) Solidification behaviour of the remnant liquid in the sheared semisolid slurry of Sn-15wt5Pb alloy. Scripta Materialia 46:205–210
8. Czerwinski F (2003) Size evolution of the unmelted phase during injection molding of semi-solid magnesium alloys. Scripta Materialia 48:327–331
9. Tzimas E, Zavaliangos A (1999) Mechanical behaviour of alloys with equiaxed microstructure in the semisolid state at high solid content. Acta Materialia 47:517–528
10. Schwind M, Agren J (2001) A random walk approach to Ostwald ripening. Acta Materialia 49:3821–3828
11. Lifshitz IM, Slyouzov VV (1961) Journal of Physics and Chemistry of Solids 19:35
12. Wagner C (1961) Zeitung der Electrochemie 65:581
13. Wan G, Sahm PR (1992) In SB Brown and MC Flemings (eds) Proceedings of the 2nd international conference on semisolid processing of alloys and composites. Cambridge, MA, TMS, Warrendale, PA, pp 328–335
14. Whitton-Manson ED et al (2002) Isothermal grain coarsening of spray formed alloys in the semisolid state. Acta Materialia 50:2517–2535
15. Snyder VA, Akaiva J, Voorhees PW (1999) The influence of temperature gradients on Ostwald ripening. Metallurgical and Materials Transactions A 30:2341
16. Czerwinski F (2002) The microstructural development of Mg-9Pct Al- 1Pct Zn alloy during injection molding. Metallurgical and Materials Transactions A 32:2963–2972

10
Microstructure–Property Relationship for Molded Alloys

10.1 Introduction

The properties of alloys manufactured by semisolid forming are controlled by a unique microstructure that is essentially different from that obtained after processing using both conventional and novel technologies. Although the alloy phase composition is similar to that formed during die casting or rapid solidification, the phase morphology, and in particular the presence of primary solid particles, makes the difference in creating a kind of composite. A specific nature of the composite arises from the spherical particles imbedded in the matrix of solidified liquid fraction. As opposed to typical composites where the reinforcement particles have increased strength, in alloys processed in semisolid state, the primary particles of αMg are generally softer than the matrix. As a result, the mechanisms developed for conventional composites cannot be adopted here and a rule of mixtures does not explain the properties of molded alloys.

An understanding of the strengthening mechanism within alloys processed by semisolid methods, with implications for their properties, is of key engineering interest. It is generally anticipated that such non-dendritic morphologies, generated during semisolid processing, should exhibit beneficial properties. A present interpretation of benefits associated with semisolid processing that assumes a reduction in porosity as the only difference compared to conventional casting, is not satisfactory. This chapter provides a detailed description of molded structures of magnesium alloys and characterizes their correlation with tensile properties.

10.2 Parameters Characterizing Thixotropic Structures After Solidification

In order to establish the structure–property correlation, a detailed description of solidified semisolid slurries is required. The general problem of a microstructure characterization relates to two-dimensional (2D) observations used to

F. Czerwinski, *Magnesium Injection Molding*.

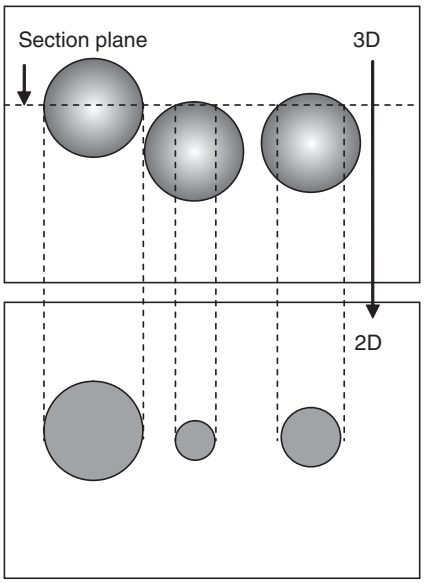

Fig. 10.1 The relationship between three-dimensional solid particles and their two-dimensional cross sections. The schematics show how three-dimensional features of the same size cause drastically different sizes of their planar equivalents after sectioning by the plane indicated

describe three-dimensional (3D) features, and this is a subject of stereology (Fig. 10.1). The quantitative parameters which describe microstructures are divided into two categories:

(i) parameters characterizing the entire material volume;
(ii) parameters characterizing individual features within the material.

10.2.1 Volume Fraction of the Primary Solid

The volume fraction of the primary solid is the basic feature of thixotropic structures. It affects not only the properties of slurries at high temperatures but also properties of alloys after solidification. A determination of the volume fraction V_v of the particulate phase is based on the assumption that it equals the surface fraction of this phase, measured on a flat section of the material:

$$V_V = \frac{\sum A_\alpha}{A_T} \tag{10.1}$$

Where:

$\sum A_\alpha$ – sum of the areas of the α phase;
A_T – total measurement area.

10.2.2 Size of the Primary Solid Particles

The particle size also affects the properties of both the slurry and solidified structures. It has special importance during thin wall molding where small gates may act as flow obstacles. Although there is no quantitative evidence available, the finer particles are considered more beneficial. Various parameters are used to determine the size of the primary solid particles. While for the spheroidal shape, the diameter is a sufficient estimator, for irregular features such as rosettes, the Feret diameter is more appropriate. It provides a dimension that does not make the assumption that a particle is spherical. As explained in Fig. 10.2, the Feret diameter is a distance between two tangents on opposite sides of the particle—parallel to an arbitrary fixed direction. In addition to the average size of the particle, size distribution is used to provide a closer description of the particle population.

10.2.3 Shape of the Primary Solid

The shape of primary solid particles is essential since it distinguishes spheroidal features from irregular ones, including rosettes and dendrites. In practice, several shape factors are applied. The most frequently used parameter, SF_1, is defined as follows:

$$SF_1 = \frac{4\pi A}{L_p^{\,2}} \tag{10.2}$$

Where:

L_p - particle perimeter;
A – particle's cross section area.

For a sphere, the value of SF_1 is 1, and it decreases below 1 as the particle becomes less spherical; for a very complex shape $SF_1 \to 0$. Examples of SF_1 distributions for globular and rosette morphologies are shown in Figs. 10.3 and 10.4, respectively. The inversion of equation (10.2) is also used, so in that case the values for complex shapes $\frac{1}{SF_1} \to \infty$.

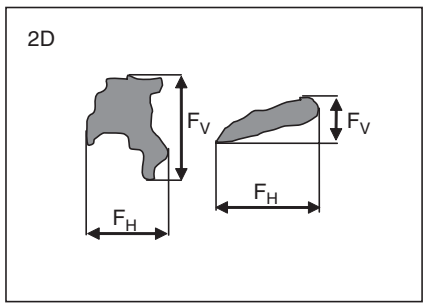

Fig. 10.2 Schematics explaining a definition of the Feret diameter used for characterizing the size of particles with irregular shape. F_H–horizontal Feret diameter; F_V–vertical Feret diameter

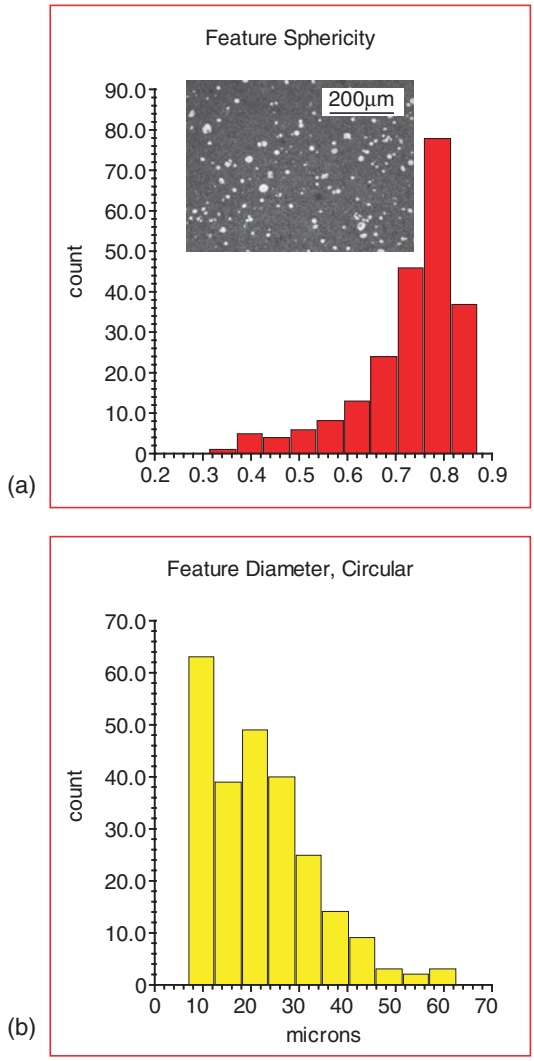

Fig. 10.3 The distribution of shape factor for Mg-9Al-1Zn spheroidal structure **a**, measured according to the formula 10.2. The distribution of particle size is shown in Fig **b**.

A different approach to globule characterization is expressed by the parameter SF_2, defined as [1]:

$$SF_2 = \frac{1}{6\pi f_S} \frac{S_V{}^2}{N_A} \tag{10.3}$$

Where:

S_V – solid-liquid interfacial area per unit volume;

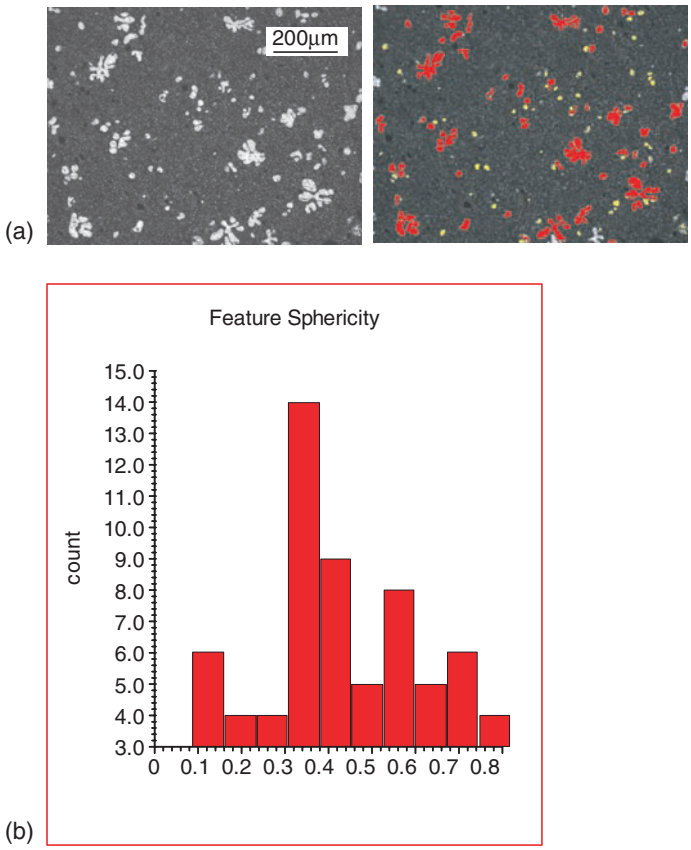

Fig. 10.4 The distribution of shape factor, measured according to Formula 10.2, for rosette-type Mg-9Al-1Zn structure: **a** (left) optical micrograph; **a** (right) image created by a computer software with shadowed particles, which were considered during measurements; **b** shape distribution graph

N_A – number of particles per unit area;
f_S – solid fraction.

It is belived that the dimensionless factor SF_2 describes more precisely the particle morphology than SF_1. SF_2 becomes unity for the perfect spherical shape and increases beyond 1 for complex morphologies. A modification of the formula (10.3) is also used and the format is written as follows [1] :

$$SF_3 = \frac{8N_L^{\,2}}{3\pi f_S N_A} \tag{10.4}$$

Where:

N_L – number of solid-liquid interfaces per unit length;
N_A – number of particles per unit area;
f_S – solid fraction.

10.2.4 Volume of Entrapped Liquid

Entrapped liquid is understood as liquid generated inside solid particles that does not have a connection with overall liquid, filling the space between particles. It is contained to one or a number of pools within solid particles. In semisolid state, the entrapped liquid affects negatively the flow behavior since being separated, it does not contribute to the overall liquid volume. An assessment of its volume fraction is not straightforward and requires 3D measurements. In practical measurements, therefore, the same rules as those used for analysis of the primary solid particles are applied. After solidification, the entrapped liquid affects the internal structure of globules and thus changes the properties of the entire microstructure. Since the solvent-rich alloy increases the strength of αMg globules, in this respect the effect is understood as positive.

10.2.5 Interfaces

At high temperatures, two types of interfaces exist in thixotropic structures (Fig. 10.5):

(i) interfaces between solid and liquid phase;
(ii) interfaces between solid and solid phase.

The solid–liquid interface transforms after solidification to the interface that separates the solid and former (i.e. solidified) liquid.

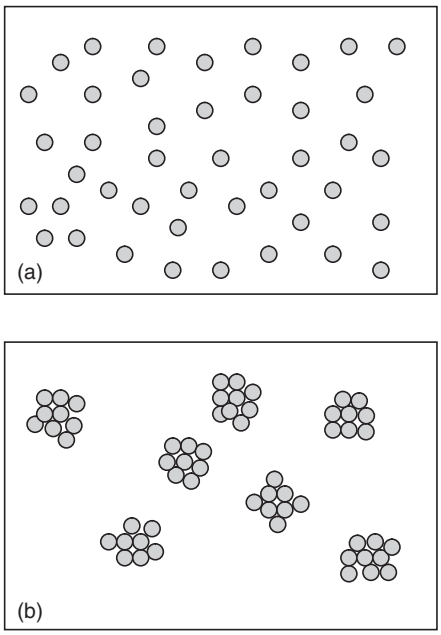

Fig. 10.5 The schematics explaining the contiguity phenomenon during semisolid processing: **a** well-dispersed structure with no solid-solid interfaces; **b** heavily agglomerated structure with high contiguity

10.2.5.1 Primary Solid–Former Liquid

These interfaces relate mainly to the area between the primary solid particles and the matrix. In general both the primary solid and the matrix may represent multiphase systems, so the interface is usually complex. For many Mg based alloys, the matrix is predominantly a two- phase structure, and the interface is anticipated to consist of fragments of αMg- αMg and αMg-intermetallics. During slow solidification, however, the solid particles may act as substrates for nucleation and be covered with a continuous single-phase layer.

10.2.5.2 Primary Solid–Primary Solid

The solid–solid interface in a semisolid slurry involves the common area between the primary solid particles and is characterized by a *contiguity*. The contiguity is understood as connectivity between solid particles in semisolid state and describes the fraction of the surface area of a particle that is shared with other particles (Fig. 10.5). The degree of contact of the surfaces of specific particles mainly exerts influence on the flow behavior at high temperatures. Although it also affects properties of a solid alloy this role is less pronounced. The contiguity $C_{\alpha\alpha}$ is defined as:

$$C_{\alpha\alpha} = \frac{2S_{v,\alpha\alpha}}{2S_{v,\alpha\alpha} + S_{v,\alpha\beta}} \tag{10.6}$$

Where:

$S_{v,\alpha\alpha}$ – interfacial contact area per unit volume between touching α particles;
$S_{v,\alpha\beta}$ – interfacial contact area per unit volume between α particles touching β matrix.

10.3 General Constituents of Thixotropic Microstructures of Magnesium Alloys

Morphologically, the molded structure is unique and essentially different from that created by conventional casting techniques. Moreover, it is also different from structures produced by other semisolid technologies. The most typical feature is a lack of large dendritic forms of growth. This refers not only to primary solid particles having globular shapes, but also to products of the molten fraction after solidification, i.e., the eutectic mixture in Mg–Al–Zn and Mg–Al systems. A variety of microstructures can be generated by changing the temperature distribution along the injection machine barrel. The most evident difference, imposed by the barrel temperature and easily revealed under magnifications of optical microscopy, is the morphology and volume content of the primary solid.

10.3.1 Primary Solid

The characteristics of primary solid particles for a volume range between 5% and 60% and evaluated on the basis of the stereological analysis of polished cross sections, are listed in Table 10.1. Reducing the processing temperature does not essentially affect their morphology (Fig. 10.6). The only exception is the range of a very low solid fraction, where particles may be less spherical. The irregular shape of solid particles is frequently obtained after substantial overheating of an alloy above the liquidus, and some authors even report the presence of rosettes. It is unlikely that this morphology was formed as a result of structure agglomeration due to bond formation among solid particles caused by impingement and reaction [2]. Rather, the morphology of the rosette-like shape suggests a re-solidification from the liquid alloy before injection into the mold cavity.

10.3.2 As-Solidified Liquid

A visual assessment indicates that, in addition to variations in the content of the primary solid particles, caused by changes in processing temperature, there is also a difference in the morphology of the eutectic component (Fig. 10.7). The eutectics is seen as a mixture of αMg and an intermetallic compound. Morphologically, the αMg has the form of rather regular grains and the intermetallics, as a film with a thickness of about 1μm, fills spaces between them. Since the growth of αMg within the eutectic is diffusion controlled, the lower processing temperature results in its smaller size. An increase in a volume fraction of the primary solid is accompanied by a refinement of the secondary αMg grains in the eutectic, approximately from 10μm for 5% (Fig. 10.7a) to 5μm for a 43% solid (Fig. 10.7c). In summary, lowering the processing temperature, necessary to achieve a higher percentage of the primary solid within the slurry, affects the subtle microstructure of the primary solid as well as the morphology and structure of the solidified liquid fraction.

A distribution of major chemical elements, including Mg, Al and Zn within the microstructure indicates differences in the chemistry of micro-regions [3].

Table 10.1 The stereological parameters describing primary solid particles and the eutectics in microstructures analyzed in this study. Numbers in brackets represent standard deviations from analysis of over 500 particles [3]. [a)] shape factor calculated according to equation 10.2

	Primary solid particles				Eutectics
	Volume fraction	Average diameter	Average area	Shape factor SF[a)]	Average diameter of αMg
Alloy	%	μm	μm^2	μm	μm
1	4	34.6	939.8	0.56	10
2	22	43.9	1512.8	0.64	8
3	43	45.3	1610.9	0.65	5
4	58	66.6	3481.9	0.61	-

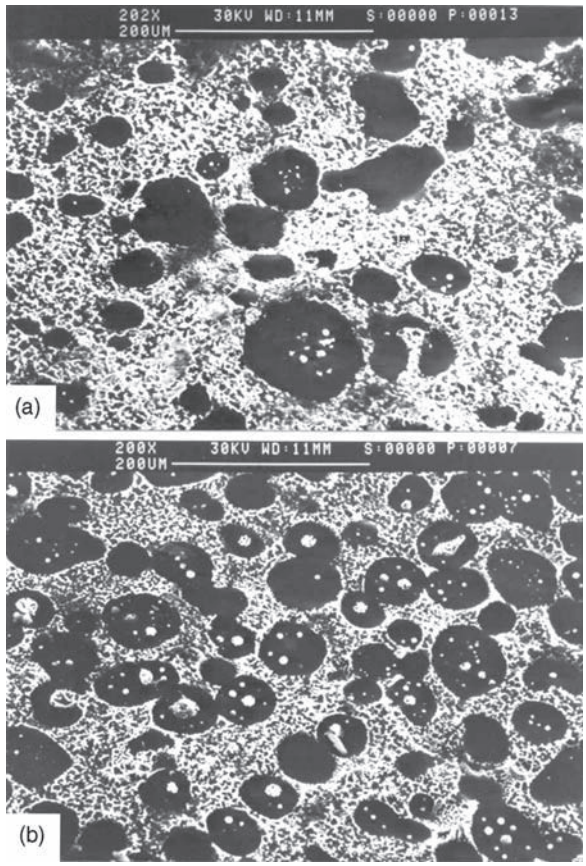

Fig. 10.6 SEM images of Mg–9Al–1Zn thixotropic microstructures showing the primary solid and eutectic components within alloys containing: **a** 22%; **b** 43% solid. The dark areas represent αMg and the bright areas correspond to the intermetallic phase. The surface after Ar ion etching [3]

The center of the αMg grain containing some traces of Al and Zn, is below the detection level. While moving toward the interface with the intermetallic phase, the content of Al and Zn also increases. The intermetallic compound itself contains almost an equal proportion of Mg and Al as well as a significant amount of Zn.

10.3.3 Phase Composition

For the Mg–Al–Zn alloys, the $Mg_{17}Al_{12}$ (γ) phase exists in an equilibrium with Mg-rich solid solution; the same phase as in the binary Mg–Al alloy. The γ phase forms by an eutectic reaction and, even if the particular alloy upon slow cooling passes from the liquid into the Mg-rich solid solution region without the occurrence of the eutectic

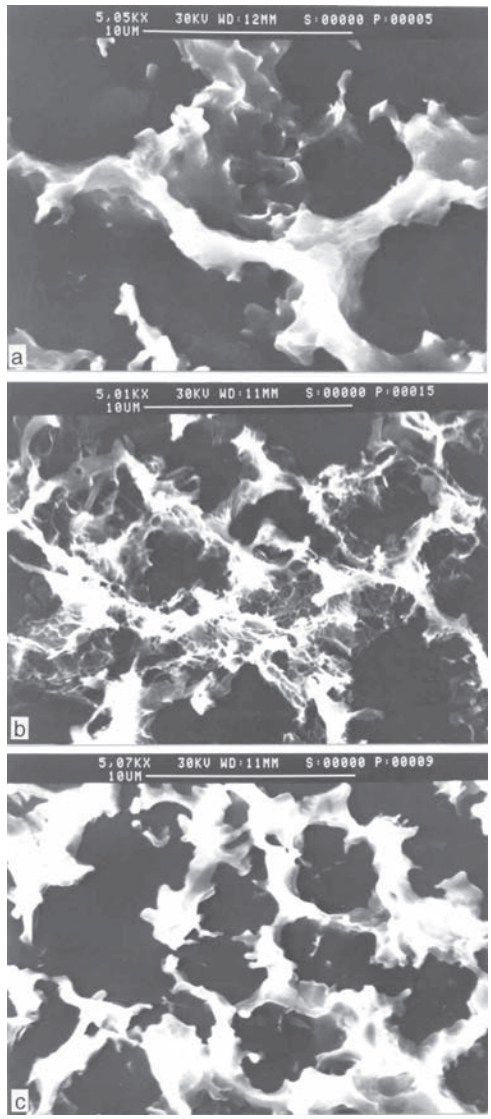

Fig. 10.7 The morphology of the eutectic component within Mg–9Al–1Zn microstructures containing different volume fractions of primary solid particles: **a** 5%; **b** 22%; **c** 43%. The dark areas represent αMg, and the bright areas represent intermetallics. SEM images after Ar ion etching [3]

reaction, the eutectic reaction may take place as a result of segregation (coring). From the shape of the αMg–γ boundary at the equilibrium phase diagram of Mg–Al–Zn, it is seen that the addition of Zn allows more γ precipitate to form at a fixed Al content of 8%. The γ compound has a part of the Al atoms substituted by Zn. Since for Mg–9Al–1Zn alloy at temperatures below 437 °C it has a form of $Mg_{17}(Al,Zn)_{12}$, likely

$Mg_{17}Al_{11.5}Zn_{0.5}$, the Zn content is expected to be higher [4]. Moreover, the increased Zn content is expressed by the sporadic presence of Zn rich inclusions and a higher Zn amount dissolved in αMg solid solution. Although due to their large size, the fragmented particles of the massive intermetallic phase are not effective in inhibiting the grain growth, grain boundaries rest on them. As a result they play a key role in the transformation of equiaxed structures into globular forms during melting.

The phases present in molded Mg–9Al–1Zn alloy are essentially the same as those obtained after die casting: αMg being a solid solution of Al and Zn in Mg, and the intermetallic compound of $Mg_{17}Al_{12}$. Under equilibrium conditions, the solubility of Al in αMg is 11.5 at % at 437 °C, but in as-cast alloys a solid solution below 437 °C is enriched only with 3–4 at % of Al. Al is not distributed uniformly and segregation typical for conventionally cast alloys is also present after semisolid processing. There are data showing that in rheocast Mg–9Al–1Zn, the Al content increased from 4.5% to 9% while moving from the center to the αMg grain boundary [5]. The same tendency of rising Al content towards the primary particle edge observed in a molded alloy would suggest that solid particles inherit the solidification segregation from an ingot. An original factor of semisolid processing is that solid particles during processing are surrounded by a liquid alloy having a higher content of Al. Assuming that the diffusion coefficient of Al in Mg at 560 °C equals 1.29×10^{-12} m^2s^{-1} [6] for the processing time of 180 s, the root mean square displacement of Al atoms is 15 μm. So, this represents another possibility of Al enrichment observed in the primary particle edge.

10.3.4 Structural Integrity

In order to assess the hardening, strengthening and fracture mechanisms of molded alloys, the role of internal integrity has to be clarified. For the as-molded state the integrity is mainly expressed by a porosity. Porosity is an important structural factor of any casting, and it is reported that molding assures up to 50% of its reduction. The above assessment is attributed to the fact that the presence of solids during the casting process will reduce volumetric shrinkage in direct proportion to the solid fraction present just before the freezing of the liquid fraction of the slurry. A calculation reveals that for pure magnesium, a volumetric shrinkage is 5% (equivalent to 1.7% linear shrinkage) during solidification, followed by 4.2% (1.5% linear) during subsequent cooling to room temperature. At the same time, in an experiment by Gosh et al. [7], for a solid fraction between 1.0% and 23.0%, the porosity stayed fairly constant at a level of 1.48%–1.96%. It appears that in that case the overall porosity was not affected by processing parameters. Also the mechanical properties appear to be independent of the porosity level. Similarly, experiments by Carnahan [8] leading to a change in the volume fraction of the primary solid between 12.0% and 63.2%, resulted in an apparently constant porosity of 2.38%–2.70%. The above results are somehow misleading. To avoid confusion, the specimens considered in this chapter were selected without evident localized porosity. Average porosity, as estimated by the Archimedes test, was of the order of 1.0%–1.5%, which is the

same as the level of the test accuracy. Such an approach allows us to focus the analysis on microstructure related factors.

10.4 Internal Structure of the Primary Solid and Matrix

10.4.1 Entrapped Liquid in As-Cast State

The majority of primary solid particles have in their interiors entrapped liquid in the form of precipitates with predominantly spherical shapes (Fig. 10.8a). Its content in the range of several percent, is similar to values quoted in the literature for other techniques of semisolid processing. The data for Sn–Pb rheocasting suggests that the volume fraction depends on the shear rate, and that there is less entrapped liquid within the particles that experience the higher shear rate. As explained earlier, for a magnesium alloy, the entrapped liquid originates from a chemical segregation and the presence of an intermetallic phase inside the grains.

Imaging under high magnification reveals that entrapped liquid precipitates are not structurally homogeneous but are composed of two phases with an image contrast corresponding to the αMg and an intermetallic compound. The origin of these morphologies should be traced to the spheroidization, melting and re-solidification of the low melting fraction of the alloy entrapped inside solid particles as a result of chemical segregation. On polished surfaces, the αMg area does not contain any visible grain or sub-grain boundaries. As it was deduced from low magnification imaging, some particles, especially in alloys with a lower content of the primary solid, do not reveal evident precipitates in their interiors (Fig. 10.8b). Their cross-section area looks morphologically homogeneous and the electron image revealed a crystallographic difference expressed by the presence of grain boundaries. The boundaries are mainly located within the near-surface region and their geometric configuration, particularly within triple junctions, suggests their high-angle character. For all solid fractions, the interface between the primary solid phase and the eutectic is not flat, but well developed and covered with numerous protrusions of an intermetallic compound.

10.4.2 Changes of Entrapped Liquid Due to Diffusion

At high temperatures, the Al-rich phase, usually composed of complex geometry coagulates, partially dissolves and acts as a source of Al, diffusing subsequently within the particle matrix. Since at processing temperatures the Al-rich phases transform to a liquid, the accompanying processes are different from those observed during the annealing of steel with lamellar pearlite. The range of Al diffusion can be estimated based on a simple consideration. The coefficient for the chemical interdiffusion of aluminum in magnesium $D_{Al(Mg)}$ at a temperature T is given by [6]:

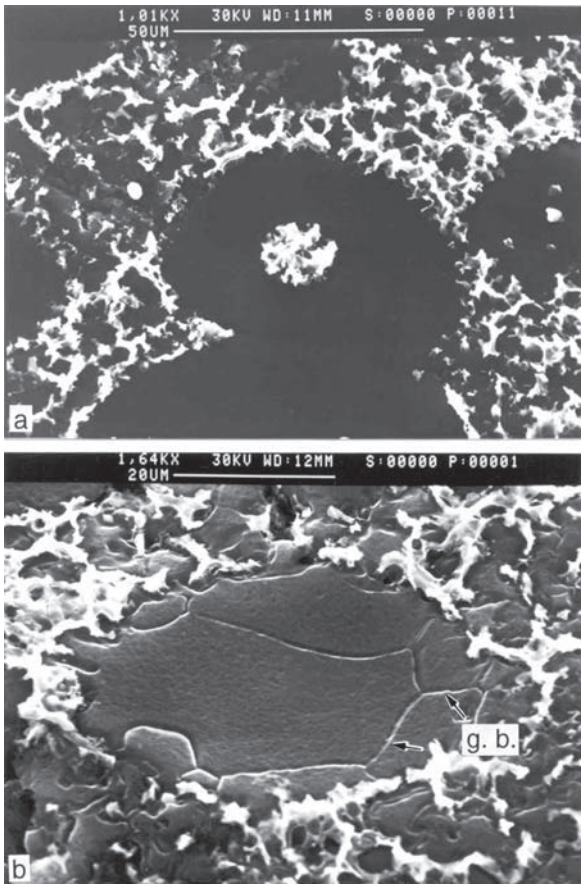

Fig. 10.8 SEM images of primary solid particles: **a** particle containing in the center a solidification product of "entrapped liquid"—alloy containing 43% of the primary solid; **b** particle without any precipitate of a second phase with grain boundaries in near-surface region—alloy with 5% of the primary solid. Surface after Ar ion etching [3]

$$D_{Al(Mg)} = 1.2 \times 10^{-3} \exp(-143{,}000\ \mathrm{J\ mol^{-1}}/RT) \quad \mathrm{m^2 s^{-1}} \tag{10.7}$$

where R is the gas constant. At a processing temperature of 580 °C, $D_{Al(Mg)}$ equals 2.09×10^{-12} m²/s. Assuming an average residency time of magnesium alloy within the system of 300 s, the root mean square displacement equals 25 μm. Thus, typical processing conditions do not allow for equal distribution of Al, and the remaining liquid, still rich in Al, will solidify as a mixture of γ and αMg inside the primary solid particles. The above calculation indicates, however, that for longer processing times, Al may reach a uniform distribution and the morphologies of entrapped liquid transformation could not be seen. Therefore, the absence of entrapped liquid alone cannot be considered as evidence of processing above the liquidus temperature.

10.4.3 Detailed Features of Molded Structures

The primary solid particles have an internal substructure that depends mainly on their content in the slurry. For 5% of the primary solid fraction, the primary solid phase comprises a solid solution with the αMg matrix, and observations under magnifications of up to 100,000 times did not reveal precipitates of a second phase (Fig. 10.9a). While some areas are dislocation free, others contain relatively high dislocation density. The latter are usually separated from the surrounding regions by well-defined boundaries. The dark phase is the intermetallic compound extended into a particle from the surrounding eutectics. The imaging of intermetallic phase sections, thin enough to be transmittable for electrons in 100 kV TEM, revealed that it contains evident grain boundaries and is essentially dislocation free (Fig. 10.9b). As indicated by the SAD diffraction pattern accompanying Fig. 10.9b, the intermetallic phase was identified as $Mg_{17}Al_{12}$ compound with a tetragonal lattice. The general view of the eutectics is depicted in Fig. 10.9c where the αMg grains, mainly with a globular shape, are surrounded by the intermetallic phase of $Mg_{17}Al_{12}$. Although the size of the majority of αMg within the eutectics is about 10 μm, there is also some fraction with a dimension as small as 1 μm.

The microstructure of the primary solid in the alloy with 20% of its content is characterized by higher dislocation density. A pile up of dislocations against the αMg grain boundary are frequently observed. An example is shown in Fig. 10.10a,

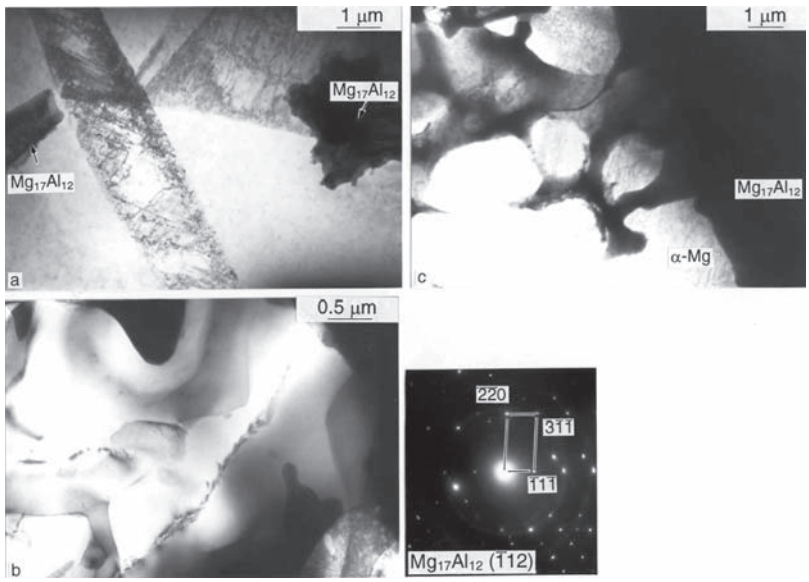

Fig. 10.9 The TEM microstructure of the Mg–9Al–1Zn sample containing 5% of primary solid particles: **a** primary solid particle; **b** intermetallic compound with corresponding SAD pattern; **c** eutectic mixture with phases indicated [3]

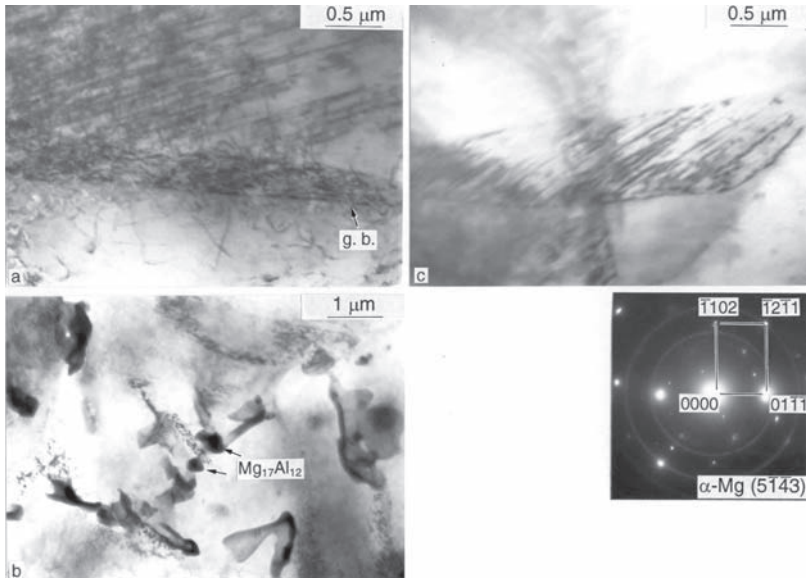

Fig. 10.10 The TEM microstructure of the Mg–9Al–1Zn sample containing 22% of the primary solid: **a** αMg grain with a concentration of dislocations in front of the grain boundary marked as g.b.; **b** $Mg_{17}Al_{12}$ precipitates inside the αMg grain due to chemical segregation; **c** unidentified fine precipitates within αMg grain and corresponding SAD pattern [3]

where the upper grain contains a significantly higher density of dislocations than the grain located beneath the boundary, marked as g. b. In some cases, the αMg grains contain sub-micron size precipitates of a second phase which, due to the low signal generated, was not detected previously by the SEM technique. As suggested by the image contrast and proving the SAD pattern, the $Mg_{17}Al_{12}$ is the major compound of these precipitates. The microstructural inhomogeneity inside the primary solid particle is shown in Fig. 10.10b. It is highly probable that this feature was caused by the chemical segregation. Another example of microstructural inhomogeneity within the αMg grains is depicted in Fig. 10.10c. The image contrast shows that in addition to a higher density of dislocations, the structure contains sub-micron precipitates of a second phase. While the strong spots on the SAD pattern are ascribed to the αMg, there are evidently additional diffraction spots of lower intensity that could be formed by a new, presently unidentified phase. The continuous rings are formed by the MgO thin film, easily grown during thin-foil preparation as a result of a high affinity of magnesium to oxygen.

An increase in the primary solid fraction up to 43% causes further changes in their general microstructure, accompanied by an increase in dislocation density (Fig. 10.11a). The microstructure comprises 1 μm to 5 μm thick laths, with essentially a different density of dislocations. This type of microstructure, termed as massive ferrite, is frequently observed in some ferrous alloys [9]. As indicated by the SAD pattern, the entire region imaged has one major crystallographic

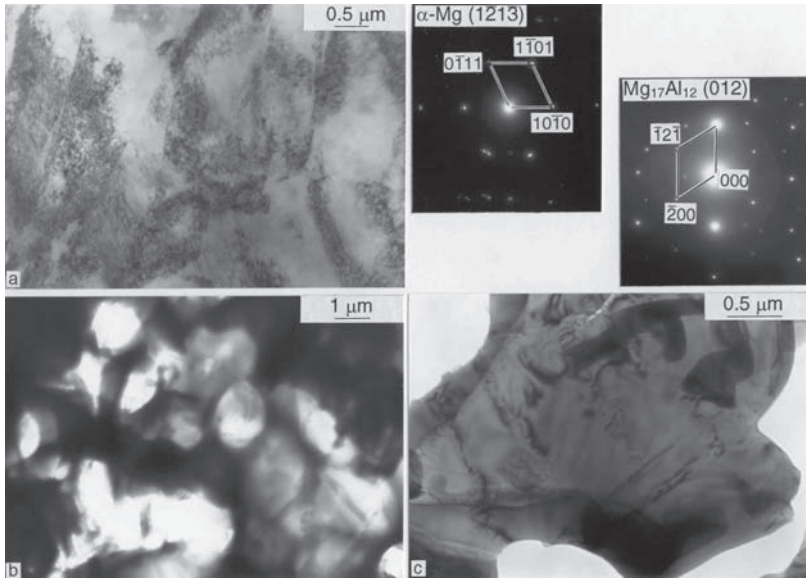

Fig. 10.11 The TEM microstructure of the Mg–9Al–1Zn sample containing 43% of primary solid phase: **a** primary solid with laths having different dislocation densities and corresponding SAD pattern; **b** fine-grained eutectic mixture with αMg grains of the order of 1 μm; **c** thin section of $Mg_{17}Al_{12}$ intermetallics with corresponding SAD pattern [3]

orientation expressed by the zone axis of $[1\,\bar{2}\,1\,\bar{3}]$. However, the wide, and in some cases double, diffraction spots suggest a small misorientation existing between individual laths. The eutectic component in the alloy containing the 43% solid is more fine grained than that observed for the low-solid fraction. Some αMg grains are as small as 1 μm (Fig. 10.11b). The intermetallic compound is also identified as $Mg_{17}Al_{12}$, and its microstructure contains grain boundaries, as observed previously in alloys with a low fraction of the primary solid (Fig.10.11c).

10.5 Tensile Properties

Tensile properties of as-cast alloys are determined using cast bars, so no machining is involved. The values of tensile strength for molded alloy Mg–9Al–1Zn, plotted as a function of the primary solid fraction, are shown in Fig. 10.12 together with literature data, selected for the same alloy chemistry. Although there are some differences, especially for a low–solid fraction of the order of 5% and caused in part by different processing parameters, all the data exhibits the same general tendency, expressed by a reduction in tensile strength with an increasing content of the primary solid particles. It should be mentioned that for the as-cast Mg–9Al–1Zn alloy the ASTM standard predicts a tensile strength of 230 MPa and a yield stress of 150 MPa. A comparison of the standard data and values in Fig. 10.12 shows that

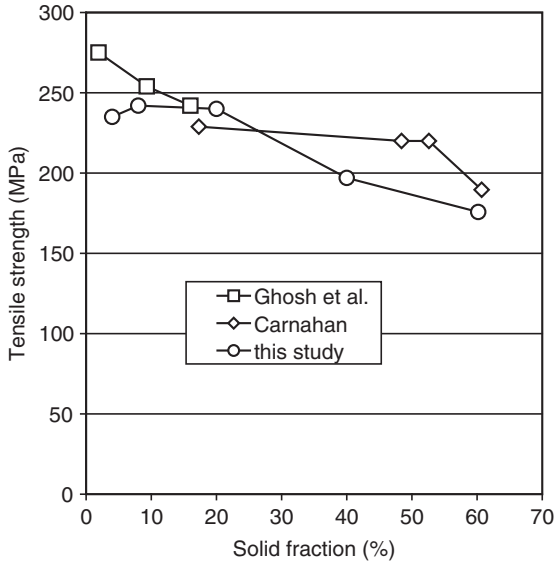

Fig. 10.12 The tensile strength of the molded Mg–9Al–1Zn alloy plotted as a function of the volume fraction of the primary solid phase. Literature data: Carnahan [8] injection velocity 2.11 m/s; Ghosh et al. [7] injection velocity of 2.29 m/s [3]

up to approximately 20% of the primary solid, the strength of molded alloy is above that limit.

A similar tendency toward a reduction in elongation, with an increase in primary solid fraction, is depicted in Fig. 10.13. It seems that the alloy ductility expressed by percent elongation, exhibits a stronger dependence on the fraction of primary solid phase than that observed for tensile strength. An especially large reduction in the ductility of molded Mg–9Al–1Zn is exhibited by data reported by Ghosh et al. [7]. This behavior is not supported by the results of our study and, for up to about 20% of the primary solid, elongation fluctuates at a level of 4.5% to 5%. In general, however, molded Mg–9Al–1Zn possesses a good ductility that, for a wide range of solid fractions, is above the value of 3% given by ASTM standard for as-cast Mg-9Al-1Zn. A comparison of data demonstrates that an increase in alloy strength is accompanied by a simultaneous increase in alloy ductility. A possible reason for such behavior will be discussed later.

10.6 Decohesion Characteristics

A common feature of all decohesion surfaces is that the crack propagates along the alloy matrix, and the solid particles are not noticeably involved in cracking. For low-solid fractions, the crack penetrates along the interface between the $Mg_{17}Al_{12}$

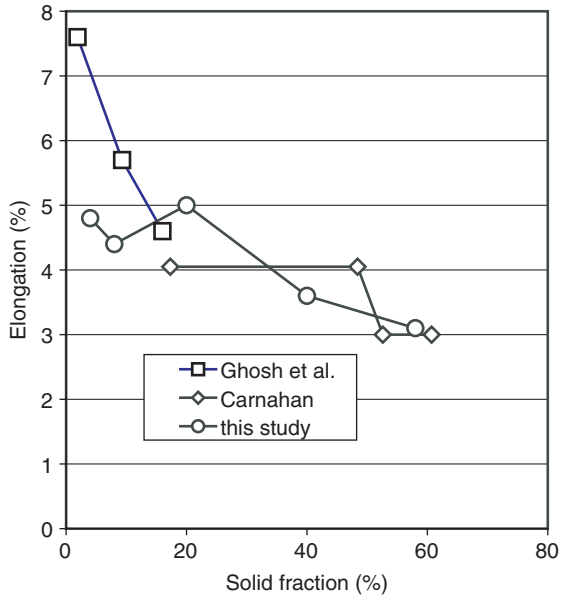

Fig. 10.13 Elongation of the molded Mg–9Al–1Zn alloy plotted as a function of the volume fraction of the primary solid phase. Literature data: Carnahan [8] injection velocity 2.11 m/s; Ghosh et al. [7] injection velocity of 2.29 m/s [3]

phase and the secondary αMg. Since the $Mg_{17}Al_{12}$ phase does not form a continuous network, the neighboring islands are connected by crack bridges that form across the αMg (Fig. 10.14a,b). The microstructure of the transformed liquid consists of secondary αMg regions surrounded by a network of the intermetallic phase of $Mg_{17}Al_{12}$. It is assumed that each αMg region exhibits the same crystallographic orientation, and that optical contrast is caused by the chemistry gradient. No evident grain boundary network was revealed within secondary αMg areas. For structures with higher solid fractions, the crack penetrates preferentially between the primary solid and the matrix (Fig. 10.15a-c). In the regions of the transformed liquid bridges that connect solid particles, the crack propagation is the same as that observed for low solid fractions.

The ruptured surfaces provide mainly morphological information, and it is rather difficult to distinguish precisely individual phases. Although there is no evidence of significant plastic deformation, there is an essential difference in morphology of the fracture surface between the alloy with low and high content of the primary solid. The morphology of the fracture surface for the low-solid fraction does not contain features that could be associated with the presence of primary solid particles (Fig. 10.16a). It seems that the decohesion surface represents an interface between two components of the eutectic: αMg and $Mg_{17}Al_{12}$ intermetallic compound with connecting bridges through both phases (Fig. 10.16b). Some flat areas with a brighter contrast, marked by arrows, presumably indicate decohesion of the

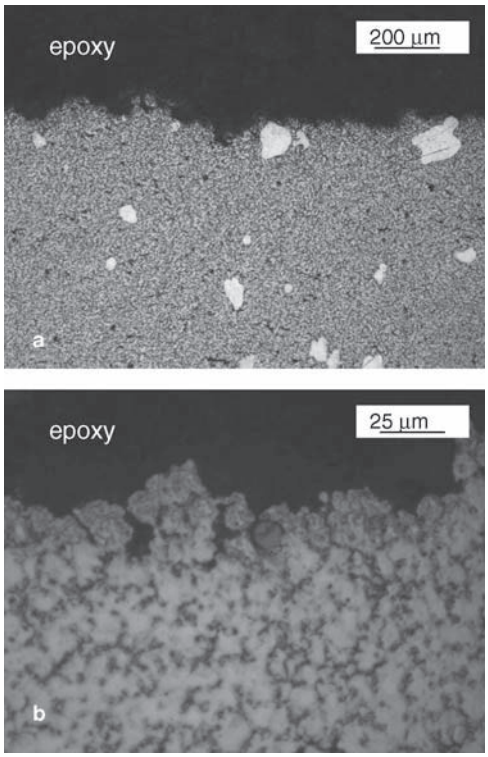

Fig. 10.14 The crack propagation path in the Mg–9Al–1Zn alloy with low solid content **a** and a magnified view of the matrix cracking **b**

intermetallic phase itself. Conversely, for structures with a high volume fraction of the primary solid, the fracture surface exhibits cauliflower-like features indicating decohesion at the interface between the eutectic and the particle (Fig. 10.16c). The high magnification image (Fig. 10.16d) represents the eutectic with finer topographic features than those observed for the low-solid fraction. Brighter contrast suggests a higher concentration of $Mg_{17}Al_{12}$ on the decohesion surface.

10.6.1 Failure Mode Under Cryogenic Conditions

Cryogenic conditions are known to promote brittle cracking, which helps to expose structural features originally existing in the as-cast state They provide an additional insight into the fractographic interpretation. The fracture surface of the alloy with a low fraction solid reveals the location of primary solid particles. Some of them are indicated by arrows in Fig. 10.17a. It is seen that in this case the cracking took place across the primary particles and evidently changed its direction while propagating throughout their interior (Fig. 10.17b). The fracture surface of the alloy with a high content of the primary solid shows that at cryogenic

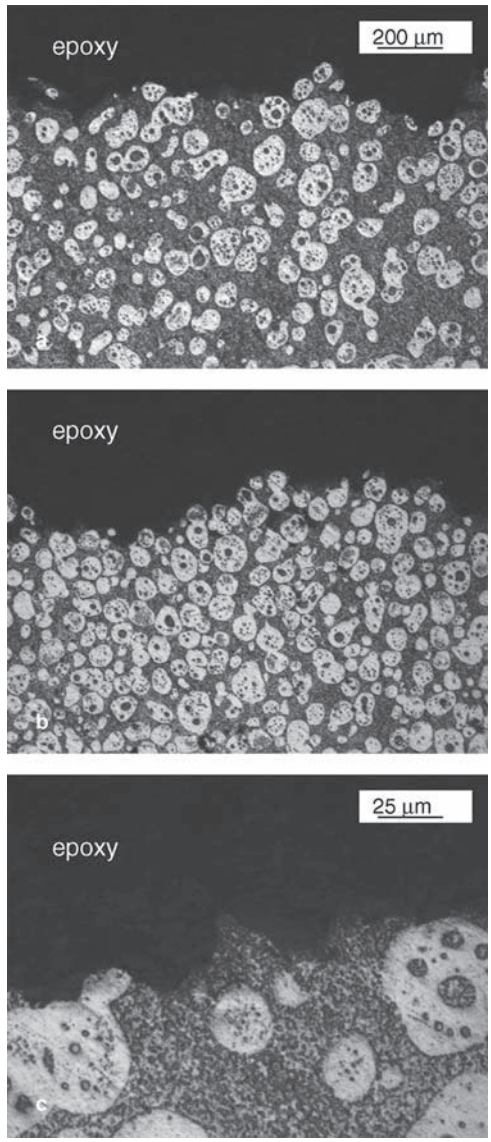

Fig. 10.15 The crack propagation path in the Mg–9Al–1Zn alloy with high solid contents **a,b** and a magnified view of the separation along interface of matrix-solid particle **c**

temperatures the particles exhibit decohesion predominantly at the interface matrix/particle (Fig. 10.17c). A detailed view of this type of failure is shown in Fig. 10.17d, revealing the complex morphology with a crack penetrating along the well developed interface.

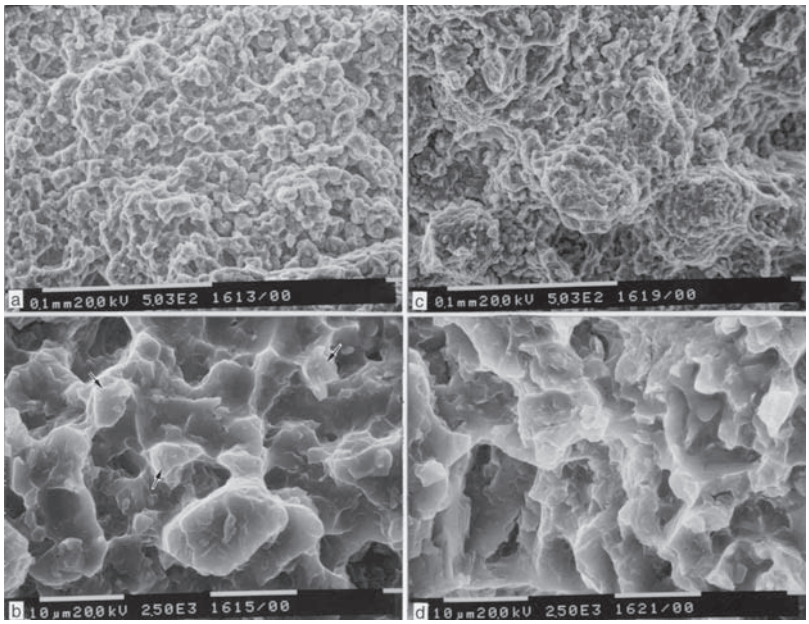

Fig. 10.16 The SEM image of the decohesion surfaces of tensile bars of Mg–9Al–1Zn containing 5% of the primary solid **a,b** and 43% of the primary solid **c,d**. The fracture was formed at room temperature [3]

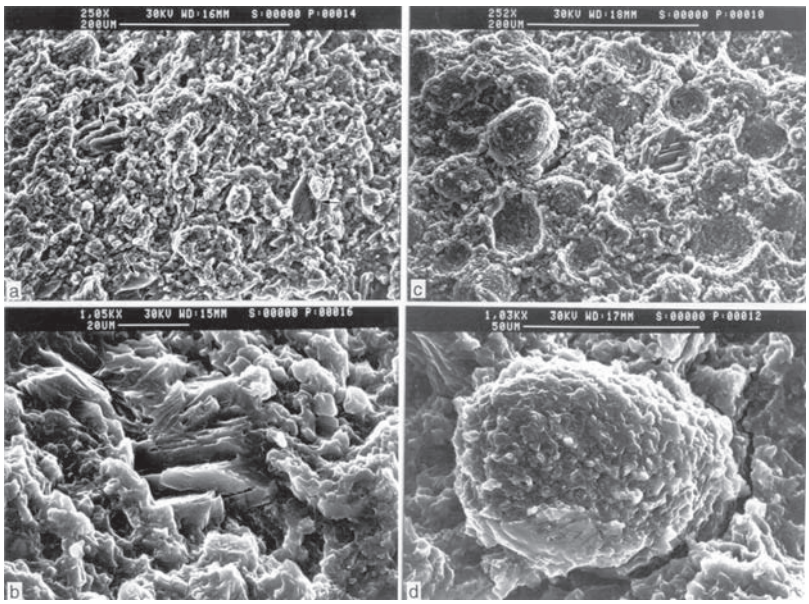

Fig. 10.17 The SEM images of molded Mg–9Al–1Zn, fractured at the temperature of liquid nitrogen: **a,b** 4% of the primary solid and **c,d** 43% of the primary solid [3]

10.7 Structure–Property Correlation

The tensile properties of molded alloys show a dependence on the processing temperature represented by a volume fraction of the primary solid. Similar findings were published earlier with the general conclusion of a reduction in strength, yield stress and ductility caused by a higher contribution of the primary solid [7, 8]. A comparison of various literature findings reveals the complex character of this relationship.

10.7.1 Role of Alloy Matrix

Two major phases, characterized above in detail, affect the tensile properties of molded Mg–9Al–1Zn alloy. The magnesium matrix is considered to be difficult to deform because of the hexagonal, close-packed lattice which, in tension, cannot use twinning to activate new slip systems. Having the hardness of approximately 60 HV it is, however, more susceptible to deformation than the over three times harder intermetallic phase with the higher strength and lower ductility. An essential difference of dislocation density in both phases after tensile testing positively proves this finding. To explain the tensile behavior, the morphological changes of both phases that take place during injection molding should be considered.

10.7.2 Role of Solid Particle Substructure

A reduction in the processing temperature causes not only an increase in volume fraction of the primary solid, but also a change in its internal microstructure. This involves an increase in microchemical inhomogeneity, the formation of nano-size precipitates of $Mg_{17}Al_{12}$ or other phases and large inclusions of solidified entrapped liquid. Since the deformation of Mg–Al alloys at temperatures below 200 °C is interpreted in terms of obstacle-controlled dislocation motion [10], the above changes, creating a drag force around the dislocations that impede their motion, will lead to a higher strength of the primary solid particles. Direct support of this thesis is provided by the SEM and TEM analysis of tensile bar fractures and sections.

Low-strength particles result in their intercrystalline cracking. Moreover, an increase in dislocation density in the primary solid particles, in the direction of reduced processing temperature, supports their higher resistance to deformation. At the same time, a reduction in processing temperature results in the refinement of the αMg grains within the eutectic mixture. The grain size of the αMg matrix operating by means of a Hall–Petch type of relationship has already been identified as a major factor determining the proof strength of cast magnesium alloys [11]. There is also data for a strengthening mechanism in materials with non-uniform

grain size [12]. Up to approximately 20% of the primary solid, refinement of the eutectic αMg grain and strengthening of the αMg primary solid fully compensated for the reduction that resulted from the increased solid fraction. A weak maximum on the strength and elongation plots, detected around 10% of the primary solid, indicates that the overall increase in strength exceeds the above described reduction.

10.7.3 Role of Solid Particle Content

A reduction in both the strength and ductility, especially clear above 40% of the primary solid, and a simultaneous change in the alloy fracture mechanism suggest that a new factor controls the tensile properties. A molded Mg–9Al–1Zn with a larger fraction of the primary solid, exhibits some features of a special composite. Since the primary solid and the eutectics have quite different elastic moduli, a complex stress distribution will be developed when a composite body is subjected to tension. The research on the failure mechanism of metal matrix composites indicated that numerous factors, including the matrix/reinforcement interface or reinforcement cracking, brittle cracking of the intermetallic particles, and microstructural inhomogeneity are associated with the composite failure [9]. However, the complexity of these materials has made it difficult to identify the contributions by each mechanism to the failure and to identify the dominant failure mechanism. While the same is essentially valid for molded Mg–9Al–1Zn, the fracture surface indicates the critical role of the interface between the primary solid and the eutectics. Although the structure of this interface depends primarily on the processing temperature, the other parameters, including injection velocity, injection pressure and mold temperature are also of importance. It is reasonable to assume, therefore, that their optimization will lead to an improvement in strength and ductility of a molded alloy with a given volume fraction of the primary solid.

10.8 Attempts at a Quantitative Description of the Structure–Property Relationship

A link between the microstructure and properties of magnesium alloys has been the subject of several studies. There were also attempts to correlate mechanical behavior with alloy chemistry and microstructure. For rapidly solidified Mg–Al–Zn alloys in which the αMg solid solution is the major phase exhibiting hardening, the contribution of alloying elements to hardening was expressed by an empirical relationship [13].

For injection molding, an empirical formula was also developed based on a statistical analysis of the metallographic and tensile data. Assuming that the porosity, αMg and matrix strengths affect the tensile properties, it aimed to calculate the ultimate and yield strengths σ in the as-molded condition [8]. The fundamental

assumption is that overall properties follow the rule of mixtures where the primary solid phase and the matrix are the weighted contributors:

$$\sigma = K_1 f_s + K_2(1 - f_s) \tag{10.8}$$

Where:
K_1 – constant for primary solid Mg phase;
K_2 – matrix strength at 0% porosity;
P_{eff} – porosity (%);
f_s – solid fraction.

For $0<f_s<0.64$ and the porosity level P_{eff} between 0.5% and 4.1% the following empirical expressions were developed [8]:

$$\sigma_{YS}(MPa) = 95 f_S + (1 - f_S)\left\lfloor 184.9 \exp(-0.12 P_{eff}) \right\rfloor \tag{10.9}$$

$$\sigma_{UTS}(MPa) = 95 f_S + (1 - f_S)\left\lfloor 311 \exp(-0.128 P_{eff}) \right\rfloor \tag{10.10}$$

A graphical representation is shown in Fig. 10.18. The limited nature of this model was later proven when in some cases a difference between predicted and measured values was almost 100% [7]. Thus, early experiments conclude that a simple rule of mixtures cannot explain the properties of molded alloys, and a more detailed microstructural model should be involved.

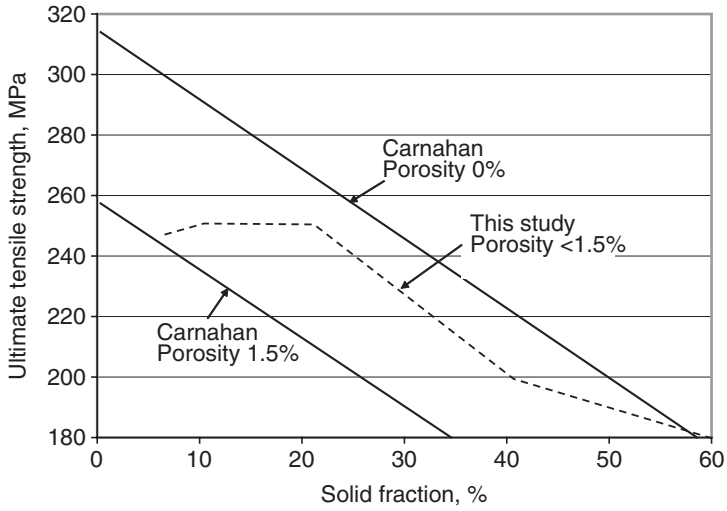

Fig. 10.18 The correlation of ultimate tensile strength and solid fraction established based on the relationship (10.10). Carnahan data from [8]

10.9 Structure–Property Correlation for Magnesium Alloys, Processed with Other Semisolid Techniques

The properties of magnesium alloys manufactured using other semisolid techniques cover rheomolding, rheocasting and thixocasting of typical Mg–Al–Zn and Mg–Al grades. For twin-screw rheomolded Mg–9Al–1Zn alloy the trend of changes is shown in Fig. 10.19 [14]. The overall values of tensile strength and particularly elongation are lower than those achieved for injection molding. The lower numbers are claimed to be due to hardware that was not optimized. In Fig. 10.19, the strength values are included for the same alloy, which was thixocast using a billet method. The data from [15] was converted from temperature to a solid fraction based on a correlation in Fig. 8.21. Although the strength values are generally higher than obtained after rheomolding, the general tendency with reducing the processing temperature is very similar.

For rheocast Mg–9Al–1Zn alloy, the empirical formulas were developed for hardness and ultimate tensile strength. While exploring the Hall–Petch type format, the hardness and strength were correlated with the size and the content of solid particles. The average hardness HV of two-phase alloy, being an average of the matrix and solid particles, is expressed as follows [16]:

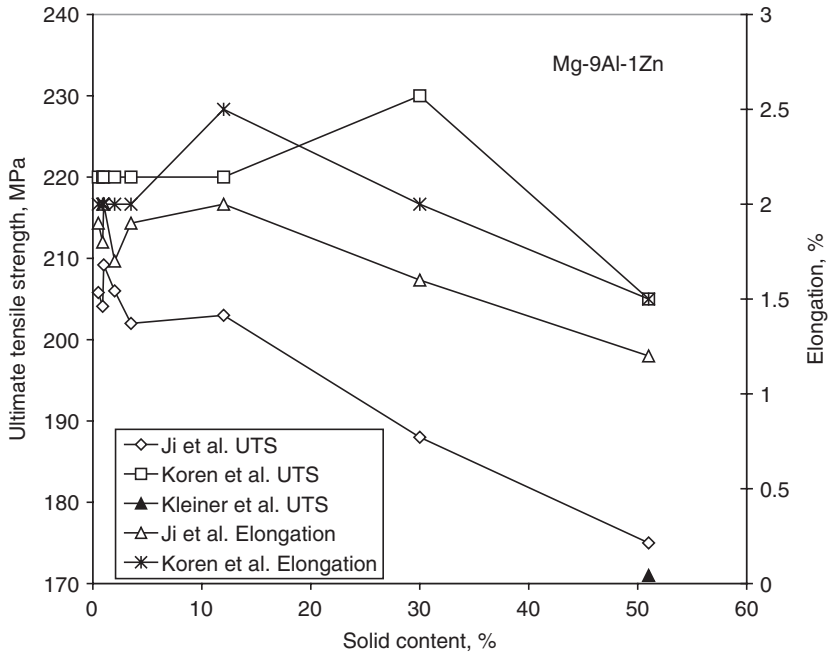

Fig. 10.19 The tensile and elongation data versus solid content achieved for Mg–9Al–1Zn alloy processed by other semisolid techniques: Ji et al.—twin screw rheomolding [14]; Koren et al. — billet casting [15]; Kleiner et al.—new rheocasting [19]

$$HV = 64\left(1 - f_s\right) + \left(44 + 190d^{-1/2}\right) f_s \tag{10.11}$$

According to the same authors [16], the ultimate tensile strength σ_{UTS} is expressed as:

$$\sigma_{UTS}(MPa) = 124\left(1 - f_s\right) + \left(72 + 547d^{-1/2}\right) f_s \tag{10.12}$$

Where: d in equations 10.11 and 10.12 is the grain size expressed in μm; f_s represents the solid fraction.

The authors conclude that the empirical equations can correctly predict the properties of rheocast magnesium alloys obtained under different processing conditions, for example by changing the stirring temperature and stirring rates.

10.10 Modification of Mechanical Properties by the Post-Molding Heat Treatment

The high integrity of alloys after semisolid processing makes them heat treatable. Since the semisolid structure is different than after casting of overheated melts, in addition to conventional processing routes (T5, T6 treatments), new treatments may also be effective.

The exposure of thixocast Mg–9Al–1Zn at temperatures from 395 °C to 435 °C substantially modified the structure through redistribution of solute elements and partial dissolution of the $Mg_{17}Al_{12}$ phase [17]. As a result the new grains were formed in the previous eutectic zone. Based on age-hardening measurements the solution temperature was indicated to be closer to 435 °C than 415 °C.

The influence of heat treatment on rheo-diecast Mg–9Al–1Zn alloy shows that during a solution annealing at 413 °C four processes are active including dissolution of the $Mg_{17}Al_{12}$ phase, formation of fine grain structure, changes in phase morphology and grain coarsening [18]. During subsequent aging at 216 °C, both types of precipitation take place: discontinuous at the grain boundary and continuous inside grains. The age hardening effect is accelerated as compared to die cast alloy and a finer and more uniform αMg grain is responsible for this behavior. The T4 solution treatment improves ductility but decreases strength. On the other side, T6 aging increases tensile strength but reduces yield strength and ductility. A new treatment, comprising direct aging of rheocast structure at 365 °C for 2 hr increases ductility while maintaining the tensile strength.

10.11 Summary

Although the tensile properties of an injection molded Mg–9Al–1Zn alloy are affected by the unmelted fraction, the alloy's tensile strength and elongation remain relatively stable at the level of 240 MPa and 4.5%, respectively, up to approximately

20% of the primary solid. A further increase in the primary solid content resulted in a gradual reduction in both strength and ductility to the level of 170 MPa and 3% respectively for the solid fraction of 40%. An apparent reduction in tensile properties, caused by an increased volume of the primary solid, is compensated for by the increased strength of the primary solid particles due to an inhomogeneity of the internal microstructure and the reduced size of αMg grains within the eutectic mixture.

The fracture mechanism and resultant morphology of the decohesion surface of tensile bars depend on the primary solid content within the thixotropic microstructure. While for solid fractions below 20% the intercrystalline cracking of the eutectics is accompanied by the transcrystalline cracking of the primary solid particles, for large solid fractions over 40% a decohesion along the particle-matrix interface is predominant. It looks like for a high volume fraction of the primary solid, the interface between the primary solid and the eutectic mixture is a key factor that controls the tensile properties of an injection molded Mg–9Al–1Zn alloy.

References

1. Loue WR, Suery M (1995) Microstructural evolution during partial remelting of Al-Si7Mg alloys. Materials Science and Engineering A 203(1):1–13
2. Chen CP, Tsao CYA (1998) Semisolid deformation of non-dendritic structures: 1-phenomenological behaviour. Acta Materialia 45(5):1955–1968
3. Czerwinski F et al (2001) Correlating the microstructure and tensile properties of a thixomolded AZ91D magnesium alloy. Acta Materialia 49(7):1225–1235
4. Aghion E, Bronfin B (1997) In Proceedings of 3rd International Magnesium Conference. The Institute of Materials, London, England, pp 313
5. Tissier A, Apelian D, Pegazoni G (1990) Journal of Materials Science 25:1184
6. Li Y, Langdon TG (1999) Creep behaviour of an AZ91D magnesium alloy reinforced with alumina powder. Metallurgical and Materials Transactions A 30(8):2059–2066
7. Ghosh DS et al (1995) In Proceedings of the 34th Conference of Metallurgists CIM, Vancouver, Canada, CIM, pp 481
8. Carnahan R (1994) Thixomolded magnesium: Its status and model relating structure and solid state properties. In Proceedings 3rd International Conference on Semisolid Processing of Alloys and Composites. Institute of Industrial Science, Tokyo, Japan, pp 1–11
9. Dieter GE (1976) Mechanical Metallurgy. McGraw-Hill, New York
10. Galiev A, Kaibyshev R (1996) The Physics of Metals and Metallography 81:451
11. Jones B (1991) Formation of microstructure in rapidly solidified materials and its effect on properties. Materials Science and Engineering A 137:77–85
12. Czerwinski F, Szpunar JA, Zielinska-Lipiec A (1999) Thermal instability of Ni electrodeposits applied in replication of optical recording devices. Acta Materialia 47(8):2053–2566
13. Shaw C, Jones H (1997) The contribution of different alloying additions to hardening in rapidly solidified magnesium alloys. Materials Science and Engineering A 226–228:856–860
14. Ji S (2002) Twin screw rheomolding of AZ91D magnesium alloys. In Y Tsutsui, M Kiuchi, K Ichikawa (eds) 7th International Conference on Semisolid Processing of Alloys and Composites, National Institute of Advanced Industrial Science and Technology, Tsukuba, Japan, pp 683–688
15. Koren Z et al (2002) Development of semisolid casting for AZ91 and AM50 magnesium alloys. Journal of Light Metals 2:81–87
16. Yim CD, Shin KS (1999) Interrelationship between microstructure and mechanical properties of rheocast AZ91D magnesium alloys. In F. Klein (ed) Proceedings of the 7th Magnesium Automotive Seminar, Allen, Germany, IMA, pp 333–339

17. Cerri E, Cabibbo M, Evangelista E (2002) Microstructural evolution during high-temperature exposure in a thixocast magnesium alloy. Materials Science and Engineering A 333:208–217
18. Wang Y, Liu G, Fan Z (2006) Microstructural evolution of rheo-diecast AZ91D magnesium alloy during heat treatment. Acta Materialia 54(3):689–699
19. Kleiner S et al (2002) Microstructure and mechanical properties of squeeze cast and semisolid cast Mg-Al alloys. Journal of Light Metals 2:277–280

11
Semisolid Extrusion Molding

11.1 Introduction

Extrusion is the plastic deformation process by which a metal is forced to flow by compression through the die orifice of a smaller cross-sectional area than that of the original billet. Since the material is subjected to compressive forces only, the extrusion is an excellent method for breaking down the cast structure of the billet with little or no cracking. Although room temperature (cold) extrusion is also exercised, most metals are extruded hot when the billet is preheated to facilitate plastic deformation. So far, commercial extrusion applications do not utilize preheating materials above the solidus temperature to enter the semisolid range.

Of all semisolid technologies, injection molding provides the largest flexibility in terms of the processed solid contents. This feature is attributed to the fact that injection molding combines the slurry making and component-forming operations into one step, and the slurry is accumulated in the direct vicinity of the mold gate. Conventional injection molding is limited to a solid content of 60%. The major cited obstacles to using high-solid contents are freezing of the premature alloy and incomplete filling of the mold cavity [1]. It was revealed that a drastic increase in solid content above 60% transforms the flow through the machine nozzle, runners, and mold gate into the mold cavity, thus activating an intense interaction between solid particles within the slurry, which facilitates mold filling [2]. As a result, a novel processing technique was developed as a combination of semisolid processing, extrusion and injection molding. The features of this technique, termed semisolid extrusion molding (SSEM), are described in this chapter.

11.2 General Features of SSEM

Major questions accompanying semisolid processing at ultra-high solid contents are as follows: (i) What is the minimum liquid required to create a semisolid thixotropic slurry and (ii) at what pre-heating temperature will this state be attained? Theoretical calculations predict a maximum solid fraction of 64% as the random

F. Czerwinski, *Magnesium Injection Molding*.

packing limit for spheres, and even small deviations from the spherical shape substantially depress this limit [3].

11.2.1 Deformation Behavior of Slurries at Ultra High Solid Contents

In general, thixotropic alloys are considered as deformable semi-cohesive spheroidal solids saturated with liquid. When applying a macroscopic stress to a thixotropic material, stress is carried by both the solid and liquid phases. The literature data on mechanical behavior of thixotropic alloys at very high solid contents is only available for aluminum alloys. Experiments under unconstrained compression of AA2014 and Al–4Cu rheocast alloys at f_s>0.6 revealed that at all stages of deformation the resistance of semisolid alloy was related to [4]:

(i) electroplastic deformation of grain contacts;
(ii) destruction of cohesive bonds between solid grains;
(iii) resistance of the flow of liquid relative to the solid;
(iv) resistance to grain re-arrangement.

Mechanisms (i) and (ii) are particularly active at early stages of deformation. This indicates that initial resistance to flow depends on the cohesion of solid grains not their yield strength. The transition from localized deformation and damage to macroscopically homogeneous and damage-free deformation occurs at solid content of the order of 80% and is affected by the alloy nature and deformation conditions (Fig. 11.1). This deformation behavior is unique for thixotropic structures. Alloys with dendritic features cannot be deformed by grain re-arrengement due to significant geometric interference of solid features, leading to high flow resistance.

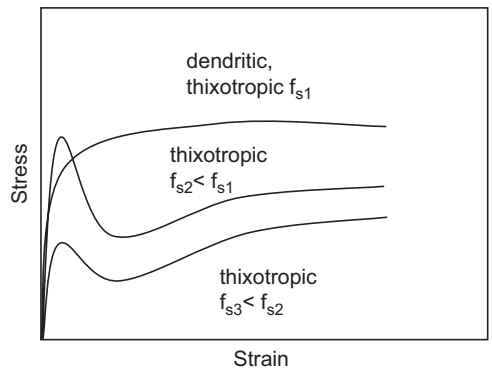

Fig. 11.1 The typical shape of stress–strain curves for dendritic and thixotropic alloys. Solid fraction f_{s2} represents the upper limit of processability of an alloy in semisolid state

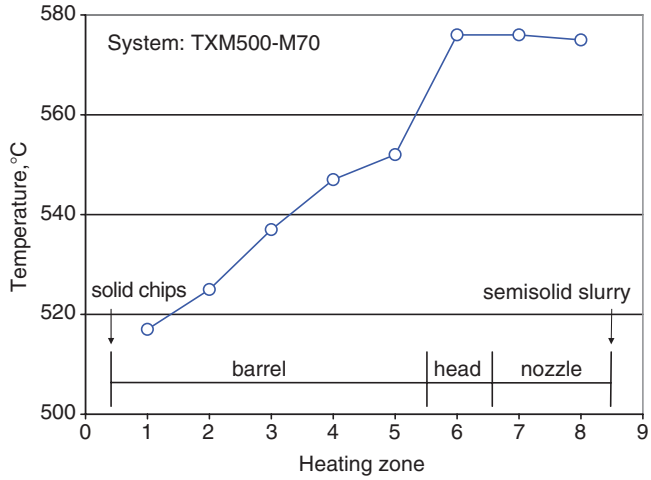

Fig. 11.2 The temperature distribution along the machine barrel and nozzle, designed to achieve over 75%–85% of an unmelted fraction within the Mg–9%Al–1%Zn alloy. Thermocouples were located deep inside the barrel and nozzle walls [8]

11.2.2 Temperature Requirements for SSEM

The melting process of an alloy starts during heating when the solidus temperature is exceeded. The ultra-high solid content requires relatively low processing temperatures. Due to the shape of the solid versus temperature graphs, the process control is generally easier than that for low-solid contents. This is because relatively large changes in temperature cause rather small variations of solid fractions. The complication arises since the alloy is heated while conveyed through a barrel exhibiting a temperature profile. A profile example used to process Mg–9Al–1Zn alloy at solid contents exceeding 70% is shown in Fig. 11.2.

11.3 Mold Filling Characteristics and Part Integrity

11.3.1 Flow Behavior of the High-Solid Slurries

An amount of alloy required to fill the mold cavity of a clutch-clamp housing is approximately 582 g, which is divided between the part of 487 g and the sprue with runners of 93 g. The mold design predicts one gate around the internal diameter of the part with a total opening area of 221.5 mm^2. The mold filling parameters, calculated for screw velocities of 2.8, 1.4 and 0.7 m/s, are summarized in Table 11.1. Since the calculation involves an assumption regarding the efficiency of a non-return valve, the screw velocity is used further as it represents the directly

Table 11.1 The mold filling characteristics at various velocities of the injection screw. The calculation was performed for the gate opening area of 221.5 mm^2 under assumption of 100% efficiency of a non-return valve [8]

Screw velocity	Alloy velocity at the gate	Mold cavity filling time
m/s	m/s	s
2.8	48.65	0.025
1.4	24.32	0.050
0.7	12.16	0.100

measured value. While combined with gate dimensions it allows estimating other parameters required for analyzing the injection process. For the existing gating system, an injection at the screw velocity of 2.8 m/s produced compact parts with high surface quality and precise dimensions (Fig. 11.3a). Experiments with partial filling revealed that at this screw velocity the slurry flow was rather turbulent (Fig. 11.3b). A 50% reduction in the screw velocity did not allow the slurry to completely fill the mold cavity (Fig. 11.3c). The part weight was 74% of that in Fig. 11.3a, and major unfilled areas were situated at the outer edge. Although the flow front showed some improvement in comparison with that recorded at a velocity of 2.8 m/s, it was still non uniform (Fig. 11.3d). This is especially clear in thin-wall regions between ribs, where local flow fronts moving from thicker ribs solidified instantly after contacting the mold surface. A further reduction of the screw velocity to 0.7 m/s resulted in only partial filling of the mold cavity (Fig. 11.3e). The part weight of 381 g corresponds to 66% of the fully compact product. The component ribs with their larger cross section still acted as runners distributing alloy to thin wall areas, but the flow front, including thin wall regions, was relatively uniform (Fig. 11.3f).

11.3.2 Part Integrity

A measurement of the internal porosity by the Archimedes method does not have high accuracy, and results should be interpreted with caution. However, significant differences between samples measured here make it useful for comparison purposes. A summary is given in Table 11.2, where data is listed separately for the part and for sprue with runners. The porosity of 2.3%, obtained for parts manufactured under full injection conditions, is at the acceptance level by industry standards. A reduction in the screw velocity to 1.4 m/s caused an increase in the part porosity to over 5%, which is generally beyond the acceptance limit. Surprisingly, further reduction in the screw velocity to 0.7 m/s led to a very low porosity at a level of 1.7%. This also applied to sprue and runners which, according to the Archimedes test, were almost completely dense. The porosity of parts manufactured under partial injection conditions was significantly higher, reaching two-digit numbers for the screw velocity of 1.4 m/s. An exception was the screw velocity of 0.7 m/s, which, similarly to conditions of full injection, created low porosity within both the part and sprue.

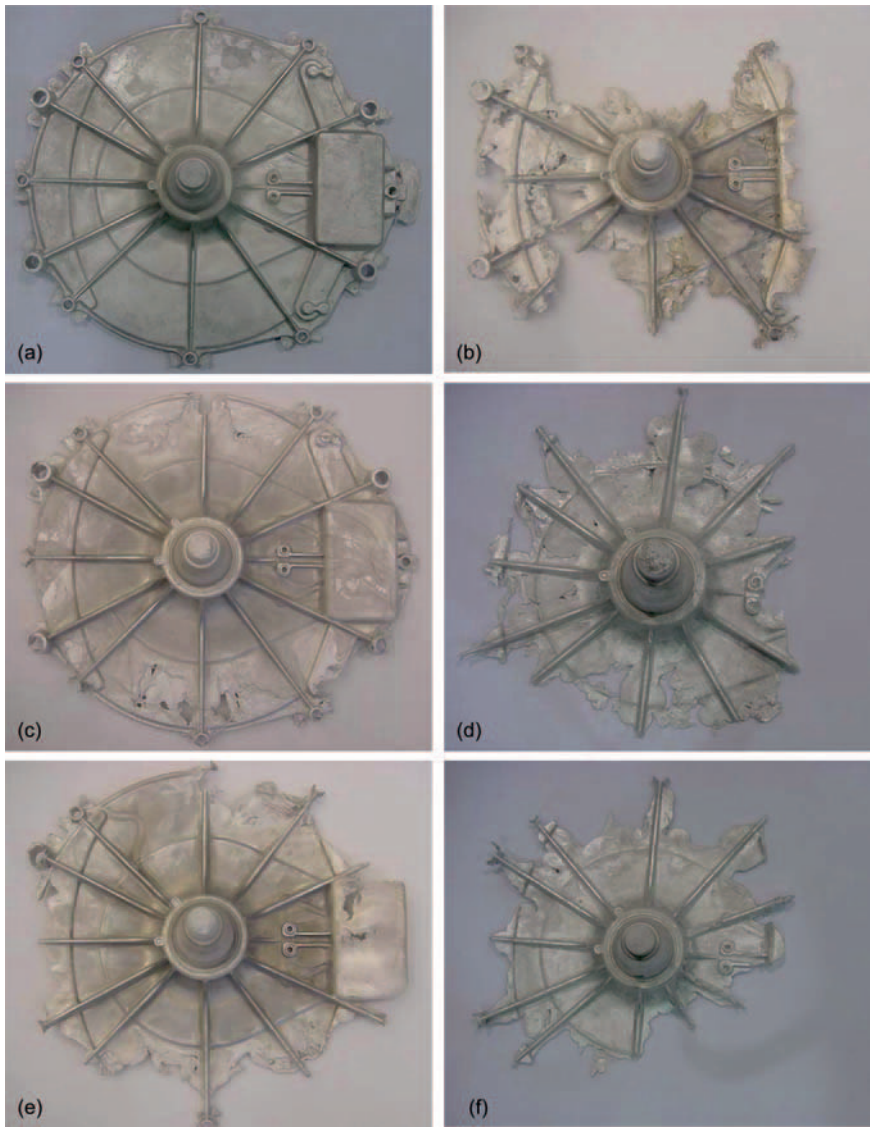

Fig. 11.3 Top views of the clutch clamp housing, injection molded at various screw velocities and shot weights: **a** velocity of 2.8 m/s, full shot, part weight of 582 g; **b** velocity of 2.8 m/s, half shot, part weight of 308 g; **c** velocity of 1.4 m/s, full shot, part weight of 428 g; **d** velocity of 1.4 m/s, half shot, part weight of 263 g; **e** velocity of 0.7 m/s, full shot, part weight of 381 g; **f** velocity of 0.7 m/s, half shot, part weight of 268 g. The maximum part diameter is approximately 290 mm [8]

While the general porosity value gives overall part assessment, the porosity distribution is crucial, since it may localize the failure. Therefore, the porosity content should be verified metalographically on cross sections in critical locations. An image of the part

Table 11.2 The weight and porosity of parts produced at various velocities of the injection screw. The internal porosity was determined by the Archimedes method, described in ASTM D792-9 [8]

	Screw velocity	Alloy weight		Alloy porosity	
		Total	Part	Part	Sprue with runners
Injection size	m/s	g	g	%	%
Full injection	2.8	582	462.6	2.3	4.6
	1.4	428	414.3	5.3	6.1
	0.7	381	334.3	1.7	0.2
Partial injection	2.8	308	177.8	7.4	2.6
	1.4	263	172.9	17.4	7.7
	0.7	268	183.6	3.1	4.0

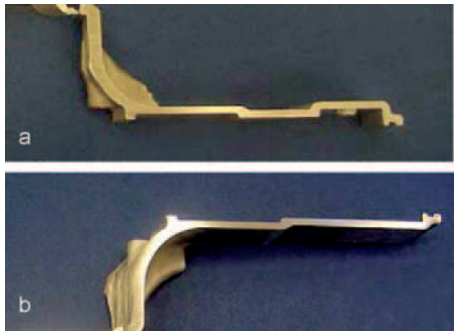

Fig. 11.4 Cross-sectional views of the clutch clamp housing: **a** full injection, screw velocity of 2.8 m/s; **b** full injection, screw velocity of 0.7 m/s

cross section, filled at a screw velocity of 2.8 m/s, is shown in Fig. 11.4a. The part is compact, and no localized porosity is revealed at the macroscopic scale. The same conclusion is valid for the part molded at a screw velocity of 0.7 m/s (Fig. 11.4b). A visual assessment does not permit distinguishing the difference between both cross-sections.

The porosity within parts injected at 1.4 m/s is described later at the microscopic scale. The location and morphology of pores are shown in Fig. 11.5. The predominant type of porosity represents an entrapped gas, presumably argon, used to shield the alloy against oxygen within the barrel. Despite the low content of the liquid phase, there is also shrinkage porosity, formed as a result of contraction during solidification. While shrinkage is usually associated with larger islands of eutectics, entrapped gas bubbles are more randomly distributed, sometimes being seen between solid particles.

11.3.3 Mold Filling Time as the Critical Factor

An important difference between magnesium and aluminum alloys is in their density and heat content. The lower density of magnesium relative to aluminum means

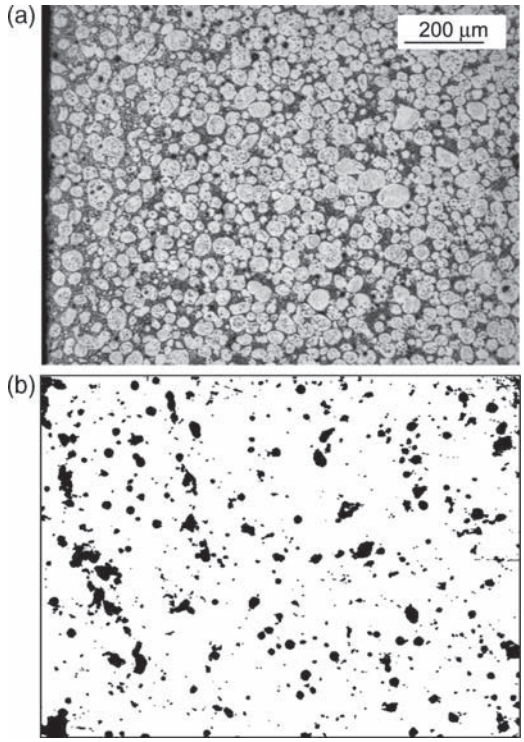

Fig. 11.5 The microstructure in the near surface region of parts molded at: **a** screw velocity of 0.7 m/s and **b** 1.4 m/s under conditions of full injection. A surface in **b** is shown as polished without etching [8]

that inertia is less, and for the same metal pressure a higher flow speed results. It will hence take a shorter time to fill a mold with liquid magnesium than with aluminum. The exact changes introduced by the solid fraction are so far not known. At the same time, a difference in density, accompanied by similar specific heat capacities of magnesium (1.025 kJ/kg K at 20 °C) and Al (0.9 kJ/kg K at 20 °C), means that the heat content of a magnesium part of the same volume will be substantially lower, and the metal will solidify faster than aluminum. The latter factor is of particular importance during the semisolid processing of magnesium alloys, particularly those with a very high umelted fraction. In this case, the solidification time is very short because only a part of the alloy is liquid. According to some estimations, for a 25%–50% solid fraction, the solidification lasts only one tenth of the time that is required in high-pressure die casting. For the content of the 15%–25% solid investigated here, this time should be even shorter. The filling time of 25 ms found for the screw velocity of 2.8 m/s does not entirely support this expectation, since it is of the same order of magnitude as the values obtained for die casting (previous Table 11.1). Accidentally, the calculated gate velocity of 48.65 m/s also falls into a range of 30 m/s to 50 m/s, being typical for magnesium die casting. A lack

of drastic differences could be explained while assuming the generation of heat during mold filling. Such a possibility is indicated by microstructural changes.

11.3.4 Role of the Flow Mode

It is well established that during semisolid processing, the slurry should exhibit laminar flow behavior, and there are many benefits associated with it. Moreover, the higher the solid content in the slurry, the higher the injection velocity it is possible to employ before reaching the turbulent flow. The practice demonstrates, however, that despite the extremely high solid content within the slurry, its flow mode might be quite turbulent. Such a flow regime not only creates an internal porosity (Table 11.2), but also increases the solidification rate by reducing the heat flow from the barrel through the continuous alloy stream. For existing gates, however, the laminar flow had to be sacrificed by applying high injection velocity in order to fill completely the mold cavity and manufacture high quality parts. The outcome of this test indicates that injection molding exhibits flexibility in terms of the flow mode of the slurry. A significant difference in porosity between partially and completely filled parts at an injection velocity of 2.8 m/s suggests that the porosity generated during mold filling was reduced during final densification. It is natural to expect that the semisolid state of the magnesium alloy is a prerequisite for successful densification. It should be mentioned at this point that due to the low heat content of the magnesium part, final densification should not be compared directly to the pressure intensification act during the final stage of aluminum die casting. At an intermediate velocity of 1.4 m/s, neither the flow mode is laminar, nor the injection velocity high enough to completely fill the mold cavity. When the laminar flow mode is finally achieved at 0.7 m/s, the alloy solidifies after filling only 66% of the mold. The low porosity obtained for partially filled parts shows that the porosity is not created while filling the mold cavity under the laminar flow regime. Moreover, it indicates that the slurry residing within the machine barrel does not contain excessive amounts of entrapped gas used for its shielding against oxidation.

11.4 Structural Transformations During Molding and As-Solidified Structure

11.4.1 Structural Transformations During SSEM

The summary of major structural transformations during semisolid extrusion molding is shown in Fig. 11.6. As a result of interaction with the chipping tool, the alloy experiences cold work. The chips' deformation is inhomogeneous with an increased

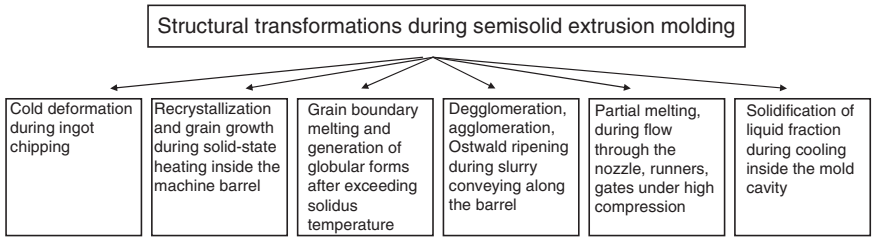

Fig. 11.6 The schematics of alloy transformation steps active during SSEM [9]

strain in the immediate location of the second-phase particles. As proven by chips melting outside the molding system, dendritic structure is disintegrated completely by the solid-state reaction. During heating inside the machine barrel, the structure recrystallizes by nucleation and the growth of equiaxed grains. The second phase, intermetallic compound $Mg_{17}Al_{12}$, is distributed mainly along grain boundaries. In addition, grain boundaries are enriched in the solute element Al. After exceeding the solidus temperature, the melting starts at grain boundaries, leading first to the generation of equiaxed, then globular solid particles, surrounded by the liquid metal.

Thus, during further conveying of the slurry along the barrel, the globular structure of the unmelted phase experiences breakdown and agglomeration due to the combined effect of external heat and strain. As a result of diffusion, the solid phase is also subjected to coalescence and Ostwald ripening, as discussed in detail in Chap. 9. After melting of the grain boundary network, the semisolid slurry, with globular solid particles, is essentially ready for the component-forming step, i.e., the injection into a mold cavity.

11.4.2 General Microstructure After Solidification

The microstructure of an alloy with ultra high-solid content is substantially different from that obtained for low- and medium-solid fractions. The major component, i.e., primary αMg, practically occupies the entire volume, while the eutectics as a mixture of secondary αMg and γ, are only distributed along particle boundaries and triple junctions. The microstructure is fine grained with an average diameter of αMg equal to 40 μm, being smaller than that reported previously for solid fractions below 60%.

A distribution of phases among microstructural constituents is shown in Fig. 11.7. As identified in Chap. 10 by the TEM/SAD technique, near globular particles with a bright contrast represent the αMg solid solution. The phase with a dark contrast is intermetallics γ ($Mg_{17}Al_{12}$). The distinct boundaries between globular particles are composed of eutectics, similar to the islands at the triple junctions. Under high magnification, a difference is revealed between the morphology of the eutectic

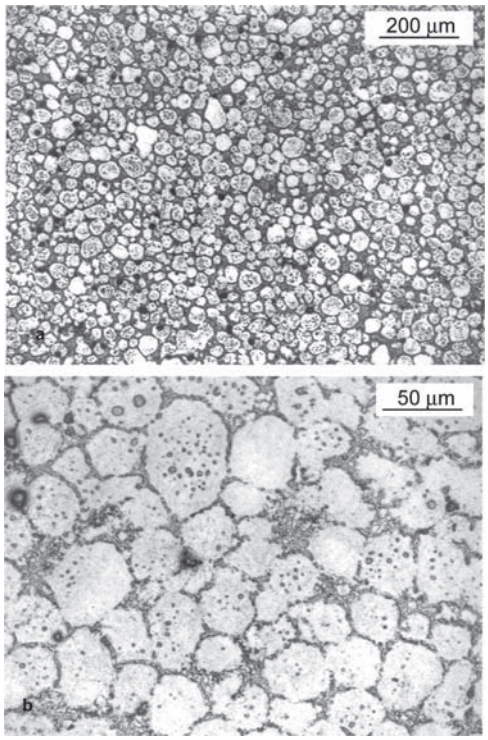

Fig. 11.7 The microstructure of the Mg9%Al1%Zn alloy, molded at 75% of the unmelted fraction. A planar view near the middle of a wall thickness [8]

constituents within thin boundary films and larger islands at triple-junctions. The difference refers mainly to the shape and size of the secondary αMg grains. The dark precipitates within solid particles appear to be pure intermetalics γ. A volume fraction of these constituents corresponds to the liquid phase during alloy residency within the barrel. The microstructure is essentially porosity free; the dark features in Fig. 11.7a resembling pores represent, in fact, Mg_2Si, as clearly seen under higher magnifications (Fig. 11.7b). This phase is considered an impurity that remained from a metallurgical rectification of the alloy, and it has a Laves type structure. Since Mg_2Si has a melting point of 1085 °C, its morphology was not modified during the processing of Mg alloy within the semisolid range.

11.4.3 Role of the Solidification Rate

One of several factors controlling the solidification rate is the part wall thickness. In order to verify changes experienced during flow through the mold gate, the

semisolid alloy was injected into a partly open mold. This caused significant increase in the gate size and wall thickness of the component, and as a result, only part of the mold cavity was filled. A typical microstructure for a roughly 5 mm thick section is composed of equiaxed grains with eutectics distributed along the grain boundary network (Fig. 11.8a). It reveals that the slower cooling rate created a microstructure that is essentially different from that obtained after rapid solidification. The role of the cooling rate, examined also on sprues, having larger size, shows that for thick walls the microstructure evolves much further than that in Fig. 11.8a. As depicted in Fig. 11.8b, not only grain boundaries show the evidence of their migration but also eutectics, distributed along grain boundaries, change morphology. The amount of former liquid within the alloy is significantly lower than the theoretical packing limit. In fact, it is slightly higher than the volume fraction of the eutectics of 12.4 % usually observed for Mg–9%Al [5]. This is caused by the fact that the near-globular forms evolve from the equiaxed grain precursor of recrystallized chips by melting of the γ phase at triple junctions and αMg/αMg grain boundaries. While solidifying slowly, the globular forms return to an equiaxed grain structure.

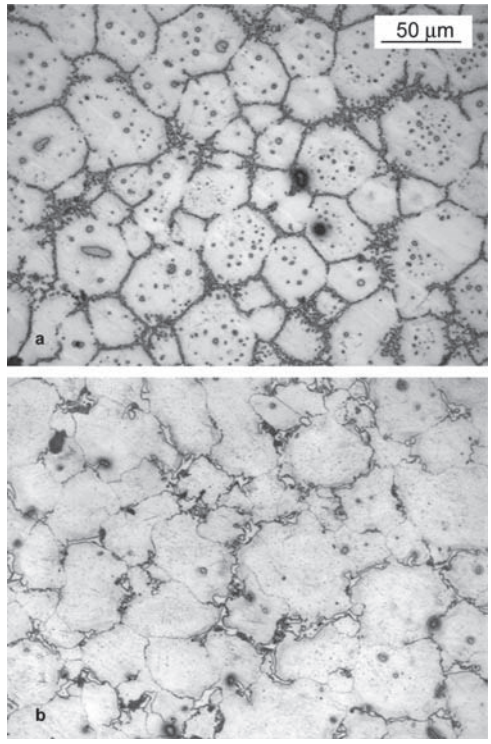

Fig. 11.8 The role of the cooling rate in the microstructural development of the Mg 9%Al 1% Zn alloy: **a** 500 µm thick section, molded under conditions of a partly open mold, screw velocity of 0.7 m/s; **b** a sprue section with a diameter of 15 mm, screw velocity of 2.8 m/s [8]

11.4.4 Phase Composition

An X-ray diffraction pattern, measured from the outer surface of a roughly 250 μm thick section of the molded part, is depicted in Fig. 11.9. In addition to the strong peaks of Mg, being characteristic of a solid solution of Al and Zn in Mg, several weaker peaks are present that allow for identification of the γ ($Mg_{17}Al_{12}$) phase. An analysis of the angle location of diffraction peaks did not reveal a significant shift due to the eventual change in the lattice parameter as a result of Al and Zn content. Due to an overlap of the major diffraction peaks for Mg_2Si (JCPDS 35-773) with peaks for Mg and $Mg_{17}Al_{12,}$ its presence cannot be unambiguously confirmed. In particular, the strongest Mg_2Si peak, located at 2θ of 40.121deg coincides with $Mg_{17}Al_{12}$. Two other peaks at 47.121 deg and 58.028 deg overlap with (102)Mg and (110)Mg, respectively. It seems that within the range examined, the only Mg_2Si peak is at 2θ of 72.117deg. A comparison of the peak intensities of the Mg-based solid solution with the JCPDS 4-770 standard indicates a random distribution of grain orientation within the area of X-ray beam penetration. Similarly, the intensities of $Mg_{17}Al_{12}$ peaks and JCPDS-ICDD 1-1128 standard do not indicate any preferred crystallographic orientation of the intermetallic phase. This imposes isotropic properties in all directions, a feature that is different from that reported for conventionally cast alloys where the skeleton of the solid dendritic phase is known for creating a crystallographic texture.

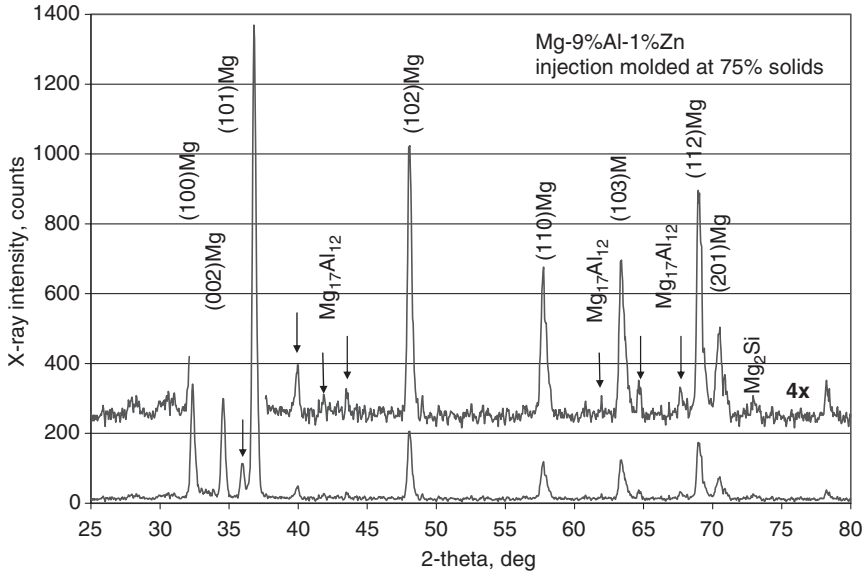

Fig. 11.9 X-ray diffraction pattern of the Mg9%Al1%Zn alloy, injection molded at 75% of the unmelted fraction. Analysis was conducted at room temperature using $Cu_{K\alpha}$ radiation [8]

11.5 Characterization of Primary Solid

For SSEM the primary solid particles represent the essential constituents of the alloy microstructure, and their stereological analysis is of primary importance.

11.5.1 Factors Affecting Solid Distribution

There are differences in the particle content between the runner and the part. Moreover, there is a segregation of particles across the wall thickness. The cross-sectional views of an approximately 1.5 mm wide surface zone within a part molded at the different screw velocities are shown in Fig.11.10. It is clear that more homogeneous distribution of the primary solid is observed within parts molded at lower screw velocities.

The quantitative description of the particle segregation is commonly assessed based on the stereological analysis, which is conducted on parts' cross sections. For detailed measurements of the solid distribution as a function of the distance from the surface, a linear method is quite effective. The graph shows that the solid content within the essential portion of the part, molded at a screw speed of 0.7 m/s, was constant at the level of 75% to 85% (Fig. 11.11). The solid content within the runner is over 10% higher. Both the runner and the part itself contain less solid within the near-surface region. The depleted zone is approximately 400 µm wide, but essential reduction to a 10% to 15% solid takes place within a 100 µm thick film.

An important finding of microstructural analysis is a lower solid content within the part than within the runner. In particular, a monotonic reduction in solid content occurs as a function of the distance from the mold gate and these changes are mainly present in the near surface zone. Although cross-sectional segregation might be explained by changes in flow behavior due to differences in density between solid alloy (1.81 g/cm^3) and liquid alloy (1.59 g/cm^3), the lower average solid content within the part than in the runner points toward another mechanism. A segregation of the liquid phase often occurs when the solid grains deviate substantially from spherical form or when the fraction of the solid is large. Under such circumstances solid grains do not move together with the liquid, but the liquid phase moves substantially with respect to the solid grains. This explanation cannot be, however, entirely adopted because of another finding, indicating the dependence of the solid content on the injection screw velocity. It is more likely that the shear during the flow of the slurry with a high solid content through the gate and within the mold cavity generate heat, which, in turn, contributes to the alloy melting. It is reasonable to assume that without this factor it would be impossible to fill the mold. A similar observation was documented for the back extrusion of partially remelted semisolid Sn–Pb alloy where the extruded product had a higher liquid fraction than the non-extruded precursor [6]. Moreover, the liquid fraction in the extruded product was a function of the extrusion ratio and increased as the wall thickness decreased.

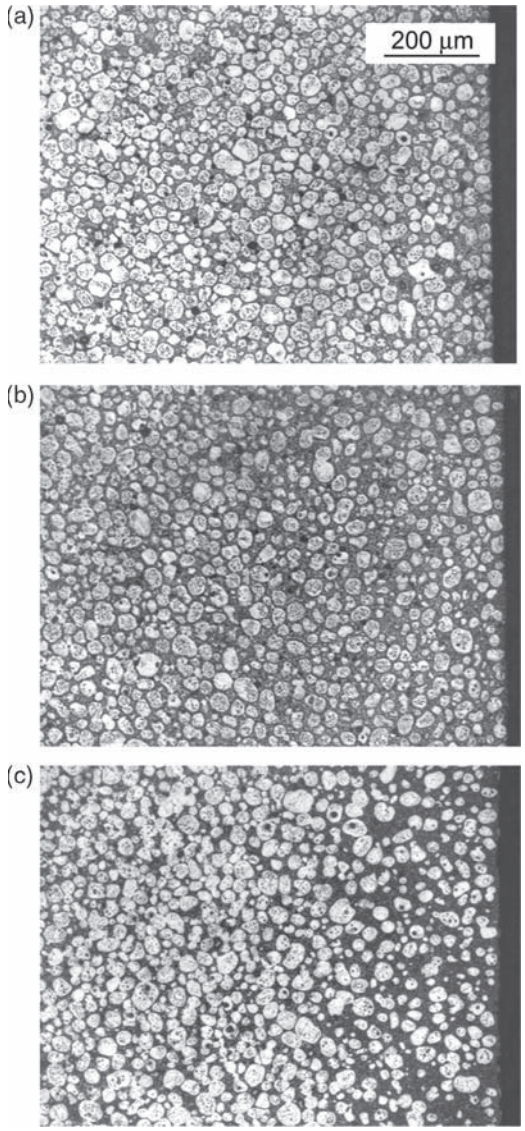

Fig. 11.10 The microstructure in the near surface region of a part manufactured at the screw velocity of 2.8 m/s under conditions of full injection: **a** runner, area 15 mm from the gate; **b** part, area 15 mm from the gate; **c** part, area situated 10 mm from the outer edge [8]

11.5.2 The Size of Solid Particles and Its Change During Processing

As a parameter characterizing size, the average Feret's diameter, measured on polished cross sections, was used. The average values and histogram of distribu-

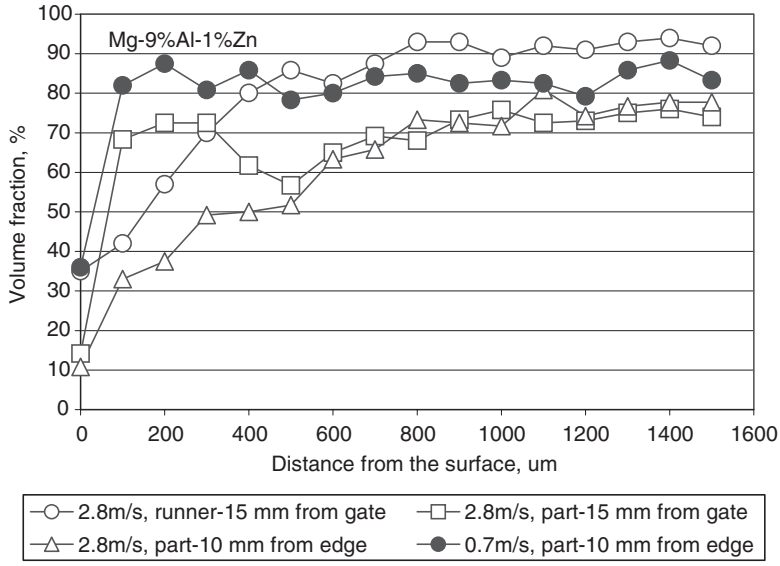

Fig. 11.11 A variation in the solid content as a function of the distance from the outer surface at various locations of the part and runners [8]

tions of particle diameter, measured at various locations within components, are depicted in Fig. 11.12. In this graph, additional data is included that characterizes the role of cycle time in controlling the solid particle size. The primary αMg particle size is affected by the residency time of the alloy at the processing temperature. For a shot size required to fill the 580 g part and the machine barrel size used here, the typical residency time is of the order 75 s to 90 s. An increase in residency time caused coarsening of the primary solid diameter, and for the residency time of 400 s, the average particle size increased by 50%. The histogram shows that a shift in the average value is accompanied by the increased contribution of large particles, with some of them having diameters over 100 μm. Such a change in the size distribution indicates the coarsening process taking place during slurry residency within the barrel.

As verified by experiments with varied cycle times, the short residency time of the alloy within the barrel is crucial in controlling particle size. First of all, the short residency of the alloy at high temperatures within the solid state prevents grain growth following recrystallization. Since there are no effective blockades which would hinder migrating boundaries in the Mg–9%Al–1%Zn alloy, the grains grow easily. Then, solid particles grow while suspended in a liquid alloy. Residency in a semisolid state leads to the solid particle coarsening by mechanisms of coalescence and Ostwald ripening. It is expected that the short residency time, which reduces diffusion, would diminish the role of Ostwald ripening, and the coalescence should be considered to be the leading mechanism.

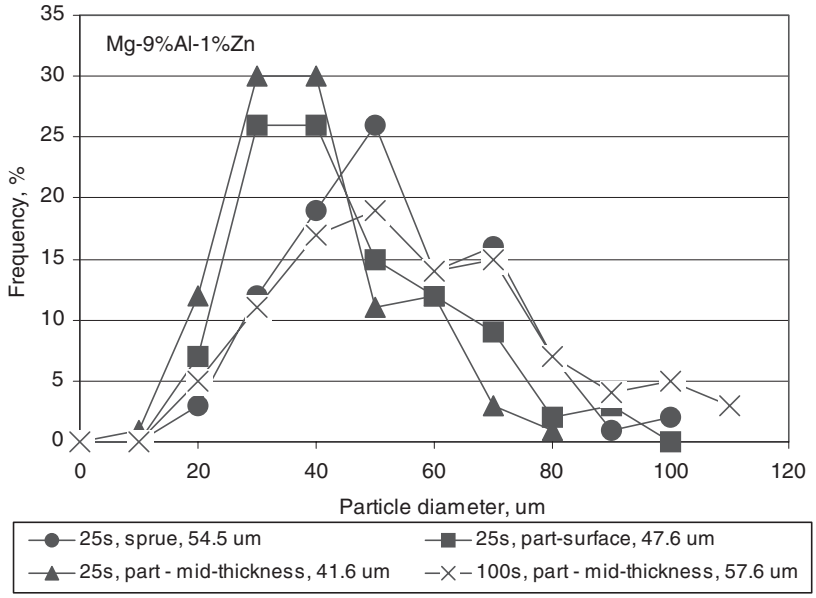

Fig. 11.12 The histogram of particle diameters for various locations within molded components. Numbers in the legend represent average values [8]

The role of shear is of particular importance here since, as opposed to low-solid fractions, there is a continuous interaction between particles that involves sliding between solid particles and their plastic deformation. The interaction between particles of the solid phase leads to structure breakdown due to shearing and collision but also to structure agglomeration due to bond formation among particles caused by impingement and reaction. It was postulated for Al semisolid processing that there is a critical shearing time below which the particle size decreased, and further increase in shearing caused a coarsening of the particles [7]

11.6 Application Areas for SSEM

Among other benefits associated with SSEM, two relate directly to the low processing temperature:

(i) minimized shrinkage;
(ii) maximized energy savings.

The advantage of minimum shrinkage is maintaining tight tolerances. This is important for thick-wall components. The experiments described here were designed to use the existing gating system with its geometry and dimensions in order to investigate the effect of processing parameters. A defined requirement of

the short time for mold filling and the simultaneous laminar flow mode suggests the modification necessity of the gating system. The experiments further point to the cold sprue as the possible obstacle with the transport of the slurry to the gates. It seems that a conventional approach, using large runners to prevent premature freezing of the alloy, does not provide a satisfactory solution for ultra-high-solid content, and some novel ideas should be attempted.

11.7 Summary

The SSEM represents a novel processing technique that can be successfully applied for manufacturing components with varying geometry and wall thickness. The mold filling time represents the primary factor controlling the SSEM of magnesium alloys at ultra-high contents of the unmelted phase. The process exhibits flexibility in terms of the slurry flow mode during the mold filling. As a result, highly dense parts are obtained under turbulent flow conditions unless the injection velocity is high enough to preserve the semisolid state until final densification. A laminar flow of the slurry, occurring for lower injection velocities, creates highly dense structures at all stages of the mold filling, and the final densification is not critical for microporosity reduction.

References

1. Carnahan RD (ed) (1999) in Avedesian MM and Baker H (1999) Magnesium and magnesium alloys. ASM International, Metals Park, Ohio
2. Czerwinski F and Kadak D (2005) Process for injection molding semi-solid alloys, US Patent 6,892,790B2, 17 May 2005
3. Underwood EE (1970) Quantitative stereology. Addison-Wesley, New York
4. Tzimas E, Zavaliangos A (1999) Mechanical behaviour of alloys in the semisolid state at high solid content. Acta Materialia, 47:517–528
5. Uggowitzer PJ, Wahlen A (2000) in 6th Conference on Semisolid Processing of Alloys and Composites. Turin, Italy, p 429
6. Basner T, Pehlke R, Sachdev A (2000) Metallurgical and Materials Transactions A 31:57
7. Yang YS, Tsao CA (1994) Thixotropic behaviour and structure evolution of A356 alloy in the semisolid state. Scripta Metallurgica et Materialia 30:1541–1546
8. Czerwinski F (2005) The processing phenomena of semisolid Mg–9%Al–1%Zn alloy at ultra-high contents of the unmelted phase. Materials Science and Engineering A 392 (1–2):51–56
9. Czerwinski F (2004) Semisolid extrusion molding of Mg–9%Al–1%Zn alloys. Journal of Materials Science 39:463–468

12
Near-Liquidus Molding

12.1 Introduction

The injection molding system is well suited for processing alloys at tightly controlled temperatures. First, the slurry making and component forming operations are combined into one step and the slurry is accumulated in the direct vicinity of the mold gate. Second, the melt transfer from the barrel to the mold is enhanced by application of hot sprue and hot runners that convey the melt to the mold during injection and maintain it at processing temperatures between injection cycles. As a result, the flow distance between the slurry with a controlled temperature and the mold gates is reduced, thus minimizing a drop in temperature. Preventing heat losses has a particular meaning for magnesium alloys, known for their low thermal capacity and tendency to quick solidification, which disrupts the complete filling of the mold.

A novel method of net-shape forming that requires a precise control of the alloy's temperature, called near-liquidus molding (NLM) [1], is described in this chapter. The technique shows that tight control of the alloy's temperature within a narrow range around the liquidus level generates structures with high integrity and diminishes some disadvantages inherent for conventional casting, which utilizes superheated melts. The structural integrity and fine microstructure improves mechanical properties that for the magnesium alloys tested, exhibit a superior combination of strength and ductility.

12.2 Growth of Globular Structures by Nucleation

The essential step of semisolid processing is the creation of a slurry free of dendrites. When rheocasting was invented, it was believed that one had to break up the dendritic structure during the freezing process either by mechanical stirring or via other forms of agitation. Then, the fragments of dendrites within the melt volume are supposed to act as nuclei of new grains that transform to spheroids. Experimental evidence mounted during recent years seriously questions this mechanism. Direct observations of the solidification of transparent liquids with metal-like crystallization characteristics and numerical modeling suggest rather

F. Czerwinski, *Magnesium Injection Molding*.

that globular crystals form through direct nucleation from a liquid instead of from fragments of broken dendrites [2, 3].

In general, the morphology of a solid in the slurry is controlled by cooling, convection or their combination. The particular role in generating globular forms, however, is associated with the melt temperature. As shown by the casting practice, lowering the pouring temperature promotes the formation of equiaxed solidification structures [4]. When superheating is sufficiently low, the whole melt is undercooled, and copious heterogeneous nucleation takes place throughout it. This leads to complete elimination of the columnar zone in the casting and to the formation of fine equiaxed grains in the entire volume. A number of attempts were made to explain the mechanism of spherical growth in a supercooled melt. As we learned to better apply physics to explain experimental findings, we have come closer to answering the question: Is it dendrite fragmentation or heterogeneous nucleation that leads to dendrite-free structure?

12.2.1 Mullins–Sekerka Stability Criterion of Globular Growth

A general condition for a solidification to proceed is that the interface temperature falls below the melting point. The theoretical Mullins–Sekerka (M–S) criterion of an alloy with a very small undercooling, accompanied by a high saturation of nucleation sites, was earlier used to explain the mechanism of formation of non-dendritic structures [5]. It describes the morphological stability of a solid sphere growing in a uniformly supercooled melt while a perturbation in the spherical shape is introduced. The growth rate is controlled by the heat transfer from the solid–liquid interface. The following are approximations used in M–S theory:

(i) the bulk and interface properties are isotropic;
(ii) thermal fields are described by Laplace's equation;
(iii) solid–liquid interface is in the state of equilibrium.

According to the M–S theory the spherical shape is unstable if the radius exceeds the critical size R_c:

$$R_c = \left(7 + \frac{4k_s}{k_L}\right) r^* \tag{12.1}$$

Where:

k_S – thermal conductivity of solid magnesium at temperature T_m;
k_L – thermal conductivity of liquid magnesium at temperature T_m;
r^* – the critical nucleus radius defined by the classical theory of nucleation specified by the following expression:

$$r^* = \frac{2\gamma_{SL} T_m}{L_v \Delta T} \tag{12.2}$$

Where:

γ_{SL} – solid-liquid interfacial free energy of magnesium at temperature T_m;
L_v – latent heat of fusion per unit volume.

After substitution of thermochemical and physical data for Mg, the equation is created that describes the critical radius for spherical growth of magnesium crystal, R_c as a function of supercooling ΔT [6]:

$$R_c = \frac{4.84}{\Delta T}(\mu m) \tag{12.3}$$

As shown graphically in Fig. 12.1, for undercooling of the order of 0.2 K features with a size of roughly 25 μm will still grow as globular. While undercooling is raised to 1 K, only features with a size of about 5 μm will grow as globules. The larger sizes will transform into dendrites. Since Equation 12.3 does not consider a solute, it is strictly applicable to pure metals or systems with solute in front of the solidification interface homogeneously distributed.

12.2.2 Growth of Globular Forms During Non-Agitated Solidification

Progress in understanding globular growth during partial crystallization was achieved by numerical modeling. The modeling allows us to predict the morphology of a solidified alloy based on the solute re-distribution in solid and liquid phases and the solid's curvature effect. According to this approach the supercooling ΔT at the growing interface is expressed by [7]:

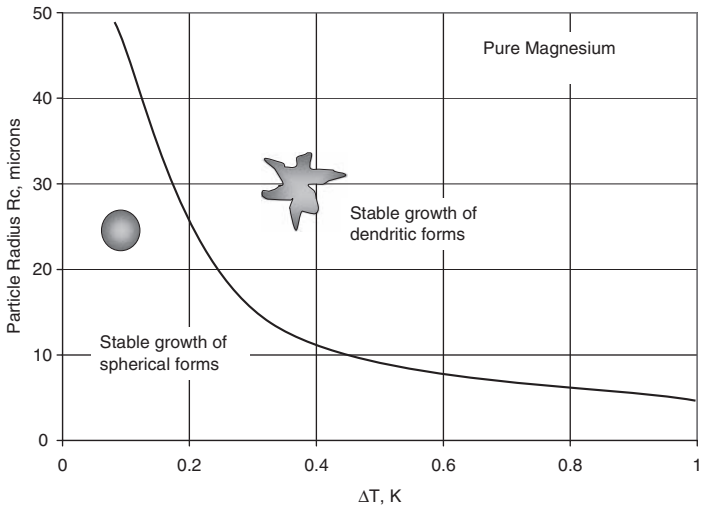

Fig. 12.1 The critical radius for spherical growth of a magnesium crystal as a function of ΔT [6]

$$\Delta T = \Delta T_L + \Delta T_C + \Delta T_R \tag{12.4}$$

Where:

ΔT_L – supercooling caused by the local temperature of the melt;
ΔT_C – supercooling caused by the local solute concentration (constitutional supercooling);
ΔT_R – supercooling caused by the curvature of the growing phase (Gibbs-Thompson effect).

A temperature reduction ΔT_R is related to additional free energy, required for the formation of a nucleus with a critical radius R:

$$\Delta T_R = \frac{2\gamma}{\Delta S}\frac{1}{R} \tag{12.5}$$

γ – solid-liquid interfacial free energy;
ΔS – solid-liquid entropy difference.

The growth model, based on formula 12.5 is shown in Fig. 12.2. When a protrusion with a very small radius $r \ll R$ is formed during early stages, the related ΔT_R will be larger than the sum of $|\Delta T_L + \Delta T_C|$, which will cause its dissolution. During the steady stage, when the primary solid continues to grow, the importance of the $|\Delta T_L + \Delta T_C|$ contribution increases. In order to minimize these two factors, forced convection or slow cooling should be introduced. When convection/diffusion are active, the solute distribution close to the solidification front is more homogeneous than during quick quenching. A resulting lower ΔT_C affects ΔT_R, leading to the higher interface stability.

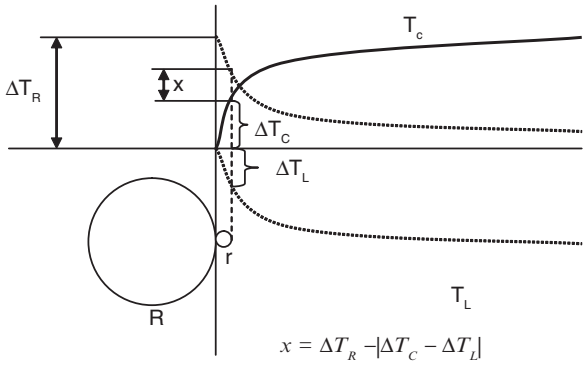

Fig. 12.2 The schematics showing the undercooling at the solid–liquid interface of a small nucleus. Under conditions specified, the particle–curvature effect compensates the constitutional and thermal undercooling [7]

12.2.3 Growth of Globular Forms Under Forced Convection

When any form of agitation is applied during solidification, convection occurs in the liquid. A consideration of the crystal growth mechanism under conditions of convection in the liquid explores the solidification velocity, which is mainly affected by cooling conditions and flow rate of the melt. An example of analysis utilizes the shape factor, defined as the ratio of the volume of sphere having the same volume of a grain and the volume of spheroid formed by encircling of tips of the grain [8]. Selecting the maximum section of the grain, the encircling radius is R_g and the radius of the circle having the same area with section area of the grain is R_s (Fig. 12.3a). The shape factor f_i is defined as [3]:

$$f_i = \left(\frac{R_s}{R_g} \right)^3 \tag{12.6}$$

$0 < f_i \leq 1$.

The larger values of f_i are typical for increased sphericity with a value of 1 for the perfect sphere.
The solidification velocity is affected by several factors such as latent heat and heat release conditions. After reaching steady stage the following assumptions control the growth:

(i) the growth conditions of all grains in the liquid are identical;
(ii) the melt temperature decreases uniformly.

The morphology of semisolid microstructure can be predicted by using mathematical models and computer simulation. As a result, the following equation was developed that relates the grain shape fraction f_i with growth conditions of the grain and describes the influence of growth conditions on grain shape [3]:

$$f_i = e^{-\frac{2v_{sol}}{v_{con}}} \tag{12.7}$$

Where:

v_{sol} is the solidification rate, i.e., flow rate of the fluid relatively to the growing surface;
v_{con} is the convection velocity.

According to the equation 12.7, an increase in convection rate and decreasing the solidification velocity lead to growth of more globular morphologies. Examples of shapes and corresponding f_i values are shown in Fig. 12.3b.

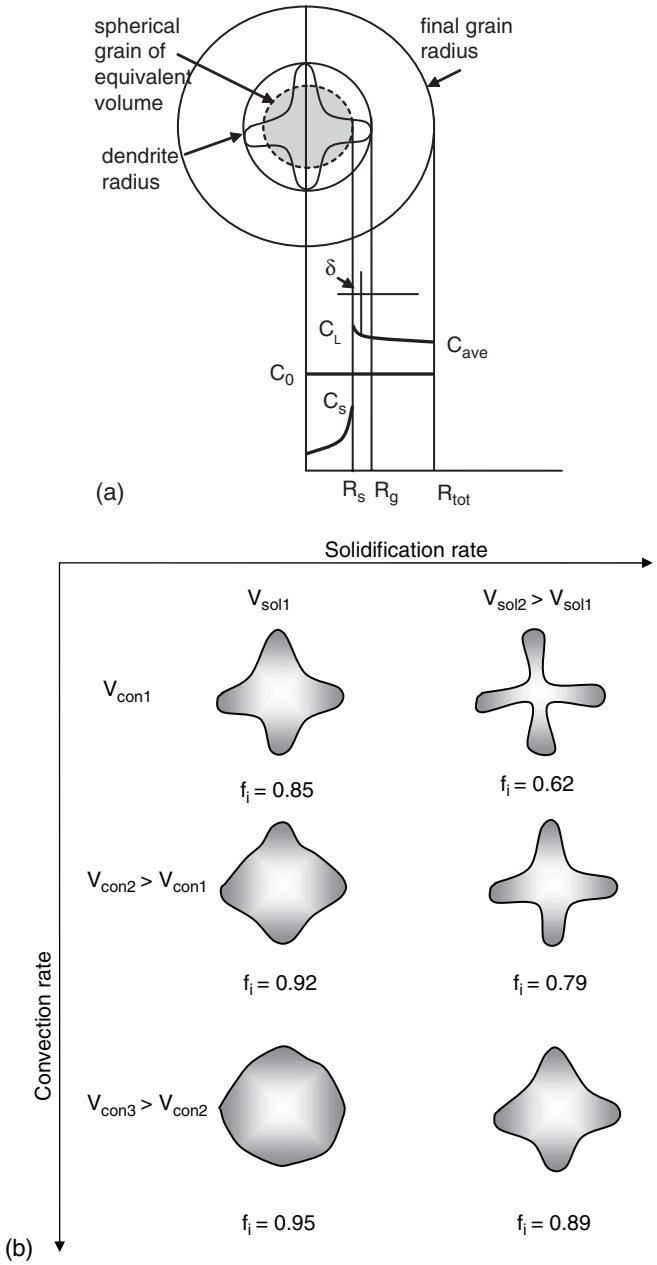

Fig. 12.3 Schematics of the solute distribution in front of the solid–liquid interface of a single grain **a**: R_{tot}— final grain radius; R_g—grain radius determined by dendrite tip; R_s—spherical grain having volume equal to dendrite; C_o, C_{ave}—initial and average solute concentration; C_s, C_L—solute concentration in solid and liquid at the solid-solid interface; δ—diffusion layer thickness. **b** Numerically simulated grain shape factor depending on the solidification rate V_{sol} and convection rate V_{con} [3]

12.3 The NLM Concept and Its Experimental Implementation

The concept of near-liquidus molding assumes that the alloy's temperature during injection is close to its liquidus value, so the solid content is very low. Although the primary assumption is to operate at solid fraction below 5%, there is a tendency to further reduce this limit. The objective of precise control of the temperature is to take advantage of copious nucleation within the entire melt's volume.

12.3.1 Technical Implications of the Preheating Range Required

Maintaining very low solid content requires tight temperature control. As opposed to the high solid fractions where relatively large temperature changes correspond to small variations in solid contents, in the near-liquidus range, small temperature variations cause relatively large changes in solid content. Thus, temperature control is very challenging. Although the basic route involves partial melting, the same solid fraction can be obtained after complete melting and subsequent re-solidification. As another option, the completely liquid alloy may be injected at a temperature slightly exceeding the liquidus. At present, there is still no quantitative assessment of that superheating increment. As a result, NLM represents a family of processing techniques with the common feature that the melt or slurry temperature is maintained in near-liquidus range. In all cases, the content and morphology of solid particles provide convenient verification.

12.3.2 Preheating Range for Mg–Al–Zn Alloys

The idea of NLM application for Mg–Al–Zn and Mg–Al alloys is shown in Fig. 12.4. When compared with conventional casting, the temperature is lower by 70 °C to 100 °C. Due to a deviation from the equilibrium state, both Mg–9Al–1Zn and Mg–6Al alloys, under typical solidification conditions, contain the $Mg_{17}Al_{12}$ phase. The phase forms by a eutectic reaction during sufficiently rapid cooling from the liquid as a result of coring. The presence of 1%Zn does not lead to the generation of new phases. According to the ternary phase diagram of Mg–Al–Zn, under equilibrium conditions, up to 4% of Zn, the phases present in ternary Mg–Al–Zn alloys are the same as those known from Mg–Al binary systems. If zinc exceeds 4%, a three-phase region is entered involving the ternary intermetallic phase ϕ. This compound leads to a eutectic reaction at a temperature of about 360 °C.

The Mg–9Al–1Zn and Mg–6Al alloys exhibit approximately 20 °C difference in liquidus temperatures. As shown in Fig. 12.5, in the sub-liquidus range, very small changes in the temperature result in substantial variations of solid fractions.

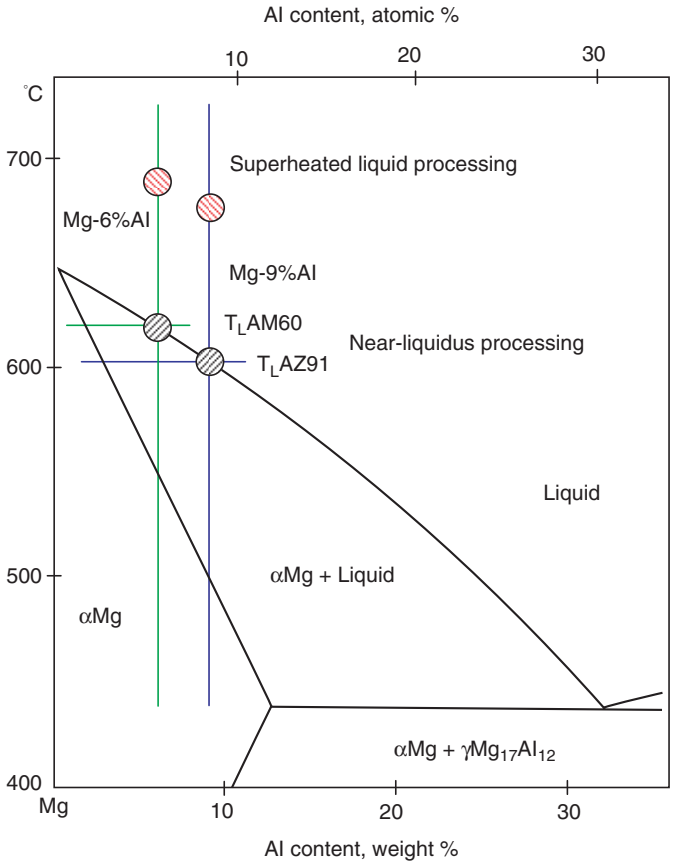

Fig. 12.4 The Mg-rich portion of Mg–Al phase diagram with marked chemistries and preheating temperatures of Mg–6Al and Mg–9Al–1Zn alloys

For Mg–9Al–1Zn alloy, an increase in solid from 0 to 5% takes place after reducing the temperature by 2 °C intervals below liquidus. The alloy of Mg–6Al is even more sensitive and the same variation in solid content from 0% to 5% requires a 1 °C reduction below the liquidus point. The values indicate why processing in the sub-liquidus range imposes a challenge on tight temperature control.

12.4 Microstructure After NLM

The microstructure comparison is conducted based on two commercial die cast alloys—Mg–9Al–1Zn and Mg-6Al—processed following NLM route and conventional high-pressure die casting, as detailed in Table 12.1.

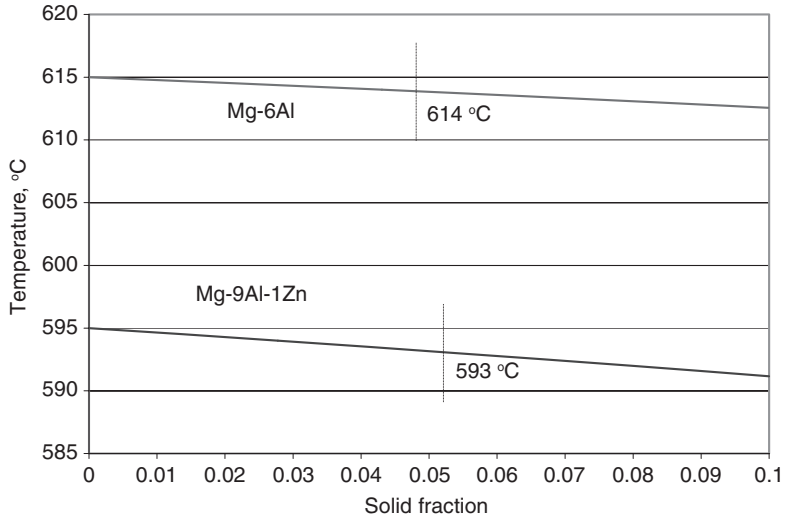

Fig. 12.5 The solid fraction versus temperature for sub-liquidus regions of Mg–9Al–1Zn and Mg–6Al alloys, calculated based on Scheil's formula. The approximate solid fractions corresponding to 614 °C and 593 °C for Mg–6Al and Mg–9Al–1Zn, respectively, are indicated [14]

Table 12.1 Chemical compositions of AZ91D and AM60B alloys processed by near-liquidus molding and die casting. Analysis was performed according to ASTM E1097-97 modified and E1479-99 standards. All values are in weight %. (*) Buehler Evolution 420D high-pressure die casting machine at Hydro Research Park, Porsgrunn, Norway

Processing technique	Alloy grade	Mold temp	Melt temp	Al	Zn	Mn	Si	Cu	Fe	Ni	Mg
Near liquidus molding	AZ91D (Mg–9Al–1Zn)	200		8.69	0.66	0.29	0.02	<0.01	<0.01	<0.01	Base
	AM60B (Mg–6Al)	200		5.82	<0.01	0.31	0.03	na	<0.01	<0.01	Base
Superheated liquid die Casting (*)	AZ91D (Mg–9Al–1Zn)	200	670 °C	8.70	0.58	0.24	0.017	0.0031	0.0021	0.0009	Base
	AM60B (Mg–6Al)	200	680 °C	6.00	0.008	0.27	0.017	0.0021	0.0006	0.0007	Base

12.4.1 Alloy's Structural Integrity

As factors affecting structural integrity of the alloy, only those defects that are inherent to the given processing method are discussed here. The defects that

are associated with incorrect injection and thermal settings or the specific part geometry are not considered. Due to very simple geometry of the mold (die), virtually no macro porosity occurred in the 5.9 mm and 6.3 mm sections of tensile bars (Fig. 12.6a). At the same time, however, there is a substantial difference in microstructure integrity after processing from a superheated liquid. Both alloy

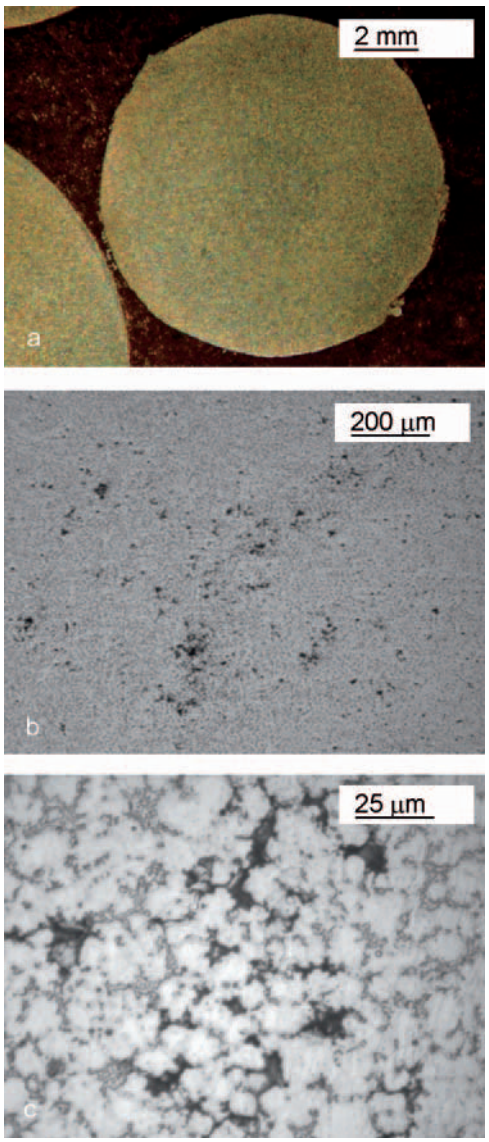

Fig. 12.6 The structural integrity of the Mg–9Al–1Zn alloy after die casting from a superheated state: **a** cross section of tensile bar, macro image showing no evident defects; **b** microscopic image with a general view of shrinkage porosity; **c** detailed view showing intercrystalline nature of pores formed during solidification shrinkage [14]

grades show shrinkage porosity, according to metallographic estimation at a level of several percent. The porosity has a form of randomly distributed individual gaps or their clusters (Fig. 12.6b). The pores occupy intercrystalline spaces and are surrounded by the last solidified phase, with the lowest melting temperature (Fig. 12.6c). Their typical size is of the order of 10 µm, so they are not easily detectable during macroscopic observations.

12.4.2 Matrix Morphology

The predominant or exclusive component of microstructures generated during molding in near-liquidus range is the solidification product of the liquid fraction (Fig. 12.7a). At low magnifications, the microstructure appears uniform with randomly distributed undissolved Mn–Al–Fe intermetallics and Mg_2Si inclusions, which originate from a metallurgical rectification. Due to their dark contrast, these phases may be misinterpreted as pores. The dominant component represents a divorced eutectic, where discontinuous precipitates of the $Mg_{17}Al_{12}$ compound

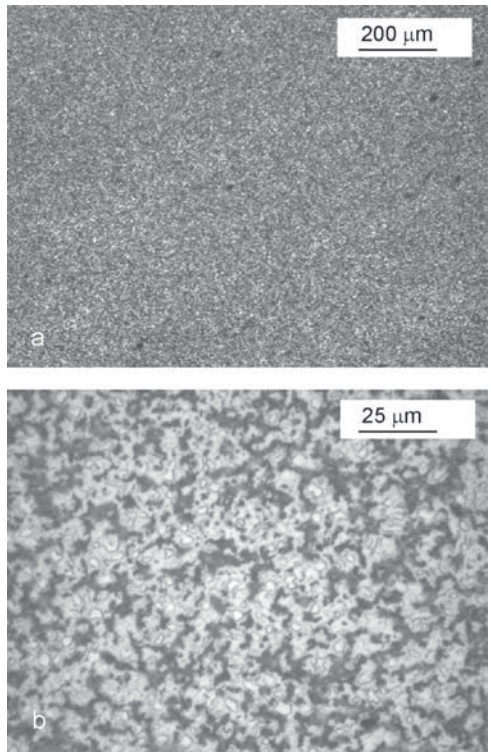

Fig. 12.7 The microstructure of Mg–9Al–1Zn alloy after near-liquidus molding at 0% solid: **a** general view, dark spots represent Mn–Fe–Al intermetallics; **b** details showing segregation within αMg and distribution of $Mg_{17}Al_{12}$ intermetallics [14]

decorate the boundaries of equiaxed αMg regions. At high magnifications, the αMg islands, with a size of the order of 20 μm, exhibit a distinct contrast caused by differences in chemistry (Fig. 12.7b).

12.4.3 Morphology of Solid Particles

In addition to the matrix, a negligible fraction of the primary solid phase is present (Fig. 12.8). For very low solid contents the optical microscope magnification may be too high to portray the representative (homogeneous) image and cannot be used directly to measure the solid content based on stereological principles. The solid's morphology depends on the thermal profile of the barrel; however, differences are less distinct than observed for high-solid fractions. When the alloys are preheated to sub-liquidus temperature they have the form of rough spheroids (Fig. 12.8b,c). The characteristic feature of the unmelted phase, observed during partial melting, i.e., the

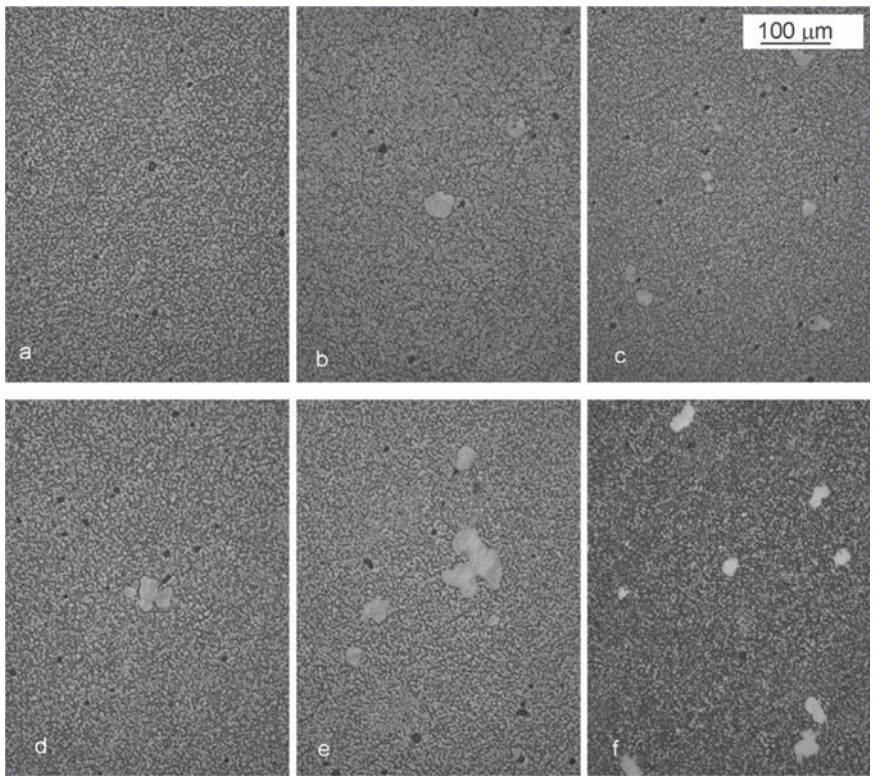

Fig. 12.8 The morphology of solids after molding in near liquidus range: **a** matrix at 0% solid; **b** globular shape at 1% volume fraction; **c** globular shape at 2% fraction; **d** rosette shape at 1% fraction; **e** mixture of rosettes and globules at 2% fraction; **f** near globular shapes at 3% of volume fraction. Alloys: **a–e**, Mg–9Al–1Zn; **f**, Mg–6Al.[14]

entrapped liquid, is absent here. When the alloy is overheated above the liquidus and followed by cooling back to a sub-liquidus range, the precipitated solid may have the form of degenerated rosettes (Fig. 12.8d). The role of shear in affecting the rosettes' shape is not clear here, and they are sometimes observed coexisting with spheroids (Fig. 12.8e). The change in the solid's morphology and content within the range from 0 to approximately 5% is not accompanied by evident differences of the matrix (Fig. 12.8a–f). Moreover, it is difficult to distinguish the morphological difference of the matrix and solid between the Mg–9Al–1Zn and Mg–6Al grades.

12.4.4 Features of Die Cast Microstructure

The microstructures produced from a superheated liquid by die casting are shown in Fig. 12.9. For both alloys, they are inhomogeneous and contain dendrite-type precipitates, formed prior to the solidification in the mold, seen as bright contrast features in Fig. 12.9a,c. Some of the precipitates are large with a size of 300 µm to 400 µm. No notable morphological differences between Mg–6Al and Mg–9Al–1Zn alloys are observed (Figs. 12.9b,d). It is known that the Mg–9Al–1Zn contains more $Mg_{17}Al_{12}$ phase, but this difference is not obviously seen from optical microscopy images. The only difference appeared to be more discontinuous precipitates of $Mg_{17}Al_{12}$ in the Mg–6Al grade.

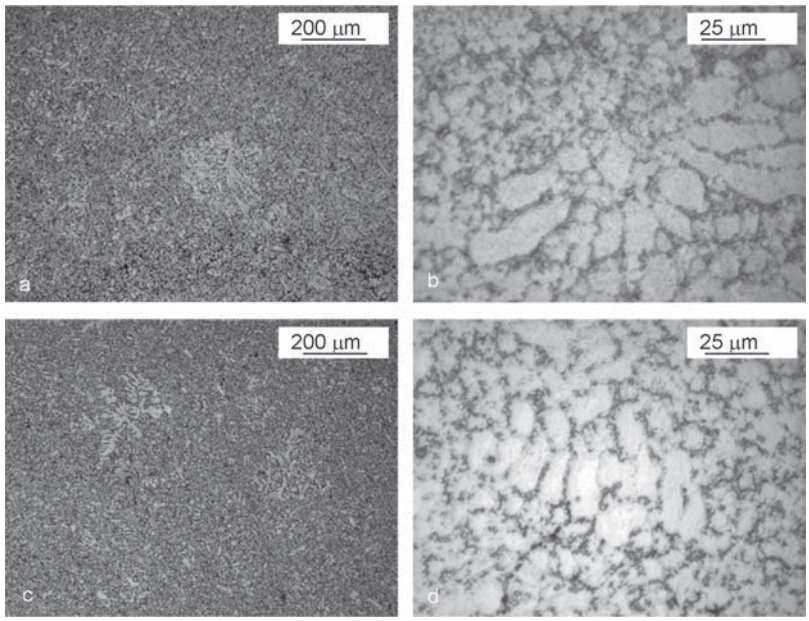

Fig. 12.9 The microstructure of alloys processed starting from overheated liquid by die casting: **a** Mg–9Al–1Zn-general view; **b** Mg–9Al–1Zn-detail showing coarse pre-eutectic dendrites within the matrix; **c** Mg–6Al-general view; **d** Mg–6Al-magnified view of pre-eutectic dendrites [14]

12.4.5 Crystallographic Orientation

The technique of color etching is useful as a method for the qualitative assessment of differences in crystallographic orientation between microstructural constituents. The color distribution within the microstructure, obtained by near liquidus molding, reveals that there is no dominant preferred orientation (Fig. 12.10a). No clustering is present and each small grain/cell is differently oriented.

The alloys die cast from the superheated liquid range show large dendrites of the same color, suggesting that all features within the dendrite had the same or very similar crystallographic orientation, as indicated by the arrow in Fig. 12.10b. Some of them have the morphology of primary dendrites, formed prior to injection into a mold cavity. The color etching shows that many features portrayed on conventional micrographs as individual grains are in fact a part of the large multi-grain conglomerates.

12.4.6 Phase Composition

The X-ray diffraction provides information about the crystallography of phases, their contents and an estimation of the preferred orientation. The Mg–9Al–1Zn

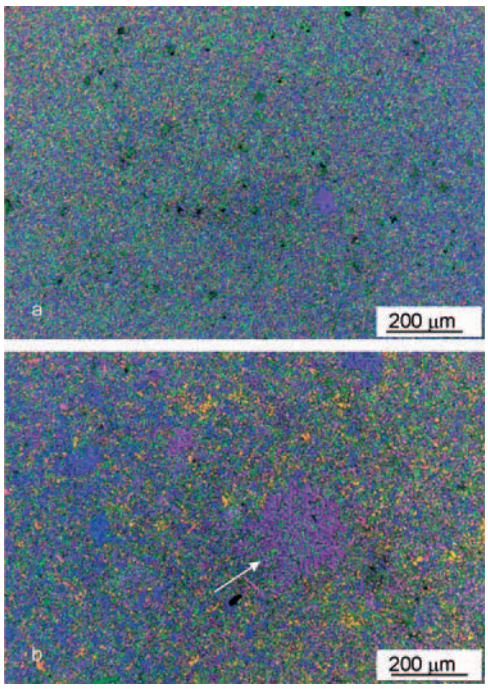

Fig. 12.10 The color etching, revealing the differences in crystallographic orientation of structural components of Mg–9Al–1Zn alloy: **a** near-liquidus molded; **b** die cast [14]

alloy, molded from near liquidus range, contains the αMg and intermetallic phase of $Mg_{17}Al_{12}$ (Fig. 12.11a). A comparison of peak intensities on the diffraction pattern and JCPDS standard suggests that both phases are randomly oriented. At least six peaks of $Mg_{17}Al_{12}$ are detectable, and estimation indicates a volume fraction of about 9%. The Mg–6Al alloy, molded from its liquidus range, exerts a different X-ray diffraction pattern with virtually only an αMg phase (Fig. 12.11b).

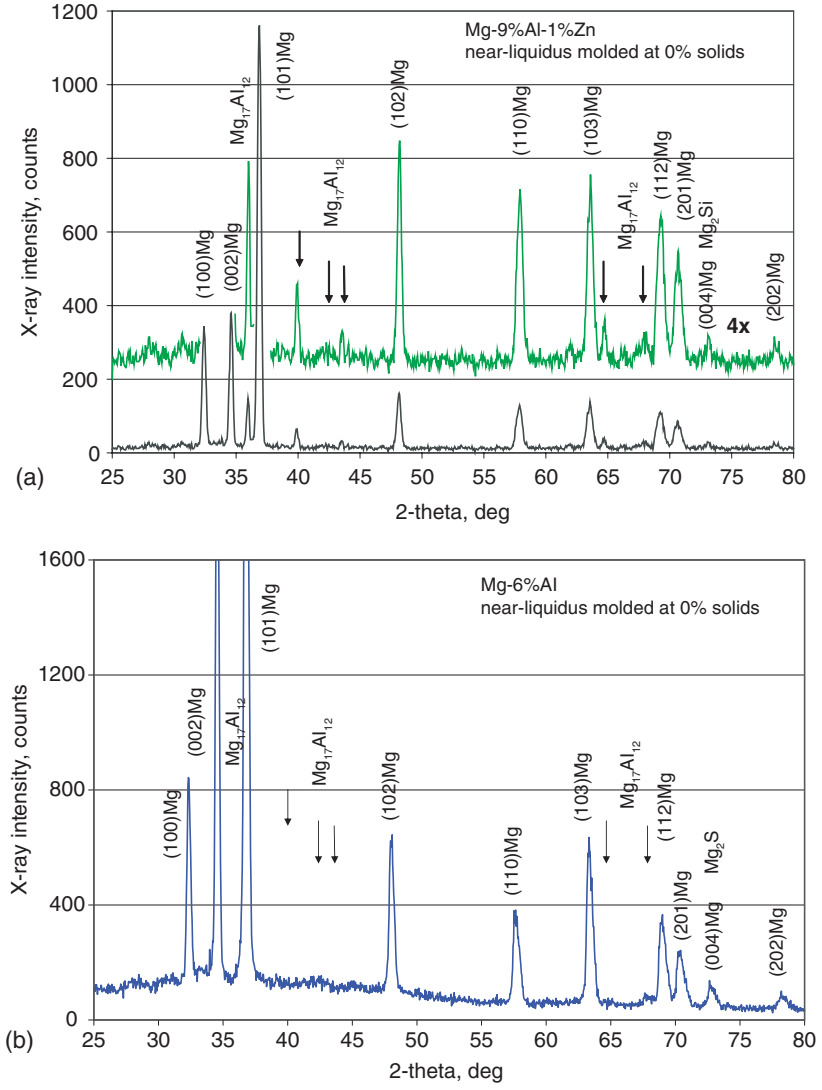

Fig. 12.11 X-ray diffraction patterns for processed alloys: **a** Mg–9Al–1Zn alloy near-liquidus

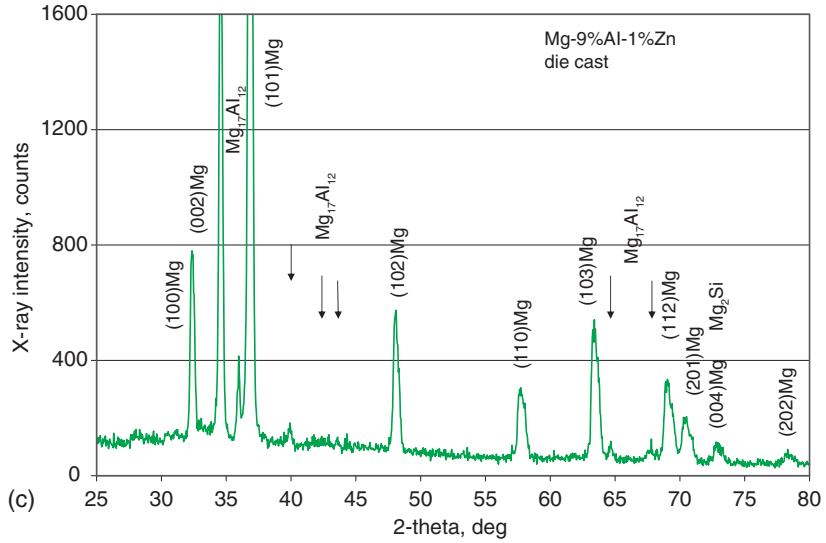

Fig. 12.11 (continued) molded at 0% solid; **b** Mg–6Al alloy near-liquidus molded at 0% solid; **c** Mg–9Al–1Zn alloy die cast starting from superheated liquid [14]

The anticipated locations of $Mg_{17}Al_{12}$ peaks are indicated by arrows where their intensities are at a level of the background noise. The volume contribution of the $Mg_{17}Al_{12}$ phase, estimated from a computer analysis of the diffraction pattern, is as low as 1%. The diffraction pattern of the Mg–9Al–1Zn alloy, die cast from a melt superheated to 670 °C, is shown in Fig. 12.11c. It exhibits visually detectable lower intensities of $Mg_{17}Al_{12}$ peaks than those after near-liquidus molding, shown above in Fig. 12.11a. The estimated content of the $Mg_{17}Al_{12}$ phase is around 7%.

12.4.7 Decohesion Characteristics

There is a significant difference in the morphology of the decohesion surface between the near-liquidus molded and the superheated liquid die-cast structures. The typical cross-sectional view of an Mg–9Al–1Zn tensile bar after near-liquidus molding is shown in Fig. 12.12a. The crack penetrates along the $Mg_{17}Al_{12}$ intermetallic phase, in particular along the interface between the αMg and the intermetallics. There is no noticeable coarsening of pores in the crack vicinity, and no transcrystalline cracking of the primary solid is observed. Instead, the crack penetrates along the interface between the primary solid and surrounding matrix. There are numerous particles of Mn–Al–Fe and Mg_2Si, undissolved during alloy melting. Since they are not observed on the decohesion surface, their contribution to cracking is not clear.

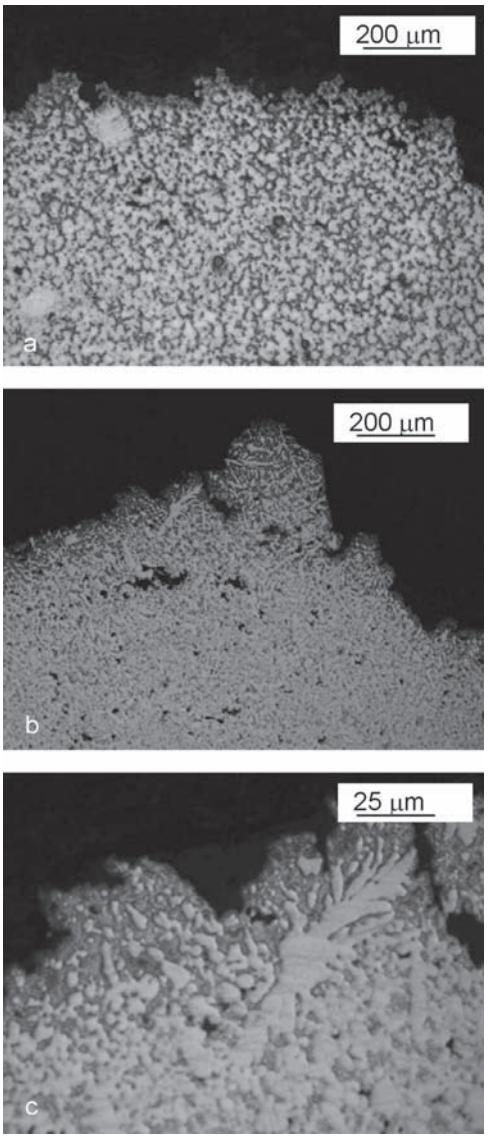

Fig. 12.12 The decohesion surfaces of the Mg–9Al–1Zn tensile bars: **a** alloy injection molded from the near-liquidus range; **b** Mg–9Al–1Zn alloy die cast from an overheated liquid; **c** details of **b** showing the crack propagation path between the coarse dendrite and surrounding matrix [14]

The dendritic morphologies present within the alloy cast from the superheated liquid exert a profound influence on the fracture mechanism (Fig. 12.12b). The regions that separate the coarse dendrites and have different crystallographic orientation than the remaining matrix are the weakest paths, susceptible to cracking (Fig. 12.12c). Outside such coarse dendrites, the αMg–$Mg_{17}Al_{12}$ intermetallic interface is the typical propagation path. Under stress, the shrinkage pores are enlarged significantly, and this is particularly obvious for pores residing in the direct vicinity of the decohesion surface.

12.5 Tensile Properties

Tensile properties are commonly used to assess alloys processed by various techniques. The comparative graph of tensile strength plotted, versus corresponding elongations for both alloys and processing techniques, is shown in Fig. 12.13. The highest strength of 275 MPa is achieved for Mg–9Al–1Zn alloy, molded from near liquidus temperatures. The Mg–9Al–1Zn alloy, which was processed from a superheated liquid, exhibits strength of up to 252 MPa. The strength of Mg–6Al alloy is similar, and after molding from its near-liquidus range, achieved the maximum value of 271 MPa. Again, after processing from the superheated liquid by die casting, the strength of the Mg–6Al alloy is lower and does not exceed 252 MPa. The elongations achieved for both processing routes are comparable and reach up to 8% for Mg–9Al–1Zn and up to 12.5% for Mg–6Al grade. Similar tendencies are revealed for yield stress measured for both alloys and processing routes (Fig. 12.14). The average values obtained for near-liquidus molding reached 166 MPa and 146 MPa for Mg–9Al–1Zn and Mg-6Al, respectively. The average yield stress

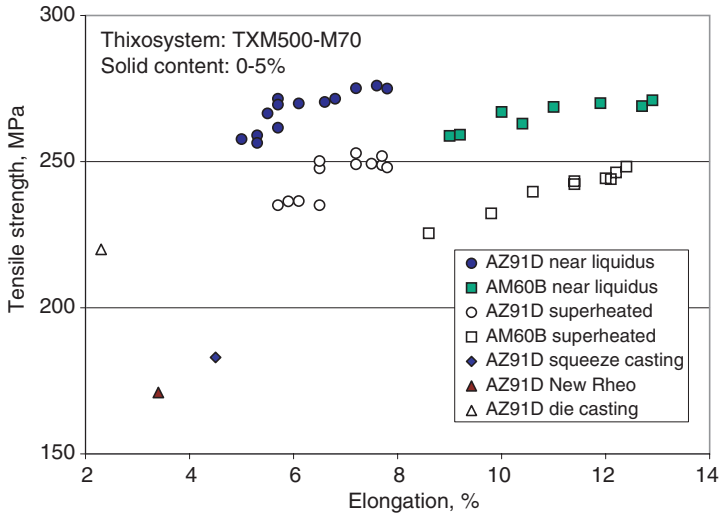

Fig. 12.13 The plot of tensile strength versus corresponding elongation for Mg–9Al–1Zn and Mg–6Al alloys molded from near liquidus temperatures and die cast from superheated state. For a comparison, some literature data are included. ASTM B94 Standard requirements: AZ91D: UTS = 230 MPa, YS = 150 MPa, elongation = 3% in 50.8 mm; AM60B: UTS = 220 MPa, YS = 130 MPa, elongation = 6% in 50.8 mm (UTS: ultimate tensile strength; YS: yield strength). Tensile testing was conducted according to ASTM B557 using cylindrical samples with a reduced section diameter of 6.3 mm for molding and 5.9 mm for die casting, and a gauge length of 50.8 mm. Measurements were performed using an Instron 4476 machine equipped in an extensometer at a crosshead speed of 0.5 mm/min [14]. Literature data: squeeze cast and New Rheomolding [15]; die cast [16]

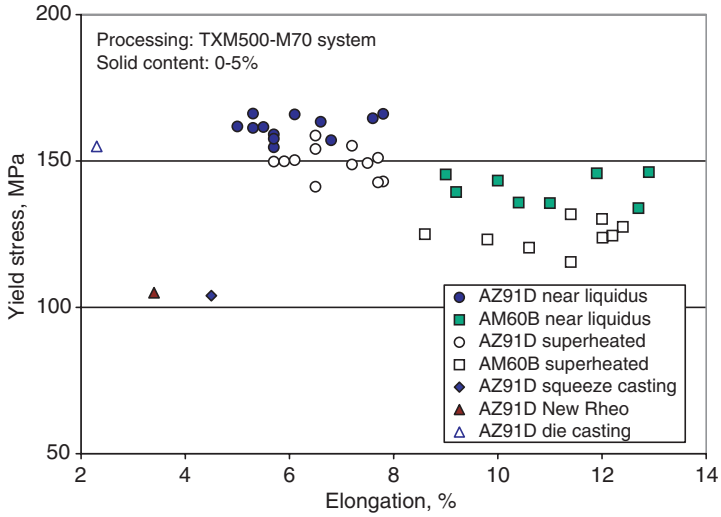

Fig. 12.14 The plot of yield stress versus corresponding elongation for Mg–9Al–1Zn and Mg–6Al alloys molded from near liquidus temperatures and die cast from superheated state. For a comparison, some literature data is included [14]. Literature data: squeeze cast and New Rheomolding [15]; die cast [16]

after die casting is 149 MPa and 124 MPa for Mg–9Al–1Zn and Mg–6Al, respectively. It is seen that the tensile-test data, achieved after NLM, is significantly higher than that required by the ASTM B94 specification.

For each alloy composition, there is a scatter of experimental data points in Figs. 12.13 and 12.14, and processing method, with a general tendency for the higher strength to correspond to the higher elongation for near-liquidus molded alloys, the solid content in the 0% to 5% range is the major variable, contributing to the scatter. Although for superheated alloys processed by die casting, the same tendency in strength and elongation changes is observed, there is no obvious correlation with microstructural components. In addition to pre-eutectic precipitates of αMg dendrites, shrinkage porosity complicates the quantification. In contrast to strength, the larger scatter of yield stress values and limited number of experimental data points do not reveal a correlation between the yield stress and elongation.

12.6 Structure-Property Correlation After NLM

A number of factors contribute to advantages of NLM over other methods of semi-solid processing and conventional casting. Some of them are analyzed below.

12.6.1 Benefits of Reduced Temperatures During NLM

The injection molding of magnesium alloys, preheated to tight temperatures around the liquidus value, diminishes some disadvantages typical for the casting of superheated melts. Both the hot- and cold-chamber die castings start from a superheated liquid and suffer from the disadvantage that it is difficult to produce fully sound components [9, 10]. Superheating is required to compensate for the heat loss during transfer to and delay time in the shot sleeve. Operating at temperatures around 70 °C to 100 °C lower also brings advantages expressed by energy savings, reduced deterioration of machine/mold components and reduced alloy losses by evaporation and oxidation. Negligible porosity after NLM is most likely attributed to the specific solidification mechanism and resultant fine, uniform structure, as discussed below. There are a number of key differences between die casting and injection molding at all stages of processing, and the alloy's temperature is only one of them. This should be kept in mind while comparing results obtained by both techniques.

12.6.2 Melt Agitation During NLM

Another factor, potentially affecting the solidification process of a molded alloy, is the agitation exerted by the reciprocating screw during conveyance along the barrel and high injection speed during mold filling. In fact, it is difficult to separate those two contributions. According to Ref. [11], turbulence introduced by high intensity shear affects destabilization of the diffusion boundary layer and also prevents solute build up ahead of the solid–liquid interface and thus suppresses dendritic growth due to compositional undercooling. As seen earlier in Fig. 12.8, solidification does not lead either to the growth of existing, or the formation of new, solid globules. This aspect may also be affected by shear. It is argued that a compact spherical morphology of the primary particles and the absence of a prominent diffusion boundary layer around them restrict the growth of these particles due to less available kinks at the solid-liquid interface. For this reason, solidification by a means of fresh nucleation within the melt volume is kinetically favored over the growth of existing particles. Thus the shear rate promotes intense turbulence in the semisolid slurry and establishes a uniform temperature distribution throughout the melt, and this condition is ideal for nucleation throughout the melt.

For semisolid processing, the room temperature microstructure allows us to reproduce a thermal history of the alloy. While exploring near-liquidus temperatures, the features that provide the link to the processing parameters are less distinct. For sub-liquidus molding, the alloy's temperature may be estimated based on metallographic measurements of the unmelted solid fraction. A lack of entrapped liquid within the primary solid particles makes

it difficult to distinguish between rheo- and thixo- routes of processing. When the liquidus temperature is exceeded, and the last granules of the primary solid dissolve, the estimation becomes even more ambiguous. In general, for cooling the completely molten and then partially re-solidified alloy, solid morphology is controlled by the external shear imposed. Evidence of overheating would be the presence of rosettes or dendrites precipitated when the melt temperature was subsequently reduced below the liquidus prior to injection. A generally low sphericity of globules, frequently co-existing in mixtures with rosettes, suggests the rather low effectiveness of the shear at such negligible solid fractions, and therefore an increased error in assessment of the processing conditions.

12.6.3 Separating the Microstructure and Internal Integrity

While considering the beneficial changes of mechanical properties after semisolid processing, two factors are frequently mixed:

(i) an improvement caused by a reduction in porosity and
(ii) a change due to a modification of the microstructure.

It is clear that high integrity structures generated after near-liquidus molding take advantage of the first factor. A variation in tensile properties of molded alloys is caused by the structure-related factor, and it is of the same nature as described previously for higher solid contents (Chap. 11). The reduction in strength for the individual alloys Mg-9Al-1Zn and Mg-6Al is associated with an increased content of coarse globules in the primary solid. Moreover, a presence of primary solid fraction results in an enrichment of the remaining liquid in Al, thus creating more $Mg_{17}Al_{12}$ precipitates, which affect matrix ductility.

12.6.4 Influence Of Alloy's Chemistry

When comparing the Mg-9Al-1Zn and Mg-6Al alloys, the major difference is the higher elongation of the latter. It is generally accepted with the quantitative evidence published that the first alloying approach for better toughness is to reduce the volume fraction of the $Mg_{17}Al_{12}$ intermetallic phase: The content of $Mg_{17}Al_{12}$ was in the range of 2% to 7% for Mg-6Al grade and from 5% to 16% for Mg–9Al–1Zn [12]. Thus, the higher elongation of Mg–6Al is associated with a significantly lower fraction of the intermetallic phase, primarily caused by the lower content of Al. The rough estimation based on X-ray measurements of this research provides $Mg_{17}Al_{12}$ fractions between 1% for Mg–6Al and 9% for Mg–9Al–1Zn. It appears at the same time that die cast alloys showed a slightly lower content of the $Mg_{17}Al_{12}$ phase, around 7% for Mg–9Al–1Zn

grade. Since the strength of Mg–6Al and Mg–9Al–1Zn grades is very similar, this finding would suggest that for optimum properties a further increase in elongation the Mg–9Al–1Zn alloy, molded from near liquidus ranges, would require a reduced content of Al.

It is generally expected that semisolid processing provides properties that are superior over those obtained after conventional casting. For Mg–Al and Mg–Al–Zn alloys an increased solid content led so far to a reduction in both strength and ductility. The metallurgical characteristics gathered here and in Chapter 10 suggest that Mg–Al and Mg–Al–Zn alloys with their solidification structures may not be best suited for semisolid processing with substantial content of the unmelted fraction. It is therefore anticipated that for Mg–Al and Mg–Al–Zn alloys, the near-liquidus molding should be a technology of choice to achieve the high integrity structures with the maximum combination of strength and ductility.

12.7 Application Areas of NLM

NLM best suits applications where the solidification shrinkage can be controlled, e.g., for components with low wall thicknesses.

12.7.1 Thin-wall Molding

Thin-wall components represent the most typical application for NLM. The homogeneous alloy flows long distances and fills the mold completely. As a result of rapid cooling by contact with a mold surface, there is instantaneous solidification within the entire part volume, leading to structures achievable only after rapid solidification. For a component with a wall thickness around 0.5 mm to 0.7 mm, the microstructure is much finer-grained than that created within tensile bars with a diameter of 6.2 mm. The homogeneous matrix is filled with fine precipitates, having a diameter of 0.5 µm to 1 µm (Fig. 12.15). Since in magnesium alloys, the Hall–Petch factor is key in strengthening, it is believed that the mechanical properties of such a structure will be higher than measured on tensile bars. As seen in Fig. 12.16, thin-wall structure after NLM exhibits extraordinary ductility, demonstrated by the 180 deg bending test. This implies that NLM may be used to improve ductility of alloys known of inherent embrittlement.

12.7.2 Matrix for Composites

The homogeneous structure generated after NLM is also well suited for matrices of composites [13]. For reinforcement particles exhibiting a tendency to react

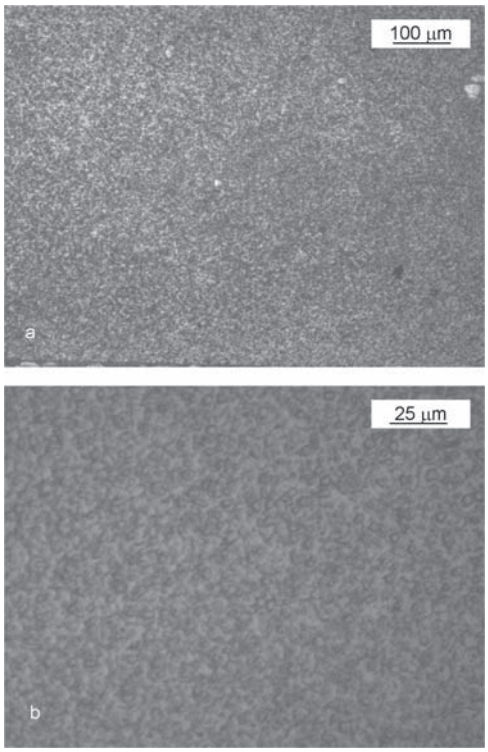

Fig. 12.15 The microstructure of a thin-wall component molded under NLM regime. The rapid solidification rates accompanied by melt temperature resulted in extremely fine-grain features with a size below 1 µm (Mg–9Al–1Zn)

Fig. 12.16 The 180 deg bending test of a component with a wall thickness of 0.7 mm showing a superior ductility after NLM (Mg–9Al–1Zn)

with magnesium, lower processing temperature will minimize reactions at the interfaces. The presence of reinforcement particles, especially those with high heat content, may potentially affect the solidification characteristics of NLM matrix. In general, however, the strong matrix after NLM benefits overall properties of the composite.

12.8 Summary

Processing following the NLM route leads to the formation of high-integrity structures. Shrinkage porosity, unavoidably present after conventional casting, which utilizes superheated melts, is minimized to a negligible level. The matrix of near-liquidus molded Mg–9Al–1Zn and Mg–6Al alloys is macroscopically homogeneous and microscopically consists of fine equiaxed structures of αMg with a typical size of 20 μm and no coarse directional dendrites that would result from pre-eutectic solidification. The αMg grains are surrounded by mostly discontinuous precipitates of the $Mg_{17}Al_{12}$ intermetallic phase with a slightly higher content than after casting from superheated melts. The primary solid is either completely absent or present in negligible amounts, not exceeding 5% of volume fraction. The solid particles do not contain an entrapped liquid and represent a morphology from spheroids to degenerated rosettes, depending on the thermal profile along the alloy's flow path within the system. The near-liquidus molded Mg–9Al–1Zn and Mg–6Al alloys exhibit a combination of strength and elongation superior to their counterparts produced from the superheated liquid and by the semisolid route. The tensile properties benefit from high structural integrity and fine microstructure.

References

1. Czerwinski F (2007) Near-liquidus injection molding process. US Patent 7, 237, 594 B2, 3 Jul 2007
2. Li T, Huang WD, Lin X (2000) Chinese Journal of Non-ferrous Metals 10:635
3. Wu S, Wu X, Xiao Z (2004) A model of growth morphology for semi-solid metals. Acta Materialia 52:3519–3524
4. Chalmers B (1963) Journal of Australian Institute of Metals 8:255
5. Mullins WW, Sekerka RF (1963) Journal of Applied Physics 34:323
6. Qian M (2006) Creation of semisolid slurries containing fine and spherical particles by grain refinement based on the Mullins–Sekerka stability criterion. Acta Materialia 54:2241–2252
7. Uggowitzer PJ, Kaufmann H (2004) Evolution of globular microstructure in New Rheocasting and Super-Rheocasting semi-solid slurries. Steel Research International 75:525–530
8. Wu S, Wu X, Xiao Z (2004) A model of growth morphology for semisolid metals. Acta Materialia 52:3519–3524
9. Flemings MC, Gallo S (2003) Hot chamber die casting of semisolids. US Patent Application 2003/0079854 A1, 1 May 2003
10. Avedesian MM, Baker H (eds) (1999) Magnesium and Magnesium Alloys. ASM International, Materials Park, Ohio, USA
11. Ji S, Das A, Fan Z (2002) Solidification behaviour of the remnant liquid in the sheared semisolid slurry of Sn–15 wt.%Pb alloy. Scripta Materialia 46(3):205–210
12. Bowles A et al (2000) The effect of low-temperature aging on the tensile properties of high-pressure cast Mg–Al alloys. In Magnesium Technology 2000, JN Hryn, Nashville, TN, USA, pp 295–300
13. Czerwinski F (2007) Near liquidus injection molding process. US Patent 7, 255, 151 B2, 14 Aug 2007

14. Czerwinski F (2005) Near-liquidus molding of Mg–Al and Mg–Al–Zn alloys. Acta Materialia 53(7):1973–1984
15. Kleiner S et al (2002) Microstructure and mechanical properties of squeeze cast and semisolid cast Mg–Al alloys. Journal of Light Metals 2(4):277–280
16. Koren Z et al (2002) Development of semisolid casting for AZ91 and AM50 magnesium alloys. Journal of Light Metals 2(2):81–87

13
Alloy and Composite Generation in a Semisolid State

13.1 Introduction

Although the conventional alloys are formed mainly in a molten phase, the ideas of incomplete melting were attempted in the past. A technique based on particulate precursors with different melting points and described as semisolid forming of elementally blended powders, was applied in the 1970s to the Ti-Al system [1]. Similarly, Al and Al-30%Mg powders were partially melted to create a family of Al–Mg alloys [2]. In contrast to the homogeneous mixing of precursors during complete melting, partial melting selectively distributes alloying elements and phases derived from each precursor between the matrix and the unmelted component. As a result, the properties of created alloys vary in a more complex way than those anticipated from a simple rule of mixtures. The separate control of the chemical composition of a liquid matrix and primary solid phase creates an opportunity for building unique structures required for specific properties. Thus, combining two or more thixotropic slurries would allow the creation of new alloys, essentially different from those obtained after the complete melting of metallic ingredients. The experiments with several magnesium alloys show that the control of chemistry and the proportion of precursors, as well as the solid to liquid ratio during their partial melting, allow the selective partition of alloying elements between the solid and liquid phases, thus designing unique solidification microstructures.

This chapter explains the concept and provides the phenomenological description of processes that take place during the formation of magnesium alloys by Semisolid-State Mixing of coarse particulate precursors with different chemistries. The mixing opportunities are further extended by an addition of reinforcement particles to create a special form of composites that have a semisolid matrix.

13.2 Concept of Semisolid-State Mixing

The melting behavior of mechanically comminuted chips and the formation of thixotropic slurries from individual precursors are of key importance during the creation of alloys by Semisolid-State Mixing. The melting progress is driven by

F. Czerwinski, *Magnesium Injection Molding*.

cold-work introduced to chips during ingot fragmentation which, after exceeding the solidus temperature, transform to globular solid particles suspended in the lower-melting range liquid. The new alloy is formed, therefore, by combining the solid spheroids and the liquid phase originating from individual chips. As opposed to the conventional mixing of completely molten ingredients, in this concept, the preheating temperature allows only partial melting of precursors to their semisolid coexistence.

13.2.1 Methods of Practical Implementation

Since the precursors are in the form of particulates, there are two ways to create alloys (Fig. 13.1). The first one relies on room temperature mixing of particulates originating from different alloys, followed by preheating them to temperatures where the alloys reach a semisolid state. This method is the simplest to implement in the present injection-molding environment, which utilizes a single barrel. An alternative solution relies on separate partial melting of individual feedstocks followed by mixing semisolid slurries formed from them. Some differences in microstructures obtained by both methods are expected. For example, melting of a mixture of a solid feedstock from all alloys will allow a longer residency of a solid within a matrix having the final chemistry. In the second case, during separate melting, solids will soak in melts coming from individual precursors. Such a procedure will introduce changes at the solid–liquid interface and within the solid phase as well.

13.2.2 Phenomenology of Structural Transformations

The concept of alloy formation during the semisolid mixing of alloy ingredients can be explained based on a hypothetical phase diagram under assumption of thixotropic nature of both alloys in a semisolid state (Fig. 13.2). To simplify, the binary alloys X and Y of the same metals A and B are considered here. Due to differences in contents of A and B and resulting solidus–liquidus ranges, the alloys, while melted separately, have various solid fractions. After increasing the temperature, the solid's chemistry, volume fraction and proportion of solid originating from individual alloys, as well as changes in the liquid chemistry, take place.

According to the phase diagram, for two hypothetical chemistries, C_X and C_Y, when alloy X enters the semisolid state, the melting of alloy Y is already well advanced. As a consequence, the predominant portion of the liquid phase, which is rich in metal B, is derived from alloy Y. For the two alloys considered here, at all mixing temperatures, X contributes more solid while Y supplies more liquid. While increasing the temperature, the B content in the liquid is reduced due to a solution of the solid phase rich in A. Assuming equilibrium conditions, represented by the phase diagram, at temperatures of the semisolid coexistence of X and Y, the

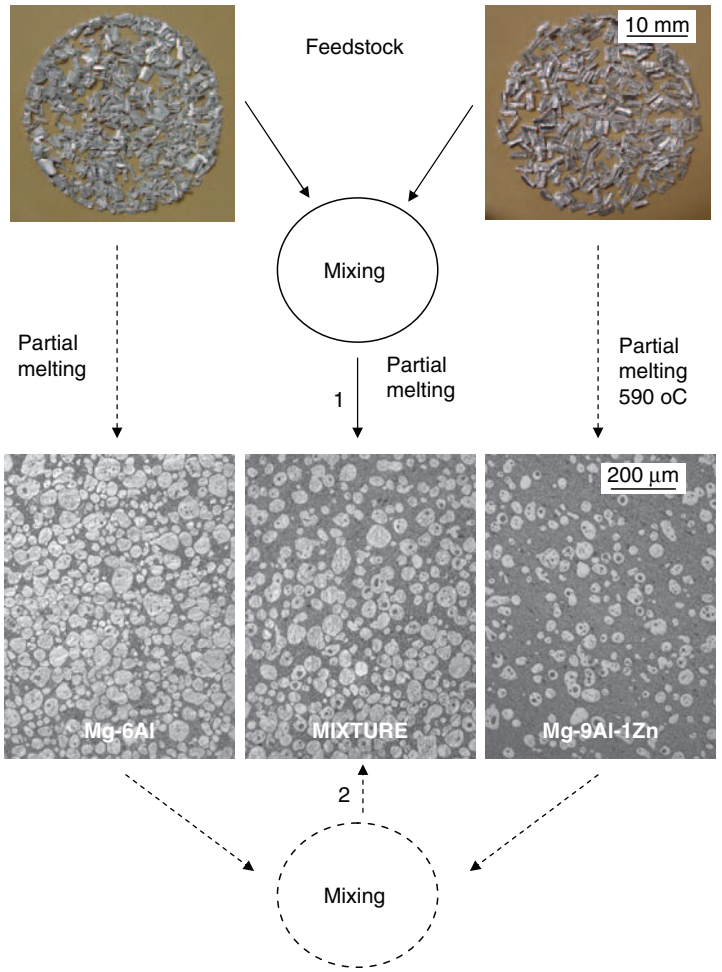

Fig. 13.1 The routes of practical implementation of the alloy generation concept by mixing of particulate precursors followed by their partial melting or by separate melting of individual precursors followed by mixing semisolid slurries. As an example, there are shown the morphology of chipped Mg–9Al–1Zn and Mg–6Al particulates and resultant microstructures after preheating to 590 °C [14]

compositions of solid and liquid derived from both alloys are the same. The short molding time, however, does not allow for substantial changes in the chemistry of the solid phase, which remains close to its initial stage—typical for a completely solid alloy. At temperatures equal to or higher than the liquidus of Y, marked as T_{LY}, this precursor becomes completely liquid and all solids are derived from the X ingredient. Above temperature T_{LY}, the alloy Y contributes exclusively liquid with the same chemistry as that of the original solid state. The liquid is then diluted in B by mixing it with the A-rich liquid, originating from the X ingredient.

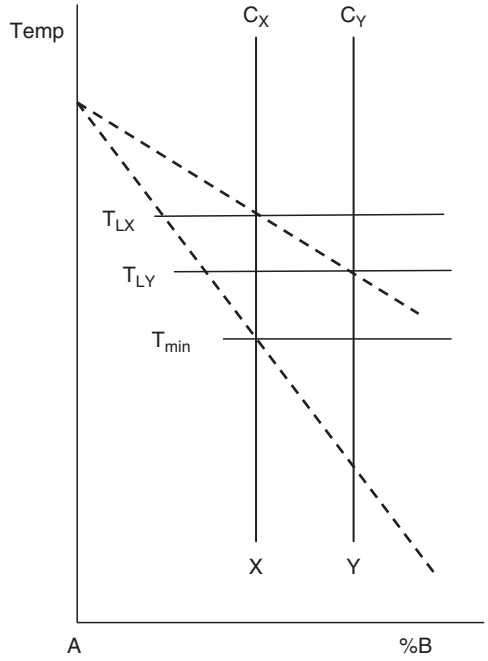

Fig. 13.2 The hypothetical phase diagram, explaining mixing of two alloys X and Y of the same metals A and B

The transformations experienced are portrayed schematically in Fig. 13.3. Mixing of two equal volumes of thixotropic slurries with matrices C1 and C2 leads to a new alloy with a matrix C3. Different contrasts of solid particles indicate their origin. Further increasing the temperature causes selective melting of solid particles, thus further modifying chemistry of the matrix, which is now marked as C4.

13.3 Effect of Temperature on Semisolid-State Mixing

Since during injection molding the feedstock is conveyed within a barrel by an injection screw, there is mixing and redistribution of chemical elements in a liquid state. During solidification/melting considerations it is generally assumed that, at the same time, there is a negligible diffusion in a solid state. It is also assumed that the formation of an alloy is possible when both precursors coexist in a semisolid state, and this condition is used during the selection of the lowest mixing temperatures. It should be understood that during injection molding the temperature represents, in fact, complex thermal profiles along the alloy flow path (Chap. 3). A combination of the temperature profile (Fig. 13.4) and residency time within the barrel has to be linked with the specific temperature reading that characterizes the

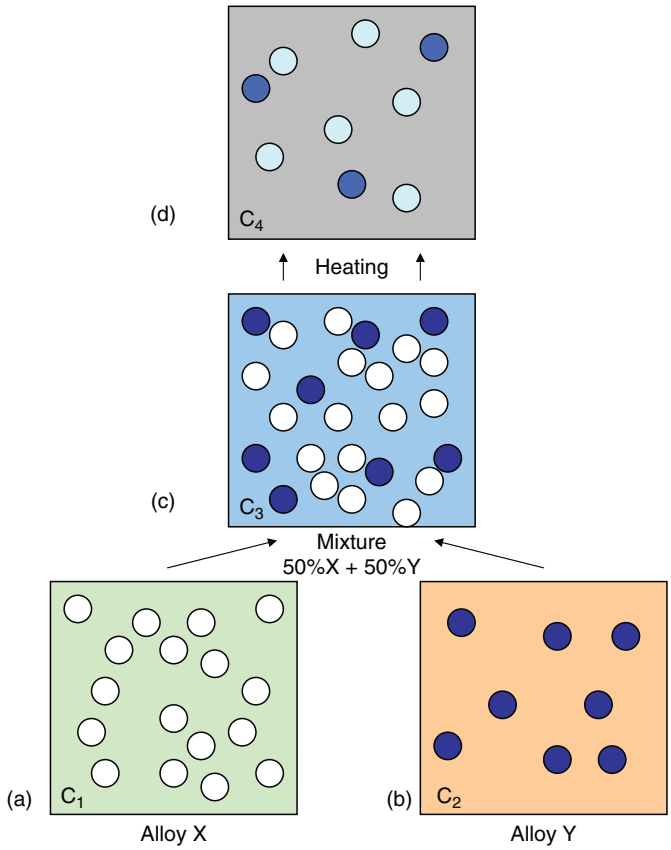

Fig. 13.3 The simplified schematics explaining the concept of alloys generation by semisolid-state mixing: **a,b** alloys X and Y in semisolid state with different solid fractions and matrices C_1 and C_2; **c** alloy with a matrix C_3, formed after mixing of X and Y; **d** alloy with a matrix C_4, formed after heating of C_3 at higher temperatures [15]

alloy location on the phase diagram (Fig. 13.5). The non equilibrium state of an alloy further complicates considerations.

13.3.1 Chemistry and Phase Composition

The starting materials are two commercial alloys, Mg–9Al–1Zn and Mg–6Al, in the form of mechanically comminuted chips. The contents of major elements in starting alloys satisfied the ASTM specifications for AZ91D and AM60B grades (Table 13.1). While mixing them in a volume ratio of 1:1, the calculated contents of Al and Zn correspond to 7.25% and 0.33%, respectively. Values of

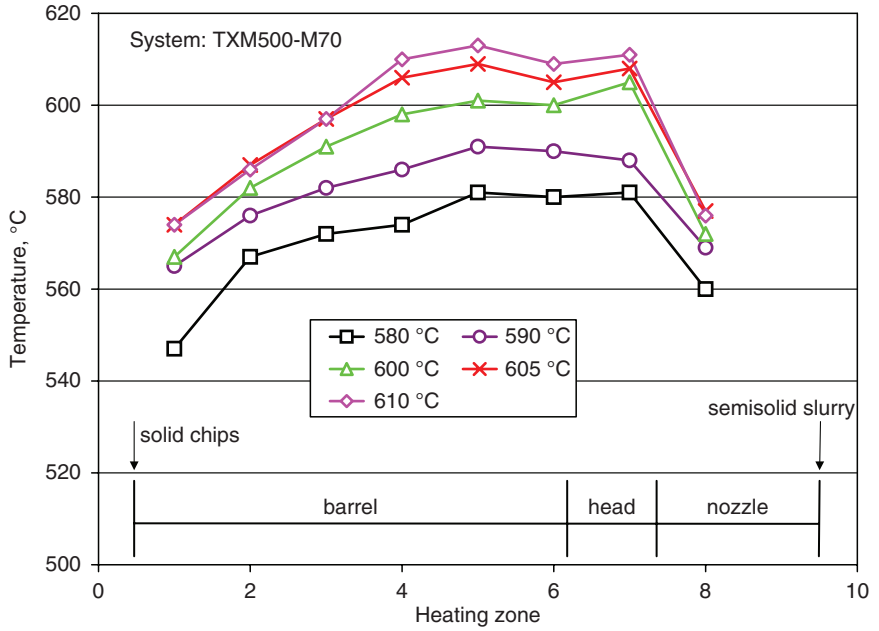

Fig. 13.4 Examples of thermal profiles along the alloy flow path within the injection molding system [16]

7.44% Al and 0.35% Zn, obtained from spectral analysis, indicate that Al and the easily evaporating Zn, provided by the precursors, were completely preserved. Since the microstructure and behavior of the alloy with overall chemistry of Mg–7.5%Al–0.35%Zn are affected by the processing temperature and are not entirely typical for this composition, it is referred to further as AZXY. Due to a deviation from the equilibrium state, both Mg–9Al–1Zn and Mg–6Al alloys, under typical solidification conditions, contain the $Mg_{17}Al_{12}$ phase. The phase forms by a eutectic reaction during sufficiently rapid cooling from the liquid as a result of coring. The same phenomenon is expected to take place within alloys obtained by Mg–9Al–1Zn and Mg–6Al mixing. Some amounts of zinc are carried from Mg–9Al–1Zn to the created alloy and its influence on phase composition should be assessed. As seen from the cross section of the ternary phase diagram Mg–Al–Zn (Fig. 13.6), under equilibrium conditions up to 4% of Zn, the created alloy should not form any new phase beyond those present in Mg–9Al–1Zn and Mg–6Al. If zinc exceeds this amount, a three-phase region is entered involving the ternary intermetallic phase ϕ. This compound creates a eutectic reaction at a temperature of about 360 °C. According to X-ray measurements conducted on Mg–9Al–1Zn alloy after molding, αMg and $Mg_{17}Al_{12}$ were identified as the only phases; the same should apply to the created alloy.

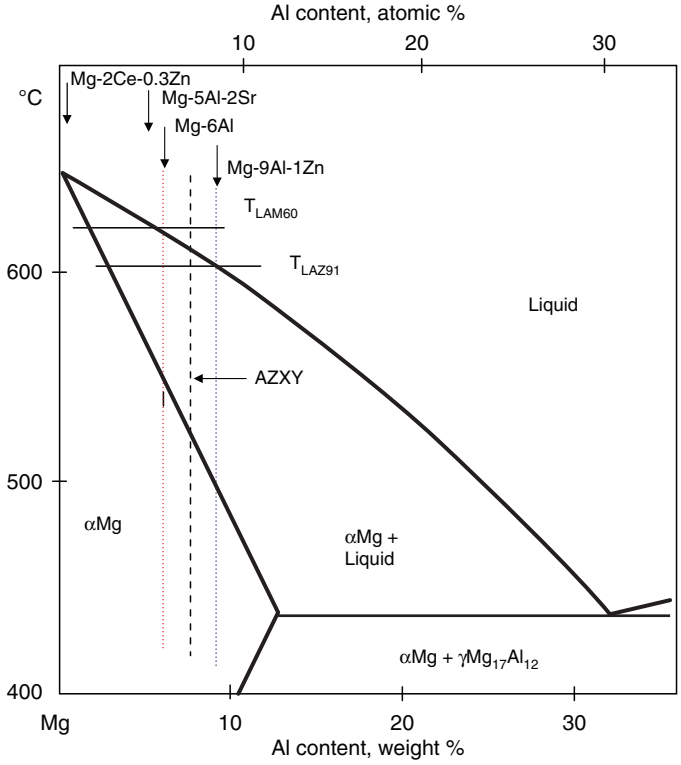

Fig. 13.5 The Mg-rich portion of the Mg–Al binary phase diagram with indicated locations of alloys examined

Table 13.1 Chemical compositions of alloys used during mixing. AZXY alloy was obtained by mixing equal proportions of AZ91D and AM60B.Analysis was performed according to ASTM E1097-97 modified and E1479-99 standards. All values are in weight %, and Mg represents a balance. * Ce-rich misch metal

	Al	Zn	Mn	Si	Cu	Fe	Ni	Sr	Ce*	Soli dus °C	Liqui dus °C
AZ91D(Mg– 9Al– 1Zn)	8.69	0.66	0.29	0.02	<0.01	<0.01	<0.01			468	595
AM60B (Mg– 6Al)	5.82	<0.01	0.31	0.03	na	<0.01	<0.01			565	615
AJ52x(Mg– 5Al– 2Sr)	5.1		0.3					1.7		512	616
MEZ(Mg– 2Ce– 0.3Zn)	<0.1	0.3	0.2						2.5	640	645
AZXY (50% Mg–9Al– 1Zn + 50% Mg– 6Al)	7.44	0.35	0.31	0.02	na	<0.01	<0.01				

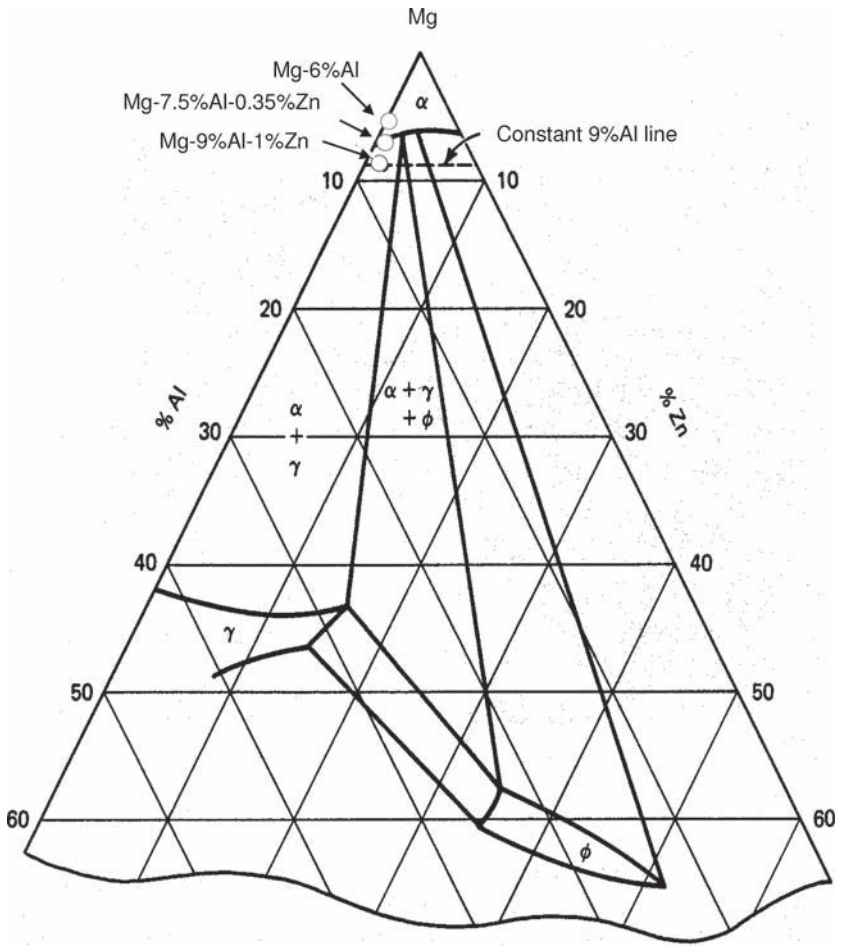

Fig. 13.6 A section of the ternary phase diagram for Mg–Al–Zn at a temperature of 335 °C. The locations of alloys examined are indicated. γ represents the $Mg_{17}Al_{12}$ compound. Adopted from [17]

13.3.2 Role of Particulate Nature of the Feedstock During Mixing

As explained earlier, the key importance during semisolid mixing is the melting behavior of mechanically comminuted chips. During conversion of the as-cast ingots into coarse particulates, as a result of interaction with the cutting tool, the alloys are subjected to cold work. The cold-worked chips experience recrystallization during heating in a solid state, which transforms the as-cast structure into equiaxed grains with a size in the range 50 μm to 80 μm. After exceeding the

solidus temperature and the melting of the grain boundary network, it leads to the generation of globular solid particles suspended in the Al-rich liquid. The created alloy is formed, therefore, by mixing the solid globules and the liquid phase originating from both grades of chips.

13.3.3 Microstructure Evolution

The overall microstructure of the created alloy is similar to those described previously for Mg-based alloys and consists of unmelted spheroids surrounded by the solidified liquid. For some alloys, magnifications of optical microscopy are sufficient to reveal unique features within the primary solids, such as content and morphology of entrapped liquid, and to link their origin to the precursor's grade. More detailed analysis with SEM\EDX proves that the microstructure does not represent the homogeneous mixture, but it is selectively influenced by individual ingredients, depending on the pre-heating temperature. As a rule, the lower the temperature, the higher contribution of the precursor with the lower melting range to the liquid matrix, and the precursor with the higher melting range to the unmelted solid of the created alloy.

The microstructures in Fig. 13.7 are described by temperatures that represent thermal profiles along the alloy flow path, characterized earlier in Fig. 13.4. Therefore the temperature values given there should not be directly compared with phase diagrams. The reason is that the alloy melting within the injection molding system is essentially different from that within the furnace. As a consequence of the short residency time, there may be no temperature equilibrium between the barrel walls and its content. Short residency time, moreover, does not homogenize the microstructure of the magnesium feedstock, known for its segregation phenomena. The steep reduction in temperature at the end of thermal profile shown previously in Fig. 13.4 corresponds to the nozzle exit and is necessary to create a cold plug and to seal the barrel between injection periods (Chap. 5). This temperature reduction is within the narrow nozzle channel, and the solid portion is then isolated into a plug catcher. Thus it does not practically affect the overall structure of the slurry residing in the barrel volume.

The selection of microstructures in Fig. 13.7a–k emphasizes the differences in melting temperatures of Mg–9Al–1Zn and Mg–6Al precursors. The heat provided during the cycle of 580 °C was not sufficient for the smooth processing of Mg–6Al. However, after mixing with Mg–9Al–1Zn, having 27% solid (Fig. 13.7k), it created the alloy with 62% solid (Fig. 13.7h). During molding at the 590 °C cycle, both precursors (Fig. 13.7d and j) were individually in a semisolid state and the created alloy exhibited 53% solid (Fig. 13.7g). The mixing scenario changed after a rising the temperature to a 600 °C cycle, when the Mg–9Al–1Zn alloy became practically molten (Fig. 13.7i). The Mg–6Al alloy separately molded following this cycle contained 49% solid (Fig. 13.7c). As shown in Fig. 13.7f the alloy generated after their mixing reached 15% solid. Changing the thermal cycle to 605 °C caused the creation of an almost completely

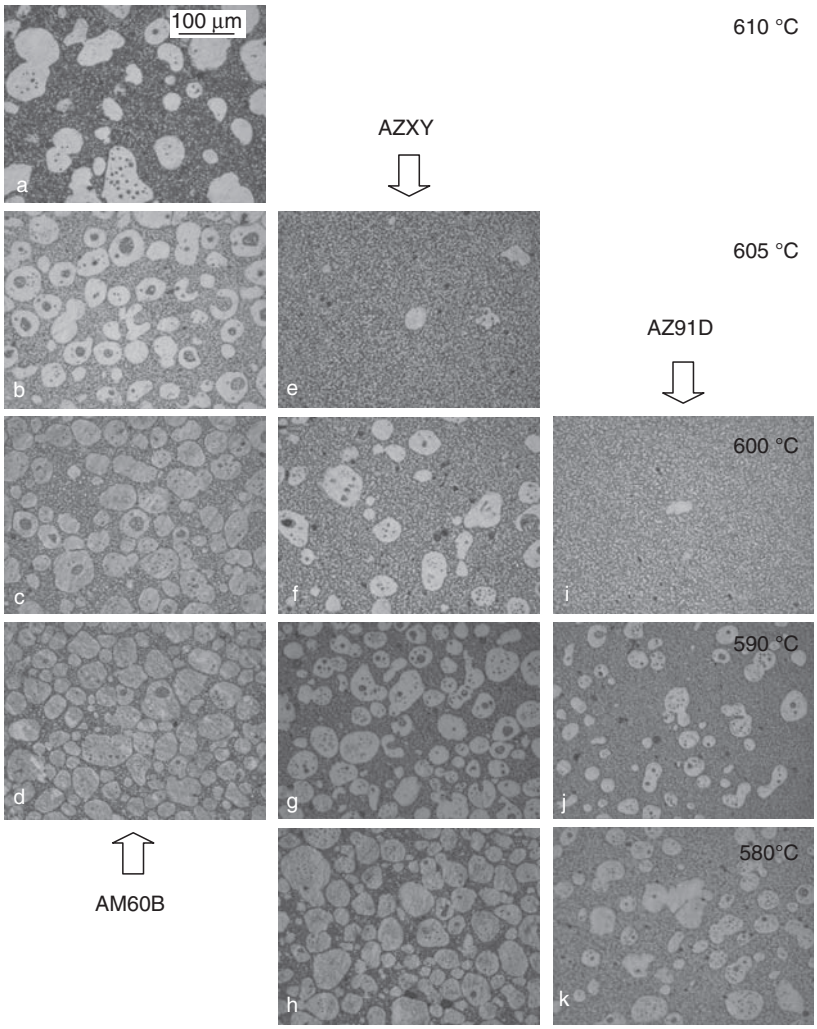

Fig. 13.7 The comparison of microstructures of Mg–9Al–1Zn and Mg–6Al precursors and the alloy generated by their mixing. Temperatures indicate thermal profiles, specified in Fig. 13.4 [16]

Table 13.2 Microchemical analysis of unmelted solid particles within alloy AZXY processed at a thermal cycle of 580 °C. All values are in weight %

	Mg		Al		Zn	
	%	3σ	%	3σ	%	3σ
Particle 1	96.06	2.49	3.07	1.03	0.88	0.64
Particle 2	98.99	2.55	0.71	0.21	0.31	0.30
Particle 3	96.18	2.19	3.58	0.85	0.25	0.15

molten alloy (Fig. 13.7e). For this cycle, separately molded Mg–9Al–1Zn and Mg–6Al exhibited 0% and 37% solid, respectively (Fig. 13.7b). Further raising the temperature resulted in generating the completely molten alloy, which has gradually overheated in respect to its liquidus position.

13.3.4 Effect of Solid State Diffusion

The inhomogeneity in chemistry of unmelted globules is expressed not only by entrapped liquid pools, but also by globule edges which were enriched in Al (Table 13.2). Globules, present in low solid microstructures, do not contain Zn, indicating their origin from the Mg–6Al precursor. There are differences in the chemistry of solid globules with Al level, with occasional ones containing below 1% of Al. Such differences represent an additional factor controlling the selective melting of solids within thixotropic structures. No obvious differences in chemistry of the transformed liquid are seen, and Al content within regions within the solidified matrix is between 12.44% and 12.95%.

A contribution of solid-state diffusion to alloy generation is not fully clear. It is reasonable to assume that there is no direct diffusion-controlled transport between solid particulates originating from different precursors because they are mostly separated by the liquid alloy. Since the material is conveyed within the machine barrel by an injection screw, there is an intense mixing and redistribution of chemical elements in the liquid state. The solid-state diffusion, therefore, relates to interiors of the solid particles and their interaction with the liquid. The diffusion impact is suppressed mainly by the alloy residency time within the system, being of the order of 3 min, of which the exposure to the maximum temperature may be below 1 min. For this short residency period and the diffusion coefficient of Al in Mg at 600 °C of 3.33×10^{-12} m^2s^{-1}, the root mean square displacement of Al atoms equals between 14 μm (for 1 min) and 25 μm (for 3 min). Thus, although for an average granule size of the order of 60 μm to 80 μm, solid-state diffusion is difficult to neglect, short residency time does not allow for substantial enrichment of the globule surface in Al. Such enrichment would reduce the solidus–liquidus location and cause melting. The ambiguity is created since the potential melting due to a diffusional change in chemistry is superimposed on other size evolutions within thixotropic structures caused by the interaction between particles leading to coagulation, spheroidization and Ostwald ripening. As a consequence, particle size reduction due to eventual melting may be compensated.

13.4 Role of Other Parameters in Semisolid-State Mixing

In the mixing experiments described above equal proportions of alloy ingredients were assumed. In that case the only variables are preheating temperature and to some extent, the residency time. In practice, there are also other factors that allow modifying properties of the generated alloys.

13.4.1 Proportions of Mixed Ingredients

The proportion of ingredients affects directly the structure and properties of the alloy generated. Due to the particulate nature of the feedstock, mixing proportions can be adjusted directly before the material is introduced into the barrel. Combining it with a preheating temperature allows it to expand substantially the range of changes in chemistry and structure of created alloys. An influence of proportions of mixed ingredients is shown using Mg–9Al–1Zn and Mg–5Al–2Sr alloys. In this case the precursors not only have different melting ranges, but also different phase compositions. The Mg–5Al–2Sr alloy contains 2% of alkali earth metal Sr to improve its high temperature properties—mainly creep resistance. An addition of Sr to Mg–9Al–1Zn almost entirely eliminates $Mg_{17}Al_{12}$, leading to the formation of Al_4Sr, $Mg_{17}Sr_2$ and ternary Al–Mg–Sr phases (Chap. 14). This feature is useful in mixing experiments because a lack of the entrapped liquid allows distinguishing solid particles coming from this alloy. The mixture rich in Mg–5Al–5Sr exhibits the primary solid free of entrapped liquid (Fig. 13.8a,b). While further diluted with Mg–9Al–1Zn at the same temperature, the increasing number of solids contains entrapped liquid, characteristic of the Mg–9Al–1Zn original (Fig. 13.8c, d). At the same time, the liquid portion experiences enrichment in Al and Zn.

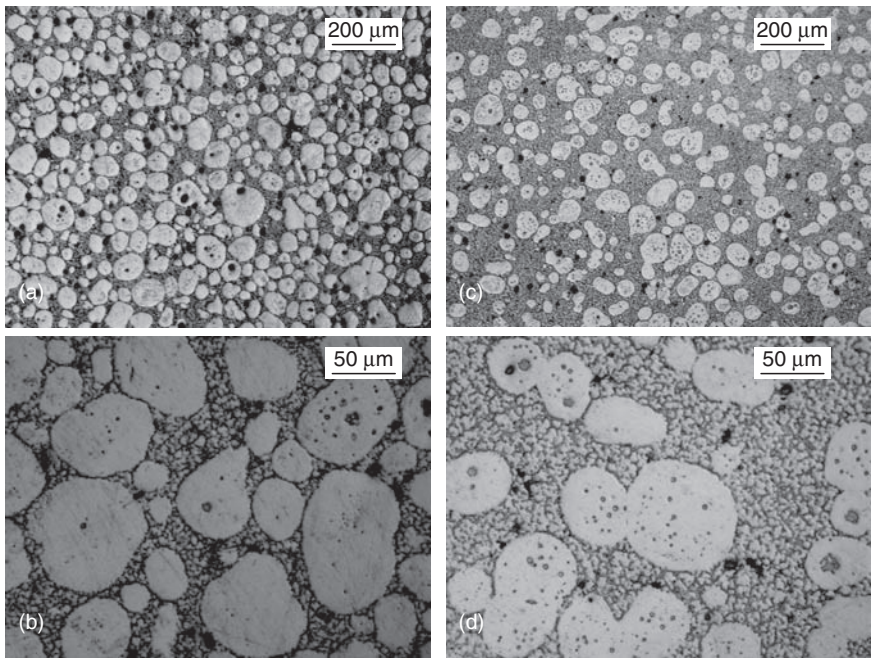

Fig. 13.8 The influence of mixing proportions on the microstructure formed by semisolid-state mixing at temperature of 580 °C: **a,b** 75% Mg–5Al–2Sr and 25% Mg–9Al–1Zn, solid fraction 59%; **c,d** 25% Mg–5Al–2Sr and 75% Mg–9Al–1Zn, solid fraction 32% [15]

13.4.2 Differences in Melting Ranges

A difference in melting ranges of individual precursors may also be used to engineer properties of the created alloy. To examine the role of this factor, two alloys with drastically different melting ranges were selected. The melting range of the Mg–2Ce–0.3Zn alloy, being 640-645 °C, is narrower and located at significantly higher temperatures than that of Mg–9Al–1Zn. Such a difference represents a challenge to Semisolid-State Mixing with Mg–9Al–1Zn. At temperatures of the semisolid state and overheated liquid of the Mg–9Al–1Zn, the Mg–2Ce–0.3Zn alloy still exists in a form of solid chips (Fig. 13.9a, b). As a result, a thixotropic slurry is formed by mixing semisolid Mg–2Ce–0.3Zn with completely molten Mg–9Al–1Zn. The mixture contains the primary solid that originates exclusively from Mg–2Ce–0.3Zn and the matrix that is formed by combining liquid portions of both alloys (Fig. 13.9c). The original phase composition

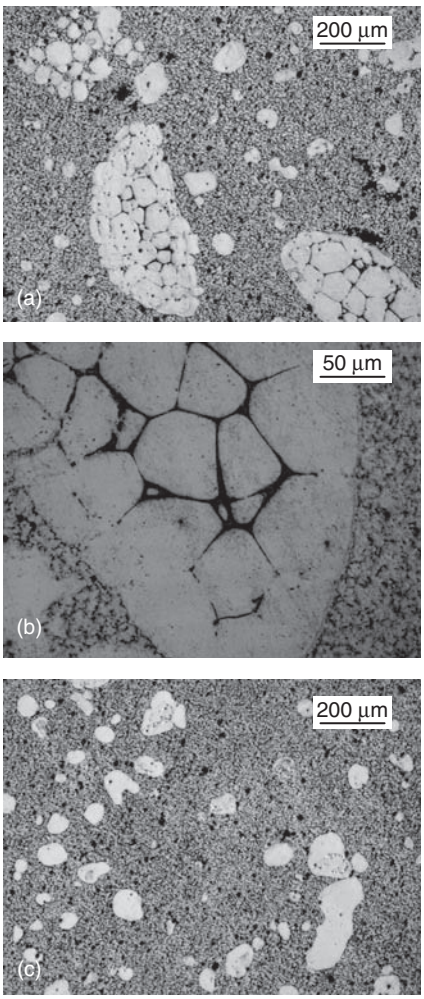

Fig. 13.9 The challenges of mixing Mg–2Ce–0.3Zn and Mg–9Al–1Zn alloys: **a** mixture of Mg–2Ce–0.3Zn solid chips and Mg–9Al–1Zn liquid; **b** magnified view of Mg–2Ce–0.3Zn chip at the very early stage of its melting; **c** primary solid originated from the Mg–2Ce–0.3Zn precursor suspended in a solidified liquid fraction [15]

of Mg–2Ce–0.3Zn, being αMg and Mg_{12}(RE), RE-rare earth, intermetallics located at grain boundaries where final solidification takes place, is therefore modified.

13.5 Tensile Properties of Alloys Created by Semisolid-State Mixing

13.5.1 Correlation of Strength and Elongation

The tensile properties of Mg–9Al–1Zn and Mg–6Al precursors and created alloys exhibit a general tendency where a reduction in solid content causes an increase in strength and ductility. Tests of over 120 tensile bars, representing all three groups of alloys and molded under various thermal profiles along their flow-path within the injection system led to these conclusions. The two-dimensional plot shows the correlation between tensile strength and elongation, where higher strength values correspond to larger elongations (Fig. 13.10). It is also clear that the correlation depends on the alloy's chemistry, since experimental points for three groups of alloys are separated. When a linear regression is used to describe tensile strength versus elongation, the correlation coefficients reach values between 0.94 and 0.96 (Table 13.3). The maximum tensile strengths achieved were 275.1 MPa and

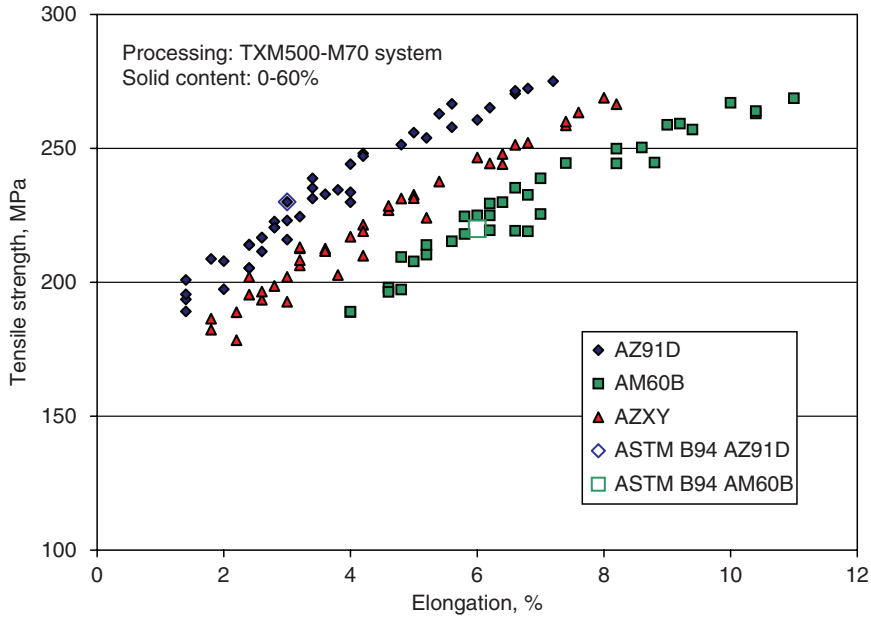

Fig. 13.10 The plot of tensile strength versus corresponding elongations for Mg–9Al–1Zn, Mg–6Al and the created alloy. Each data point represents an individual tensile test [16]

Table 13.3 Tensile properties of AZ91D and AM60B precursors as well as the alloy (AZXY) created by their mixing in equal proportions.

	Tensile strength		Yield stress		Elongation in 50.8 mm		TS =A * El + B			YS= A * El + B		
	MPa		MPa		%		MPa			MPa		
Alloy	max	min	max	min	max	min	A	B	R^2	A	B	R^2
AZ91D	275.1	189.1	168.3	139.8	7.2	1.4	14.6	178.1	0.951	1.7	153.5	0.162
AM60B	268.7	188.9	146.2	112.0	11.0	4.0	11.4	150.8	0.936	2.6	112.9	0.312
AZXY	268.9	178.4	158.7	122.8	8.2	1.8	13.4	162.1	0.963	1.4	138.7	0.244

ASTM B94 Standard requirements:
AZ91D: UTS = 230 MPa, YS = 150 MPa, Elongation = 3% in 50.8 mm;
AM60B: UTS = 220 MPa, YS = 130 MPa, Elongation = 6% in 50.8 mm

268.7 MPa for Mg–9Al–1Zn and Mg–6Al, respectively. Thus both values are close to each other and to the strength of 268.9 MPa, measured for the created alloy. Similarly, the minimum strength of all alloys is close to 188 MPa. There are also differences in values of elongation achieved. The maximum elongation of created alloys—8.2%—is located between 7.2% and 11%, the highest values measured for Mg–9Al–1Zn and Mg–6Al, respectively. The minimum elongation of created alloys reaching 1.8% is very close to the 1.4% exhibited by Mg–9Al–1Zn and quite far away from the Mg–6Al group.

The relationship of yield stress versus elongation is mainly controlled by the alloy's chemistry, and there is a clear distinction between both precursors and the created alloy (Fig. 13.11). The experimental points exhibit relatively large scatter, and correlation coefficients for regression lines are very low (Table 13.3). For the entire elongation range the yield stress of created alloys is located between those for the Mg–9Al–1Zn and Mg–6Al precursors. The requirements of tensile properties specified by the ASTM B94 standard are also included in Figs 13.10 and 13.11. A comparison shows that values measured exceed the requirements by up to 20% in strength and up to 140% in elongations.

13.5.2 Influence of Mixing Temperature on Properties

13.5.2.1 Ultimate Tensile Strength/Yield Stress

In order to evaluate the role of the molding temperature, the values of tensile strength, yield stress and elongation are plotted as a function of the solid content, measured metallographically. The major finding is that the tensile strength is mainly affected by the solid content, and the alloy's chemistry has very limited effect (Fig. 13.12). An increase in solid content from 0 to 60% resulted in a 25% reduction of the alloy's strength. For the same change in solid content, the yield stress experiences a smaller reduction (Fig. 13.13). This is more clearly shown by the yield-to-strength ratio in Fig. 13.14. In contrast to tensile strength, yield stress

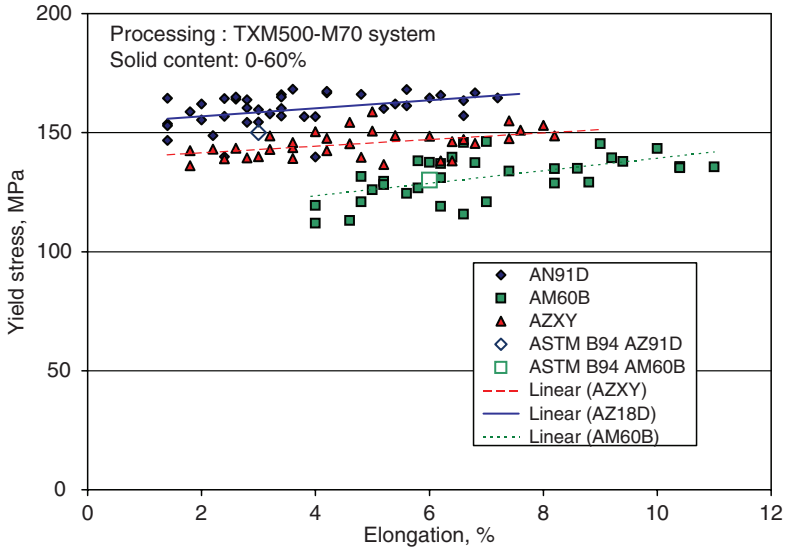

Fig. 13.11 The plot of yield stress versus corresponding elongations for both precursor and the created alloy. Each data point represents an individual tensile test [16]

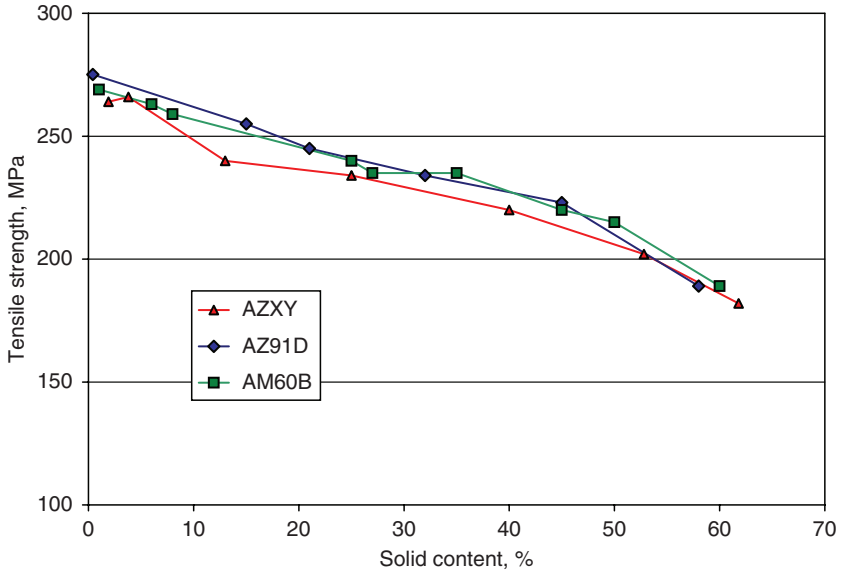

Fig. 13.12 The plot of tensile strength as a function of solid content for alloys indicated [16]

is affected by chemistry. Due to a large scatter of experimental points, the tendency of changes is indicated using regression lines.

Thus for alloys processed at various temperatures of the semisolid range, the tensile strength shows a strong correlation with corresponding elongations. The tensile

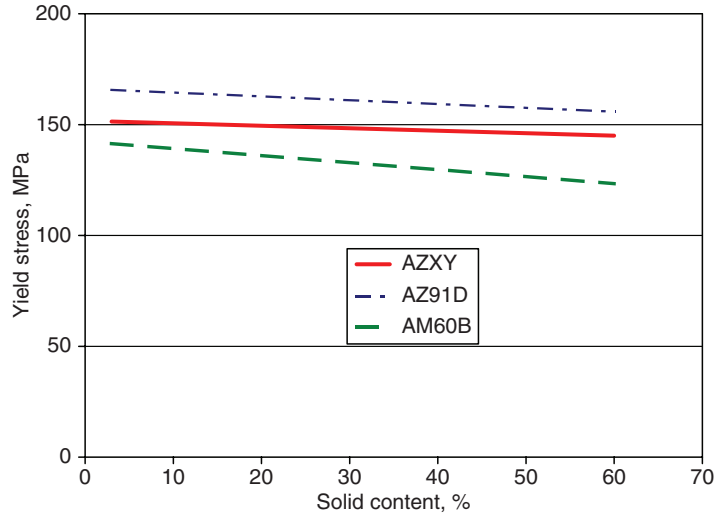

Fig. 13.13 The plot of yield stress as a function of the solid content for alloys indicated [16]

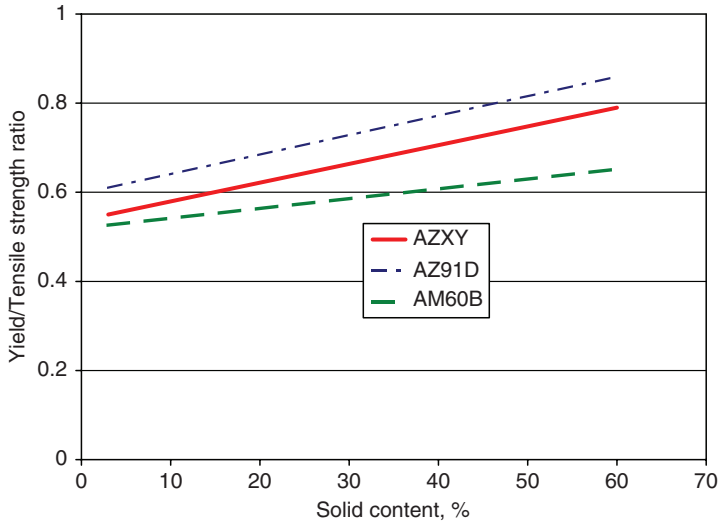

Fig. 13.14 The plot of yield to tensile strength ratio as a function of solid content for alloys indicated [16]

strength is predominantly controlled by the solid content within the microstructure with negligible influence derived from changes in the alloy's chemistry. On the contrary, yield stress is less sensitive to variations in processing temperature and is additionally affected by the alloy's chemistry. Although the elongation is affected by both the solid content and the alloy's chemical composition, the larger role is still exerted

by the former. An increase in solid content leads to a reduction of tensile strength and yield stress, as well as elongation, with a more pronounced effect on the latter.

13.5.2.2 Elongation

Significantly larger changes are exhibited by the alloy's elongation (Fig. 13.15). For Mg–9Al–1Zn alloys, elongation starts from a maximum of 7% for a very low-solid fraction and decreases to almost 2% for 60% solid. The alloy Mg–6Al has a much higher initial elongation of 11%, located also at a low-solid fraction. While increasing the solid content to 60%, elongation fell to 4%. The created alloys show elongations between values corresponding to two precursors. For a low-solid content, the elongation is an average for two precursors. With increasing solid contents it shifts closer to results typical for the Mg–9Al–1Zn alloy. For a 60 % solid it reaches the value of almost 2%, which is practically the same as that found for the Mg–9Al–1Zn alloy.

The general correlation between the solid content and properties described in Chap. 10 is also valid for alloys created by semisolid mixing: An increase in solid content causes a reduction in both the strength and elongation (Fig. 13.16). Since, in mixing experiments, three alloys with different chemistries are involved, the comparison of them sheds more light on the complex nature of the microstructure-properties' relationship in alloys subjected to semisolid processing. For all three alloy compositions and a wide range of solid contents, the following behavior is revealed: (i) For a given alloy a higher elongation is achieved by a reduction in a solid content; (ii) for a given solid content, a higher elongation is achieved by a reduction in Al content. In order to understand the nature of these changes, two factors, namely the solid content and chemistry of the transformed liquid, have to be separated.

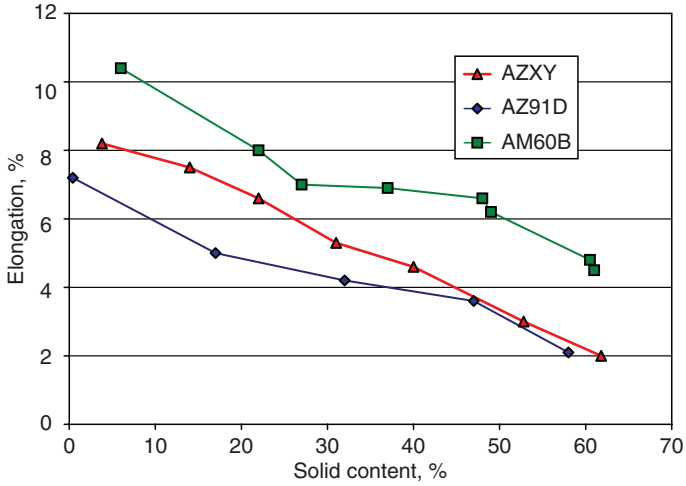

Fig. 13.15 The plot of elongation as a function of solid content for both precursors and the created alloy [16]

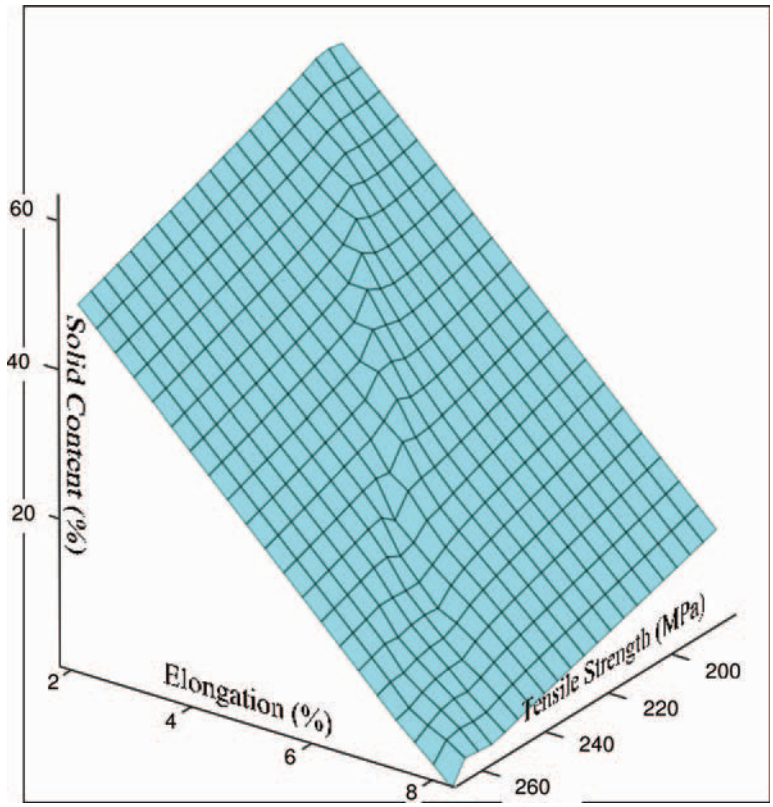

Fig. 13.16 Three-dimensional plot of tensile strength, elongations and solid contents for the alloy formed after mixing of Mg–9Al–1Zn and Mg–6Al precursors [16]

13.5.2.3 Role of Solid Content

At present, the roles of the solid and transformed liquids in controlling the properties of molded structures are not fully explained, and attempts at their quantification, based on the rule of mixtures, are still in progress (Chap. 10). In particular, the role of primary solid globules and their internal structure is not clear, since cross-sectional observation of decohesion surface does not show their involvement in a crack propagation. The microscopy indicates rather that the crack is located within the transformed liquid. Precisely, the crack propagates along the interface between the intermetallic phase and secondary αMg grains within the eutectics. With an increasing solid fraction, there is a tendency toward crack penetration along the interface between the primary solid and the eutectics. The observation that for the same solid fraction, the elongation increased while moving from Mg–9Al–1Zn through AZXY to Mg–6Al seems to point toward the chemistry of the transformed liquid and increased Al content in it, as is the case in die cast alloys.

13.5.2.4 Chemistry of Solid and Liquid Phases

The common factor accompanying the reduction in processing temperature is the increase in Al content within the molten component of the semisolid slurry. As a result there is a change in content of the $Mg_{17}Al_{12}$ intermetallic compound. An additional difference is the morphology and distribution of this intermetallic phase. The fracture toughness measurements confirmed the dominant influence of the amount and distribution of $Mg_{17}Al_{12}$ on the mechanical properties of Mg alloys, where ductility is enhanced by a decrease in volume fraction and a finer dispersion of the $Mg_{17}Al_{12}$ phase.

13.5.3 Applicability of the Rule of Mixtures

The issue that requires explanation is how to determine the contribution of both precursors to the properties of the alloy created by semisolid alloying. Although tensile properties are between the characteristics of both precursors, their particular value depends upon mixing temperature. According to previous plots in Figs 13.10 and 13.12, the pure rule of mixtures is valid for the mixing of completely molten alloys. At temperatures close to the complete melting of both alloys, the properties are almost equally affected by both precursors. With a reduction in processing temperature, there is an increased deviation from the rules of mixture. At high-solid contents the deviation is so high that properties are entirely controlled by the lower melting range component. For example, for solid contents close to 60%, properties of the created alloy are typical for the Mg–9Al–1Zn precursor. This finding points again towards the chemistry of the transformed liquid and its eventual influence on the structure of the interface between the primary solid and transformed liquid. Therefore, since the solid phase is not involved in cracking, its role may be indirect through the control of the chemistry and morphology of the transformed liquid. Thus the properties of alloys produced in the semisolid state are not a simple function of their mixing proportions and resultant average chemistry. As shown for a case of equal volume mixing, the properties are affected selectively either by Mg–6Al or by Mg–9Al–1Zn, depending on the processing temperature.

13.6 Generation of Magnesium Matrix Composites

Metal matrix composites (MMC) are created by mixing into a single material a metallic matrix and a reinforcing constituent that is usually non-metallic and is frequently a ceramic. There are also composites of a ceramic in a ceramic or a ceramic in the polymer. MMCs have been studied since the early 1960s and the initial work was driven by high-performance needs of the aerospace industry. After two decades without significant commercialization, other industries joined the new developmental path that, in addition to performance, started paying attention to cost.

A classic example of a composite is aluminum reinforced with SiC fibers, which combines the strength and stiffness of SiC with the ductility of aluminum. Although the aluminum matrix dominates both the studies and applications, magnesium is explored for this purpose as well.

13.6.1 Magnesium as a Composite's Matrix

A number of different Mg-based alloys are used as matrices for composites. Although the conventional composites are based on crystalline matrices, the amorphous state is also applied.

13.6.1.1 Homogeneous Crystalline Matrix

The most frequently explored crystalline matrix represents common alloys: Mg–9Al–1Zn and Mg–6Al. To a lesser extent, other alloys, including those containing rare earth elements, are also used. For crystalline Mg alloys, additions of fine reinforcement particles reduce grain size, which improves properties according to the Hall–Petch law. The grain refinement is caused by a heterogeneous nucleation of Mg grains on the reinforcement particles. It is commonly accepted that the crystalline magnesium composite shows substantial improvements in stiffness, strength, wear resistance and other properties over the unreinforced state (Fig. 13.17). For example, hybrid reinforced composites based on a AM60B matrix containing 12% of B_4C and 12% of SiC whisker reached elastic modulus of 80.2 GPa and tensile strength of 420 MPa, which are 100% and 35% higher, respectively [3].

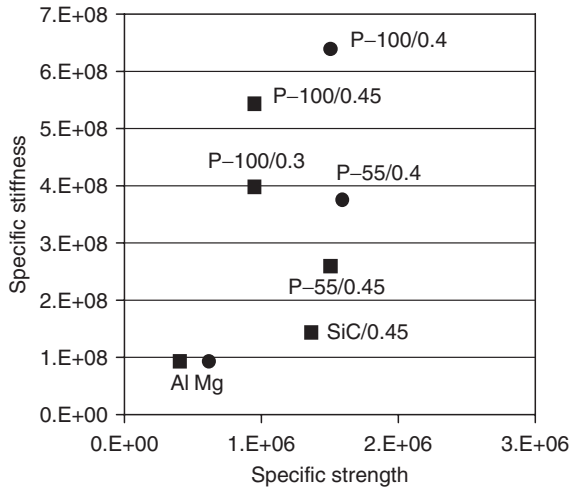

Fig. 13.17 The increase in properties of Mg based and Al based composites as compared to the pure matrices [18]

Composites of a magnesium matrix reinforced with aligned long fibers of Mg_2Si, C or SiC, as well as short fibers of Al_2O_3 have shown damping capacity 10 to 100 times higher than die cast AZ63 alloy [4].

13.6.1.2 Amorphous Matrix

The magnesium amorphous alloys (metallic glasses) and methods of their manufacturing are described in Chap. 1. A major concern that limits the use of metallic glasses for composites is that solid particle dispersions may adversely affect their glass forming ability. Despite this, a number of chemical compositions were successfully applied as composite matrices. Although the strength of Mg based amorphous alloys is two to four times greater than their crystalline equivalents, it can be further increased by additions of reinforcements. An example of strengthening and toughening effects of TiB_2 particles with a size of 10 μm on $Mg_{65}Cu_{7.5}Ni_{7.5}Zn_5Ag_5Y_{10}$ bulk metallic glass is shown in Fig. 13.18 [5]. The compressive fracture strength of

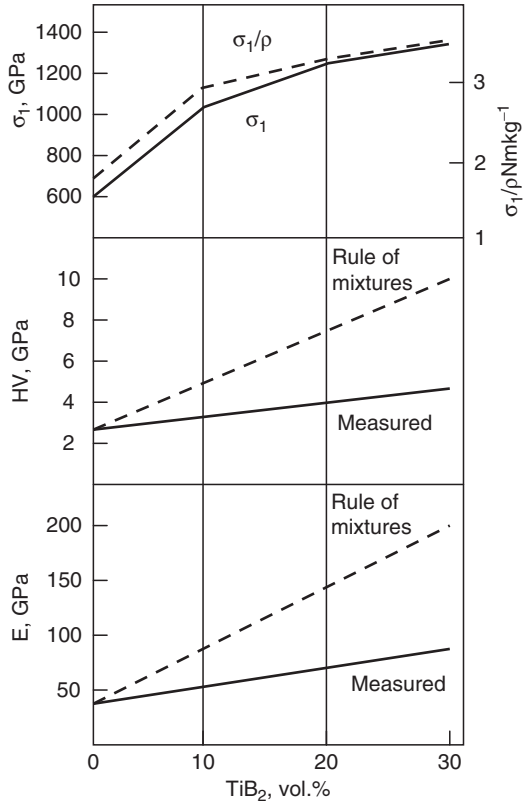

Fig. 13.18 The influence of a volume of the TiB_2 reinforcement particulates on selected properties of a composite based on the amorphous matrix of $Mg_{65}Cu_{7.5}Ni_{7.5}Zn_5Ag_5Y_{10}$ [5]

1.3 GPa was achieved for a plastic strain-to-failure of 2-3% (Fig. 13.18a). A variation of hardness and elastic modulus deviates significantly from the prediction of the rule of mixtures (Fig. 13.18b,c).

13.6.2 Reinforcements Applicable for Magnesium

A variety of reinforcements in terms of size, shape and chemistry are available for composite formation. In fact, the class of composites is defined based on the shape of their reinforcement, and the major grades include:

(i) particles;
(ii) short fibers and whiskers;
(iii) continuous fibers;
(iv) monofilaments;
(v) interpenetrating (three dimensionally percolating) phase, e.g., foam ;
(vi) hybrids.

In terms of chemistry, the most widely used are ceramics since the properties make them very desirable as reinforcements (Table 13.4). Other possibilities include metallic and intermetallic compounds. For metallic powders, a requirement is low solubility in magnesium. Elemental powders of Ti, Cu or Ni with a size of few micrometers were found to act as reinforcements. The size of reinforcement is important. High effectiveness was exerted by nano-particles of Al_2O_3,which increased the yield stress, tensile strength and ductility combination of pure magnesium to a level higher than that of AZ91D alloy [6]. Alumina δ-Al_2O_3 fibers with a size of 3×150μm and a volume fraction of 20% were found to improve the creep of AZ91 alloy. The true stress exponent was close to 3 at the lower stress levels and exceeded 3 at higher stresses. Moreover, the true activation energy for creep was close to the value anticipated for interdiffusion of Al in Mg [7]. The carbon and graphite fibers improve physical properties of magnesium, such as specific strength, stiffness, electrical and thermal conductivity [8].

Table 13.4 Properties of typical reinforcements, applicable for magnesium matrix composites

Property	Unit	SiC	B_4C	BN	Al_2O_3	ZrO_2	Mg_2Si
Crystallographic structure		Hexagonal	Rhombohedral	Cubic	Rhombohedral	Tetragonal/monoclinic	Cubic
Density	g/cm^3	3.1	2.5	3.5	3.9	6.0/5.7	1.9
Melting point	°C	2600	2450	3027	2054	2681-2847	1085
Specific heat	J/kg K	750		793	880		
Coefficient of thermal expansion	$10^{-6}°C^{-1}$	4.0	5.0	11.9	8.4	10.3	7.5
Microhardness	Kgf/mm^2	2800	2500		1440		350-700
Elastic modulus	GPa	410	450	46.9	375	200	120
Compressive strength	MPa	3900		143	2600	1750	

13.6.3 Challenges with Manufacture of the Magnesium Matrix Composites

Processes commonly explored for composite fabrication include:

(i) stir-casting;
(ii) squeeze infiltration;
(iii) liquid phase sintering;
(iv) diffusion bonding;
(v) powder metallurgy.

During stir casting the metal base and reinforcement particles are heated in a furnace until the metallic phase is molten. The key step of this method is mechanical stirring in the furnace. The alloy is then transferred for further processing by sand casting, permanent mold casting or die casting. The squeeze infiltration allows the incorporation of a larger volume fraction of reinforcement, up to 50%. In this method, a preform of a reinforcement is combined with a molten matrix, shaped and solidified under high pressure. In another attempt, pressureless melt infiltration under protective atmosphere of argon at temperatures from 850 °C to 950 °C was used to produce a TiC/Mg composite. As a result, an increase in tensile strength up to 172–233 MPa was achieved [9]. Powder metallurgy is considered the key technique for composite formation, but due to the very high affinity of magnesium for oxygen and its explosive nature, it has certain limitations here.

The combination of stir casting and partial remelting represents another method, tested on the TiB_2–Mg–11Al–0.5Zn system [10]. TiB_2 addition had no influence on the remelting characteristics of the eutectic but affected the remaining liquid, which is located at grain boundaries. No reaction occurred between TiB_2 particles and the matrix, indicating thermodynamic stability of the system. A combination of disintegrated melt deposition technique followed by hot extrusion was applied to manufacture a hybrid composite of AZ91 alloy reinforced with Cu metallic particulates [11]. The addition of Cu increased elastic modulus, yield strength and tensile strength while ductility was marginally affected. It is of interest that an increase in mechanical properties was higher than in the case of SiC additions. Some reinforcements can be formed *in situ* inside the composite. For example, Mg_2Si dispersions may be introduced by employing *in situ* formation of Mg_2Si in a solid state. A similar *in situ* mechanism is used to obtain reinforcements of TiC.

13.6.4 Injection Molding as a Fabrication Method of Composites

The major disadvantage of MMCs is usually the high cost of their manufacturing. In this case injection molding offers a cost-effective solution. When composites are fabricated exploring semisolid routes, they inherit all the benefits typical for semisolid processing.

13.6.4.1 Semisolid Matrix

The matrix represents a unique feature of composites formed using semisolid injection molding. Although it generally has a semisolid nature, in some cases a fully molten state may also be explored. The content of primary solids within the matrix is reduced to accommodate reinforcement particles, e.g., if the composite contains 20% reinforcements, the maximum solid content allowed is reduced by 20%. In cases of practical importance, the size of reinforcement particles is smaller than the primary solid.

13.6.4.2 SiC Reinforcement Particles

SiC particles have lower thermal conductivity and heat diffusivity than magnesium. During solidification the particle's temperature is higher than the surrounding magnesium melt, which slows down the solidification. Based on this assumption, αMg could not nucleate on SiC particles, and as the solidification progresses, SiC particles would travel with the molten alloy.

For an SiC size of 20 μm to 25 μm with volume fractions of 20%, 35% and 40%, the reinforcement particles are distributed uniformly within the matrix (Fig. 13.19). No signs of nucleation of αMg on SiC particles are detected. The solids are generally smaller but uniformly distributed within the matrix (Fig. 13.20). In some cases the Mg matrix in direct vicinity of SiC particles reveals darker contrast, suggesting changes in chemistry due to a reaction between SiC and the AZ91 alloy.

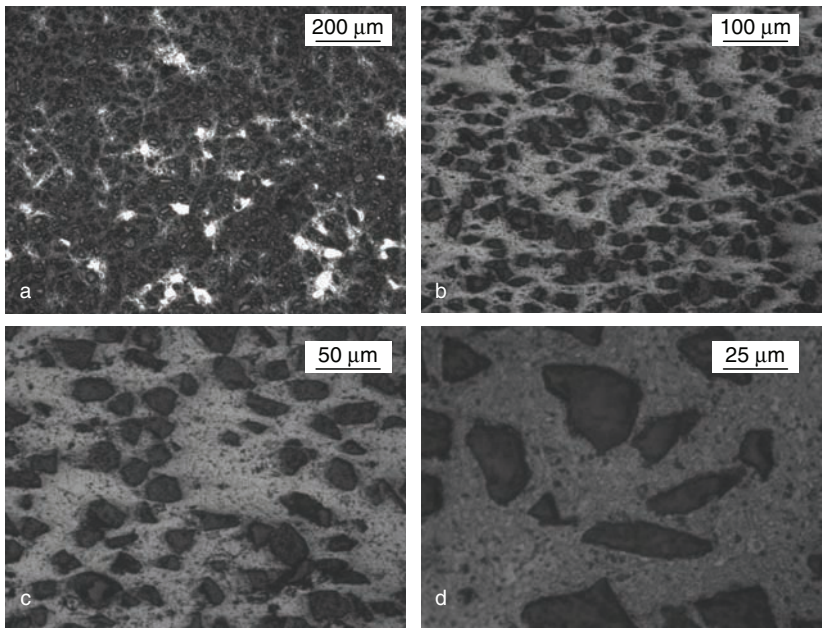

Fig. 13.19 The microstructure of Mg–SiC composite with 35vol% of large particle reinforcements

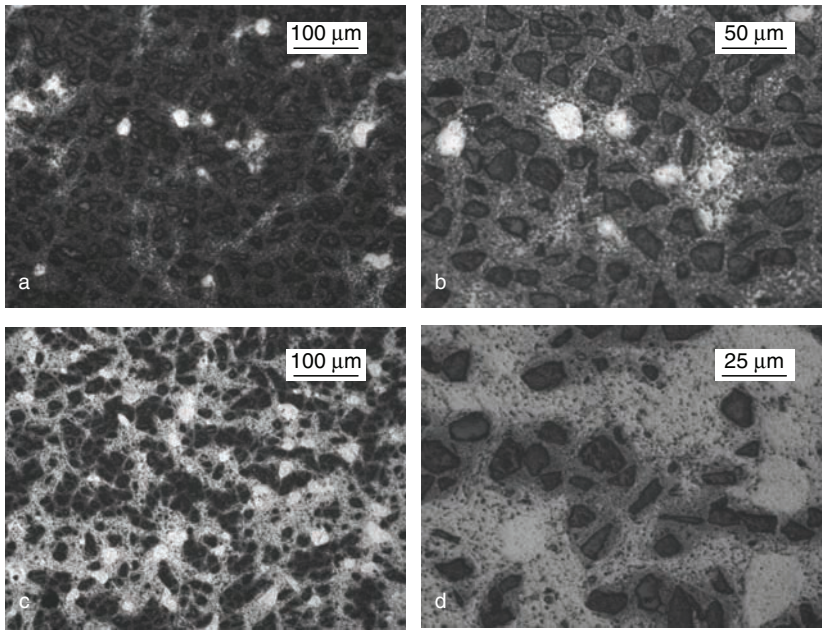

Fig. 13.20 The microstructure of Mg–SiC composite with large particles: **a,b** 20 vol%; **c,d** 40 vol%

For smaller SiC with a size of 1 µm, the role that the particles play during composite crystallization is different. The particle location inside the microstructure in Fig. 13.21 indicates that they act as nucleation sites for αMg growth. There is a tendency for the smaller particles to be more active as nucleation substrates while the larger remain in the molten alloy. Thus after solidification they are present in regions between αMg grains. In general, the αMg grains are not globular, but their external surface is rather well developed.

13.6.4.3 Interfacial Reaction SiC/AZ91

For a short residency time, typical for continuous molding, no substantial dissolution of SiC particles is observed. For longer residency time of the order of 0.5-1 h, the reaction of SiC particles with the AZ91 matrix occurs, and the extent of the reaction depends on the alloy's chemistry. For a pure Mg matrix, SiC particles are inert. For Mg–Al–Zn alloys, interfacial reactions with Al take place, leading to the precipitation of Mg_2Si. The compound is formed by a two step reaction, where the first step is controlled by the content of Al [12]:

$$4Al + 3SiC = Al_4C_3 + 3Si \tag{13.1}$$

$$Si + 2Mg = Mg_2Si \tag{13.2}$$

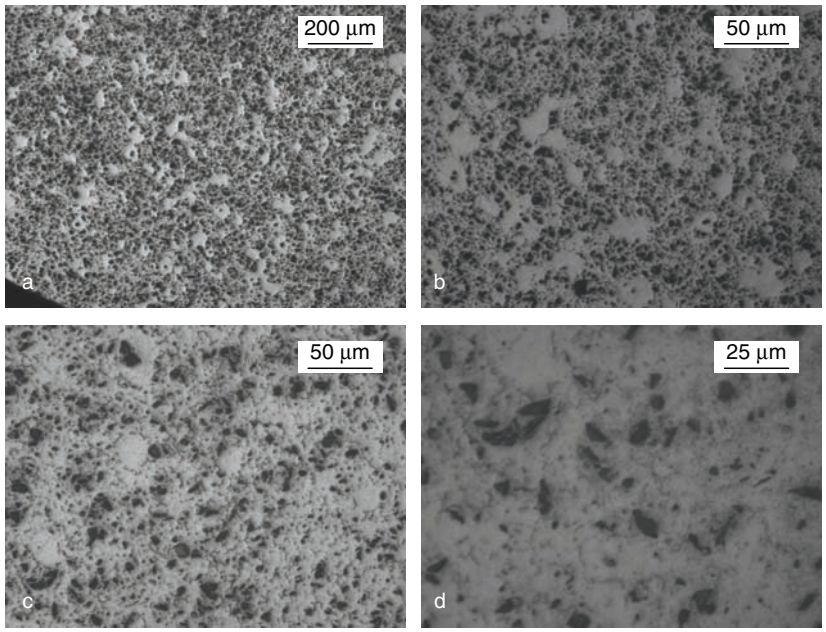

Fig. 13.21 The microstructure of Mg–SiC composite with 20vol% of fine particle reinforcements

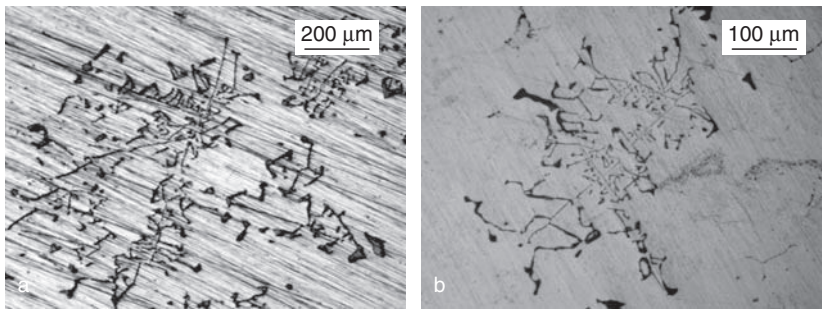

Fig. 13.22 Chinese script-like precipitates of Mg_2Si formed after dissolution of SiC reinforcement

The role of Mg_2Si depends on its morphology. While the polygonal Mg_2Si improves mechanical properties, the Chinese script precipitates (Fig. 13.22) are detrimental by reducing ductility and causing brittle fracture along the Mg_2Si/matrix interfaces. In order to eliminate the Chinese script morphologies and promote the polygonal type precipitates, microalloying elements are added. It was found that for this purpose, additions of P, Ca, Sr, Nd or Sb are very effective.

13.7 Engineering Importance of Semisolid-State Mixing

The concept of alloy generation during semisolid injection molding is of great engineering importance, and the potential advantages are clear when considering the examples described below.

13.7.1 Application to Conventional Alloys

It should be emphasized that alloys Mg–9Al–1Zn, Mg–6Al, Mg–5Al–2Sr and Mg–2Ce–0.3Zn were selected exclusively to demonstrate the concept of semisolid-state mixing. Particular applications will require precursors with appropriate chemistries. The experiments show, however, how the semisolid mixing concept may be used to engineer the required properties of alloys. While Mg–9Al–1Zn shows high strength with excellent castability, Mg–6Al is known for its high ductility and toughness. The alloys formed by mixing will cover an intermediate range of properties. On the other hand, alloy Mg–5Al–2Sr has excellent creep resistance at high temperatures but limited castability. An increase in Al content during alloying with Mg–9Al–1Zn improves castability and room temperature strength while still preserving satisfactory creep resistance at moderate temperatures. Similarly, the alloy Mg–2Ce–0.3Zn is designed for high creep resistance. An absence of Al results in reduced tensile properties at room temperature and demanding castability. Combining it with Mg–9Al–1Zn could allow for balancing between the alloy's castability, room temperature yield, tensile strength and creep resistance. The properties of alloys produced in the semisolid state are not a simple function of their mixing proportions and resultant average chemistry. As shown for a case of equal volume mixing, the properties are affected selectively either by Mg–6Al or by Mg–9Al–1Zn, depending on the processing temperature. The advantages of mixing are superimposed on the well-established benefits of semisolid processing described in Chap. 2.

13.7.2 Application to Immiscible Alloys

A related opportunity of semisolid mixing during injection molding is through generating alloys using ingredients that are generally immiscible [13]. These systems are characterized by their specific thermodynamic features such as positive deviation from Raoult's law and large positive enthalpy of mixing (Fig. 13.23). The immiscible systems of potential engineering importance include Al–Pb, Zn–Pb, Ga–Pb, Al–Bi or Al–In. It is likely that future interests will also include Mg and the Mg–Ti system as an example. So far, there are no casting techniques capable of generating fine and uniformly dispersed microstructures.

The two-step rheomixing strategy was developed to create homogeneous microstructure from immiscible alloy systems [13]. The first step takes place above the melting temperature, when the initial stabilization is achieved by applying an

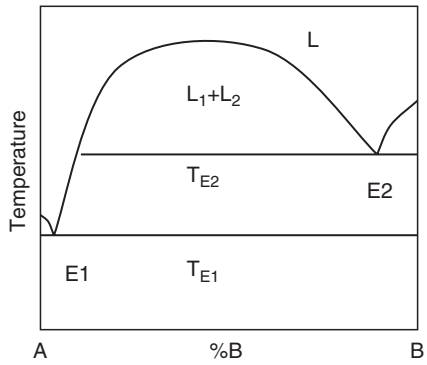

Fig. 13.23 The hypothetical phase diagram of two metals A and B, which do not mix to form an alloy

intensive shear stress-strain field to create a fine homogeneous liquid dispersion. In the second step, this fine dispersion is stabilized by shearing it while in semisolid range. The high viscosity of the slurry is considered as the factor preventing coarse separation. Experiments conducted using Ga–Pb and Zn–Pb systems provided the positive confirmation.

13.7.3 Application to Magnesium Matrix Composites

The application of injection molding to create metal matrix composites offers a clear advantage. This advantage is magnified in the case of magnesium alloys due to their high affinity for oxygen, which does not allow for a direct adoption of techniques used for aluminum. The capabilities of net shape molding are of particular importance for composites with hard reinforcements, which are very difficult and costly to machine.

The semisolid nature of the matrix is not explored commercially. The composite generation by injection molding of a semisolid matrix along with reinforcements will benefit from all of the inherent features, combining high component quality with lower manufacturing cost.

13.8 Summary

Mixing of thixotropic slurries formed during partial melting of coarse particulate precursors represents a novel technique of alloy generation. The microstructure of the created alloy consists of a mixture of unmelted spheroidal solids originating from individual precursors and the matrix that results from combining their liquid fractions. In this process, a critical role is played by the thixotropic structure of the semisolid alloy that is formed from the particulate nature of the precursor. Microstructural inhomogeneity, associated with a selective partition of alloying elements, becomes more evident with temperature reduction, whereupon the liquid fraction is increasingly influenced by an alloy with a lower melting range.

A selection of the feedstock chemistry, mixing proportions and preheating temperature allows controlling of the selective partition of alloying elements between the solid and liquid, thus generating alloys with unique microstructures that are essentially different from those formed after the conventional mixing of completely molten ingredients. It is anticipated that alloys with microstructures created by semisolid-state mixing will exhibit unique properties required for specific applications. The generation of novel materials by semisolid-state mixing is further extended after addition of various reinforcements to magnesium. The composites with a semisolid magnesium matrix, formed this way, may be engineered to meet properties required for certain applications.

References

1. Young, RMK, Clyne TW (1986) Journal of Materials Science 21:1025
2. Yasue K et al (2003) Journal of Materials Science 38:3591
3. Jining Q et al (2006) Mechanical behaviour of a hybrid reinforced magnesium composite fabricated by pressure infiltration method. Key Engineering Materials 313:151–157
4. Mayencourt C, Schaller R (1999) A high damping magnesium matrix to limit fatigue in composite. Journal of Reinforced Plastics and Composites 18(18):1677–1688
5. Xu YK et al (2005) Mg-based metallic glass composites with plasticity and gigapascal strength. Acta Materialia 53:1857–1866
6. Gupta M, Hassan SF (2005) Development of high performance magnesium nano-composites using nano-Al2O3 as reinforcement. Materials Science and Engineering A 392:163–168
7. Y L, Langdon TG (1999) Creep behaviour of an AZ91 magnesium alloy reinforced with alumina fibers. Metallurgical and Materials Transactions A 30:1999–2059
8. Wu F, Zhu J (1997) Morphology of second-phase precipitates in carbon-fiber and graphite-fiber reinforced magnesium based matel-matrix composites. Composites Science and Tecchnology 57:661–667
9. Contreras A, Lopez VH, Bedolla E (2004) Mg/TiC composites manufactured by pressureless melt infiltration. Scripta Materialia 51(3):249–253
10. Jiang QC et al (2004) Effect of TiB_2 particulate on partial remelting behaviour of Mg-11Al-0.5Zn matrix composite. Materials Science and Engineering A 381(1–2):223–229
11. Ho KF, Gupta M, Srivatsan TS (2004) The mechanical behaviour of magnesium alloy AZ91D reinforced with fine copper particulates. Materials Science and Engineering A 369(1–2):302–308
12. Ye HZ, Liu XY (2004) Review of recent studies in magnesium matrix composites. Journal of Materials Science 39:6153–6171
13. Fan Z, Ji S, Zhang J (2001) Processing of immiscible metallic alloys by rheomixing process. Materials Science and Technology 17:837–842
14. Czerwinski F (2004) The concept and technology of alloy formation during semisolid injection molding. In Magnesium Technologies SP-1947, SAE International, Warrendale, Pa, USA, pp 45–49
15. Czerwinski F (2005) A novel method of alloy creation by mixing thixotropic slurries. Materials Science and Engineering A 404(1–2):19–25
16. Czerwinski F (2004) The generation of Mg–Al–Zn alloys by semsolid state mixing of particulate precursors. Acta Materialia 52(17):5057–5069
17. Brooks CR (1982) Heat Treatment, Structure and Properties of Non-ferrous Alloys. ASM International, Metals Park, Ohio, USA
18. Mortensen A, Cornie JA, Flemings MC (1988) Solidification processing of metal-matrix composites. Journal of Metals 12 Feb. 1988

14
Molding Creep-Resistant Alloys

14.1 Introduction

Creep resistance is a major requirement for consideration of magnesium in high-temperature applications. It is believed that the most significant area of future growth for magnesium is in automotive engines and power-train components, but progress is still limited by the substantial weakness of magnesium alloys expressed by their behavior at elevated temperatures. While Mg–Al and Mg–Al–Zn combinations exhibit moderate tensile strength at ambient temperatures, they are all prone to excessive creep when exposed to even low-level loads above approximately 120 °C.

In addition to an alloy's chemistry, the creep properties are also affected by the method of a component's manufacture. Different casting techniques have been investigated to explore slower die filling, solidification under high pressure or semisolid forming [1]. Creep resistant alloys are generally more difficult to process; thus, during die casting, they require higher temperatures with values quoted in the literature as high as 820 °C and 350 °C for melt and mold, respectively [2]. Such conditions might be difficult to implement in an industrial environment. A successful processing of these grades at significantly lower temperatures of their semisolid existence would prove to be a substantial advantage over conventional casting. While semisolid injection molding offers tight temperature control and a closed environment, it operates at significantly lower temperatures. Thus, partial melting introduces differences caused by a partition of alloying elements between the remaining solid and liquid. As a result, it modifies the microstructure and possibly the precipitation phenomena that affect high temperature properties, and in particular its resistance to creep.

This chapter discusses the challenging aspects of injection molding for high temperature alloys of magnesium. First, the nature of creep in magnesium alloys, methods of its control and key families of creep resistant alloys are described. Then, for a selected alloy of Mg–5Al–2Sr the influence of semisolid molding on the microstructure development is analyzed.

F. Czerwinski, *Magnesium Injection Molding*.

14.2 Elements of Creep Deformation Theory

As mentioned in Chap. 4, a metal subjected to a constant tensile load (or constant stress) at elevated temperatures will experience a time-dependent elongation called creep. Since creep processes are diffusion-controlled, they are relevant during exposure over extensive time periods at temperatures exceeding roughly 0.4 of the absolute melting temperature of the material. During engineering tests of creep, the load is maintained at a constant level; thus, stress increases due to a decrease in cross-sectional area.

14.2.1 The Creep Deformation Curve

The idealized creep curve reveals three stages when material degradation progresses at different creep rates (Fig. 14.1a). During the first stage, called *primary creep*, the creep rate decreases. An increase in the creep resistance is associated with material deformation. The initial strain = σ_o /E is the elastic response to the applied stress σ_o.

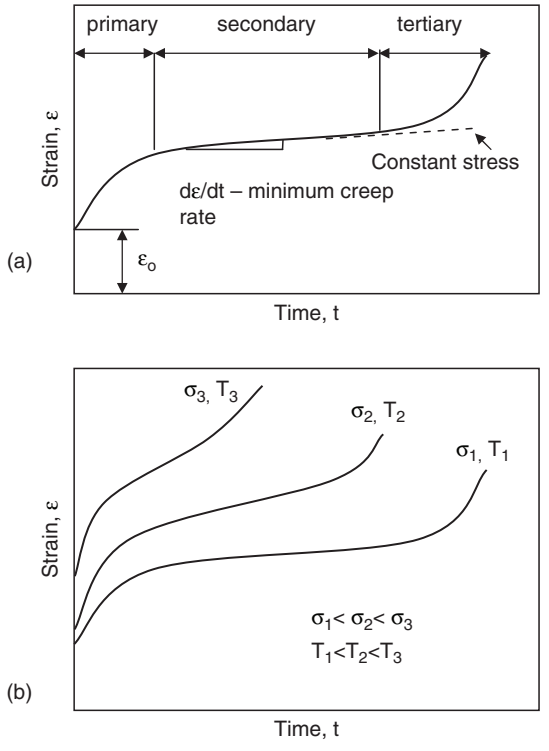

Fig. 14.1 The idealized creep curve showing the three stages of creep **a** and changes of the curve shape caused by strain and temperature **b**

During the second stage, known as *secondary creep* or *steady-state creep*, the creep rate remains almost constant. The slope of the creep curve, being a measure of the creep rate, at this stage reaches minimum. The final stage, called *tertiary creep*, manifests in a rapid increase in creep rate. It is accompanied by a reduction in material cross-section due to void formation or necking, which leads to fracturing.

The creep rate is affected by stress and temperature: Higher temperature and higher stress result in greater creep. It is clear that the creep curve with three stages that are well defined is obtained only for certain stresses and temperatures. In practice, the creep stages are less pronounced and a direction of changes is portrayed in Fig. 14.1b.

There were attempts to mathematically describe the creep curve as a function of time. Early relationships assumed that the creep strain ε increases with time t raised to the third power ($t^{1/3}$ law) [3]. Later, more complex equations were developed, providing a better fit [4, 5]:

$$\varepsilon = \varepsilon_o + \varepsilon_t \left(1 - e^{-rt}\right) + \dot{\varepsilon}_s t \tag{14.1}$$

Where:

ε_o – instantaneous strain on loading;
ε_t – limit for transient creep;
r – ratio of transient creep rate to transient creep strain;
$\dot{\varepsilon}_s$ – steady state creep rate;
t – exposure time.

Since all relationships are of an empirical nature they usually apply to certain materials only.

The most important from a design perspective is the steady state creep rate $\dot{\varepsilon}$. A change of steady state creep may be described by functional relationships involving external empirical parameters, such as stress and temperature. An example is given below [6]:

$$\dot{\varepsilon} = \frac{ADGb}{kT}\left(\frac{b}{d}\right)^p \left(\frac{\sigma}{G}\right)^n \tag{14.2}$$

Where:

D – diffusion coefficient;
A – dimensionless constant;
G – shear modulus;
n – stress exponent;
b – Burger's vector;
k – Boltzmann's constant;
T – absolute temperature;
σ – applied stress;
d – grain size of the material;
p – inverse grain size exponent.

An analysis of the plot of $\dot{\varepsilon}$ versus σ, allows one to distinguish different mechanisms that control the creep rate.

14.2.2 Creep Mechanisms

There are a number of deformation processes at high temperatures. In addition to the primary mechanisms listed below, secondary processes can also occur. While the atomistic mechanisms of creep at intermediate and high stresses are well documented, the interpretation of creep at low stress levels is still controversial.

14.2.2.1 Slip

At elevated temperatures new slip systems are activated. For example, in magnesium non-basal slip systems may occur. The structure of slip bands formed at high temperature is different from those formed at room temperature.

14.2.2.2 Grain-Boundary Sliding

During creep the individual grains of a polycrystalline material may displace with respect to each other, leading to intergranular cracks. The process may be controlled by the generation of dislocations in areas of blockage followed by their pile up and climb on the opposite side of the grain [7]. A model of the formation of wedge cracks during grain boundary sliding is shown in Fig. 14.2. A characteristic feature of grain boundary sliding is that the shape of individual grains is preserved. The process is favored by increasing the temperature and decreasing the strain rate.

14.2.2.3 Diffusional Creep and Harper–Dorn Creep

Diffusional creep is understood as the stress-directed flow of vacancies occurring to restore a condition of equilibrium [6, 8]. During diffusional creep the concentration of vacancies close to a grain boundary, which is normal to an applied tensile stress, increases (Fig. 14.3). At the same time the excess of vacancies flows to the grain boundaries parallel to the tensile stress. Such a diffusion of vacancies leads to a plastic deformation. In a case where the vacancy flow takes place through the crystalline matrix, typical for high temperatures, the process is called Nabarro–Herring creep. At lower temperatures, when the vacancy flow occurs along the grain boundaries, the process is described as Coble creep.

A distinct creep mechanism acting at very low stresses was identified as Harper–Dorn creep [6]. For example, during tests on single crystals and polycrystalline Al at temperatures close to the melting point, the measured creep rate was more than two

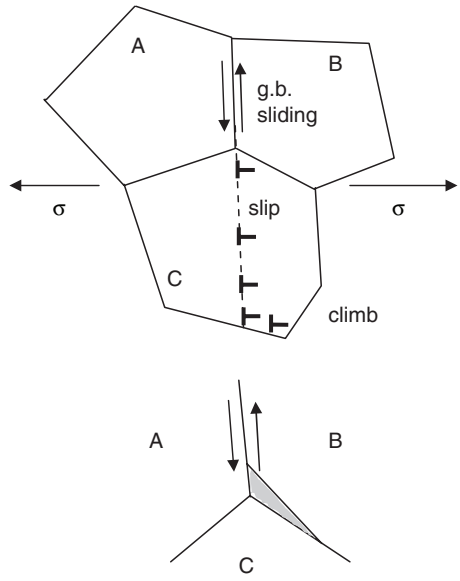

Fig. 14.2 The concept of grain boundary sliding during creep, which involves dislocation glide and climb (top) and a formation of wedge crack at the triple junction (bottom)

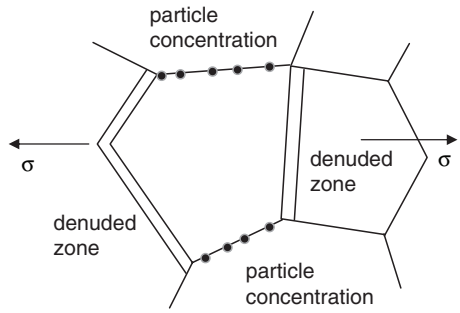

Fig. 14.3 The idea of diffusional creep involving of formation of denuded zones along grain boundaries perpendicular to the load axis and particle precipitation along grain boundaries parallel to the load axis

orders of magnitude higher than that which would be predicted based on the diffusional creep theory. Although the precise deformation mechanism of Harper-Dorn creep is not known, it is generally attributed to an intergranular dislocation process.

14.3 Creep in Magnesium and Its Alloys

For engineering applications of magnesium alloys the creep deformation is relevant in the temperature range 100 °C to 200 °C, with stress reaching the yield stress level of the alloy. However, the creep phenomenon is also registered at slightly elevated temperatures. The general mechanisms of creep characterized above are applicable to magnesium and magnesium alloys. They include diffusion controlled climbing

of dislocations on the basal plane, and cross slip of dislocations [9] or dislocation gliding hampered by solved impurity atoms. The dominant mechanism will depend on the alloy type, temperature and the stress level.

14.3.1 Creep in Pure Magnesium

According to [10] the activation energy of creep in pure magnesium at temperatures 0.5-0.67 T_m is 92 kJ/mol and reaches 230 kJ/mol at higher temperatures. According to [11], for temperature interval 0.5-0.78 T_m the creep activation energy is 134 kJ/mol. For higher temperatures exceeding 0.78 T_m the value is the same as in the previous assessment, i.e., 230 kJ/mol. The same activation energy of 230 kJ/mol is also proposed by [12]. As the major mechanism that controls the creep rate is seen, the dislocation climb is accommodated by self-diffusion [13]. The map of deformation mechanisms for pure magnesium with a grain size of 100 μm is shown in Fig. 14.4.

14.3.2 Factors Affecting Creep in Magnesium Alloys

As compared to metals having a single-phase structure, the creep mechanism in alloys is more complex. The presence of other phases, as well as their microstructure, morphology and distribution within the matrix are the major differences. In addition, the matrix itself is subject to changes, depending on the alloy system. Due to poor creep characteristics of the magnesium matrix there is a vital role for alloying elements. The main concepts to suppress creep include solid solution

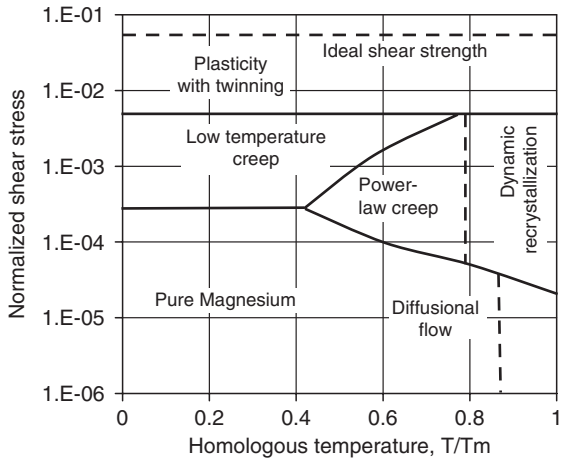

Fig. 14.4 The map of deformation mechanisms of pure magnesium at different temperature and stresses. Normalized shear stress – σ/μ; Homologous temperature – T/T_m [11]

strengthening and grain boundary strengthening by stable compounds to prevent local deformation and sliding in the vicinity of grain boundaries.

14.3.2.1 Solid Solution Additions

The matrix of high temperature magnesium alloys is a solid solution with other elements occupying positions within the crystallographic lattice. In order to be effective, the solvent should have high solubility and due to its atomic size cause substantial strengthening effect. Moreover, its diffusion rate within magnesium should be rather low at high temperatures. Unfortunately, elements having high solubility in Mg, such as Zn or Al, due to their low melting temperatures, are not effective.

14.3.2.2 Precipitates Formed Internally

Precipitates that are stable at high temperatures represent the key source for the improvement of creep resistance in magnesium alloys. They may be distributed within grains or along grain boundaries. In order to be effective, precipitates should fulfill certain conditions, such as:

(i) stability at high temperatures;
(ii) fine size and dense distribution;
(iii) crystallographic coherence with the matrix.

14.3.2.3 Externally Introduced Particle Dispersions

It is well-established that magnesium based composites exhibit increased creep resistance due to a presence of reinforcement particles. The major improvement is derived from (i) the existence of a temperature-dependent threshold stress and (ii) good bonding between the matrix and reinforcement during creep exposure. Experiments with AZ91 alloy, reinforced with 20vol% Al_2O_3 short fibers, revealed an improvement of creep at 150 and 200 °C [14]. An example of creep curves at 150 °C for the AZ91–Al_2O_3 fiber system is shown in Fig. 14.5. The creep life of the composite was found to be one order of magnitude longer. Moreover, the reinforcements led to a substantial decrease in the creep plasticity, exhibiting no clear trend with respect to the influence of stress and temperature on the strain to fracture. Detailed TEM analysis indicates that the matrix microstructure has no significant influence on the creep properties. It suggests that the mechanism controlling creep strengthening in the composite is an effective load transfer that separates the external load between the matrix and the fibers as a result of the matrix-fiber interface bond [15].

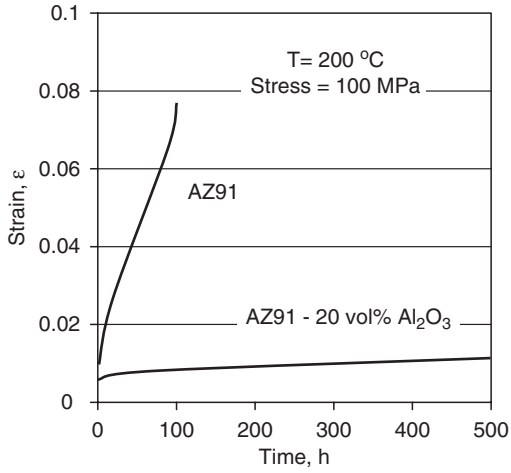

Fig. 14.5 Influence of Al_2O_3 fiber reinforcement on creep behavior of AZ91 alloy [14]

14.4 Creep Control in Modern Commercial Alloys

The directions of Mg alloy development that are recommended for high temperature applications include [16]:

(i) to improve AZ91 by introducing minor changes;
(ii) to develop economic alternatives with application temperatures up to 200 °C;
(iii) to develop alloys with RE or other additions with application temperatures up to 300 °C.

It is interesting to note that gathered empirical evidence, rather than basic understanding, is still used for the practical design and development of magnesium alloys. Creep investigations have shown significant improvement, but a real understanding, and hence further development, will depend on microstructural investigations. The key explanation that is missing relates to the precipitation details of compounds controlling creep and their thermal stability.

The majority of the creep data in the literature is reported for tensile stress. However, there is a significant compression tension asymmetry of creep in magnesium alloys with higher deformation rates in tension than in compression. For AM60B alloy, tested at 150 °C, the minimum creep rate in compression is equivalent to that during tension under half of the applied load [13]. The creep asymmetry is associated with processes enhanced by tension and suppressed under compression:

(i) strain induced by the precipitation reaction;
(ii) precipitation reaction from a supersaturated Mg solution causing lattice dilation;
(iii) cavity growth.

14.4.1 Alloying Systems

The earliest die cast creep-resistant alloys were Mg–Al–RE (AE grades) and Mg–Al–Si (AS grades). The downside of both alloy systems, expressed by less than optimal properties or/and high cost, led to further search. Considerable effort has been devoted to the identification of low cost alloying elements with a better effect on improving creep [16]. The number of possible alloying additions is limited and, according to accumulated experimental evidence for high performance alloys, rare or alkaline earth metals are the best choice where the criterion is the formation of highly stable precipitates. In parallel, the modification of their matrix was attempted by limiting or even completely eliminating Al [17]. The low creep resistance of Mg–Al alloys is frequently attributed to softening of the $Mg_{17}Al_{12}$ phase with a melting point of about 470 °C, which when located at grain boundaries allows grain boundary sliding at temperatures below 150 °C.

Thorium is the most effective alloying element to improve the high temperature properties of magnesium. The benefits are associated with high thermal stability of the equilibrium precipitates $Mg_{23}Th_6$. Due to the radioactivity issue, Th-containing alloys were phased out. Presently, most alloys for applications at 150 °C to 200 °C are Mg–Al systems with single or combined additions of Si, Zn, Ca, Sr or RE. The creep resistant grades are listed together with other commercial alloys in Table 1.7 (Chap. 1).

14.4.1.1 Mg–Al–Si

The veteran family of Mg–Al–Si alloys, developed in the 1970s, exhibits better creep resistance than conventional AZ and AM alloys and may be applied up to 150 °C. The major chemistries explored include Mg–2Al–1Si and Mg–4Al–1Si, but an intermediate Al content in Mg–3Al–1Si was also recently tested by the USCAR program. An increase in Al content in AS grades leads to higher strength at room temperature and better castability at the expense of creep resistance.

The creep resistance of AS alloys is achieved due to the stable Mg_2Si phase, precipitated at grain boundaries. The positive influence of Mg_2Si requires its fine morphology achievable only after rapid cooling. When the solidification rate is slow the Mg_2Si phase crystallizes in dendritic forms that impair the mechanical properties. A modification with rare earth elements or calcium leads to a transformation of the dendritic morphologies of Mg_2Si into finely dispersed globular structures [18].

14.4.1.2 Mg–Al–RE

The beneficial effect of rare earths on high temperature behavior of Mg was discovered in the 1930s. When considering binary alloys the effect of rare earths is divided into two groups: the Ce group (La–Eu) and the Y group (Y and Gd–Lu) [16].

All rare earths form with Mg eutectic phase diagrams with limited solubility, thus being suitable for age hardening. The solubility of the Ce group in solid Mg is substantially lower than elements from the Y group. The most popular system of this group is Mg–4Al–2RE, developed in the 1980s. Since Ce and La are the major rare earth elements in this alloy (RE equals 50%Ce–25%La–20%Nd–5%Pr), the creep is controlled by a mixture of Al_4Ce and Al_4La. Both phases are located at grain boundaries, thus preventing grain boundary sliding, which is the creep mechanism in Mg–Al based systems.

New ways to control creep that not only combine rare earths with calcium but also try to verify various rare earth elements are being researched. It was found that changing the rare earths in Mg–0.5Zn–6Al–1Ca–3RE with lanthanum further improves the creep properties of the alloy (Fig. 14.6) [19]. Lanthanum additions result in crystallization of a large amount of acicular $Al_{11}RE_3$ ($Al_{11}La_3$) compound along grain boundaries and across grain interiors. The improvement in creep is attributed to the control of the grain boundary sliding and dislocation motion in the vicinity of grain boundaries by $Al_{11}La_3$ precipitates.

14.4.1.3 Mg–Al–Ca

The beneficial nature of Ca in Mg-base alloys is associated with [20]:

(i) significant improvement of high temperature strength and creep;
(ii) possibility of further improvement by quaternary additions;
(iii) low density and low cost.

The addition of Ca can refine the grain size, break down the coarse dendrites and form spheroidal structures. The chemistry explored in the 1970s was Mg–8Al–1Zn

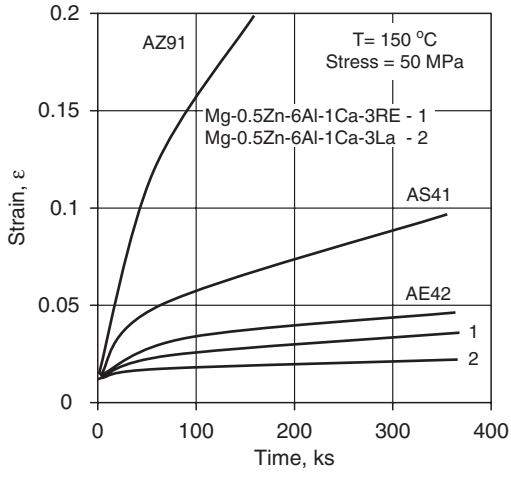

Fig. 14.6 A comparison of creep behavior of magnesium alloys [19]

with an addition of 1%Ca [21]. There are, however, processing issues caused by Ca that include severe die sticking and hot cracking.

In order to improve processing behavior, the Ca content was increased to 2% and 0.1% of Sr was added [18] [22] [23]. In Ca containing alloys, the Al_2Ca Laves phase with a cubic structure is blamed for hot cracking, thus the beneficial effect of Sr is seen in reducing the temperature of Al_2Ca formation. In another solution, implemented in MRI family alloys, rare earth elements are combined with Ca additions.

The beneficial influence of Ca on creep is associated with the presence of the Al_2Ca phase dispersed within the matrix and with the formation of Al_2Ca at grain boundaries during eutectic solidification. In fact, due to the presence of other elements, the actual phase containing Ca appears to be $(Zn, Al, Mg)_4Ca$ [24]. For Mg–5Al–3Ca composition, the eutectic compound contains Al_2Ca, Mg_2Ca, $(Mg, Al)_2Ca$ or a mixture of all three phases [25].

14.4.1.4 Mg–Al–Sr

The development of Mg–Al–Sr alloys was aimed at replacing RE elements, mainly for economic reasons. The latter factor is questioned, pointing towards Ca-containing master alloys or Ce-based mischmetal as less expensive solutions [2]. The major development direction was to modify the AM50 alloy with 1.7-2.2% of Sr. Another alloy of this family has an increased Al content to 6% [26]. A detailed characterization of Mg–Al–Sr alloys is provided later in this chapter.

14.4.2 Role of Alloy Processing in Creep Properties

For a given chemical composition of an alloy, the technique of component manufacture affects the microstructural factors that control creep. Thus, the potential implications of structural transformations during manufacturing should be considered during an alloy selection for high temperature application.

14.4.2.1 Conventional Techniques

Creep resistant alloys containing rare or alkaline earth elements are more difficult to process and, as such, during conventional casting, they require higher melt temperatures. A substantial superheating above liquidus may cause changes in alloy chemistry due to evaporation or oxidation. Die casting is the major technique for manufacturing a variety of components. Due to solidification conditions die cast microstructures are in a non-equilibrium state. For Mg–Al–Zn and Mg–Al alloys, a large amount of Al remains in a supersaturated solid solution. A precipitation of $Mg_{17}Al_{12}$ compound at high temperatures leads to a reduction in creep resistance [27].

14.4.2.2 Semisolid Techniques

Manufacturing techniques that rely on partial melting affect redistribution of alloying elements within the alloy volume. A presence of solid phase causes an enrichment of the liquid in some elements. It is anticipated that after solidification the microstructure will be different than that after complete melting. A difference in microstructure will affect creep properties.

14.4.2.3 Heat Treatment

Heat treatment changes properties of the matrix as well as the structure and distribution of precipitates. As a result, it affects creep behavior. In Mg–Al alloys, a T4 treatment leads to increased creep rate. If the Al content is high enough to generate precipitation hardening, the T6 treatment that follows will reduce the creep rate. There is also conflicting information on the role of precipitates: While according to [27] the formation of precipitates deteriorates creep, according to [28] the occurrence of precipitates after annealing led to an improvement in creep resistance. Pre-aging of Mg–5Al–3Ca–0.15Sr alloy at 200 °C for 100 h caused a reduction in creep resistance. The higher creep rate was associated with a decrease in solid-solution strengthening in αMg grains due to depletion of Al and Ca atoms to form precipitates [25]. For the Mg–5Al–8Zn alloy, an over-aging at 190 °C for 300 h led to the activation energy of creep being significantly lower than directly after die casting. During a creep test at 150 °C to 190 °C the over-aged alloy had an activation energy of 143 kJ/mol, which is close to lattice self-diffusion in magnesium [29]. The value of activation energy after die casting was 183 kJ/mol.

14.5 Characteristics of Mg–5Al–2Sr Feedstock for Injection Molding

Semisolid molding introduces unique changes to the alloy microstructure. Detailed structural changes experienced by Mg–5Al–2Sr alloy are described below. The results not only provide transformations during molding of this particular alloy but also allow the estimation of the direction of potential changes that may be experienced in alloys with other chemistries.

14.5.1 Alloy Chemistry and Melting Range

The Mg–5Al–2Sr alloy was developed by Noranda Inc. for high temperature applications and exhibits a superior creep behavior, acceptable castability and good corrosion resistance. The contents of major chemical elements in the as-cast ingot

Table 14.1 The chemical composition of the ingot precursor and semisolid processed alloy, determined by inductive coupled plasma spectrometry. An analysis performed according to ASTM E1097 (modified) and E1479-99 specifications. All values are in weight % [37]

	Al	Sr	Mn	Si	Ni	Cu	Fe	Mg
As-cast ingot	5.15	1.64	0.31	0.01	<0.001	0.002	0.06	Balance
After semisolid processing	4.62	1.67	0.42	0.03	<0.001	0.002	<0.01	Balance
Noranda specification for AJ52x	4.5-5.5	1.7-2.3						Balance

precursor, molded products along with standard requirements are listed in Table 14.1. A comparison indicates that injection molding preserved the alloy chemistry, and the strontium content remained at the same level of 1.64-1.67%, which is slightly below the specification requirement. The molded alloy contains 4.62% Al, which is less than its cast precursor, showing 5.15% of Al. Since Mg is known to have a high evaporation rate, one should rather expect an increase in Al content during any process involving melting.

Knowledge of an alloy's melting range is crucial for semisolid processing. According to thermal calorimetry measurements, the solidus and liquidus for the chemistry of Mg–5%Al–2%Sr are 512 °C and 616 °C, respectively (Fig. 14.7). Temperatures evaluated from the transformation curve serve as input for designing thermal profiles along the magnesium flow path inside the machine barrel.

14.5.2 Effect of Sr on Phase Composition in As-Cast Ingot

The as-cast ingot provides a good reference for understanding changes caused by semisolid processing, which involves a partial melting during slurry preparation followed by rapid solidification after injection into a mold cavity. A relatively slow solidification makes an ingot structure more suitable for examination of changes caused by the presence of Sr, through comparison with the equilibrium phase diagram. The key obstacle is, however, a lack of a well-defined Mg–Al–Sr ternary diagram [30]. The prediction of phases is presently conducted based on three binary diagrams of Al–Mg, Al–Sr and Mg–Sr. Within the Al–Sr system, in addition to solid solutions of Al, γ-Sr (bcc) and α–Sr (fcc), there are three intermetallic compounds: Al_4Sr, Al_2Sr and Al_7Sr_8 [31]. The Mg–Sr system also contains, in addition to solid solutions of Mg, γ–Sr and α–Sr, four intermetallic compounds: $Mg_{17}Sr_2$, $Mg_{38}Sr_9$, $Mg_{23}Sr_6$ and $MgSr_2$ [32].

X-ray diffractometry revealed that, similar to binary Mg–Al systems rich in Mg, a matrix represents the αMg solid solution with Al as the major solvent (Fig. 14.8). The intensities of αMg peaks are roughly proportional to data from the JCPDS standard, indicating the random distribution of grain orientations. The second major phase identified is the hexagonal structured Al_4Sr with eight diffraction peaks, starting from (101) at 2-theta of 21.446 deg (all numbers represent standard positions). The strongest experimentally measured (112) peak for Al_4Sr at

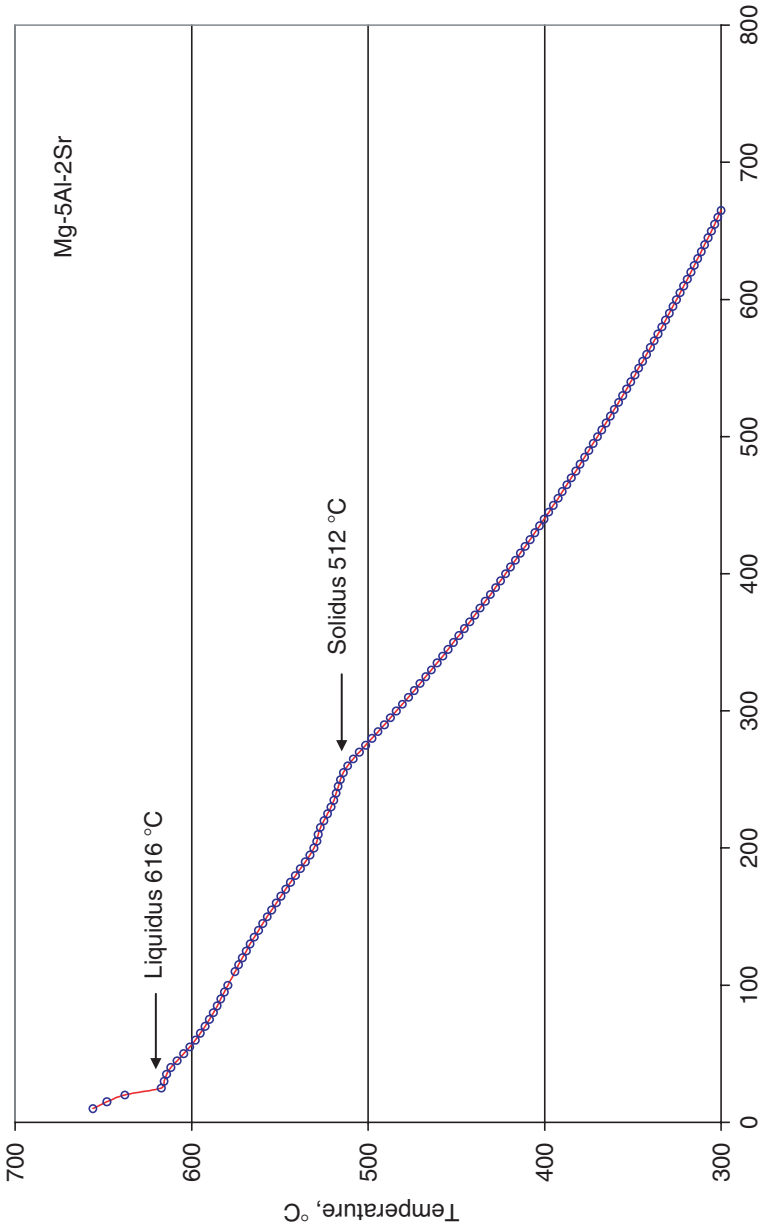

Fig. 14.7 The thermal analysis of Mg–5Al–2Sr alloy, revealing the liquidus and solidus temperatures

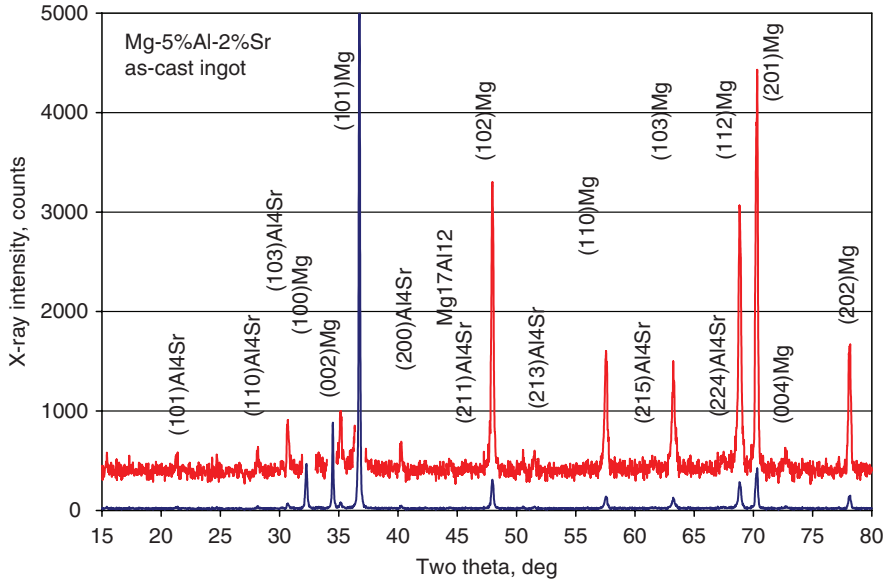

Fig. 14.8 The X-ray diffraction pattern of as-cast Mg–5Al–2Sr ingot with descriptions of phases detected [37]

32.765 deg, corresponds to the strongest according to the JCPDS standard. Fitting software indicates that traces of two binary Mg–Sr phases: Mg_4Sr and $Mg_{5.2}Sr$, both with hexagonal structures, can also be present. Since both phases have many peaks whose locations coincide with Al_4Sr and overall peak intensity is slightly above the background noise, in order to avoid ambiguity, additional verification using other analytical techniques is required.

According to a planimetric estimation of the X-ray diffraction pattern, αMg occupies 92% of the sample volume, Al_4Sr—4% with a remaining 4% for other phases, including about 1% of $Mg_{17}Al_{12}$. Because of the overlap of major diffraction peaks between αMg, and $Mg_{17}Al_{12}$ (JCPDS 1-1128) the presence of the latter is not clearly stated on the 2-theta scan: The strongest peaks of αMg and $Mg_{17}Al_{12}$ are at 36.601 and 36.191 deg, respectively. The key peak, confirming the presence of $Mg_{17}Al_{12}$, is at 43.917 deg, with significantly weaker ones at 65.186 deg and 76.084 deg. In addition, there are some other phases involving elements present in small amounts, as Mg_2Si. Again, peaks for Mg_2Si overlapped with both αMg and $Mg_{17}Al_{12}$.

14.5.3 General Microstructure

The microstructure created during a slow solidification of the standard size ingot, is shown in Fig. 14.9. Under the contrast of a scanning microscope, the dark phase of αMg matrix is divided by bright precipitates, forming a network of grains/cells with

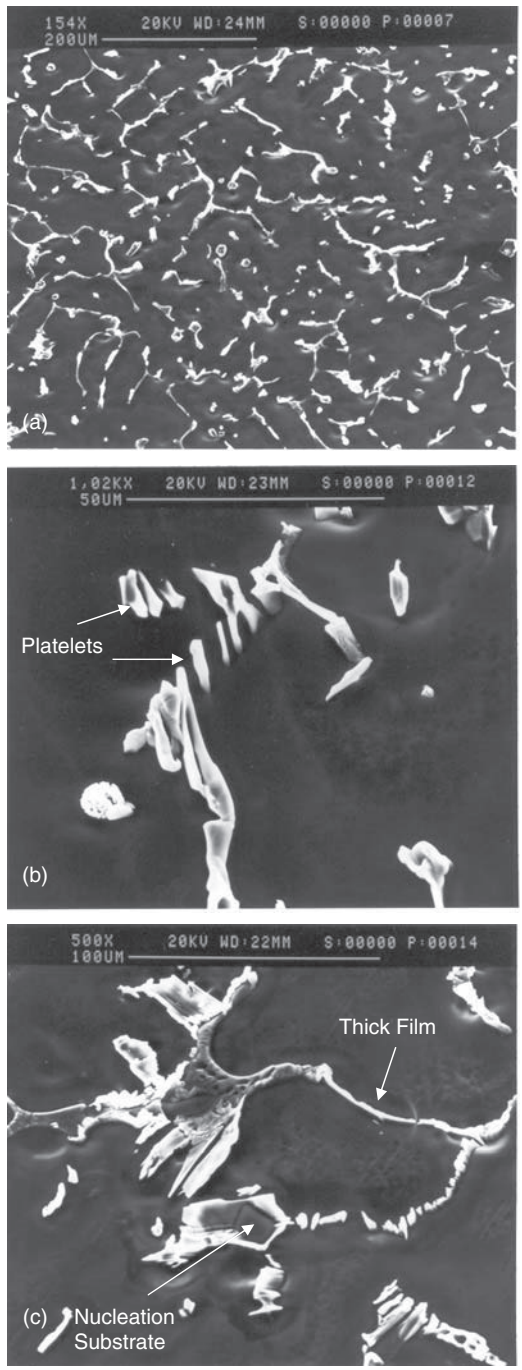

Fig. 14.9 The SEM micrographs of as-cast Mg–5Al–2Sr ingot: **a** distribution of the intermetallic compounds at grain/cell boundaries; **b** detailed morphology of plate-like precipitates in chain-like arrangements; **c** complex-shape aggregates of an intermetallic; the arrow indicates the Mn–Al particle surrounded by a Mg–Al–Sr compound [37]

a size typically below 100 µm. At a flat cross section, the network is not continuous and requires connections via αMg bridges (Fig. 14.9a). The dark matrix of Mg exhibits differences in etching features, most likely caused by a combination of crystallographic orientation and chemical segregation. The precipitates are not morphologically homogeneous and two major types are distinguished. In addition to the thick film located along grain boundaries, the plate-like compounds in chain arrangements are the most typical. The platelets, approximately 20 µm long, are oriented at an angle to the grain boundary direction and roughly parallel to each other. A distance between them is of the same order of magnitude as their thickness (Fig. 14.9b). Some precipitates, especially those located at triple junctions, have a complex shape, frequently referred to as Chinese script (Fig. 14.9c). The minor precipitates of blocky shapes with a higher melting point, e.g., manganese aluminum compound, act as preferred nucleation sites for other intermetallic phases, as marked in Fig. 14.9c. Although a majority of precipitates reside at grain/cell boundaries, in some cases single blocky compounds appear to be located inside larger grains. It is suspected that their location coincides with subgrain boundaries, not revealed by etching.

A correlation is identified between the precipitate morphology at the scale of SEM magnifications and their chemistry. The plate-like and complex shapes contain Al and Sr (Fig. 14.10a,b). By contrast, the film-like compounds contain

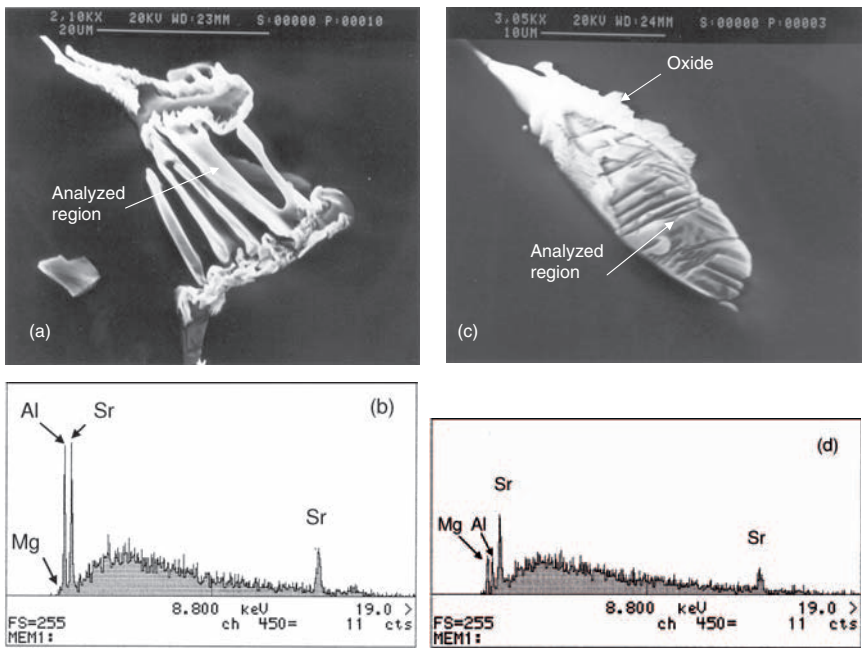

Fig. 14.10 The SEM detailed view of typical morphologies and EDAX energy spectra: **a** plate-like precipitates arranged in Chinese script shape and **b** corresponding EDAX spectrum detecting exclusively Al and Sr; **c** film-shaped precipitates at αMg grain boundaries and **d** EDAX spectrum indicating Sr rich compound with Al and Mg [37]

Mg in addition to Al and Sr (Fig. 14.10c,d). Since the dimensions of both types of precipitates are roughly the same, there should be no error involved due to the collection of the Mg signal from the surrounding matrix. In addition, precipitates exhibit differences in surface contrast. This is not caused by the basic chemistry of precipitates but rather by surface oxidation. Thus, the bright color oxides, apparently having lower electrical conductivity, lead to gathering electrons. As seen in both Figs. 14.10a and 14.10c, the dark contrast portion extends clearly from beneath the bright surface layer.

14.5.4 Ingot's Phases and Their Morphology

As revealed by microscopic examinations, Sr combined with the Mg–5Al base creates a number of compounds with different morphologies and distributions. TEM thin foil examinations provide the characteristics of a subtle microstructure of the matrix grains and fine precipitates that are not detected by optical and SEM techniques. The αMg grains are composed of thin laths having a distinct contrast caused by different densities of dislocations. According to SAD diffraction, laths are separated by low angle grain boundaries, and the imaged region of Fig. 14.11a reflected electrons as a single crystal (Fig. 14.11b). In some cases, however, twin orientation relationship between lath-type features is observed. The precipitates revealed at TEM magnifications represent at least three categories. In addition to relatively large plate like Al–Sr precipitates detected above by SEM, TEM revealed small islands of parallel platelets arranged in eutectic colonies (Fig. 14.12a). SAD identified them as Al_4Sr and they formed the eutectics with Mg (Fig. 14.12b).

Another types of precipitates fill some αMg grain interiors and represent a fine Mg–Al compound identified as $Mg_{17}Al_{12}$ (Fig. 14.13a). They reside at certain habit planes and exhibit a clear crystallographic relationship with the matrix as shown by the SAD pattern (Fig. 14.13b). Their morphology resembles tiny platelets with several different crystallographic arrangements within the matrix. It is not clear why there is a substantial difference in the precipitate density between individual grains with some grains being almost precipitate-free. A segregation of Al within the ingot is the likely explanation. The third category represents tiny precipitates located at sub-boundaries. This is another type of precipitate containing Sr, revealed by TEM in an as-cast state (Fig. 14.14a). They had a small size, a morphology of fine discs and a single crystal type of SAD, suggesting their strict crystallographic orientation–relationship with the matrix (Fig. 14.14b).

The major new phase, created after modification with Sr, is Al_4Sr. It has a tetragonal structure (a = 4.46 A and c = 11.07 A) and a melting point of 1025 °C [33]. Its presence is clearly confirmed by X-ray diffractometry and TEM/SAD diffraction. According to metallography and microchemical spectra from SEM/EDX, the second major phase is Mg–Al–Sr with a film-type morphology, located at grain/cell boundaries. Its existence is, however, confirmed neither

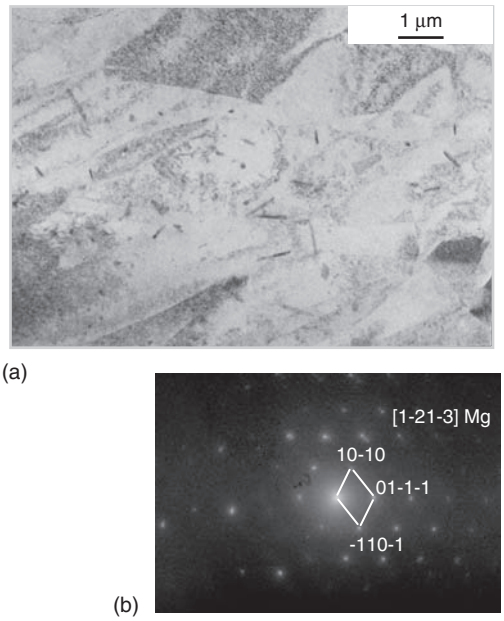

Fig. 14.11 The TEM image **a** and SAD diffraction pattern **b** of the αMg matrix grain, which consists of laths with different dislocation density [37]

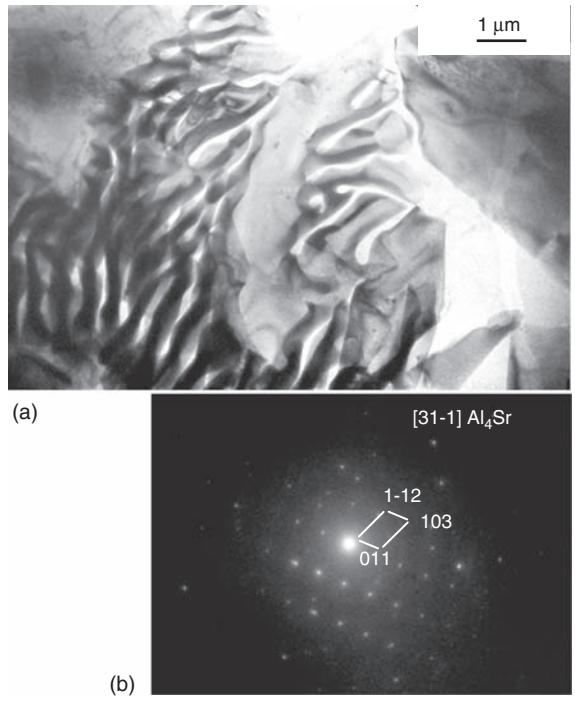

Fig. 14.12 The TEM image **a** and SAD diffraction pattern **b** of an island of platelets identified as Al_4Sr [37]

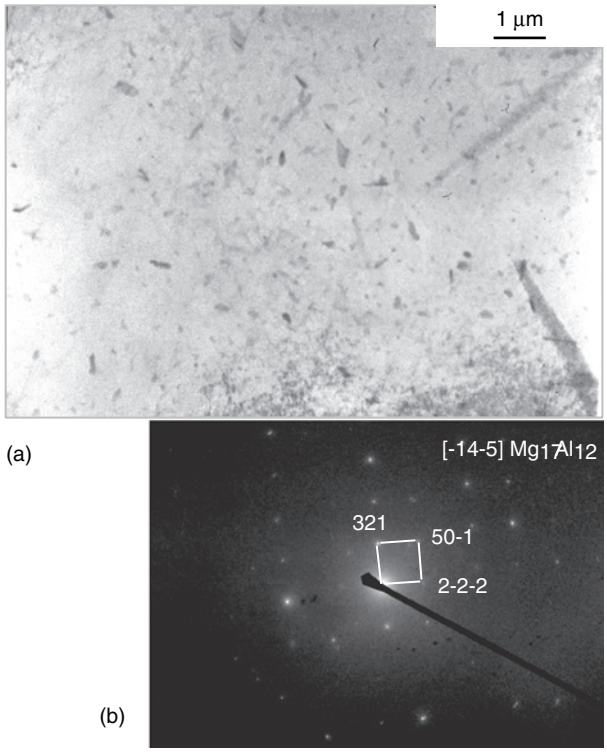

Fig. 14.13 The TEM image **a** and SAD diffraction pattern **b** of the αMg matrix with fine precipitates of $Mg_{17}Al_{12}$ [37]

by bulk X-ray diffraction nor by TEM to establish the precise characteristics. For a die-cast state the stechiometry of $Al_3Mg_{13}Sr$ is reported [26]. The common feature of Sr-containing phases in as-cast ingot is their location at grain or sub-grain boundaries. The presence of $Mg_{17}Al_{12}$ would suggest an insufficient amount of Sr to bind all Al. At the same time, however, Sr reacted exclusively with Mg forming $Mg_{17}Sr_2$. Hence, it is very likely that the local segregation of Al and Sr leads to a variety of phases observed. A variation in the morphology of intermetallic compounds indicates different mechanisms of their formation.

14.5.5 Changes During Manufacturing of Particulates

When considering the microstructure evolution from an as-cast precursor to a semi-solid molded component, changes that take place during the conversion of an ingot into coarse particulates (chips) should be included (Fig. 14.15a). As described earlier

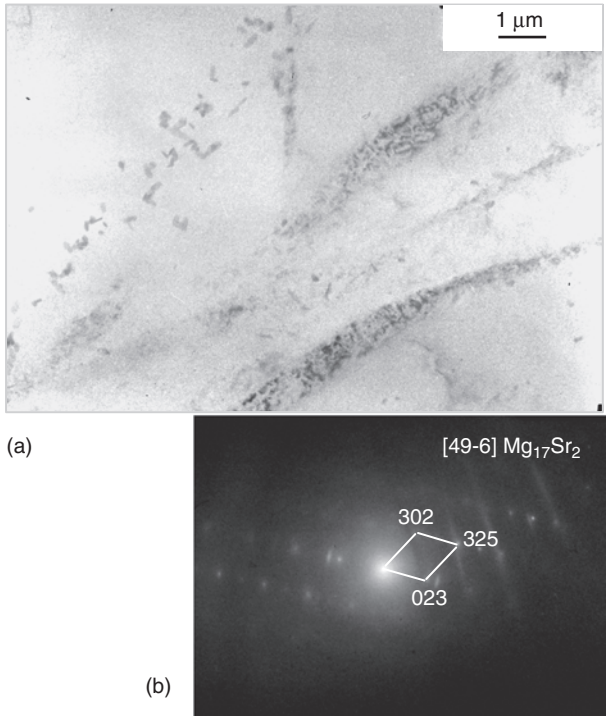

Fig. 14.14 The TEM image and SAD diffraction pattern **b** of Sr containing precipitates distributed at sub-grain boundaries of αMg. The precipitates were identified as $Mg_{17}Sr_2$ [37]

for other alloys (Chap. 6) an interaction with a chipping tool at room temperature introduces structural changes to the as-cast material. The brittle intermetallic compounds that reside at grain/cell boundaries, experience cracking and are fragmented into small particles (Fig.14.15b). The αMg matrix, being more ductile, is subjected to plastic deformation. Cold work introduced during mechanical comminuting activated recrystallization during solid state reheating, as described in Chap. 8.

14.6 Effect of Semisolid Molding on Mg–5Al–2Sr Microstructure

The additions of strontium affect the morphology, distribution and chemical composition of precipitates in both the ingot precursor and semisolid molded components. The precipitation phenomena in Mg–5Al alloy, which serve as the base for Sr modifications, involve solely the formation of the equilibrium phase $Mg_{17}Al_{12}$. The nucleation of $Mg_{17}Al_{12}$ from a supersaturated solid solution is energetically difficult, and it forms preferentially by discontinuous precipitation

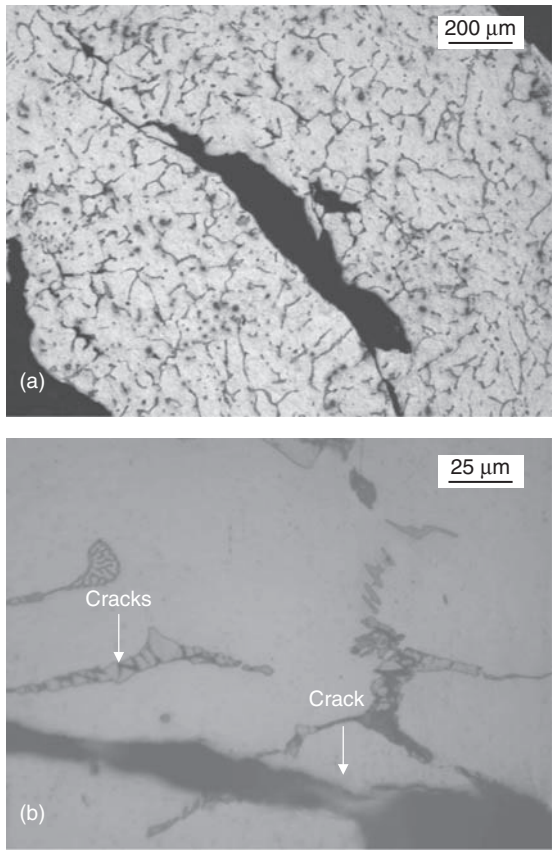

Fig. 14.15 The microstructure of mechanically comminuted chips: **a** general view; **b** detailed image of deformation features with fragmentation of intermetallic compounds and cracking of the matrix. Optical microscopy image after etching with a nital

at grain boundaries [34]. It is commonly accepted that $Mg_{17}Al_{12}$ facilitates grain boundary migration and increases creep. Thus a systematic reduction, or elimination, of the $Mg_{17}Al_{12}$ volume would lead to improvement in creep resistance. The aim of modifications with rare or alkaline earth metals is to suppress the formation of $Mg_{17}Al_{12}$ and activate the growth of more stable phases.

14.6.1 Phase Composition

The X-ray diffraction pattern of as-molded alloy exhibits some differences when compared to the ingot state (Fig. 14.16). The changes in intensity ratios for (100)Mg and (002)Mg do not have any significance; the sample orientation was random. Of importance are, however, higher intensities of the Al_4Sr peaks when compared to

the Mg matrix. Again, the strongest experimentally measured (112) peak for Al_4Sr at 32.765 deg, corresponds to the strongest according to the JCPDS standard. According to planimetric estimation, there is still about 1% of $Mg_{17}Al_{12}$. Another difference is the presence of two diffraction peaks at low 2-theta values, approximately, 18.26 deg and 23.68 deg. Those peaks are not present for the ingot precursor. So far, it is not clear what phase could be associated with them.

14.6.2 General Microstructure

The as-molded microstructure is essentially different from the ingot precursor. It comprises unmelted solid particles surrounded by a transformation product of the former liquid (Fig. 14.17a). In an optical microscope imaging contrast, the unmelted phase is seen as bright. The solid's morphology is generally globular, but there are also larger particles with truncated shapes and size much larger than the spherical particles. As opposed to Mg–Al alloys, no extensive "entrapped liquid" pools are present inside the primary solids. The alloy matrix, formed by solidification of a former liquid from a partially molten state, consisted of very fine Mg grains densely surrounded by intermetallics. The grey contrast precipitates, larger than the matrix grains are minor phases, identified as Mn–Al compound (Fig. 14.17b).

The molded microstructure observed in the contrast of SEM microscopy, which is the reverse of that in optical imaging, is shown in Fig. 14.18. The interiors of the

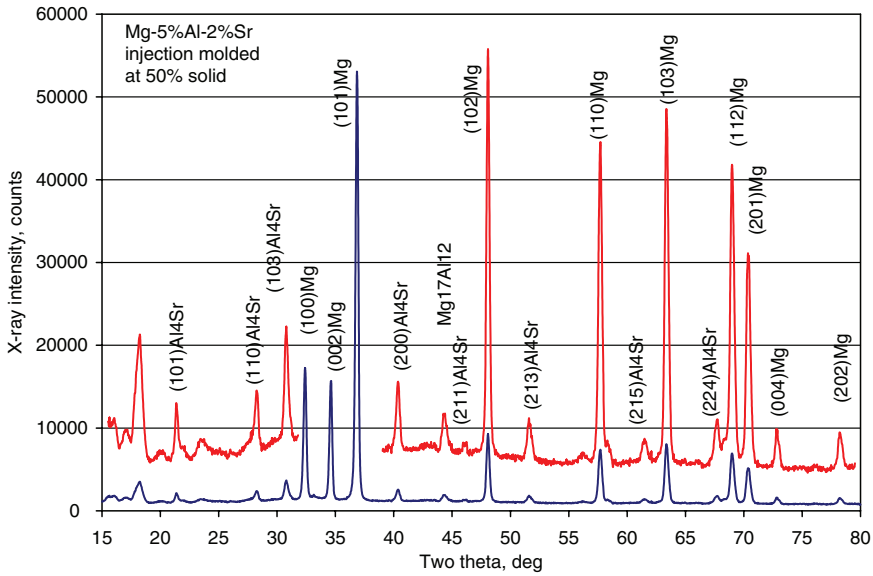

Fig. 14.16 The X-ray diffraction pattern of the injection molded Mg–5Al–2Sr alloy with a description of phases detected. An approximate solid content of 50% [37]

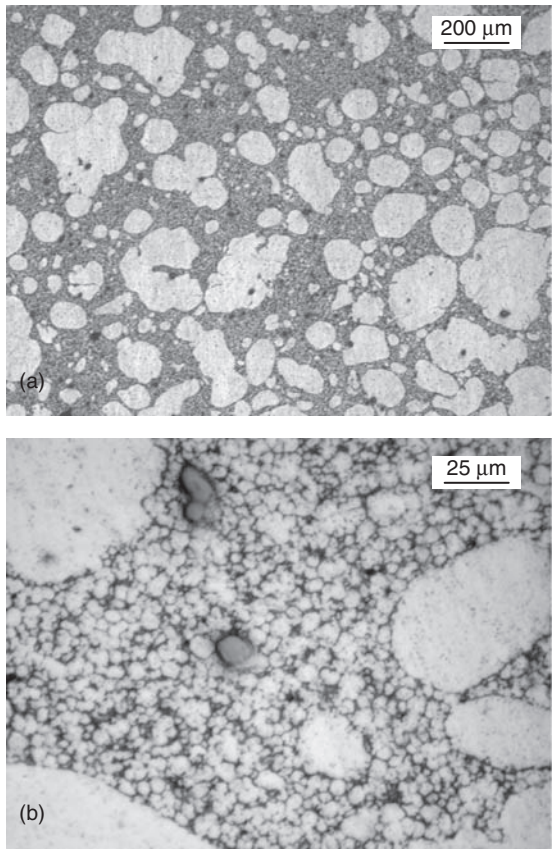

Fig. 14.17 The optical microscopy image of the semisolid molded alloy with a solid content of 45%: **a** morphology of the primary solid particles; **b** morphology of the solidified liquid portion forming the alloy's matrix [37]

primary solid contain trace quantities of brightly contrasted spherical precipitates, which can be interpreted as equivalent to an entrapped liquid in the Mg–Al alloy without Sr. Since the precipitates are located inside the globules, only the sections through the globule center are able to reveal them. Smaller globules, seen in Fig 14.18a, were sectioned at a distance from their centers.

The structure of the transformed liquid comprises secondary Mg grains with a typical size below 10 μm, with a dense network of intermetallics at grain boundaries (Fig. 14.18b). The small size of Mg grains, hence the high contribution of grain boundaries, causes a relatively high density of precipitates. At higher magnifications, the sub-structure of bright contrast precipitates is revealed. The predominant fraction is represented by platelets tightly combined to form colonies, some of them as large as 5 μm (Fig. 14.18c). In addition, some grain boundaries are covered with a film-like layer; this type is, however, in the minority. It should be kept in mind

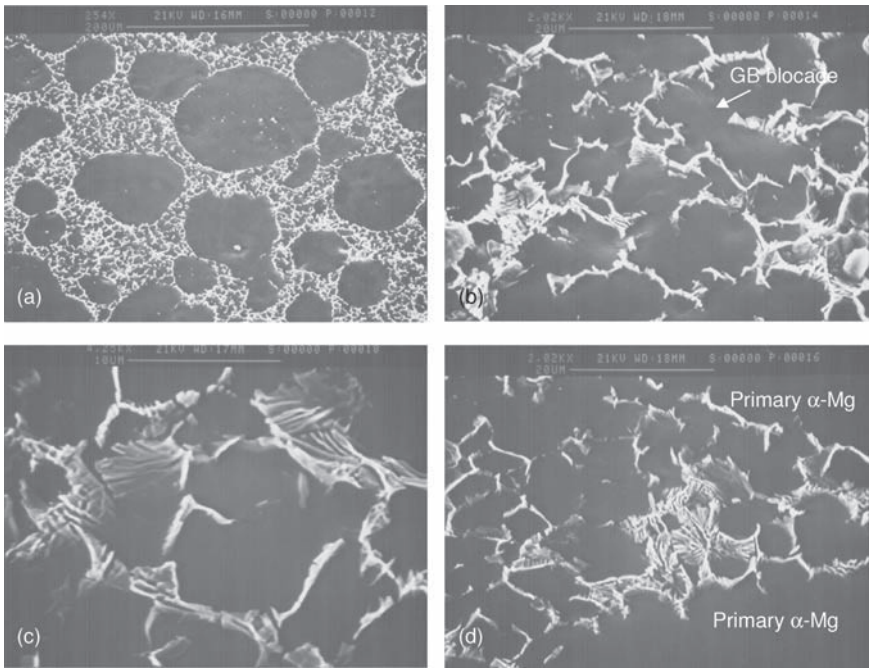

Fig. 14.18 The SEM contrast images of the semisolid molded microstructure: **a** primary solid particles separated by a matrix of solidified liquid; **b** morphology and distribution of the intermetallic phases within the solidified liquid; the arrow indicates small precipitates blocking the grain boundary; **c** magnified view of lamellae nature of intermetallics; **d** interface between the primary solid and solidified liquid [37]

that in some cases this image might represent artifacts caused by a sectioning direction. In some areas the platelets formed large aggregates, comparable to the size of the secondary αMg. Not all grain boundaries are rich in coarse precipitates, and grain boundaries evidently free of precipitates are present, as identified by the arrows in Fig.14.18b. The interface between the primary αMg and transformed liquid is shown in Fig. 14.18d. There is no increased content of the intermetallic phase and rather secondary Mg grains were formed on the primary αMg surface.

14.6.2.1 Effect of Strontium on Primary Solid

The noticeable differences in the morphology of thixotropic structures between Mg–Al alloys with and without Sr additions are distinguished. First, they include the shape of the primary solid, which in Mg–5Al–2Sr alloy also contains, in addition to well-developed globules, particles with truncated shapes and a larger size. As a result, the particle size distribution tends to be bimodal. The average size of the highly globular fraction, of 75 μm for 50 % solid, is generally smaller than

that in pure Mg–Al alloy [35]. These findings are in partial agreement with studies of the influence of Mg and rare earth element additions on the semisolid microstructure in zinc based alloys. Those authors found that rare earth elements decreased the coarsening rate of the primary solid phase and improved the uniformity in particle size [36]. Moreover, the influence of rare earth elements in zinc alloys was concentrated within the liquid regions between particles, suppressing atom diffusion and welding particles together. Another feature of the Mg–5Al–2Sr alloy is a lack of entrapped liquid in the interior of primary solids. This suggests that Sr reduced the Al segregation effects by confining its presence to grain boundaries. Globule interiors experienced, therefore, less Al coring and did not form liquid pools while heated to the solidus–liquidus range. The subtle details with tiny laths and their twin nature indicate deformation, possibly experienced as a result of stress imposed by solidified liquid.

14.6.2.2 Effect of Strontium of Liquid Fraction

The addition of Sr also affects the liquid portion of thixotropic slurry. Since the Al and Sr containing eutectics have lower melting temperatures, the partial melting leads to the selective partition of alloying elements between the solid and liquid phases. As a result, the chemistry of the liquid fraction, forming the alloy's matrix, is different than the average for the alloy. Furtherfore, the melt's chemistry is controlled by the alloy preheating temperature. For low temperatures within the solidus–liquidus range, corresponding to the high-solid contents, the liquid is highly enriched in Al and Sr. Increasing temperature causes a solution of Mg-rich solid that reduces the concentration of Al and Sr. After solidification, the chemistry of the liquid fraction affects the type and morphology of the phases. This also applies to $Mg_{17}Al_{12}$. To eliminate completely the formation of the $Mg_{17}Al_{12}$ phase, a certain ratio of Al to Sr is required. Thus the higher Al/Sr ratio leads to increased volumes of Al_4Sr and results in fewer Mg–Al–Sr compounds. The higher volume fraction of Al_4Sr, projected from X-ray diffractometry, is magnified when one assumes that the existence of Al_4Sr phase is restricted to the former liquid area. This area may occupy only 50% of the material volume. Similarly as in an as-cast ingot, traces of $Mg_{17}Al_{12}$ are still present after semisolid molding. Their location in as-molded state within grain interiors of the primary αMg seems to indicate that they are formed as the result of a coagulation of the continuous precipitates observed after casting.

The beneficial feature of the semisolid microstructure is very small size and mostly equiaxed shape of the secondary αMg grains. Microscopy revealed two contributing factors. First, the nucleation of αMg grains is controlled not only by the primary αMg spheroids but also by fine precipitates of Mn–Al–Sr. Due to the high melting temperatures, the Mn–Al–Sr compounds were suspended in a molten alloy and acted as nucleation substrates. Then, the growth of grains was hindered not only by Al_4Sr lamellae conglomerates distributed around them but also by small and highly effective precipitates located at grain boundaries.

14.6.3 Phase Morphology

TEM thin foil imaging of unmelted solid globules reveals a substructure composed of thin laths with a contrast generated by a variation in dislocation density (Fig. 14.19a). Excluding αMg, no other phases are detected. Also, there is a specific difference in laths' orientation, and according to SAD, individual laths exhibit a twin orientation relationship (Fig. 14.19b). The $Mg_{17}Al_{12}$ compound, occasionally discovered, is of irregular morphology. The particle shown in Fig. 14.20a,b was thinned in some areas to a level where it reveals the dislocation substructure within Mg grain located beneath. In addition to lamellae structures observed by SEM, the Sr containing phases also exhibit a dendritic morphology (Fig. 14.21a). Moreover, much smaller precipitates containing Sr were detected at a twin boundary (Fig. 14.21b). Their disc-like shape and arrangements suggest that they could be formed by a continuous mode of precipitation.

The secondary αMg grains are generally spheroidal with a size below 5 μm. (Fig. 14.22a,b). Their substructures resembled mainly areas with various densities of dislocations. The grains are surrounded by lamellae-type morphologies of the

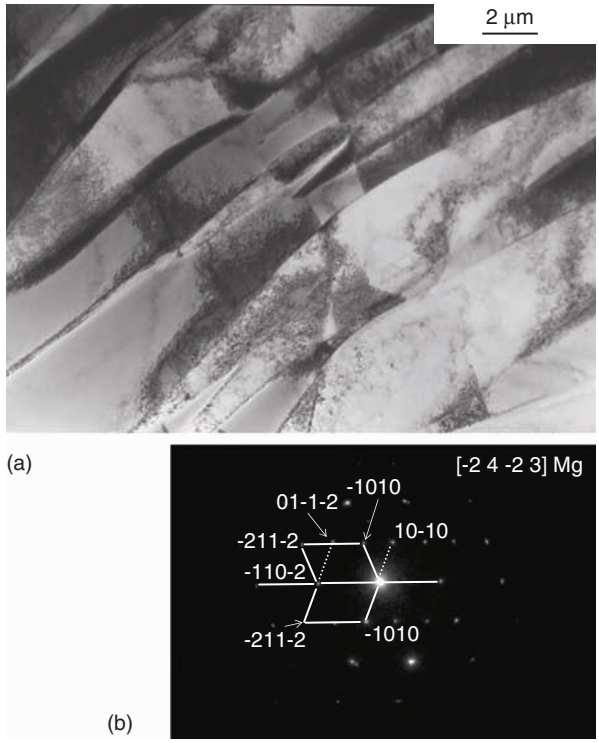

Fig. 14.19 The TEM image **a** and corresponding SAD pattern **b** of the primary solid particle with the lath-shaped sub-structure exhibiting a twin orientation relationship [37]

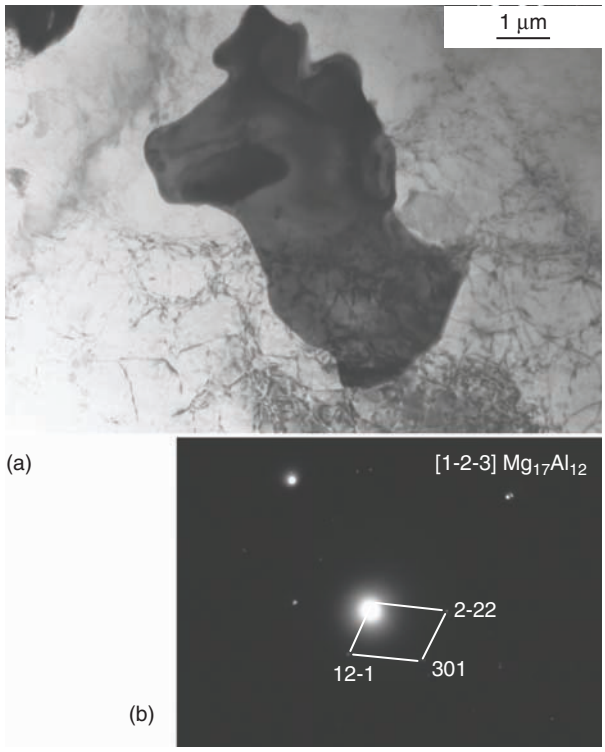

Fig. 14.20 The TEM images of $Mg_{17}Al_{12}$ trace compounds: **a** massive particle with irregular shape located near the grain boundary; **b** SAD pattern identifying the $Mg_{17}Al_{12}$ phase [37]

Al_4Sr phase. In some grains, small spheroidal precipitates with a dark contrast are present. An EDAX analysis within TEM revealed contents of Mn and Al with some traces of Sr (Fig. 14.22c). Since the particles are very small, the Mg signal was picked up from the matrix. It appears that they represent a Mn–Al compound of metallurgical origin, known from other Al alloys. The location in the αMg center suggests that the particles act as a nucleation substrate during a solidification of the liquid fraction.

14.7 Summary

The application opportunities in automotive engines and power-train components drive the development of magnesium alloys with increased creep resistance. Although a search for the optimum alloy is still in progress, there are already alloy grades suitable for applications at certain temperature and stress ranges. A use of rare and alkali earth elements can be further extended by precipitates introduced

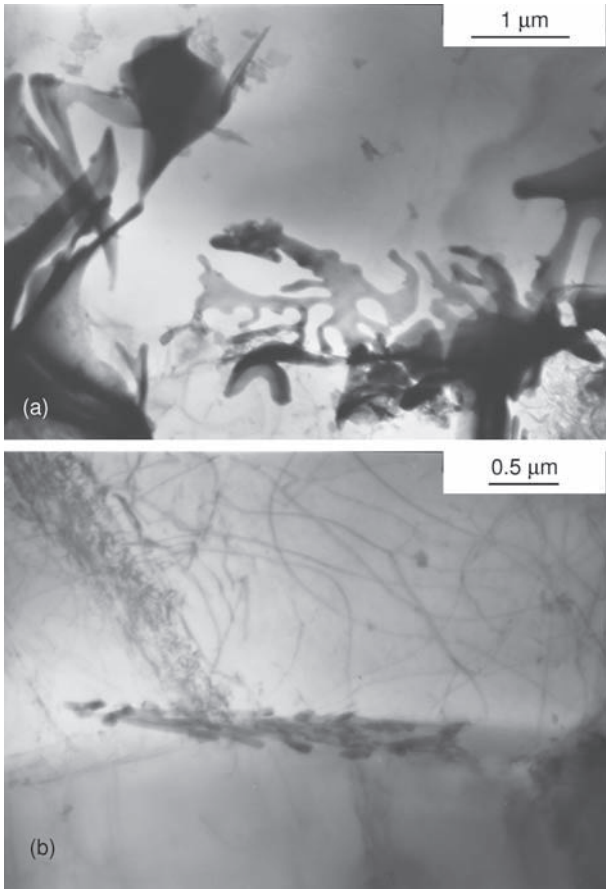

Fig. 14.21 The TEM morphology of Sr containing phases in semisolid molded structure; **a** Mg–Al–Sr phase with dendritic shapes; **b** continuous type precipitates at a twin boundary [37]

externally. The preliminary trials suggest that semisolid injection molding may represent an effective method of manufacturing automotive components from creep-resistant alloys, considered more difficult to process. The experiments show that semisolid processing using the injection molding technique, conducted at temperatures of the solidus–liquidus range, being significantly lower than that used during casting of overheated melts, allowed the manufacturing of high integrity parts from the Mg–5Al–2Sr grade. It is suspected that an improvement in the processibility of the semisolid alloy is caused by the fact that the liquid fraction contained increased Al content, known for improving castability. At the same time, however, semisolid processing creates microstructures essentially different from those after conventional casting of superheated melts. Partial melting during semisolid injection molding causes the selective partition of alloying elements

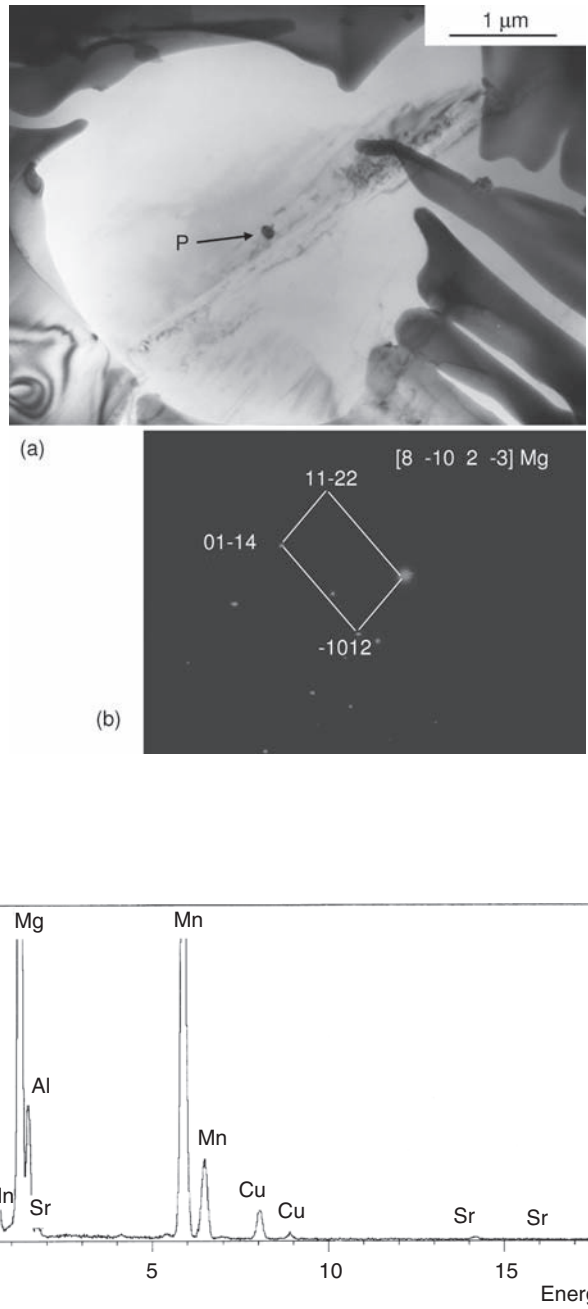

Fig. 14.22 The TEM image of a secondary αMg grain surrounded by plate shaped compound containing Sr **a** and corresponding SAD pattern **b**. The TEM/EDAX analysis from the dark contrast particle, marked as P in Fig **a** is shown in **c**. The Cu signal originates from the sample holder [37]

between solid and liquid. Thus a liquid portion, which is enriched in Al and Sr, after quick solidification, leads to the formation of increased volumes of the Al_4Sr phase. Moreover, the alloy's interfaces include not only grain boundaries in solidified liquid but also the interface between primary solid and former liquid and the primary solid itself with its own substructure.

References

1. Czerwinski F (2003) Assessing capabilities of thixomolding system in semisolid processing of magnesium alloys. International Journal of Cast Metals Research 16(4):389–396
2. Agnion E et al (2003) Newly developed magnesium alloys for powertrain applications. Journal of Metals 54(11):30
3. Anrade END (1914) Proceedings of Royal Society A 90:329–342
4. Garofalo F (1960) Properties of Crystalline Solids. ASTM Special Technical Publication vol. 283. p 82
5. Dieter, GE (1976) Mechanical Metallurgy. McGraw-Hill, New York
6. Langdon TG (2002) Creep at low stresses: An evaluation of diffusion creep and Harper–Dorn creep as viable creep mechanism. Metallurgical and Materials Transactions A 33(2):249–259
7. Wadsworth J, Ruano OA, Sherby O (2002) Denuded zones, diffusional creep, and grain boundary sliding. Metallurgical and Materials Transactions A 33(2):219–229
8. Nabarro FRN (2002) Creep at very low rates. Metallurgical and Materials Transactions A 33(2):213–220
9. Mordike BL, Lukac P (1997) In Proceedings of the 3rd International Magnesium Conference, The Institute of Materials, London, p 419
10. Crossland IG, Jones RB (1972) Met. Sci. J. 6:162
11. Frost HJ, Ashby MF (1982) Deformation mechanisms maps. Pergamon, Oxford
12. Tegar, WJM (1961) Acta Metallurgica 9:614
13. Agnew SR et al (2000) Tensile and compressive creep behavior of die cast magnesium alloy AM60B. In HI Kaplan et al (eds) Magnesium technology 2000, TMS, Warrendale, PA, USA, pp 285–289
14. Svoboda M et al (2002) The role of matrix microstructure in the creep behaviour of discontinuous fiber-reinforced AZ91 magnesium alloy. Materials Science and Engineering A 324:151–156
15. Sklenicka V et al (2000) Key Engineering Materials 593:171–174
16. Mordike BL (2002) Creep-resistant magnesium alloys. Materials Science and Engineering A 324:103–112
17. King JF (2000) In KU Kainer (ed) Magnesium Alloys and their Application. Wiley, VCH, New York
18. Luo AA (2004) Recent magnesium alloy development for elevated temperature applications. International Materials Review 49(1):13–30
19. Anyanwu IA et al (2004) Effect of substituting cerium-rich mischmetal with lantanum on high temperature properties of die-cast Mg-Zn-Al-Ca-RE alloys. Materials Science and Engineering A 380(1–2):93–99
20. Suzuki A et al (2005) Solidification paths and eutectic intermetallic phases in Mg-Al-Ca ternary systems. Acta Materialia 53:2823–2834
21. Hollrigl-rosta F et al (1980) Light Metal Age, March 1980:22–29
22. Tang B et al (2005) Effect of Ca/Sr composite addition into AZ91D alloy on hot-crack mechanism. Scripta Materialia 53:1077–1082
23. Hirai K, Somekawa H, Tagikawa Y, and K, H (2005) Effects of Ca and Sr addition on mechanical properties of a cast AZ91 magnesium alloy at room and elevated temperatures, Materials Science and Engineering A 403:276–280

24. Sohn KY, JW, J, and Allison JE (2000) The effect of calcium on creep and bolt retention behaviour of die cast AM50 alloy, in Magnesium Technology 2000, H Kaplan, J Hryn, and | B Clow H Kaplan, J Hryn, and B Clow, TMS, Warrendale, PA, USA, pp 271–279
25. Suzuki A, Saddock ND, Jones JW, and Pollock TM (2005) Phase transformation and creep of Mg-Al-Ca based die-cast alloy, in Magnesium Technology 2005, NR Neelameggham, HI Kaplan, and BR Powell NR Neelameggham, HI Kaplan, and BR Powell, TMS, Warrendale, PA, USA, pp 111–116
26. Pekguleryuz M, Labelle P, Argo D, and Baril E (2003) Magnesium diecasting alloy AJ62X with superiour creep resistance, ductility and diecastability, in Magnesium Technology 2003, H Kaplan H Kaplan, TMS, Warrendale, PA, USA, 201
27. Regev M, Botstein O, Bamberger M, and Rosen A (2001) Continuous versus interrupted creep in AZ91D magnesium alloy, Materials Science and Engineering A 302(1):51–55
28. Dargusch M, Hisa M, Caceres CH, and Dunlop GL, (1997) in Proceedings 3-rd International Magnesium Conference, The Institute of Materials, London, UK, 153
29. Vogel M, Kraft O, and Arzt E, (2003) Creep behaviour of magnesium die cast alloy ZA85, Scripta Materialia 48(8):985–990
30. Chartrand P and Pelton AD (1994) Journal of Phase Equilibria 15:591
31. Alcock CB and Itkin VP (1989) Bulletin of Alloy Phase Diagrams 10:624
32. Nayeb-Hashemi AA and Clark JB (1986) Bulletin of Alloy Phase Diagrams 10:624
33. Nowotny H and Wesenberg H (1939) Zeitung von Metallkunde 31:363
34. Polmear JS (1994) Materials Science and Technology 10:1
35. Czerwinski F (2003) Size evolution of the unmelted phase during injection molding of semi-solid magnesium alloys, Scripta Materialia 48(4):327–331
36. Chen TJ, Hao Y, Sun J, and Li YD (2003) Science and Technology of Advanced Materials 4:495
37. Czerwinski F and Zielinska-Lipiec A (2005) The microstructure evolution during semisolid molding of a creep resistant Mg–5Al–2Sr alloy, Acta Materialia 53(12):3433–3444

Index

A
Abrasive wear, 210, 211
Advanced thixotropic metallurgy, 129
Alcan multi polar cell, 12
Alloy chemistry effect on morphology of chips manufacture, 297, 298
Alloy composition
  equilibrium solidification lever rule, 381, 382
  non-equilibrium solidification lever rule, 383–385
  solid fraction calculation, 381
Alloy formation, semisolid-state mixing
  alloy microstructure, 521–523
  chemical compositions, 517–520
  element proportions, 524
  feedstock behavior, 520, 521
  melting ranges, 525, 526
  metal matrix composites, formation, 520–527
  methods in, 514
  solid-state diffusion, 523
  structural transformation methods, 514–516
  tensile properties, 526–532
    mixing temperature on, 527–532
    rule of mixtures, 532
    strength and elongation, 526, 527
Alloying additions (Mg), and role
  in aluminum, 18, 20, 21
  manganese, 20–22
  silicon, zirconium, and beryllium, 22, 23
  zinc, 20, 21
Alloying systems (AS), creep resistance of, 551
Alloy matrix, decohesion characteristics, 457–460
Alloy microstructures, 521–523
Alloy protection
  environmental impact, 345, 346
  fluorinated ketones (Fks), 343, 344
  hydro-fluorocarbons (HFC), 344
  inert gases, 344, 345
  magshield, 342, 343
  protective atmospheres for heat treatment, 345
  solid or gaseous CO_2, 344
  sulphur dioxide (SO_2), 342
  sulphur hexafluoride (SF_6), 340–342
Alloy steels
  martensite, structure of, 183, 184
  temperature and exposure time effects, 182, 184
Aluminum alloys, 474, 475
  low creep resistance of, 551
  T4 treatment of, 554
AM50 alloy
  gravity filling permanent mold casting, 33
  Searle type viscometer measurements for, 104
  tensile ductility and porosity, relationship between, 47–49
AM60B alloy
  chemical composition, 495
  tensile properties of, 527–530
Amorphous alloys (metallic glasses)
  compressive fracture strength and specific strength of, 38
  embrittlement and yield stress, 39
  thermal stability, 40
Annealing, 62
Archimedes method, 472
As-cast ingot
  compression deformation of, 357
  melting, 392–394
  Mg-9Al-1Zn morphologies, 394
  for semisolid processing, 555

ASTM E276-68 sieve test, 292
Automotive industry and magnesium application, 73–75
AZ91 alloy, 348, 349
AZ91D alloy, 33, 34
  chemical composition, 495
  compression and backward extrusion measurements of, 104
  effect of rest time on viscosity of, 106
  flow pattern of fully molten, 251, 252
  rheological behavior of, 106, 107
  tensile properties, 527–530
AZ91D chips morphologies, 291
AZXY alloy
  formation, 518, 519
  tensile properties, 527

B

Back extrusion viscometer
  apparent viscosity, 103
  experimental setup, 102
  extrusion ratio and viscosity, 101
Barrel and screw maintenance stations, 170, 171
Barrel temperature profile
  magnesium flow path
    accumulation zone, 219, 220
    melting and conditioning region, 219
    preheat zones, 218, 219
Basal slip, 41
Basal systems, crystallographic slip in, 41
Beryllium (Be), metal, 330–333
Bingham fluids, 84, 85
Boltzmann's constant, 545
Brasmag process, 10
Brittle cracking, cryogenic conditions, 459–461
Burger's vector, 545

C

Cable (tubular) heater, 158, 161
Carbon inoculation, 25
Carbothermic reduction, 14–16
Casting, magnesium alloy
  chemistry of, 282
  cold chamber die casting, 55, 56
  experimental, 58
  hot chamber die casting
    heat loss minimization, 53
    multi-slide die casting, 54, 55
  integrity testing techniques, 277–280
    porosity measurement by Archimedes method, 280, 281
    porosity measurement by X-ray tomography, 280
  investment casting, 57
  permanent mold and sand casting, 57
  squeeze casting
    alloy solidification, 56
    microstructure and applied high pressure, 56, 57
Cast structures, segregation in
  fragmentation mechanisms, 428
  macrosegregation, 427
  microsegregation, 426, 427
Cavitation wear, 211
Chemical grain refinement, 110
Chips C2, size distribution and aspect ratio of, 295. *See also* Particulates manufacture
Clamp (sub-system)
  hydro-mechanical design, 151
  mold, 149
Cleaning (surface treatment), 71
Closed-packed hexagonal lattices, twinning in, 42
Clutch-clamp housing, 471, 473, 474
Coalescence ripening, 434–453
Co based superalloys
  hardness and aging, 188
  for Mg processing, 186
Cold chamber die casting, 55, 56
Cold-deformed ingot recrystallization, 367
Cold-deformed metal phenomena, 365, 366
Combined DTA and heat-transfer modeling, 380, 381
Compression viscometer, 99
Contiguity, semisolid state, 447
Continuous rheo-conversion process, 111, 112
Controlled slow cooling, 113
Conventional alloys, semisolid-state mixing in, 540
Cooling curves method, Mg–9Al–1Zn alloy, 378, 379
Corrosion fatigue, 194
Corrosion prevention techniques, 68–73
Corrosion resistance
  magnesium alloy, 65, 66
    alloy chemistry effects on, 67, 68
    alloy microstructure, 68
Couette method (viscosity measurement), 97
Creep
  definition of, 194
  deformation curve, 544–546
  failure, 196
  resistance alloys
    Al_2O_3 influence on, 550

commercial alloys control, 550
alloying systems, 551–553
alloy processing role, 553, 554
die casting, 543
diffusion-controlled, 544
in magnesium
factors affecting, 548–550
pure magnesium, 548
mechanisms, 546, 547
pre-aging, 554
stages in, 544–546
CRP. *See* Continuous rheo-conversion process
Crystallographic slip, 40, 41
Cushion size, 220
Cyclic cooling, 192
Cylindrical viscometer
based on Couette method, 98
shear rate generated by, 97

D
Damping capacity
sand cast alloys, 50
vibration energy absorption, 49
Decohesion characteristics, alloy, 457
Dendrite arm spacing (DAS), 426
Dendrites formation, factors affecting, 426
Die casting alloys
fluidity and flow length, 33, 34
Mg12Al1Zn5Sn and Mg12Al3Zn5Sn alloys, 34
thin wall applications, 33
Die casting cycle
packing, 221
phases of, 220, 221
Differential scanning calorimetry (DSC) method, 378
Differential thermal analysis (DTA) method, 377, 380, 381
Diffusional creep, 546, 547
Direct semisolid forming, 130
Direct structure theories
rate of structure breakdown, 89
viscosity, 90
Drop forge viscometer
designed on, 99
shear rates and viscosity, 100, 101

E
Electric resistance heaters
cable (tubular) heater, 158, 161
mica band heaters, 158
Electrolytic/ion plate coating, 68–70
Electrolytic isolation, magnesium, 10–12
Electrolytic microplasma anodizing, 70
Electromagnetic interference (EMI) shielding, metal, 51
Electroplastic deformation, of grain contacts, 470
Erosive wear, 211
Evaporation characteristics, magnesium, 332–334
External characteristics, injection molding applications, 308–310
Extruded pellets
annealing phenomena in
general microstructure development, 370
grain growth, 373, 374
intermetallic phases changes of, 371–373
microstructure evolution during, 361
thermal instability of, 362
Extrusion
AZ31 alloy, 61
billet breaking, cast structure of, 469
direct and indirect, 60, 61
plastic deformation process, 469

F
Feedstock
conveying
compaction stage, 224, 225
initial forwarding, 223, 224
solid bed conveying, 225
loading devices, 166–168
mechanical effect on, 409
melting
behavior of, 355
dissipative and conduction melting, 226
microstructure evolution during, 374
extruded pellets, 387–392
liquid penetration along grain boundaries, 375, 376
mechanically comminuted chips, 385–389
non-equilibrium melting, 375
solid to liquid ratio, 376–385
thermal conductivity, 225
oxidation
behavior of, 315
growth morphologies, 320–324
kinetics, 315–318
layers internal structure, 324, 325
mechanism, 334–338
phase composition, 326–329
surfaces, 319, 320

Feedstock (*cont.*)
selection, 285–313
thermal instability, factors affecting, 355–364
transformation of, 408
Feret's diameter, 482
particles size characterization, 443
FLOW-3D software applications
magnesium alloy filling pattern evaluation
cell phone housing, 92–94
laptop case cover, 92, 95
Flow length, expression for, 256
F1-MEZ and F2-AZ91 flakes, 292
Forging, magnesium alloy
grain structure, 59
open-die and close-die, 58, 59

G
Gate velocity, 258
Gating equation, for die casting
amount of heat available, 256
component of, 257
semisolid processing applications, 258
Globular structures generation techniques
chemical grain refinement, 110
continuous rheo-conversion process (CRP), 111, 112
controlled slow cooling, 113
crystallization front morphology and temperature gradient, 425
liquid phase sintering (LPS), 115
liquidus/sub-liquidus casting/pouring, 112
melt stirring/agitation
magnetohydrodynamic agitation (MHD), 108, 109
mechanical stirring, 107, 108
ultrasonic agitation, 109, 110
rapid slug cooling technology (RSCT), 112, 113
spray forming, 113, 114
stress induced melt activation (SIMA), 115
swirl enthalpy equilibration, 110, 111
Grain boundary sliding and strengthening
in creep process, 546, 547
deformation mechanism, 45, 46
flow stress, grain-size dependence of, 24
grain size control, 24, 25
Grain growth, 373, 374
Grain-refining techniques, 25, 26
Granule G1 of Mg-9Al-1Zn during melting evolution of microstructure, 398
Gravity cast alloys, 33
Growth restriction parameter (Q), 26

H
Harper–Dorn creep, 546, 547
Heat checking, 192, 269
Heat dissipation, magnesium alloys, 51, 52
Herschel-Bulkley fluids, 84, 85
High temperature effects, on materials
corrosion fatigue, 194
creep and stress rupture, 194–196
fatigue phenomenon, 188–192
oxidation, 196
Fe-Cr alloys, 198
Ni-based superalloys, 198, 199
property degradation
alloy steels, 182–184
Co based superalloys, 186–188
Ni based superalloys, 184–186
reduction, dolomite, 10
thermal fatigue, 192–194
High temperature fatigue, 188, 189
High temperature steels, temperature effect on tensile properties of, 183–185
Holding pressure, 222
Homologous temperature, 188
Hot chamber die casting
molten metal, 53
multislide dies, 54, 55
Hot runners, 172–174
exit plug and thermal sealing in, 251
processing benefits of, 251
slurry distribution to mold, 249
Hot sprue, 172
benefit of, 246–249
slurry transfer using, 246
thermal gating during molding, 246
Husky machines, 134
Hydrostatic extrusion, 60, 61

I
Ignition behavior, magnesium alloys, 338, 339
Immiscible alloys, semisolid-state mixing in, 540, 541
Inconel 718 alloy
creep crack growth, 196
high-temperature exposure, 186
tensile properties, 186
Indirect microstructural theories, 88, 89
Inductive heaters, 161, 162
Inert gas apparatus, 288
Injection molded alloys, microstructures of, 407, 415, 418
Injection molding, 469
alloy degradation from, 347–352
application characteristics, 308

mechanically fragmented chips, 309
rapidly solidified granules, 309, 310
defects
causes of, 269–276
and flow modeling, 277
gas porosity, 266, 268
shrinkage porosity, 265, 266
injection cycle, 215, 216
die casting cycle, 220, 221
holding pressure, 222
screw velocity and packing, 221
transition position, 221, 222
injection screw functions
alloy metering, 226, 227
feedstock conveying, 223–225
feedstock melting, 225, 226
output of, 227–229
shear function of, 229–232
Mg–5Al–2Sr alloy for
alloy chemistry and melting range, 554, 555
Sr effect on phase composition, 555–557
microstructure development, 407
slurry generation, 408
solidification conditions and secondary changes, 409
practice implications, 346, 347
product quality control
dimensional verification and surface quality, 277
internal integrity examination, 277–281
recovery, 223
thermal gating with hot sprue, 246
various stages of, 217
X-ray diffraction pattern of, 565
Injection molding machine
barrel and screw maintenance stations, 170, 171
clamping force, 152
clamp (sub-system)
hydro-mechanical design, 151
mold, 149
feedstock drying and preheating devices, 168, 169
feedstock loading devices, 166–168
heating systems for barrel assembly components
electric resistance heaters, 158–161
inductive heaters, 161, 162
process monitoring systems, 162–165
hydro-electric machine platform, 151
injection screw assembly
injection screw, 164, 165
non-return valves, 165, 166
injection units
injection loads, 155
single-stage and two-stage plunger, 154
machine barrel assembly
barrel and barrel head, 155, 157
injection nozzle, 157, 158
mist filtration devices, 169
processing route selection, factors affecting, 436
thick wall components, 436, 437
thin wall components, 437–439
protective gas supply to barrel, 169
robots, 169, 170
slurry distribution systems
cold sprue, 171, 172
hot runners, 172–174
slurry transfer using hot sprue, 246
Injection screw, 164, 165
alloy metering
Poiseuille flow, 226
feedstock conveying, 223–225
feedstock melting, 225, 226
output of
machine throughput, 227
volumetric metering rate, 226, 227
shear function of
polymer and metal molding, 229, 230
shear rate in screw channel, 231, 232
Injection units
flow path of magnesium alloy through, 216, 217
injection loads, 155
single-stage and two-stage plunger, 154
Internal defect
component scrapping, 269
X-ray detection of, 278, 279
Inverted-stream apparatus, 289
Investment casting, 57

J
JSW machines, 134

L
Lanthanum, for creep properties, 552
Laths separation, 560, 561
Liquid fraction, solidification microstructure of, 429
Liquid metal forging. *See* Squeeze casting
Liquid phase sintering (LPS), 115

Liquidus/sub-liquidus casting/pouring, 112
Lost wax process. *See* Investment casting
Low-temperature Pouring (LTP), 397
LSW theory, 433, 434

M
Machine barrel assembly
  barrel and barrel head, 155, 157
  injection nozzle, 157, 158
  semisolid-state transformations within
    under partial melting, 414–416
    thixotropic slurry formation, 412, 413
  solid-state transformations, feedstock, 409–412
Machine nozzle
  alloy flow path, 216, 218
  hot sprue, 172
Magnesia. *See* Magnesium oxide
Magnesium
  alloys solid fraction and temperature data, 385
  cold deformation of, 356, 357
  corrosion resistance of, 65
  etching chemicals for, 283
  evaporation, 348–350
  extrusion deformation features, 360, 361
  flow path for injection
    melting, conditioning and accumulation zone, 219, 220
    preheat zones and, 218
    thermal profiles along, 419, 555
  galvanic corrosion, 66, 67
  particulates, global manufacturing market of, 310–312
  production techniques, 9
    carbothermic reduction, 14, 15
    electrolytic isolation, 10–12
    Mintek Thermal Magnesium Process (MTMP), 12, 13
    recycling, 15–18
    thermal processes, 10
    using solid oxide membrane (SOM), 12–14
  properties of pure, 19, 20
  recrystallization phenomena, 366
Magnesium alloys, 18, 474, 475
  amorphous alloys (metallic glasses)
    compressive fracture strength and specific strength of, 38
    embrittlement and yield stress, 39
    thermal stability, 40
  application markets
    aerospace industry, 75
    automotive industry, 73–75
    general purpose market, 76
  casting alloys, 29–32
    die, 33–35
    gravity, 33
    wrought, 35–38
  in composites matrix, 533–535
  corrosion prevention
    cleaning and protective painting, 71, 72
    electrolytic/ion plate coating, 68–70
    electrolytic microplasma anodizing, 70
    surface passivation, 71
  corrosion resistance of, 66, 67
    alloy chemistry effects, 67, 68
    alloy microstructure, 68
  creep in, 547–549
  dark matrix of, 559
  deformation mechanisms
    basal slip, 41
    slip displacement, 40
    superplastic deformation, 44, 46
    texture effect on plastic deformation, 44, 45
    twinning, 42–44
  etching chemicals for, 283
  fluidity of, 256
  grains, 566
  heat treatment of, 61, 554
    annealing and stress relieving, 62
    solution treatment and aging, 62–65
  high temperature, 549, 550
  ignition behavior, 338, 339
  impurities, 23, 24
  low creep resistance of, 551
  mechanical properties
    alloy integrity effect on, 46–49
    damping capacity, 49
    electromagnetic interference (EMI)/radio interference frequency (RFI) shielding, 49, 51
    heat dissipation, 51, 52
  mixing
    distributive and dispersive mixing, 233
    mechanisms, 233, 234
    particle size effects, 236, 237
    re-solidification (re-melting), 238
    in screw channel, 234, 235
    segregation, 235
    wall slip effect, 236
  processing techniques
    casting, 53–58
    extrusion, 60, 61
    forging, 58, 59
    rolling, 59, 60

strengthening mechanisms for
grain boundary strengthening, 24–26
particle dispersion strengthening, 28
solid solution strengthening, 26–28
thermal diffusivity and thermal conductivity of, 52, 53
Magnesium industry
application markets
aerospace industry, 75
automotive industry, 73–75
general purpose market, 76
market development
raw metal consumption, 4–9
raw metal production, 1–4
Magnesium molding
advantages of, 130
automotive applications, 142–144
commercialization, 134, 135
consumer electronics applications, 135–137
manufacturing challenges, 138–142
market geography and structure, 142
general purpose equipment, 144
technological origin of, 130–134
Magnesium molding system. *See* Injection molding machine
Magnesium oxide
carbothermic reduction of, 14
direct magnesium production using SOM from, 12–14
Magnetherm process, 10
Magnetohydrodynamic agitation
molten metals, vibration of, 108
non-dendritic structures generation, 109
Magnola electrolysis system, 10–12
MagShield protection method, 342
Mechanically comminuted chips annealing phenomena
grain size-chip size correlation, 369, 370
recrystallization microstructure, 368, 369
Mechanically cut chips deformation, 357, 358
Mechanical stirring, 107, 108
Melting temperature (T_m), 332, 365, 375, 391
Melt superheating, 25
Metallic glasses, 38, 39, 534
Metallic slurries
rheological behavior of
apparent viscosity *vs.* solid fraction, 86
steady state apparent viscosity *vs.* shear rate, 87
viscosity measurements of
back extrusion viscometer, 101–103
compression viscometer, 99
Couette method, 97
drop forge viscometer, 99–101
rotational viscometers, 97, 98
wall slip effect in flow, 236
Metallographic image analysis of Mg–9Al–1Zn alloy, 378
Metal matrix composites (MMCs), formation
injection molding, 536–539
magnesium alloys in, 533–535
processes in, 536
reinforcements application of magnesium, 535
semisolid-state mixing in, 541
Mg-5Al-2Sr alloy
for high temperature applications, 554
ingredient proportions, 524
semisolid molding effect on, 563, 564
general microstructure, 565–568
phase composition, 564, 565
phase morphology, 569, 570
SEM micrographs of, 558
thermal analysis of, 556
X-ray diffraction pattern of, 557, 565
Mg-9Al-1Zn alloy
color etching technique, 500
cooling rate in, 479
crack propagation, 459
decohesion surfaces, 502, 503
ingredient proportions, 524
migrating boundaries, 483
spheroidal structure, distribution of shape factor, 444, 445
structural integrity, 496, 497
tensile strength, 457
thixotropic microstructures, 449
eutectic component within, 450
TEM microstructure of, 454–456
X-ray diffraction pattern of, 480, 500–502
1Mg–9Al–1Zn and Mg–6Al alloys
comparisions, 507, 508
microstructures, 521–523
mixing in alloy formation, 517–520
preheating range, 493, 494
tensile properties, 526–532
tensile strength, 504
yield stress *vs*. corresponding elongation, 505
MHD. *See* Magnetohydrodynamic agitation
Mica band heaters, 158
Mintek Thermal Magnesium Process, 12
Mist filtration devices, 169
Mixing
distributive and dispersive mixing, 233
mechanisms, 233, 234
particle size effects, 236, 237

Mixing (*cont.)*
re-solidification (re-melting), 238
for screw
shear strain, 235
striation thickness, 234
segregation, 235
wall slip effect, 236
Mold filling
characteristics
flow mode role, 476
high-solid slurries, flow behavior of, 471, 472
part integrity, 472–474
surface region, microstructure of, 475
structural transformations
phase composition, 480
solidification, general microstructure after, 477, 478
during SSEM, 476, 477
time, 256
Mold processing, 251
mold filling time
gate velocity, 258
gating equation for die casting, 256–258
metal injection pressure, 260
metals, flow modes of, 259, 260
process operating window, 260
mold spraying, 261
heat transfer during, 262–264
mold lubricants, 262
part cooling after ejection, 264
mold temperature, 260, 261
molten alloy fluidity
magnesium, 256
and solidification time, 255
surface tension, 252, 254
Mold spray equipment
needle-type and spool type poppet shutoff nozzles, 177
parameters affecting spray, 177–178
Mold temperature
cavity filling characteristics and solidification structures, 260
cycle time and, 261
Mold (tool)
heating-cooling systems, 175–177
mechanisms and features of, 174, 175
temperature control methods, 176, 177
temperature distribution, 176
Mold vacuum systems
static and dynamic valves, 179, 180
vacuum molding, 178
Molten magnesium alloys, corrosive behavior of
reactivity with iron and steel, 199–202
reactivity with nickel-containing alloys, 202–210
Monotonic reduction, in solid content, 481
M-S theory of alloy, 488, 489
MTMP. *See* Mintek Thermal Magnesium Process
Multi-slide die casting, 54, 55

N
Near-liquidus molding
application areas, 508, 509
globular structures growth, 487–492
microstructure, 494, 495
alloy structural integrity, 495–497
crystallographic orientation, 500
decohesion features, 502, 503
die cast microstructure characteristics, 499
matrix morphology, 497, 498
phase composition, 500–502
solid particles morphology, 498, 499
structure-property correlation, 505–508
tensile properties, 504, 505
New rheocasting, 126, 127
Newtonian/non-Newtonian fluids
apparent viscosity, 84
shear stress, 83, 84
Nickel based superalloys
chemistry of, 187
creep crack growth, 196
high-temperature exposure, 186
NLM. *See* Near-liquidus molding
Non-return valve
magnesium molding, role in, 241, 242
plastics injection and, 241
role in die casting, sleeve sealing, 238–241
Nozzle plug
formation of, 242, 243
induction heating, 245, 246
release and disintegration mechanism, 245
temperature and microstructure, 243, 244
as thermal shut off valve, 242
transformations associated with
alloy temperature and plug microstructure, 420
microstructure effect on flow behavior, 423–425
plug, decomposition and microstructure of, 421, 422
release behavior during preheating, 420, 421
NRC. *See* New rheocasting
Nucleus, solid-liquid interface, 490

O
Ostwald ripening
for coarsening in semisolid mixtures, 402
Gibbs–Thompson effect, 433
Oxidation
failure mechanisms, 196
resistance
at high temperatures, 198
nickel-based superalloys, 198, 199
of steels, 198
volumetric change, 198

P
Particle coarsening
shear and coalescence effects, 436
temperature gradients effect on, 435
Particle dispersion strengthening, 28
Particulates manufacture
by mechanical fragmentation
bulk density, 295
external defects, 295, 296
morphological features, 290–292
phase composition and microstructure, 296, 297
sieve analysis, 292–295
techniques
mechanical comminution, 285–288
rapid solidification, 288–290
Particulates, non-conventional morphologies of, 292
Pellets
microstructure of, 389
P1-AZ91D, 292, 299
Permanent mold casting, 57
Phase diagrams
Al–Fe equilibrium, 201
Mg–Al equilibrium, 20
Mg–Al–Zn equilibrium, 450, 493, 518, 520
Mg–Fe equilibrium, 200
Mg–Mn equilibrium, 22
Mg–Si equilibrium, 23
Mg–Zn equilibrium, 21
Ni–Al equilibrium, 206
Ni–Mg equilibrium, 205
Pidgeon process, 10, 11
Pilling–Bedworth ratio (PBR), 198
Pismatic sytems, crystallographic slip in, 41
Plastic deformation processes
extrusion, 60
rolling, 59
Post-molding heat treatment and mechanical properties modification, 466
PQ2 diagram. *See* Process window
Precipitation phenomena in magnesium alloy, 63, 64
Primary solid
characterization of, 481–484
and matrix, internal structure
entrapped liquid, 452, 453
molded structures features, 454–456
Strontium effect on, 567, 568
Primary solid phase evolution, 429
mechanisms controlling, 431–433
coalescence ripening, 434, 435
high solid fractions coarsening, 435
Ostwald ripening, 433, 434
temperature gradients effect on particle coarsening, 435, 436
microstructure, 430
particle size *vs*. solid volume fraction, 430, 431
Process window, 260
Protective painting, 71, 72
Pseudoplasticity. *See* Shear thinning
Pure magnesium, properties of, 19, 20
Pyramidal slip system, polycrystalline structures, 40, 41

R
Rapidly solidified granules heating phenomena, 394
as-solidified microstructure features of, 395, 396
granule melting, 396–398
heating in solid state, transformations during, 396
particulate feedstock, melting features of, 398, 399
Rapid slug cooling technology
globular dendrites production, 112
temperature effects, 113
Rapid solidification
casting of large droplets, 288–290
granulation using inert gas apparatus, 288, 289
granules characterization
bulk density, 301
chemical composition and, 303–304
dimensional features, 299–301
external defects, 301–303, 307, 308
internal microstructure, 305–307
morphological features, 297–299
phase composition, 304, 305
Reactive element effect, Beryllium (Be), 331
Recrystallization temperature (Tr), 365, 366

Recrystallized alloy
boundaries in, 411
equiaxed grains of, 410, 411
Recycled feedstock (R1-AZ91D), 292
Recycling, magnesium
coating removal methods, 17
flux-based batch wise and fluxless continuous method, 17
recycling circuit, 18
scrap classification, 15–17
Remnant liquid, solidification of, 429
Rheocasting, 124–126
Rolling
hot and cold, 59, 60
magnesium alloy sheet production, 60
RSCT. *See* Rapid slug cooling technology

S
SAD diffraction pattern
αMg matrix grain, 561
Sr containing precipitates, 563
Sand casting, 57
Scheil model, 381
Screw velocity reduction, 472
Searle viscometer, 97
Semisolid extrusion molding
application areas for, 484, 485
as-cast Mg–5Al–2Sr ingot, micrographs of, 558
EDAX energy spectra view, 559
features, 469, 470
semisolid molded microstructure, 567
structural transformations, 476, 477
temperature requirements for, 471
Semisolid magnesium alloys, rheological measurements
continuous cooling measurements
apparent viscosity, 104
shear rate, 106
isothermal holding measurements
apparent viscosity, 103
extrusion and Searle type viscometer, 104
Semisolid metallurgy (SSM). *See* Semisolid metal processing
Semisolid metal processing
advanced thixotropic metallurgy, 129
benefits of, 115, 116
and component's integrity and microstructure, 118, 119
direct semisolid forming, 130
for magnesium alloys
alloy composition, 123
processing techniques, 123
microstructure evolutions, factors affecting, 407
mechanical effect, 409
slurry generation, 408, 409
thermal effect, 408
new rheocasting process (NRC), 126, 127
reduced temperature effects on hardware performance, 116–118
rheocasting, thixocasting, and thixoforging, 124–126
semisolid rheocasting (SSR), 127, 128
semisolid slurry, 83
shear rate, 87
solid fraction and, 269
sub-liquidus casting (SLC), 128, 129
suitability criteria of alloys for, 119
morphological and rheological characteristics of slurry, 122
solidification range, 120
temperature sensitivity of solid fraction, 121
thermodynamic characteristics, 121, 122
Semisolid processing, contiguity phenomenon, 446
Semisolid rheocasting
cycle time, 128
graphite agitator and superheated alloy, 127
Semisolid slurries
flow modeling of, 92
heat and shearing force effects on, 428
mixing, 232
morphology of, 122
partial cooling of, 415
rheological behavior of
flow characteristics of, 91–96
Newtonian and non-Newtonian fluids, 83–85
thixotropy and pseudoplasticity, 85, 86
Semisolid-state mixing in alloy formation, 513–516
advantages of, 540, 541
alloy microstructure, 521–523
chemical compositions, 517–520
element proportions, 524
feedstock behavior, 520, 521
melting ranges, 525, 526
metal matrix composites, formation, 520–527
solid-state diffusion, 523
tensile properties
mixing temperature on, 527–532
rule of mixtures, 532
strength and elongation, 526, 527

Semisolid-state transformations, feedstock
under complete melting and partial re-solidification
overheating level above liquidus, 417, 418
residency in screw, 418
sub-liquidus cooling range in barrel, 416, 417
under partial melting, 414–416
shear during mold filling, 418, 419
thixotropic slurry formation, 412, 413
Shear thinning, 86
Shot size, 220
SiC particles in MMCs formation, 537, 538
SIMA. *See* Stress induced melt activation
Simple viscosity theories
rate of change of viscosity, 90
thixotropic breakdown, 91
SLC. *See* Sub-liquidus casting
Slip systems for hcp magnesium lattice, 40, 41
Slurries, deformation behavior of, 470, 471
Slurry distribution systems
cold sprue, 171, 172
hot runners, 172–174
Solid and semisolid state
microstructure correlation between, 399
internal changes of globular solid, 403
size-evolution of solid phase within slurry, 401, 402
solid-state grain and semisolid-state solid globule, 400, 401
Solidification range, 120
Solidification rate, 477–479
Solidification time, 255
Solid oxide membrane
direct magnesium production from magnesium oxide using, 12, 13
experimental electrolytic SOM cell, 12–14
Solid solution strengthening
alloying elements on magnesium, 26, 27
for AZ91D alloy, 28
hardening and softening, 26, 27
Solid-state mechanical comminution
fragmentation and chipping, 286, 287
solid-state extrusion, 287, 288
Solid-state transformations
feedstock, 409, 410
during heating, 364–374
Solution treatment and aging
precipitates, crystallography of, 64
precipitation phenomena in magnesium alloy
alloy strengthening, 63
continuous and discontinuous, 64
temperature-time parameters of, 62, 63
SOM. *See* Solid oxide membrane
Spray forming
liquid metal, atomization of, 113
rapid solidification, 114
Squeeze casting
direct and indirect, 56
high pressure effects, 57
SSEM. *See* Semisolid extrusion molding
SSP. *See* Semisolid metal processing
SSR. *See* Semisolid rheocasting
Steady state creep rate, 545
Steels
erosive wear and impact wear of, 213
oxidation resistance of, 198
Stellites
fatigue crack, 192
fatigue failure, 195
hot hardness of, 191
wear resistance, 211, 212
wear resistance and ductility, 186
Strain-hardening rate, magnesium alloys, 27
Stress induced melt activation, 115
Stress relieving, 62
Stress-strain curves, 470
Strontium effect
liquid fraction, 568
primary solid, 567, 568
Sub-liquidus casting
grain refinement, 128
shot piston and sleeve wall temperatures, 129
Superplastic deformation, magnesium alloys, 45, 46
Surface defects
analysis, 277
component scrapping, 269
sub, 275
thin wall components molded using AZ91D alloy, 273
Surface oxidation, 196
Surface passivation, 71
Surface treatments, corrosion prevention, 70–73
Swirl enthalpy equilibration, 110, 111

T

TEM images
island of platelets, 561
αMg matrix grain, 561
of secondary αMg grain, 572
Sr containing precipitates, 563

Temperature sensitivity of solid fraction, 120, 121
Tempering effect, 182
Tensile properties, as-cast alloys, 456, 457
  alloy matrix, role of, 462
  solid particle content, role of, 463
  solid particle substructure, role of, 462, 463
Texture effect on plastic deformation, 44, 45
Thermal fatigue
  cyclic stresses, 192
  of H13 steel, 192, 193
  service parameters, 194
Thermal shock, 192
Thermal stress, 196
Thin-wall molding, 508
Thixocasting, 125, 126
  methods, 119
Thixoforging, 125, 126
Thixotropic
  alloys, 470
  materials, 85
  microstructures of magnesium alloys, 447
    phase composition, 449–451
    primary solid particles, characteristics of, 448
    solidified liquid, 448, 449
    structural integrity, 451, 452
    structure–property relationship
    semisolid techniques, 465, 466
    structure–property relationship, 463, 464
Thixotropic slurry
  melting and formation of, 412, 413
  partial melting, 414
  residency time of, 418
Thixotropic structures, after solidification
  interfaces, 446, 447
  primary solid particle
    entrapped liquid volume, 446
    size and shape of, 443–445
    volume fraction of, 442
Thixotropy, 81, 82
  floc structural arrangement, changes in, 85
  structure models
    direct structure theories, 89, 90
    indirect microstructural theories, 88, 89
    simple viscosity theories, 90, 91
Thorium, 551
Torque dynamometer, 97
Transient-state viscosity, 87
T6 treatment, creep rate reduction, 554
T4 treatment, in Mg-Al alloys, 554
Twinning deformation
  for Mg-Zn alloy, 42–44
  shear and shape change, 42

U
Ultrasonic agitation, 109, 110

V
Vacuum molding
  entrapped gases in mold cavity, 178
  vacuum system, 179, 180
Volumetric metering rate, 227

W
Wall slip effect, 236
Wear mechanisms, classification of, 210, 211
Wrought alloys, 35–38

Z
Zn based alloys, tear-drop-like shape particulates, 299